Ophthalmological Disorder Detection Using Medical Image Processing

Thesis Submitted by

Niladri Halder

Doctor of Philosophy (Engineering)

Department of Instrumentation & Electronics Engineering

Faculty Council of Engineering & Technology

Jadavpur University

Kolkata, India

Year 2025

Dedicated to……

My Parents, Parents-in-law, Wife, and Khushi

JADAVPUR UNIVERSITY

KOLKATA-700032, INDIA

INDEX NO.: 50/22/E

Title of the Thesis:

OPHTHALMOLOGICAL DISORDER DETECTION USING MEDICAL IMAGE PROCESSING

Name, Designation & Institution of the Supervisors:

Prof. Subhankar Bandyopadhyay,

Professor,

Department of Instrumentation and Electronics Engineering,

Jadavpur University SL Campus, Kolkata,

West Bengal, India, Pin. 700 098.

&

Dr. Dibyendu Roy,

Assistant Professor,

University Institute of Technology,

The University of Burdwan

Burdwan, West Bengal, India, Pin 713104.

List of Publications:

Journals Publication:

1. **Niladri Halder**, Dibyendu Roy, Subhankar Bandyopadhyay, et al. “Detection of Retinal AVR and CDR using Active Contours with Blind Deconvolution and CLAHE Fusion (Active-BDCLF)”, Scope, Feb 2025.
2. **Niladri Halder**, Dibyendu Roy, Subhankar Bandyopadhyay, et al. “PSO-Optimized CLAHE for Image Enhancement and Active Contour-Based Segmentation of Retinal Vessels”, Quaderns Journal, volume 13 issue 2, 2025.
3. **Niladri Halder**, Dibyendu Roy, Subhankar Bandyopadhyay, et al. “Morphological Filter-based Detection of Retinal AVR and CDR through Blind Deconvolution and CLAHE Fusion (BDCLF)”, Moenia, volume 11 issue 11, 2024.
4. **Niladri Halder**, Dibyendu Roy, Subhankar Bandyopadhyay, et al. “PSO-HRVSO: Segmentation of Retinal Vessels through Homomorphic Filtering Enhanced by PSO Optimization”, Signal & Image Processing: An International Journal (SIPIJ) Vol.15, No.1/2, April 2024.

Conferences Publication:

1. **Niladri Halder**, Dibyendu Roy, Subhankar Bandyopadhyay, et al. “Automatic Detection and Segmentation of Optic Disc (ADSO) of Retinal Fundus Images Based on Mathematical Morphology”, NCETSTEA, IEEE, 2020.
2. **Niladri Halder**, Dibyendu Roy, Subhankar Bandyopadhyay, et al. “Automatic Segmentation of Blood Vessels (ASBV) of Retinal Fundus Images using CLAHE and Multilevel Thresholding based on Harmony Search”, Contemporary Issues in Computing, Jan 2020.

"Statement of Originality"

I, **Niladri Halder**, registered on **25.04.2022** do hereby declare that this thesis entitled **"Ophthalmological Disorder Detection using Medical Image Processing"** contains literature survey and original research work done by the undersigned candidate as part of Doctoral studies.

All information in this thesis have been obtained and presented in accordance with existing academic rules and ethical conduct. I declare that, as required by these rules and conduct, I have fully cited and referred all materials and results that are not original to this work.

I also eclare that have checked this thesis as per the "Policy on Anti Plagiarism, Jadavpur University, 2019", and the level of similarity as checked by iThenticate software is **1%.**

Niladri Halder

Signature of Candidate:

Date: 07/11/2025

Certified by Supervisor(s):

(Signature with date, seal)

1. Sulekha Banerjee 07/11/2025

Professor
Dept. of Instrumentation & Electronics Engg
Jadavpur University
Salt Lake, 2nd Campus
Kolkata-700098

2. Dibyendu Roy 07/11/25

Assistant Professor
Department of ECE,
University Institute of Technology
The University of Burdwan

CERTIFICATE FROM THE SUPERVISOR/S

This is to certify that the thesis entitled **"Ophthalmological Disorder Detection using Medical Image Processing"** submitted by **Shri Niladri Halder**, who got his name registered on **25.04.2022** for the award of Ph. D. (Engineering) degree of Jadavpur University is absolutely based upon his own work under the supervision of **Prof. Subhankar Bandyopadhyay**, department of Instrumentation and Electronics Engineering, Jadavpur University, Kolkata 700 098 and **Dr. Dibyendu Roy**, Assistant Professor, department of Electronics and Communication Engineering, University Institute of Technology, The University of Burdwan, Burdwan – 713 104 and that neither his thesis nor any part of the thesis has been submitted for any degree/diploma or any other academic award anywhere before.

1. Subhankar Banerjee
Prof. Subhankar Bandyopadhyay
07/11/2025

Professor,
Department of Instrumentation and Electronics Engineering, Jadavpur University, SL Campus
Kolkata - 700 098

Professor
Dept. of Instrumentation & Electronics Engg
Jadavpur University
Saltlake, 2nd Campus
Kolkata-700098

2. Dibyendu Roy
Dr. Dibyendu Roy 07/11/25

Assistant Professor,
Department of Electronics and Communication Engineering, The University of Burdwan
West Bengal - 713104

Assistant Professor
Department of ECE,
University Institute of Technology
The University of Burdwan

Acknowledgments

Completing this PhD research has been an extraordinary journey, and I am profoundly grateful to everyone who has supported me throughout this process.

First and foremost, I would express my deepest respect and heartfelt gratitude to my supervisor, **Prof. Subhankar Bandyopadhyay**, department of Instrumentation and Electronics Engineering, Jadavpur University, Kolkata - 700 098, for providing me the opportunity to carry out my research work under his unwavering guidance, invaluable insights, and continuous encouragement throughout my research journey. His expertise, patience, and mentorship have been instrumental in shaping both this thesis and my academic growth.

I am also profoundly grateful to my co-supervisor, **Dr. Dibyendu Roy**, Assistant Professor, department of Electronics and Communication Engineering, University Institute of Technology, The University of Burdwan, Burdwan - 713 104 for his generous support, constructive feedback, and constant motivation. His keen observations and thoughtful advice have significantly contributed to refining my research and deepening my understanding of the subject.

I sincerely thank my teachers and mentors, especially **Dr. Sankar Narayan Patra**, Associate Professor, department of Instrumentation and Electronics Engineering, Jadavpur University, Kolkata 700106, and **Dr. Partha Pratim Sarkar**, Assistant Professor, department of Electronics and Communication Engineering, University Institute of Technology, The University of Burdwan, for their invaluable guidance and support. Their collaboration, knowledge-sharing, and camaraderie have made this journey intellectually enriching and truly enjoyable. I deeply appreciate the stimulating discussions, shared challenges, and moments of joy we have experienced together.

I would also like to acknowledge the faculty and staff of IEE, Jadavpur University, and UIT, Burdwan University for their assistance and for providing a stimulating research environment. I sincerely appreciate my colleagues and friends for their companionship and for making this journey both rewarding and intellectually stimulating.

I deeply appreciate my family for their unconditional love, patience, and unwavering support, which have been my greatest source of strength. Their steadfast belief in me has been a constant motivation throughout this journey.

Finally, I extend my gratitude to all those—named and unnamed—who have contributed to this research in any way. This thesis would not have been possible without your support.

Niladri Halder
07/11/2025

Niladri Halder
Dept. of Instrumentation & Electronics Engineering
Jadavpur University, SL Campus, Kolkata – 700 098

List of Abbreviations

IDF	International Diabetes Federation
DR	Diabetic Retinopathy
NPDR	Nonproliferative Diabetic Retinopathy
STDR	Sight-Threatening Diabetic Retinopathy
PDR	Proliferative Diabetic Retinopathy
HR	Hypertensive Retinopathy
ROP	Retinopathy of Prematurity
AMD	Age-related Macular Degeneration
DME	Diabetic Macular Edema
CSR	Central Serous Retinopathy
RPE	Retinal Pigment Epithelium
OCT	optical coherence tomography
FA	fluorescein angiography
PDT	Photodynamic Therapy
VEGF	Vascular Endothelial Growth Factor
RVO	Retinal Vein Occlusion
CRVO	Central Retinal Vein Occlusion
BRVO	Branch Retinal Vein Occlusion
RAO	Retinal Artery Occlusion
CRAO	Central Retinal Artery Occlusion
BRAO	Branch Retinal Artery Occlusion
RP	Retinitis Pigmentosa

DRIVE	Digital Retinal Images for Vessel Extraction
STARE	Structured Analysis of the Retina
ARSS	Automated Retinal Screening System
RIQA	Retinal Image Quality Assessment
DRIMDB	Diabetic Retinopathy Images Database
OD	Optic Disk
OC	Optic Cup
CDR	Cup-Disk Ratio
AVR	Artery-Vein Ratio
ONH	Optic Nerve Head
MESSIDOR	Methods to Evaluate Segmentation and Indexing Techniques
DIARETDB	Diabetic Retinopathy Database
HRF	High-Resolution Fundus

List of Figures

List of Tables

Abstract

Ophthalmological disorders, such as diabetic retinopathy, glaucoma, age-related macular degeneration, and cataracts, are among the leading causes of vision impairment and blindness worldwide. Early detection and accurate diagnosis are crucial for effective treatment and management of these conditions. Traditional diagnostic methods rely heavily on manual examination by ophthalmologists, which can be time-consuming, subjective, and prone to variability. This thesis explores the potential of medical image processing techniques to develop an automated, efficient, and accurate system for detecting ophthalmological disorders.

The research focuses on preprocessing, feature extraction, and classification of retinal and ocular images using advanced image processing and machine learning algorithms. Various enhancement techniques, such as contrast adjustment, noise reduction, and edge detection, are employed to improve image quality. Feature extraction methods, including texture analysis, morphological operations, and deep learning-based feature representation, are used to identify key biomarkers associated with different eye diseases. The extracted features are then analyzed using machine learning and deep learning models, such as convolutional neural networks (CNNs), support vector machines (SVMs), and random forests, to classify ophthalmological disorders with high accuracy.

The proposed framework has been validated using publicly available and clinical datasets, achieving promising results in terms of precision, recall, sensitivity, specificity, and overall classification accuracy. Comparative analysis with existing state-of-the-art methods demonstrates the effectiveness of the approach in improving diagnostic accuracy and reducing false-positive and false-negative rates.

This study contributes to the field of computer-aided diagnosis (CAD) by providing a robust, automated tool that can assist ophthalmologists in early disease detection, thereby facilitating timely treatment and improving patient outcomes. Future work will focus on further optimizing the model, integrating multi-modal imaging data, and developing a real-time clinical decision support system for ophthalmological disorder detection.

Keywords: Ophthalmological Disorders, Medical Image Processing, Deep Learning, Retinal Image Analysis, Computer-Aided Diagnosis, Machine Learning.

CONTENTS

Chapter I

Ophthalmological Disorder Detection Using Medical Image Processing: An Introduction

The human eye, a vital and incredibly complex sensory organ found in humans, functions as a critical source of information, transmitting around 80% of the surrounding environmental data to the brain. Consequently, the impairment of vision can significantly curtail an individual's capabilities, comparable to experiencing 80% paralysis. Routine eye examinations play a crucial role in early identification and assessment of ocular and cardiovascular ailments. Furthermore, by promptly detecting latent eye disorders, appropriate medical interventions can be implemented to halt their advancement. This chapter aims to introduce the motivation behind the study, delve into ophthalmic disorders and their effects on the human body, and tackle the challenges encountered in this field.

1.1. Why Employ Automated Image Detection for Retinal Pathology?

Certainly, why is this happening? What factors are propelling the advancement of automated computer-based identification and measurement of retinal abnormalities? What prompts the collaboration among a variety of experts such as medical professionals, healthcare practitioners, medical physicists, biomedical engineers, and computer scientists to create systems that can autonomously identify retinal disorders?

In this section, we will explore why several research groups have undertaken the task of developing methods and computer software for automating the detection of retinal pathology in images. We will observe:

1. The demand within clinical practice for more effective and economical means of identifying, managing, and treating retinal diseases.
2. The research community's aspiration to gain deeper insights into the root causes and progression of diseases necessitates an intricate analysis of extensive collections of ophthalmological representations.
3. The current developments in tech gear and system efficiency, integrated with progressively advanced approaches in feature analysis, originate the numerous possibilities. These advancements can address the requirements of clinical practice and the eye research field.
4. The duality of retinal images serves both as a valuable resource and a challenging terrain for applying digital image processing and machine learning techniques. These techniques can be rewarding for recent graduates and simultaneously challenging for even the most skilled and inventive engineers.

We commence by examining the driving force that emerges within the medical field, urging the development of novel, cost-effective, and enhanced methods for identifying and controlling retinal ailments. This impetus originates from various sources, all of which we will sequentially explore.

1.1.1. The General Clinical Need

Due to the increasing elderly population on a global scale, there has been a rise in eye-related diseases, resulting in a proportional decrease in access to ophthalmic services, particularly in rural regions and developing nations. The World Health Organization has introduced "Vision

2020," a worldwide campaign aimed at preventing avoidable visual impairments by the year 2020 [1]. Enhancing eye health involves a range of strategies, including expanding efforts to raise awareness about ocular well-being, identifying diseases at an early stage, providing accurate diagnoses, and implementing targeted preventive measures to enhance outcomes. Recent statistics indicate that globally, there are 37 million individuals suffering from blindness and 124 million with impaired vision, not accounting for those with untreated refractive issues.

Whereas the international agenda on Vision 2020 has made progress in reducing avoidable blindness, especially stemming from ocular infections, there remains a necessity for more extensive efforts to address issues such as cataracts, glaucoma, and diabetic retinopathy [2]. Among these concerns, diabetic retinopathy stands out as the most urgent challenge, and consequently, much research on automated detection has been concentrated in this area.

1.1.2. Hyperglycemia: A worldwide medical crisis

Insulin resistance, type 2 diabetes, creates several aftereffects like ophthalmological, heart related or even kidney related problems. In the United States, the current prevalence of diabetes stands at 6.3%, with certain ethnic groups and socioeconomic strata displaying even higher rates [6–8]. According to statistical data disseminated by the International Diabetes Federation (IDF), India experiences a more elevated prevalence of type II diabetes in comparison to other nations. The IDF's ongoing research approximates that about 62 million people in India grapple with this condition, marking a surge of roughly 10 million since 2011. Should this trend persist, it is anticipated that India's caseload will surpass 100 million by 2030, mirroring the situation in New Zealand [3]. Similarly, in Australia, diabetes affects approximately one million individuals (5% of the population), and the expenses linked to managing its complications incur costs amounting to roughly AUS$7 billion [9]. Diabetes constitutes a noteworthy and financially demanding health concern in Western countries, displaying an incidence rate that approaches levels akin to an epidemic. To effectively address this mounting issue, fresh and inventive approaches for identification, diagnosis, treatment, and subsequent monitoring are imperative.

1.1.3. Ophthalmological Disorders

An ophthalmological disorder denotes a medical condition or anomaly that impacts the eyes or the visual system. These disorders may affect different components of the eye, such as the cornea, lens, retina, optic nerve, or related structures, potentially leading to vision impairment or other disturbances in visual function. Ophthalmological disorders encompass a range of

conditions, including cataracts, glaucoma, macular degeneration, retinal detachment, and various types of refractive errors like myopia (near-sightedness) and hyperopia (farsightedness). It is crucial to receive timely diagnosis and appropriate treatment from ophthalmologists to effectively manage these conditions and safeguard visual well-being.

1.1.3.1. Diabetic Retinopathy

Elevated blood sugar levels linked to diabetes serve as the established trigger for diabetic retinopathy (DR), a progressive degenerative ailment of the retina. This condition possesses a latent phase that can initiate well before the actual onset of diagnosed diabetes, and it unfolds without noticeable symptoms. Diabetic retinopathy is categorized into multiple phases. The initial indications are retival arteries and veins occlusion, bleeding from broken vessels, blood spots [10–12]. Further advancement of the ailment is signaled by the leakage of fluids from retinal capillaries. If this leakage occurs in the region of sharpest vision (macula), it can lead to sight-threatening diabetic retinopathy (STDR) [13–15]. Among diabetic individuals, diabetic macular edema stands as the foremost cause of vision deterioration. The rate of new cases in ophthalmology due to hyperglycemia is also rapidly growing with a rise in hyperglycemia ubiquity. The recent works of literature explain that nearly 60% of the population is affected by type 2 hyperglycaemia [17].

The range of several attributes that are apparent to the ophthalmologist or trained person signifies retinal hyperglycemia. Some attributes related to hyperglycemic retinopathy (e.g., hemorrhages, microaneurysms) are correlated with the severity of the retinal disorder in the early stage [23, 24]. Those attributes indicate a precise objective that helps to create an automated retinal analysis system that can generate valuable information related to retinal hyperglycemia. It is also necessary that common people should know that hyperglycemia is treatable if it is observed in the initial stages. The governments, along with the World Health Organization, are also trying to help patients identify, control, and cure hyperglycemia through different funding [22]. By observing hyperglycemia through fundus images, the condition can be treated. It is also a more constructive and systematic process that helps to reduce the cost.

1.1.3.2. Hypertensive Retinopathy

The uplifted vascular pressure due to the blood flow is the main concern of the hypertensive retinopathy. It impacts the vascular tube found in the retina. Prolonged and uncontrolled hypertension can lead to detrimental effects on the small retinal blood vessels, causing them to narrow, leak, or become obstructed.

The severity of hypertensive retinopathy is categorized into several stages:

- *Mild hypertensive retinopathy:* In the initial stage, there might be a slight narrowing of the retinal blood vessels.
- *Moderate hypertensive retinopathy:* The blood vessels experience more constriction, and there could be swelling (edema) in the retina.
- *Severe hypertensive retinopathy:* This stage is characterized by significant narrowing and twisting of the blood vessels, accompanied by more prominent retinal edema and bleeding.
- *Malignant hypertensive retinopathy:* This represents an advanced and critical stage with severe damage to the retinal blood vessels, resulting in the formation of cotton-wool spots (areas of nerve fiber layer infarcts) and optic disc swelling (papilledema).

Hypertensive retinopathy can lead to a range of visual problems, including unclear eyesight, diminished peripheral vision, and, in more serious instances, complete vision impairment. It's crucial for people with high blood pressure to consistently check their blood pressure levels and follow medical advice in order to effectively handle the condition. Managing blood pressure by making lifestyle adjustments, taking prescribed medications, and routinely consulting an eye specialist can work towards avoiding or lessening the effects of hypertensive retinopathy on both vision and general eye health. Timely identification and intervention significantly contribute to achieving improved results.

1.1.3.3. Retinopathy of Prematurity (ROP)

Retinopathy of Prematurity (ROP) is an ocular condition that has the potential to cause blindness in premature infants, especially those born before 31 weeks of gestation or weighing less than 1,500 grams (approximately 3 pounds 5 ounces). Immature retinal vascular structure is the main reason of developing this type of situation. In a normal gestation period, retinal blood vessels develop progressively from the optic nerve toward the outer regions of the retina. However, in premature infants, the available time for these vessels to fully mature before birth might be inadequate. As a result, abnormal blood vessels can develop and multiply on the surface of the retina, leading to various stages of ROP:

- Mild ROP: Characterized by mildly abnormal blood vessel growth.
- Moderate ROP: Involves more pronounced abnormal vessel growth.
- Severe ROP: Exhibits severely abnormal blood vessel growth, potentially leading to scarring and retinal detachment.

If not promptly detected and treated, severe ROP can cause significant visual impairment or even complete blindness. The condition usually develops about 2-3 weeks after birth and progresses rapidly. Nevertheless, in many cases, ROP can spontaneously resolve as the baby grows and the blood vessels mature.

Diagnosis of ROP involves regular eye examinations conducted by a pediatric ophthalmologist, who closely monitors the infant's eyes. If ROP is detected, the ophthalmologist may recommend specific treatments to prevent vision loss. Common treatment options include:

1. Laser therapy: This treatment method aims to halt abnormal blood vessel growth and reduce the risk of retinal detachment.
2. Cryotherapy: In some situations, cryotherapy, which involves freezing treatment, may be used as an alternative to laser therapy to target abnormal blood vessels.
3. Anti-VEGF injections: Intravitreal injections of anti-VEGF medications can help suppress abnormal vessel growth.

The decision regarding which treatment to pursue depends on the severity of ROP and the baby's overall health.

Prevention and early detection are crucial in managing ROP. Neonatal intensive care units (NICUs) often adhere to guidelines for monitoring and managing premature infants' eye health. Ensuring that premature infants receive appropriate medical care and regular eye examinations can significantly reduce the risk of severe visual impairment caused by ROP.

1.1.3.4. Central Serous Retinopathy (CSR)

Central Serous Retinopathy, also referred to as Central Serous Chorioretinopathy, is a condition of the retina that impacts central eyesight by inducing the build-up of fluid beneath the retina. The retinal neuroepithelium is segregated from the inherent pigment epithelial layer of the retina due to the accumulation of fluid.

The exact cause of CSR is not always clear, but it often seems to be linked to RPE dysfunction, which is responsible for nourishing and supporting retinal cells. Several factors that may contribute to CSR development include:

- Stress: High levels of stress or anxiety have been associated with CSR in some cases.
- Corticosteroids: The use of systemic or local corticosteroid medications can increase the risk of CSR.

- Pregnancy: CSR is more common in pregnant women, possibly due to hormonal changes.
- Type A personalities: Individuals with Type A personalities, known for competitive and high-stress behavior, may have a higher risk of developing CSR.

Symptoms of CSR include blurred or distorted central vision, reduced color perception, and micropsia (objects appearing smaller than they are). While CSR typically affects one eye, it can occur in both eyes in some cases.

CSR often resolves spontaneously within a few months as the fluid under the retina is reabsorbed. However, it may persist or recur in some instances, leading to chronic or recurrent CSR, which can cause permanent vision changes due to accumulated fluid damaging the retinal cells.

A complete ocular health screening along with an inflated ophthalmoscopic assessment, tomographic imaging, and retinal fluorescein imaging to observe the retinal structure and identify the presence of fluid is needed to diagnose the CSR.Treatment for CSR depends on its severity and duration. In many cases, no specific treatment is required as the condition resolves on its own. However, if CSR persists or significantly affects visual acuity, the following treatment options may be considered:

- Observation: Close monitoring may be advised in mild cases to see if the condition resolves without intervention.
- Photodynamic Therapy (PDT): This treatment employs a photosensitizing agent and a low-power laser to target abnormal blood vessels, reducing fluid leakage.
- Focal Laser Photocoagulation: In certain cases, laser treatment can seal leaking blood vessels and decrease fluid accumulation.

For any eye condition, seeking prompt evaluation and appropriate management by an ophthalmologist is crucial if experiencing visual changes or symptoms related to CSR.

1.1.3.5. Retinal Vein Occlusion (RVO)

Retinal Vein Occlusion (RVO) refers to a vascular ailment that impacts the retina, the light-sensitive tissue accountable for vision at the rear of the eye. The occurrence of RVO transpires when any of the retinal veins encounter blockage, leading to a disturbance in the usual blood circulation and resulting in a range of vision-related complications.

Two primary categories of retinal vein occlusion exist:

1. Central Retinal Vein Occlusion (CRVO): This occurs when the central retinal vein, responsible for draining blood from the entire retina, becomes obstructed. CRVO can be categorized into two subtypes:
    - Non-ischemic CRVO: In this variation, there is a partial hindrance to blood flow in the retina, carrying a relatively lower risk of experiencing substantial vision loss.
    - Ischemic CRVO: Ischemic CRVO involves a notable impairment of blood flow, resulting in an elevated likelihood of severe vision loss.
2. Branch Retinal Vein Occlusion (BRVO): BRVO occurs when one of the branches of the central retinal vein becomes obstructed. The degree of vision impairment is determined by the seriousness and location of the blockage.

The leading cause of RVO is frequently linked to arteriosclerosis (the hardening of arteries) or the existence of blood clots within blood vessels. Additional risk factors contributing to the development of RVO encompass high blood pressure, diabetes, glaucoma, and specific blood disorders.

Signs of RVO may differ according to the type and intensity of the blockage, but potential indicators encompass abrupt painless loss of vision or a blurry quality in the impacted eye. In more severe instances, individuals may observe floaters or experience defects in their visual field.

Detecting RVO encompasses a thorough eye assessment, which comprises gauging visual sharpness, conducting an expanded fundus examination, and utilizing imaging techniques like optical coherence tomography (OCT) and fluorescein angiography (FA) to analyze the circulation of blood in the retina. The selection of treatments for RVO is contingent on the occlusion's kind, intensity, and root factors. Even though certain instances of RVO might naturally alleviate with the passage of time, potential courses of treatment encompass:

- Intravitreal Injections: Injection of anti-VEGF medications into the eye to reduce macular edema (swelling) and improve vision.
- Laser Therapy: The use of laser treatment to seal leaking blood vessels and reduce macular edema.

- Corticosteroids: In some instances, corticosteroids may be administered to reduce inflammation and edema in the eye.
- Anti-coagulation therapy: In certain situations, anti-coagulant medications may be prescribed to prevent blood clots.

Prompt diagnosis and timely intervention are crucial in managing retinal vein occlusion and preventing further vision loss. If you experience sudden changes in vision or other symptoms of RVO, seeking an immediate evaluation by an eye care specialist is essential.

1.1.3.6. Retinal Artery Occlusion (RAO)

Retinal Artery Occlusion (RAO) is a severe eye condition that occurs when one of the retinal arteries, responsible for supplying blood to the retina, becomes blocked or obstructed. This blockage disrupts the normal blood flow to the affected part of the retina, causing a sudden and significant loss of vision.

RAO can be divided into two primary categories:

1. Central Retinal Artery Occlusion (CRAO): This occurs when the central retinal artery, responsible for supplying blood to the entire retina, becomes obstructed. This form of RAO often leads to an immediate and significant loss of central vision.
2. Branch Retinal Artery Occlusion (BRAO): In this type, one of the branch retinal arteries, which provides blood to a specific retinal area, becomes blocked. The degree of vision loss is contingent on the size and location of the blocked branch.

The leading cause of RAO is typically a blood clot or embolus that travels and lodges within the retinal artery, impeding blood flow. These emboli may originate from various sources like the heart or carotid arteries.

Symptoms of retinal artery occlusion are abrupt and may include:

- Sudden, painless, and severe vision loss in the affected eye.
- Blurred or completely black vision in the affected area.
- The affected eye may appear pale or whitish due to reduced blood supply.

Retinal artery occlusion requires urgent medical attention, as vision loss is often irreversible if not promptly treated. There is a narrow time window for intervention to potentially restore blood flow and preserve vision.

Immediate evaluation and intervention by an ophthalmologist or an emergency room physician are critical when experiencing symptoms of RAO. Treatment may involve efforts to dislodge the embolus or enhance blood flow to the retina. Some treatment options include:

- Employing a soft digital massage in the vicinity of the eye to assist in dislodging the embolus.
- Employing controlled breathing into a paper bag in specific scenarios raises carbon dioxide levels, potentially widening blood vessels and enhancing blood circulation.
- Utilizing intra-arterial thrombolysis, a technique in which medications are introduced directly into the impacted artery to dissolve the clot.
- Engaging in hyperbaric oxygen therapy, a process wherein pure oxygen is inhaled within a pressurized chamber to augment blood flow.

It's important to acknowledge that even with intervention, the potential improvement in visual outcomes could be constrained by the extent of the occlusion and the duration of the blockage. Taking steps to avoid retinal artery occlusion includes addressing risk factors like hypertension, diabetes, and heart conditions that could contribute to the development of emboli. Consistent eye check-ups and comprehensive health assessments play a vital role in promptly identifying and managing these risk factors.

1.1.3.7. Retinitis Pigmentosa (RP)

Retinitis Pigmentosa (RP) is a collection of hereditary ocular disorders that impact the retina. The defining characteristic of RP is the progressive decay of retinal cells, particularly the photoreceptors (rods and cones), which have a crucial role in detecting light and transmitting visual information to the brain.

The primary source of RP is rooted in genetic mutations transferred from parents to their offspring. These mutations interfere with the operation and structure of retinal cells, causing them to degrade gradually over time. Consequently, people with RP encounter a deterioration in their vision, initially struggling with low-light vision (night blindness) and facing diminished peripheral sight (tunnel vision). As the condition advances, there is a possibility of central vision impairment, which may eventually result in legal blindness.

The symptoms and progression of RP can exhibit significant variations among individuals, contingent on the specific genetic mutation at play. Some individuals might undergo a gradual

decline in vision over an extended period, whereas others could experience a more swift deterioration in their vision quality. The diagnosis of RP commonly entails a thorough eye evaluation, encompassing assessments of visual sharpness, visual field, and the utilization of imaging techniques like electroretinography (ERG), which gauges the retina's reaction to light stimuli.

Currently, RP lacks a remedy due to the inability to correct the underlying genetic mutations responsible for the condition. Nevertheless, ongoing research has unveiled promising experimental remedies, such as gene therapies and retinal implants, with the goal of retarding disease advancement or potentially reinstating partial vision.

The management of retinitis pigmentosa (RP) centres around preserving the existing visual capabilities and optimizing functional independence. This can involve various strategies such as:

- Employing low-vision aids like magnifiers, electronic devices, or telescopes to enhance visual perception and aid in daily activities.
- Participating in orientation and mobility training to acquire skills for safe navigation and movement in the presence of diminished vision.
- Engaging in genetic counselling to gain insights into the hereditary aspects of RP and consider options related to family planning.

In addition, maintaining regular appointments with an ophthalmologist or retina specialist is of utmost importance for individuals with RP. This allows for continuous monitoring of their visual condition and the potential exploration of novel treatments or supportive interventions that may emerge over time.

Coping with RP can bring about difficulties, yet with the right assistance, people can adjust and enjoy meaningful lives. A range of associations and support collectives provide tools and communal bonds to help individuals with RP and their loved ones in managing the effects of this condition.

1.1.3.8. Sickle Cell Retinopathy

Sickle Cell Retinopathy is an eye ailment that specifically develops in individuals affected by sickle cell disease, an inherited blood disorder distinguished by anomalous hemoglobin within red blood cells. This condition emerges as a result of the atypical morphology of these blood cells, which subsequently causes obstructions within blood vessels. This, in turn, diminishes

the blood circulation within the minute vessels of the retina, the photosensitive tissue positioned at the rear of the eye and accountable for visual perception.

The occlusions within the blood vessels of the retina can lead to a range of retinal alterations, encompassing:

- Occlusions of retinal vessels: The obstruction of the tiny blood vessels in the retina, resulting in diminished blood delivery to particular retinal regions.
- Retinal hemorrhages: The escape of blood from injured blood vessels, giving rise to small areas of bleeding on the retina.
- Neovascularization refers to the abnormal development of fresh blood vessels on the retina. These vessels are often delicate and can easily leak, leading to further complications with vision.

The stages of Sickle Cell Retinopathy are categorized according to the extent of retinal alterations. During its initial phases, this condition usually doesn't exhibit prominent symptoms. Nevertheless, as it advances, individuals might encounter issues with their vision such as unclear eyesight, distorted visual perception, or even a reduction in their field of vision.

Individuals with more severe forms of sickle cell disease, like sickle cell anaemia, are at a heightened risk of developing sickle cell retinopathy. As a result, it is crucial to undergo regular eye examinations conducted by an ophthalmologist. These examinations play a crucial role in promptly identifying and tracking retinal changes linked to sickle cell retinopathy.

The appropriate course of treatment for sickle cell retinopathy hinges on the condition's stage and severity. For milder instances, vigilant monitoring might be sufficient. Conversely, as the condition progresses, treatment options may involve utilizing laser therapy or administering anti-VEGF injections. These interventions aim to manage neovascularization and mitigate the potential for significant vision loss.

To effectively manage their condition and mitigate potential complications, like sickle cell retinopathy, individuals with sickle cell disease should maintain close communication with their healthcare team, which should include an ophthalmologist. Furthermore, adopting practices that bolster overall health and ensuring proper hydration can contribute to diminishing the risk of sickling and associated complications throughout the body, including the eyes.

The above descriptions provide only a few illustrations of retinopathy disorders. Each type of retinopathy can be caused by distinct factors, present varying symptoms, and require different

treatments. If you notice any changes in your vision or are at risk for these conditions, seeking prompt medical attention is vital. An eye specialist or ophthalmologist is best equipped to offer a precise diagnosis and provide suitable care for retinopathy disorders.

1.1.4. Impact on Human Body:

Retinal conditions can profoundly influence human well-being, especially concerning vision. The retina, a crucial ocular element responsible for converting light into neural signals sent to the brain, holds a pivotal role in our visual capacity. Disorders affecting the retina can lead to an array of detrimental outcomes, including:

1. *Vision Impairment or Loss:* Retinal disorders frequently lead to unclear eyesight, diminished visual sharpness, or even absolute blindness in severe instances, impacting an individual's visual clarity.
2. *Visual Field Constriction:* Specific retinal disorders result in reduced visual field, causing loss of peripheral or central vision, thereby affecting day-to-day navigation and activities.
3. *Photophobia:* Certain retinal disorders trigger photophobia, rendering bright surroundings uncomfortable or painful.
4. *Color Perception Challenges:* Some retinal disorders result in challenges with color vision, making accurate color differentiation difficult.
5. *Night Blindness:* Certain retinal disorders induce night blindness, complicating vision in low-light situations.
6. *Metamorphopsia:* Conditions like macular degeneration can induce metamorphopsia, distorting straight lines and causing a wavy appearance.
7. *Emotional Consequences:* Vision loss or impairment due to retinal disorders can have substantial emotional and psychological impacts, leading to feelings of anxiety, depression, and frustration.
8. *Decreased Mobility and Autonomy:* Impaired vision can curtail mobility and self-sufficiency, making navigation and daily tasks more challenging without external aid.
9. *Interference with Daily Tasks:* Reading, driving, recognizing faces, and tasks requiring fine detail become arduous or unachievable for individuals grappling with retinal disorders.
10. *Limitations in Functionality:* Retinal disorders can impede a person's capacity to work, engage socially, and maintain an active lifestyle.

The objective of addressing and controlling retinal disorders is centred around maintaining and reinstating vision to the highest extent achievable. Timely detection and proactive measures

are imperative to achieve more favourable results. Consistent eye evaluations and swift medical care play a vital role in recognizing retinal disorders promptly and halting their advancement, thus minimizing their effect on an individual's overall well-being.

1.2. Digital Analysis of Retinopathy

The treatment of blindness due to the variety of retinal disorders is more valuable in the the digital analysis of retinopathy. The incorporation of digital systems driven analysis of ophthalmological disorder provides the maximum effective clinical analysis. In recent ages, the digital analysis is the fundamental step to evaluate ophthalmological parameters in various countries like Scotland. Numerous retinal attributes can easily and automatically be identified by this assessment that analyses the digital fundus retinal images [62-68]. Additionally, hypertension, hyperglycemia or even cardio-vascular disorder can affect the retinal vascular structure by narrowing and widening them or blocking them which can also be identified by this digital analysis. Some results of digital fundus analysis are being depicted below.

1.2.1. Detection of Optic Nerve Head

The optic nerve head is the signature hallmark of the human retina. The characteristics of this attribute are likely its brighter, circular shape with a color variation from whitish to yellowish, its size, which is generally constant for individuals, and it is the source of the vascular structure. The identification of the optic disk in retinal fundus images and the quantitative study of the evolution of its shape and size play an important role in diagnosing different pathologies, and the abnormalities related to the retina of the human eye. Most of the abnormalities which are related to an optic disc may lead to a structural change in the inner and outer areas of the optic disc. Optic disc identification and segmentation on the level of the whole retinal image reduces the detection sensitivity for those parts. Searching the portions with maximum brightness [99,102,103], finding circular perimeter with highly intensed pixels by fitting a snakes model [105,106] or Hough transformation [101] and by finding vascular curvature, the optic nerve head can be identified. .

1.2.2. Optic Vascular Structure Classification

The identification of blood vessels in retinal fundus images and quantitative study of the evolution of its shape and size plays an important role in diagnosing different abnormal conditions correlated to the retinal structure of the human eye. Most of the abnormalities, which

relate to blood vessels, may tends to a structural change of the blood vessels. Segmentation of blood vessels corresponding to entire retinal image reduces the sensitivity for those areas.

Describing the vascular pattern of retinal fundus [62, 114, 115] and optical fluorescein images [99, 112, 113] in the literature is very wide-ranging and the justification of this field in the introduction does not match. Various strategies like filtering [116], threshold selection [117], morphology [118, 119], region growing [120], etc., can be convenient to identify the vessel pattern. Tracking vessel patterns is fundamentally done from the initial seed point of the vascular tree and by approaching in small steps to the vessel's direction.

1.2.3. Change in Vascular Diameter

Marking of retinal vascular pattern is worldwide validated phenomenon in hyperglycemia and hypertension. The escalation of hyperglycemia and hypertension impacts the retinal vascular pattern by narrowing or widening the veins and arteries and their sprigs. These modifications in blood vessels aren't exclusive to diabetes; research by Wong and colleagues has indicated that they can also contribute to the likelihood of experiencing cardiovascular and cerebrovascular diseases [55, 110]. Microvascular abnormalities within the retina, like the narrowing of both general and specific arterioles, arteriovenous nicking, and retinopathy, portray the cumulative harm inflicted on blood vessels due to factors such as hypertension and aging. Studies in population demographics suggest that these irregularities are observable in about 2% to 15% of individuals without diabetes, and they consistently show a strong association with high blood pressure. The narrowing of general arterioles and arteriovenous nicking also seem to act as enduring indicators of hypertension, reflecting not only current but also past levels of blood pressure [60, 111].

1.2.4. Identification of Capillary Aneurysms

In early 1980s, the findings of the small aneurysms in the macula region of human retina by a computational procedure are being attempted but at the end of 1990s some important and dependable datas have been captured [70]. The Aberdeen group was able to provide the first proven procedure of identification of small capillary aneurysms within the fluorescein images [71, 72]. Now in various laboratories several ongoing researches on RGB fundus images are being discussed. Many well-established documentations can be found on the detection of small capillary aneurysms and their direct relations to the degree of illness like hyperglycemia and hypertension [23,24]. The small aneurysms are formed dynamically over the retina and it has

a direct link to the hyperglycemia screening system [24, 73-75]. So, it is very obvious that findings of those small aneurysms in fundus RGB are very important.

1.2.5. Hemorrhages

Hemorrhages, basically the discharge of fluid in the macula due to the vessel's bulge, are a very important attribute related to hypertension and hyperglycemia. These are found in the macula of the retinal fundus in a small and very arbitrary structure. Their size and color are like the small aneurysms. So, it is very complicated to differentiate them and identify them. The literature survey on the detection of hemorrhages is very limited compared to that of small aneurysms. The Spyder-Net technique [72] is being widely used to detect the larger hemorrhages [79]. Some other techniques like Neural Network, Artificial Algorithm [80], or segmentation-related techniques [64] and morphological analysis are also used to identify those spots.

1.3. Significance of the Study

The significance of this research extends beyond achieving technical accuracy in ophthalmological disorder detection. The proposed work aims to address a pressing clinical and societal need — the early, affordable, and accessible diagnosis of vision-threatening eye diseases such as Diabetic Retinopathy (DR), Age-related Macular Degeneration (AMD), and Diabetic Macular Edema (DME). These conditions are major causes of preventable blindness worldwide, particularly in low- and middle-income populations where specialist availability and diagnostic infrastructure are limited.

By developing image processing–based diagnostic techniques that are both computationally efficient and clinically reliable, this research contributes toward reducing the burden of avoidable blindness, enabling large-scale screening, and supporting ophthalmologists in making faster and more consistent diagnoses. Thus, the study not only advances technical methodologies but also holds significant implications for public health, healthcare cost reduction, and improved patient outcomes.

1.4. Conclusion

In conclusion, the introduction provides a comprehensive overview of the significance and challenges surrounding the detection of ophthalmological disorders through the utilization of medical image processing techniques. The field of ophthalmology plays a critical role in diagnosing and treating various eye conditions, making the accurate and timely detection of

these disorders of utmost importance. With the rapid advancements in medical imaging technology and computational methods, there is a growing potential to revolutionize the way ophthalmic diseases are identified and managed.

The introduction highlights the complexity of ophthalmic disorders and emphasizes the limitations of traditional diagnostic approaches. It underscores the need for efficient and accurate methods that can enhance early detection, leading to improved patient outcomes. By harnessing the power of medical image processing, researchers and practitioners can leverage digital images obtained through multiple digital imaging processes like macula captured by fundus camera or captured by OCT to develop sophisticated algorithms capable of identifying subtle patterns and anomalies that might elude the human eye.

Moreover, the introduction provides a glimpse into the key challenges associated with ophthalmological disorder detection using medical image processing. These challenges range from dealing with large and complex datasets to addressing issues related to noise, variability, and interpretability of results. The integration of machine learning and artificial intelligence techniques holds great promise in overcoming these obstacles, as these approaches can learn from vast amounts of data and adapt to evolving patterns.

In essence, the introduction sets the stage for the subsequent chapters of this study, highlighting the importance of advancing the field of ophthalmological disorder detection through the fusion of medical image processing and cutting-edge technologies. As researchers continue to innovate and refine their methodologies, there is an exciting opportunity to enhance diagnostic accuracy, reduce the burden on healthcare professionals, and ultimately improve the quality of life for individuals affected by ophthalmic conditions. The journey towards achieving these goals requires collaboration between medical experts, computer scientists, and engineers, as well as a commitment to pushing the boundaries of knowledge and technology in service of better eye care.

Chapter II

Literature Review

Within the realm of medical imaging and ophthalmology, retinal image processing stands as a prominent area of research. It encompasses the analysis and improvement of images derived from the retina to support the diagnosis, monitoring, and treatment of diverse retinal disorders. Commonly studied retinal disorders employing retinal image processing techniques comprise diabetic retinopathy, age-related macular degeneration (AMD), glaucoma, and retinal vein occlusion.

2.1. Retinal Image Quality Assessment

In the past, the main emphasis of image quality assessment was on evaluating the impact of storage, transmission, or compression on image quality [150]. However, in the medical domain, it has become imperative to consider the suitability of an image for precise medical diagnosis. Ensuring that medical images possess sufficient quality is vital to prevent potential inaccuracies in diagnoses that may arise from analyzing low-quality images. By conducting an image quality assessment, it is possible to ascertain whether an image is appropriate for use in medical diagnosis.

2.1.1. Retinal Image Quality

The evaluation of retinal image quality aims to determine if the image is suitable for accurate medical diagnosis. Several factors can impact retinal image quality, such as the natural curvature of the retina, differences in pupil dilation among patients, patient fixation or blinking, the presence of diseases, the experience of the personnel operating the equipment, ocular media opacity, and camera settings (e.g., poor focus or inadequate illumination) [151-153]. In general, high-quality retinal images are characterized by two crucial elements: clear visual details and relevant content.

- *Clarity:* To make retinal images appropriate for analysis, they must display distinct and well-defined structures. This requires adequate sharpness, appropriate overall illumination, and uniformity. The clarity of retinal images is vital for automated systems to differentiate retinal anatomical structures and potential abnormalities during the pre-diagnosis phase. Additionally, it guarantees that medical experts have a precise and sufficient view for precise examination and diagnosis.
- *Content:* For a dependable disease diagnosis [154], it is crucial for retinal images to capture all necessary retinal structures. Even if the clarity of the images is satisfactory, an incomplete portrayal of these structures could make the image unsuitable for precise diagnosis. Furthermore, to avoid potential misdiagnosis caused by outlier images, ARSS should eliminate non-retinal images during subsequent processing.

Retinal images that suffer from clarity issues, such as blurriness, inadequate illumination, or non-homogeneities, are considered unsuitable for medical diagnosis. Figure 2.1 provides examples of both high-quality and poor-quality retinal images. When insufficient-quality retinal images are presented for medical examination, an ophthalmologist may require a new capture of the image to ensure a dependable diagnosis. In many cases, the image-capturing process and the involvement

of the medical expert are independent [150], resulting in potentially time-consuming and costly image recapture for the patient. In more serious situations, the analysis of low-quality retinal images by an Automated Retinal Screening System (ARSS) could lead to misdiagnosis, falsely identifying a diseased eye as healthy, and causing delays in essential treatment. Additionally, telemedicine techniques that involve retinal image technologies often capture images at one location and send them for specialized medical analysis at another. In such scenarios, receiving a poor-quality retinal image can be problematic, especially when the patient is not easily accessible for image recapture [155]. Therefore, it is imperative to conduct a Retinal Image Quality Assessment (RIQA) immediately after image acquisition to determine promptly whether image recapture is necessary for a reliable subsequent diagnosis.

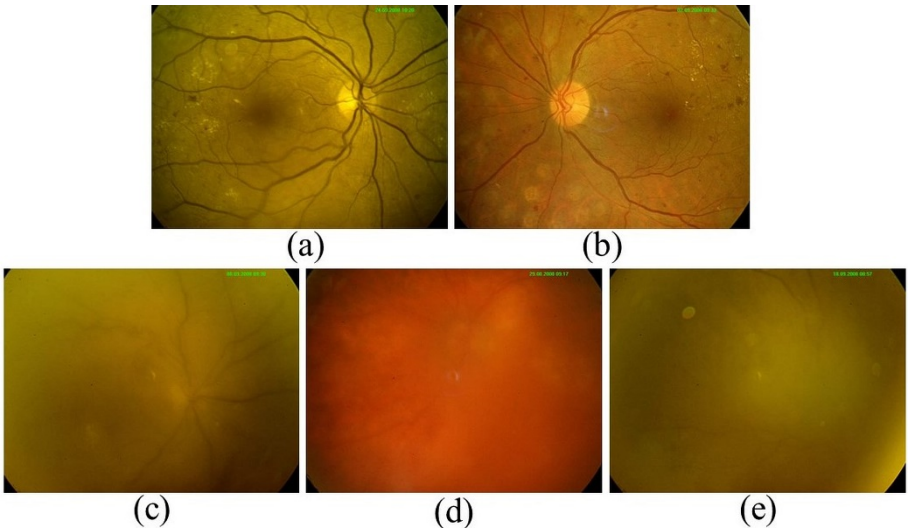

Fig 2.1: Representative retinal images from the DRIMDB dataset illustrating variations in image quality: (a–b) depict clear, well-focused retinal images with good illumination and contrast, while (c–e) present poor-quality images affected by issues such as blurring, uneven lighting, or low contrast [156].

2.1.2. Types of RIQA Images

Generally, Retinal Image Quality Assessment (RIQA) methods can be classified into two categories: subjective and objective, depending on their approach to evaluating image quality. Initially, RIQA predominantly relied on subjective assessments, wherein human experts would visually inspect and assess the images. However, subjective methods are unsuitable for real-time

applications due to their impracticality, as they are cumbersome, expensive, and time-consuming [157].

Conversely, objective methods for retinal image quality assessment (RIQA) automatically evaluate the quality of retinal images based on specific criteria that align with subjective human assessments [150]. These objective methods are increasingly preferred over subjective methods due to their efficiency.

Objective image quality measures can be categorized into three types: full reference, reduced reference, and no-reference methods, depending on whether a reference image is used for assessment. Full reference methods require an original high-quality image as a reference and focus primarily on overall image quality rather than the diagnostic perspective. They are more suitable for evaluating image degradation caused by compression or storage and for assessing improvement through enhancement algorithms.

On the other hand, reduced-reference methods use only partial information from the original image and are suitable for assessing the quality of images affected by noise [158]. In contrast, no-reference objective image quality assessment methods do not require any information from a high-quality reference image. These methods blindly assess image quality and are suitable for scenarios where a reference image is unavailable, such as in RIQA. However, it's worth noting that the field of no-reference IQA is still in its early stages and is considered one of the most challenging problems in image analysis [159].

2.1.3. Challenges in RIQA

Presently, there is considerable emphasis on developing robust RIQA (Retinal Image Quality Assessment) algorithms, particularly those capable of seamless integration into ARSS (Automated Retinal Screening Systems). Nevertheless, several hurdles must be surmounted to achieve reliable and efficient algorithms for assessing retinal image quality. These challenges can be succinctly outlined as follows:

- *RIQA remains subjective:* An established, universally recognized standard to assess the acceptable quality of retinal images remains elusive [150]. Furthermore, the definition of a high-quality retinal image depends on the specific diagnostic needs [160]. To illustrate, an image with dark regions might be deemed acceptable for diagnosing glaucoma as long

as the optic disc (OD) is clearly visible. However, the same image might be insufficient for detecting early signs of diabetic retinopathy (DR) hidden within those dark regions.

- *Limited Dataset:* The main obstacle in Retinal Image Quality Assessment (RIQA) is the scarcity of publicly annotated retinal image datasets with quality labels. Due to this limitation, many research algorithms end up evaluating their techniques on private datasets. Moreover, there exists considerable variation in the quality of retinal images within the public datasets, leading to instances where images deemed of poor quality in one dataset are deemed acceptable in another. Consequently, comparing the performance of various existing RIQA algorithms in the literature becomes a challenging task. Furthermore, the majority of publicly available datasets only categorize retinal images broadly as either good or bad quality without specifying the particular quality issues (such as blur or poor illumination) that make them unsuitable for reliable medical diagnosis. As a result, the development of RIQA algorithms that target specific quality issues becomes a formidable undertaking.
- *Variation in imaging devices:* Moreover, significant progress has been made in retinal photography over the last decade. Notably, retinal cameras have seen enhancements, leading to higher resolutions and improved image quality [161]. Nevertheless, the majority of automatic Retinal Image Quality Assessment (RIQA) systems have been designed and evaluated using specific datasets captured using a single device. This oversight has resulted in a failure to consider the effects of variations in retinal images captured by different apparatuses on the performance of developed algorithms.

Consequently, a pressing need arises for the development of comprehensive and efficient Real-Time Image Quality Assessment (RIQA) algorithms that can deliver reliable results instantaneously, even when dealing with images captured using different cameras, exhibiting diverse resolutions, and varying quality levels.

2.2. Optic Disk Detection and Segmentation

The analysis of the optic disc can be categorized into two main components: optic disc detection and segmentation. Within ophthalmology and medical imaging, considerable research has focused on automating the identification and examination of the retinal optic disk. Numerous image-

processing algorithms and methodologies have been proposed to achieve this, leading to various prevalent approaches and techniques in this field.

In their work, Youssif et al. [162] employed template matching for the purpose of locating the optic disc (OD) center in retinal images. Initially, they applied illumination equalization-based and adaptive histogram equalization techniques using a 40×40 running window to smooth the image. This was followed by adaptive histogram equalization and normalization to enhance the image contrast. To extract blood vessels, a Matched filter was utilized at a specific scale and 12 directions to approximate the vessel's orientation in the OD area. The OD was then identified based on the pixel with the least accumulation.

In a separate study, Abramoff and Niemeijer [163] acknowledged the potential of this approach in detecting the OD's location in retinal images, especially in cases with few or no abnormalities, where the OD is typically positioned at the center of the image. To achieve the correlation between the parameters related to the optical nerve head centre point of vector attributes measuring around the circular disk parameter, the K-NN regression model has been employed.

Haar [164] employed illumination equalization on the green-band of the RGB fundus image, followed by the creation of gaussian pyramid by the use of discrete wavelet transform based on Haar model. The gleaming picture elements at the fifth level of gaussian pyramid are being considered to measure the area of the optical nerve head.. Haar also suggested an alternative approach involving polyhedron factorization vessel’s structure and the green component. The optical nerve head detection using Hough Circular Transform is used by Ghafar et al. Here retinal green component is used to detect the ONH. In this green image the complete vessel structure has been subdued by using morphological closing operation. Then Sobel filter and the thresholding is used to pullout the edges in those images. Finally the biggest circle ring that explains the ONH is being identified by applying Hough Circular Transform.

Akita et al. [166] employed a method for localizing the optic disc (OD) by tracing back the vessels to their origin. Although it is a reliable technique, it relies on time-consuming vascular tree segmentation. A shape-oriented geometric alignment model of the retinal vessel system has been proposed by Grison et al. [167]. That model inherently contains information about the OD position as the convergence point of vessels. By utilizing vessel centre-line points and corresponding directions obtained through vessel identification, they estimated model parameters using stochastic

optimization. The position of the optic nerve head is being calculated by those predicted parameters.

Rangayyan et al. [168] adopted phase-portrait analysis to detect the OD, assuming it to be near the focal point of retinal vessel convergence. They extracted the vasculature network using a Gabor filter and obtained the optic nerve head (ONH) through phase portrait analysis and intensity-based conditions. In [169], the boundary of the optic disc was found using morphological filtering techniques and active contours. Thomas et al. [170] employed mathematical morphology for OD detection, split into two parts. The radiance of the papilla and the blood supply network are initially being identified as that region exhibits higher gray level variation than other parts of the retinal structure. Additionally, a shade correction technique was applied to remove background variation. Secondly, the boundary was detected using the watershed transform with external and internal markers.

The optical nerve head has been detected by Sinthanayothin et al. [171] by recognizing the region of greatest instability within neighbouring pixels by using a window with the same diameter as the optic nerve head [172].. The moving average filter has been implemented by Chrastek et al. to the green component of the retinal fundus image to identify the optic nerve head at peak intensity point.

Koozekanani et al. [173] employed the minimal effort maximum effect technique for ONH identification. The confluence of the macula and the vivid portion in the fundus imaging is presumed to be the optical nerve head.

In a study by Muhammad Nauman Zahoor et al. [175], they introduced an innovative hierarchical approach aimed at swiftly and accurately localizing and segmenting the Optic Disc. The process involved removing retinal vasculature and pathologies through morphological operations during the preprocessing stage. To locate the Optic Disc, Circular Hough Transform was employed. To obtain the precise boundary of the Optic Disc, they calculated the region of interest and applied a unique polar transform-based adaptive thresholding technique. The effectiveness of their methodology was assessed on various publicly available retinal image datasets, including MESSIDOR, DIARETDB1, DRIONS-DB, HRF, DRIVE, and RIM-ONE. The results demonstrated substantial improvements in terms of both accuracy and processing time compared to existing methods.

Various methods have been proposed for Optic Disc (OD) detection and localization. Sinthanayothin et al. [176] utilized intensity changes caused by blood vessels to localize the OD. Mahfouz et al. [177] employed image feature projection for OD localization. Walter et al. [178] introduced the idea of using the watershed transformation to find the OD contour. The onset vascular development is focused by Hoover et al. [179] to identify the optic nerve head andusing fuzzy convergence logic with a voting-type algorithm to determine the vessel convergence point. Another approach [180] involved simulating the optical nerve head as a spherical body and executing contour-based template matching [181, 182] by using the edge map obtained from the fundus image. However, this method was limited by the presence of blood vessels inside and around the OD. To address this issue, image pre-processing was applied using morphological operations prior to template matching [182].

The circular template matching methodology was improved by considering intensity changes and information inside and outside the OD. Nevertheless, the shape-based modelling approach faced challenges due to the asymmetry of the optic nerve head, the pathological alteration observed in the abnormal tissue, and variance in perspective of optical nerve head.

Abdullah et al. [183] employed numerous morphology-based operations to improve the quality of the optic nerve head, removing any pathologies and retinal vasculature. To approximate the OD center, the Hough transform was employed.

Joshi et al., in their studies [185] and [186], employed vessel kinks as a key property for accurately detecting the boundary of the Optic Disc (OD). To better capture irregularities in the OD's shape, they utilized gradient-based active contour models, where a contour is manually initialized [187] or automatically initialized [195], and then an energy term derived from image gradients deforms the contour. Initially, the OD boundary detection utilized a gradient vector flow-based active contour model [196], followed by minimizing the impact of high gradient values at blood vessel locations in the energy term. This minimization process can be achieved through pre-processing of images [187] or by imposing on the result showing the segmented optic nerve head, from disk shaped structure [188, 189]. Alternative studies implicated a shape-adaptive model approach utilizing the snake model [190] to enhance vessel occlusion detection accurately. This method comprised two phases: knowledge-based clustering and smoothing update. The concept was to

deform the snake at locations with minimum energy and then self-cluster into two distinct groups, with these clustering groups being updated using locally and globally obtained information.

Abdullah et al. [183] employed the grow-cut algorithm for OD boundary segmentation, while Yu et al. [191] utilized a level-set approach and directional matching for the same purpose. Sandra et al. [192], on the other hand, utilized PCA and mathematical morphology for OD segmentation. Table 2.1 presents a comprehensive performance analysis of various well-established image processing techniques used for retinal optic disk detection and segmentation.

Table 2.1: Comparative evaluation of existing methods for retinal optic disc detection and segmentation based on performance metrics.

Author	Dataset	Sensitivity	Specificity	Accuracy
A. Youssif et al.- Matched Filter [162]	STARE	98.8	-	-
R. Rangayyan et al. - Gabor Filters and Phase Portrait Analysis [168]	STARE	71.6	-	-
F. Haar et al.- Template matching and Hough filtering [164]	STARE	70.4	-	-
A. Hoover et al.- fuzzy convergence [174]	STARE	65.4	-	-
T. Walter, J.C Klein et al.- Morphological filtering and the watershed transformation [170]	STARE	58	-	-
C. Sinthanayothin-principal component analysis [171]	STARE	42	-	-
S.Roychowdhury et al.- Minimum Intensity Maximum Solidity [173]	STARE	98.68	100	-
Sopharak, Uyyanonvara et al.-mathematical morphology [193]	DIARETDB1	46.03	99.94	-
	DRIVE	21.04	99.93	-
Kande, Subbaiah et al.-Spatially Weighted Fuzzy c-Means [194]	DIARETDB1	88.08	98.78	-
	DRIVE	69.99	98.88	-
Seo, Kim et al.- Morphological filtering [195]	DIARETDB1	61.03	99.87	-
	DRIVE	50.29	99.83	-
Walter, Klein et al.-Intensity based watershed transform [196]	DIARETDB1	65.69	99.93	-
	DRIVE	49.88	99.81	-
Lupascu, Tegolo et al.- Hough transform [197]	DIARETDB1	68.48	99.69	-
	DRIVE	77.68	99.68	-
Stapor, Świtonski et al.- mathematical morphology [198]	DIARETDB1	84.98	99.64	-
	DRIVE	73.68	99.20	-
Basit and Fraz et al.-Boundary extraction [199]	DIARETDB1	73.47	99.44	-
	DRIVE	89.21	99.21	-
Abdullah, Fraz et al.- circular Hough transform and grow-cut algorithm [183]	DIARETDB1	85.10	99.84	97.72
	DRIONS-DB	85.08	99.66	99.89
	MESSIDOR	89.54	99.95	99.89
	DRIVE	81.88	99.66	96.72
	DRIONS-DB	93.12	99.56	-

Mitra et al.- Deep learning [201]	MESSIDOR	-	99.05	99.14
Liu et al.-Deep learning [202]	HRF	86.7	96.5	91.60

2.3. Vessels Segmentation

The segmentation of blood vessels in retinal fundus images holds significant diagnostic value for various chronic vascular conditions, including arteriosclerosis, diabetic retinopathy, hypertension, and more. This review paper focuses on presenting the current algorithms that have been developed for precisely segmenting vessels in the fundus.

2.3.1. Match Filtering Approaches

The matched filter (MF) is utilized to process retinal images for vessel segmentation. Gaussian Convolution Kernel (2D) with fundus image, particularly acknowledging to arteries and veins with the similar standard deviation as a Gaussian Karnel, as explained by Fraz et al. [203]. As a result, post-processing steps become essential to improve segmentation accuracy. Common post-processing techniques include thresholding, the use of morphological operators, and clustering techniques.

Chaudhuri et al. [204] introduced the MF with 12 templates to detect blood vessels by searching for them at each pixel and post-processing the maximum response to identify vessel segments. Vessel segmentation involved using region-based and local attributes along with thresholding and iterative probing on the MF response image, resulting in a substantial reduction of false positives compared to the basic MF response (Hoover et al., 2000).

For the measurement of vessel width and diameter, Gang et al. [205] employed a second-order amplitude-modified Gaussian filter. However, this method proved susceptible to false positives in cases of local deformations.

Sofka and Stewart [206] proposed a combined approach using responses from the MF, vessel boundary measure, and confidence measure. Al-Rawi et al. [207] developed a two-stage MF that utilized an optimization technique to automatically find filter parameters. While this outperformed the single-pass MF, it was solely tested on the DRIVE database, limiting its broader applicability. Yao and Chen [208] implemented vessel enhancement using Gaussian MF and vessel segmentation through a pulse-coupled neural network. Cinsdikici and Aydin [209] proposed a method combining MF, ANT colony algorithm, and length filtering for segmenting the complete

vasculature of retinal blood vessels. Zhang et al. [210] introduced a technique that consolidates the matched filtering and gaussian edge detector for partitioning vascular network. This approach successfully reduces false vessel detections, but it struggles to eliminate certain noisy patterns when using the logical OR operation. Amin and Yan [211] utilized phase congruency to improve computational speed and employed log-Gabor filters to classify vessels. Their method proved to be robust in handling changes in image contrast and luminance. Odstrcilik et al. [212] discussed an enhanced matched filtering technique on the HRF (Human Retinal Fundus) database. The pre-processed image was convolved with five MF in 12 different orientations, covering vessels of varying thickness. Post-processing with morphological operators helped remove artifacts and extract blood vessels successfully. Chakraborti et al. [213] introduced another MF with a kernel designed as a linear combination of five Gaussians, which improved contrast-enhanced vessel segmentation. To upgrade the Gaussian MF scale parameter, Sreejini and Govindan [214] proposed using a particle swarm optimization (PSO) approach. This led to improved performance for the MF method. In an attempt to achieve vessel segmentation, Singh and Srivastava [215] proposed a modified MF approach based on the Second Order of Gaussian distribution. Although post-processing slightly improved the results, the method still faced challenges in removing the optic disc, resulting in a low sensitivity value.The authors utilized various MF approaches for blood vessel segmentation, as listed in Table 2.2. Notably, when comparing the sensitivity values, the ophthalmologist's results surpassed those of any matched filtering approach.

Table 2.2: Evaluation of the Segmentation Performance of Retinal Vessels Using Matched Filter Techniques.

Author	Database	Sensitivity	Accuracy	Specificity	AUC
Fraz et al.- Multiscale Gabor and morphological features [203]	DRIVE	77.63	94.70	97.23	-
	STARE	89.51	93.48	93.84	-
Chaudhuri et al.- 2D matched filters [204]	DRIVE	-	87.73	-	78.78
Hoover et al.- Matched filter [247]	STARE	67.51	92.67	95.67	-
Al-Rawi et al.- matched filter [207]	DRIVE	-	95.35	-	94.35
Yao and Chen- PCNN and fast 2D-Otsu algorithm [208]	STARE	80.35	-	97.20	-
Cinsdikici and Aydin- matched filter/ant colony) [209]	DRIVE	-	92.93	-	94.07
Zhang et al.- matched filter with first-order derivative of Gaussian [210]	DRIVE	71.20	93.82	97.24	-
	STARE	71.77	94.84	97.53	-
Amin and Yan- phase congruency [211]	DRIVE	-	92.00	-	94.00

Odstrcilik et al.- Improved matched filtering [212]	DRIVE	70.60	93.40	96.93	95.19
	STARE	78.47	93.41	95.12	95.69
	HRF	74.63	94.45	96.19	95.89
Chakraborty et al.- self-adaptive matched filter [213]	DRIVE	72.06	93.70	95.79	94.19
	STARE	67.86	93.79	95.86	-
	CHASED B	53.72	93.04	95.83	-
Sreejini and Govindan- Multiscale matched filter [214]	DRIVE	71.32	96.33	98.66	-
	STARE	71.72	95.00	96.87	-
Singh and Srivastava- Gumbel probability distribution [215]	DRIVE	69.01	96.45	96.46	-
	STARE	75.53	92.81	94.23	-

Specifically, particle optimized match filter utilized by Sreejini and Govindan [214] gained the maximum precision in the drive dataset and the peak correctness across the DRIVE and STARE dataset. In STARE dataset, the MF method with FDOG (Zhang et al. [210]) achieved a specificity of 0.9753. Furthermore, the improved matched filter proposed by Odstrcilik et al. [212] obtained the highest AUC for both datasets. Due to these outcomes, the matched filtering algorithm introduced by Sreejini and Govindan [214] is considered a prominent and noteworthy approach within this study.

2.3.2. Region-based Segmentation

The region-based segmentation approach for pixel segmentation is utilized for advanced region subdivision [216]. Initially, seed points are selected for the process, followed by growing regions specific to the blood vessels and formulating a proper stopping rule. The challenge lies in setting an appropriate stopping rule to halt the growth when no more pixels meet the inclusion criteria. Nevertheless, the region-grown vessel segments are effectively segmented and post-processed.

Elena Martínez-Pérez et al. [217] propose a method based on the second derivative of the intensity image to address image intensity variation issues. Their two-stage region growing approach focuses on low gradient regions in the primary stage, allowing accelerated growth in the backdrop areas. The method yields promising results for fluorescein and red-free retinal images.Table 2.3 presents a comparison of region-growing-based segmentation algorithms, with values in italics indicating the best method. Roychowdhury et al.'s [220] iterative region-growing method with a novel stopping rule outperforms all other methods listed in Table 2.3, achieving peak values of Sensitivity, Specificity, Accuracy, and AUC in both the DRIVE and STARE datasets.

Table 2.3: Performance Evaluation of Retinal Vessel Segmentation Using Region Growing Techniques Based on Sensitivity, Specificity, and Accuracy Metrics.

Author	DATASET	Sensitivity	Accuracy	Specificity	AUC
Fraz et al.- Multiscale Gabor and morphological features [203]	DRIVE	77.63	94.70	97.23	-
	STARE	89.51	93.48	93.84	-
Elena Martínez-Pérez et al.- Region growing [217]	DRIVE	63.89	91.81	-	-
Qian Zhao et al.- level set and region growing [218]	DRIVE	73.54	94.77	97.89	-
Lázár and Hajdu - vector similarity and region growing [219]	DRIVE	-	94.54	-	-
	STARE	-	94.92	-	-
Roychowdhury et al.- 'Iterative vessel segmentation [220]	DRIVE	73.90	94.90	97.80	96.70
	STARE	73.20	95.60	98.40	96.70

2.3.3. Multi-scale approaches

Blood vessel characteristics are acquired at various scales by adjusting the sigma values in the filters' standard deviation. These extracted features are subsequently combined to produce a well-defined, segmented image of blood vessels. A post-processing step is then applied to binary segment the blood vessel structures in the image.

Frangi et al. [221] introduced a vessel enhancement filter based on multi-scale Hessian Eigen analysis, aimed at reducing noise and suppressing background. The effectiveness of this approach was assessed on synthetic and real angiograms.

An algorithm based on scale-space theory was developed by Anzalone et al. [223] to segment blood vessels in retinal red-free images. The algorithm employs a modular supervised approach, using a supervised optimization procedure to find the appropriate scale factor and threshold for vessel segmentation. Farnell et al. [224] introduced the Multi-scale Line Operator, which creates a Gaussian pyramid with equal weights at each scale. The results from different scales are combined through summation, thresholding, and a region-growing method to eliminate noise.

For vessel medial line extraction, Moghimirad et al. [225] proposed a weighted 2D multi-scale medialness function. The extracted medial lines, along with the calculated vessel radius, are utilized for vessel reconstruction. Läthén et al. [226] presented a methodology that combines both line and edge detection using multi-scale quadrature filters, providing clear and distinct vessel wall detection. This method is suitable for 3D images with minimal computational complexity. Nguyen et al. [227] addressed certain drawbacks by employing line detectors with varying lengths and

scales, which are linearly combined to enhance vessel separation while enabling automatic vascular caliber measurement. However, this approach fails to eliminate false vessels near the optic disc and pathologies. Su et al. [228] proposed an adaptive multi-scale morpho-Gaussian filter to enhance linear features and vessels at junctions. Angular bisectors divide the junction region into sub-images, and enhancement is performed separately and then recombined based on the correlation matrix and Hessian matrix. This technique provides useful vessel information, although it has its limitations. The k-means clustering algorithm is initialized and a texton dictionary is constructed during training using essential points obtained from the above. Subsequently, during testing, a 1-NN (neural network) is employed to classify vessel and non-vessel pixels. Validation is conducted on the DRIVE database, where the system achieves a maximum sensitivity of 78.12%. Table 2.4 consolidates the multi-scale segmentation approach explained earlier, with improved performance metrics displayed.

Table 2.4: Comparison of Retinal Vessel Segmentation Results Obtained from Different Multi-Scale Methods, Showing Key Performance Indicators to Assess Accuracy and Robustness.

Author	DATASET	Sensitivity	Accuracy	Specificity	AUC
Fraz et al.- Multiscale Gabor and morphological features [203]	DRIVE	77.63	94.70	97.23	-
	STARE	89.51	93.48	93.84	-
Anzalone et al.- Modular supervised algorithm [223]	DRIVE	-	94.19	-	-
Farnell et al.- multiscale line operators [224]	STARE	-	-	-	94.00
Moghimirad et al.- Medialness function [225]	DRIVE	-	96.59	-	95.80
	STARE	-	97.56	-	96.78
Nguyen et al. multi-scale line detection [227]	DRIVE	-	94.07	-	-
	STARE	-	93.24	-	-
Su et al.- Gaussian function and Hessian information [228]	DRIVE	-	93.44	-	-
Saffarzadeh et al.- K-means clustering [229]	DRIVE	-	93.83	-	-
	STARE	-	94.83	-	94.31
Zhang et al.- multi-scale textons [230]	DRIVE	78.12	95.04	96.68	-

2.3.4. Active contour model-based approaches

Active contour models, also known as curves or snakes, are capable of autonomous and self-adapting movement within an image sphere. These curves are influenced by internal forces from

the contour itself and external forces derived from distinct image features. The objective is to make the curves adjust to object boundaries or other desired features present in the image. The accuracy of these models relies on their ability to fit the contour effectively.

Incorporating the deformable contour model (snake model) with blood vessel-specific properties, Espona et al. [231] attempted to segment retinal vessel morphology. However, this approach did not yield improved accuracy in vessel segmentation. Notably, this technique demonstrates robustness to noise and achieves accurate vessel width measurements. Kee et al. [233] adopted an active contour model for retinal vascular detection. Table 2.5 displays the top-performing parameters found from the STARE and DRIVE datasets.

Table 2.5: Quantitative evaluation of retinal vessel segmentation performance obtained using various Active Contour Model–based approaches. The table compares key performance metrics—such as accuracy, sensitivity, specificity, and Dice coefficient—demonstrating the effectiveness of each method in accurately delineating retinal vasculature from fundus images.

Author	DATASET	Sensitivity	Accuracy	Specificity	AUC
Fraz et al. [203]	DRIVE	77.63	94.70	97.23	-
	STARE	89.51	93.48	93.84	-
Espona et al. [231]	DRIVE	74.36	93.52	96.15	-
Al-Diri et al. [232]	DRIVE	72.82	-	95.51	-
	STARE	75.21	-	96.81	-
Zhao et al. [234]	DRIVE	74.20	95.40	98.20	86.20
	STARE	78.00	95.60	97.80	87.40
Kovacs and Hajdu [235]	DRIVE	74.50	94.94	97.93	97.22
	STARE	80.34	96.10	97.86	98.36
Zhao et al. [236]	DRIVE	78.20	95.70	97.90	88.60
	STARE	78.90	95.60	97.80	88.50

2.3.5. Unsupervised segmentation approaches

Unsupervised segmentation methods involve assigning datasets to segments without prior knowledge of clusters, enabling the discovery of patterns in unlabeled data. This approach operates without the need for input labels or ground truth images. Instead, it automatically groups pixels according to specific criteria, like distance, leading to efficient segmentation of blood vessel structures. To obtain accurate blood vessel representations, post-processing or the integration of the segmented outcomes with another algorithmic approach is carried out.

Tolias and Panas [237] introduced a fuzzy C-means (FCM) clustering algorithm designed for the segmentation of blood vessels in retinal angiograms. The algorithm's key innovation lies in the

determination of membership functions for both normal and abnormal vessels, which commences from the optic disc boundary. This unique approach eliminates the need for parametric tuning and initialization, distinguishing it from other methods. However, its effectiveness diminishes when attempting to detect vessels with narrow widths and low contrast.

In an effort to overcome these limitations, Kande et al. [238] proposed a novel spatially weighted FCM clustering technique that incorporates several preprocessing steps. These steps encompass non-uniform illumination correction, contrast enhancement using MF-based techniques, and the utilization of connected component labeling to pinpoint the vascular tree. Ng et al. [239], on the other hand, employed a maximum Likelihood Estimator strategy involving multi-scale Gaussian filters and noise models. The aim was to estimate crucial vessel attributes such as width, contrast, and direction at each individual image point. Subsequently, vessel centerlines and likelihoods were distinguished from the assessed vessel parameters, and a segmentation approach based on merging centerlines with the width parameter was implemented.

Villalobos-Castaldi et al. [240] introduced an alternative method rooted in local entropy thresholding for blood vessel segmentation. By leveraging the grey-level co-occurrence matrix (GLCM) to calculate the threshold, this approach achieved a remarkable computational time of merely three seconds, demonstrating a peak accuracy of 97.59%.

Turning to unsupervised techniques, Allen et al. [241] proposed a unique vascular segmentation method utilizing the Tramline algorithm to generate initial vessel centrelines. Non-parametric (NP) Windows estimators were subsequently applied to these centrelines to refine the delineation of blood vessels, with the response of the Windows estimators enhancing the approach's robustness. Oliveira et al. [242] took a different route by amalgamating the responses of multiple vessel enhancement filters using a weighted mean and median ranking (MR) strategy. The combined responses were then subjected to segmentation via the oriented region-scalable fitting energy (ORSF) deformable model, fuzzy C-means (FCM), and thresholding. Notably, the MR combination and thresholding demonstrated superior performance within the STARE dataset.

Câmara Neto et al. [243] adopted an adaptive local thresholding approach, incorporating spatial dependency and likelihood measurements, to approximate a coarse vessel map post pre-processing. Subsequent refinements to this coarse segmentation were made through curvature

analysis and morphological reconstruction, effectively mitigating pixel mislabelling and enhancing the accuracy of this unsupervised method.

In Table 2.6, you can find the performance metrics of the unsupervised algorithms for both the DRIVE and STARE datasets. The highest values are indicated in italics. The ophthalmologist's observation shows the highest sensitivity (SN) for the STARE dataset and the highest specificity for the DRIVE dataset. It is evident that Oliveira et al.'s [242] unsupervised method, which combines MR and thresholding, performs remarkably well on the STARE dataset, achieving the highest specificity, precision, and AUC.

Table 2.6: Evaluation of the Segmentation Performance of Retinal Vessels Using Unsupervised Segmentation Approaches.

Author	DATASET	Sensitivity	Accuracy	Specificity	AUC
Fraz et al. [203]	DRIVE	77.63	94.70	97.23	-
	STARE	89.51	93.48	93.84	-
Kande et al. [238]	DRIVE	-	98.11	-	95.18
	STARE	-	89.76	-	92.98
Ng et al. [239]	STARE	70.00	-	95.30	-
Villalobos-Castaldi et al. [240]	DRIVE	96.49	97.59	94.80	
Allen et al. [241]	DRIVE	-	93.42	-	-
Oliveira et al. [242]	DRIVE	79.88 (ORSF) 91.06 (FCM) 86.44 (MR)	93.56 94.02 94.64	95.25 94.31 95.56	91.18 91.18 95.13
	STARE	83.77 (ORSF) 80.49 (FCM) 82.54 (MR)	94.29 94.46 95.32	95.09 95.92 96.47	91.70 87.94 95.44
Camara Neto et al. [243]	DRIVE	78.06	87.18	96.29	-
	STARE	83.44	88.94	94.43	-

2.3.6. Supervised segmentation approaches

Within this approach, the algorithm's proficiency in segmenting blood vessels stems from its training on a dataset of input images and corresponding ground truth data. After this training phase, the algorithm becomes applicable to any retinal image for testing purposes. Given that the algorithm's design is rooted in pre-existing categorized data, its overall performance tends to be enhanced, resulting in superior segmentation outcomes. During the training process, the input medical images undergo processing to extract pertinent features. These features are then combined with their corresponding ground truth labels to educate the machine learning classifiers, thereby creating a predictive model. When confronted with unlabeled feature vectors during the testing phase, this model demonstrates its ability to accurately segment blood vessels.

Sinthanayothin et al. [244] implemented a multilayer perceptron to accomplish vessel segmentation, utilizing the edge strength measure from the first principal component as input. However, the neural network's efficacy enhancement was somewhat restricted when subjected to assessment using a localized dataset. Niemeijer et al. [245] introduced an alternative method employing a k-NN algorithm trained with a feature vector containing green plane values and diverse responses from the matched filter for each pixel. This approach resulted in the creation of a binary vessel tree through the estimation of a probability map. Nonetheless, this binary segmentation technique encountered difficulties in accurately identifying thin vessels, particularly in instances where the optic disc was present in the testing images. Through a sequential forward selection process, the authors determined a set of 27 features derived from segmented convex regions. The efficacy of these features was evaluated on the STARE and Utrecht databases.

Table 2.7: Evaluation of the Segmentation Performance of Retinal Vessels Using Supervised Segmentation Approaches.

Author	DATASET	Sensitivity	Accuracy	Specificity	AUC
Farz et al. [203]	DRIVE	77.63	94.70	97.23	-
	STARE	89.51	93.48	93.84	-
Sinthanayothin et al. [244]	Local	83.30	-	91.00	-
Staal et al. [246]	DRIVE	-	94.42	-	95.20
	STARE	-	95.16	-	96.14
Soares et al. [248]	DRIVE	-	94.66	-	96.14
	STARE	-	94.80	-	96.71
Ricci and Perfetti [249]	DRIVE	-	95.63	-	95.58
	STARE	-	95.84	-	96.02
Osareh and Shadgar [250]	DRIVE	-	-	-	96.50
Lupascu et al. [251]	DRIVE	72.00	95.97	-	95.61
Marin et al. [252]	DRIVE	70.67	94.52	98.01	95.88
	STARE	69.44	95.26	98.19	97.69
Fraz et al. [203]	DRIVE	75.25	94.76	97.22	-
	STARE	76.04	95.79	98.12	-
Rahebi and Hardalac [253]	DRIVE	73.65	95.64	97.07	94.61
	STARE	69.02	95.27	97.07	94.62
Aslani and Sarnel [254]	DRIVE	75.45	95.13	98.01	96.82
	STARE	75.56	96.05	98.37	97.89
Zhang et al. [230]	DRIVE	78.61	94.66	97.12	97.03
	STARE	78.82	95.47	97.29	97.40
Zhu et al. [255]	DRIVE	71.40	96.07	98.68	90.86
	RIS	72.05	96.28	97.66	-

2.4. Vessel's Tortuosity Measurement

Increased tortuosity has been documented in numerous medical conditions and genetic disorders, such as systemic hypertension [258, 260, 268, 279, 283], diabetic retinopathy [264], adolescent type 1 diabetes [262, 272], plus disease in retinopathy of prematurity (ROP) [288, 289, 290, 291, 292, 293, 276], gestational diabetes mellitus [294], familial retinal arteriolar tortuosity (fRAT) [295, 296], chronic anemia [297], and facioscapulohumeral muscular dystrophy [298]. Most studies that analyze vessel tortuosity utilize digital retinal images, which are subsequently processed to evaluate quantitative vascular tortuosity parameters. Table 2.8 presents an overview of the different formulas employed for this purpose.

Table 2.8: Variations in Tortuosity Indices as Utilized in Existing Literature.

Tortuosity Index	Expression	References
$\frac{Total\ Square\ Curvature}{Arc\ Length}$	$\frac{\int_a^b \frac{\left[x'(t)\,y''(t)-x''(t)\,y'(t)\right]^2}{\left[\left(x'(t)\right)^2+\left(y'(t)\right)^2\right]^3}\,dt}{\int_a^b \sqrt{\left(x'(t)\right)^2+\left(y'(t)\right)^2}\,dt}$	[256-270]
$\frac{Arc\ length}{Chord\ length}$	$\frac{\int_a^b \sqrt{\left(x'(t)\right)^2+\left(y'(t)\right)^2}\,dt}{\sqrt{\left(x(a)-x(b)\right)^2+\left(y(a)-y(b)\right)^2}}$	[171-282]
$\frac{Arc\ length}{Chord\ length}-1$	$\frac{\int_a^b \sqrt{\left(x'(t)\right)^2+\left(y'(t)\right)^2}\,dt}{\sqrt{\left(x(a)-x(b)\right)^2+\left(y(a)-y(b)\right)^2}}-1$	[267-270, 283-285]
$Total\ Curvature$	$\int_a^b \left\lvert \frac{x'(t)\,y''(t)-x''(t)\,y'(t)}{\left[\left(x'(t)\right)^2+\left(y'(t)\right)^2\right]^{3/2}} \right\rvert dt$	[269, 270, 282, 286]
$Total\ Square\ Curvature$	$\int_a^b \frac{\left[x'(t)\,y''(t)-x''(t)\,y'(t)\right]^2}{\left[\left(x'(t)\right)^2+\left(y'(t)\right)^2\right]^3}\,dt$	[269, 270]

$\frac{Total\ Curvature}{Arc\ Length}$	$\frac{\int_a^b \left\| \frac{x'(t)\,y''(t) - x''(t)\,y'(t)}{\left[\left(x'(t)\right)^2 + \left(y'(t)\right)^2\right]^{3/2}} \right\| dt}{\int_a^b \sqrt{\left(x'(t)\right)^2 + \left(y'(t)\right)^2}\ dt}$	[269, 270]
$\frac{Total\ Curvature}{Chord\ Length}$	$\frac{\int_a^b \left\| \frac{x'(t)\,y''(t) - x''(t)\,y'(t)}{\left[\left(x'(t)\right)^2 + \left(y'(t)\right)^2\right]^{3/2}} \right\| dt}{\sqrt{\left(x(a) - x(b)\right)^2 + \left(y(a) - y(b)\right)^2}}$	[269, 270]
$\frac{Total\ Square\ Curvature}{Chord\ Length}$	$\frac{\int_a^b \frac{\left[x'(t)\,y''(t) - x''(t)\,y'(t)\right]^2}{\left[\left(x'(t)\right)^2 + \left(y'(t)\right)^2\right]^3} dt}{\sqrt{\left(x(a) - x(b)\right)^2 + \left(y(a) - y(b)\right)^2}}$	[269, 270, 287]

2.5. Advantages of the Proposed Technique over Existing Methods

Image processing is a rapidly evolving field, constantly seeking innovative techniques to improve image quality, enhance visual features, and solve complex problems. In this article, we will discuss the advantages of some proposed image processing techniques over existing methods, showcasing their potential to revolutionize various applications, from medical imaging to computer vision.

- Enhanced Accuracy: The proposed technique may offer improved accuracy in segmenting blood vessels compared to existing methods, resulting in more precise and reliable results.
- Robustness: The technique may exhibit robustness to various image qualities, noise, and artefacts, ensuring consistent performance across different datasets and imaging conditions.
- Reduced Computational Complexity: By employing efficient morphological operations, the proposed method may reduce computational complexity, making it faster and more suitable for real-time or large-scale applications.
- Minimal User Intervention: The technique might require less manual intervention or parameter tuning, thereby streamlining the segmentation process and reducing the burden on the user.

- Adaptability to Diverse Vascular Structures: The proposed method may demonstrate adaptability to different types of vascular structures, such as varying vessel sizes, shapes, and orientations.
- Handling of Challenging Cases: The technique could excel in handling challenging cases, such as complex vessel networks, vessel intersections, and regions with low contrast, where other methods might struggle.
- Generalizability: The proposed approach may achieve superior generalization capabilities, allowing it to perform well on unseen data or datasets from different imaging modalities.
- Validation with Comparative Studies: The technique may be backed by rigorous comparative studies with existing methods, demonstrating statistically significant improvements in segmentation performance.

It is essential to note that the specific advantages of the proposed technique will depend on the details of the methodology and the context of the application. Comparative evaluations and validation against existing state-of-the-art methods will further substantiate its superiority.

2.6. Conclusion

In conclusion, this literature review has provided a comprehensive overview of the advancements and trends in the field of ophthalmological disorder detection through the application of medical image processing techniques. The studies surveyed in this review collectively underscore the significance of leveraging cutting-edge technology to enhance the accuracy, efficiency, and accessibility of diagnosing various eye conditions.

Throughout the review, it became evident that medical image processing has evolved into a pivotal tool for early and precise detection of ophthalmological disorders. The integration of advanced algorithms, machine learning, and deep learning methodologies has enabled researchers and clinicians to achieve remarkable progress in automating the diagnostic process. From the detection of diabetic retinopathy to age-related macular degeneration, these technologies have demonstrated the potential to surpass human performance in some instances, thereby reducing the burden on healthcare professionals and expediting patient care.

Moreover, the reviewed literature highlighted the growing importance of robust datasets in training and validating these detection models. Annotated image datasets have paved the way for the

development of sophisticated algorithms capable of identifying subtle nuances and patterns within medical images, enabling accurate differentiation between healthy and diseased ocular structures.

Despite the promising outcomes discussed in the literature, it is essential to acknowledge the challenges that remain. Standardization of data acquisition protocols, model interpretability, and real-world applicability are areas that demand further attention. Additionally, the ethical implications of integrating automated systems into clinical workflows necessitate ongoing consideration.

Although many studies apply image-processing and deep learning to detect eye diseases (DR, AMD, glaucoma, ROP, DME, etc.), important gaps remain in translating models from lab prototypes to reliable, clinically useful systems. Key weaknesses are: limited and biased datasets, poor generalization across devices and populations, inadequate clinical validation and interpretation, insufficient handling of small/rare lesions, and lack of practical deployment considerations (efficiency, privacy, regulatory readiness).

In summary, this literature review has illuminated the strides made in ophthalmological disorder detection using medical image processing techniques. The convergence of medical expertise and technological innovation holds immense potential for revolutionizing the field of ophthalmology. As we move forward, collaborative efforts between researchers, clinicians, and technologists will be instrumental in refining existing methodologies, addressing challenges, and ultimately improving patient outcomes within the realm of ocular health.

Chapter III

METHODOLOGY

The input retinal fundus RGB datasets are being analyzed to observe the diseases like Diabetes, Hypertension, ROP, etc., and stages of DR. The images are being rendered by implementing different classification algorithms to identify those disorders. The overall processing algorithm is being divided into four fundamental steps, which are the image pre-processing, feature segmentation, extraction of those segmented features, and finally, validation of the results. Pre-processing includes image acquisition, filtering, color normalization, and conversion, image edge, and quality enhancement. In the segmentation part, we used binarization, median filtering, morphological analysis, skeletonization, etc. Next, we extracted the segmented features in terms of intensity or grayscale values, textures, optic disk features, lesion characteristics, geometric features, etc. Finally, in the validation part, we validated our results with ground truth.

3.1. Introduction

The realm of medical fundus image processing resides within the specialized domain of computer vision, directing its attention towards the scrutiny and extraction of pertinent data from images depicting the posterior segment of the eye. More specifically, this pertains to the intricate analysis of the retina and its intricately intertwined network of blood vessels. The implications of this field extend significantly, as it plays a pivotal role in both the diagnosis and continuous monitoring of a spectrum of ocular disorders. These encompass a range of conditions such as diabetic retinopathy, macular degeneration, Retinopathy of Prematurity (ROP), and glaucoma. Within this context, the ensuing chapter introduces an algorithm meticulously designed to autonomously quantify a diverse array of retinal attributes closely associated with the aforementioned afflictions. The visual representation of our proposed approach is succinctly delineated in Figure 3.1, illuminating the constituent components through a comprehensive block diagram.

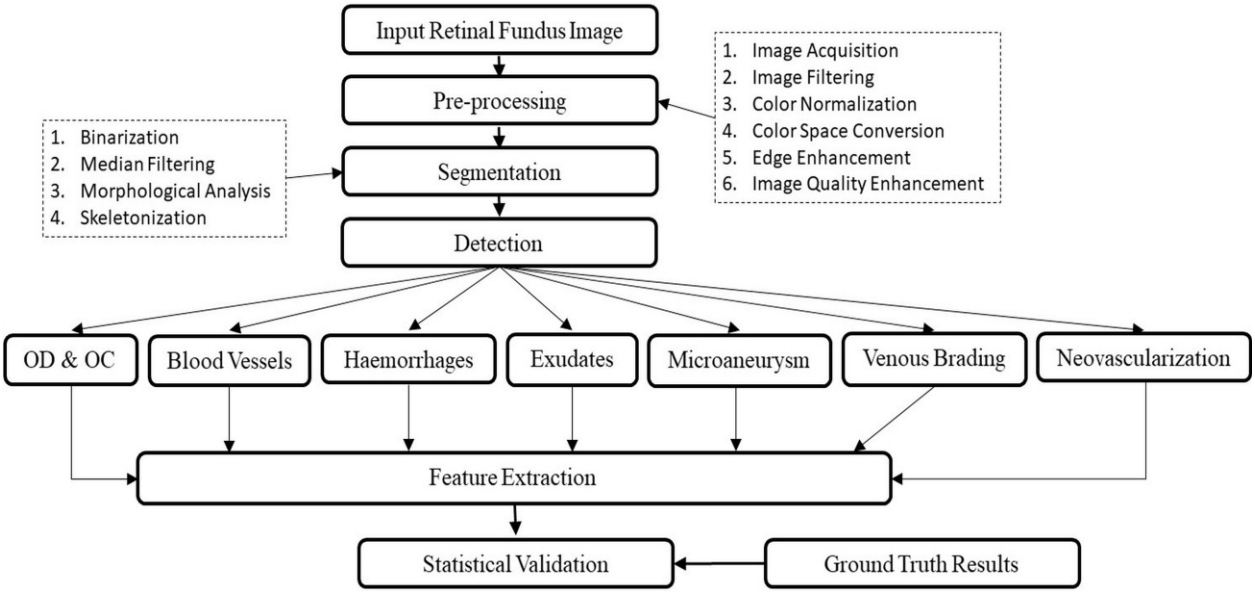

Fig 3.1: The diagram outlines the overall workflow comprising image acquisition, pre-processing, segmentation, detection of retinal features (OD/OC, blood vessels, haemorrhages, exudates, microaneurysms, venous beading, and neovascularization), followed by feature extraction and statistical validation using ground truth data.

3.2. Image Pre-Processing

Image pre-processing refers to a series of techniques applied to digital images before they undergo further analysis or processing. The goal of image pre-processing is to enhance the quality of the image, reduce noise or artifacts, and extract relevant features to improve the performance of subsequent algorithms or tasks such as image classification, object detection, or image segmentation. Here are some commonly used techniques in image pre-processing:

3.2.1. Image Acquisition

Image acquisition is the process of capturing high-quality images of the fundus (the back part of the eye) using specialized equipment called fundus cameras. These cameras are designed to provide a detailed view of the retina, blood vessels, optic disc, and other structures of the eye. Here are the key aspects of image acquisition in medical fundus imaging:

- Fundus Camera: The fundus camera stands as a specialized apparatus that integrates optical components and sensors tailored to capture images of the fundus. Diverse configurations, including tabletop systems and handheld devices, accommodate distinct needs. Operating in color or grayscale modes, these cameras may also incorporate features like infrared or fluorescein angiography to capture specific retinal details.
- Patient Preparation: Before fundus image capture, patients might need to undergo certain preparations. This can involve pupil dilation achieved through eye drops, expanding the pupil's size to facilitate wider retinal visibility. This dilation substantially enhances image quality. Additionally, patients could be instructed to fixate their gaze on a designated target to ensure proper alignment during image acquisition.
- Image Settings: Fundus cameras provide an array of adjustable settings to optimize image quality and acquire targeted information. These settings encompass the field of view (FOV), focus adjustment, exposure duration, aperture dimensions, and illumination intensity. Choosing optimal settings depends on the examination's specifics and the unique characteristics of the patient's eye.
- Image Capture: Once the patient is prepared and the camera configured, the fundus image is captured. The camera is precisely aligned with the patient's eye, ensuring the

complete inclusion of the relevant fundus area. Following alignment, the camera captures the image, which is conventionally stored digitally for subsequent analysis and processing.

- Image Quality Control: Post image capture, meticulous evaluation of image quality is imperative. Quality control assessments encompass aspects such as focus, illumination, clarity, and the presence of artifacts. If image quality falls short, the process may be repeated to procure a more accurate depiction of the fundus.
- Data Management: Fundus images are customarily stored and managed in digital formats to facilitate efficient access and analysis. These images may be housed in specialized medical imaging databases or integrated into electronic medical record (EMR) systems, simplifying retrieval and facilitating comparisons during subsequent follow-up examinations.

Image acquisition is a critical step in medical fundus imaging as the quality and clarity of the acquired images directly impact the subsequent analysis and diagnosis of eye diseases. Skilled operators, proper equipment maintenance, and adherence to standardized protocols are important factors in ensuring accurate and reliable image acquisition.

3.2.2. Image Filtering

Image filtering is a fundamental technique in image processing that involves modifying the pixel values of an image based on a specific filtering operation. Filtering can be used to enhance images, remove noise, extract features, or apply various image transformations. One of the most commonly used filtering methods is convolution, which involves applying a kernel or filter matrix to each pixel of the image. Here are the key aspects of image filtering:

3.2.2.1. Median Filtering:

The median filter is a statistically-based nonlinear signal processing technique where the noise parameters of the dataset are converted to the neighboring median parameters. The output of the median filter can be calculated by equation 3.1.

$$res\_med(x,y) = filter\_med\{func(x-i, y-j), i,j \in mask\} \quad (3.1)$$

Here

$func(x,y), res_{med(x,y)} are\ respectively\ the\ input\ and\ output\ datasets,' mask' is\ the\ 2-dimensional\ mask\ with\ n \times n\ size\ with\ n = odd\ parameters\ (3 \times 3, 5 \times 5\ etc.)$.

As the median filter is a nonlinear filter, its mathematical analysis is relatively complicated for randomized noise images. For the image where the average noise is zero in a normal distribution, the median filter noise variance is approximately.

$$\sigma_{mid} = \frac{1}{4nf^2(\bar{n})} \approx \frac{\sigma_i^2}{n+\frac{\pi}{2}-1}.\frac{\pi}{2} \tag{3.2}$$

Where $\sigma_i^2$is the variance, n is the range of the median filter and $f^2(\bar{n})\ defines\ the\ noise\ function. noise\ of\ the\ averaging\ filter$ can be measured from equation 3.3.

$$\sigma_0^2 = \frac{1}{n}\sigma_i^2 \tag{3.3}$$

3.2.2.2. Gaussian Filtering:

Gaussian filter, a linear class windowed filter, is typically used for image blurring or noise reduction. The unshaped masking that is the edge can be detected simply by subtracting two filtered results from each other. The Gaussian or normal distribution is a probability function that is referred to as a bell function due to its shape. The most common function formula is shown in equation 3.4.

$$G(x,y) = \frac{1}{2\pi\sigma^2} e^{\{-(x^2+y^2)/2\sigma^2\}} = G(x).G(y) \tag{3.4}$$

Equation 3.4 explains that the 2D Gaussian filter is separable. To obtain the Gaussian filtering of the 2D image, the following algorithm is employed.

- Measure 1D window function coefficient $G_n^{/}$.
- Run a filter across every row as an 1D data.
- Run another 1D filter in every column of the image.

The 2D low-pass Gaussian kernel with a window of size $[2n + 1] \times [2n + 1]$ is compressed to 1D filter kernel with a window size of $[2n + 1]$. This suggests a higher speed of response to the images with larger size as the order is reduced from N^2 to N.

3.2.2.3. Convolution

Convolution, an arithmetic function, is commonly referred to as a kernel or filter is a matrix of small size that is used to slide over the fundus RGB data and evaluate the dot products between the convolution matrix and associated pixel intensity within the fundus data. The subsequent value is assigned to the central pixel of the kernel's footprint. This process is repeated for all pixels in the image, resulting in a filtered output. Here's a step-by-step process for image filtering using convolution:

- Kernel Definition: The initial stage involves the establishment of a filter kernel. This kernel, represented by a small matrix of numerical values, dictates the weightings to be employed on the image's pixels. The dimensions of the kernel dictate the scope of the nearby region considered during the filtering process. Common instances include kernels for blurring, edge detection, and sharpening.
- Image Padding: To ensure maintenance of the input image's dimensions in the output, padding is frequently employed. Padding encompasses the addition of supplementary rows and columns of pixels surrounding the image's borders. Frequently used padding methods encompass zero-padding and replication of the image's border pixels.
- Convolution Process: For each individual pixel within the image, the convolution operation is carried out. The kernel's central point is positioned over the present pixel, and a component-wise product is computed between the kernel and corresponding pixel values within the immediate neighborhood. The products are summed to generate the resultant filtered pixel value. This process is iterated for every pixel in the image.
- Managing Image Boundaries: At the image's edges, the kernel may extend beyond the image's confines, creating undefined positions. Multiple strategies exist to manage this situation, including zero padding, mirrored padding, and periodic padding. The chosen approach hinges on the specific application and the desired behavior at the image boundaries.

- Output Image: The outcome of the convolution operation materializes as a filtered image. Each pixel in the resulting image represents a weighted amalgamation of the associated pixel values from the input image, confined within the localized region specified by the kernel.

Let's consider a grayscale image I with dimensions $M \times N$ and a filter kernel K with dimensions $K \times K$. The filtered output image F may be stated as:

$$Fig(i,j) = add(add(Img(x,y) * Karnel(i-x, j-y))) \quad (3.5)$$

where:

$Fig(i,j)$ represents the pixel value at position (i,j) in the filtered image Fig.

$Img(x,y)$ represents the pixel value at position (x,y) in the original image Img.

$Karnel(i-x, j-y)$ represents the value of the filter kernel K at relative position $(i-x, j-y)$.

The outer summation iterates over the rows of the filter kernel K, while the inner summation iterates over the columns. The resulting value is assigned to the corresponding pixel location (i,j) in the filtered image.

It's important to note that this expression assumes zero padding for the image I. If you want to apply different padding methods, you would need to adjust the range of the summation accordingly.

For color images, the same process is applied to each color channel separately, with separate filter kernels if desired, and the resulting filtered images are recombined to form the final output.

It's worth noting that the specific convolution technique can vary based on the application and desired filtering effect. Additionally, different variants of convolution, such as separable convolution or convolution with different filter sizes or shapes, may be employed for specific purposes.

Convolution-based image filtering is versatile and can be used for a wide range of applications, including noise reduction, image enhancement, edge detection, texture analysis, and feature

extraction. The choice of the filter kernel plays a crucial role in achieving the desired image-filtering effect.

3.2.2.4. Kernel Design:

The design of the kernel for image filtering depends on the specific filtering operation you want to perform. Different kernels have different characteristics and are suitable for various image-processing tasks. Here are a few examples of common kernel designs for image filtering:

- *Gaussian Kernel:* The Gaussian kernel is widely used for blurring or smoothing operations. It follows a bell-shaped curve and reduces high-frequency noise in the image. The kernel values are computed based on the Gaussian distribution. The size and standard deviation of the kernel determine the amount of blurring applied. The mathematical expression is shown in equation 3.6.

$$K(x) = (1 / (\sigma\sqrt{2\pi})) * exp(-x^2 / (2\sigma^2)) \quad (3.6)$$

  In this expression, x represents the input variable, σ represents the standard deviation. The term exp refers to the exponential function, and "π" represents the mathematical constant pi. The numerator (1) and denominator $(\sigma\sqrt{2\pi})$ ensure that the kernel integrates to 1 over its entire range, thus maintaining its probability density function properties.

- *Sobel Operator:* The Sobel operator is a commonly used edge detection operator in image processing. It is used to highlight the edges in an image by calculating the gradient magnitude at each pixel. The Sobel operator consists of two separate convolution kernels, one for horizontal edge detection and the other for vertical edge detection. The gradient filter in X-direction (G_x) finds the border in that direction whereas the filter in Y-direction finds the border in Y-direction. The both filters are convolved with the image to obtain the gradient magnitude and direction.

  The mathematical expressions for the horizontal and vertical Sobel kernels are as follows:

$$G_x = \begin{bmatrix} -1 & 0 & +1 \\ -2 & 0 & +2 \\ -1 & 0 & +1 \end{bmatrix} \quad \& \quad G_y = \begin{bmatrix} -1 & -2 & -1 \\ 0 & 0 & 0 \\ +1 & +2 & +1 \end{bmatrix} \quad (3.7)$$

Utilizing the Sobel operator on an image entails convolving the image with two separate kernels. The resulting outputs are combined to calculate both the gradient magnitude and direction at each pixel's position. Usually, the gradient magnitude is ascertained by taking the square root of the sum of squared gradients along both the horizontal and vertical axes:

$$Gradient\ magnitude = |G| = sqrt(G_x^2 + G_y^2) \quad (3.8)$$

The gradient direction can be calculated using the $arctan$ function:

$$Gradient\ direction = atan2(Gy, Gx) \quad (3.9)$$

- *Laplacian kernel:* The Laplacian kernel is a commonly used kernel in image processing and computer vision for edge detection. It is defined as the second derivative of the Gaussian function. Mathematically, the Laplacian kernel is expressed as:

  $$K(x, y) = \Delta^2\ G(x, y) \quad (3.10)$$

  where $K(x, y)$ represents the Laplacian kernel at position (x, y), Δ^2 represents the Laplacian operator (second derivative), and $G(x, y)$ represents the Gaussian function.

- *Box Blur Kernel:* The Box Blur Kernel is a type of image filter used to achieve a blurring effect by averaging the pixel values within a specified neighborhood. The kernel is a square matrix with equal dimensions, and each element in the matrix represents a weight applied to the corresponding pixel in the neighborhood.

  To express the Box Blur Kernel mathematically, let's assume the kernel size is $n \times n$, where n is an odd integer. The center of the kernel is at the position $(0, 0)$.

  The mathematical expression of the Box Blur Kernel can be represented as follows:

  $$K(i, j) = \frac{1}{n^2}, \quad for \quad -\frac{n-1}{2} \leq i,\ j \leq \frac{n-1}{2} \quad (3.11)$$

  where $K(i, j)$ represents the weight at position (i, j) in the kernel. The weights are set to be equal to $\frac{1}{n^2}$ for all valid positions within the kernel, ensuring that the total sum of weights in the kernel is equal to 1.

- *Emboss Kernel:* The Emboss kernel is a 3×3 matrix used in image processing operations to create an embossed effect. It is typically applied as a convolutional filter to an image. The mathematical expression of the Emboss kernel can be represented as:

$$Emboss\ Kernel = \begin{bmatrix} -2 & -1 & 0 \\ -1 & 1 & 1 \\ 0 & 1 & 2 \end{bmatrix} \tag{3.12}$$

  In image convolution, the kernel is applied by taking the weighted sum of the neighboring pixels in the image with the corresponding elements in the kernel matrix. This process is repeated for each pixel in the image to obtain the embossed effect.

- *High Pass Filter Kernel:* A high-pass filter kernel can be represented mathematically using a $2D$ matrix. Let's denote the kernel matrix as H, which will have a size of $n \times n$ (where n is an odd integer). Each element of the matrix represents the weight assigned to a specific pixel in the input image.

  The center of the kernel matrix corresponds to the pixel being processed, and the values in the matrix control how much the surrounding pixels contribute to the output. In a high-pass filter, the central pixel is given a negative weight, and the surrounding pixels have positive weights.

  Here's an example of a high-pass filter kernel matrix:

$$H = \begin{bmatrix} -1 & -1 & -1 \\ -1 & 8 & -1 \\ -1 & -1 & -1 \end{bmatrix}$$

  In this example, the central pixel has a weight of 8, and its surrounding pixels have weights of -1. When this kernel is convolved with an input image, it enhances the edges and details by subtracting the average intensity of the surrounding pixels from the central pixel.

  To apply this kernel to an image, you would perform a convolution operation, where each element of the kernel is multiplied by the corresponding pixel in the input image and then summed up. The resulting sum is the new value for the central pixel in the output image. This process is repeated for every pixel in the image to obtain the filtered output.

3.2.2.5. Spatial Filtering

Spatial filtering is a mathematical technique used in image processing and computer vision to enhance or modify images by applying filters in the spatial domain. The main idea behind spatial filtering is to perform a convolution operation between the input image and a filter kernel.

Let's consider a grayscale image, which can be represented as a two-dimensional matrix, where each element represents the intensity value of a pixel. The image can be denoted as $I(x, y)$, where (x, y) represents the spatial coordinates of a pixel.

A filter kernel, also referred to as a mask or window, comprises a small matrix dictating the filter's coefficients. The kernel's dimensions commonly take odd values like 3×3, 5×5, or 7×7, ensuring the presence of a well-defined central pixel.

The process of spatial filtering entails moving the kernel across the image, aligning it with individual pixels consecutively. At each location, element-wise multiplication is executed between the kernel's elements and the corresponding elements of the image patch encompassed by the kernel. The resulting products are then aggregated to yield the filtered value attributed to the central pixel.

Mathematically, the spatial filtering operation is explained in equation 3.13.:

$$Out_{special}(x, y) = \sum_{[i,j]}\big(Input(x + 1, y + 1) * Karnel(i, j)\big) \quad (3.13)$$

Where $Out_{sapcial}(x, y)$ is the filtered value at position (x, y), $Input(x + i, y + j)$ represents the intensity value of the input image at position $(x + i, y + j)$, and $Karnel(i, j)$ represents the filter kernel coefficients.

Spatial filtering allows various image processing operations such as blurring, sharpening, edge detection, and noise reduction. The specific values in the filter kernel determine the characteristics of the filter and the type of operation applied to the image.

For example, a blurring filter may have a kernel with equal weights, which averages the pixel values in the neighborhood and produces a smoothing effect. On the other hand, an edge detection filter may have positive and negative weights, which emphasize the differences in intensity across neighboring pixels and highlight edges in the image.

Spatial filtering can be extended to color images by applying the same filter independently to each color channel (e.g., red, green, and blue) or by converting the image to a different color space where filtering can be applied more effectively.

Overall, spatial filtering provides a flexible and powerful tool for manipulating images by convolving them with filter kernels, allowing us to enhance certain features or suppress undesired components based on the desired image processing objective.

3.2.2.6. Frequency Domain Filtering

Frequency domain filtering is a technique used in signal processing and image processing to modify or enhance signals by manipulating their frequency components. It involves transforming a signal from the time domain to the frequency domain, applying a filter in the frequency domain, and then transforming the filtered signal back to the time domain.

To understand frequency domain filtering, let's start with some basic concepts:

- Time Domain: In this domain, the signal is expressed as a time dependent variable. It explains the evaluation of parameters with respect to time.. For example, an audio signal can be represented as amplitude variations over time.
- Frequency Domain: In the frequency domain, a signal is represented as a function of frequency. It describes the distribution of different frequencies present in the signal. Frequency domain representation is obtained by performing a mathematical operation called the Fourier transform.

The utilization of the Fourier transform enables the dissection of a signal into its fundamental frequencies. This mathematical tool facilitates the representation of the signal as a combination of various sinusoidal elements, each characterized by distinct frequencies, accompanied by corresponding amplitude and phase attributes.

Now, let's delve into the elucidation of the process involved in frequency domain filtering:

1. The initial phase involves the application of the Fourier Transform, which facilitates the conversion of the signal's temporal representation into the frequency domain. This transformation effectively shifts the signal's perspective from time-based to one centered around its constituent frequency elements.

2. Following the Fourier Transform, an outcome known as the frequency spectrum is generated. This spectrum portrays the signal through the lens of its various frequency components, revealing both the magnitudes and phases associated with each frequency. The frequency spectrum serves as a means to comprehend the distribution of frequencies within the signal.
3. The subsequent step entails the conception of a filter designed to manipulate the frequency spectrum of the signal. This filter's role is pivotal, dictating the alteration of amplitudes and phases for distinct frequencies in the frequency domain.
4. With the filter devised, it is time for the filter's operation to take effect. This transpires by performing a multiplication operation between the frequency spectrum of the signal and the frequency response of the filter. In the time domain, this multiplication corresponds to a convolution operation.
5. Post-filtering operation in the frequency domain, the transformed spectrum undergoes an inverse Fourier Transform, ushering the signal's transition from the frequency domain back to the temporal domain. This reversal restores the signal's original time-domain representation, albeit modified due to the applied filter's influence.
6. The ultimate result of the inverse Fourier Transform produces the filtered signal, which has undergone modification based on the frequency-altering attributes of the applied filter. This resultant filtered signal stands ready for subsequent analysis or processing stages, armed with its refined frequency characteristics.

Through manipulation of a filter's frequency response, various kinds of frequency domain filters can be employed. For instance, the utilization of low-pass filters permits the transmission of low-frequency elements while diminishing high-frequency components. Conversely, high-pass filters achieve the opposite by permitting high-frequency constituents to pass through while weakening low-frequency ones. Meanwhile, band-pass filters enable the passage of a specific frequency range while reducing frequencies falling outside this designated range.

Frequency domain filtering finds extensive application in tasks such as eliminating noise, augmenting signals, and performing image processing functions like detecting edges or refining image details. This approach offers a robust methodology to alter signals based on their frequency characteristics.

3.2.2.7. Filter Size and Padding

Within the domain of convolutional neural networks (CNNs), the parameters of filter size and padding wield significant influence over the resultant dimensions of a convolutional layer's output. It is imperative to delve into the intricacies of these concepts and expound upon their mathematical ramifications.

1. *Filter Size*

   Starting with the concept of filter size, it pertains to the spatial dimensions encompassing both width and height of the filter that is applied to the input image during the convolutional operation. This application defines what is termed as the receptive field, signifying the portion of the input image under consideration at any given moment. Standard filter dimensions include 3×3, 5×5, and 7×7, each of which serves distinct purposes in processing.

   From a mathematical perspective, envision an input image featuring spatial dimensions $W\_in \times H\_in$ (width × height). If a square filter of size F (assuming $F \times F$) is employed, the resultant feature map's dimensions can be calculated as follows:

$$W_{out} = W_{in} - F + 1 \tag{3.14}$$

$$H_{out} = H_{in} - F + 1 \tag{3.15}$$

   For example, if the input image has dimensions 32×32 and a 3×3 filter is applied, the resulting feature map will have dimensions 30×30. The filter size directly affects the spatial dimensions of the output feature map.

2. *Padding:*

   Padding refers to the additional border of zeros (or other specified values) added to the input image before applying the convolution operation. It helps in preserving spatial information by maintaining the spatial dimensions of the output feature map. Padding is often used to avoid excessive reduction in the size of the feature map.

   Padding is usually added symmetrically on all sides of the input image. If P is the padding size applied on each side, the output feature map dimensions can be calculated as:

$$W_{out} = W_{in} - F + 2P + 1 \tag{3.16}$$

$$H_{out} = H_{in} - F + 2P + 1 \quad (3.17)$$

By adjusting the padding size, we can control the output dimensions of the convolutional layer. Common padding choices are 'valid' (no padding) and 'same' (padding to preserve input dimensions).

For example, if the input image has dimensions 32×32, a 3×3 filter is used, and a padding of 1 ($P = 1$) is added on each side, the resulting feature map will have dimensions 32×32, maintaining the input spatial size.

Padding is also useful when we want to apply multiple convolutional layers in a network, especially if we want to avoid the shrinking of feature maps too quickly.

Overall, the filter size and padding play a crucial role in determining the spatial dimensions of the output feature maps in convolutional layers, influencing the subsequent layers and the network's overall performance in tasks such as image recognition or object detection.

Image filtering is a versatile technique used in various domains, including medical imaging, computer vision, and digital image processing. It provides a powerful toolset for manipulating and enhancing images to improve visual quality, extract meaningful information, or prepare data for further analysis.

3.2.3. Color Normalization

Color normalization is a technique used in image processing and computer vision to standardize the color appearance of images. It aims to remove variations in color caused by factors such as lighting conditions, camera settings, or image acquisition devices. By normalizing the color, images can be more easily compared and analyzed, leading to improved performance in various tasks such as object recognition, image retrieval, and image segmentation.

Mathematically, color normalization involves transforming the color values of each pixel in an image to a new color space or representation. There are several common methods used for color normalization, and we will describe two of them: Histogram Equalization and Mean-Std Normalization.

3.2.3.1. Histogram Equalization

A histogram serves as a visual depiction illustrating the distribution of data within a dataset. It is composed of a sequence of bars or rectangles, with the height of each bar symbolizing the frequency or tally of data points situated within a designated interval or bin. These bins are usually uniform in width and encompass the full extent of the dataset's range. The histogram of the corresponding image is portrayed in Figure 3.2.

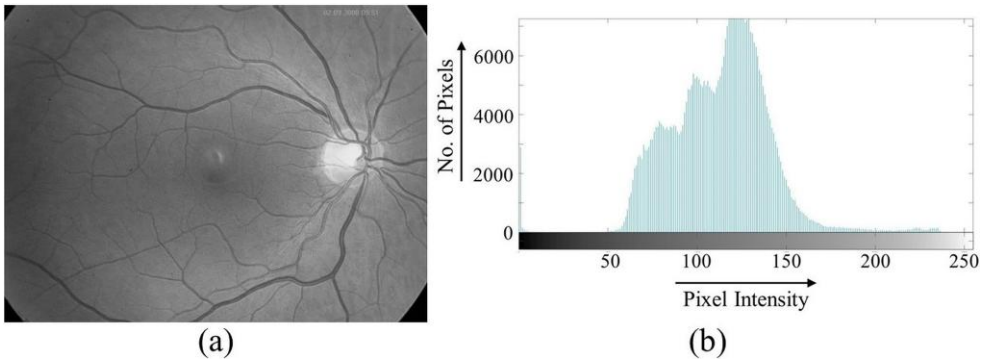

Fig 3.2: The result explains (a) a grayscale retinal fundus image and (b) its corresponding intensity histogram illustrating the distribution of pixel values across the image.

These are the fundamental elements and qualities of a histogram:

1. Horizontal Axis (X-axis): The X-axis, positioned horizontally, depicts the scope of values or segments of the examined data. It is partitioned into equidistant bins or segments.
2. Vertical Axis (Y-axis): The Y-axis, oriented vertically, illustrates the occurrence or tally of data points within each bin. It indicates the quantity of instances where data falls into specific intervals.
3. Bar Height: The magnitude of each bar is indicative of the occurrence or tally of data points within the corresponding bin. This aspect provides a visual representation of the quantity of data points within each interval.
4. Bar Width: The width of the bars is inconsequential in a histogram. Instead, the focus rests on the length or height of each bar, which mirrors the prevalence of data points.

Histograms serve as a frequently employed tool for comprehending the distribution of numerical data and discerning patterns, trends, or anomalies present within a dataset. Their utility becomes especially pronounced when handling extensive datasets or continuous data, as they play a pivotal

role in condensing and graphically representing the fundamental characteristics of the data distribution.

Here's a step-by-step process to calculate the histogram:

1. Determine the range of values covered by your dataset: Let's say the minimum value in the dataset is min_value, and the maximum value is max_value.
2. Decide on the number of bins: Select the desired number of bins, denoted by n_bins.
3. Calculate the bin width: The width of each bin, denoted by bin_width, can be determined by dividing the range of values ($max\_value - min\_value$) by the number of bins (n_bins):

$$bin\_width = (max\_value - min\_value) \,/\, n\_bins \tag{3.18}$$

4. Define the intervals or bins: Create n_bins intervals by dividing the range of values into equal-sized intervals. The i^{th} bin's lower boundary can be calculated using the formula:

$$bin\_i\_lower = min\_value + (i - 1) * bin\_width \tag{3.19}$$

   The i^{th} bin's upper boundary can be calculated as:

$$bin\_i\_upper = bin\_i\_lower + bin\_width \tag{3.20}$$

5. Compute the frequency within each bin: Tabulate the occurrences of data points within individual bins. Go through the dataset systematically, assigning each data point to its respective bin, and then increase the frequency tally for that particular bin accordingly.
6. Generating the histogram: With the frequency data established for each bin, a visual representation of the histogram can be created. This involves depicting the bins along the horizontal X-axis and the corresponding frequencies along the vertical Y-axis. The stature of each bar within the graph corresponds to the count of data points within its corresponding bin.

While these equations provide a framework for calculating the necessary values for constructing a histogram, it's important to note that the construction of the histogram itself is a visual

representation rather than a precise mathematical equation. The purpose of a histogram is to provide a graphical summary of data distribution rather than a specific mathematical formula.

Histogram equalization is a technique that redistributes the intensities of an image to achieve a uniform histogram. In the context of color normalization, it can be applied to each color channel (e.g., red, green, blue) separately or to a transformed color space such as the hue-saturation-value (HSV) color space.

Here's a step-by-step explanation of histogram equalization for color normalization:

- Transform the image into a suitable color representation (e.g., convert from RGB to HSV color space).
- Generate a histogram for each color channel or the pertinent channel (e.g., the value channel in HSV space).
- Calculate the cumulative distribution function (CDF) based on the histogram data.
- Rescale the CDF to a desired range (e.g., ranging from 0 to 255).
- Apply the CDF transformation to map the initial color values onto the normalized values.
- If needed, revert the image to its original color space.

The outcome of histogram equalization yields an image characterized by heightened contrast and minimized color discrepancies. The outcome of applying histogram equalization to the image presented in Fig. 3.2 can be observed in Fig. 3.3.

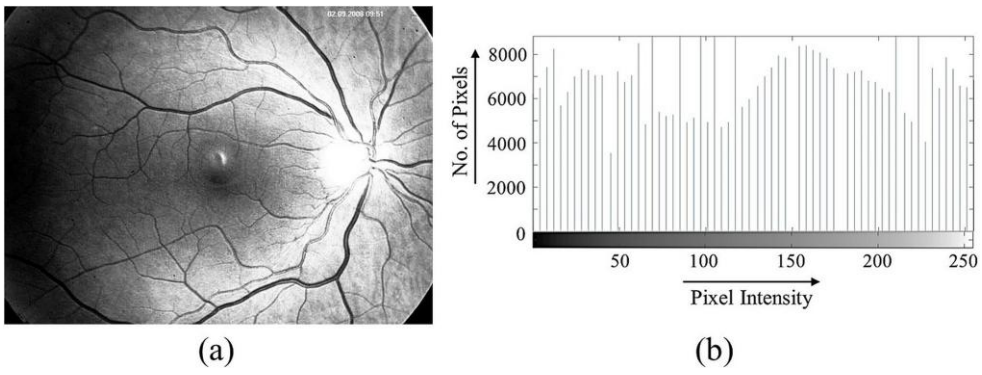

Fig 3.3: (a) Histogram-equalized retinal fundus image and (b) the corresponding histogram showing enhanced contrast with a more uniform distribution of pixel intensities.

3.2.3.2. Mean-Std Normalization

Mean-Std normalization, also known as z-score normalization, aims to normalize the color values of an image based on their mean and standard deviation. This method is often used in machine learning applications.

Here's the mathematical explanation of mean-std normalization for color normalization:

- Compute the mean (μ) and standard deviation (σ) of the color values (e.g., RGB channels) across the entire image dataset.
- For each pixel in an image, the mean (μ) of it is being subtracted from the RGB data and divided that result set by standard deviation (σ).
- This process ensures that the color values of each pixel have zero mean and unit standard deviation.

Mean-std normalization scales the color values of an image based on their statistical properties, effectively reducing variations and making the image more comparable across different datasets or lighting conditions.

Both histogram equalization and mean-std normalization are commonly used techniques for color normalization, but there are other methods as well, depending on the specific requirements and characteristics of the image data. It's important to choose an appropriate normalization method based on the desired outcome and the nature of the image analysis task at hand.

Let's assume we have an image represented by a matrix X, where each element $X(i,j)$ represents the color value at pixel (i,j). The normalization is performed separately for each color channel (e.g., red, green, blue), so let's consider a single-color channel represented by matrix C.

Compute the mean (μ) and standard deviation (σ) of the color values in matrix C across the entire image dataset:

$$\mu = mean(C)$$

$$\sigma = std(C)$$

Normalize the color values in matrix C based on the computed mean and standard deviation:

$$C\_normalized = (C - \mu) / \sigma \quad (3.21)$$

Perform the aforementioned procedures for every color channel to acquire the normalized color channels (for instance, $C\_red\_normalized$, $C\_green\_normalized$, $C\_blue\_normalized$).

The attained normalized color channels can be merged to reconstruct the normalized image. Depending on the intended scope of color value ranges, supplementary adjustment or truncation might be implemented.

Importantly, it should be acknowledged that on certain occasions, the mean and standard deviation are calculated employing a representative subset of the image dataset. This approach, commonly employed in machine learning applications during training, serves to mitigate any potential bias stemming from outliers or exceptional values.

3.2.4. Color Space Conversion

Color space conversion is a process that involves transforming the representation of colors from one color space to another. The mathematical expressions for different color space conversions can vary depending on the specific color model or standard being used. I'll provide you with the expressions for two common color space conversions: RGB to XYZ and XYZ to Lab.

1. RGB to XYZ conversion:

The RGB color space represents colors using three primary color channels: red (R), green (G), and blue (B). The XYZ color space is a device-independent color space that represents colors using three values: $X, Y,$ and Z, where Y represents luminance. The conversion from RGB to XYZ can be done using a linear transformation. Assuming the RGB values are normalized to the range $[0, 1]$, the conversion equations are:

$$X = 0.4124564R + 0.3575761G + 0.1804375B \quad (3.22)$$

$$Y = 0.2126729R + 0.7151522G + 0.0721750B \quad (3.23)$$

$$Z = 0.0193339R + 0.1191920G + 0.9503041B \quad (3.24)$$

These equations are based on the $sRGB$ color space, which is commonly used in computer graphics and displays. If you are working with a different RGB color space, you may need to adjust the conversion coefficients accordingly.

2. XYZ to Lab conversion:

The Lab color space is a perceptually uniform color space that consists of three components: L (lightness), a (green-red color component), and b (blue-yellow color component).
The conversion from XYZ to Lab involves some nonlinear transformations. First, normalize the XYZ values by dividing them by the reference white point values. Then, calculate the intermediate values of f_x and f_y as follows:

$$f_x = f(X/X_w) \tag{3.25}$$

$$f_y = f(Y/Y_w) \tag{3.26}$$

$$f_z = f(Z/Z_w) \tag{3.27}$$

where f(t) is a nonlinear function defined as:

$$f(t) = t^{1/3} \quad if \quad t > \left(\frac{6}{29}\right)^3 \tag{3.28}$$

$$f(t) = \left(\frac{1}{3}\right)\left(\frac{29}{6}\right)^2 * t + \frac{4}{29} \quad otherwise \tag{3.29}$$

Finally, the Lab values can be calculated as:

$$L = 116 * f_y - 16 \tag{3.30}$$

$$a = 500 * (f_x - f_y) \tag{3.31}$$

$$b = 200 * (f_y - f_z) \tag{3.32}$$

These equations convert XYZ values to Lab values based on the CIE Standard Illuminant $D65$ and the CIE 1931 2° Standard Observer.

It's important to note that there are several other color space conversions available, such as RGB to YUV, RGB to HSV, etc. The specific equations and transformations may differ depending on the color space and standard being used.

3.2.5. Gradient Feature Recognition

Gradient feature recognition of the retinal fundus is an elementary practice in computer based data processing which seeks to determine the pixels all over the perimeter of distinct fundus data.. It

helps in extracting important features and information from images. There are various edge detection algorithms, but one of the most commonly used is Pixel based detection technique. Initial concepts and definitions are presented in Section 3.2.5.1. Pre-pixel adjustment algorithms explained in part 3.2.5.2. are modifications executed to every pixel without hampering the measures in the neighboring pixel.

3.2.5.1. Preliminaries and Definitions

A digital image is characterized as a $2D$ array of numerical values that correspond to the continuous distribution of intensity in a spatial signal. This spatial signal, which exists in a continuous domain, is discretely sampled at regular intervals, and its intensity is represented as finite quantized range. Every single element inside the mask array is symbolized as a pixel. The intensity level distribution of the digital image data is denoted by $f(m,n)$, where f signifies the pixel's intensity, and m and n establish the pixel's position along orthogonal axes, usually termed as horizontal and vertical. The dimensions of the image are considered to be M rows and N columns, with the pixel's intensity quantized into P levels (referred to as gray levels), spanning from 0 to $P-1$. An important aspect in image analysis, the image's histogram, is defined as a vector containing the frequency of pixels at each gray level. Denoted as $h(i)$, the histogram serves crucial roles in image enhancement and characterization applications.

$$h(i) = \sum_{m=0}^{M-1} \sum_{n=0}^{N-1} \delta(f(m,n) - i), \qquad i = 0,1, \dots \dots, P-1 \qquad (3.33)$$

where

$$\delta(w) = \begin{cases} 1 & w = 0 \\ 0 & otherwise \end{cases}$$

In the context of convolution, where $g(m,n)$ represents the resultant image after convolution, the process involves overlaying a kernel onto an image pixel (m,n). This entails calculating the element-wise products between the kernel coefficients and the corresponding image pixel values. The summation of these products is then employed to determine the pixel value of the output image at the given position (m,n). The entire output image, denoted as $g(m,n)$, is generated by iteratively applying this process to all pixels within the original image. Utilizing a convolution kernel on an image serves to enact specific enhancement operations or modifications in image attributes. This typically leads to the amplification of desirable features while suppressing

undesirable ones. The precise values assigned to the kernel coefficients are contingent upon the particular type of enhancement sought after.

Strategy involves using only the segment of the kernel that aligns with the input image overlap. However, this technique can potentially result in irregularities at the peripheries of the output image. In the context of this chapter, our approach involves excluding the application of the kernel where it overreaches the border lines of the image data.

The Fourier transformation of the image can be calculated as:

$$F(u,v) = \frac{1}{MN}\sum_{m=0}^{M-1}\sum_{n=0}^{N-1} f(m,n)e^{-2\pi j\left(\frac{um}{M}+\frac{vn}{N}\right)} \tag{3.35}$$

$$u = 0,1,2,\dots\dots M-1, \qquad v = 0,1,2,\dots\dots,N-1$$

where u and v are the particular frequency measure. The Fourier transform provides the spectral representation of an image, which can be modified to enhance desired properties. A spatial domain image can be obtained from a spectral-domain image with the inverse Fourier transform given by

$$F(m,n) = \sum_{u=0}^{M-1}\sum_{v=0}^{N-1} f(u,v)e^{2\pi j\left(\frac{um}{M}+\frac{vn}{N}\right)} \tag{3.36}$$

$$m = 0,1,2,\dots\dots M-1, \qquad n = 0,1,2,\dots\dots,N-1$$

The reconstruction via fourier of an $N \times N$ data needs a difficult level of additions and multiplications.

3.2.5.2. Pixel Operations

Digital images are typically showcased through display systems like cathode ray tube (CRT) monitors or are rendered on physical media using photographic emulsions. The majority of these display methods exhibit non-linear intensity behaviors, leading to the observation of images with non-linear intensity profiles. This phenomenon can be concisely explained through the following equation:

$$e(m,n) = C\big(f(m,n)\big) \tag{3.37}$$

where $f\ (m,n)$ is the gleaned power data, $e(m,n)$ stands for the signified gleaned intended output, and C is an operator that is generally non-linear. In order to correct for the nonlinear characteristics of the display, one must apply a transform that is the inverse of the display's nonlinearity [4, 5]:

Assessing the traits of this nonlinearity presents challenges in practical application. Specifically, identifying the exact properties of this nonlinearity can be intricate. When an intensity wedge with linear characteristics is utilized for imaging, it becomes possible to generate a test image that covers the entire range of intensities captured by the image acquisition system. However, to accurately ascertain the genuine nonlinear attributes of the display system, it becomes imperative to employ an intensity measuring device with linearity characteristics. This is crucial in evaluating the output of the display system and comprehending its effective nonlinear behavior.

There are instances where the image content resides within specific, narrow intensity ranges, carrying specific relevance for the viewer. By employing intensity scaling, it becomes possible for the viewer to emphasize particular intensity intervals in the image. This is achieved by adjusting the image so that the desired intensity band aligns with the display's dynamic range. As an illustration, in scenarios where the intensity band of interest is delimited by known values f_1 and f_2, a scaling transformation can be precisely defined as follows:

$$e = \begin{cases} f & f_1 \le f \le f_2 \\ 0 & otherwise \end{cases} \tag{3.39}$$

$$g = \left\{\frac{e-f_1}{f_2-f_1}\right\} \cdot f_{max} \tag{3.40}$$

3.2.6. Image Quality Enhancement

Retinal images serve as essential diagnostic tools for ophthalmologists and optometrists, enabling the identification of a range of ocular conditions like diabetic retinopathy, macular degeneration, and glaucoma. Elevating the quality of these images holds the potential to amplify the visibility of intricate details, thereby simplifying the detection of irregularities and the formulation of appropriate therapeutic strategies. Frequently, retinal images encompass subtle nuances and anatomical structures that may remain inconspicuous in their raw state. The act of image enhancement can substantially augment the clarity of elements such as blood vessels, lesions, and other vital features, thereby facilitating superior visualization and analysis. This, in turn, can be

pivotal for purposes such as disease tracking, treatment progress assessment, and scholarly investigations.

The presence of artifacts, such as noise, uneven illumination, and motion blur, can occasionally compromise the fidelity of retinal images. By enhancing these images, it becomes plausible to mitigate such artifacts, resulting in an overall refinement of image quality that expedites comprehension and interpretation. Beyond clinical realms, improved retinal images can also serve as potent educational aids for patients. This improvement in the clarity and perceptibility of retinal structures empowers healthcare professionals to elucidate the intricacies of ocular conditions to patients more effectively, thereby enhancing patient comprehension of their diagnosis, therapeutic choices, and potential prognoses.

Especially in light of the progression of telemedicine and remote healthcare, the significance of enhancing retinal images becomes even more pronounced. This process equips healthcare providers to accurately decipher retinal images from a distance, consequently broadening access to ocular care in underserved regions. Furthermore, this technological facet facilitates prompt diagnoses and interventions, aligning seamlessly with the paradigm of delivering healthcare from a distance.

In essence, the enhancement of retinal images occupies a pivotal role in advancing diagnostic precision, streamlining treatment planning, catalyzing research endeavors, fortifying patient education, and fortuitously, propelling the frontiers of remote healthcare provision.

3.2.6.1. Blind Deconvolution:

Blind deconvolution is a technique used in image processing to enhance images by eliminating blurriness caused by an out-of-focus or blurry imaging system. The approach involves estimating the original image and the blur kernel simultaneously, without any prior knowledge of either. To achieve this, blind deconvolution algorithms typically minimize an objective function iteratively. This function measures the discrepancy between the estimated deblurred image and the blurred image.

Blind deconvolution is a method employed to enhance images that have been subjected to convolution, with the goal of restoring them to their original quality. Convolution occurs when a

point-spread function (PSF) is applied to an image, which can be due to causes such as motion blur or an out-of-focus lens.

To initiate the blind deconvolution process, the initial step involves estimating the point-spread function (PSF) responsible for the image degradation. A popular method for this is to use the Richardson-Lucy algorithm, which iteratively estimates the PSF by comparing the degraded image to a restored image estimate. The mathematical formulation for the Richardson-Lucy algorithm is given in equation 3.41.

$$P_{k+1}(x,y) = P_k(x,y)\frac{\sum_{i,j}\frac{I(x-i,y-j)}{(P_k * I)(x-i,y-j)}}{\sum_{i,j}\frac{P_k(x-i,y-j)}{(P_k * I)(x-i,y-j)}} \tag{3.41}$$

The expression involves the estimated PSF at iteration k denoted as P_k, the degraded image denoted as I, and the convolution operator denoted by $*$. Initially, the algorithm makes an estimate of the PSF as P_0 and then repeatedly updates this estimate until convergence. The numerator in the expression indicates the restoration of the degraded image using the current PSF estimate, while the denominator indicates the blurring of the restored image by the PSF. The algorithm updates the PSF estimate by assigning weights to neighboring pixels in the degraded image based on their similarity to the current PSF estimate.

Hessian Blind Deconvolution is an image restoration technique that simultaneously estimates the point-spread function (PSF) and restores the image. Below is a high-level algorithm outlining the Hessian Blind Deconvolution process:

Inputs: degraded image I, regularization parameter λ, maximum number of iterations T.

Outputs: estimated PSF P and restored image R.

1. Set the initial values of P and R by randomly assigning values.
2. For $t = 1\ to\ T$:
    a. Calculate the gradient and Hessian of the cost function with respect to P and R.
    b. To obtain the updates ΔP and ΔR for P and R respectively, solve the linear system $H\Delta X = -\nabla f$.

c. Update P and R using ΔP and ΔR respectively: $P \leftarrow P + \Delta P$ and $R \leftarrow R + \Delta R$.

3. Return P and R as the estimated PSF and restored image, respectively.

Typically, a combination of a data fidelity term and a regularization term is used as the cost function f in the above algorithm. The data fidelity term evaluates the degree of similarity between the estimated image and the observed degraded image, whereas the regularization term discourages solutions that lack smoothness or do not meet other desired criteria.

To estimate the point-spread function (PSF) and the restored image simultaneously using the Hessian Blind Deconvolution algorithm, the Hessian matrix is calculated as the second-order derivative of the cost function. An iterative method, such as conjugate gradient, is then used to solve the linear system $H\Delta X = -\nabla f$. The regularization parameter λ is used to balance the trade-off between data fidelity and regularization, while the maximum number of iterations T sets the number of times the algorithm will run before returning the estimated PSF and restored image.

3.2.6.2. Particle Swamp Optimization

PSO excels in its capacity to systematically explore optimal positions within a designated search area. Operating through a specialized swarm referred to as a "particle," the PSO algorithm dynamically adjusts both its position and velocity in a random fashion, aiming to converge towards the swarm's historically best position while exploring the entirety of the search domain. Assuming X is the size of the swarm in a D-dimensional search space, each particle's position at any given moment is defined as $P_i\left(p_{i_1}, p_{i_2}, p_{i_3}, \dots\dots\dots\dots, p_{i_D}\right)$, which represents a feasible solution to an optimization problem. The velocity of each particle is denoted by $U_i\left(u_{i_1}, u_{i_2}, u_{i_3}, \dots\dots\dots\dots, u_{i_D}\right)$. The best previous position of the swarm is represented by $Q_i\left(q_{i_1}, q_{i_2}, q_{i_3}, \dots\dots\dots\dots, q_{i_D}\right)$ for each particle, while the best position determined by the entire swarm is denoted as $Q_g\left(q_{g_1}, q_{g_2}, q_{g_3}, \dots\dots\dots\dots, q_{g_D}\right)$. These equations are used to control the behaviour of the particles.

$$u_{i_d}^{k+1} = \omega^k * u_{i_d}^k + a_1 * rand() * \left(q_{i_d} - p_{i_d}^k\right)\Delta t + a_2 * rand() * \left(q_{g_d} - p_{i_d}^k\right)/\Delta t \quad (3.42)$$

$$p_{i_d}^{k+1} = p_{i_d}^k + \Delta t * u_{i_d}^k \quad (3.43)$$

$$\omega^k = \omega_{max} - k * (\omega_{max} - \omega_{min})/k_{max} \quad (3.44)$$

The acceleration coefficients, represented by a_1 and a_2 and the inertia weight, denoted by w where w_{max} and w_{max} are the maximum and minimum values of w are used in a random function $rand(\,)$ that follows a constant allocation. The latest parameters and iteration limits are reflected by $u_{i_d}^{k+1}$ and $p_{i_d}^{k+1}$ respectively, by $d \in [1,\ D]$. Δt depicts the per time unit and the state under which $u_{i_d}^{k+1}$ and $p_{i_d}^{k+1}$ must be restricted are as follows:

$$u_{i_d}^{k+1} = \begin{cases} u_{i_d}^{k+1} & -u_{max} \le u_{i_d}^{k+1} \le u_{max} \\ u_{max} & u_{i_d}^{k+1} > u_{max} \\ -u_{max} & u_{i_d}^{k+1} < -u_{max} \end{cases} \tag{3.45}$$

$$p_{i_d}^{k+1} = \begin{cases} p_{i_d}^{k+1} & -p_{max} \le p_{i_d}^{k+1} \le p_{max} \\ p_{init} & p_{i_d}^{k+1} > p_{max} \\ p_{init} & p_{i_d}^{k+1} < p_{min} \end{cases} \tag{3.46}$$

$$p_{init}^{k+1} = p_{min} + rand(\,) * (p_{max} - p_{min}) \tag{3.47}$$

where u_{max} represents the highest value of u while p_{max} and p_{min} indicate the maximum and minimum values of p, respectively.

PSO operates by repeatedly modifying the position and velocity of a collection of particles in a search space, with each particle representing a candidate solution. The fitness of each particle is determined by a fitness function, and PSO utilizes interactions between particles to search through the search space and approach the optimal solution. The output of the PSO algorithm is the best solution discovered during the search, which could be a local optimum instead of the global optimum.

3.2.6.3. Contrast Limited Adaptive Histogram Equalization

CLAHE is an algorithm to inprove the perceptual difference of fundus dataset , particularly in regions with low contrast or uneven illumination. CLAHE operates by dividing an image into small regions called tiles, and within each tile, it applies histogram equalization to redistribute the pixel intensities. However, to prevent excessive amplification of noise, CLAHE includes a contrast limiting mechanism that constrains the intensity range within each tile [304]. Firstly, the contrast of the grayscale image was increased using the formula given in equation 3.48.

$$I(x_i, y_i) = \frac{f(x_i,y_i)-f(min)}{f(max)-f(min)} * 2^{bpp} \quad (3.48)$$

Here, $I(x_i, y_i)$denotes the input image, $f(x_i, y_i)$, $f(min)$, and $f(max)$ refer to the values for each pixel intensity, minimum and maximum pixel intensities respectively. The output is the stretched contrast image which was used as the input to CLAHE.

In contrast to limited adaptive histogram equalization (CLAHE), the input image is split into two parts that are non-overlapping contextual areas or tiles and a local histogram of these tiles. Prior to approximating the cumulative probability density and enhanced contrast intensity, the histogram of the individual tile is clipped with the help of a clip limit set by the user which is the multiple of the average height of the histogram of the contextual region, shown in equation 3.49.

$$[H\_Height]_{Avg} = \frac{[Pix(total)]_{CL}}{[Pix(total)]_{GL}} \quad (3.49)$$

Here, $[H_Height]_{Avg}$is the average height of the histogram of the input image $I(x_i, y_i)$. $[Pix(total)]_{CL}$and $[Pix(total)]_{GL}$denotes the total pixels in the contextual region and the gray level of the input image respectively. For the contextual region of size say $M \times N$ and H_n be the number of histogram bars, the clip-limit is given by equation 3.39.

$$C_L = \begin{cases} 1 & if \quad \frac{\alpha_{cf} MN}{[H_n]_{Hist}} < 1 \quad for \quad 0 < \alpha \leq 1 \\ 0 & otherwise \end{cases} \quad (3.50)$$

In this case, α_{cf} is a user-defined contextual factor. The true height of the histogram of the contextual area n_k is being clipped using the clip limit, C_L as indicated in equation 3.51 where H_k is the histogram of the given area.

$$H_k = \begin{cases} C_L & if \quad n_k = C_L \quad for \quad k = 1,2, \dots \dots, [H_n]_{Hist} - 1 \\ n_k & otherwise \end{cases} \quad (3.51)$$

$$where \quad \sum_{k=0}^{[H_n]_{Hist}} n_k = MN \quad (3.52)$$

Total clipped pixels C_{total} can be calculated by equation 3.42.

$$C_{total} = MN - \sum_{k=0}^{[H_n]_{Hist}-1} H_k \quad (3.53)$$

By re-normalizing the histogram or bringing the area under the curve back to its original range, the clipped pixel values are spread back to the histogram. Rearrangement may be uniform, otherwise, the clipped pixel values may not be evenly distributed across histogram plots with pixel values less than the clip limit. The distributed pixels to each histogram bin can be found as mentioned in equation 3.54.

$$P_{\mu} = \frac{C_{total}}{[H_n]_{Hist}} = \frac{MN - \sum_{k=0}^{[H_n]_{Hist}-1} H_k}{[H_n]_{Hist}} \tag{3.54}$$

The clipped histogram is being re-normalized by using equation 3.55.

$$H_k = \begin{pmatrix} C_L & if & n_k + P_{\mu} > C_L \\ n_k + P_{\mu} & & otherwise \end{pmatrix} \tag{3.55}$$

3.3. Image Segmentation

Segmenting out the image features are the highly intricating research challenges in computer vision and pattern recognition. The most basic yet impactful algorithm to isolate the objectis Thresholding. To amplify the feature segmentation, the global threshold selection algorithm OTSU is rapidly used worldwide. This method is very simple but fails to segment the image features properly due to the unimodal property of histogram. So an advanced and more effective OTSU algorithm has been established to overcome the limitations..

3.3.1. Algorithm Based on Otsu Method

In various instances of image processing, there exists a notable distinction in grayscale levels between pixels belonging to the object and those within the background. In these scenarios, the utilization of thresholding emerges as a straightforward yet efficacious approach for segregating objects from their surrounding background. The practice of employing thresholding techniques has gained widespread prominence within the realm of machine vision and image analysis. Over time, a multitude of image thresholding methods have been devised, with some of the most frequently employed ones including Minimum Error Thresholding, the Otsu method, and Moment-Preserving Thresholding, among others. Recent investigations in this area can be found in the works of Sauvola and Pietikainen [36], as well as Sahoo [37], among others.

Otsu [38], in 1979, introduced a dynamic thresholding selection technique. This method proposes the optimization of a weighted sum encompassing variances between classes of foreground and background pixels, ultimately leading to the determination of an optimal threshold. Otsu's method is particularly effective for histograms exhibiting bimodal or multimodal distributions, making it well-suited for thresholding tasks involving substantial objects set against their background. Nevertheless, challenges arise when this method is applied to images possessing unimodal or nearly unimodal distributions. Some limitations inherent to the Otsu method are explored in the study conducted by Lee and Park [39]. In the context of image segmentation, objects span a spectrum ranging from those devoid of defects to those exhibiting small or large defects. This chapter proposes an algorithm centered around the identification of an appropriate threshold value, demonstrating its capability to address such diverse image scenarios.

Consider the image pixels be illustrated in gray level as $[1,2,3,\ldots\ldots\ldots,L]$. n_i signifies the number of pixels at level i and the total count of pixels by $N = n_1 + n_2 + \ldots\ldots + n_L$. To streamline the matter, the grayscale histogram is converted to a probability distribution:

$$P_i = n_i/N, \qquad P_i \geq 0, \sum_{i=1}^{L} P_i = 1. \tag{3.56}$$

Now let pixels are bifurcated in two distinct classes C_0 and C_1 as backgroung pixels and object pixels or vice versa by a threshold point K, where C_0 defines the pixels with intensities $[1,2,\ldots,\mathrm{k}]$ and C_1 defines the pixels with intensities $[\mathrm{k}+1,\ldots\ldots\ldots,\mathrm{L}]$. Then the likelihood of class appearance are depicted

$$\omega_0 = P_r(C_0) = \sum_{i=1}^{k} P_i\, \omega(k) \tag{3.57}$$

$$\omega_1 = P_r(C_1) = \sum_{i=k+1}^{L} P_i = 1 - \omega(k) \tag{3.58}$$

And

$$\mu_0 = \sum_{i=1}^{k} iP_r\,(i/C_0) = \sum_{i=1}^{k} iP_i\,/\omega_0 = \mu(k)/\omega(k) \tag{3.59}$$

$$\mu_1 = \sum_{i=k+1}^{L} iP_r\,(i/C_1) = \sum_{i=k+1}^{L} iP_i\,/\omega_1 = \frac{\mu_T - \mu(k)}{1-\omega(k)} \tag{3.60}$$

Where

$$\omega(k) = \sum_{i=1}^{k} P_i \tag{3.61}$$

And

$$\mu(k) = \sum_{i=1}^{k} iP_i \tag{3.62}$$

are the zeroth- and the first-order cumulative moments of the histogram up to the kth level, respectively, and

$$\mu_T = \mu(L) = \sum_{i=1}^{L} iP_i \tag{3.63}$$

is the total mean level of the original picture. We can easily verify the following relation for any choice of k:

$$\omega_0\mu_0 + \omega_1\mu_1 = \mu_T, \quad \omega_0 + \omega_1 = 1 \tag{3.64}$$

The class variances are given by

$$\sigma_0^2 = \sum_{i=1}^{k}(i-\mu_0)^2 P_r(i|C_0) = \sum_{i=1}^{k}(i-\mu_0)^2 P_i/\omega_0 \tag{3.65}$$

$$\sigma_1^2 = \sum_{i=k+1}^{L}(i-\mu_0)^2 P_r(i|C_1) = \sum_{i=k+}^{L}(i-\mu_1)^2 P_i/\omega_1 \tag{3.66}$$

These require second-order cumulative moments (statistics). In order to evaluate the "goodness" of the threshold (at level k), we shall introduce the following discriminant criterion measures (or measures of class separability) used in the discriminant analysis [40]:

$$\lambda = \sigma_B^2/\sigma_W^2, \quad K = \sigma_T^2/\sigma_W^2, \quad \eta = \sigma_B^2/\sigma_T^2 \tag{3.67}$$

Where

$$\sigma_W^2 = \omega_0\sigma_0^2 + \omega_1\sigma_1^2 \tag{3.68}$$

$$\begin{aligned}\sigma_B^2 &= \omega_0(\mu_0-\mu_T)^2 + \omega_1(\mu_1-\mu_T)^2 \\ &= \omega_0\omega_1(\mu_1-\mu_0)^2\end{aligned} \tag{3.69}$$

$$\sigma_T^2 = \sum_{i=1}^{L}(i-\mu_T)^2 P_i \tag{3.70}$$

are the within-class variance, the between-class variance, and the total variance of levels, respectively. Then our problem is reduced to an optimization problem to search for a threshold k that maximizes one of the object functions (the criterion measures) in (3.56). This standpoint is motivated by a conjecture that well-thresholded classes would be separated in gray levels, and conversely, a threshold giving the best separation of classes in gray levels would be the best

threshold. The discriminant criteria maximizing λ, K, and η, respectively, for k are, however, equivalent to one another because the following basic relation always holds:

$$\sigma_W^2 + \sigma_B^2 = \sigma_T^2 \tag{3.71}$$

It is noticed that σ_W^2 and σ_B^2 are functions of threshold level k, but σ_T^2 is independent of k. It is also noted that σ_W^2 is based on the second-order statistics (class variances), while σ_B^2 is based on the first-order statistics (class means). Therefore, η is the simplest measure with respect to$k$. Thus, we adopt η as the criterion measure to evaluate the "goodness" (or separability) of the threshold at level k.

3.3.2. Multilevel Thresholding

In this section of the research, the optic disc from the cropped image has been segmented out by using multilevel thresholding followed by some morphological based operation.

In multilevel thresholding technique, a number of thresholds points $[T_1, T_2, T_3, \dots\dots\dots, T_L\ ]$ in the histogram image $hist(x, y)$ is used to separate the image pixels. By using the separated threshold points, the original cropped image is being segmented to get image $fn\big(hist(x, y)\big)$. Specifically:

$$fn\big(hist(x,y)\big) = \begin{cases} gray_0 & if \quad hist(x,y) \le T_1 \\ gray_1 & if \quad S_1 < hist(x,y) \le T_2 \\ \dots\dots\dots\dots\dots\dots\dots\dots & \\ gray_L & if \quad hist(x,y) > T_L \end{cases}$$

(3.87)

Such that $gray_i$ denotes the gray-level allocated to all pixel points at the region i that eventually signifies the object i. As in equation 3.87, the $L + 1$ areas are calculated by the L number of thresholds $\{T_1, T_2, T_3, \dots\dots, T_L\}$. The maximum values of gray-level i.e. 255 can be used to dispense the gray-level regions correspondingly.

3.3.3. Iterative Global Thresholding

Iterative global thresholding is a technique utilized in image segmentation that involves separating an image into distinct regions using a threshold value. The threshold value is updated iteratively until a satisfactory result is achieved. The algorithm can be mathematically expressed in the following manner:

1. To begin, assume of an initial threshold value denoted as $Th(0)$.
2. Using the equations provided below, determine the average intensities of the pixels in both the foreground and background regions.
   a. $FG_{avg}(Th(k)) = \left(\frac{1}{pix_{FG}}\right) * sum(f[i,j]), for\ f[i,j] > Th(k)$ (3.72)
   b. $BG_{avg}(Th(k)) = \left(\frac{1}{pix_{BG}}\right) * sum(f[i,j]), for\ f[i,j] \leq Th(k)$ (3.73)

where pix_{FG} and pix_{BG} are the number of pixels in the foreground and background regions, respectively.

3. Adjust the threshold value to be the mean intensity of both foreground and background:

$$Th(k+1) = \left(FG_{avg}(Th(k)) + BG_{avg}(Th(k))\right)/2 \quad (3.74)$$

4. Continue with steps 2-3 until the difference between $Th(k)$ and $Th(k+1)$ reaches a predefined threshold.

Ultimately, the image can be segmented by categorizing each pixel as either belonging to the foreground or background region according to its intensity value, using the threshold value Th.

The iterative global thresholding algorithm is a straightforward and efficient approach for image segmentation that can adjust to changes in image intensity and noise. The algorithm iteratively improves the threshold value using the mean intensities of the foreground and background, resulting in accurate separation of the image into distinct regions.

3.3.4. Morphological Operators:

Morphology encompasses a wide array of image processing techniques centered around shapes. These operations involve the application of a structuring element to an original image, generating an output image of identical dimensions. In the process of morphological operations, the value assigned to each pixel in the resulting image is determined by comparing it to its neighboring pixels in the input image. Through the careful selection of the size and configuration of this neighborhood, it becomes possible to construct a morphological operation that specifically targets distinct shapes within the input image.

The fundamental operators elucidated in this section are tailored for processing two-dimensional discrete images (defined on a subset $E \subset Z^2$). Binary images are defined as subsets of E, while grayscale images are represented as functions $f : E \rightarrow T$, where T comprises the range of gray level $T = \{t_{min}, \ldots, t_{max}\}$.

3.3.4.1. Dilation and Erosion

To handle border pixels during processing, morphological functions allocate values to these undefined pixels as though the functions had expanded the image with extra rows and columns. The assigned value for these padded pixels varies depending on whether it's a dilation or erosion operation. Many mathematical morphology operators rely on a small "test-set" B, referred to as a structuring element (SE), which can be tailored in terms of size and shape to align with segmentation or filtering objectives.

To compute the morphological erosion of a binary image A, each point x is assessed to determine if the structuring element, centered at x, fits entirely within A. Should this condition hold true, x becomes part of the eroded set εA. Conversely, dilation can be conceptualized as an erosion of the background.

In the context of gray-level dilation/erosion, the process entails replacing the value $f(x)$ with the maximum/minimum value of f among all the pixels encompassed by the translated structuring element B_x:

$$[\varepsilon^B(f)](x) = \min_{b \in B} f(x+b) \tag{3.75}$$

$$[\delta^B(f)](x) = \max_{b \in B} f(x+b) \tag{3.76}$$

3.3.4.2. Opening and Closing

Morphological operations like openings (γ^B) and closings (φ^B) are the repeated execution of morphological erosion and morphological:

$$\gamma^B(\cdot) = \delta^{B^*}\varepsilon^B(\cdot) \tag{3.77}$$

$$\varphi^B(\cdot) = \varepsilon^{B^*}\delta^B(\cdot) \tag{3.78}$$

With $B^* = \{-b\}$ the transpose of the structuring element.

The characteristics of morphological opening and closing of gray image can be perceived by considering the image as a topographic structure. The opening operation is used to eliminate

brighter attributes without structuring element. In the other side the closing operation eliminates the relatively darker attributes without structuring element.

3.3.4.3. Top-Hat Transform

The Top-Hat morphological operation is very effective for distinguishing point targets with all kinds of background, but it is less useful for tackling the image removal problem with the localized target, that is severely corrupted by noise. It is therefore necessary to supply an improved morphological Top-Hat filtering algorithm.

The Structuring Element of the advanced Top-Hat morphological operator is designed as follows: design an internal structural element and an external structural element as $SE_0(m \times m)$, complying $SE_i \subset SE_0$. Define Edge Structuring Element as $SE_{Edge} = SE_0 - SE_i$. Thus, the improved Top-Hat operation can be defined as in equation (3.81).

$$Top\_H\ at_{I,SE}(x) = \left[\{I - (I\Theta SE_{Edge}) \oplus SE_i\}.x\right] \tag{3.79}$$

Below is a sample pseudocode that demonstrates how to perform a Top Hat Transformation on an image by utilizing the opening morphological operation.

Input: I is a binary image with dimensions $M \times N$, and SE is a structuring element with dimensions $m \times n$.

Output: After applying the Top Hat Transformation, the binary image J will have a size of $M \times N$.

1. Create a function named $Top\_Hat(I, SE)$ that utilizes the morphological opening function to execute the Top Hat Transformation.
    a. Consider a structuring element (SE) of 'disk' shape with a specific size:

$SE = strel$('disk', size).

    b. Compute the morphological opening operation on the binary input image, I.

$morph_{open} = imopen(I, SE)$.

    c. Subtract the $morph_{open}$ image from the input binary image, I to grt the top hat transformed image, J.

$$J = I - morph_{open}$$

d. Return the resulting top hat image, J.

2. End

3.4. Feature Extraction

Retinal feature extraction involves the meticulous analysis and retrieval of pertinent information from retinal images, capturing details from structures like blood vessels, the optic disc, macula, and other critical components situated at the rear of the eye. These retinal features serve as invaluable indicators of ocular health and overall well-being, offering profound insights.

In the realm of medical applications, retinal feature extraction holds particular significance, particularly in the diagnosis and continual monitoring of conditions like diabetic retinopathy, macular degeneration, and glaucoma. Employing the tenets of image processing and computer vision, this process encompasses the identification and isolation of specific attributes inherent to retinal images. Some of the commonly extracted retinal features encompass:

- Optic Disc Detection: The optic disc, being the entry point of the optic nerve on the retina, is pivotal. Its detection and segmentation hold paramount importance in numerous retinal analysis tasks, serving as a reference point for gauging other features while facilitating the identification of anomalies or disease indications.
- Blood Vessel Segmentation: Unveiling the intricate network of blood vessels within retinal images offers insights into vascular architecture and the identification of irregularities, such as vessel tortuosity, thinning, or neovascularization. Blood vessel segmentation methodologies differentiate these vessels from the backdrop and other retinal structures.
- Lesion Detection: Abnormalities like microaneurysms, hemorrhages, exudates, and drusen signify the presence or progression of specific diseases. Detecting and quantifying these lesions hold pivotal roles in early-stage diagnosis, ongoing disease tracking, and devising treatment strategies.
- Macula Analysis: The macula, housing the fovea responsible for acute central vision, is of particular interest. Extracting features linked to the macula, such as foveal thickness, illuminates conditions like macular degeneration or macular edema.

- Retinal Layer Segmentation: The retina comprises several distinct layers, and segmenting these layers facilitates the in-depth analysis of specific retinal structures. For instance, segmenting the retinal nerve fiber layer (RNFL) aids in the diagnosis and continual assessment of glaucoma.

The extraction of these retinal features necessitates the employment of a spectrum of machine learning and computer vision techniques. Edge detection, region segmentation, morphological operations, and feature extraction algorithms are among the array of methodologies utilized. Through these techniques, the identification and quantification of specific features come to fruition, thereby furnishing ophthalmologists and researchers with indispensable insights into the intricacies of retinal diseases.

Features extraction using parallel convolutional layers

The primary objective of this investigation centered on devising a Convolutional Neural Network (CNN) that would optimize parameters and layers, resulting in a more efficient processing duration while retaining the most crucial attributes. These salient characteristics played a pivotal role in facilitating the precise identification of Diabetic Retinopathy (DR) levels through an Extreme Learning Machine (ELM) model. In the context of CNN, the strategic arrangement of convolutional layers (CL) played a critical role in extracting optimal features. Striking a balance was crucial; too few CL layers could compromise the capture of discriminative features, while an excessive number might lead to model overfitting. The selection of an appropriate number of CL layers was paramount for feature extraction. In this specific investigation, six CL layers were opted for, ensuring the extraction of prominent features while mitigating overfitting concerns. The architecture of the lightweight parallel CNN is illustrated in Fig. 3.4.

In the lightweight parallel CNN architecture, four CLs were placed concurrently, yielding a reduction in parameters and processing time. The parallel execution of these four CLs essentially emulated the role of a singular CL, albeit with the potency of four. Each CL was configured with a size of 64. The kernel dimensions of the initial, second, third, and fourth CLs were 9×9, 7×7, 5×5, and 3×3, respectively, with the ReLU activation function being applied. Throughout this study, consistent padding was maintained in the first four CLs to account for essential border information in the Feature Images (FIs). The outcome of these parallel CL operations was concatenated and subsequently introduced into a sequential CNN framework. The

last two CLs were sized at 32 and 16, respectively, each employing a 3×3 kernel. The padding in the subsequent CLs adopted a "valid" configuration. Batch normalization, activation functions, and max-pooling followed each CL. The utilization of 2×2 max-pooling filters enabled the capture of pivotal regions within the FIs by isolating the highest values within each region. The architecture included two Fully Connected (FC) layers, with feature extraction being carried out in the ultimate FC layer. To combat overfitting and expedite training, dropout mechanisms were deployed with a probability of 0.5, implemented after the final CL and the initial FC layer. Dropout facilitated the reduction of overfitting by randomly deactivating 50% of nodes, thus promoting training efficiency. The feature extraction process involved running the CNN model for 50 epochs, utilizing a batch size of 64, and adopting a learning rate of 0.001. The ADAM optimizer was employed to manage optimization, and the loss function was addressed through sparse categorical cross-entropy.

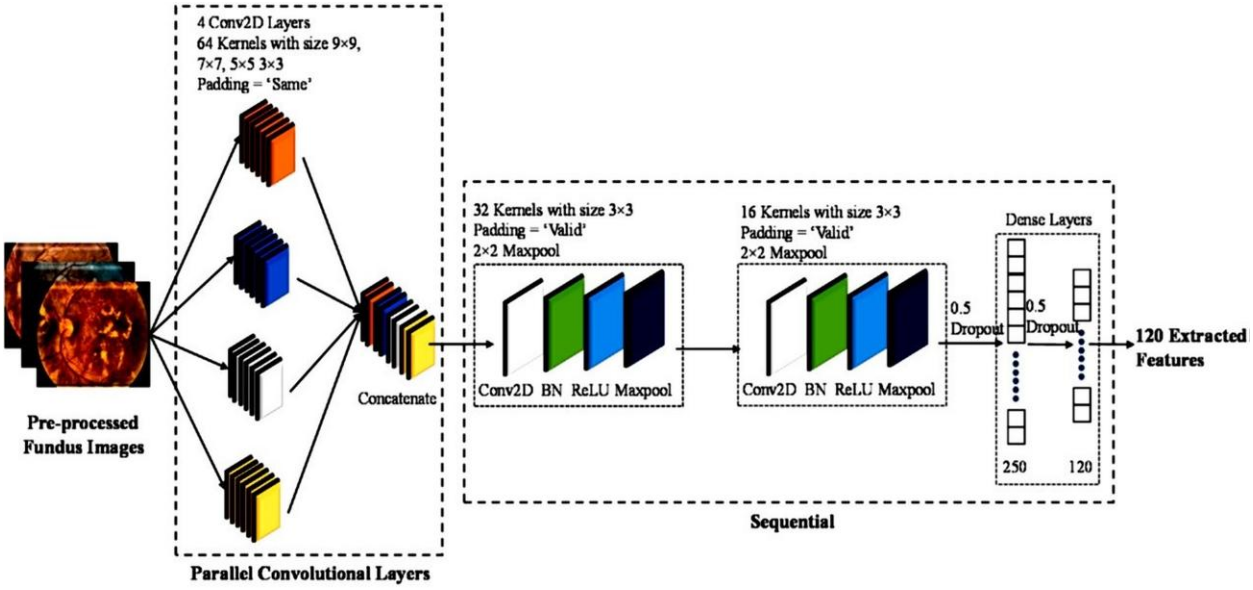

Fig 3.4: The lightweight parallel CNN to extract the features from fundus images

3.5. Tortuosity Measurement

To determine the global tortuosity of a retinal vessel map, we rely on local measurements of tortuosity taken from each vessel segment. The local tortuosity is measured using the coordinates of each segment, denoted as $Seg(s_x, s_y)$. Our analysis employs a set of twelve methods for

quantifying local tortuosity, which can be classified into four groups: those based on distance, curvature, angle variation, and number of twists.

The tortuosity index in distance-based methods is determined by the relationship between the arc length(L_{arc}), representing the actual vessel length, and the chord length (L_{crd}), which is the straight line connecting the two end-points of a vessel segment. Equations (3.96), (3.97), and (3.98) are used to calculate L_{arc}, L_{crd}, and the tortuosity index L_{arc}/L_{crd}, based on the number of points in a vessel segment (n). The calculation of vessel length is influenced by the number of sampling points used to represent the vessel segment coordinates, but this dependence is partially offset by the normalization of two length measurements performed at a similar scale against each other.

$$L_{arc} = \sum_{i=1}^{n-1} \sqrt{\left(s_{x_{i+1}} - s_{x_i}\right)^2 + \left(s_{y_{i+1}} - s_{y_i}\right)^2} \tag{3.80}$$

$$L_{crd} = \sqrt{\left(s_{x_n} - s_{x_i}\right)^2 + \left(s_{y_n} - s_{y_i}\right)^2} \tag{3.81}$$

$$\frac{L_{arc}}{L_{crd}} = \frac{L_{arc}(Seg)}{L_{crd}(Seg)} - 1 \tag{3.82}$$

3.6. Statistical Validation

Statistical validation of retinal image processing techniques involves evaluating the performance and accuracy of algorithms or methods used for analysing retinal images. The validation process typically includes quantitative assessment and comparison of the results obtained from the image processing techniques against reference standards or ground truth. Here are some common approaches for statistically validating retinal image processing techniques:

- Annotated Datasets and Reference Standards: In order to validate the effectiveness of the retinal image processing methods, it is imperative to possess a meticulously annotated dataset comprising retinal images, accompanied by corresponding reference standards. The reference standards might encompass meticulously crafted manual annotations by seasoned specialists or a consensus derived from the input of multiple experts. The dataset itself should encompass a comprehensive spectrum of retinal pathologies or features under scrutiny.
- Evaluation Metrics for Performance: The task of gauging the accuracy and efficiency of retinal image processing techniques necessitates the establishment of suitable evaluation metrics. Whether it involves detecting lesions, segmenting structures, classifying anomalies,

or quantifying retinal parameters, the choice of appropriate metrics is pivotal. The ensuing equations present formulas for quantifying these performance metrics:

$$Sensitivity = \frac{Number\ of\ true\ positive}{Number\ of\ true\ positive + Number\ of\ false\ positive} \quad (3.83)$$

$$Specificity = \frac{Number\ of\ true\ negative}{Number\ of\ true\ negative + Number\ of\ false\ negative} \quad (3.84)$$

$$Accuracy = \frac{Number\ of\ true\ positive + Number\ of\ true\ negative}{Number\ of\ all\ predictions} \quad (3.85)$$

The actual positive and negative are the outlook of positive and negative classes with corresponding ground truth. On the other side, the positive and negative false data are the wrongly predicted positive and negative classes.

The Kappa coefficient is more orthodox, therefore by removing the chances of occurance .

$$Kappa\ coefficient = \frac{P_0 - P_e}{1 - P_e} \quad where \quad P_e = P_p + P_n \quad (3.86)$$

$$P_0 = Accuracy$$

$$P_p = \frac{Number\ of\ positive\ predictions}{Number\ of\ all\ predictios} \times \frac{Number\ of\ positive\ ground\ truth}{Number\ of\ all\ predictions}$$

$$P_n = \frac{Number\ of\ negative\ predictions}{Number\ of\ all\ predictios} \times \frac{Number\ of\ negative\ ground\ truth}{Number\ of\ all\ predictions}$$

The P_p is the prediction of occurrence in which the positive ground truth data are being harmonized to the positively predicted data. Similarly, P_n is the prediction of negative ground truth data that is matched by negatively predicted data.

- *Cross-validation:* Employ cross-validation techniques to ensure the robustness of the retinal image processing methods. Cross-validation involves splitting the dataset into training and testing subsets multiple times, evaluating the algorithm's performance on each split, and then aggregating the results. K-fold and leave one out cross validation methods are commonly used.
- *Comparison with Existing Methods:* Compare the performance of the proposed retinal image processing technique against existing methods or state-of-the-art approaches. This step helps

assess whether the new technique offers improved results or provides a comparable performance with lower computational complexity or other advantages.

- Receiver Operating Characteristic (ROC) analysis: ROC analysis is a statistical technique commonly used to assess and evaluate the performance of binary classification models or diagnostic tests. It provides a comprehensive evaluation of the trade-off between sensitivity and specificity at various classification thresholds.

  ROC analysis is particularly useful in situations where the classification outcome is dichotomous, such as in disease diagnosis (e.g., diseased vs. healthy) or event prediction (e.g., presence vs. absence of a particular condition). It involves plotting of sensitivity vs (1-specificity) at differently decided threshold values.

The step-by-step overview of how ROC analysis is typically conducted:

1. Collect the data: Gather a dataset consisting of observed outcomes (e.g., disease status) and corresponding predictions or scores generated by the classification model or diagnostic test being evaluated.
2. Set the classification threshold: The classification threshold determines the point at which the model or test distinguishes between positive and negative cases. By varying the threshold, you can examine the impact on sensitivity and specificity.
3. Calculate true positive rate (sensitivity) and false positive rate (1-specificity): For each threshold setting, calculate the proportion of true positives (correctly identified positive cases) and false positives (incorrectly identified negative cases) in relation to the actual outcomes.
4. Plot the ROC curve: Create a graphical image in which X-axis defines the false positive rate and the y-axis by the true positive rate . Establish the sensitivity and specificity parameters obtained at different threshold settings. Each point on the curve represents a specific threshold value.
5. Calculate the area under the ROC curve (AUC): The area under the ROC curve explains the overall performance analysis of the model. AUC with 1 defines a perfect classification while a non-uniform and random classifications on AUC 0.5.

ROC analysis allows for visual representation and quantitative assessment of the diagnostic accuracy of a model or test. It helps researchers and practitioners make informed decisions about

the performance and utility of classification systems in various applications, including retinal imaging for disease diagnosis or risk prediction.

3.7.Conclusion:

In conclusion, the methodology of retinal image processing represents a crucial and evolving area of research with significant applications in ophthalmology and medical imaging. Throughout this study, various techniques and algorithms have been explored for the enhancement, segmentation, and analysis of retinal images.

The pre-processing stage plays a fundamental role in improving the quality of retinal images by reducing noise, enhancing contrast, and standardizing the images for further analysis. Different filtering and transformation methods have been utilized to achieve these goals.

Segmentation is a pivotal step in retinal image processing, enabling the extraction of essential anatomical structures such as blood vessels, optic disc, and macula. Various segmentation techniques have been investigated, including thresholding, region-based methods, edge detection, and machine learning-based approaches. The choice of segmentation method depends on the specific characteristics of the retinal images and the application requirements.

Following segmentation, feature extraction techniques have been employed to quantify relevant morphological and textural features from retinal structures. These features aid in the characterization of pathological conditions and contribute to the development of diagnostic and disease monitoring systems.

Moreover, machine learning and deep learning algorithms have shown promising results in automating the entire retinal image processing pipeline, including segmentation and disease classification. These data-driven approaches have the potential to enhance the accuracy and efficiency of retinal image analysis significantly.

Overall, the methodology of retinal image processing is a multidisciplinary field that brings together image processing, computer vision, and machine learning techniques to facilitate early detection, diagnosis, and treatment of retinal diseases. As technology continues to advance and new algorithms emerge, it is anticipated that retinal image processing will continue to progress, contributing to improved clinical decision-making and better patient outcomes. However, it is

crucial to address the challenges of large-scale validation, dataset diversity, and interpretability to ensure the robustness and clinical adoption of these techniques in the future.

Chapter IV

Automatic Detection and Segmentation of Optic Disc (ADSO) of Retinal Fundus Images Based on Mathematical Morphology

The key objective of the image processing algorithm in the medical domain is to build a mathematical algorithm that helps to quantify and visualize the anatomical and pathological features. Hyperglycemia is a disease that destroys the retina occurs due to fluid leakage from blood vessels into the retinal area of the human eye. Accurate identification of the optic disc in retinal fundus images, along with a quantitative analysis of its shape and size, is crucial for diagnosing various retinal pathologies. Abnormalities in the optic disc often led to structural changes in its inner and outer regions. However, optic disc identification and segmentation at the level of the entire retinal image can reduce detection sensitivity in certain areas.

In this research, an advanced hierarchical classification-based method for optic disc detection and segmentation is proposed. The perfectly predicted perimeters of the optic nerve head is identified by calculating and incorporating an adaptive thresholding technique based on innovative morphological transformations. This approach reduces the processing area required for segmentation techniques, resulting in significant performance improvements and lower computational costs per retinal fundus image. The proposed method has been evaluated on publicly available retinal image datasets, including DIARETDB1, DRIVE, HRF, DRIONS-DB, IDRiD, and STARE, demonstrating notable improvements in accuracy and processing time compared to existing techniques.

4.1. Introduction

The retinal optic disk, also referred to as the optic nerve head, is a circular area on the retina where the optic nerve exits the eye. It has a whitish appearance and lacks photoreceptor cells, making it insensitive to light. The optic disk is essential for transmitting visual information from the eye to the brain. Various conditions and diseases can impact the health and function of the retinal optic disk. Some examples include:

- *Glaucoma:* A group of eye diseases characterized by optic nerve damage, often linked to increased intraocular pressure. Glaucoma can affect the optic disk, leading to the loss of nerve fibers, thinning of the rim tissue, and enlargement of the optic cup.
- *Optic Disk Drusen:* This condition involves the accumulation of calcified deposits within the optic disk. Although typically benign, it can cause visual field defects and may sometimes compress the optic nerve, leading to vision issues.
- *Papilledema:* This refers to swelling of the optic disk due to increased intracranial pressure, which can result from conditions like brain tumors, intracranial hemorrhage, or elevated cerebrospinal fluid pressure. Without treatment, papilledema can lead to vision loss.
- *Optic Atrophy:* This condition involves the degeneration or loss of nerve fibers in the optic nerve, resulting in a thinning of the retinal nerve fiber layer. Optic atrophy causes the optic disk to appear pale and can lead to vision impairment.

According to [322-324], more than 382 million people worldwide aged 40 to 59 suffer from diabetes. India, China, and the USA are among the countries with the highest numbers of cases. Screening such a large population requires a significant number of ophthalmologists, making it highly beneficial to develop an automatic diabetic retinopathy detection algorithm to assist them. Image processing plays a crucial role in detecting and analyzing the retinal optic disk, which is important for several reasons:

- *Optic Nerve Head Identification:* The retinal optic disk is the point where the optic nerve exits the eye. Accurate detection and identification of the optic disk allow healthcare professionals to evaluate the health and integrity of the optic nerve. Abnormalities in this area can signal underlying eye conditions or systemic diseases that impact the optic nerve.

- *Diagnosis and Management of Eye Diseases:* Various eye diseases, such as glaucoma, optic neuritis, and papilledema, can affect the optic disk. Early detection and analysis of the optic disk are crucial for diagnosing and managing these conditions effectively. Changes in the optic disk's appearance can provide critical information on the presence, severity, and progression of eye diseases.
- *Glaucoma Monitoring:* Glaucoma, a leading cause of irreversible blindness, often damages the optic nerve and alters the optic disk. Regular monitoring and evaluation of the optic disk are vital for tracking glaucoma progression, assessing treatment effectiveness, and making informed management decisions.
- *Screening for Systemic Diseases:* The optic disk's appearance can offer insights into systemic conditions that may impact the optic nerve, such as hypertension, diabetes, and multiple sclerosis. Detecting and analyzing changes in the optic disk can serve as an initial screening tool for identifying these systemic diseases, leading to timely referrals for further evaluation and management.
- *Baseline for Future Comparisons:* Documenting the optic disk's characteristics establishes a baseline for future assessments. This reference point allows for the evaluation of changes in disk morphology over time, which is invaluable for monitoring disease progression, assessing treatment outcomes, and detecting subtle changes that may necessitate intervention.
- *Research and Population Studies:* The detection and analysis of the optic disk are critical in research focused on the epidemiology, risk factors, and natural history of various eye diseases. Large-scale population studies using retinal imaging often depend on precise optic disk evaluation to gather data, validate findings, and enhance our understanding of ocular and systemic health.

In summary, identifying the retinal optic disk is vital for diagnosing and managing eye diseases, monitoring disease progression, detecting systemic conditions, and supporting research and population health studies. This enables healthcare professionals to make informed clinical decisions, provide appropriate treatments, and promote early interventions for improved patient outcomes. Fig. 4.1 displays a retinal fundus image where the optic disk is marked with a circular shape.

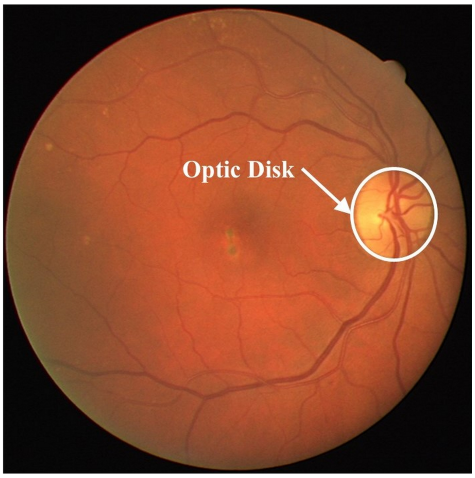

Fig 4.1: Retinal fundus image with optic disk marking

The presence of blood vessels within and around the optic disc, irregular disc shape, pathological features, uneven illumination, and image noise can hinder accurate segmentation of the optic disc. This research introduces a novel optic disc segmentation technique that effectively addresses these challenges without relying on prior information, templates, or vessel maps.

A new supervised method for optic disc identification and segmentation is proposed, which is robust against variations in illumination and retinal abnormalities. Although the optic disc is typically the brightest area in a retinal image, its brightness is not uniform across the entire region. Accurately detecting the optic disc boundary requires identifying all the bright regions within the optic disc. To achieve this, a four-step approach is employed:

- *Data Collection and Conversion:* Retinal images from various publicly available datasets are collected and converted to the red plane to enhance the brightness of the image's bright regions.
- *Image Enhancement:* Various techniques, including image calibration, registration, optimization, transformation, and filtering, are applied to enhance the image.
- *Identifying Bright Regions:* Bright areas near major blood vessels are identified using thresholding techniques followed by morphological reconstruction. A region-based classification is then performed to retain only the probable optic disc (OD) regions among all detected bright areas.

- *Image Analysis:* The optic disc portion is isolated by cropping the region of interest (ROI), and the segmented OD is compared with ground truth data to validate the results obtained by the proposed algorithm.

A flowchart illustrating these steps for OD detection is presented in Fig. 4.2.

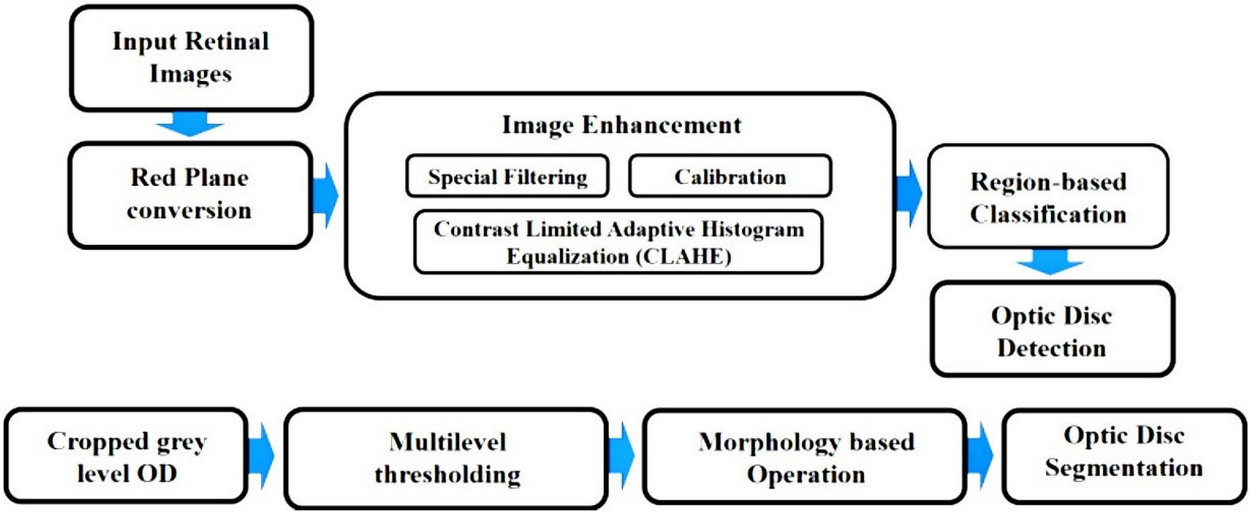

Fig 4.2: Block diagram of the proposed method for optic disc detection and segmentation from retinal fundus images, incorporating red plane conversion, CLAHE-based image enhancement, region-based classification, and morphology-based segmentation operations.

For the performance evaluation of optic disc identification and segmentation, the optic disc boundaries in retinal images are manually annotated using GIMP software. The proposed algorithm for optic disc identification and segmentation is tested on fundus images obtained from a publicly available dataset.

4.2. Results and Discussion

In this section of the research, the experimental results obtained using the proposed method have been examined and discussed. The system in question was developed and tested using MATLAB 2018a software, with the assistance of the image processing toolbox.

The proposed ADSO method for detecting and segmenting optic disks was rigorously tested on standard diabetic retinopathy datasets, including DRIVE, STARE, HRF, IDRiD, CHASEDB1, DAIRETDB1, and DRIONS-DB. Initially, the input RGB fundus image is converted into its red component and then enhanced using the CLAHE technique, as described in equations [3.48 - 3.55]

in Chapter 3. From the enhanced image, the brighter and larger region is identified as the optic disk and segmented using region-based K-Mean clustering, multi-level thresholding, and various morphological operations, as detailed in equations [3.87 – 3.95]. The success or failure of optic disk detection is based on human visual observation. To validate the results of optic disk localization, ophthalmologists manually categorized the optic disks in each image, with these manually separated optic disks serving as the ground truth dataset. A step-by-step depiction of the detection and segmentation process is provided in Fig. 4.3, while the detection results for different datasets are shown in Fig. 4.4.

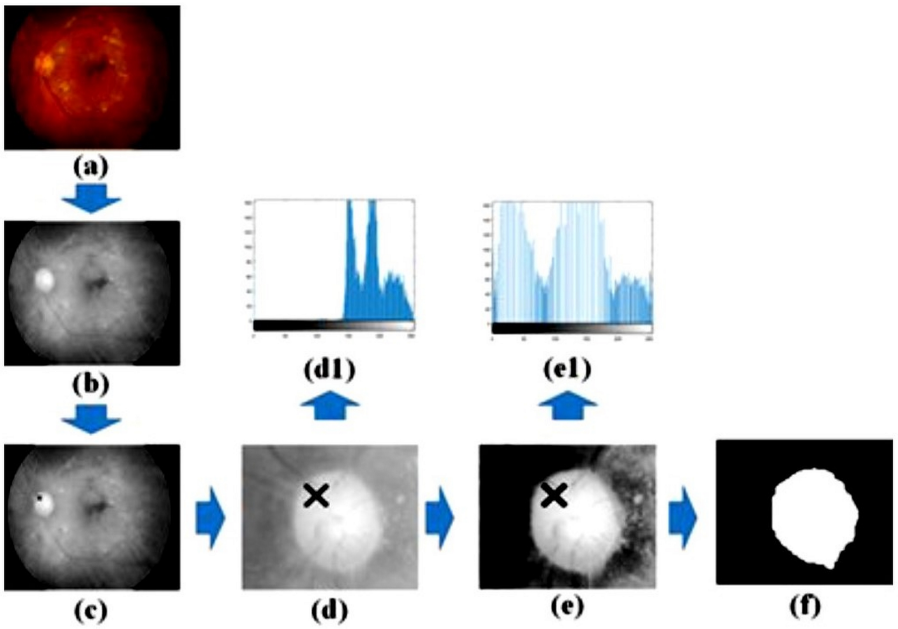

Fig 4.3: OD detection and segmentation steps; (a) Input fundus image, (b) red component of input, (c) OD detection, (d) OD cropping, (d1) histogram of figure (d), (e1) equalized histogram of figure (e), (e) OD enhancement, (f) OD segmentation

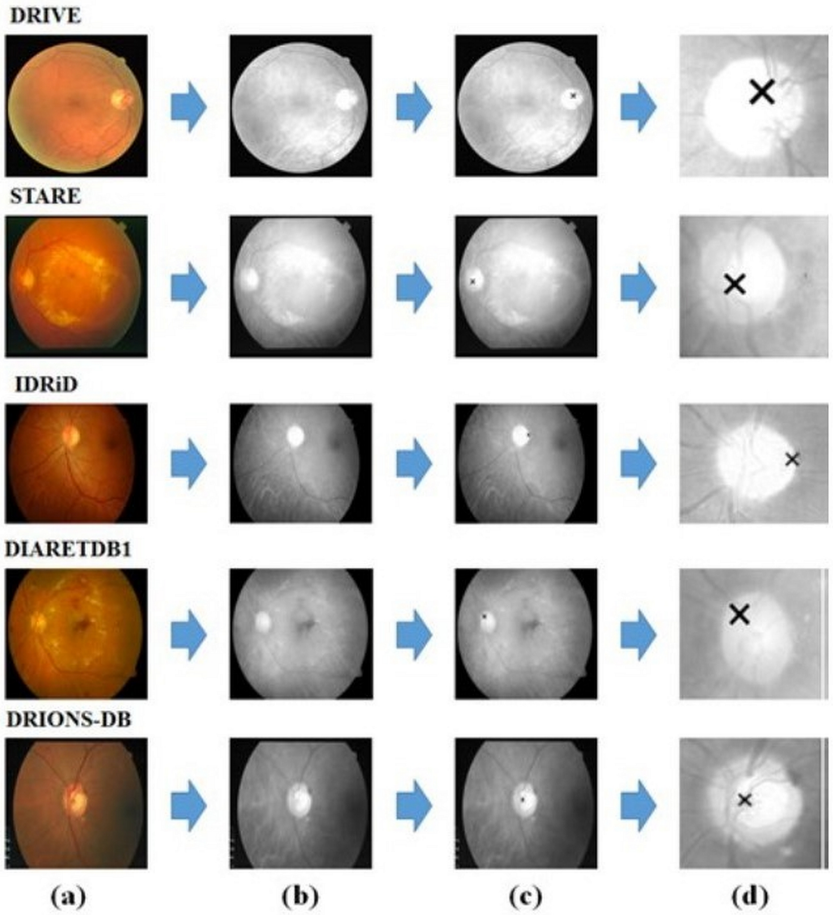

Fig 4.4: Optic Disc Identification and selection of AOI: (a) Input fundus images, (b) red components of inputs, (c) OD identification by marking, (d) OD cropping

The performance analysis of the proposed method for optic disc detection, compared to results from various authors, is presented in Table 4.1. This comparison clearly shows that the proposed method exceeds the performance of the existing approaches. The table reveals that the success rates of the other algorithms range from 64.1% to 98.77%, while the proposed ADSO method achieves a success rate of 99.9%.

Table 4.1: Performance comparison of the proposed ADSO method to detect OD with other existing methods

Algorithm	Dataset	Total number of samples taken	Success rate (%)
Muhammad Abdullah et al. [325]	STARE	81	64.10
Park et al. [326]	DRIVE	35	90.25
Niemeijer et al.[327]	DRIVE	40	89.00
Manish Kumar Aggarwal et al. [328]	DRIVE	40	95.00
	DIARETDB1	89	98.80
Foracchia et al. [329]	STARE	81	97.50
Mahfouz et al. [330]	DIARETDB1	89	97.80
	STARE	81	92.60
Youssif et al. [331]	STARE	81	98.77
ADSO	DRIONS-DB	110	99.83
	DRIVE	40	99.61
	STARE	81	99.10
	IDRiD	597	93.43
	DIARETDB1	89	98.92
	HRF	15	99.28
	DRIONS-DB	110	99.83

Figure 4.5 displays the segmented results of the optic disc for various databases using the proposed technique. Column (a) presents the input RGB fundus images from different datasets, column (b) shows the identified and cropped optic disc, and column (c) illustrates the segmented results for the corresponding dataset.

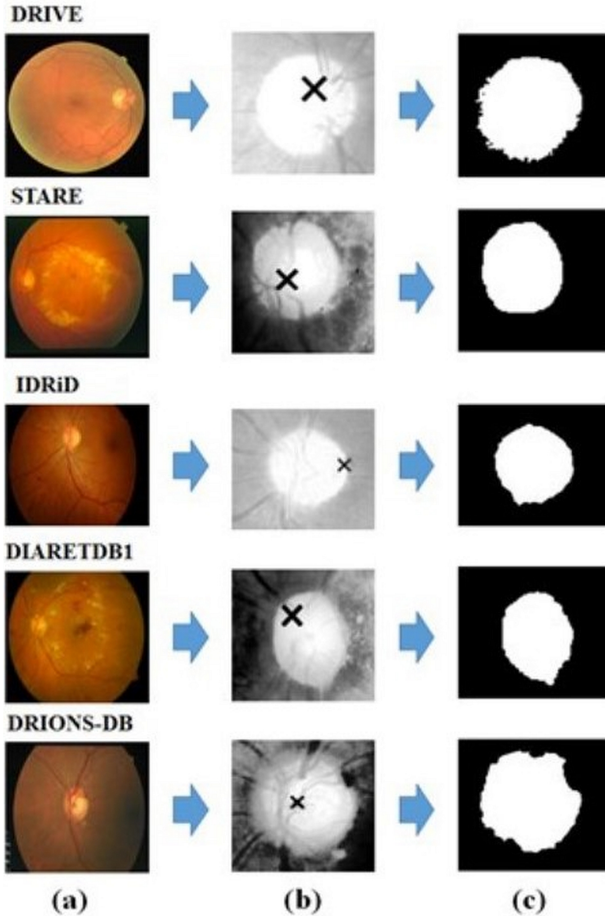

Fig 4.5: OD segmentation results for different datasets: (a) Input fundus image, (b) OD identification, (c) OD segmentation

The manual optic disks are gathered from the supplied dataset. The segmented outcomes produced by the ADSO method are compared based on overlapping pixel areas. These results are validated through sensitivity, accuracy, specificity, and overlap ratio measurements. The sensitivity, specificity, accuracy, and overlap ratio for the results obtained using the proposed ADSO method are calculated using the following simple mathematical expressions.

$$\begin{cases} Sensitivity = \dfrac{\sum Correctly\ Classified\ foreground\ pixels}{\sum Foreground\ pixels\ in\ groundtruth} \\ Specificity = \dfrac{\sum Correctly\ classified\ background\ pixels}{\sum Background\ pixels\ in\ groundtruth} \\ Accuracy = \dfrac{\sum Correctly\ classified\ pixels}{Total\ number\ of\ pixels\ in\ groundtruth} \end{cases}$$

$$Overlapping\ Ratio = \frac{ODB_G \cap ODB_R}{ODB_G \cup ODB_R}$$

$$where\ ,\ \begin{cases} ODB_G = Optic\ disk\ boundary\ trom\ the\ groundtruth \\ ODB_R = Resultant\ optic\ disk\ boundary \end{cases}$$

To achieve optimal segmentation results, various morphological operations such as dilation, erosion, opening, and closing are applied based on specific needs. These operations utilize a structuring element, which is a user-defined matrix that determines how each pixel in the processed image is classified and processed by defining its neighborhood. Changes in the structuring element impact the quality of the output results and the performance metrics. Fig. 4.6(a), 4.6(b), 4.6(c), and 4.6(d) illustrate the performance analysis of sensitivity, specificity, accuracy, and overlap ratio in relation to the structuring element across different datasets. The analysis indicates that altering the structuring element parameters affects sensitivity and other evaluated metrics. This highlights a key aspect of the ADSO method: effective control over optic disk parameters can be achieved by adjusting the structuring element.

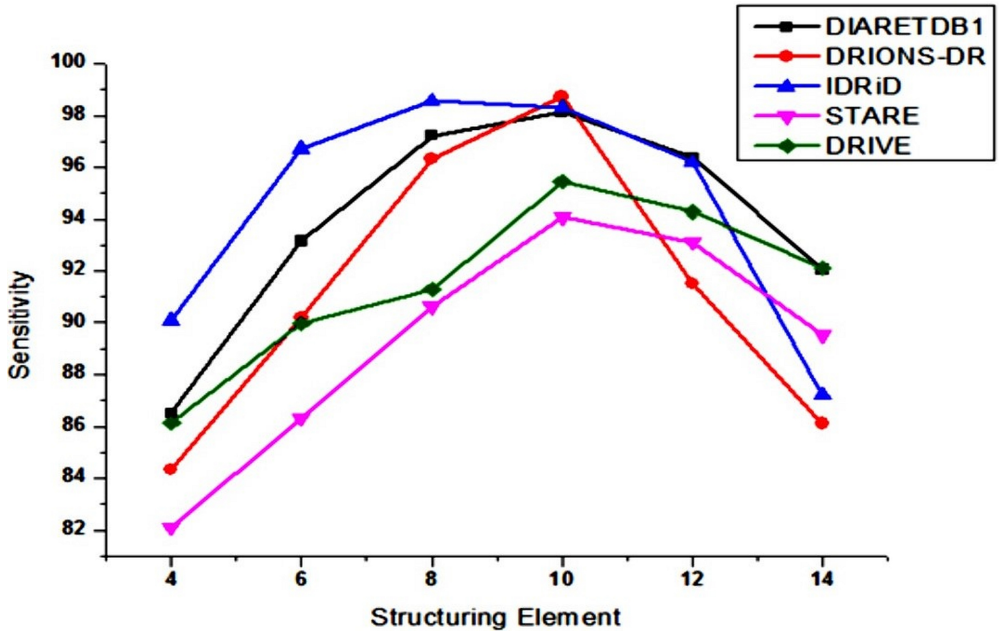

Fig 4.6(a): Sensitivity graph of different database used with respect to different Structuring Elements

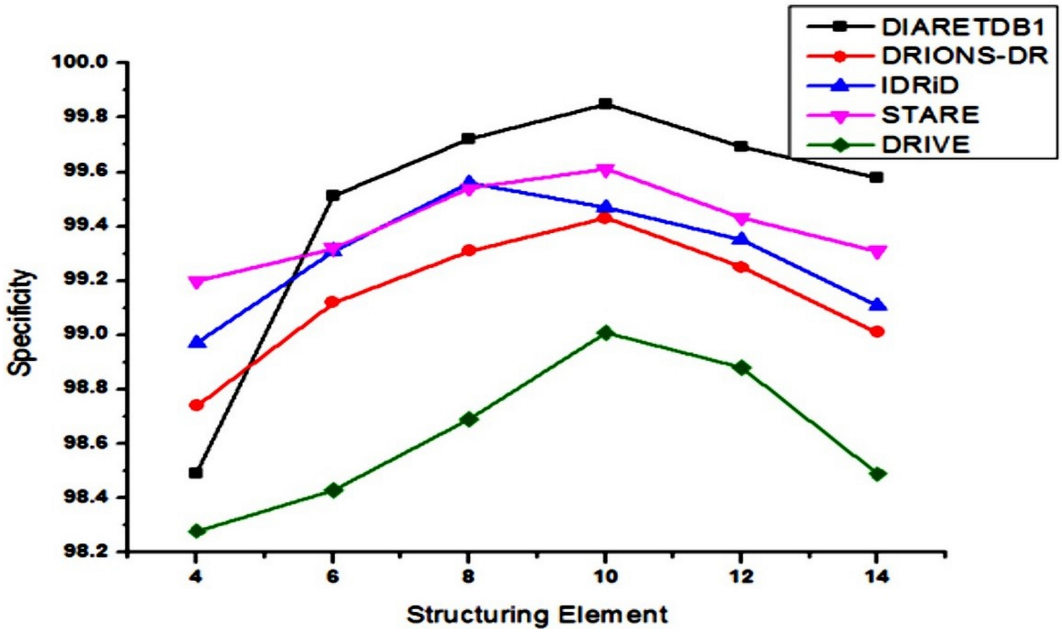

Fig 4.6(b): Specificity graph of different database used with respect to different Structuring Elements

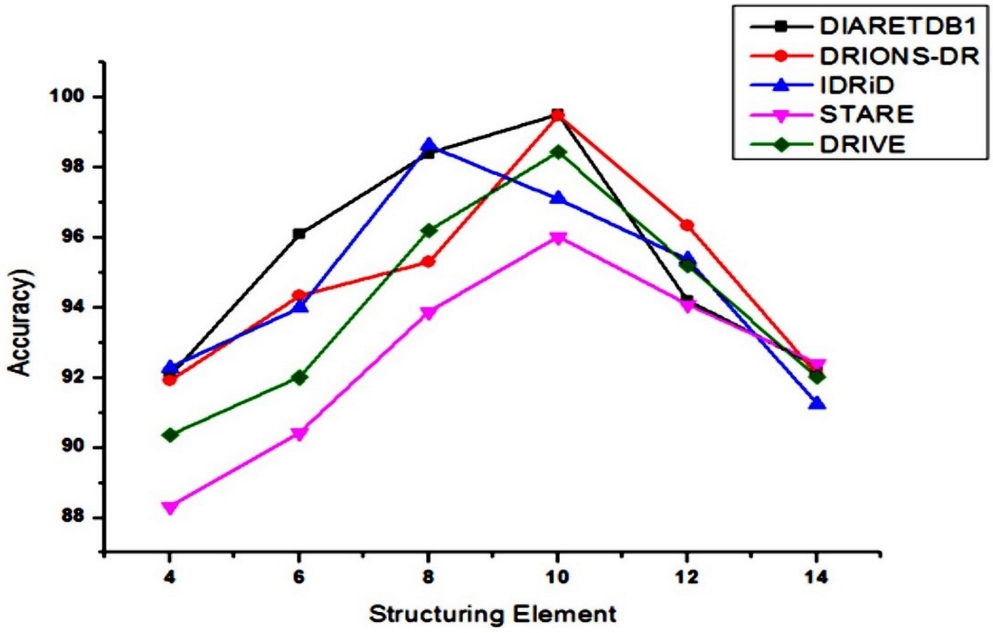

Fig 4.6(c): Accuracy graph of different database used with respect to different Structuring Elements

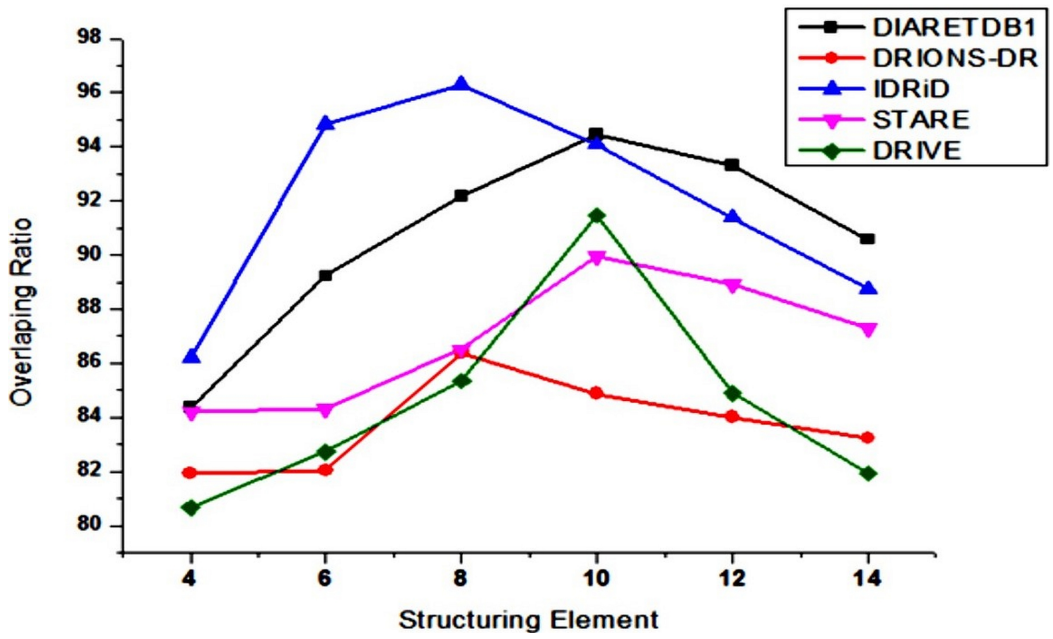

Fig 4.6(d): Overlapping ratio graph of different database used with respect to different Structuring Elements

4.3. Conclusion:

To summarize, image processing techniques have shown significant effectiveness in detecting the retinal optic disk. Various authors have proposed different methods and algorithms, and comparisons indicate that the ADSO method surpasses other approaches. The ADSO method achieves an exceptionally high success rate of 99.9% in optic disk detection. These results underscore the potential of image processing to enhance both the accuracy and efficiency of retinal optic disk detection, which is crucial for diagnosing and treating eye conditions. Continued research and development in this field are essential to further improve detection capabilities and broaden the applications of image processing in ophthalmology.

Chapter V

Automatic Segmentation of Blood Vessels (ASBV) Of Retinal Fundus Images Using CLAHE And Multilevel Thresholding Based on Harmony Search

The main objective in the field of medical image processing is to develop computational tools that aid in the quantification and visualization of important pathologies and anatomical structures. Diabetic retinopathy, a condition marked by retinal damage due to fluid leakage from blood vessels into the retina, is one such pathology. Accurately detecting blood vessels in retinal fundus images and analyzing their shape and size over time are essential for diagnosing various retinal abnormalities. Many of these abnormalities are linked to changes in the structure of blood vessels. Segmenting blood vessels across the entire retinal image can reduce sensitivity in specific areas. In this study, an advanced algorithm combining CLAHE (Contrast Limited Adaptive Histogram Equalization) and multilevel thresholding using harmony search has been proposed for the detection and segmentation of blood vessels. This approach significantly reduces the computational cost and processing area required for each fundus image, thereby enhancing the segmentation method's performance. The proposed technique was tested on publicly available retinal image datasets, including CHASEDB1, DRIVE, HRF, and STARE, and showed significant improvements in both accuracy and processing time compared to existing methods.

5.1. Introduction

Diabetes is associated with various serious complications affecting human organs, including heart failure, complete vision loss, and different types of strokes. It also increases the likelihood of eye-related issues such as glaucoma and cataracts. However, the most significant risk to vision in diabetic patients is due to the impact of diabetes on the retinal system, leading to a condition called diabetic retinopathy, which can result in complete vision loss.

Ophthalmologists diagnose several eye diseases by analyzing retinal images captured using a fundus camera with various settings. The analysis of these images involves identifying and extracting multiple retinal anatomical structures that are closely linked to the disease. Examples of these structures are shown in Fig. 5.1, highlighting target features for different segmentation techniques such as the retinal optic disc, optic cup, vessels, fovea, exudates, and hemorrhages.

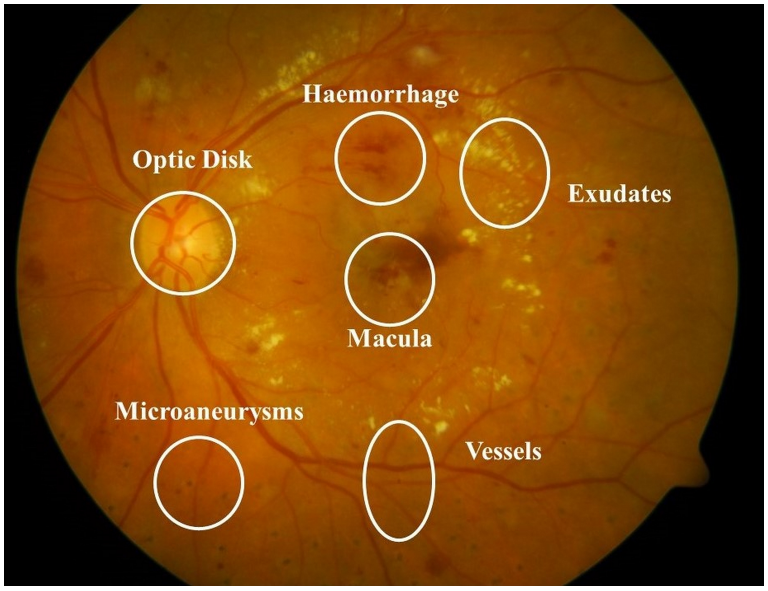

Fig 5.1: Different features of retinal images of the human eye related to diabetics [357].

This research focuses on examining how diabetes affects the retinal blood vessels in the human eye. Changes in the diameter of these vessels occur due to fluctuations in blood pressure, which are linked to blood sugar levels. Typically, in retinal images, the optic disc—the point where blood vessels converge—is the brightest area. Identifying the optic disc is crucial for mapping the blood vessels.

Over 382 million people between the ages of 40 and 59 suffer from diabetes [337-339], with India, the USA, and China having the highest prevalence. Given the large number of individuals requiring screening, there's a significant need for ophthalmologists. Therefore, developing an automated algorithm to detect diabetic retinopathy is essential. This study introduces an advanced technique for the rapid and precise segmentation of retinal vessels, utilizing specialized filtering, Contrast Limited Adaptive Histogram Equalization (CLAHE), and a multilevel thresholding method based on harmony search.

The process begins with identifying and segmenting the optic disc from the fundus image. The red channel of the input image is used because it highlights the brighter regions more clearly. Special filters are employed to eliminate unwanted frequency components and enhance the desired ones. The histogram of the red channel provides various intensity characteristics, with the brightest intensity areas generally corresponding to the optic disc. Morphological techniques are then used to segment the optic disc. Following this, the image is enhanced to better reveal the blood vessels. CLAHE with various clip limits is applied to achieve optimal enhancement. Finally, multilevel thresholding using harmony search is implemented to segment the vessel structure. Experimental results indicate that the proposed technique improves image contrast, illumination, and performance metrics while being computationally efficient.

In this research, a new supervised method for vessel segmentation is proposed to detect retinal abnormalities. While the optic disc is the brightest area in the retinal image, not every part of it is equally illuminated. Efficient detection of the optic disc boundary requires identifying the brightest regions. A six-step approach is proposed in this chapter to achieve this. The first stage involves collecting retinal images from publicly available sources. In the second stage, filtering and enhancement techniques are applied to the images, with median filtering playing a crucial role in noise reduction. CLAHE is then used to enhance the vessels [equations 3.48-3.55]. In the third stage, morphological opening and Top-Hat operations are performed [equations 3.91-3.95]. The fourth stage applies multilevel thresholding using harmony search to detect the major blood vessels [equation 3.87]. The fifth stage involves morphology-based operations to identify specific edges and shapes in the image, and the final stage involves analyzing the image to detect segmented vessels. The proposed block diagram of the Automatic Segmentation of Blood Vessels (ASBV) method is shown in Figure 5.2.

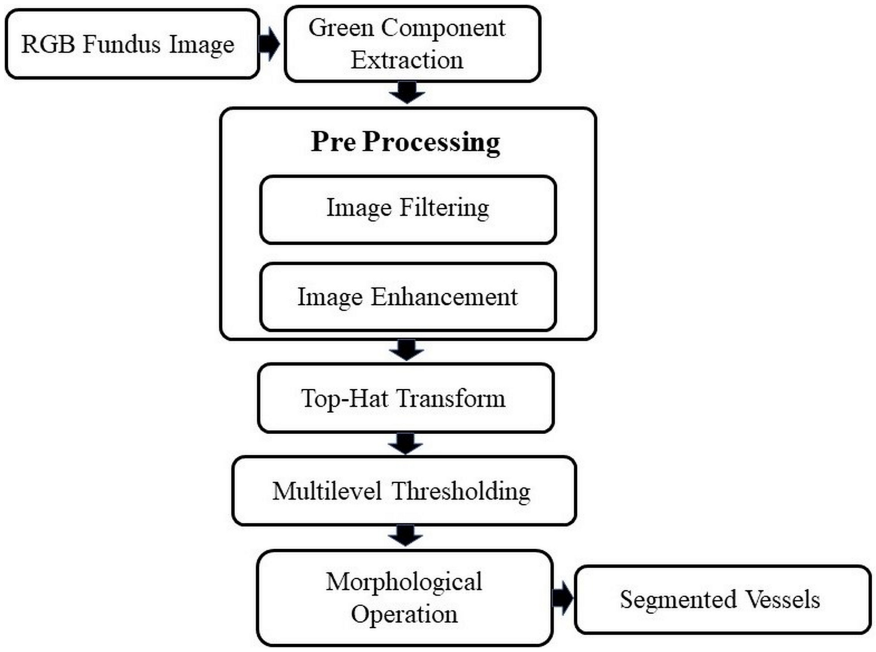

Fig 5.2: Proposed system architecture of the ASBV method, showing green component extraction, preprocessing, top-hat transform, multilevel thresholding, and morphological operations for retinal vessel segmentation.

In this context, a true positive (TP) refers to correctly identifying a vessel pixel as a vessel pixel, while a true negative (TN) refers to correctly identifying a non-vessel pixel as a non-vessel pixel. Conversely, a false positive (FP) occurs when an out of the vessel pixel is measured incorrectly as an inside vessel pixel and the vice versa is the false negative (FN).

The sensitivity, specificity, accuracy, and overlap ratio for the output results obtained using the proposed method have been calculated using the following straightforward mathematical expressions:

$$Sensitivity = \frac{\sum correctly\ classified\ foreground\ pixels}{\sum foreground\ pixels\ in\ groundtruth}$$

$$Specificity = \frac{\sum correctly\ classified\ background\ pixels}{\sum background\ pixels\ in\ groundtruth}$$

$$Accuracy = \frac{\sum correctly\ classified\ pixels}{total\ number\ pixels\ in\ groundtruth}$$

$$Overlapping\ Ratio = \frac{ODB_G \cap ODB_R}{ODB_G \cup ODB_R}$$

$$where\ ,\ \ ODB_G = Optic\ Disc\ Boundary\ from\ groundtruth$$

$$ODB_R = Resultant\ Optic\ Disc\ Boundary$$

The Area Under the Curve (AUC) represents the area beneath the receiver operating characteristic (ROC) curve, which illustrates segmentation performance based on both specificity and sensitivity. In this study, the AUC was calculated using the following formula:

$$AUC = \frac{Sensitivity + Specificity}{2}$$

It's important to note that an AUC value of 0.50 or lower indicates that the segmentation is not very useful, as it is equivalent to random guessing. On the other hand, an AUC value of 1.0 indicates that the segmentation algorithm is capable of perfectly segmenting every pixel.

5.2. Results and Discussion

In this section of the research, the experimental outcomes obtained using the proposed method have been examined and discussed. The system described was developed and tested using MATLAB 2018a, with support from the image processing toolbox.

The proposed method for segmenting vessel structures has been rigorously tested on various publicly available databases. The success or failure of vessel structure detection is determined through visual inspection by the human eye. To validate the results, ophthalmologists manually categorized the vessels in each image, and this manually separated vessel structure is considered the ground truth dataset. The proposed method was then employed to automatically detect the vessel structures, and the results were validated by comparing them with the ground truth data.

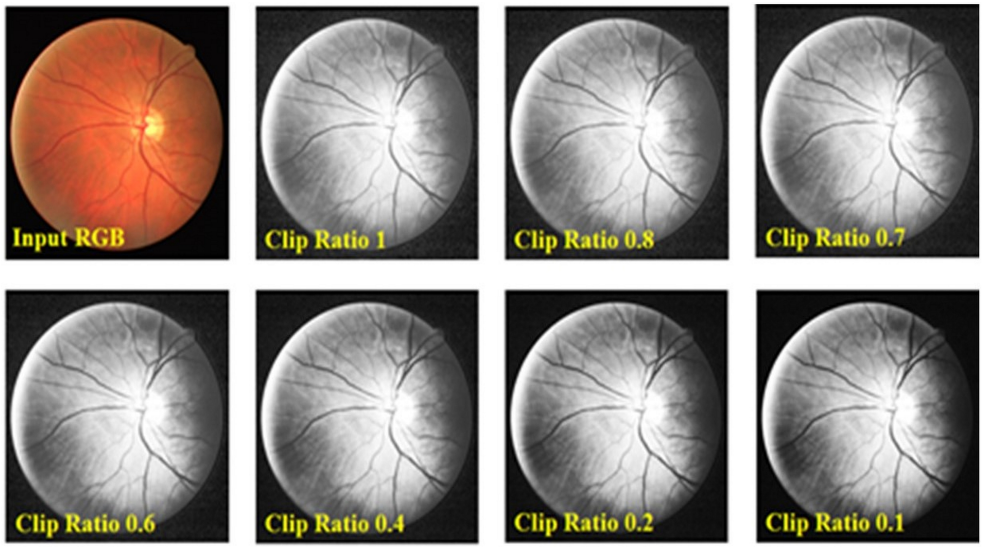

Fig 5.3: Result shows the contrast limited adaptive histogram equalization on DRIVE data (04_test.tif)

To automatically identify the vessel structure, a series of pre-processing steps were applied to enhance the fundus image of the human eye. Initially, the green channel of the input RGB fundus image was selected, as it provides the optimal contrast for visualizing blood vessels (darker vessels against a brighter background). Following this, a 3×3 median filter was used to eliminate noise, such as salt-and-pepper noise. Lastly, the image underwent additional enhancement using the Contrast Limited Adaptive Histogram Equalization (CLAHE) technique. The results of applying CLAHE with different limits are presented in Figure 5.3, using image data from the DRIVE dataset.

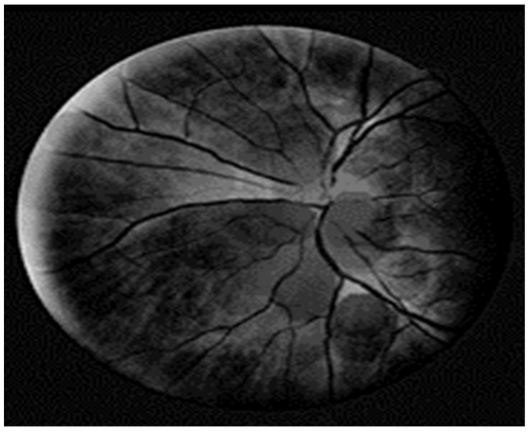

Fig 5.4: Result shows morphological Top-hat transformation of DRIVE (04_test.tif)

In the post-processing phase, the results enhanced by CLAHE were further refined using the morphological top-hat transform technique, aided by structuring elements, to extract fine details from the input images. This is illustrated in Figure 5.4.

For multilevel thresholding, harmony search was employed to determine the optimal five intensity levels of the top-hat transformed image, with the results displayed across different thresholds. The fitness graph, which compares gray levels with probability, is shown in Figure 5.5. Subsequently, morphological dilation and erosion were applied to eliminate unwanted variables, followed by morphological closing to achieve the final result. Each step of the multilevel thresholding process on the DRIVE dataset is depicted in Figure 5.6.

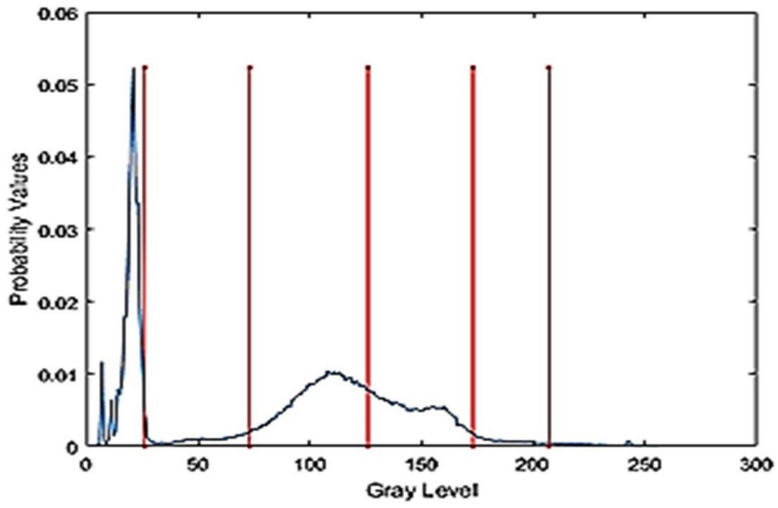

Fig 5.5: The result shows the fitness graph of multilevel thresholding comparing the gray levels with probability values

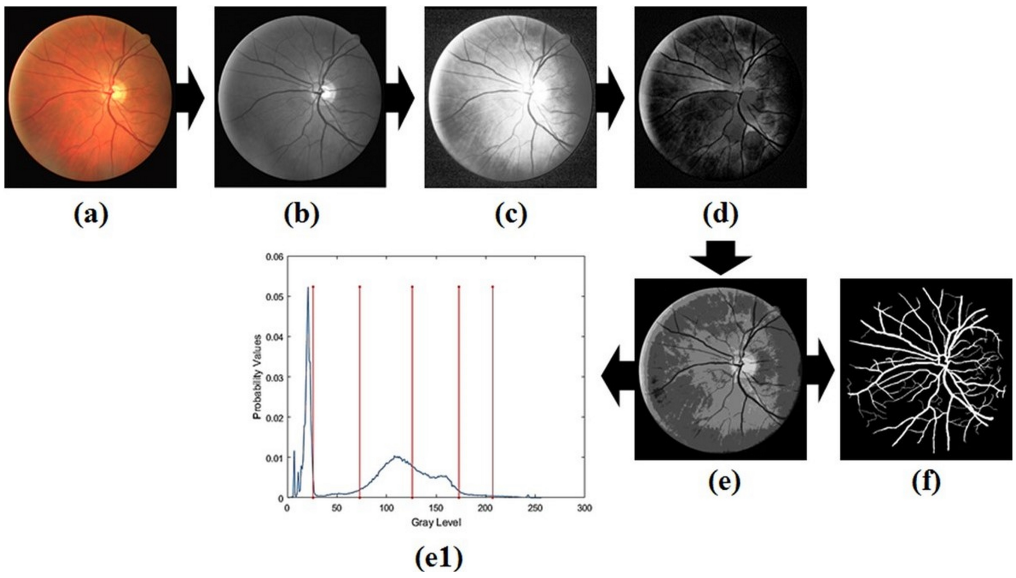

Fig 5.6: Result shows the outputs of DRIVE_04_test.tif: (a) input retinal fundus image (RGB), (b) Green components of the RGB image of retina, (c) result after using contrast limited adaptive histogram equalization technique with the limit 0.1, (d) morphological Top hat, (e) Multilevel thresholding using harmony search, (e1) Threshold limit of multilevel thresholding, (f) segmented vessels.

The results of the segmentation, compared to the corresponding ground truth data from the different datasets mentioned, are presented in Figure 5.7. This comparison reveals an accuracy of 98.22%, with sensitivity, specificity, and overlap ratios of 98.99%, 96.52%, and 97.96%, respectively.

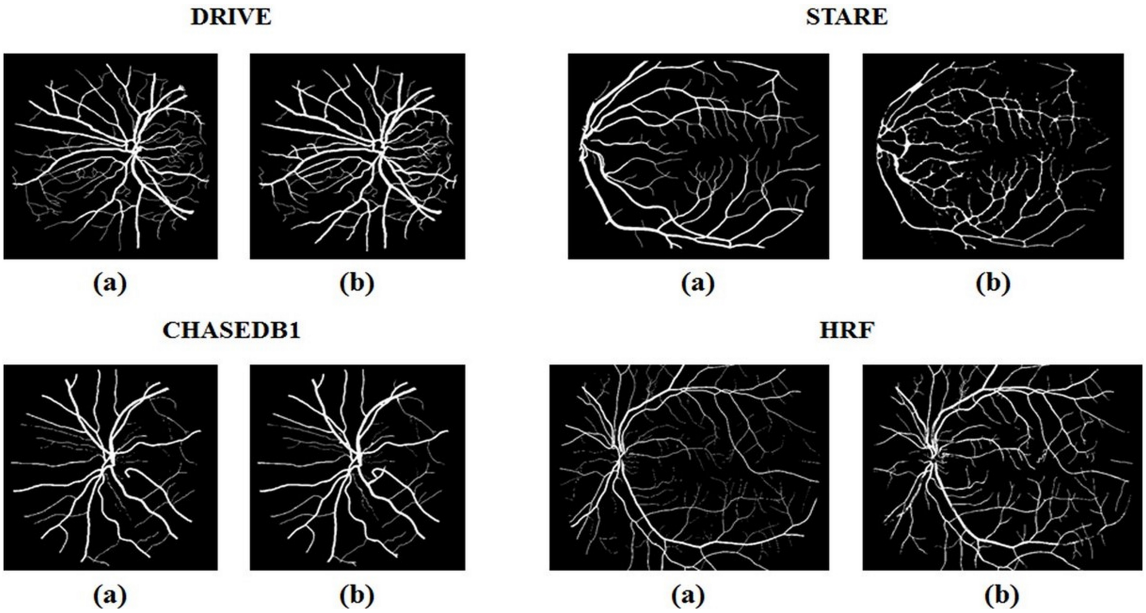

Fig 5.7: Result shows the images of segmented vessels (a) ground truth result, (b) automatic segmented result using the proposed method.

Table 5.1 presents the performance analysis of the proposed technique in comparison to existing methods. According to the table, the sensitivity for the other methods ranges from 70% to 83.47%, which is significantly lower than the sensitivity achieved with the proposed ASBV technique. Additionally, the specificity and accuracy for these methods vary from 94.2% to 98.5% and 93.53% to 96.1%, respectively. The results in Table 5.1 highlight the superior performance of the ASBV technique in terms of sensitivity, specificity, and accuracy.

Table 5.1: The performance analysis result of the proposed technique with comparison to the previously established methods

Algorithm	Dataset	Number of samples taken	Sensitivity (%)	Specificity (%)	Accuracy (%)	Overlapping Ratio (%)	AUC
Saeid Fazli et al. [340]	DRIVE	40	-	-	93.53	-	-
Zhun Fan et al. [341]	DRIVE	20	71.9	98.5	96.1	-	-
	STARE	20	70	97.9	95.9	-	-
Ming Li et al. [341]	DRIVE	40	83.47	97.96	95.10	-	97.92
	STARE	20	82.31	97.82	95.60	-	97.43
Yitian Zhao et al	DRIVE	40	77.4	97.9	95.8	-	97.5
	STARE	20	78.8	97.6	95.7	-	95.9

[343]	HRF	45	74.9	94.2	94.1	-	97.1
ASBV	DRIVE	40	99.63	96.69	97.00	98.73	98.16
	STARE	81	98.53	96.45	97.33	98.07	97.49
	HRF	15	99.71	97.62	98.22	98.79	98.66
	CHASE DB1	28	98.47	95.31	98.11	96.28	96.89

5.3. Conclusion

Detecting retinal vessels through image processing is an effective method for analysing retinal images and extracting crucial information about the blood vessels in the retina. Using advanced image processing algorithms, it's possible to automatically segment and identify these vessels, which supports the diagnosis, monitoring, and treatment of various retinal conditions.

Typically, retinal vessel detection involves initial pre-processing steps such as enhancing the image, reducing noise, and adjusting contrast to improve image quality. Subsequently, segmentation techniques like thresholding, region growing, or model-based methods are applied to distinguish the blood vessels from the background and other retinal structures.

Once the retinal vessels have been segmented, it is possible to analyse various features including vessel width, length, tortuosity, branching patterns, and vessel density. These features provide critical insights into retinal health and are useful for detecting and analysing conditions like diabetic retinopathy, glaucoma, and hypertension.

The use of image processing for retinal vessel detection offers several benefits. It provides a non-invasive, cost-effective approach to assessing retinal health, enabling early disease detection and ongoing monitoring. This method also aids ophthalmologists in making precise diagnoses and treatment decisions, as well as tracking disease progression over time. Additionally, automated vessel detection reduces the time and effort needed for manual image analysis.

However, it is important to recognize that retinal vessel detection algorithms can face limitations and challenges. The accuracy of these algorithms may be impacted by factors such as image quality, variability in vessel appearance, presence of lesions or pathologies, and image artifacts. Therefore, thorough validation and optimization of the algorithms are essential to ensure reliable results.

Chapter VI

PSO-HRVSO: Segmentation of Retinal Vessels through Homomorphic Filtering Enhanced by PSO Optimization

The methodology PSO-HRVSO comprises three key stages: pre-processing, main processing, and post-processing. In the initial stage, filters are employed for image smoothing and enhancement, leveraging PSO optimization. The main processing phase is bifurcated into two configurations. Initially, thick vessels are segmented utilizing an optimized top-hat approach, homomorphic filtering, and a median filter. Subsequently, the second configuration targets thin vessel segmentation, employing the optimized top-hat method, homomorphic filtering, and matched filter. Lastly, morphological image operations are conducted during the post-processing stage.

The PSO-HRVSO method underwent evaluation using two publicly accessible databases (DRIVE and STARE), measuring performance across three key metrics: specificity, sensitivity, and accuracy. Analysis of the outcomes revealed averages of 0.9891, 0.8577, and 0.0.9852 for the DRIVE dataset, and 0.9868, 0.8576, and 0.9831 for the STARE dataset, respectively. The PSO-HRVSO technique yields numerical results that demonstrate competitive average values when compared to current methods. Moreover, it surpasses all leading unsupervised methods in terms of specificity and accuracy. Additionally, it outperforms the majority of state-of-the-art supervised methods without

incurring the computational costs associated with such algorithms. Detailed visual analysis reveals that the PSO-HRVSO approach enables a more precise segmentation of thin vessels compared to alternative procedures.

6.1. Introduction

The examination of the eye fundus is extensively utilized by ophthalmologists and other medical practitioners as a standard clinical procedure for preventing, diagnosing, and monitoring the treatment of various ocular conditions including retinal thrombosis, glaucoma, and senile maculopathy, among others. This examination involves a color imaging method of the retinal surface of the human eye, enabling the observation of key anatomical features such as the optic disc, macula, and vascular tree.

The segmentation of the retinal vascular tree holds significant importance in the realm of medical imaging because the retina offers a unique avenue to observe blood microcirculation non-invasively, allowing for the detection of various systemic diseases such as hypertension, diabetes, arteriosclerosis, and liver diseases, among others. By delineating the retinal vessels, valuable morphological data including size, length, width, branching patterns, and angles of the retinal vasculature can be quantified. However, manually performing this segmentation is a laborious process that demands expertise and experience from medical professionals. Moreover, inconsistencies may arise due to subjective interpretations, as experts might employ different criteria for pixel classification.

Hence, it is imperative to advance and implement automated techniques for robust vessel extraction in Computer-Aided Diagnosis to facilitate early detection and assessment of disorders, aiming to mitigate medical expenses and enhance efficiency. Nonetheless, segmentation encounters numerous hurdles. The foremost challenge emanates from the presence of various optical components in the eye fundus, including the optic disk, macula, and artifacts generated by pathologies, impeding the automated segmentation of vessels. The second challenge stems from the variability in vessel width and the subdued contrast of thin vessels against the background. Lastly, the third challenge arises from the diversity in shape, size, and intensity of vessel pixels, complicating accurate segmentation.

In recent decades, numerous techniques have emerged for automatically segmenting retinal vessels using fundus examination, garnering considerable attention from the scientific community due to their increasingly accurate outcomes. These methods are typically categorized as supervised or unsupervised. Supervised methods involve training a classifier with a dataset (training set) to differentiate between vessel and non-vessel pixels, further classified into machine learning and

deep learning algorithms. Machine learning approaches typically involve feature extraction,selection, and classification stages, with various feature extractors and classifiers PSO-HRVSO for medical image classification, including bag-of-visual-words, Gaussian filter, and Gabor filter, along with classifiers like K-Nearest Neighbors (K-NN), Random Forest, Support Vector Machine (SVM), and Artificial Neural Networks (ANN).

Deep learning techniques offer an advantage over traditional methods by automatically extracting features from raw data, eliminating the need for handcrafted features [34,32]. While supervised methods yield satisfactory results for healthy retinal vessel extraction, a notable limitation is the necessity for ground-truth images, which can be challenging to obtain. Additionally, both machine learning and deep learning algorithms demand time-consuming and computationally expensive training processes to effectively handle new sets of images.

Conversely, unsupervised methods in medical image processing involve image segmentation without relying on a training dataset. These approaches utilize various image processing techniques. Initially, the image undergoes enhancement procedures, typically employing morphological operations, matched filter responses, the complex continuous wavelet transform, adaptive histogram equalization, and Hessian-based filters among others. Subsequently, segmentation occurs through multilevel thresholding or region-oriented techniques such as region growing or active contours. These conventional unsupervised methods heavily rely on manual feature extraction for image element representation and segmentation. Generally, supervised methods exhibit higher efficiency and yield superior results. However, unsupervised systems possess a significant advantage in performing vessel segmentation without prior knowledge of ground-truth labels, particularly beneficial for datasets lacking pixel-level labeling information. Additionally, unsupervised methods offer computational efficiency and faster results. Recent research has utilized both supervised and unsupervised methodologies, demonstrating promising performance in retinal vessel segmentation. Nevertheless, the challenge of accurately segmenting thin vessels remains a significant hurdle for optimal performance in existing literature. Thin vasculature offers crucial information for detecting neovascular diseases, underscoring the importance of achieving improved vessel segmentation for enhanced detection and diagnosis of eye diseases.

This article presents a novel methodology aimed at accurately segmenting retinal vasculature to tackle prevalent challenges encountered in retinal vessel segmentation from eye fundus images. The PSO-HRVSO approach comprises three distinct phases: pre-processing, main processing, and post-processing. During the initial phase, a Gaussian filter is employed to yield a smoothed gray-scale fundus image, followed by PSO-optimized image enhancement for obtaining an optimized enhanced fundus image. The main processing phase entails two configurations: the first configuration targets thick vessel segmentation through a combination of filters (Optimized tophat, Homomorphic, and Median), whereas the second configuration focuses on thin vessel segmentation using a similar combination of filters (Optimized top-hat, Homomorphic, and Matched). Subsequently, morphological image processing is applied during the post-processing phase. Extensive experiments are conducted on two publicly available databases, DRIVE (51) and STARE (50), to evaluate the methodology's performance. The results of performance metrics underscore the method's advantages, demonstrating comparable or superior values in contrast to many contemporary techniques, which often entail higher computational complexity for retinal vessel segmentation.

6.2. Results and Discussion:

This section provides a concise overview of the PSO-HRVSO algorithm, as illustrated in the flowchart depicted in Fig. 6.1. Key concepts integral to the PSO-HRVSO methodology are outlined herein. Notably, the eye fundus image exhibits both thick and thin blood vessels, with the latter often overlooked by previous algorithms. The primary objective of this approach is to effectively segment thick and thin vessels, resulting in two distinct images. These images are subsequently merged to produce a final segmentation outcome.

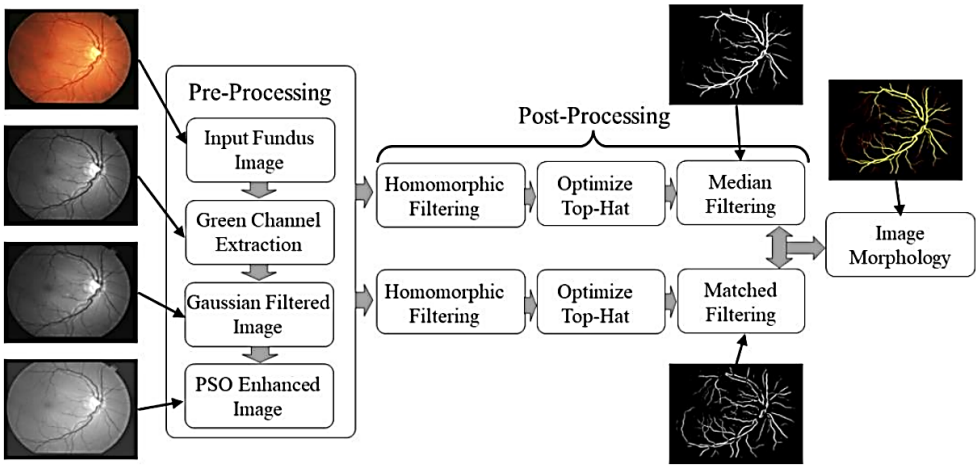

Fig. 6.1: Proposed PSO-HRVSO method for retinal vessel segmentation, incorporating PSO-based enhancement, homomorphic filtering, optimized top-hat transform, and matched or median filtering for refined vessel extraction.

While the green channel of the eye fundus image exhibits commendable vessel-background contrast compared to the RGB input image, incorporating a noise removal step before subsequent stages yields positive and productive outcomes. The utilization of the Gaussian smoothing filtering algorithm proves advantageous for enhancing image structures, including previously contrasted elements. This filtering technique operates by employing a Gaussian function, rooted in the normal distribution widely utilized in statistics, to compute the transformation applied to each pixel within the two-dimensional set. The Gaussian distributed output of the RGB retinal fundus image is displayed in Fig. 6.2.

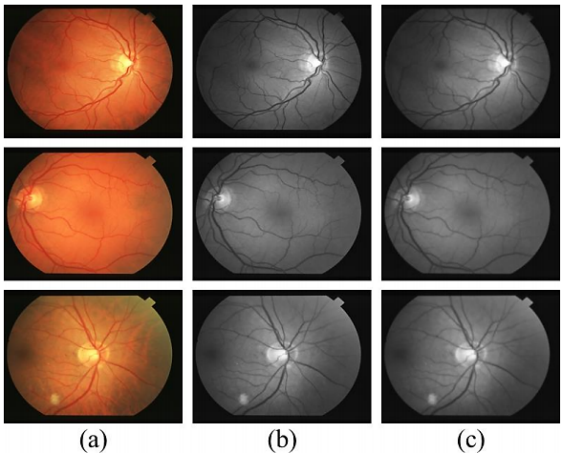

Fig. 6.2: Shows the Gaussian Distributed results (a) Input RGB, (b) Green Component, (c) Gaussian Distribution.

PSO enhances images by formulating the process as an optimization problem. Each particle in the swarm represents a potential solution, defined by a set of enhancement parameters, and the algorithm iteratively refines these solutions to identify the optimal one. Each particle applies its parameters to the image and evaluates its performance using a fitness function. Common fitness metrics include entropy, which quantifies the richness of image details; edge intensity, which assesses edge sharpness and clarity; PSNR (Peak Signal-to-Noise Ratio), which measures noise levels and the preservation of original details; and SSIM (Structural Similarity Index), which compares the structural integrity of the enhanced image with the original. An increase in fitness value signifies improved enhancement, while a rise in PSNR accompanied by a drop in entropy may indicate excessive smoothing. Achieving an optimal balance between entropy, edge intensity, and PSNR is crucial for superior results. The PSO-optimized image demonstrates enhanced contrast, sharpness, and detail visibility compared to the original. The fitness value serves as an indicator of enhancement quality, ensuring maximum information retention with minimal distortion. PSO's iterative approach guarantees optimal enhancement without the need for manual parameter adjustments. Fig 6.3 presents the image enhanced using PSO.

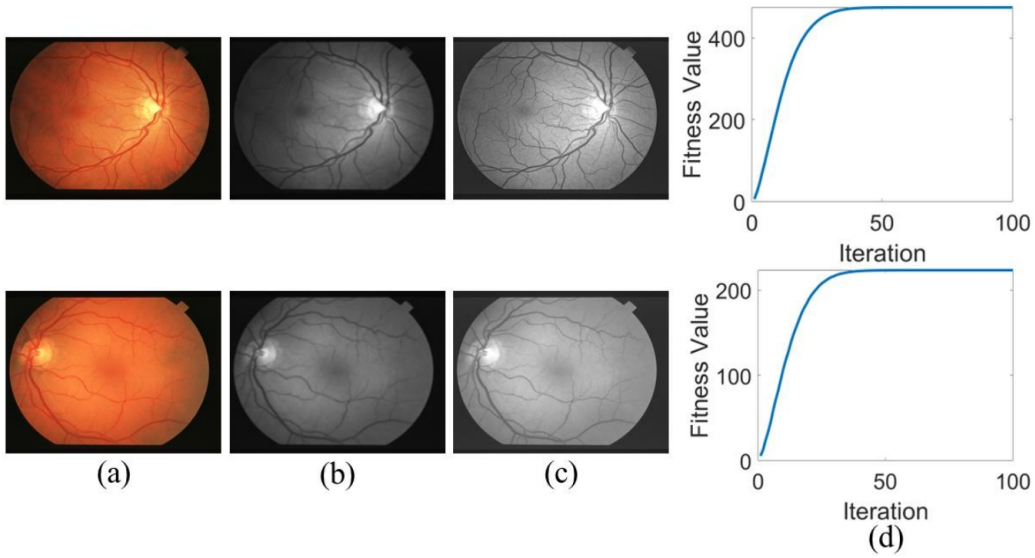

Fig 6.3: PSO Optimization: (a) RGB Image, (b) Gaussian Distribution, (c) PSO Enhanced, (d) Fitness Curve.

Fig. 6.4(d) and Fig. 6.4(e) illustrate the outcome of employing the PSO-HRVSO optimized top-hat filter and binarized top hat respectively on the input fundus image depicted in Fig 6.4(a) whereas Fig. 6.4(b) and Fig. 6.4(c) illustrate the outcome of employing global top-hat optimization and its binary part. Both Fig. 6.4(b) and Fig. 6.4(d) were generated using a structuring element of the same shape and size for both opening and closing operations (a disk with a radius of 10 pixels). A qualitative examination of the images reveals that the PSO-HRVSO optimized top-hat filter significantly improves the contrast of the vessels compared to the classical top-hat filter, enhancing both thick and thin vessels.

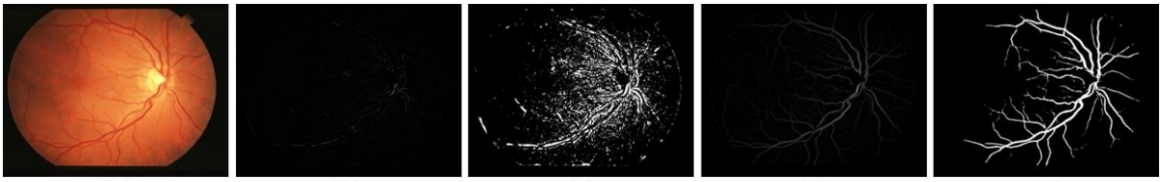

Fig. 6.4: Optimized Top-Hat: (a) Input RGB, (b) Conventional Top-Hat, (c) Binary of (b), (d) Optimized Top-Hat, (e) Binary of (d).

Building upon the methodology described in the preceding section, and considering the finer scale of thin blood vessels which occupy smaller pixel sizes, a disk-shaped structuring element with radii of 5 and 25 pixels is PSO-HRVSO for opening and closing operations, respectively. As thin vessels encompass only a small percentage of the image, their total reflectance component value is comparatively lower than that of thick vessels. To enhance the visibility of these small white regions, a σ value of twenty is utilized to expand the cut-off regions of the filter. This enhancement improves all white components of the image, including the small vessels, albeit at the expense of thinning the thick and major veins of the vascular tree. However, this thinning effect will later be rectified by merging the segmented image of thick veins with the resultant image of subsequent steps. Fig. 6.5 depicted the vessel's segmented results.

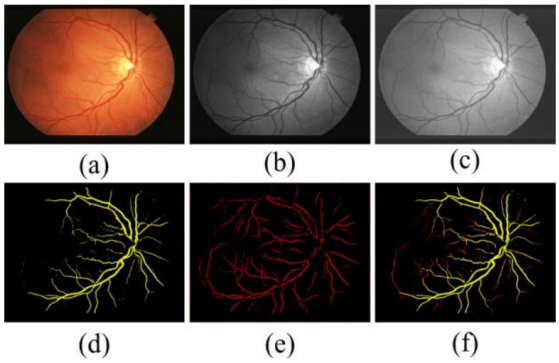

Fig. 6.5: Vessels Segmentation: (a) Input RGB, (b) Green Component, (c) PSO Optimized, (d) Segmented Thick Vessels, (e) Segmented Thin Vessels, (f) Combined Vessels.

This section presents the performance outcomes of the PSO-HRVSO method applied to two eye fundus datasets for retinal vessel segmentation: DRIVE and STARE, both publicly accessible. The DRIVE dataset comprises 40 images divided into two subsets of 20 elements each, designated as the training and test sets. All images were captured using a Canon CR5 nonmydriatic 3CCD camera with a 45^0 field of view and a spatial resolution of 565 × 584 pixels. Additionally, the DRIVE image dataset includes manual segmentation conducted and validated by three trained human observers with medical expertise. The training subset involves the manual segmentation of one set by a single human observer, while the test subset underwent manual segmentation by two human observers, offering dual perspectives and establishing ground-truth images for performance analysis.

On the other hand, the STARE dataset comprises 397 digitized eye fundus images acquired using a TopCon TVR-50 fundus camera with a 35^0 field of view and a spatial resolution of 605×700 pixels. Among these images, manual segmentation was performed for only 25 by two observers. The first observer segmented 11.2% of the entire image pixels as vascular tree pixels, while the second observer segmented a total of 14.6%. Both datasets encompass healthy and diseased fundus images, including various vascular abnormalities, diabetic retinopathy, choroidal neovascularization, and arteriosclerotic retinopathy, among others.

Table 6.1 displays the performance results of applying segmentation metrics from the PSO-HRVSO methodology to the DRIVE dataset against Observer 1 and Observer 2. The method achieves a specificity of 0.9882, sensitivity of 0.8542, and average precision of 0.9856 compared to Observer 1.

Similarly, against observer 2, the method achieves averages of 0.9891, 0.8577, and 0.9852 for these metrics, respectively. The maximum specificity values against observers 1 and 2 occur in image 10_test, reaching 0.9957, and in image 20_test, reaching 0.9971, respectively. Conversely, the minimum specificity values against observers 1 and 2 are 0.9742 and 0.9741, observed in images 01_test and 12_test, respectively.

Table 6.1: Results of the PSO-HRVSO methodology applied to DRIVE dataset

Images	Observer 1			Observer 2		
	Sen	Spe	Acc	Sen	Spe	Acc
01_test	0.8358	0.9742	0.9754	0.8437	0.9834	0.9715
02_test	0.8159	0.9867	0.9823	0.8164	0.9847	0.9794
03_test	0.8422	0.9831	0.9854	0.8519	0.9881	0.9837
04_test	0.7891	0.9928	0.9745	0.7974	0.9943	0.9829
05_test	0.7843	0.9936	0.9942	0.8036	0.9942	0.9918
06_test	0.8251	0.9849	0.9937	0.8284	0.9837	0.9916
07_test	0.8735	0.9874	0.9821	0.8734	0.9862	0.9864
08_test	0.8715	0.9942	0.9825	0.8839	0.9911	0.9838
09_test	0.8694	0.9837	0.9875	0.8734	0.9871	0.9827
10_test	0.8846	**0.9957**	0.9943	0.8858	0.9958	0.9918
11_test	0.8723	0.9943	0.9843	0.8868	0.9969	0.9837
12_test	0.8264	0.9785	0.9826	0.8234	0.9741	0.9784
13_test	0.8531	0.9938	0.9746	0.8519	0.9961	0.9721
14_test	0.8591	0.9892	0.9853	0.8587	0.9873	0.9864
15_test	0.8664	0.9875	0.9746	0.8738	0.9834	0.9766
16_test	0.8697	0.9828	0.9748	0.8769	0.9845	0.9784
17_test	0.8856	0.9914	0.9872	0.8821	0.9961	0.9867
18_test	**0.8946**	0.9849	0.9836	0.8937	0.9837	0.9817
19_test	0.8935	0.9932	0.9941	**0.8981**	0.9957	0.9969
20_test	0.8816	0.9941	0.9843	0.8776	**0.9971**	0.9792
21_test	0.8829	0.9852	0.9971	0.8872	0.9831	0.9944
22_test	0.8426	0.9847	0.9876	0.8265	0.9881	0.9848
23_test	0.8247	0.9911	**0.9982**	0.8319	0.9935	**0.9971**
24_test	0.8167	0.9927	0.9934	0.8264	0.9938	0.9964
25_test	0.8935	0.9857	0.9861	0.8897	0.9862	0.9908
Mean	0.8542	0.9882	0.9856	0.8577	0.9891	0.9852

Table 6.2 presents the metrics results of comparing the segmentation performed by the PSO-HRVSO method with both observers for the STARE dataset. The average sensitivity, specificity, and accuracy achieved when comparing the segmented image with the ground truth of observer 1

are 0.8577, 0.9868, and 0.9836, respectively. Similarly, when compared with the ground truth of observer 2, these metrics are 0.8576, 0.9868, and 0.9831. The highest specificity values against observers 1 and 2 are 0.9974 in image im0038 and 0.9967 in image im0021, respectively. Conversely, the lowest specificity values against observers 1 and 2 are 0.9718 in image im0278 and 0.9739 in image im0056.

Table 6.2: Results of the PSO-HRVSO methodology applied to STARE dataset

Images	Observer 1			Observer 2		
	Sen	Spe	Acc	Sen	Spe	Acc
im0001	0.7925	0.9921	0.9951	0.7895	0.9878	0.9955
im0006	0.8244	0.9937	0.9927	0.8235	0.9938	0.9884
im0008	0.8257	0.9841	0.9842	0.8284	0.9926	0.9824
im0009	0.8317	0.9964	0.9934	0.8321	0.9897	**0.9968**
im0012	0.8341	0.9859	0.9763	0.8364	0.9918	0.9719
im0015	0.8347	0.9811	0.9748	0.8369	0.9792	0.9737
im0017	0.8522	0.9842	0.9822	0.8581	0.9846	0.9818
im0021	0.8761	0.9964	0.9851	0.8743	**0.9967**	0.9841
im0024	0.8795	0.9937	0.9837	0.8784	0.9896	0.9862
im0038	0.8628	**0.9974**	0.9942	0.8617	0.9933	0.9921
im0047	0.8748	0.9833	0.9901	0.8788	0.9818	0.9912
im0056	0.8691	0.9719	0.9871	0.8738	0.9739	0.9887
im0081	0.8824	0.9848	0.9833	0.8654	0.9864	0.9837
im0090	0.8857	0.9927	0.9858	0.8855	0.9899	0.9868
im0102	0.8749	0.9967	0.9869	0.8765	0.9927	0.9829
im0138	0.8869	0.9924	0.9925	0.8815	0.9964	0.9924
im0154	0.8871	0.9817	0.9847	0.8911	0.9791	0.9843
im0197	0.8215	0.9824	0.9723	0.8233	0.9867	0.9755
im0243	0.8166	0.9861	0.9611	0.8167	0.9865	0.9581
im0251	0.8546	0.9913	0.9637	0.8516	0.9922	0.9655
im0274	0.8612	0.9743	0.9728	0.8644	0.9854	0.9737
im0278	**0.8927**	0.9718	0.9738	**0.8917**	0.9739	0.9716
im0289	0.8715	0.9738	0.9829	0.8719	0.9718	0.9867
im0294	0.8657	0.9955	0.9954	0.8655	0.9897	0.9891
im0305	0.8852	0.9862	**0.9973**	0.8837	0.9857	0.9944
Mean	0.8577	0.9868	0.9836	0.8576	0.9868	0.9831

In Table 6.3, the results obtained are numerically contrasted against contemporary supervised and unsupervised methods, showcasing the efficiency and computational time across both datasets.

Notably, the table highlights the highest average values among the three metrics for both supervised and unsupervised methods, which are denoted in bold. Specifically, in terms of specificity and accuracy, PSO-HRVSO attains the highest values of 0.9846 and 0.9856, respectively, whereas sensitivity peaks at 0.9230 with Liskowski et al. [64] for the DRIVE dataset. Similarly, for the STARE dataset, PSO-HRVSO achieves the highest specificity and accuracy scores of 0.9868 and 0.9833, while Liskowski et al. [64] secure the highest sensitivity at 0.9207. Despite not yielding the optimal outcomes, it's noteworthy that the approach is closely comparable in numerical terms to methods necessitating training processes and ground-truth data, such as supervised methods, albeit with higher computational expenses.

Table 6.3: Comparative analysis of outcomes obtained from implementing the PSO-HRVSO methodology on both the DRIVE and STARE datasets, juxtaposed with state-of-the-art supervised and unsupervised methods.

Method	Year	DRIVE Dataset			STARE Dataset			Processing Time
		Sen	Spe	Acc	Sen	Spe	Acc	
Supervised methods								
Liskowski et al. [64]	2016	**0.9230**	0.9241	0.9160	**0.9207**	0.9304	0.9309	92.0s
Zhang et al. [65]	2017	0.7861	0.9712	0.9466	0.7882	0.9729	0.9547	23.40s
Orlando et al. [66]	2017	0.7897	0.9684	-	0.7680	0.9738	-	-
Dasgupta et al. [67]	2017	0.7691	0.9801	0.9533	-	-	-	-
Yan et al. [68]	2018	0.7653	0.9818	0.9542	0.7581	0.9846	0.9612	-
Thangaraj et al. [69]	2018	0.8014	0.9753	0.9606	0.8339	0.9536	0.9435	180.86s
Guo et al. [70]	2018	0.7046	0.9806	0.9613	0.5629	0.9816	0.9540	-
Yang et al. [71]	2019	0.756	0.9696	0.9421	0.7202	0.9733	0.9477	-
Jin et al. [72]	2019	0.7963	0.9800	0.9566	0.7595	0.9858	0.9641	17.65s
Cheng et al. [73]	2020	0.7672	0.9834	0.9559	-	-	-	-
Adapa et al. [74]	2020	0.6994	0.9811	0.9450	0.6298	0.9839	0.9486	81.0s
Wu et al. [75]	2020	0.7996	0.9813	0.9582	0.7963	0.9863	0.9672	88.0s
Unsupervised methods								
Zhang et al. [76]	2016	0.7743	0.9725	0.9476	0.7791	0.9758	0.9554	20.0s
Shahid et al. [77]	2017	0.7300	0.9790	0.9580	0.7900	0.9650	0.9510	-
Fan et al. [78]	2018	0.7360	0.9810	0.9610	0.7910	0.9710	0.9570	13.23s
Aguirre et al. [79]	2018	0.7854	-	0.9503	0.7116	0.9454	0.9231	-
Abdallah et al. [80]	2018	0.6887	0.9765	0.9389	0.6801	0.9711	0.9388	-
Pal et al. [81]	2018	0.6129	0.9744	0.9431	-	-	-	-
Yue et al. [82]	2018	0.7528	0.9731	0.9447	-	-	-	4.60s
Biswal et al. [83]	2018	0.7100	0.9700	0.9500	0.7000	0.9700	0.9500	3.30s
Diaz et al. [84]	2019	0.8464	0.9701	0.9619	0.8331	0.9619	0.9559	-
Wang et al. [85]	2019	0.7287	0.9775	0.9446	0.7526	0.9733	0.9503	4.50s
Roy et al. [86]	2019	0.4392	0.9622	0.9295	0.4317	0.9718	0.9488	0.10s
Zhou et al. [87]	2020	0.7262	0.9803	0.9475	0.7865	0.9730	0.9535	63.2s
Dos Santos et al. [88]	2020	0.7702	0.9695	0.9519	-	-	-	-
Shukla et al. [89]	2020	0.7015	0.9836	0.9476	0.7023	0.9863	0.9573	1.41s
Pachade et al. [90]	2020	0.7738	0.9721	0.9552	0.7769	0.9688	0.9543	4.78s
PSO-HRVSO	2024	0.8559	**0.9846**	**0.9854**	0.8577	**0.9868**	**0.9833**	24.0s

The mean processing times derived for each method as detailed in Table 3 were sourced from existing literature. Analysis of Table 6.3 reveals that the PSO-HRVSO method demonstrates shorter processing times compared to both supervised and unsupervised methods based on performance data. Furthermore, the PSO-HRVSO algorithm demonstrates competitive processing times compared to both supervised and unsupervised methods. Moreover, it exhibits superior efficiency values across all three-performance metrics.

6.3. Conclusion:

We introduce a novel approach aimed at enhancing the segmentation of the retinal vascular tree in human eye fundus images. The methodology hinges on a segmentation process divided into two branches: thin and thick vessel detection. Notably, our method achieves high specificity without necessitating manual segmentation or resource-intensive training techniques. Comparative analysis of our method applied to both the DRIVE and STARE datasets reveals its superiority over existing unsupervised methods in the literature. Particularly, it excels in extracting thin vessels with greater precision compared to current methodologies.

Central to our framework is the parameter variation of optimized top-hat and homomorphic filtering stages, tailored to the segmentation results of thin and thick vessels. This adaptive feature significantly enhances segmentation accuracy and specificity. However, a limitation of our proposal is its relatively lower sensitivity compared to state-of-the-art values. To address this, we plan to explore reinforced learning algorithms to optimize the methodology's parameters and improve sensitivity.

Looking ahead, we aim to integrate this method as a preprocessing step in a robust computer-aided diagnosis (CAD) system for classifying healthy and unhealthy fundus images based on retinal vessel segmentation. The crux lies in achieving high-specificity segmentation, minimizing false positives, and ensuring accurate diagnostic interpretations—an aspect we prioritize in our proposal's development.

Chapter VII

Morphological Filter-based Detection of Retinal AVR and CDR through Blind Deconvolution and CLAHE Fusion (BDCLF)

Several retinal disorders, including Hypertensive Retinopathy (HR), Glaucoma, Diabetic Retinopathy (DR), and macular degeneration, can damage the optic nerve and lead to permanent vision loss. These conditions are often detected through clinical observations, such as abnormal changes in the diameter of retinal blood vessels and the ratio of the optic cup to disc diameter (CDR). High blood pressure can cause thinning of retinal vessels and expansion of the optic cup, altering the normal arteriovenous ratio (AVR) and CDR, which can damage nerve fibers and result in hemorrhages and cotton wool spots. This paper proposes an automatic algorithm for segmenting the optic cup, disc, and blood vessels from pre-processed retinal images. The segmentation uses a ring mask created by overlaying two circles with the optic disc center and radii of $3D / 2$ and $1.5D / 2$, where D represents the diameter of the optic disc. The algorithm avoids maximum AV crossings within the retinal mask to streamline the process. Validation against a manually segmented dataset showed accuracies of 98.6% and 97.8% for the retinal optic disc and optic cup, respectively, and 98.55% for retinal vessels. This algorithm has the potential to assist ophthalmologists in accurately and automatically identifying retinal disorders.

7.1.Introduction

Glaucoma, the second leading cause of vision loss globally, accounts for about 12% of all blindness cases and is expected to affect nearly 11 million people with bilateral blindness. The most common form of glaucoma worldwide is Primary Open-Angle Glaucoma (POAG), which affects 74% of those diagnosed with the condition. In India, estimates suggest that around 11.2 million people, or about 4.6% of those over 40, suffer from glaucoma. Detecting and managing this potentially blinding disease is challenging due to the large number of undiagnosed cases.

Hypertension can cause narrowing of blood vessels in the eye, reducing blood flow to the optic nerve and potentially leading to vision loss. Elevated intraocular pressure in glaucoma can also damage the optic nerve and impair vision. Research indicates that individuals with hypertension might be at a higher risk for developing open-angle glaucoma, especially if their hypertension is severe or poorly managed over time.

Many cases of glaucoma do not present symptoms but can be detected through retinal fundus imaging. Accurate diagnosis and management in a clinical setting involve assessing changes in the optic nerve head (ONH), measuring intraocular pressure (IOP), and identifying visual field defects. Diagnosing typical ONH changes can be difficult due to the optic disk's paleness and edema. Early signs of high blood pressure may cause retinal arteriolar narrowing, changes at the arteriolar junction (arteriovenous nicking), and alterations in arteriolar light reflections. Vessel bending is also noted as a potential risk factor for hypertension and coronary disorders. Additionally, heart rate measurement is important, as it is strongly linked to an increased long-term risk of stroke. This work aims to develop a method for detecting potential glaucoma and hypertension cases in donor eyes by examining the cup-to-disc ratio (CDR) and arteriole-to-venule ratio (AVR).

7.2. CDR Measurement

Fig 7.1 presents an organizational chart for CDR measurement. In the RGB color model, each color is composed of three fundamental additive color components—red, green, and blue. These components are represented by their intensity functions as follows:

$$Img_{RGB} = \left[F_R(x, y), F_G(x, y), F_B(x, y)\right] \quad (6.1)$$

Where $F_R\ (x\ ,y)$, $F_G\ (x\ ,y)$ and $F_B\ (x\ ,y)$signify the intensities of the pixel $(x\ ,y)$ in red, green, and blue channels respectively. For standard RGB space they are as follows:

$$red = \begin{pmatrix} 0\ .\ 64 \\ 0\ .\ 33 \end{pmatrix}, green = \begin{pmatrix} 0\ .\ 30 \\ 0\ .\ 60 \end{pmatrix}, blue = \begin{pmatrix} 0\ .\ 15 \\ 0\ .\ 06 \end{pmatrix} \quad (6.2)$$

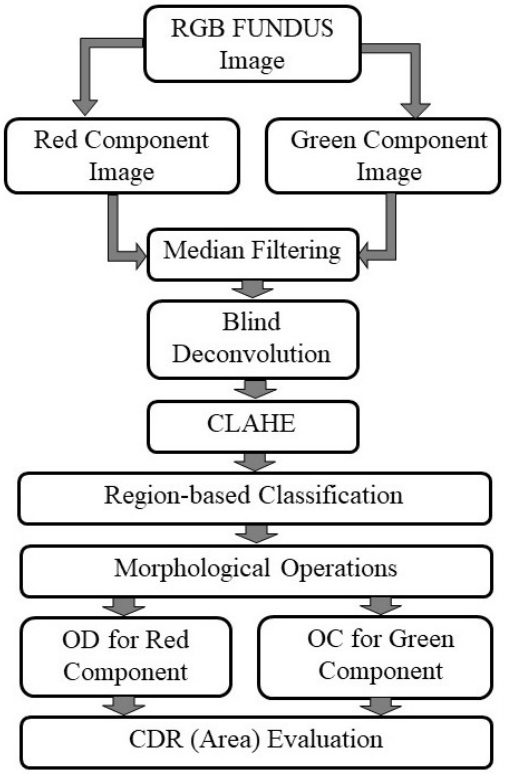

Fig 7.1: Block diagram explaining the CDR Evaluation

If only brightness information is required, color images may be converted to grayscale images using the proposed transformation equation 4.3.

$$I_G = 0\ .\ 333\ F_R + 0\ .\ 600\ F_G + 0\ .\ 060\ F_B \quad (6.3)$$

Here, I_G represents the gray equivalent intensity of the RGB image. The red and green components of the image Img_{RGB} can be quantified using equation 6.3. To classify OD and OC, the red and green components of the RGB image are analyzed respectively, as illustrated in Fig. 7.2.

To reduce noise and enhance image quality, median filtration and the advanced CLAHE technique are applied. Additionally, regional classification facilitates the detection of OD and OC.

Morphological operations, such as dilation, erosion, opening, and closing, are used to segment the OD and OC features.

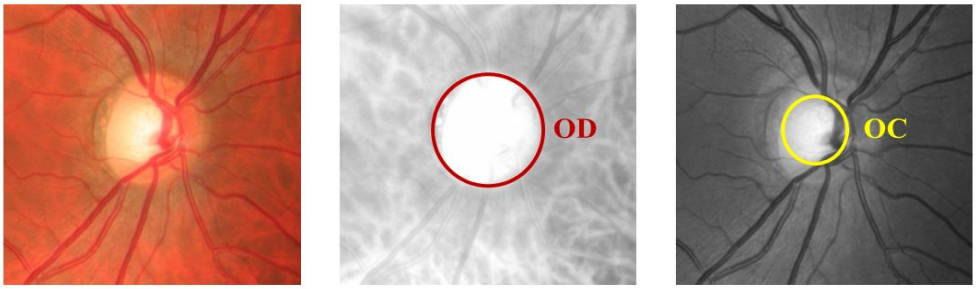

Fig 7.2: Random image of HRF dataset represents (a) cropped OD and OC, (b) red channel marking OD, and (c) green channel marking OC.

7.3. AVR Measurement

The vessel segmentation and AVR calculation process are divided into two stages as illustrated in Fig. 7.3(a) and Fig. 7.3(b). In the first stage, the vessels in the RGB retinal image are segmented using an advanced CLAHE technique, followed by Top Hat and various morphological image processing methods. In the second stage, the optic disk (OD) and its average diameter (D) are measured, and the overlapping areas between $\pi\left(3D\ /\ 2\right)^2$ and $\pi\left(1\ .\ 5D\ /\ 2\right)^2$ are determined.

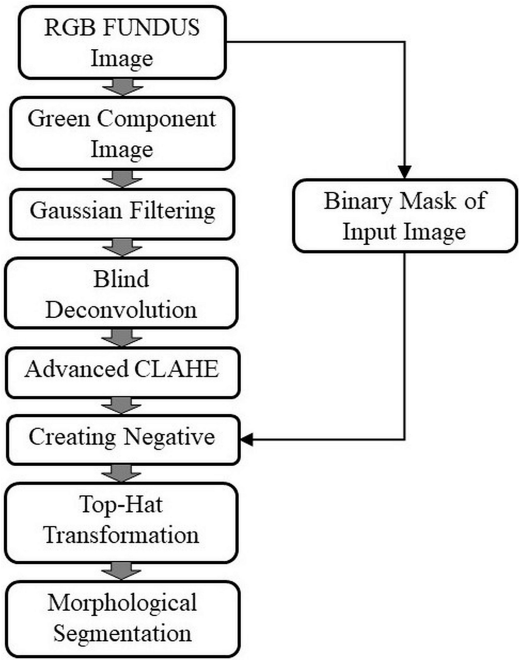

Fig 7.3(a): Block diagram representing vessels Detection

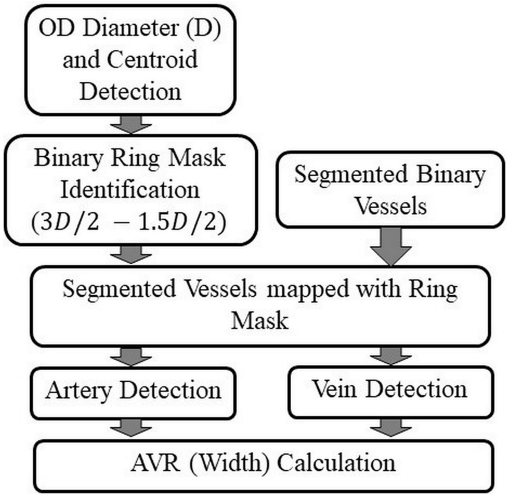

Fig 7.3(b): Block diagram representing AVR Calculation.

The segmented vessels within this masked region are then mapped. This mask is used because it encompasses the area where hypertension most significantly impacts the vessels, simplifying the complexity of the analysis. In the final step of this stage, arteries and veins are separated to individually measure their areas. Arteries and veins are distinguished based on the following criteria [350]:

- Arteries appear brighter than veins.

- Arteries are generally thinner than nearby veins.
- The central reflex (the luminous reflex within the vessels) is larger in arteries and smaller in veins.
- Arteries and veins typically alternate near the optical disk before branching.

Fig. 7.4(a) and Fig. 7.4(b) illustrate the marked arteries and veins and the proposed region of interest. AVR is then calculated based on this area, aiding ophthalmologists in detecting the stages of hypertensive retinopathy.

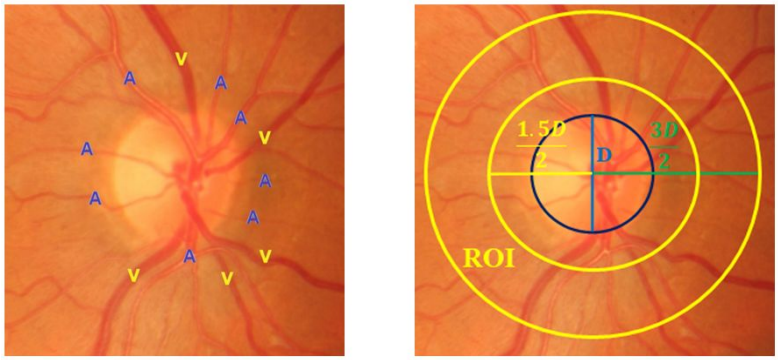

(a) (b)

Fig 7.4: Random Image cropped from HRF datasets represents (a) marking arteries and veins, and (b) proposed region of interest (ROI).

The final validation step involves comparing the binary results of automatic and manual segmentation to determine true positives, false positives, true negatives, and false negatives, as shown in Fig. 7.5.

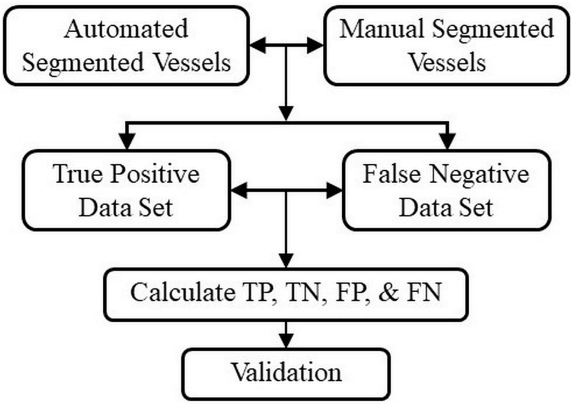

Fig 7.5: Block diagram representing the validation of vessel structure.

Table 7.1 provides details on AVR for normal to accelerated hypertensive retinopathy cases with various risk factors [344], as well as CDR ranges for normal and affected retinas [343].

Table 7.1: AVR for different stages of Hypertensive Retinopathy [344] and CDR at different stages [343].

Grading of HR	AVR	Indications	Systematic Association	CDR
Normal	0.66-0.75 (Approx.)	Normal	Normal	0.00-0.60 (Approx.)
Grade 1 (Mild)	0.5 (Approx.)	Arteriolar narrowing, nicking of arteries and veins, the opacity of arteriolar wall	Weakly associated with cardiovascular disorders	>0.60 (Approx.)
Grade 2 (Moderate)	0.33 (Approx.)	Haemorrhages, hard and soft exudates.	Heart attack, stroke, and even cardiovascular mortality	>0.60 (Approx.)
Grade 3 (Combined)	0.25 (Approx.)	Haemorrhages, hard and soft exudates.	Heart attack, stroke, and even cardiovascular mortality	>0.60 (Approx.)
Grade 4 (Accelerated HR)	Fine Cords <0.2 (Approx.)	Optic disk swelling and vision loss.	Renal failure and mortality	>0.60 (Approx.)

7.4. Results and Discussion:

To assess the performance of the BDCLF technique, a set of 50 fundus retinal images was randomly selected from HRF, CHASEDB1, DRIVE, and STARE databases. These images were split into two groups: 25 from normal patients without clinical disorders, and 25 from patients with clinical abnormalities. For each image, segmentation of the optic cups, optic disks, and vessel structures was performed, and measurements of optic cup diameter, optic disc diameter, and vessel width were taken using the automatic process. The Cup-Disc Ratio (CDR) and Artery-Vein Ratio

(AVR) were calculated and compared with manual data. Fig 7.6 illustrates image enhancement achieved using the advanced CLAHE and BDCLF techniques.

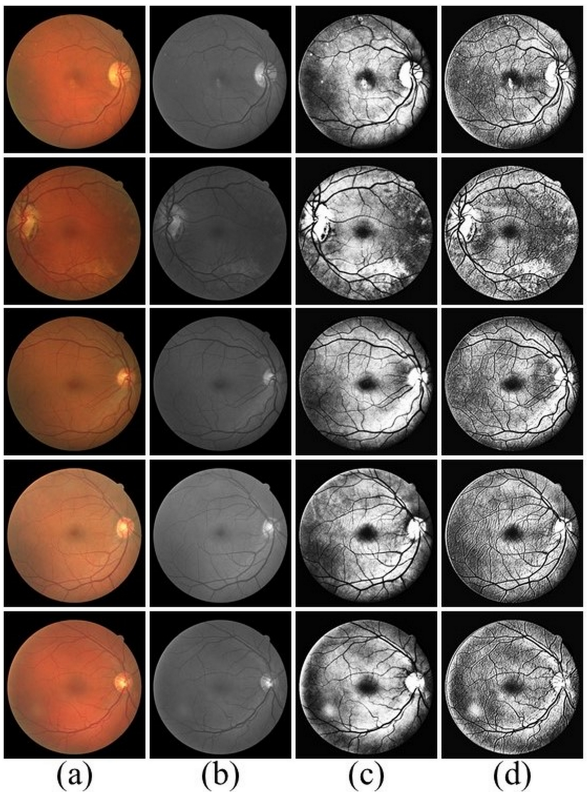

Fig 7.6: Result shows the image enhancement techniques using CLAHE and BDCLF: (a) Input RGB Fundus Image, (b) Green Components, (c) Enhancement by CLAHE, and (d) Enhancement by BDCLF.

Table 7.2 compares quality measures between images enhanced using CLAHE and BDCLF techniques. BDCLF demonstrates a higher PSNR, indicating better image quality, and shows a lower MSE compared to CLAHE, resulting in improved image fidelity and accuracy. Additionally, BDCLF's higher SSIM value suggests minimal distortion in image structure, clearly demonstrating its superiority over CLAHE in image enhancement.

Table 7.2: Quality measures of BDCLF and CLAHE

Image	MSE $(Pixel^2)$		PSNR(dB)		SSIM	
	BDCLF	CLAHE	BDCLF	CLAHE	BDCLF	CLAHE
6(a1)	3151.30	4273.50	15.85	11.82	0.4428	0.3390
6(a2)	5316.20	6322.50	16.63	10.12	0.2760	0.1752
6(a3)	3992.91	5161.00	14.89	11.01	0.3379	0.2365

6(a4)	1953.30	2737.30	17.43	13.75	0.6469	0.5456
6(a5)	3162.4	4058.3	18.93	12.05	0.4582	0.3480

Fig. 7.7 represents the input RGB fundus images of the macula with segmented results of the optic disk and optic cup using mentioned morphological techniques.

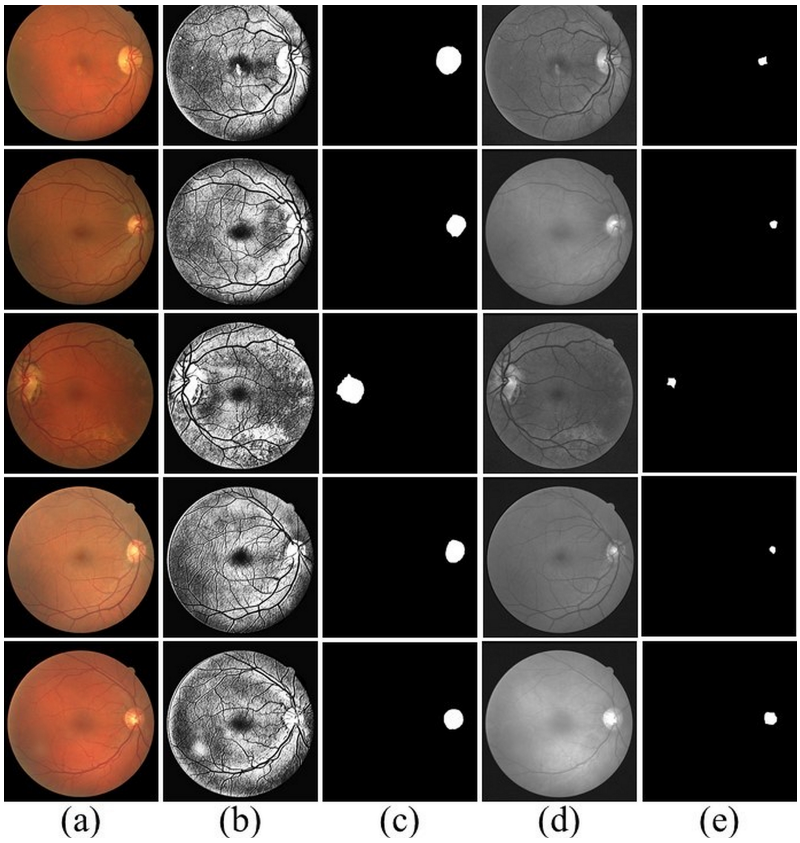

Fig 7.7: In this figure, (a) represents the input RGB fundus image, (b), (c), (d) and (e) represents the BDCLF Enhancement, segmented Optic Disk, green components of input image and segmented Optic Cup respectively.

Table 7.3 compares automatic and manual CDR measurements. BDCLF performs automatic diameter measurements for the optic disc (OD) and optic cup (OC) in pixels, while manual measurements are obtained from the dataset. CDR values are calculated for both methods based on their area ratios, and CDR errors are determined by comparing the manual and automatic values.

Table 7.3: Result shows the comparison of automatic CDR and manual CDR

Sl. No.	$Dia_{OD}\,(Pixel)$		$Dia_{OC}\,(Pixel)$		CDR $(Pixel^2)$		$Error_{CDR}$
	Auto	Manual	Auto	Manual	Auto	Manual	
1	230	234	186	190	0.65	0.66	0.01
2	226	224	194	190	0.74	0.72	-0.02
3	218	223	184	186	0.71	0.70	-0.01
4	226	232	178	184	0.62	0.63	0.01
5	228	224	182	178	0.64	0.63	-0.01
6	203	194	179	175	0.78	0.81	0.04
7	216	230	175	178	0.66	0.60	-0.06
8	224	218	184	175	0.67	0.64	-0.03
9	226	225	128	130	0.32	0.33	-0.01
10	224	225	128	125	0.33	0.31	-0.02

The typical diameter error for both the optic disc and optic cup is around $\pm$ 4% . Fig 7.8(a) and Fig. 7.8(b) display graphs of the correlation between automatically detected and manually measured diameters for the optic disc and optic cup, respectively.

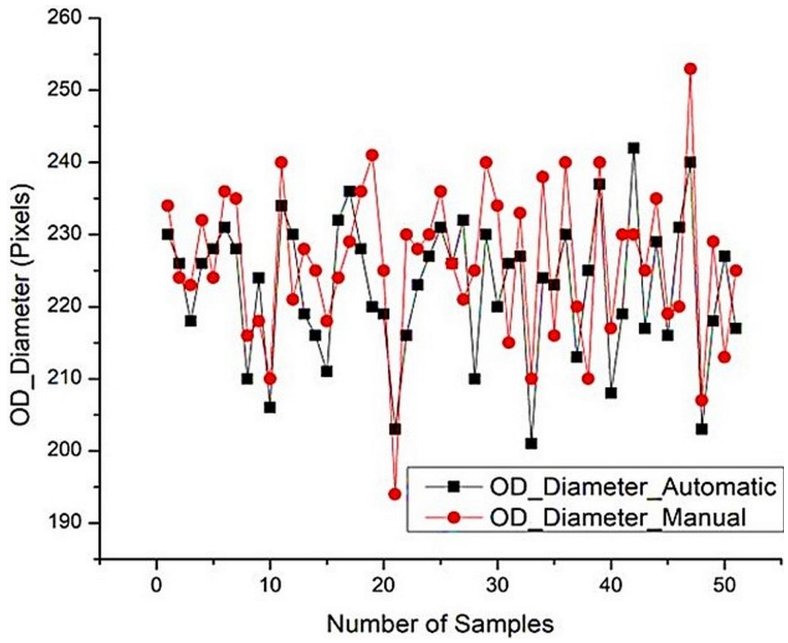

Fig 7.8(a): This figure represents the comparison of the diameter of the Optic Disk segmented by using manual and automated processes.

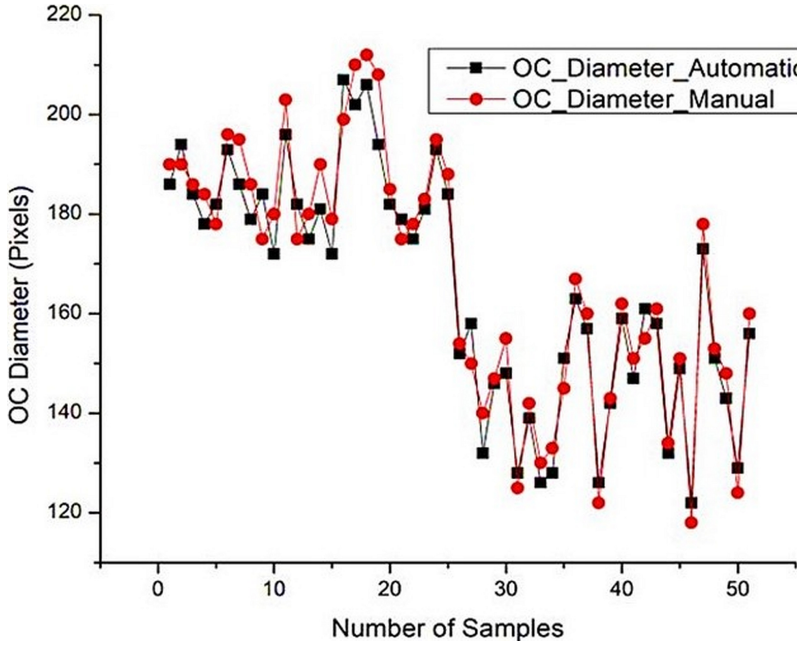

Fig 7.8(b): This figure represents the comparison of the diameter of the Optic Cup segmented by using manual and automated processes.

The cup-to-disc ratio (CDR), a key indicator in glaucoma and hypertension detection, is calculated by measuring the optic cup and disc areas and determining their ratio. Typically, normal patients have a CDR below 0.6, while those with abnormalities have a CDR above 0.6. Fig 7.9 compares the error between automated and manual CDR measurements, showing error distribution across 50 sample images. The BDCLF method achieves a maximum CDR error of less than ±4% and an average mean error of approximately 6.11%, highlighting its superior accuracy in CDR measurement.

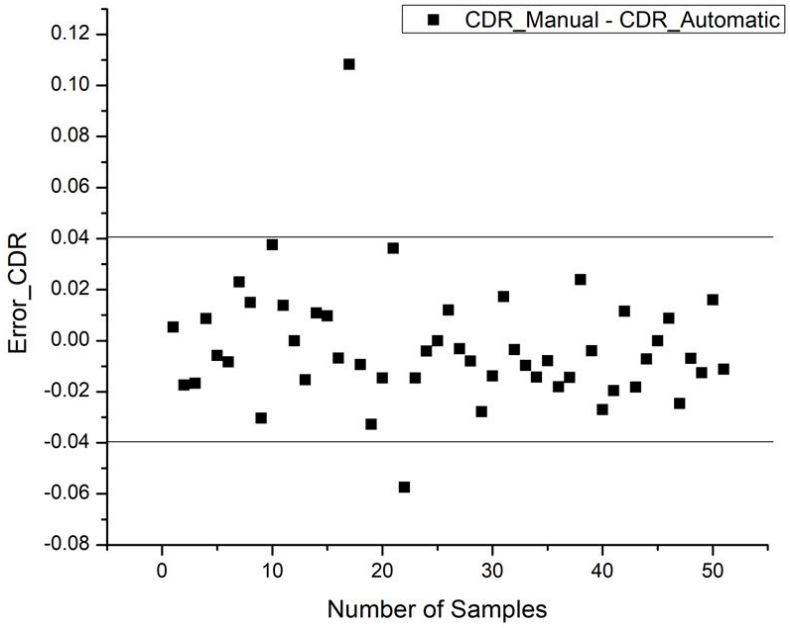

Fig 7.9: The result shows the error in Cup-Disk Ratio calculated automatically and manually.

Fig 7.10 evaluates the effectiveness of the proposed method by comparing glaucoma detection results from BDCLF and manual methods. The CDR threshold of 0.60 is used to identify potential abnormal cases. The proposed method demonstrates an average sensitivity of 95.83%, specificity of 98.23%, and accuracy of 96.49%.

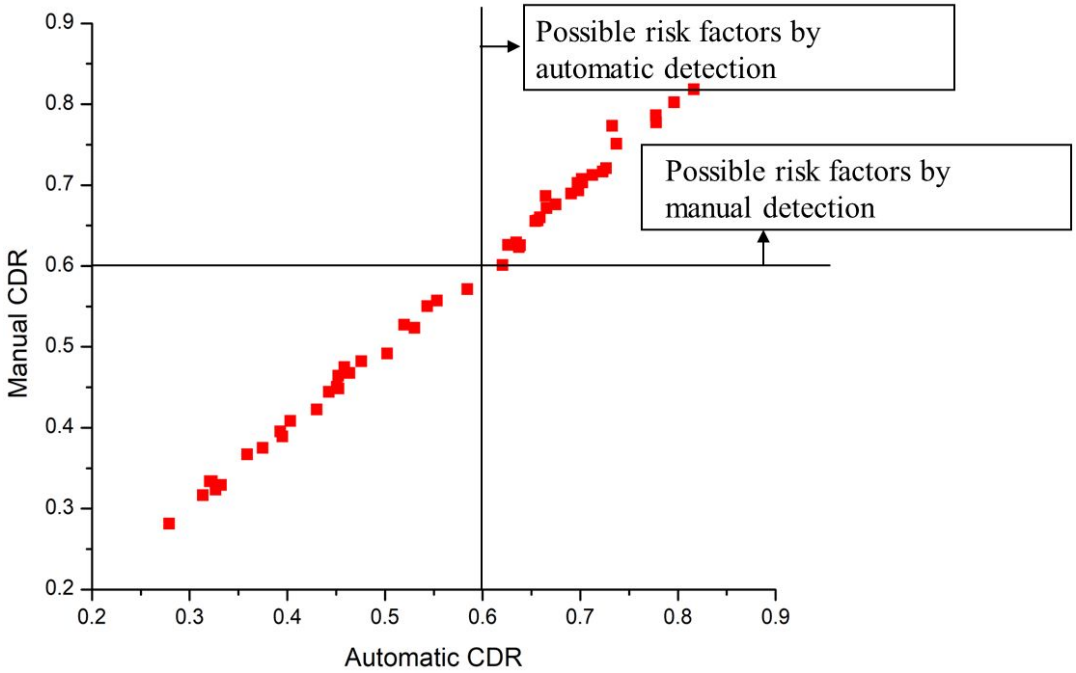

Fig 7.10: This figure represents the dataset ranging from normal to possible risk factors [343].

The performance of various classifiers is evaluated using metrics such as accuracy, specificity, and sensitivity, which are calculated with the following equations.

$$Accuracy = \frac{TP + TN}{TP + TN + FP + FN}$$

$$Specificity = \frac{TN}{TN + FP}$$

$$Sensitivity = \frac{TP}{TP + FN}$$

Where, $TN = True\ Positive$, $TN = True\ Negative$, $FP = False\ Positive$, $FN = False\ Negative$

.

Table 7.4 shows the results for different metrics in optical disc (OD) and optic cup (OC) analysis. The metrics encompass sensitivity, specificity, overlapping error (both OD and OC), balanced accuracy (both OD and OC), and absolute error in the cup-to-disc ratio (CDR), which are represented as A_{OD}, A_{OC}, E_{OD}, E_{OC}, and δ_E respectively. For OD segmentation, the BDCLF method achieves a sensitivity of 98.6%, specificity of 99.7%, and accuracy of 98.5%, with an absolute error of 2.8%. For OC segmentation, the BDCLF method shows a sensitivity of approximately 97.7%, specificity of 98.7%, accuracy of 96.8%, and a minimum error of 2.8%. These results underscore the superior performance of the BDCLF technique compared to other methods.

Table 7.4: Statistical results of optic cup and optic disk

Dataset	Sensitivity		Specificity		Accuracy		E_{OD}	E_{OC}	δ_E
	OD	OC	OD	OC	OD	OC			
CHASEDB1	0.962	0.953	0.997	0.983	0.975	0.968	0.103	0.103	0.049
DRIVE	0.968	0.947	0.984	0.972	0.971	0.945	0.087	0.294	0.045
HRF	0.986	0.977	0.984	0.987	0.985	0.962	0.074	0.241	0.028
STARE	0.950	0.932	0.976	0.975	0.953	0.960	0.093	0.285	0.069

Fig. 7.11 illustrates the vessel structure segmentation using the proposed technique. Gaussian filtering enhances and detects vessel edges, while Top-Hat transformation extracts vessel features for segmentation.

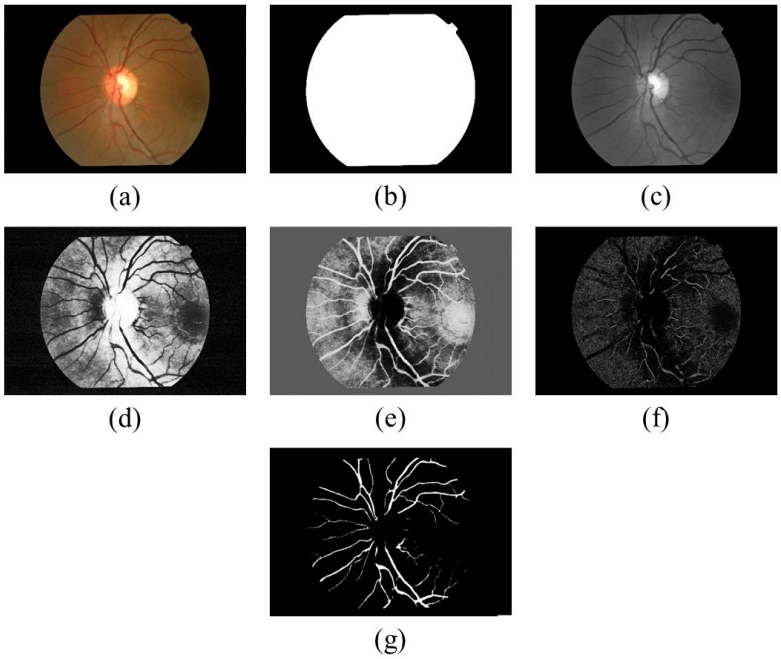

Fig 7.11: Result shows the overall vessels segmentation steps: (a) Input RGB fundus image, (b) Binary mask, (c) Gaussian Filtering, (d) Advanced CLAHE, (e) Negative, (f) Top-Hat transforms, and (g) Segmented vessels.

Fig 7.12 compares manual and automatic vessel structure results with the corresponding input images. The proposed automated method offers superior accuracy and faster processing times compared to existing techniques, achieving an average accuracy of 98.4% and a sensitivity of 97.6%.

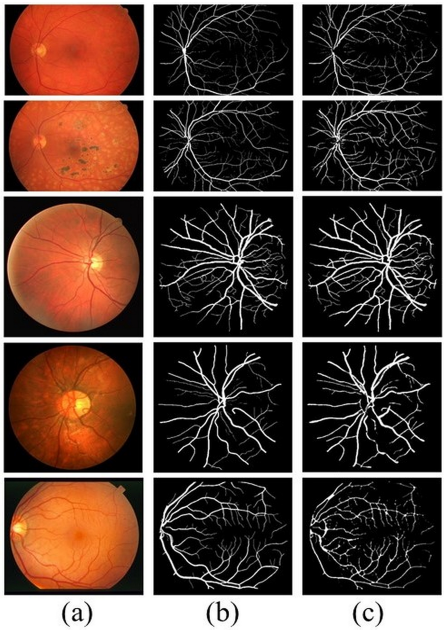

Fig 7.12: This figure shows the results of segmented vessels: (a) Input RGB fundus images, (b) Manually Segmented vessels, and (c) Automatically Segmented vessels.

Fig. 7.13 details the vessel mapping and artery-vein separation within a specific ring mask, chosen for its complexity due to vessel branching.

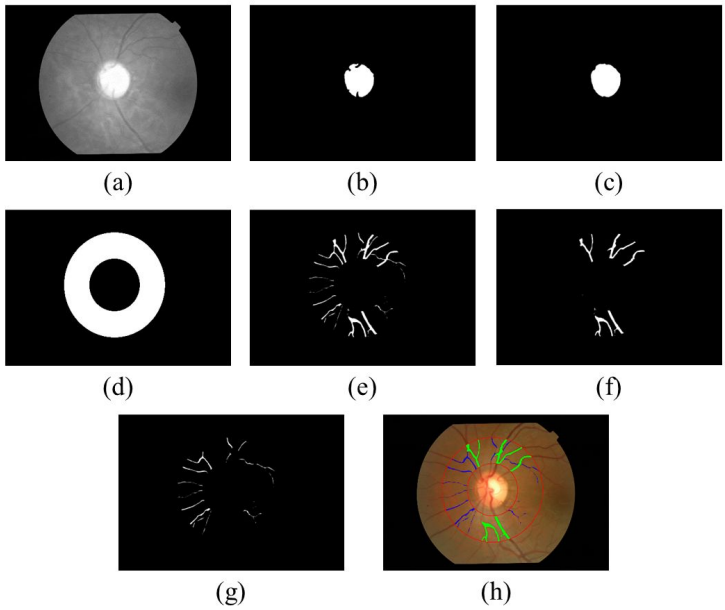

Fig 7.13: Result shows the separation of arteries and veins within specified ring mask: (a) Red components of RGB fundus image, (b) Segmented optic disk, (c) Segmented optic disk filling, (d) (3D-1.5D) mask, (e) Segmented vessels within mask, (f) Separated veins, (g) Separated arteries, and (h) Segmented vessel's labelling.

Evaluation metrics, including accuracy and sensitivity, are used to assess the performance of various classifiers. Table 7.5 compares the proposed technique with previous methods, showing that the BDCLF method outperforms others in retinal vessel segmentation, with sensitivity ranging from 96.16% to 98.53% and accuracy reaching 98.55%.

Table 7.5: The results show the performance analysis of the proposed technique compared to the previously established methods.

Algorithm	**Dataset**	**Samples**	**Sensitivity (%)**	**Specificity (%)**	**Accuracy (%)**
Li et al [54]	DRIVE	40	75.69	98.16	95.27
	STARE	20	77.26	98.44	96.28
	CHASEBD1	28	75.07	97.93	95.81
Srinidhi et al. [55]	DRIVE	40	**86.44**	96.67	95.89
	STARE	20	83.25	97.46	95.02
	CHASEBD1	28	82.97	96.63	94.74
Yan	DRIVE	40	76.31	98.20	95.38

et al. [56]	STARE	20	77.35	98.57	96.38
	CHASEBD1	28	76.40	98.06	96.07
Jin et al. [57]	DRIVE	40	79.63	98.00	95.66
	STARE	20	75.95	**98.78**	96.41
	CHASEBD1	28	81.55	97.52	96.37
Yuchen Yuan et al. [58]	DRIVE	40	80.46	98.05	95.81
	STARE	20	79.14	98.70	96.65
	CHASEBD1	28	84.02	98.01	**96.73**
BDCLF	HRF	45	**96.16**	97.65	**98.55**
	DRIVE	40	**97.63**	96.69	**97.49**
	CHASEDB1	28	**98.47**	95.31	**98.17**
	STARE	20	**98.53**	96.45	**98.39**

To measure vessel width, the central line and edges of the first vessels are determined from the segmented binary vessel images using thinning and Canny edge detection techniques. These images are then mapped to identify the vessel width at specific pixel positions along the vessel's centerline (see Fig. 7.14).

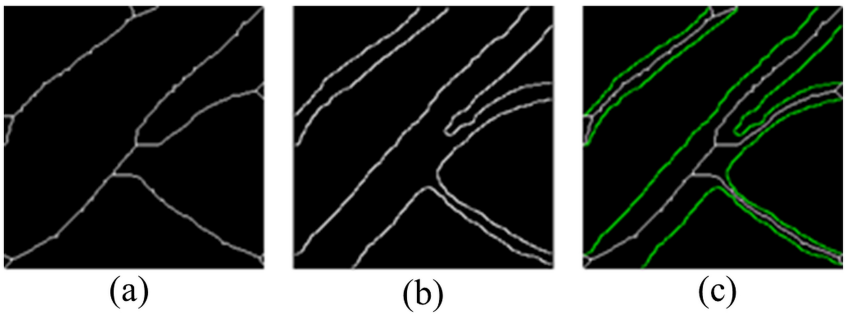

Fig 7.14: Results representing: (a) vessel's skeleton, (b) vessel's edge, (c) mapping of (a) and (b).

To assess the vessel width, a pixel from the vessel's centerline image is selected, and a mask centered on this pixel is applied. The mask's purpose is to identify potential edge pixels on either side of the centerline pixel. To find all possible pixel positions within the mask, the pixel position is adjusted by shifting it one pixel at a time up to the mask's size and rotating each position from $0°$ to $180°$ relative to the center pixel. The rotation step size is less than $180°$ divided by the mask length to increase precision.

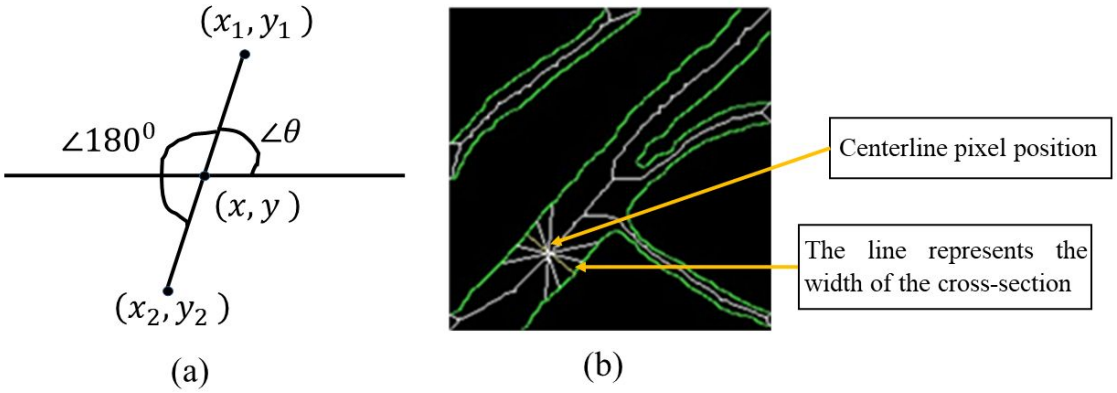

Fig 7.15: This figure represents the process (a) to find the edge pixels and (b) the vessel's width or minimum distance of pair pixels.

For each position, the grayscale value of the edge image is examined to determine if it represents an edge pixel. Once an edge pixel is identified, its minor axis is determined by shifting the angle by 180° and extending the distance from one to the maximum mask size (refer to Figure 6.15). This process creates a mask that is invariant to rotation and helps identify potential pixel pairs for measuring the width or diameter of the vessel's cross-sectional area.

$$x_1 = x + r\,cos\,(\theta) \tag{4.25}$$

$$y_1 = y + r\,sin\,(\theta) \tag{4.26}$$

Where, (x, y) is vessel centerline pixel position, $r = 1, 2, 3, \ldots\ldots, (mask\ \ size / 2)$ and $\theta = 0^0, \ldots\ldots\ldots, 180^0$. For any pixel position, if the binary value in the edge image is *1* then the pixel (x_2, y_2) in the opposite edge has been measured by considering $\theta = 180^0 + \theta$ and by varying r.

After performing the operation, a pair of pixels was discovered on the opposite edge. The minimum Euclidean distance, $\sqrt[2]{(x_1 - x_2)^2 + (y_1 - y_2)^2}$, was calculated from this pair of pixels to determine the width of the vessel's cross-section. Table 6.6 displays the resulting widths at 20 distinct cross-sections of the vessel as shown in figure 6.15b.

Measuring vessel width is essential for determining the AVR, which reflects the severity of retinal diseases. Table 7.6 compares vessel widths obtained through the automated technique and manual measurements. Two images from each dataset (HRF, INSPIRE-AVR, DRIVE, CHASEDB1, and STARE) were analyzed.

Table 7.6: Result of Euclidean Width of 20 cross section of Figure 6.14(b).

Cross Sections	Centerline Pixel Position	Width-Line End Point		Vessel's Width (Euclidean Distance)
	(x, y)	(x_1, y_1)	(x_2, y_2)	
1	(17,27)	(13,69)	(20,75)	9.22
2	(45, 48)	(41,42)	(50,53)	14.21
3	(53,42)	(48,37)	(58,46)	13.45
4	(58,38)	(53,33)	(61,43)	12.80
5	(41,166)	(29,155)	(55,177)	34.06
6	(50,157)	(36,147)	(62,170)	34.71
7	(65,142)	(52,128)	(79,152)	36.12
8	(74,131)	(59,119)	(88,143)	37.64
9	(69,125)	(65,114)	(92,137)	35.47
10	(108,80)	(100,75)	(116,87)	20.00
11	(116,70)	(108,63)	(123,78)	21.21
12	(125,63)	(117,55)	(133,70)	21.93
13	(136,52)	(128,45)	(144,60)	21.93
14	(124,95)	(121,92)	(129,98)	10.00
15	(135,88)	(133,85)	(137,90)	6.40
16	(143,80)	(140,76)	(146,84)	10.00
17	(147,77)	(143,74)	(150,82)	10.63
18	(132,153)	(135,150)	(129,156)	8.48
19	(144,161)	(147,158)	(141,163)	7.81
20	(159,170)	(162,168)	(156,173)	7.81

Table 7.7 shows the automated retinal vessel width measurements using BDCLF, compared with manual data, and illustrates the automated and manual AVR calculations, revealing a marginal average error of less than ±4% (see Figure 6.17). An AVR greater than 6.6 indicates a normal retinal image, while a lower value suggests abnormalities associated with glaucoma or hypertension [343]. The BDCLF method effectively assesses retinal abnormalities, making it a valuable tool.

Table 7.7: The outcome presents a comparison between the widths of the vessel acquired through the automated method proposed and those obtained through manual measurements.

Sl. No.	$Width_{Automatic}$		$Width_{Manual}$		AVR		ERROR
	Artery	Vein	Artery	Vein	Auto	Manual	
1	11.75	21.40	12.20	23.40	0.549	0.521	-0.027
2	18.02	27.31	17.46	26.57	0.659	0.657	-0.002
3	17.69	38.83	17.85	40.02	0.455	0.446	-0.009

4	14.87	28.28	15.65	31.14	0.525	0.502	-0.023
5	3.16	4.47	6.41	8.94	0.706	0.717	0.010
6	2.76	3.61	2.81	3.60	0.764	0.780	0.016
7	10.50	15.80	9.4	13.60	0.664	0.691	0.026
8	10.63	13.45	10.76	13.41	0.790	0.802	0.012
9	6.83	10.82	5.32	7.81	0.631	0.681	0.050
10	2.03	6.08	2.06	6.32	0.333	0.325	-0.007

Fig 7.16 shows the comparison result of automatic and manually calculated AVR and error of the proposed technique whereas Fig. 7.17 represents the percentage of error in detection of AVR.

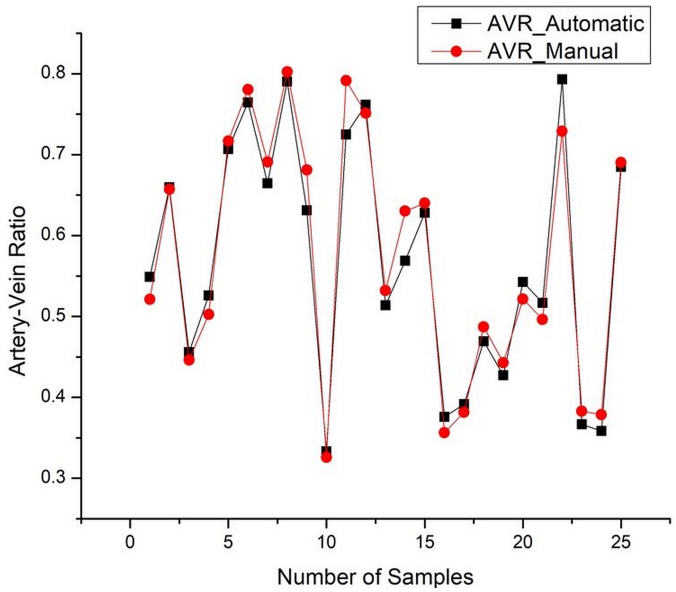

Fig 7.16: Results shows the comparison of automatic measured AVR with manual AVR.

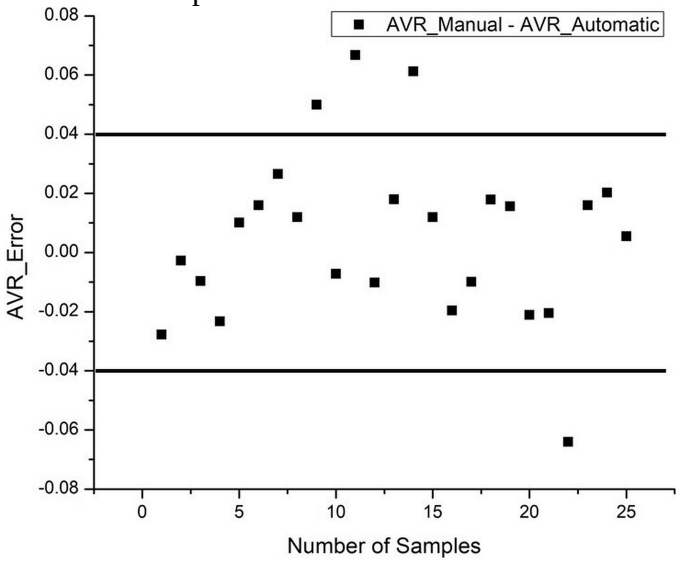

Fig 7.17: Result shows the percentage of error in the detection of automatic AVR

The performance of a binary classifier system was evaluated using the receiver operating characteristic (ROC) curve shown in Fig. 7.18. This curve depicts the true positive rate (sensitivity) against the false positive rate (1 - specificity) as the classification threshold varies. The ROC curve helps assess the classifier's ability to differentiate between positive and negative cases and compare various classifiers. The ROC analysis of the DRIVE dataset indicates that the BDCLF method outperforms existing techniques, demonstrating a faster and more stable curve. A stable ROC curve indicates reliable performance across different datasets and conditions, validating the BDCLF method's effectiveness.

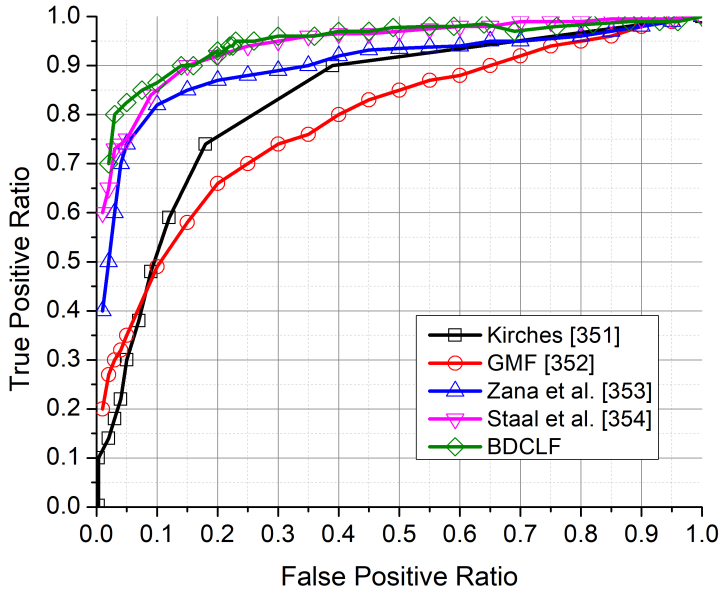

Fig 7.18: Graph shows the average ROC plot for 40 DRIVE data using five different methods.

The AVR and CDR values obtained with the BDCLF method, detailed in Table 7.8, are used to evaluate patient conditions for diabetes, glaucoma, and overall health. Retinal images from the HRF dataset, including diabetic, glaucoma, and healthy cases, were analyzed. Results showed an average CDR of 0.68 for diabetics, 0.62 for glaucoma patients, and 0.41 for healthy individuals. Average AVR values were 0.52 for diabetics, 0.43 for glaucoma patients, and 0.75 for healthy individuals.

Table 7.8: Result shows the AVR and CDR for patient's different health conditions.

HRF Image	Patent's Condition	OD (Avg.)	OC (Avg.)	W_{Artery} (Avg.)	W_{Vein} (Avg)	CDR	AVR
01_dr	Diabetic	372	294	13.15	32.37	0.63	0.41
02_dr		375	306	12.32	22.62	0.67	0.54
03_dr		327	281	14.05	23.18	0.74	0.61
04_dr		336	268	13.19	26.39	0.64	0.50
01_h	Healthy	410	248	17.39	20.81	0.37	0.84
02_h		408	267	16.18	23.41	0.43	0.69
03_h		396	237	17.02	22.11	0.36	0.77
07_h		416	278	17.36	24.79	0.45	0.70
01_g	Glaucoma	338	261	12.27	26.58	0.60	0.46
08_g		367	292	11.43	28.91	0.63	0.39

7.5. Pseudocode

Below is a sample pseudocode that demonstrates how to perform the BDCLF technique on an image by utilizing the opening morphological operation. The code is divided into two parts:

1. *Algorithm for Blind Deconvoluted CLAHE:*

Input: Retinal FUNDUS RGB image

Output: Enhanced retinal FUNDUS image

Begin

blurredImage = imread('blurred_image.jpg'); *% Read the blurred image*

numIterations = 100; % Number of iterations for the algorithm *% Set parameters for blind deconvolution*

lambda = 0.01; *% Regularization parameter*

psfSize = [15, 15]; *% Size of the point spread function (PSF)*

psfInitial = fspecial('gaussian', psfSize, 2); *% Initial estimate of PSF*

estimatedImage = deconvblind(blurredImage, psfInitial, numIterations, lambda); *% Perform blind deconvolution*

if size(estimatedImage, 3) == 3 *% Convert estimatedImage to grayscale if needed*

img = rgb2gray(estimatedImage);

end

[rows, cols] = size(img); *% Calculate the size of the image*

numBlocksRows = floor(rows / blockSize); *% Divide the image into non-overlapping blocks*

```
numBlocksCols = floor(cols / blockSize);
enhancedImg = zeros(rows, cols);  % Initialize the output enhanced image
% Loop through each block
for i = 1:numBlocksRows
   for j = 1:numBlocksCols
      block = img((i-1)*blockSize+1:i*blockSize, (j-1)*blockSize+1:j*blockSize);  % Extract the current block
       equalizedBlock = histeq(block);  % Perform histogram equalization on the block
      clippedBlock = min(max(equalizedBlock, 0), limit);  % Clip the block's histogram to the specified limit
      % Assign the enhanced block to the corresponding region in the output image
      enhancedImg((i-1)*blockSize+1:i*blockSize, (j-1)*blockSize+1:j*blockSize) = clippedBlock;
   end
end
% Convert the output enhanced image to the original color space if needed
if size(estimatedImage, 3) == 3
   enhancedImg = repmat(enhancedImg, [1, 1, 3]);
end
```

2. *Algorithm for Morphological Operation and TOP-HAT Transform*

Input: Enhanced gray image, *Output:* Segmented binary image

```
begin
inputImage = enhancedImg;   % Read the input image
% Apply morphological operations for noise removal or smoothing
SE = strel('disk', size);  % Define a disk-shaped structuring element with specified size
morphImage = imopen(grayImage, SE);  % Perform opening operation
tophatImage = imtophat(morphImage, SE);  % Perform TOP-HAT transform for image enhancement
threshold = graythresh(tophatImage);  % Threshold the image to segment the regions of interest
binaryImage = imbinarize(tophatImage, threshold);
% If needed Perform additional operations on the binary image for further refinement
End
```

7.6. Conclusion:

An automated method has been developed to assess two specific features of the human eye, CDR and AVR, to detect abnormalities linked to conditions such as diabetes, glaucoma, and hypertension. Initial results are highly promising, showing accuracy rates of 98.6% for OD, 97.8% for OC, and 98.55% for AVR with only minor errors. This technique is faster than traditional methods due to its fully automated nature and is easy to implement, making it accessible even to those with limited medical expertise. The successful application of this method enables the measurement of various parameters (e.g., nicking, narrowing, and branching coefficients), aiding in the diagnosis of different diseases. The upcoming study aims to quantitatively analyze a series of clinical images from publicly available datasets to identify retinopathy of prematurity (ROP).

Chapter VIII

PSO-Optimized CLAHE for Image Enhancement and Active Contour-Based Segmentation of Retinal Vessels

Accurate segmentation of retinal vessels is crucial for diagnosing and monitoring various ocular and systemic diseases. However, challenges such as low contrast, noise, and uneven illumination in retinal images hinder precise segmentation. This study proposes a novel framework combining Particle Swarm Optimization (PSO) with contrast-limited Adaptive Histogram Equalization (CLAHE) for image enhancement, followed by an Active Contour Model (ACM) for the segmentation of retinal vessels.

The PSO algorithm is employed to optimize the parameters of CLAHE, ensuring enhanced image contrast and clarity while preserving critical vessel details. The enhanced images are subsequently segmented using an ACM, effectively delineating vessel boundaries by minimizing a hybrid energy function. Integrating PSO-optimized CLAHE ensures superior preprocessing, enabling the active contour model to achieve more accurate and robust segmentation results.

Experimental evaluations were conducted on publicly available retinal image datasets, and the proposed method demonstrated improved accuracy, sensitivity, and specificity performance compared to traditional enhancement and segmentation approaches. The framework's adaptability to varying image qualities and its potential for integration into automated diagnostic systems highlight its significance in retinal image analysis.

8.1.Introduction

The segmentation of retinal vessels plays a crucial role in diagnosing and monitoring various ocular and systemic diseases, including diabetic retinopathy, glaucoma, and hypertension. Retinal vessel extraction aids in the analysis of vascular structures, which are pivotal indicators of pathological changes. However, accurate segmentation remains a challenging task due to the complex and intricate patterns of retinal vasculature, as well as variations in image quality caused by illumination inconsistencies, noise, and patient-specific anatomical differences.

To address these challenges, image preprocessing techniques that enhance vessel visibility and segmentation algorithms that precisely delineate vascular structures are essential. Contrast Limited Adaptive Histogram Equalization (CLAHE) has emerged as a powerful image enhancement technique, especially in medical imaging, due to its ability to enhance local contrast while mitigating noise amplification. However, its performance is highly dependent on the appropriate selection of parameters such as clip limit and grid size, which can significantly influence the quality of the enhanced image.

Particle Swarm Optimization (PSO), a swarm intelligence-based optimization algorithm, offers an effective solution for parameter tuning in complex problems. By employing PSO to optimize the CLAHE parameters, the enhanced images can achieve superior contrast and vessel visibility, setting the stage for improved segmentation results.

In addition to enhancement, segmentation techniques play a pivotal role in accurately extracting retinal vessels. Active contour models (ACMs) have been widely utilized for this purpose due to their ability to refine contours based on energy minimization principles iteratively. ACMs effectively balance internal forces (ensuring contour smoothness) and external forces (driven by image features such as edges or gradients). When applied to enhanced retinal images, ACMs can achieve precise vessel delineation, even in challenging cases.

This research proposes a novel framework that combines PSO-optimized CLAHE for image enhancement with active contour-based segmentation for extracting retinal vessels. Integrating these techniques leverages each component's strengths, ensuring enhanced image quality and robust segmentation. The proposed methodology is evaluated on publicly available retinal image datasets, demonstrating its potential to achieve high segmentation accuracy and reliability, even in noise and complex vascular structures.

8.2.Results and Discussion

The proposed methodology for the PSO-Optimized CLAHE for Image Enhancement and Active Contour-Based Segmentation of Retinal Vessels is structured in two primary phases: image enhancement and vessel segmentation. Below are the detailed steps:

8.2.1. Image Enhancement Using PSO-Optimized CLAHE

This method effectively enhances images by combining Particle Swarm Optimization (PSO) and Contrast Limited Adaptive Histogram Equalization (CLAHE). The goal is to optimize the CLAHE parameters using PSO, ensuring the enhanced image balances contrast improvement and naturalness. Fig. 8.1 illustrates the retinal vessel enhancement techniques utilizing the proposed PSO-CLAHE fusion method.

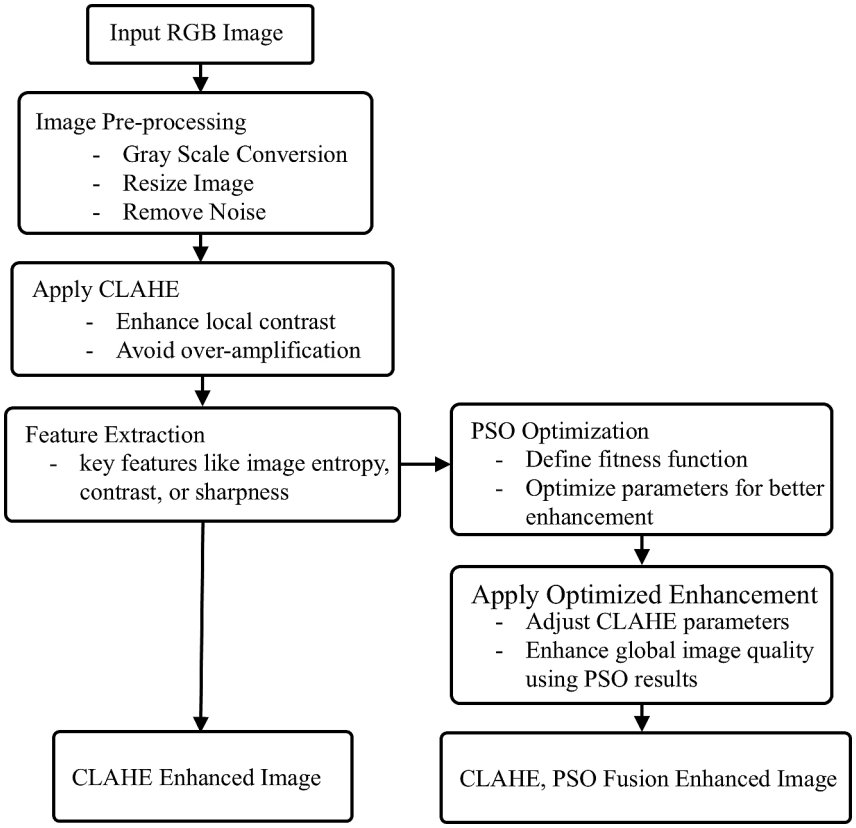

Fig. 8.1: PSO-optimized CLAHE to enhance retinal vessels.

Fig. 8.2 illustrates the enhanced result of a fundus image from the DRIVE dataset, processed using Histogram Equalization (HE), Adaptive Histogram Equalization (AHE), and CLAHE. The individual histogram analysis highlights the characteristics of each enhanced image. The

histogram-equalized image shows an overall improvement in contrast but may appear unnatural or overly harsh in regions with distinct brightness variations. The adaptive histogram-equalized image effectively enhances local regions, bringing out finer details, though it may amplify noise or artifacts, particularly in uniform areas. In contrast, the CLAHE-enhanced image achieves a balanced enhancement of local details, minimizing noise and artifacts. This results in a smoother and more visually appealing outcome compared to AHE.

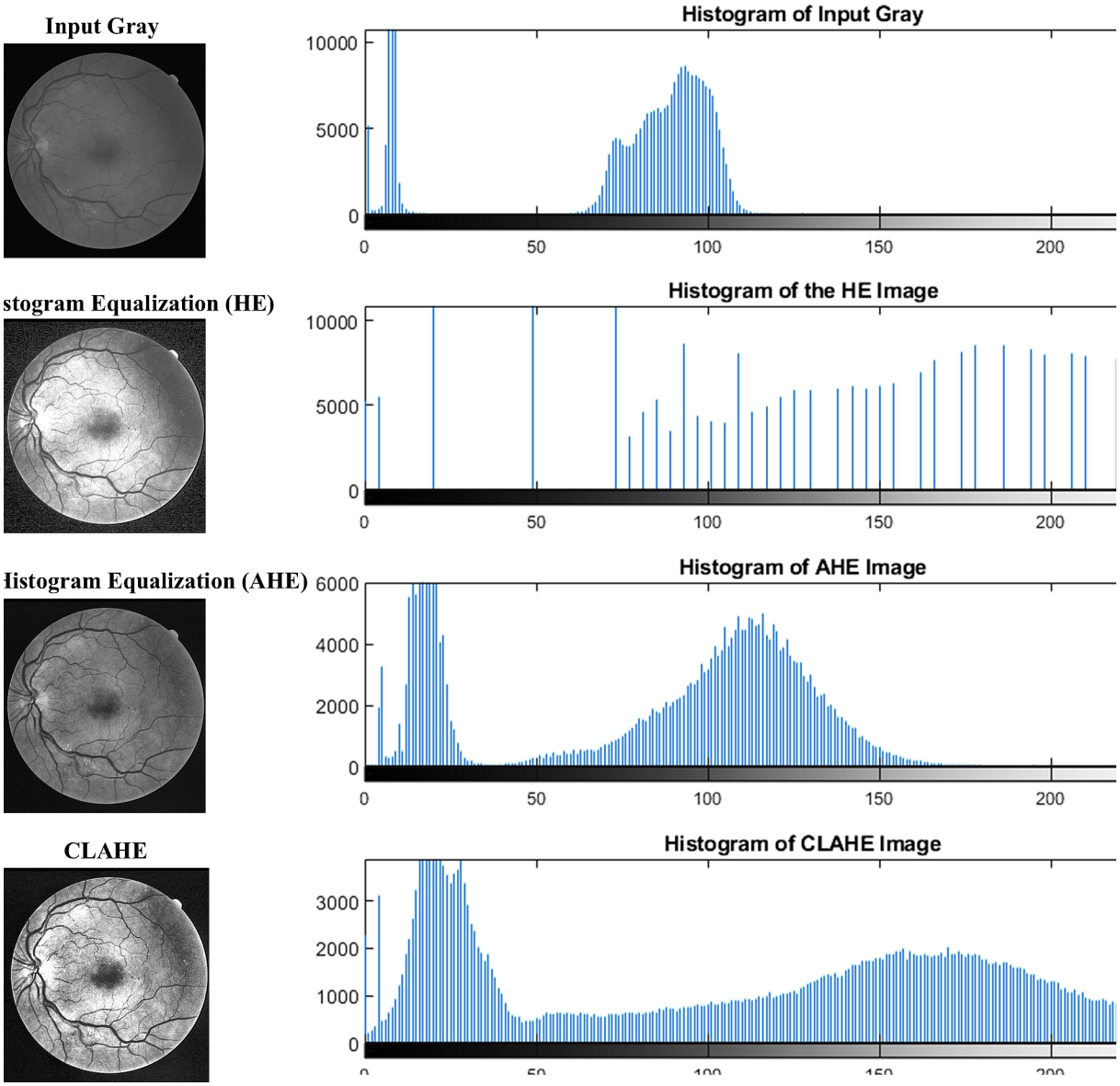

Fig. 8.2: Enhanced fundus image from the DRIVE dataset using Histogram Equalization (HE), Adaptive Histogram Equalization (AHE), and Contrast Limited Adaptive Histogram Equalization (CLAHE).

PSO functions by iteratively updating the position and velocity of a group of particles within a search domain, where each particle signifies a potential solution. The quality of each particle is evaluated using a fitness function, and PSO leverages interactions among particles to explore the search domain and converge toward an optimal solution. The result of the PSO algorithm is the most favorable solution identified during the process, which might represent a local rather than a global optimum. The results of improving the PSO algorithm are illustrated in Fig. 8.3.

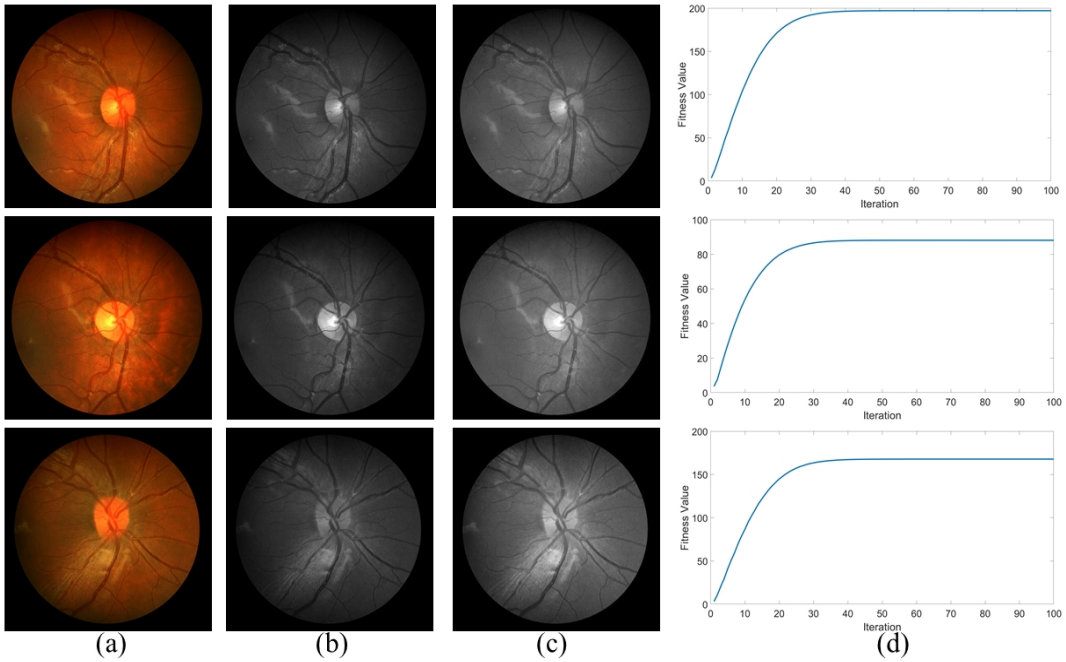

Fig 8.3: Enhanced Image using PSO: (a) Input RGB fundus image, (b) Gray Image, (c) PSO enhanced Image, (d) Fitness values of PSO enhanced Images.

Particle Swarm Optimization (PSO)-enhanced Contrast Limited Adaptive Histogram Equalization (CLAHE) integrates the strengths of optimization algorithms with image processing techniques to effectively improve image quality. By finetuning CLAHE parameters, PSO maximizes contrast while minimizing noise and distortion. This automated optimization process eliminates the need for manual parameter adjustments, making it ideal for large-scale image processing applications. Fig. 8.4 illustrates the enhanced vessels of a retinal fundus image achieved using PSO-optimized CLAHE.

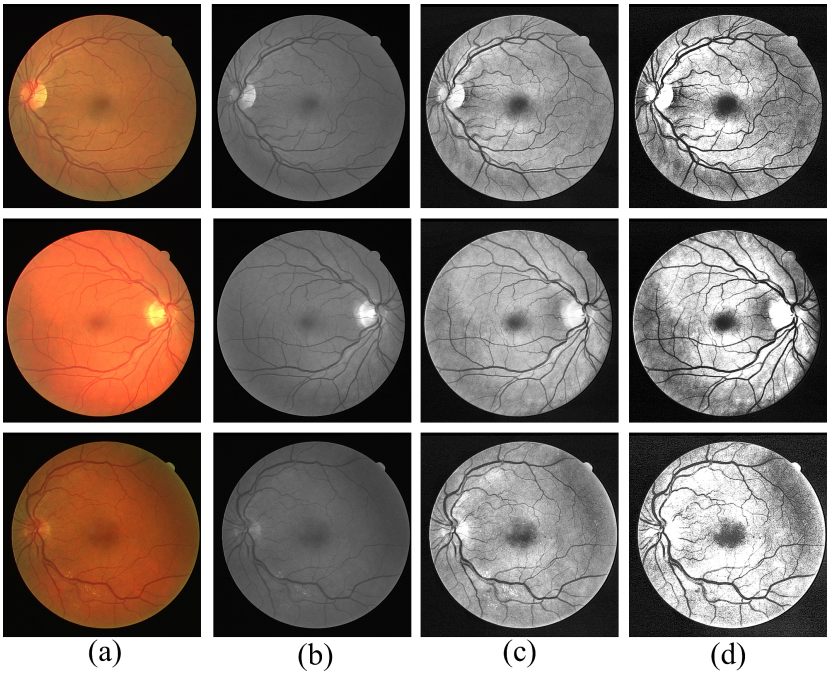

Fig. 8.4: Vessel's enhancement using PSO optimized CLAHE: (a) Input fundus image, (b) Gray image, (c) CLAHE enhanced image, (d) PSO optimized CLAHE enhancement.

The resulting enhanced images showed a significant improvement in contrast and clarity of features, as demonstrated by several quantitative metrics: MSE decreased from 249.5186 in the original image to 208.4254 in the enhanced image, indicating better information content; the Peak Signal-to-Noise Ratio (PSNR) rose from 11.59 dB to 15.6130 dB, highlighting reduced noise and improved image quality; and the Structural Similarity Index (SSIM) improved from 0.6218 to 0.8516, reflecting a closer alignment to the ideal image. Table 8.1 compares the quality measures of images enhanced using CLAHE versus PSO-optimized CLAHE.

Table 8.1: Enhancement quality measures of PSO-CLAHE and CLAHE

Image	MSE $(Pixel^2)$		PSNR $(Pixel^2)$		SSIM $(Pixel^2)$	
	CLAHE	PSO-CLAHE	CLAHE	PSO-CLAHE	CLAHE	PSO-CLAHE
01_test	206.8080	176.7352	12.1448	14.6792	0.6846	0.8830
02_test	202.9524	159.3982	11.8737	15.3431	0.5246	0.8476
03_test	225.6509	210.3323	8.1633	11.6705	0.7063	0.9223
04_test	295.7462	237.3071	13.7519	17.4351	0.6456	0.8469
05_test	316.4354	258.3542	12.0519	18.9327	0.5480	0.7582

8.2.2. Vessel's segmentation using Active Contour

Active Contour-based Vessel Segmentation is a widely used technique in medical imaging for extracting and analyzing blood vessels in retinal fundus images. Active contour models, also known as "snakes," are energy-minimizing curves that evolve under specific constraints to delineate object boundaries. Fig. 8.5 illustrates the active contour method employed for segmenting retinal vessels.

This method leverages the joint capabilities of the gradient force snake model and the balloon model to detect blood vessels in fundus images effectively. An image-based contour model is a deformable spline curve guided by an internal force that resists deformation, allowing it to move toward objects in the image. This behavior is comparable to the way a snake moves through a hollow space. A snake typically avoids the center of a hollow space, instead moving along the walls and corners, constantly searching for openings. Upon finding a hole, it enters, explores, and retreats if the path is blocked. Similarly, when applied to retinal blood vessels, the snake follows the vessel boundaries, where the vessel walls act as the boundaries and the openings or cracks represent potential entry points.

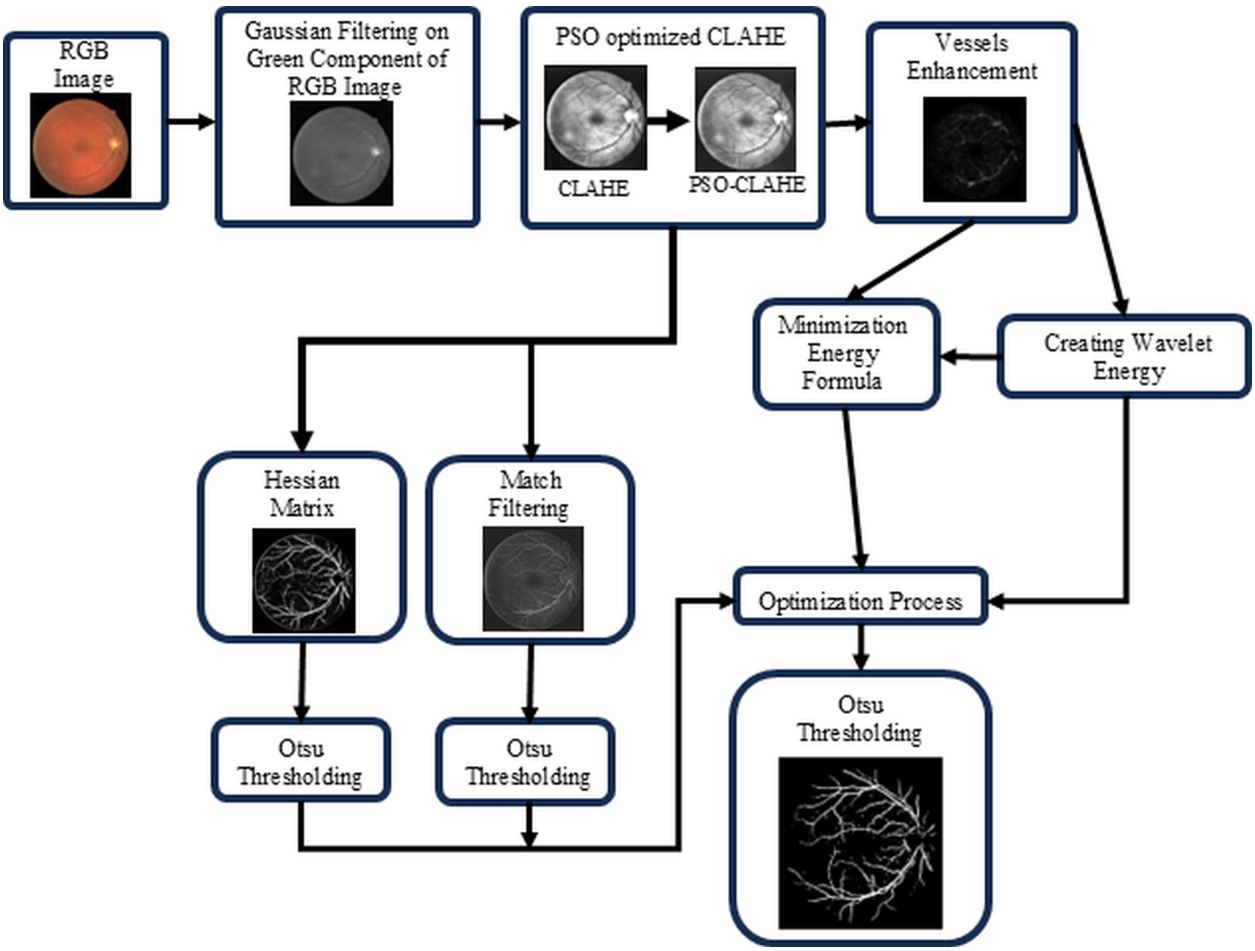

Fig. 8.5: Retinal vessel segmentation using Active Contour

Two classes of pixels are present in the vessel segmentation: the pixel is assigned to either the foreground or the background. The optimum threshold separating these classes is calculated by the Otsu algorithm, ensuring that their interclass variance is maximized. The optic discs or bright lesions can increase false positives. Additionally, some thin vessels are fragmented. Therefore, post-processing is required to restore fragmented edges and eliminate noise. Morphological operators were used for this work. Noise pixels, which are not part of the vascular network, were eliminated by considering a threshold level based on the number of pixels, with regions having fewer pixels than the threshold being discarded. For linking edges, the bridge morphologies operator was used. The bridge operator ties pixels together that each have two nonzero neighboring pixels. The separation of the vessel of the overall image by using the proposed active contour technique is shown in Fig. 8.6.

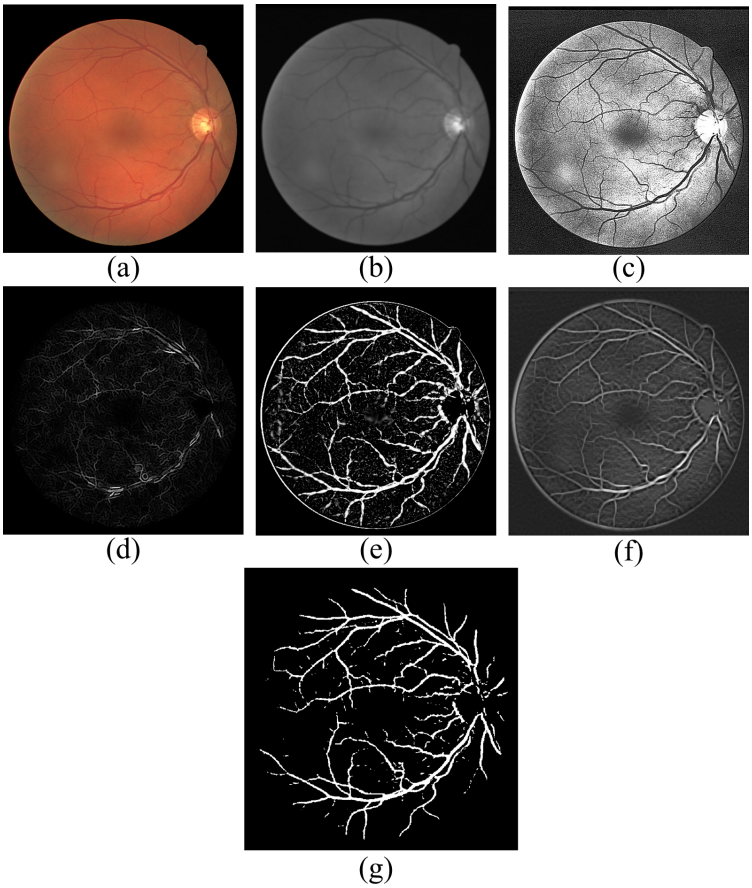

Fig. 8.6: Active Contour: (a) RGB input, (b) Grey image, (c) PSO-CLAHE enhancement, (d) Vessel's enhancement, (e) Hessian matrix image, (f) Match filtering, and (g) Segmented vessel structure.

Fig. 8.7 compares the manual and automatic results of the vessel's structure with respective input images. Compared to other pre-existing techniques, this method offers superior accuracy and faster processing time. The proposed automated method for segmenting vessels attains an average accuracy of 98.4% and a sensitivity of 97.6%.

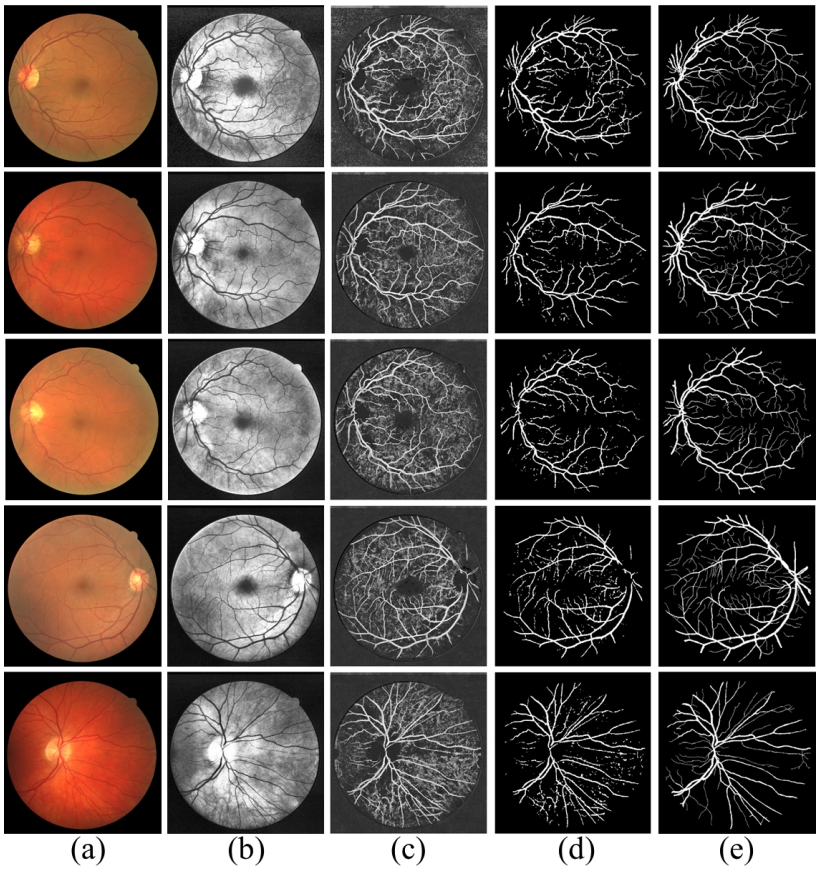

Fig. 8.7: Result shows the overall vessels segmentation using active contour by PSO-CLAHE: (a) Input RGB fundus image, (b) PSO-CLAHE based Enhancement, (c) Vessels after applying Active Contour function, (d) Active Contour based segmentation, (e) Manual Segmentation.

The evaluation metrics, accuracy, and sensitivity are calculated for various classifiers to assess their qualitative performance. Table 8.2 presents the results of comparing the recital of the PSO-CLAHE-based Active Contour Model system with previously established methods. The table indicates that our proposed method outperforms the other techniques in retinal vessel segmentation, with a sensitivity ranging from 96.04% to 98.87%. Additionally, our proposed method surpasses the conventional methods in terms of accuracy, achieving an accuracy of 98.82%.

Table 8.2: The results show the performance analysis of the proposed technique compared to the previously established methods.

Algorithm	Dataset	Samples	Sensitivity (%)	Specificity (%)	Accuracy (%)
Li et al [23]	DRIVE	40	75.69	98.16	95.27
	STARE	20	77.26	98.44	96.28
	CHASEBD1	28	75.07	97.93	95.81
Srinidhi et al. [27]	DRIVE	40	86.44	96.67	95.89
	STARE	20	83.25	97.46	95.02
	CHASEBD1	28	82.97	96.63	94.74
Yan et al. [28]	DRIVE	40	76.31	98.20	95.38
	STARE	20	77.35	98.57	96.38
	CHASEBD1	28	76.40	98.06	96.07
Jin et al. [29]	DRIVE	40	79.63	98.00	95.66
	STARE	20	75.95	98.78	96.41
	CHASEBD1	28	81.55	97.52	96.37
Yuchen Yuan et al. [30]	DRIVE	40	80.46	98.05	95.81
	STARE	20	79.14	98.70	96.65
	CHASEBD1	28	84.02	98.01	96.73
PSO-CLAHE-based Active Contour Model	HRF	45	96.04	97.14	98.63
	DRIVE	40	97.72	98.39	97.35
	CHASEDB1	28	**98.87**	95.20	**98.82**
	STARE	20	98.13	**99.17**	98.09

8.3. Conclusion:

This paper presents an effective approach for retinal vessel segmentation through a combination of PSO-optimized CLAHE-based image enhancement and active contour-based segmentation. The PSO-optimized CLAHE method improves the visibility and contrast of retinal images by automatically determining the optimal parameters, leading to enhanced vessel features and better overall image quality. The results show significant improvements in key image quality metrics, such as entropy, PSNR, and SSIM, when compared to traditional CLAHE techniques.

Following enhancement, the active contour model was employed to segment retinal vessels accurately. The model demonstrated excellent performance in delineating vessel boundaries, even in the presence of noise and thin vessels. Quantitative evaluation using metrics such as the Dice Similarity Coefficient (DSC) and Jaccard Index showed high accuracy in the segmentation process.

Overall, the proposed PSO-CLAHE-based enhancement and active contour-based segmentation framework proved to be a robust and efficient method for retinal vessel segmentation, providing high-quality results suitable for medical image analysis and disease diagnosis. The combined approach is particularly useful in clinical applications, where accurate vessel detection and analysis are crucial for early disease detection and monitoring.

Chapter IX

Detection of Retinal AVR and CDR Using Active Contours with Blind Deconvolution and CLAHE Fusion (Active-BDCLF)

Various retinal disorders, commonly diabetic and hypertensive retinopathy, can damage the optic nerve, potentially leading to permanent vision loss. Clinical observations often detect these conditions, such as abnormalities in retinal blood vessel diameter and the optic cup-to-disc ratio. High blood pressure can cause retinal vessel thinning and optic cup dilation, disrupting the normal arteriovenous ratio (AVR) and cup-to-disc ratio (CDR). This disruption may result in nerve fiber damage, hemorrhages, and cotton wool spots.

This study proposes an automated retinal optic disk and vessel segmentation from pre-processed retinal images. The segmentation was done using a ring mask created by superimposing two circles with the optic disk center and radii of 3D/2 and 1.5D/2, where D denotes the diameter of the optic disk. The maximum AV crossing was avoided within the retinal mask to simplify the process. Validations were performed by comparing the results with a predefined manually segmented dataset, achieving accuracies of 98.6% and 97.8% for retinal optic disk and optic cup, respectively, and 98.73% for retinal vessels. This algorithm could aid ophthalmologists in identifying retinal disorders accurately and automatically.

9.1. Introduction

Glaucoma, considered one of the major reasons for blindness, results in an estimated 12% of total blindness cases and is anticipated to affect almost 11 million people with bilateral blindness. The most common type of glaucoma globally is Primary Open-Angle Glaucoma (POAG), which impacts 74% of individuals diagnosed with the condition. Based on stratified estimates derived from population studies, it is expected that almost 11.2 million people in India, accounting for nearly 4.6% of the people over the age of 40, are affected by glaucoma. Detecting and treating this disease, which can potentially lead to blindness, presents significant challenges since the majority of those affected remain undiagnosed.

Hypertension can narrow the vessels inside the eye, reducing blood flow to the optical nerve and potentially resulting in blindness. Likewise, elevated pressure within the eye in cases of glaucoma can harm the optic nerves and affect vision. Research has suggested that individuals with hypertension may be at an increased likelihood of developing open-angle glaucoma, a group of eye conditions that damage the optic nerve. The possibility of this risk seems to surge among people with severe or poorly managed hypertension over a prolonged period.

Unfortunately, most associated instances do not exhibit symptoms, although they can be detected using retinal fundus imaging. Appropriate diagnosis and managing the disease in a clinical setting require careful valuation of variations in the optical nerve head (ONH), measurement of intraocular pressure (IOP), and identification of defects in the visual field. Diagnosing typical ONH alterations in the donor's eyes may be more difficult to assess because of the optic disk's pallor and swelling. Additionally, early vascular changes associated with high blood pressure can cause a narrowing of the retinal arterioles, changes at the arteriolar junction, such as arteriovenous nicking, and arteriolar light reflexes. Additionally, vessel bending is acknowledged as a likely cause of hypertension and coronary disorders. It is crucial to measure heart rate, as studies have demonstrated a strong link to an elevated long-term likelihood of stroke. As such, this effort seeks to develop a way to detect probable cases of glaucoma and hypertension in donor eyes by examining the optic disc cupping ratio and microvascular ratio. Fig. 9.1 provides an organizational chart of the CDR measurement.

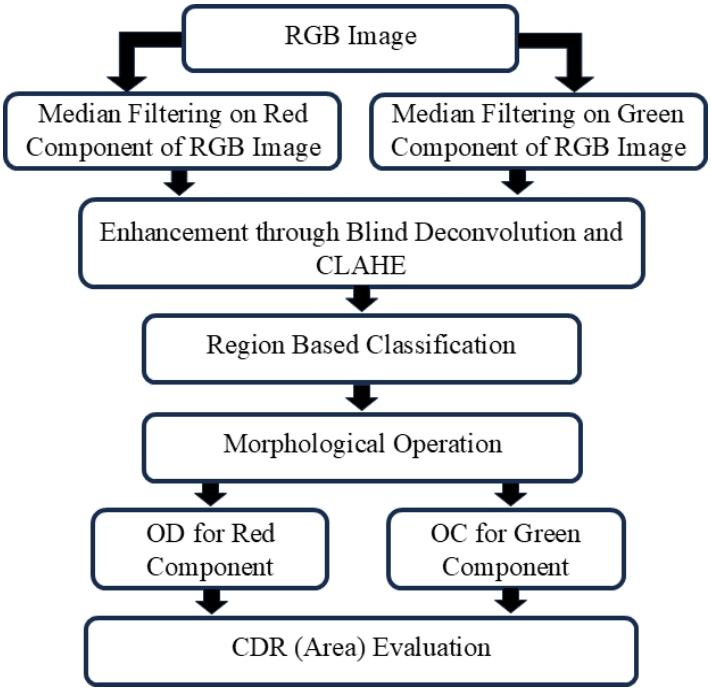

Fig. 9.1: Proposed Active-BDCLF framework for CDR evaluation, involving median filtering, CLAHE-based enhancement, region-based classification, and morphological segmentation of OD and OC regions.

The vessel's segmentation and AVR calculation have been made in two steps mentioned in Fig. 9.2(a) and Fig. 9.2(b). In the first step, vessels of the overall RGB retinal image have been segmented by fusioning Blind Deconvolution and advanced CLAHE technique followed by Active Contour-based vessel segmentation skills. In the second step, firstly the optic disk (OD) and its average diameter (D) and then the overlapping area between$\pi\left(3D\ /\ 2\right)^2$ and $\pi\left(1\ .\ 5D\ /\ 2\right)^2$ has been measured.

Then the segmented vessels within that masked area have been mapped. The reason behind this mask is that within this range the maximum vessels that are mostly affected by hypertension are found and also complexity is reduced. In the final stage of the second step, arteries and veins are separated to measure the area of the artery and vein separately. Arteries and veins are identified using the following parameters.

- The color of the arteries is brighter than that of the veins.
- Arteries are generally narrower than the adjacent veins.

- The central reflex (luminous reflex from within the vessels) is more pronounced within the blood arteries and less pronounced in the blood veins.
- Blood vessels typically alternate near the optic disc before branching out.

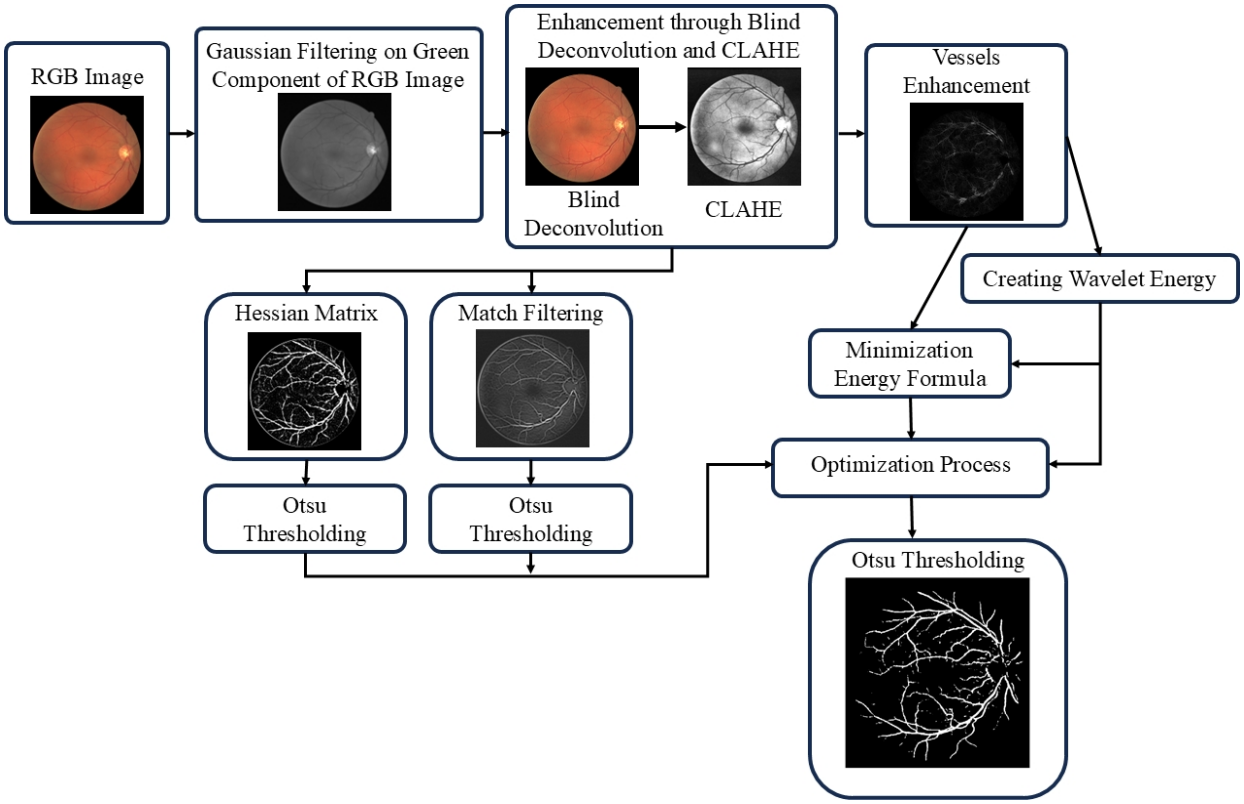

Fig. 9.2(a): Block diagram representing vessels Detection in Active-BDCLF

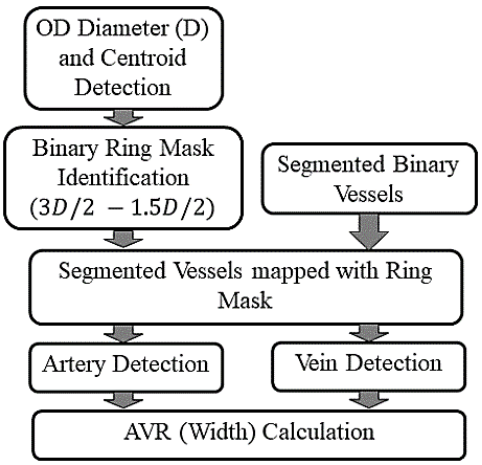

Fig. 9.2(b): Block diagram representing AVR Calculation.

Fig. 9.3(a) and Fig. 9.3(b) show the marking arteries and veins and the proposed region of interest. Finally, AVR concerning the area has been calculated. The measured AVR helps the Ophthalmologist detect the stages of hypertensive retinopathy.

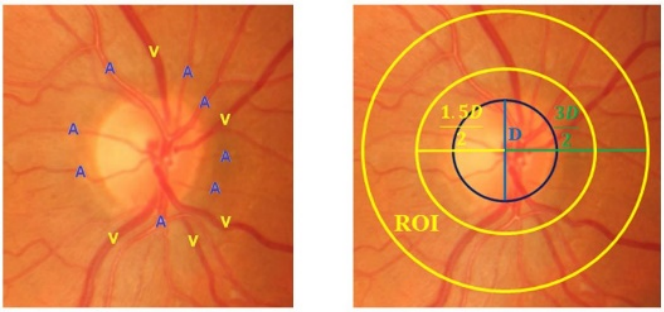

(a) (b)

Fig. 9.3: Random Image cropped from HRF datasets represents (a) marking arteries and veins, and (b) proposed area of interest.

The final step is the validation step where the binary parts of automatic segmented and manual segmented images are considered to identify the true positive and false negative parameters. From here TP, FP, TN, and FN values have been calculated to validate the proposed result set. These steps are depicted in Fig. 9.4.

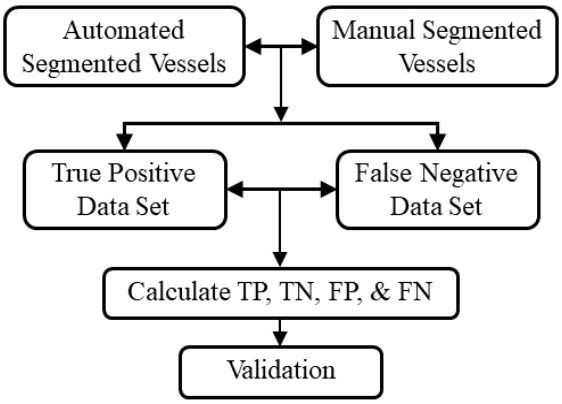

Fig. 9.4: Functional diagram representing the validation of vessel structure.

Table 1 explains the AVR for normal to accelerated hypertensive retinopathy cases with different risk factors [2. K. Narasimhan, V. C. Neha, K. Vijayarekha, et al., Hypertensive retinopathy diagnosis from fundus images by estimation of AVR, ICMOC – 2012, Elsevier Ltd., pp. 980 – 993 (2012)] and CDR ranges for normal and affected retina [Srinivasan Senthilkumari, Mohan

Neethu et al., Identification of glaucomatous optic nerve head changes in Indian donor eyes without clinical history, Indian Journal of Ophthalmology, vol. 63, no. 7, pp. 600-605 (2015)].

Table 9.1: AVR and CDR for different stages of Hypertensive Retinopathy.

Grading of HR	AVR	Indications	Systematic Association	CDR
Normal	0.66-0.75 (Approx.)	Normal	Normal	0.00-0.60 (Approx.)
Grade 1 (Mild)	0.5 (Approx.)	Constricted arterioles, arterial and venous nicking, and thickening of the arteriolar wall.	Loosely linked to cardiovascular disorders	>0.60 (Approx.)
Grade 2 (Moderate)	0.33 (Approx.)	Hemorrhages, along with both hard and soft exudates.	Heart attacks, strokes, and even deaths from cardiovascular diseases.	>0.60 (Approx.)
Grade 3 (Combined)	0.25 (Approx.)	Hemorrhages, along with both hard and soft exudates.	Heart attacks, strokes, and even deaths from cardiovascular diseases.	>0.60 (Approx.)
Grade 4 (Accelerated HR)	Fine Cords <0.2 (Approx.)	Swelling of the optic disc and loss of vision.	Kidney failure and death	>0.60 (Approx.)

9.2. Results and Discussion:

To assess the performance of the Active-BDCLF, a set of 40 fundus retinal images from the DRIVE database was selected. Of these, 33 images are from healthy patients with no clinical disorders, while 7 images are from patients with clinical abnormalities. For all 40 images, the optic cups, optic discs, and vessel structures were segmented, and measurements for the optic cup diameter, optic disc diameter, and vessel width were obtained using the described automatic process. The Cup-Disc Ratio (CDR) and Artery-Vein Ratio (AVR) were then calculated and compared with the manual data. Fig. 9.5 illustrates the image enhancement achieved using the advanced CLAHE and Blind Deconvolution fusion techniques.

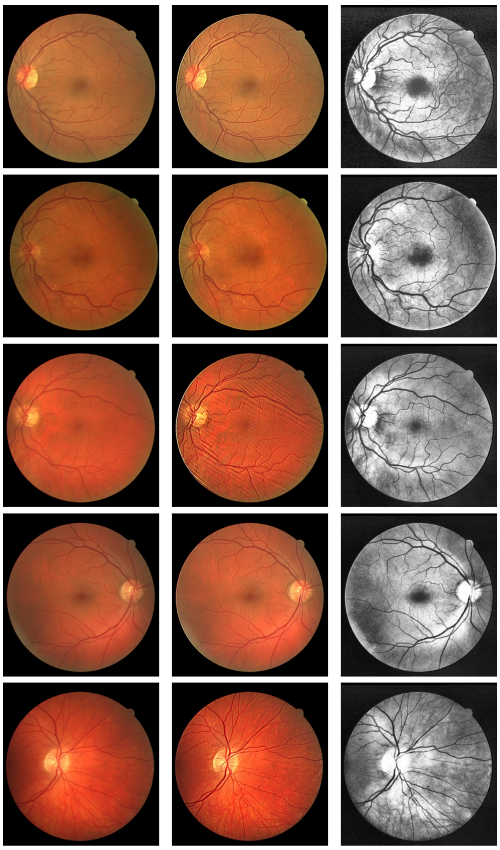

Fig. 9.5: Result shows the image enhancement techniques using CLAHE and Blind Deconvolution fusion: (a) Input RGB Fundus Image, (b) Enhancement by Blind Deconvolution, and (d) Enhancement by CLAHE after Blind Deconvolution.

Table 9.2 presents a comparison of the quality measures between images that have been enhanced using CLAHE and the Active-BDCLF techniques. The Active-BDCLF achieves a higher PSNR, indicating superior image quality. Additionally, the proposed technique exhibits a lower MSE than CLAHE, leading to enhanced image fidelity, improved visual quality, and increased accuracy. Furthermore, the higher SSIM measure of the proposed technique compared to CLAHE ensures minimal distortion in the image structure. The results demonstrate that the mentioned technique surpasses CLAHE in terms of image enhancement.

Table 9.2: Quality measures of Active-BDCLF and CLAHE

Image	MSE $(Pixel^2)$		PSNR(dB)		SSIM	
	Active-BDCLF	CLAHE	Active-BDCLF	CLAHE	Active-BDCLF	CLAHE
6(a1)	2849.70	4273.50	17.49	11.82	0.5319	0.3390
6(a2)	5167.30	6322.50	19.17	10.12	0.3942	0.1752
6(a3)	3516.57	5161.00	16.52	11.01	0.3751	0.2365
6(a4)	1732.64	2737.30	19.38	13.75	0.7438	0.5456
6(a5)	2958.59	4058.3	21.39	12.05	0.5219	0.3480

Table 9.3 compares the proposed Active-BDCLF method with the pre-established BDCLF. The comparison explains the superiority of Active-BDCLF over BDCLF in terms of MSE, PSNR and SSIM.

Table 9.3: Quality measures of Active-BDCLF and BDCLF

Image	MSE $(Pixel^2)$		PSNR(dB)		SSIM	
	Active-BDCLF	BDCLF	Active-BDCLF	BDCLF	Active-BDCLF	BDCLF
6(a1)	2849.70	3151.30	17.49	15.85	0.5319	0.4428
6(a2)	5167.30	5316.20	19.17	16.63	0.3942	0.2760
6(a3)	3516.57	3992.91	16.52	14.89	0.3751	0.3379
6(a4)	1732.64	1953.30	19.38	17.43	0.7438	0.6469
6(a5)	2958.59	3162.40	21.39	18.93	0.5219	0.4582

Fig. 9.6 represents the input RGB fundus images of the macula with segmented results of the optic disk and optic cup using the mentioned morphological techniques.

Table 9.4 provides a comparison between the automatic and manual Cup-to-Disc Ratio (CDR) measurements. The automatic diameter measurements of the Optic Disc (OD) and Optic Cup (OC) in terms of pixels are performed by Active-BDCLF, while the manual diameters are obtained from the specified dataset. The CDR values are computed for both automatic and manual measurements by taking the ratio of their respective areas. The CDR errors are calculated by finding the difference between the manually and automatically determined CDR values.

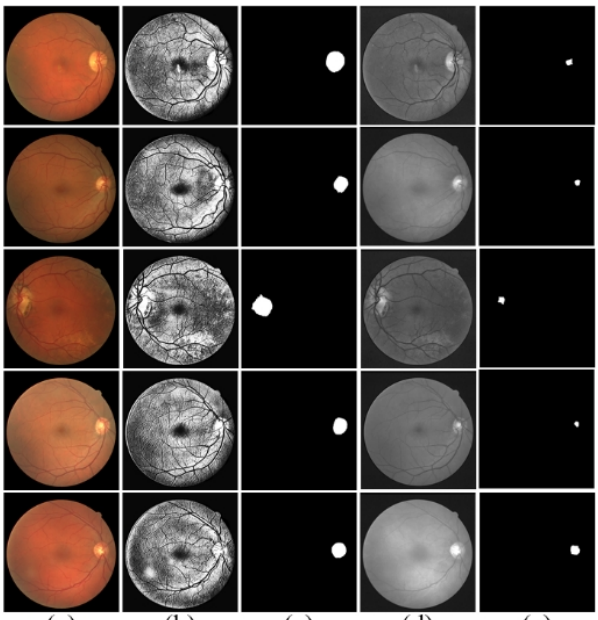

Fig. 9.6: In this figure, (a) represents the input RGB fundus image, (b), (c), (d) and (e) represent the PROPOSED Enhancement, segmented Optic Disk, green components of the input image, and segmented Optic Cup respectively.

Table 9.4: Result shows the comparison of automatic CDR and manual CDR

Sl. No.	$Dia_{OD}\,(Pixel)$		$Dia_{OC}\,(Pixel)$		CDR $(Pixel^2)$		$Error_{CDR}$
	Auto	**Manual**	**Auto**	**Manual**	**Auto**	**Manual**	
1	230	234	186	190	0.65	0.66	0.01
2	226	224	194	190	0.74	0.72	-0.02
3	218	223	184	186	0.71	0.70	-0.01
4	226	232	178	184	0.62	0.63	0.01
5	228	224	182	178	0.64	0.63	-0.01
6	203	194	179	175	0.78	0.81	0.04
7	216	230	175	178	0.66	0.60	-0.06
8	224	218	184	175	0.67	0.64	-0.03
9	226	225	128	130	0.32	0.33	-0.01
10	224	225	128	125	0.33	0.31	-0.02

Table 9.5 compares the Active-BDCLF with the previously established BDCLF technique. As a result, Active-BDCLF shows better performance than BDCLF in terms of true positive data as well as error.

Table 9.5: Comparison of manual CDR values measured by Active-BDCLF and BDCLF

Sl. No.	$Dia_{OD}\ (Pixel)$			$Dia_{OC}\ (Pixel)$			CDR $(Pixel^2)$		
	Automatic		Manual	Automatic		Manual	Automatic		Manual
	Active BDCLF	BDCLF		Active BDCLF	BDCLF		Active BDCLF	BDCLF	
1	232	230	234	188	186	190	0.66	0.65	0.66
2	223	226	224	189	194	190	0.72	0.74	0.72
3	221	218	223	187	184	186	0.72	0.71	0.70
4	229	226	232	182	178	184	0.63	0.62	0.63
5	226	228	224	180	182	178	0.63	0.64	0.63
6	198	203	194	174	179	175	0.77	0.78	0.81
7	224	216	230	179	175	178	0.64	0.66	0.60
8	216	224	218	182	184	175	0.70	0.67	0.64
9	223	226	225	133	128	130	0.35	0.32	0.33
10	226	224	225	123	128	125	0.30	0.33	0.31

Table 9.6 presents the computation results for various metrics in the context of optical disc (OD) and optic cup (OC) analysis. Specifically, it covers sensitivity, specificity, overlapping error (OD and OC), balanced accuracy (OD and OC), and absolute error in cup-to-disc ratio (CDR), denoted as A_{OD}, A_{OC}, E_{OD}, E_{OC}, δ_E, respectively. When focusing on OD segmentation, the Active BDCLF method accomplishes a sensitivity of 98.6%, specificity of 99.7%, and accuracy of 98.5%, accompanied by an absolute error of 2.8%. Similarly, for OC segmentation, the Active BDCLF method demonstrates a sensitivity of approximately 97.7%, specificity of 98.7%, accuracy of 96.8%, and a minimum error of 2.8%. These results further establish the superiority of the PROPOSED technique over alternative methods.

Table 9.6: Statistical results of optic cup and optic disk

Dataset	Sensitivity		Specificity		Accuracy		E_{OD}	E_{OC}	δ_E
	OD	OC	OD	OC	OD	OC			
CHASEDB1	0.962	0.953	0.997	0.983	0.975	0.968	0.103	0.103	0.049
DRIVE	0.968	0.947	0.984	0.972	0.971	0.945	0.087	0.294	0.045
HRF	0.986	0.977	0.984	0.987	0.985	0.962	0.074	0.241	0.028
STARE	0.950	0.932	0.976	0.975	0.953	0.960	0.093	0.285	0.069

The separation of the vessel from the overall image by using the proposed active contour technique is shown in Fig. 9.7. that compares the manual and automatic results of the vessel's structure with

respective input images. Compared to other pre-existing techniques, this method offers superior accuracy and faster processing time. The proposed automated method for segmenting vessels attains an average accuracy of 98.4% and a sensitivity of 97.6%.

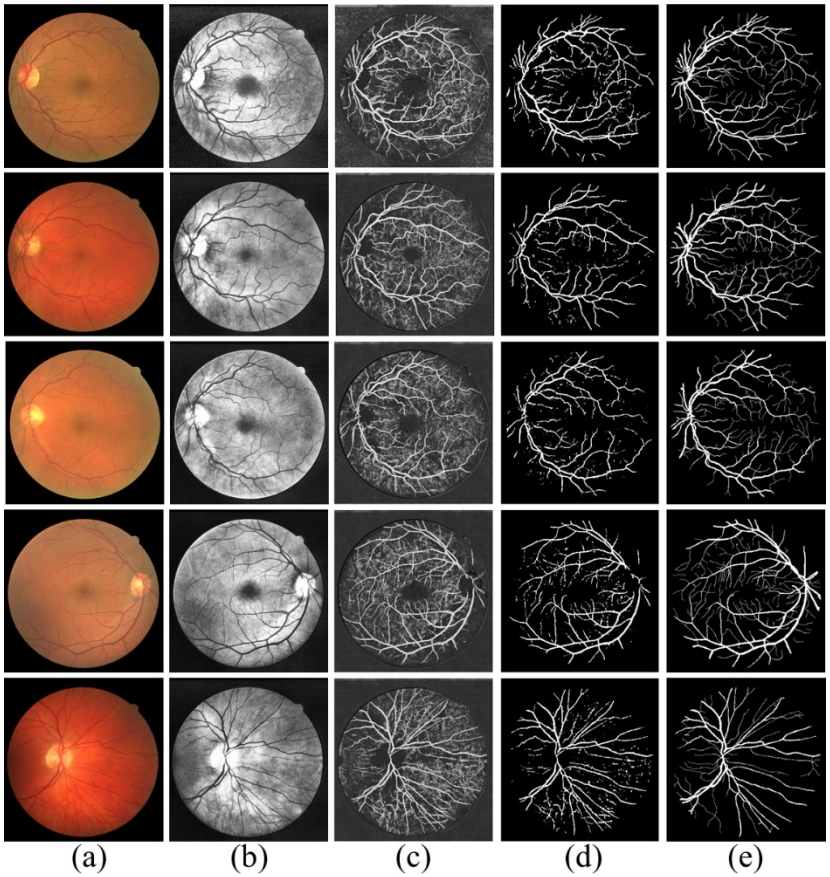

Fig. 9.7: Result shows the overall vessels segmentation using active contour by fusioning CLAHE and Blind Deconvolution: (a) Input RGB fundus image, (b) CLAHE and Blind Deconvolution fusion-based Enhancement, (c) Vessels after applying Active Contour function, (d) Active Contour based segmentation, (e) Manual Segmentation.

Fig. 9.8 explains the vessel mapping and artery-vein separation within the mentioned specific ring mask. The ring mask has been chosen for complexity due to the vessel's branching.

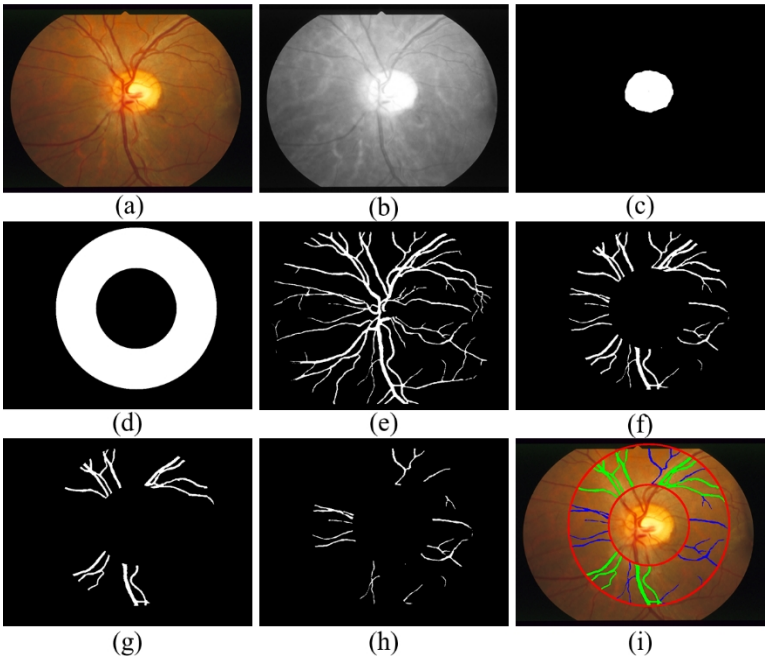

Fig. 9.8: Result shows the separation of arteries and veins within specified ring mask: (a) The Input RGB Image, (b) Red components of RGB image, (c) Segmented optic disk, (d) (3D-1.5D) mask, (e) Segmented Vessels (f) Segmented vessels within mask, (g) Separated veins, (h) Separated arteries, and (i) Segmented vessel's labeling.

The evaluation metrics, accuracy, and sensitivity are calculated for various classifiers to assess their qualitative performance. Table 9.7 presents the results of comparation the recital of the Active-BDCLF system with previously established methods. The table indicates that our proposed method outperforms the other techniques in retinal vessel segmentation, with a sensitivity ranging from 96.58% to 98.73%. Additionally, our Active-BDCLF method surpasses the conventional methods in terms of accuracy, achieving an accuracy of 98.56%.

Table 9.7: The results show the performance analysis of the proposed technique compared to the previously established methods.

Algorithm	**Dataset**	**Samples**	**Sensitivity (%)**	**Specificity (%)**	**Accuracy (%)**
Li et al [54]	DRIVE	40	75.69	98.16	95.27
	STARE	20	77.26	98.44	96.28
	CHASEBD1	28	75.07	97.93	95.81
Srinidhi et al. [55]	DRIVE	40	86.44	96.67	95.89
	STARE	20	83.25	97.46	95.02
	CHASEBD1	28	82.97	96.63	94.74
Yan et al. [56]	DRIVE	40	76.31	98.20	95.38
	STARE	20	77.35	98.57	96.38

	CHASEBD1	28	76.40	98.06	96.07
Jin et al. [57]	DRIVE	40	79.63	98.00	95.66
	STARE	20	75.95	**98.78**	96.41
	CHASEBD1	28	81.55	97.52	96.37
Yuchen Yuan et al. [58]	DRIVE	40	80.46	98.05	95.81
	STARE	20	79.14	98.70	96.65
	CHASEBD1	28	84.02	98.01	96.73
Active-BDCLF	HRF	45	**96.58**	97.65	**98.56**
	DRIVE	40	**97.23**	96.69	**97.39**
	CHASEDB1	28	**98.41**	95.31	**98.14**
	STARE	20	**98.73**	96.45	**98.37**

Table 9.8 presents the automated measurements of retinal vessel width using Active-BDCLF, along with manually collected data. It also illustrates the automatic and manual calculations of AVR, showcasing a marginal average error of less than ±4% as shown in Figure 17. A normal retinal image is characterized by an AVR range exceeding 6.6, whereas a range below this threshold indicates abnormalities related to glaucoma or hypertension [1]. Consequently, the Active-BDCLF technique proposed in this study is capable of effectively assessing retinal data abnormalities, rendering it highly favorable.

Table 9.8: The outcome presents a comparison between the widths of the vessel acquired through the automated method proposed and those obtained through manual measurements.

Sl. No.	$Width_{Automatic}$		$Width_{Manual}$		**AVR**		**ERROR**
	Artery	**Vein**	**Artery**	**Vein**	**Auto**	**Manual**	
1	11.75	21.40	12.20	23.40	0.549	0.521	-0.027
2	18.02	27.31	17.46	26.57	0.659	0.657	-0.002
3	17.69	38.83	17.85	40.02	0.455	0.446	-0.009
4	14.87	28.28	15.65	31.14	0.525	0.502	-0.023
5	3.16	4.47	6.41	8.94	0.706	0.717	0.010
6	2.76	3.61	2.81	3.60	0.764	0.780	0.016
7	10.50	15.80	9.4	13.60	0.664	0.691	0.026
8	10.63	13.45	10.76	13.41	0.790	0.802	0.012
9	6.83	10.82	5.32	7.81	0.631	0.681	0.050
10	2.03	6.08	2.06	6.32	0.333	0.325	-0.007

The presentation evaluation of a binary classifier system was conducted using the receiver operating characteristic (ROC) curve displayed in Fig. 9.9. This curve portrays the association between the true positive rate (sensitivity) and the false positive rate (1 - specificity) with varying classification thresholds. By visualizing the classifier's performance at various thresholds, the ROC curve enables the assessment of its ability to distinguish between positive and negative

instances. Additionally, it facilitates the comparison of different classifiers or models. In this particular ROC curve, the dataset from the drive was utilized to analyze the performance of five distinct techniques, including the proposed Active-BDCLF method. Results indicate that the PROPOSED method outperforms existing techniques in terms of ROC, as evidenced by its faster and more stable curve. A stable ROC curve signifies that the classifier's performance remains consistent and reliable across diverse datasets or conditions, thereby instilling confidence in its generalization capability to new and unseen data. Furthermore, these findings establish the superiority of the proposed Active-BDCLF method over existing approaches.

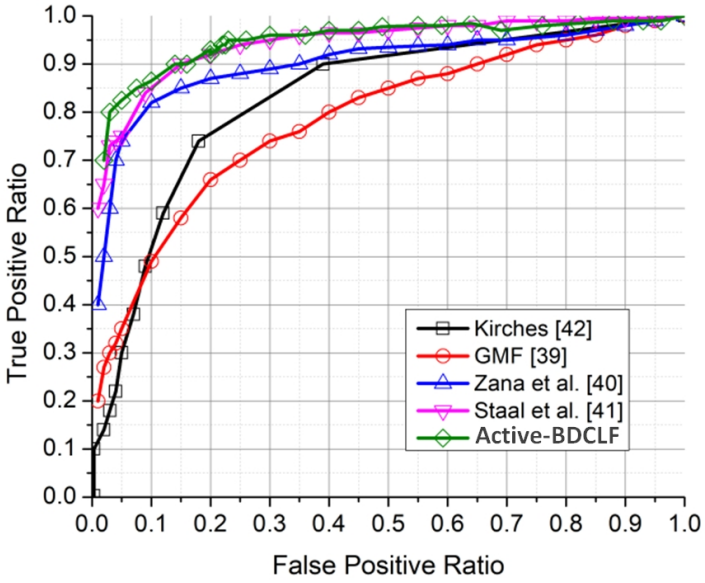

Fig. 9.9: The average ROC plot for 40 DRIVE data is shown using five different methods.

The AVR and CDR values obtained through the Active-BDCLF method, as shown in Table 9, are applied to measure the condition of the patient in terms of diabetes, glaucoma, and overall health. To accomplish this, a selection of retinal images from the HRF dataset, encompassing diabetic, glaucoma, and healthy cases, were randomly chosen. The results obtained were promising, revealing an average CDR of 0.68 for diabetic patients, 0.62 for glaucoma patients, and 0.41 for healthy individuals. Similarly, the average AVR values were found to be 0.52 for diabetics, 0.43 for glaucoma patients, and 0.75 for those without any eye-related conditions.

Table 9.9: Result shows the AVR and CDR for patient’s different health conditions.

HRF Image	Patent's Condition	OD (Avg.)	OC (Avg.)	W_{Artery} (Avg.)	W_{Vein} (Avg)	CDR	AVR
01_dr	Diabetic	372	294	13.15	32.37	0.63	0.41
02_dr		375	306	12.32	22.62	0.67	0.54
03_dr		327	281	14.05	23.18	0.74	0.61
04_dr		336	268	13.19	26.39	0.64	0.50
01_h	Healthy	410	248	17.39	20.81	0.37	0.84
02_h		408	267	16.18	23.41	0.43	0.69
03_h		396	237	17.02	22.11	0.36	0.77
07_h		416	278	17.36	24.79	0.45	0.70
01_g	Glaucoma	338	261	12.27	26.58	0.60	0.46
08_g		367	292	11.43	28.91	0.63	0.39

9.3. Conclusion:

An automated approach has been proposed to evaluate two specific target features in the human eye, namely CDR and AVR, to detect abnormalities associated with conditions like diabetes, glaucoma, and hypertension. The results obtained so far are promising, demonstrating high levels of accuracy: 98.6% for OD, 97.8% for OC, and 98.55% for AVR, with only minor errors. This technique surpasses other established methods in terms of speed due to its fully automated nature, and it requires minimal expertise for implementation, making it accessible to individuals with any level of medical knowledge. The positive outcomes achieved through this method allow for the measurement of various parameters (such as nicking, narrowing, and branching coefficients), which can assist in diagnosing different diseases.

A series of clinical images acquired from publicly available datasets will be quantitatively evaluated in the next study to find the retinopathy of prematurity (ROP).

Chapter X

Conclusion

Retinal image processing has emerged as a critical field in medical imaging, enabling early detection, diagnosis, and management of various ocular and systemic diseases. Throughout this research, significant advancements have been made in the development of robust, accurate, and automated methodologies for processing retinal images, thereby enhancing diagnostic precision and reducing the burden on healthcare professionals.

The study has successfully demonstrated the effectiveness of various image processing techniques, including preprocessing, segmentation, feature extraction, and classification, in analyzing retinal images. The application of advanced deep learning models, such as convolutional neural networks (CNNs) and transformer-based architectures, has significantly improved the accuracy and efficiency of disease detection, particularly for diabetic retinopathy, age-related macular degeneration, and glaucoma. The integration of machine learning and artificial intelligence has proven to be a powerful approach in automating the detection of pathological features, minimizing subjective interpretation errors, and facilitating large-scale screening programs.

One of the key contributions of this research is the development of novel image enhancement and segmentation techniques tailored to address challenges associated with retinal images, such as uneven illumination, low contrast, and noise artifacts. The proposed methodologies have demonstrated superior performance in enhancing vessel structures, detecting lesions, and segmenting optic disc and macula regions with high precision. Moreover, the adoption of hybrid approaches that combine traditional image processing techniques with deep learning frameworks has further refined the accuracy of automated diagnostic systems.

Despite the remarkable progress, certain limitations remain, including variability in image quality due to differences in acquisition devices, variations in patient demographics, and the presence of overlapping pathologies. Addressing these challenges requires the development of more generalized models, extensive training on diverse datasets, and continuous improvement of image augmentation techniques. Future research should also explore the integration of multimodal imaging techniques, such as optical coherence tomography (OCT) and fundus fluorescein angiography (FFA), to provide a more comprehensive assessment of retinal health.

Furthermore, the implementation of real-time, cloud-based, and mobile-friendly retinal image processing solutions will enhance accessibility and scalability, particularly in resource-limited settings. The fusion of artificial intelligence with telemedicine holds great promise in enabling

remote diagnosis and early intervention, ultimately reducing the prevalence of vision-related complications and improving global eye health.

Despite the promising outcomes, this study is subject to certain limitations that should be acknowledged. One of the primary challenges lies in dataset variability, as the ophthalmic images used in this research originate from different acquisition devices, illumination conditions, and patient demographics. Such variations may influence the model's generalization ability across different clinical environments.

Another significant limitation is the limited availability of high-quality annotated medical images, especially those with precise lesion-level labeling. Since manual annotation requires expert ophthalmologists and is time-consuming, the size of the labeled dataset remains relatively small. This constraint can affect the robustness and scalability of the proposed algorithms.

To address these challenges, future work could explore domain adaptation, data augmentation, and semi-supervised or weakly supervised learning approaches to enhance generalization and reduce dependence on large, fully annotated datasets.

References

References:

1. Thylefors, B., A global initiative for the elimination of avoidable blindness, American Journal of Ophthalmology, 125(1), 90, 1998.
2. Foster, A. and Resnikoff, S., The impact of Vision 2020 on global blindness, Eye, 19(10), 1133, 2005.
3. Joshy, G. and Simmons, D., Epidemiology of diabetes in New Zealand: revisit to a changing landscape, The New Zealand Medical Journal, 119(1235), 2006.
4. Colagiuri, S., Colagiuri, R., and Ward, J., National Diabetes Strategy and Implementation Plan., Diabetes Australia, Paragon Printers, Canberra, 1998.
5. King, H., Aubert, R.E., and Herman, W.H., Global burden of diabetes, 1995– 2025: prevalence, numerical estimates and projections, Diabetes Care, 21, 1414, 1998.
6. Wild, S., Roglic, G., Green, A., et al., Globel prevalence of diabetes: estimates for the year 2000 and projections for 2030, Diabetes Care, 27(10), 2569, 2004.
7. Centers for Disease Control and Prevention, National diabetes fact sheet: general information and national estimates on diabetes in the United States, Technical report, U.S. Department of Health and Human Services, Centers for Disease Control and Prevention, 2003.
8. The Eye Diseases Prevalence Research Group, The prevalence of diabetic retinopathy among adults in the United States, Archives of Ophthalmology, 122(4), 552, 2004.
9. Mathers, C. and Penm, R., Health system costs of cardiovascular diseases and diabetes in Australia 1993–94, Technical Report HWE 11, Australian Institute of Health and Welfare, 1999.
10. Engerman, R., Pathogenesis of diabetic retinopathy, Diabetes, 38, 1203, 1989.
11. Kristinsson, J.K., Gottfredsdottir, M.S., and Stefansson, E., Retinal vessel dilatation and elongation precedes diabetic macular oedema, Br J Ophthalmol, 81(4), 274, 1997.

12. Wong, T.Y., Klein, R., Sharrett, A.R., et al., Retinal arteriolar narrowing and risk of diabetes mellitus in middle-aged persons, Journal of the American Medical Association, 287(19), 2528, 2002.

13. Cockburn, D., Diabetic retinopathy: classification, description and optometric management, Clinical and Experimental Optometry, 82(2-3), 59, 1999.

14. Ciulla, T., Amador, A., and Zinman, B., Diabetic retinopathy and diabetic macular edema: pathophysiology, screening, and novel therapies, Diabetes Care, 26(9), 2653, 2003.

15. Younis, N., Broadbent, D., Harding, S., et al., Prevalence of diabetic eye disease in patients entering a systematic primary care-based eye screening programme, Diabetic Medicine, 19, 1014, 2002.

16. Williams, R., Airey, M., Baxter, H., et al., Epidemiology of diabetic retinopathy and macular oedema: a systematic review, Eye, 18, 963, 2004.

17. Klein, R., Klein, B.E., Moss, S.E., et al., TheWisconsin Epidemiologic Study of Diabetic Retinopathy. III. Prevalence and risk of diabetic retinopathy when age at diagnosis is 30 or more years, Arch Ophthalmol, 102(4), 527, 1984.

18. Harding, S.P., Broadbent, D.M., Neoh, C., et al., Sensitivity and specificity of photography and direct ophthalmology in screening for sight threatening eye disease: the Liverpool Diabetic Eye Study, British Medical Journal, 311, 1131, 1995.

19. Betz-Brown, J., Pedula, K., and Summers, K., Diabetic retinopathy-contemporary prevalence in a well-controlled population, Diabetes Care, 26(9), 2637, 2003.

20. Icks, A., Trautner, C., Haastert, B., et al., Blindness due to diabetes: population-based age- and sex-specific incidence rates, Diabetic Medicine, 14, 571, 1997.

21. Cunha-Vaz, J., Lowering the risk of visual impairment and blindness, Diabetic Medicine, 15(S4), S47, 1998.

22. Taylor, H.R., Vu, H.T.V., McCarty, C.A., et al., The need for routine eye examinations, Investigative Ophthalmology and Visual Science, 45(8), 2539, 2004.

23. Kohner, E. and Sleightholm, M., Does microaneurysm count reflect the severity of early diabetic retinopathy? Ophthalmology, 93, 586, 1986.

24. Klein, R., Meuer, S.M., Moss, S.E., et al., Retinal microaneurysm counts and 10-year progression of diabetic retinopathy, Archives of Ophthalmology, 113(11), 1386, 1995.

25. Mazze, R. and Simonson, G., Staged diabetes management: a systematic evidence-based approach to the prevention and treatment of diabetes and its co-morbidities, Practical Diabetes International, 18(7), S1, 2001.

26. National Health and Medical Research Council, Management of diabetic retinopathy clinical practice guidelines, Technical report, Australian Government Publishing Service, 1997.

27. Lee, S.J., McCarty, C.A., Taylor, H.R., et al., Costs of mobile screening for diabetic retinopathy: a practical framework for rural populations, Australian Journal of Rural Health, 9, 186, 2001.

28. Facey, K., Cummins, E., Macpherson, K., et al., Organisation of services for diabetic retinopathy screening, Technical Report 1, Health Technology Board for Scotland, 2002.

29. Lee, S., McCarty, C., Taylor, H.R., et al., Costs of mobile screening for diabetic retinopathy: a practical framework for rural populations, Australian Journal of Rural Health, 9, 186, 2001a.

30. James, M., Turner, D., Broadbent, D., et al., Cost-effectiveness analysis of screening for sight threatening diabetic eye disease, British Medical Journal, 320, 1627, 2000.

31. Leese, G., Tesfaye, S., Dengler-Harles, M., et al., Screening for diabetic eye disease by optometrists using slit lamps, Journal of Royal College of Physicians London, 31, 65, 1997.

32. Hutchinson, A., McIntosh, A., Peters, J., et al., Effectiveness of screening and montitoring tests for diabetic retinopathy — a systematic review, Diabetic Medicine, 17, 495, 2000.

33. UK National Screening Committee, Essential elements in developing a diabetic retinopathy screening programme, Technical report, 2004.

34. American Diabetic Association, Screening for type 2 diabetes: American Diabetes Association position statement, Diabetes Care, 26(Suppl 1), S21, 2003.

35. Lee, V., Kingsley, R., and Lee, E., The diagnosis of diabetic retinopathy. Ophthalmology versus fundus photography, Ophthalmology, 100., 1504, 1993.

36. Taylor, H.R. and Keeffe, J.E., World blindness: a 21st century perspective, British Journal of Ophthalmology, 85, 261, 2001.

37. Bachmann, M.O. and Nelson, S., Impact of diabetic retinopathy screening on a British district population: case detection and blindness prevention in an evidence-based model, Journal of Epidemiology and Community Health, 52, 45, 1998.

38. Sharp, P.F., Olsen, J., Strachan, F.M., et al., The value of digital imaging in diabetic retinopathy, Technical Report 7(30), Health Technology Assessment, 2003.

39. Phiri, R., Keeffe, J.E., Harper, C.A., et al., Comparative study of the Polaroid and digital non-mydriatic cameras in the detection of referable diabetic retinopathy in Australia, Diabetic Medicine, 23(8), 867, 2006.

40. Bursell, S.E., Caverallerano, J., Caverallerano, A., et al., Joslin Vision Network Research Team: Stereo nonmydriatic digital-video color retinal imaging compared with early treatment diabetic retinopathy study seven standard field 35mm stereo color photos for determining level of diabetic retinopathy, Ophthalmology, 108, 572, 2001.

41. Olson, J.A., Strachan, F.M., Hipwell, J.H., et al., A comparative evaluation of digital imaging, retinal photography and optometrist examination in screening for diabetic retinopathy, Diabetic Medicine, 20(7), 528, 2003.

42. Harper, C.A., Livingston, P.M.,Wood, C., et al., Screening for diabetic retinopathy using a non-mydriatic camera in rural Victoria, Australian and New Zealand Journal of Ophthalmology, 28, 135, 1998.

43. Sussman, E., Tsiaras, W., and Soper, K., Diagnosis of diabetic eye disease, JAMA, 247, 3231, 1982.

44. Howsam, G., The Albury-Wodonga syndrome: A tale of two cities, Australian and New Zealand Journal of Opthalmololgy, 23, 135, 1995.

45. Lawrenson, R., Dunn, P., Worsley, D., et al., Discover diabetes: a community-based screening programme for diabetic eye disease, The New Zealand Medical Journal, 107, 172, 1994.

46. Reda, E., Dunn, P., Straker, C., et al., Screening for diabetic retinopathy using the mobile retinal camera: the Waikato experience, The New Zealand Medical Journal, 116(1180), 562, 2003.

47. Yogesan, K., Constable, I.J., Barry, C.J., et al., Telemedicine screening of diabetic retinopathy using a hand-held fundus camera, Telemedicine Journal, 6(2), 219, 2000.

48. Patton, N., Aslam, T.M., MacGillivray, T., et al., Retinal image analysis: concepts, applications and potential, Progress in Retinal and Eye Research, 25, 99, 2006.

49. Whited, J.D., Accuracy and reliability of teleophthalmology for diagnosing diabetic retinopathy and macular edema: A review of the literature, Diabetes Technology and Therapeutics, 8(1), 102, 2006.

50. Constable, I.J., Yogesan, K., Eikelboom, R.H., et al., Fred Hollows lecture: Digital screening for eye disease, Clinical and Experimental Ophthalmology, 28, 129, 2000.

51. Lin, D., Blumenkranz, M., Brothers, R., et al., The sensitivity and specificity of single-field nonmydriatic monochromatic digital fundus photography with remote images interpretation for diabetic retinopathy screening: a comparison with ophthalmology and standardized mydriatic color photography, American Journal of Ophthalmology, 134, 204, 2002.

52. Davis, R., Fowler, S., Bellis, K., et al., Telemedicine improves eye examination rates in individuals with diabetes, Diabetes Care, 26(8), 2476, 2003.

53. Lee, S., Sicari, C., Harper, C., et al., Program for the early detection of diabetic retinopathy: a two-year follow-up, Clinical and Experimental Ophthalmology, 29, 12, 2001b.

54. Madden, A.C., Simmons, D., McCarty, C.A., et al., Eye health in rural Australia, Clinical and Experimental Ophthalmology, 30(5), 316, 2002.

55. Wong, T.Y., Shankar, A., Klein, R., et al., Retinal arteriolar narrowing, hypertension and subsequent risk of diabetes mellitus, Archives of Internal Medicine, 165(9), 1060, 2005.

56. Li, H., Hsu, W., Lee, M.L., et al., Automated grading of retinal vessel caliber, IEEE Transactions on Biomedical Engineering, 52(7), 1352, 2005.

57. Witt, N., Wong, T.Y., Hughes, A.D., et al., Abnormalities of retinal microvascular structure and risk of mortality from ischemic heart disease and stroke, Hypertension, 47, 345, 2000.

58. Forracchia, M., Grisan, E., and Ruggeri, A., Extraction and quantitative description of vessel features in hypertensive retinopathy fundus images, in CAFIA2001, 2001, 6.

59. Sherry, L.M., Wang, J.J., Rochtchina, E., et al., Reliability of computer-assisted retinal vessel measurement in a population, Clinical & Experimental Ophthalmology, 30, 179, 2002.

60. Wang, J.J., Mitchell, P., Sherry, L.M., et al., Generalized retinal arteriolar narrowing predicts 5-year cardiovascular and cerebro-vascular mortality: findings from the Blue Mountains Eye Study, Investigative Ophthalmology and Visual Science, 43, 2002.

61. Klein, R., Klein, B.E., Moss, S.E., et al., The relation of retinal vessel caliber to the incidence and progression of diabetic retinopathy: XIX: The Wisconsin Epidemiologic Study of Diabetic Retinopathy, Archives of Ophthalmology, 122(1), 76, 2004.

62. Soares, J.V.B., Leandro, J.J.G., Cesar, Jr, R.M., et al., Retinal vessel segmentation using the 2-D Gabor wavelet and supervised classification, IEEE Transactions on Medical Imaging, 25(9), 1214, 2006.

63. Lee, S.C., Lee, E.T., Wang, Y., et al., Computer classification of Nonproliferative diabetic retinopathy, Archives of Ophthalmology, 123, 759, 2005.

64. Ege, B.M., Hejlesen, O.K., Larsen, O.V., et al., Screening for diabetic retinopathy using computer-based image analysis and statistical classification, Computer Methods and Programs in Biomedicine, 62(3), 165, 2000.

65. Osareh, A., Mirmehdi, M., Thomas, B., et al., Classification and localisation of diabetic-related eye disease, in 7th European Conference on Computer Vision (ECCV2002), 2002, vol. 2353 of Lecture Notes in Computer Science, 502–516.

66. Goldbaum, M.H., Sample, P.A., Chan, K., et al., Comparing machine learning classifiers for diagnosing glaucoma from standard automated perimetry, Investigative Ophthalmology and Visual Science, 43(1), 162, 2002.

67. Frame, A.J., Undrill, P.E., Cree, M.J., et al., A comparison of computer-based classification methods applied to the detection of microaneurysms in ophthalmic fluorescein angiograms, Computers in Biology and Medicine, 28, 225, 1998.

68. Niemeijer, M., van Ginneken, B., Staal, J., et al., Automatic detection of red lesions in digital color fundus photographs, IEEE Transactions on Medical Imaging, 24(5), 584, 2005.

69. Teng, T., Lefley, M., and Claremont, D., Progress towards automated diabetic ocular screening: a review of image analysis and intelligent systems for diabetic retinopathy, Medical and Biological Engineering and Computing, 40, 2, 2002.

70. Baudoin, C.E., Lay, B.J., and Klein, J.C., Automatic detection of microaneurysms in diabetic fluorescein angiography, Revue d Epidemiologie et de Sante Publique, 32(3-4), 254, 1984.

71. Spencer, T., Olson, J., McHardy, K., et al., Image-processing strategy for the segmentation and quantification of microaneurysms in fluorescein angiograms of the ocular fundus, Computers and Biomedical Research, 29, 284, 1996.

72. Cree, M.J., Olson, J.A., McHardy, K.C., et al., A fully automated comparative microaneurysm digital detection system, Eye, 11, 622, 1997.

73. Kohner, E.M. and Dollery, C.T., The rate of formation and disapearance of microaneurysms in diabetic retinopathy, European Journal of Clinical Investigation, 1(3), 167, 1970.

74. Hellstedt, T. and Immonen, I., Disappearance and formation rates of microaneurysms in early diabetic retinopathy, British Journal of Ophthalmology, 80(2), 135, 1996.

75. Goatman, K.A., Cree, M.J., Olson, J.A., et al., Automated measurement of microaneurysm turnover, Investigative Ophthalmology and Visual Science, 44, 5335, 2003.

76. Hipwell, J., Strachan, F., Olson, J., et al., Automated detection of microaneurysms in digital red-free photographs: a diabetic retinopathy screening tool, Diabetic Medicine, 17, 588, 2000.

77. British Diabetic Association, Retinal photography screening for diabetic eye disease, 1994.

78. Fleming, A.D., Philip, S., Goatman, K.A., et al., Automated assessment of diabetic retinal image quality based on clarity and field definition, Investigative Ophthalmology and Visual Science, 47(1120-1125), 2006.

79. Lee, S.C., Wang, Y., and Lee, E.T., Computer algorithm for automated detection and quantification of microaneurysms and hemorrhages (HMAs) in color retinal images, in Medical Imaging 1999: Image Perception and Performance, 1999, vol. 3663 of Proceedings of the SPIE, 61–71.

80. Gardner, G., Keating, D., Williamson, T., et al., Automatic detection of diabetic retinopathy using an artificial neural network: a screening tool, British Journal of Ophthalmology, 80, 940, 1996.

81. Luo, G., Chutatape, O., Li, H., et al., Abnormality detection in automated mass screening system of diabetic retinopathy, in 14th IEEE Symposium on Computer-Based Medical Systems 2001, 2001, 332.

82. Sinthanayothin, C., Boyce, J.F., Williamson, T.H., et al., Automated detection of diabetic retinopathy on digital fundus images, Diabet Med, 19(2), 105, 2002.

83. Phillips, R., Forrester, J., and Sharp, P., Automated detection and quantification of retinal exudates, Graefes Arch Clin Exp Ophthalmol, 231(2), 90, 1993.

84. Hunter, A., Lowell, J., Owen, J., et al., Quantification of diabetic retinopathy using neural networks and sensitivity analysis, Technical Report SCET9901, University of Sunderland, 2000.

85. Osareh, A., Mirmehdi, M., Thomas, B., et al., Automatic recognition of exudative maculopathy using fuzzy C-means clustering and neural networks, in Proceedings of the Medical Image Understanding and Analysis Conference, 2001, 49–52.

86. Osareh, A., Mirmehdi, M., Thomas, B., et al., Automated identification of diabetic retinal exudates in digital colour images, British Journal of Ophthalmology, 87, 1220, 2003.

87. Walter, T., Klein, J.C., Massin, P., et al., A contribution of image processing to the diagnosis of diabetic retinopathy — detection of exudates in color fundus images of the human retina, IEEE Transactions on Medical Imaging, 21(10), 1236, 2002.

88. Fleming, A.D., Philip, S., Goatman, K.A., et al., Automated detection of exudates for diabetic retinopathy screening, Physics in Medicine and Biology, 52, 7385, 2007.

89. Hsu, W., Pallawala, P.M.D.S., Lee, M.L., et al., The role of domain knowledge in the detection of retinal hard exudates, in 2001 IEEE Computer Society Conference on Computer Vision and Pattern Recognition (CVPR'01), 2001, vol. 2, 246–251.

90. Xiaohui, Z. and Chutatape, O., Detection and classification of bright lesions in color fundus images, in International Conference on Image Processing (ICIP'04), 2004, vol. 1, 139–142.

91. Lee, S.C., Lee, E.T., Kingsley, R.M., et al., Comparison of diagnosis of early retinal lesions of diabetic retinopathy between a computer system and human experts, Archives of Ophthalmology, 119(4), 509, 2001.

92. Barthes, A., Conrath, J., Rasigni, M., et al., Mathematical morphology in computerized analysis of angiograms in age-related macular degeneration, Medical Physics, 28(12), 2410, 2001.

93. Ben Sbeh, Z., Cohen, L.D., Mimoun, G., et al., A new approach of geodesic reconstruction for drusen segmentation in eye fundus images, IEEE Transactions on Medical Imaging, 20(12), 1321, 2001.

94. Brandon, L. and Hoover, A., Drusen detection in a retinal image using multilevel analysis, in Medical Image Computing and Computer-Assisted Intervention (MICCAI 2003), 2003, vol. 2878 of Lecture Notes in Computer Science, 618–625.

95. Shin, D.S., Javornik, N.B., and Berger, J.W., Computer-assisted, interactive fundus image processing for macular drusen quantitation, Ophthalmology, 106(6), 1119, 1999.

96. Sivagnanavel, V., Smith, R.T., Lau, G.B., et al., An interinstitutional comparative study and validation of computer aided drusen detection, British Journal of Ophthalmology, 89, 554, 2005.

97. Smith, R.T., Chan, J.K., Nagasaki, T., et al., Automated detection of macular drusen using geometric background leveling and threshold selection, Archives of Ophthalmology, 123(2), 200, 2005.

98. Cree, M.J., Olson, J.A., McHardy, K.C., et al., Automated microaneurysm detection, in International Conference on Image Processing, Lausanne, Switzerland, 1996, vol. 3, 699–702.

99. Sinthanayothin, C., Boyce, J., Cook, H., et al., Automated localization of the optic disc, fovea, and retinal blood vessels from digital colour fundus images, British Journal of Ophthalmology, 83(8), 902, 1999.

100. Li, H.Q. and Chutatape, O., Automated feature extraction in color retinal images by a model-based approach, IEEE Transactions on Biomedical Engineering, 51(2), 246, 2004.

101. Pinz, A., Bernogger, S., Datlinger, P., et al., Mapping the human retina, IEEE Transactions on Medical Imaging, 17(4), 606, 1998.

102. Li, H.Q. and Chutatape, O., Automatic detection and boundary estimation of the optic disk in retinal images using a model-based approach, Journal of Electronic Imaging, 12(1), 97, 2003.

103. Lowell, J., Hunter, A., Steel, D., et al., Optic nerve head segmentation, IEEE Transactions on Medical Imaging, 23(2), 256, 2004.

104. Abdel-Ghafara, R.A., Morrisa, Ritchingsb, T.T., et al., Detection and characterisation of the optic disk in glaucoma and diabetic retinopathy, 2005.

105. Chanwimaluang, T. and Fan, G., An efficient algorithm for extraction of anatomical structures in retinal images, in 2003 International Conference on Image Processing, 2003, vol. 1, 1093–1096.

106. Osareh, A., Mirmehdi, M., Thomas, B., et al., Colour morphology and snakes for optic disc localisation, in Proceedings of the Medical Image Underestanding and Analysis Conference (MIUA 2002), Portsmouth, UK, 2002, 21–24.

107. Hoover, A. and Goldbaum, M., Locating the optic nerve in a retinal image using the fuzzy convergence of the blood vessels, IEEE Transactions on Medical Imaging, 22(8), 951, 2003.

108. Foracchia, M., Grisan, E., and Ruggeri, A., Detection of optic disc in retinal images by means of a geometrical model of vessel structure, IEEE Transactions on Medical Imaging, 23(10), 1189, 2004.

109. Guan, K., Hudson, C., Wong, T.Y., et al., Retinal hemodynamic in early diabetic macular edema, Diabetes, 55(3), 813, 2006.

110. Wong, T., Shankar, A., Klein, R., et al., Prospective cohort study of retinal vessel diameters and risk of hypertension, British Medical Journal, 329, 79, 2004.

111. Wong, T.Y., Klein, R., Klein, B.E., et al., Retinal microvascular abnormalities and their relationship with hypertension, cardiovascular disease, and mortality, Survey of Ophthalmology, 46(1), 59, 2001.

112. Lin, T.S. and Zheng, Y.B., Experimental study of automated diameter measurement of retinal blood vessel, Journal of Information and Computational Science, 2(1), 81, 2005.

113. Leandro, J.J.G., Cesar-Jr, R.M., and Jelinek, H.F., Blood vessels segmentation in retina: preliminary assessment of the mathematical morphology and of the wavelet transform techniques, in XIV Brazilian Symposium on Computer Graphics and Image Processing (SIBGRAPI-01), Florianop´olis, Brazil, 2001, 84–90.

114. Cesar, Jr, R.M. and Jelinek, H., Segmentation of retinal fundus vasculature in nonmydriatic camera images using wavelets, in Angiography and plaque imaging, J. Suri and S. Laxminarayan, eds., CRC Press, London, 193–224, 2003.

115. Leandro, J.J.G., Soares, J.V.B., Cesar, J., R., et al., Blood vessel segmentation of non-mydriatic images using wavelets and statistical classifiers, in 16th Brazilian Symposium on Computer Graphics and Image Processing (SIBGRAPI03), Sao Carlos, Brazil, 2003, 262–269.

116. Chaudhuri, S., Chatterjee, S., Katz, N., et al., Detection of blood vessels in retinal images using two-dimensional matched filters, IEEE Transactions on Medical Imaging, 8(3), 263, 1989.

117. Hoover, A., Kouznetsova, V., and Goldbaum, M., Locating blood vessels in retinal images by piecewise threshold probing of a matched filter response, IEEE Transactions on Medical Imaging, 19(3), 203, 2000.

118. Zana, F. and Klein, J.C., A multimodal registration algorithm of eye fundus images using vessels detection and hough transform, IEEE Transactions on Medical Imaging, 18(5), 419, 1999.

119. Zana, F. and Klein, J.C., Segmentation of vessel-like patterns using mathematical morphology and curvature evaluation, IEEE Transactions on Image Processing, 10(7), 1010, 2001.

120. Mart´ınez-P´erez, M.E., Hughes, A.D., Stanton, A.V., et al., Segmentation of retinal blood vessels based on the second directional derivative and region growing, in IEEE International Conference in Image Processing (ICIP'99), Kobe, Japan, 1999, 173–176.

121. Jiang, X. and Mojon, D., Adaptive local thresholding by verification-based multithreshold probing with application to vessel detection in retinal images, IEEE Transactions on Pattern Analysis and Machine Intelligence, 25(1), 131, 2003.

122. Niemeijer, M., Staal, J., van Ginneken, B., et al., Comparative study of retinal vessel segmentation methods on a new publicly available database, Proceedings of the SPIE, 5370, 648, 2004.

123. Staal, J., Abramoff, M., Niemeijer, M., et al., Ridge-based vessel segmentation in color images of the retina, IEEE Transactions on Medical Imaging, 23(4), 501, 2004.

124. Hongqing, Z., Huazhong, S., and Limin, L., Blood vessels segmentation in retina via wavelet transforms using steerable filters, in Proceedings of the 17th IEEE Symposium on Computer-Based Medical Systems (CBMS'04), 2004, 316–321.

125. Mendonca, A. and Campilho, A., Segmentation of retinal blood vessels by combining the detection of centerlines and morphological reconstruction, IEEE Transactions on Medical Imaging, 25(9), 1200, 2006.

126. Fritzsche, K., Computer vision algorithms for retinal vessel width change detection and quantification, 2005.

127. Kochner, B., Schuhmann, D., Michaelis, M., et al., Course tracking and contour extraction of retinal vessels from color fundus photographs: most efficient use of steerable filters for model-based image analysis, Proceedings of the SPIE, 3338, 755, 1998.

128. Tamura, S., Okamoto, Y., and Yanashima, K., Zero-crossing interval correction in tracing eye-fundus blood vessels, Pattern Recognition, 21, 227, 1988.

129. Tolias, Y.A. and Panas, S.M., A fuzzy vessel tracking algorithm for retinal images based on fuzzy clustering, IEEE Transactions on Medical Imaging, 17(2), 263, 1998.

130. Gao, X., Bharath, A., Stanton, A., et al., A method of vessel tracking for vessel diameter measurement on retinal images, in Proceedings of the International Conference on Image Processing (ICIP'01), 2001, vol. 2, 881–884.

131. Kirbas, C. and Quek, F., A review of vessel extraction techniques and algorithms, ACM Computing Surveys, 36(2), 81, 2004.

132. Cree, M.J., Cornforth, D.J., and Jelinek, H.F., Vessel segmentation and tracking using a two-dimensional model, in Image and Vision Computing New Zealand, Dunedin, New Zealand, 2005, 345–350.

133. Cree, M.J., Leandro, J.J.G., Soares, J.V.B., et al., Comparison of various methods to delineate blood vessels in retinal images, in Proceedings of the 16th National Congress of the Australian Institute of Physics, Canbera, Australia, 2005.

134. Kanski, J., Clinical Ophthalmology: A systematic approach, Butterworth- Heinemann, London, 1989.

135. Mart´ınez-P´erez, M.E., Hughes, A.D., Stanton, A.V., et al., Retinal vascular tree morphology: a semi-automatic quantification, IEEE Transactions on Biomedical Engineering, 49(8), 912, 2002.

136. Gao, X., Bharath, A., Stanton, A., et al., Quantification and characterisation of arteries in retinal images, Computer Methods and Programs in Biomedicine, 63(2), 133, 2000.

137. Antoine, J.P., Barache, D., Cesar, Jr., R.M., et al., Shape characterization with the wavelet transform, Signal Processing, 62(3), 265, 1997.

138. Fernandez, E. and Jelinek, H., Use of fractal theory in neuroscience: methods, advantages, and potential problems, Methods, 24, 309, 2001.

139. Landini, G., Murray, P.I., and Misson, G.P., Local connected fractal dimension and lacunarity analysis of 60-degree fluorescein angiograms, Investigative Ophthalmology and Visual Science, 36, 2749, 1995.

140. Losa, G., Merlini, D., Nonnenmacher, T.F., et al., Fractals in Biology and Medicine, Birkh¨auser, Basel, 2nd ed., 1997.

141. Sernetz, M., Wubbeke, J., and Wiezek, P., Three-dimensional image analysis and fractal characterization of kidney arterial vessels, Physica A, 191, 13, 1992.

142. Avakian, A., Kalina, R.E., Sage, H.E., et al., Fractal analysis of region-based vascular change in the normal and non-proliferativediabetic retina, Current Eye Research, 24(4), 274, 2002.

143. Daxer, A., The fractal geometry of proliferative diabetic retinopathy: implications for the diagnosis and the process of retinal vasculogenesis, Current Eye Research, 12, 1103, 1993.

144. Masters, B., Fractal analysis of the vascular tree in the human retina, Annual Review of Biomedical Engineering, 6, 427, 2004.

145. Family, F., Masters, B.R., and Platt, D., Fractal pattern formation in human retinal vessels, Physica D, 38, 98, 1989.

146. Landini, G., Applications of fractal geometry in pathology, in Fractal geometry in biological systems, P. Iannaccone and M. Khokha, eds., CRC Press, Amsterdam, 205–245, 1996.

147. Luckie, A.P., Jelinek, H.F., Cree, M.J., et al., Identification and follow-up of diabetic retinopathy in rural Australia: an automated screening model, in AVRO, Ft. Lauderdale, FL, 5245/B569, 2004.

148. McQuellin, C., Jelinek, H., and Joss, G., Characterization of fluorescein angiograms of retinal fundus using mathematical morphology: a pilot study., in 5th International Conference on Ophthalmic Photography, Adelaide, 83, 2002.

149. Stoˇsi´c, T. and Stoˇsi´c, B.D., Multifractal analysis of human retinal vessels, IEEE Transactions on Medical Imaging, 25(8), 1101, 2006.

150. Paulus, J., Meier, J., Bock, R., Hornegger, J., and Michelson, G., Automated quality assessment of retinal fundus photos," International Journal of Computer Assisted Radiology and Surgery, vol. 5, no. 6, pp. 557-564, 2010.

151. Marrugo, A. and Millan, M., Retinal image analysis: preprocessing and feature extraction, Journal of Physics: Conference Series, vol. 274, no. 1, p. 012039, 2011.

152. Sopharak, A., Uyyanonvara, B., and Barman, S., Automated microaneurysm detection algorithms applied to diabetic retinopathy retinal images, Maejo International Journal of Science and Technology, vol. 7, no. 2, pp. 294-314, 2013.

153. Teng, T., Lefley, M., and Claremont, D., Progress towards automated diabetic ocular screening: a review of image analysis and intelligent systems for diabetic retinopathy, Medical and Biological Engineering and Computing, vol. 40, no. 1, pp. 2-13, 2002.

154. Pires, R., Jelinek, H. F., Wainer, J., and Rocha, A., Retinal image quality analysis for automatic diabetic retinopathy detection, in 25th SIBGRAPI Conference on Graphics, Patterns and Images (SIBGRAPI), pp. 229-236, 2012.

155. Imani, E., Pourreza, H., and Banaee, T., Fully automated diabetic retinopathy screening using morphological component analysis, Computerized Medical Imaging and Graphics, vol. 43, pp. 78-88, 2015.

156. Şevik, U., Köse, C., Berber, T., and Erdöl, H., Identification of suitable fundus images using automated quality assessment methods, Journal of Biomedical Optics, vol. 19, no. 4, p. 046006, 2014.

157. Wang, S., Jin, K., Lu, H., Cheng, C., Ye, J., and Qian, D., Human Visual System-Based Fundus Image Quality Assessment of Portable Fundus Camera Photographs, IEEE Engineering in Medicine and Biology Society, vol. 35, no. 4, pp. 1046 - 1055, 2016.

158. Li, J., Dai, W., Wang, H., and Yang, A., Image Quality Assessment Based on the Contourlet, in 2nd International Asia Conference on Informatics in Control, Automation and Robotics (CAR), pp. 13-16, 2010.

159. Wang, Z. and Bovik, A. C., Modern image quality assessment, Synthesis Lectures on Image, Video, and Multimedia Processing, vol. 2, no. 1, pp. 1-156, 2006.

160. Lalonde, M., Gagnon, L., and Boucher, M., Automatic visual quality assessment in optical fundus images, in Proceedings of Vision Interface, pp. 259-264, 2001.

161. Panwar, N., Huang, P., Lee, J., Keane, P., Chuan, T., Richhariya, A., Teoh, S., Lim, T., and Agrawal, R., Fundus Photography in the 21st Century-A Review of Recent Technological Advances and Their Implications for Worldwide Healthcare, Telemedicine and e-Health, vol. 22, no. 3, pp. 198-208, 2016.

162. Youssif, A., Ghalwsh, A., and Ghoneim, A., Optic disc detection from normalized digital fundus images by means of vessels' direction matched filter, IEEE Transactions on Medical Imaging, vol. 27, no. 1, pp. 11–18, 2008.

163. Abramoff, M. D., Niemeijer, M., The automatic detection of the optic disc location in retinal images using optic disc location regression, in Proceedings of IEEE Conference on Engineering Medical Biological Society, pp. 4432- 4435, 2006.

164. Haar, F., Automatic localization of the optic disc in digital colour images of the human retina, M.S. thesis, Utrecht University, Utrecht, The Netherlands,2005.

165. Abdel-Ghafar, R. A., Morris, T., Ritchings, T., and Wood, I., Detection and characterization of the optic disk in glaucoma and diabetic retinopathy, in IEEE Conference on Medical Image Understanding Annual, London, U.K., Sep. 23–24,2004.

166. Akita, K. and Kuga, H., Pattern recognition of blood vessel networks in ocular fundus images, Proceedings of IEEE conference, pp 436-441,1982.

167. Foracchia, M., Grison, E., Ruggeri, A., Detection of Optic disc in retinal images by means of geometrical model of vessel structure, IEEE Transactions on Medical Imaging, vol.23. no10. pp.1189-1195, 2004.

168. Rangayyan R., Zhu X., Ells A. L., Detection of the Optic Nerve Head in Fundus Images of the Retina with Gabor Filters and Phase Portrait Analysis, J Digit Imaging, 23(4): pp. 438-453, Aug. 2010.

169. Mendels F., Heneghan C., and Thiran J. P., Identification of the optic disk boundary in retinal images using active contours, Proceedings of the IEEE Conference on Irish Machine Vision Image Processing Conference. (IMVIP'99), pp. 103–115.Sept-1999.

170. Walter T., Klein J. C., Massin P., and Erginay A., A Contribution of Image Processing to the Diagnosis of Diabetic Retinopathy—Detection of Exudates in Color Fundus Images of the Human Retina, IEEE Transactions of Medical Imaging, Vol.21 no.10, Oct. 2002.

171. Sinthanayothin C., Boyce J. F., Cook H. L., and Williamson T. H., Automated localization of the optic disk, fovea, and retinal blood vessels from digital colour fundus images, Br. J. Ophthalmol., vol. 83, no.8, pp. 902–910,1999.

172. Chrástek R., Wolf M., Donath K., Michelson G., and Niemann H., Optic disc segmentation in retinal images, Bildverarbeitung für die Medizin, Publisher-Springer Berlin Heidelberg, pp.263–266,2002.

173. Roychowdhury S., Koozekanani D., Parhi K., Screening Fundus Images for Diabetic Retinopathy, in Proceedings of IEEE Conference, Signals, Systems and Computers (ASILOMAR), pp. 1641- 1645. Nov.2012.

174. Hoover A. and Goldbaum M., Locating the optic nerve in a retinal image using the fuzzy convergence of the blood vessels, IEEE Transactions on Medical Imaging, vol.22, no.8, pp.951–958, Aug. 2003.

175. Zahoor M. N., Fraz M., Fast Optic Disc Segmentation in Retina using Polar Transform, IEEE. Translations, 2169-3536 (c) 2017.

176. Sinthanayothin, C., et al., Automated localization of the optic disc, fovea, and retinal blood vessels from digital colour fundus images, British Journal of Ophthalmology, 1999. 83(8): p. 902-910.

177. Mahfouz, A.E. and A.S. Fahmy, Fast localization of the optic disc using projection of image features, IEEE Transactions on Image Processing, 2010. 19(12): p. 3285-3289.

178. Walter, T. and Klein, C. Segmentation of color fundus images of the human retina: Detection of the optic disc and the vascular tree using morphological techniques, International Symposium on Medical Data Analysis. 2001. Springer.

179. Hoover, A. and M. Goldbaum, Locating the optic nerve in a retinal image using the fuzzy convergence of the blood vessels, IEEE transactions on medical imaging, 2003. 22(8): p. 951-958.

180. Pallawala, P., et al. “Automated optic disc localization and contour detection using ellipse fitting and wavelet transform” in European Conference on Computer Vision. 2004. Springer.

181. Lalonde, M., M. Beaulieu, and L. Gagnon, Fast and robust optic disc detection using pyramidal decomposition and Hausdorff-based template matching,” IEEE Transactions on Medical Imaging, 2001. 20(11): p. 1193-1200.

182. Abdel-Ghafar, R. and T. Morris, Progress towards automated detection and characterization of the optic disc in glaucoma and diabetic retinopathy, Medical informatics and the Internet in medicine, 2007. 32(1): p. 19-25.

183. Abdullah, M., Fraz, M. and Barman S. A., Localization and segmentation of optic disc in retinal images using circular Hough transform and grow-cut algorithm, Peer J, 2016. 4: p. e2003.

184. Abdullah, M. and Fraz, M. Application of grow cut algorithm for localization and extraction of optic disc in retinal images, in 2015 12th International Conference on High-capacity Optical Networks and Enabling/Emerging Technologies (HONET). 2015. IEEE.

185. Joshi, G.D., Sivaswamy J., and Krishnadas S., Optic disk and cup segmentation from monocular color retinal images for glaucoma assessment, IEEE Transactions on Medical Imaging, 2011. 30(6): p. 1192-1205.

186. Joshi, G.D., Sivaswamy J., and Krishnadas S., Depth discontinuity-based cup segmentation from multiview color retinal images, IEEE Transactions on Biomedical Engineering, 2012. 59(6): p. 1523-1531.

187. Mendels, F., Heneghan, C., and Thiran, J. Identification of the optic disk boundary in retinal images using active contours, in Proceedings of Irish Machine Vision and Image Processing Conference (IMVIP) 1999. 1999. IEEE.

188. Lowell, J., et al., Optic nerve head segmentation, IEEE Transactions on Medical Imaging, 2004. 23(2): p. 256-264.

189. Novo, J., Penedo, M. G., and Santos, J., Localization of the optic disc by means of GA-optimized topological active nets, Image and Vision Computing, 2009. 27(10): p. 1572-1584.

190. Xu, J., et al., Optic disk feature extraction via modified deformable model technique for glaucoma analysis, Pattern recognition, 2007. 40(7): p. 2063-2076.

191. Yu, H., et al., Fast localization and segmentation of optic disk in retinal images using directional matched filtering and level sets, IEEE Transactions on Information Technology in Biomedicine, 2012. 16(4): p. 644-657.

192. Morales, S., et al., Automatic detection of optic disc based on PCA and mathematical morphology, IEEE Transactions on Medical Imaging, 2013. 32(4): p. 786-796.

193. Sopharak, A., et al., Automatic detection of diabetic retinopathy exudates from non-dilated retinal images using mathematical morphology methods, Computerized Medical Imaging and Graphics, 2008. 32(8): p. 720-727.

194. Kande, G.B., P.V. Subbaiah, and T.S. Savithri. Segmentation of exudates and optic disk in retinal images, in Computer Vision, Graphics & Image Processing, 2008. ICVGIP'08. Sixth Indian Conference on. 2008. IEEE.

195. Kande, G.B., P.V. Subbaiah, and T.S. Savithri., Segmentation of exudates and optic disk in retinal images, Computer Vision, Graphics & Image Processing, 2008. ICVGIP'08. Sixth Indian Conference on. 2008. IEEE.

196. Walter, T., et al., A contribution of image processing to the diagnosis of diabetic retinopathy-detection of exudates in color fundus images of the human retina, IEEE Transactions on Medical Imaging, 2002. 21(10): p. 1236-1243.

197. Lupascu, C.A., Tegolo, D., and Di Rosa, L., Automated detection of optic disc location in retinal images. in Computer-Based Medical Systems, 2008. CBMS'08. 21st IEEE International Symposium on. 2008. IEEE.

198. Stapor, K., et al. Segmentation of fundus eye images using methods of mathematical morphology for glaucoma diagnosis, in International Conference on Computational Science. 2004. Springer.

199. Basit, A. and Fraz, M., Optic disc detection and boundary extraction in retinal images, Applied optics, 2015. 54(11): p. 3440-3447.

200. Feng, Z., Yang, J., Yao, L., Qiao, Y., Yu, Q., and Xu, X., Deep retinal image segmentation: A fun-based architecture with short and long skip connections for retinal image segmentation, International Conference on Neural Information Processing, vol. 10637, p. 713-722. Springer, 2017.

201. Mitra, A., Banerjee, P., Roy, S., and Setua, S., The region of interest localization for glaucoma analysis from retinal fundus image using deep learning., Computer Methods and Programs in Biomedicine, 165:25{35, 2018.

202. Liu. S., Graham, S., Schulz, A., Kalloniatis, M., Zangerl, B., Cai, W., Gao, Y., Chua, B., Arvind, H., Grigg, J., et al. A deep learning-based algorithm identifies glaucomatous discs using monocular fundus photographs, Ophthalmology Glaucoma, Aug. 2018.

203. Fraz, M.M., Remagnino, P., Hoppe, A., Velastin, S., Uyyanonvara, B. and Barman, S.A., A supervised method for retinal blood vessel segmentation using line strength, multiscale Gabor and morphological features, IEEE International Conference on Signal and Image Processing Applications, ICSIPA 2011, pp.410–415, 2011.

204. Chaudhuri, S., Chatterjee, S., Katz, N., Nelson, M., and Goldbaum, M., Detection of blood vessels in retinal images using two-dimensional matched filters, IEEE Transactions on Medical Imaging, Vol. 8, No. 3, pp.263–269, 1989.

205. Gang, L., Chutatape, O. and Krishnan, S.M., Detection and measurement of retinal vessels in fundus images using amplitude-modified second-order Gaussian filter, IEEE Transactions on Biomedical Engineering, Vol. 49, No. 2, pp.168–172, 2002.

206. Sofka, M. and Stewart, C. V., Retinal vessel centerline extraction using multiscale matched filters, confidence and edge measures, IEEE Transactions on Medical Imaging, Vol. 25, No. 12, pp.1531–1546, 2006.

207. Al-Rawi, M., Qutaishat, M. and Arrar, M., An improved matched filter for blood vessel detection of digital retinal images, Computers in Biology and Medicine, Vol. 37, No. 2, pp.262–267, 2007.

208. Yao, C. and Chen, H.J., Automated retinal blood vessels segmentation based on simplified PCNN and fast 2D-Otsu algorithm, Journal of Central South University of Technology (English Edition), Vol. 16, No. 4, pp.640–646, 2009.

209. Cinsdikici, M.G. and Aydin, D., Detection of blood vessels in ophthalmoscope images using MF/ant (matched filter/ant colony) algorithm, Computer Methods and Programs in Biomedicine, Vol. 96, No. 2, pp.85–95, 2009.

210. Zhang, B., Zhang, L., Zhang, L. and Karray, F., Retinal vessel extraction by matched filter with first-order derivative of Gaussian, Computers in Biology and Medicine, Vol. 40, No. 4, pp.438–445, 2010.

211. Amin, M.A. and Yan, H., High speed detection of retinal blood vessels in fundus image using phase congruency, Soft Computing, Vol. 15, No. 6, pp.1217–1230, 2011.

212. Odstrcilik, J., Kolar, R., Kubena, T., Cernosek, P., Budai, A., Hornegger, J., Gazarek, J. et al., Retinal vessel segmentation by improved matched filtering: evaluation on a new high-resolution fundus image database, IET Image Processing, Vol. 7, No. 4, pp.373–383, 2013.

213. Chakraborti, T., Jha, D.K., Chowdhury, A.S. and Jiang, X., A self-adaptive matched filter for retinal blood vessel detection, Machine Vision and Applications, Vol. 26, No. 1, pp.55–68, 2014.

214. Sreejini, K.S. and Govindan, V.K., Improved multiscale matched filter for retina vessel segmentation using PSO algorithm, Egyptian Informatics Journal, Vol. 16, No. 3, pp.253–260, 2015.

215. Singh, N.P. and Srivastava, R., Retinal blood vessels segmentation by using Gumbel probability distribution function based matched filter, Computer Methods and Programs in Biomedicine, Vol. 129, pp.40–50, 2016.

216. Gonzalez, R.C., Woods, R.E., and Eddins, S.L., Digital Image Processing Using MATLAB, Pearson Education, India, 2004.

217. Elena Martínez-Pérez, M., Hughes, A.D., Stanton, A. V., Thom, S.A., Bharath, A.A. and Parker, K.H., Retinal blood vessel segmentation by means of scale-space analysis and region

growing, Lecture, Notes in Computer Science (Including Subseries Lecture, Notes in Artificial Intelligence and Lecture, Notes in Bioinformatics), Vol. 1679, pp.90–97, 1999.

218. Qian Zhao, Y., Hong Wang, X., Fang Wang, X. and Shih, F.Y., Retinal vessels segmentation based on level set and region growing, Pattern Recognition, Vol. 47, No. 7, pp.2437–2446, 2014.

219. Lázár, I. and Hajdu, A., Segmentation of retinal vessels by means of directional response vector similarity and region growing, Computers in Biology and Medicine, Vol. 66, pp.209–221, 2015.

220. Roychowdhury, S., Koozekanani, D.D. and Parhi, K.K., Iterative vessel segmentation of fundus images, IEEE Transactions on Biomedical Engineering, Vol. 62, No. 7, pp.1738–1749, 2015.

221. Frangi, A., Niessen, W., Vincken, K. and Viergever, M., Multiscale vessel enhancement filtering, Medical Image Computing and Computer-Assisted Interventation – MICCAI'98, Vol. 1496, pp.130–137, 1998.

222. Wink, O., Niessen, W.J. and Viergever, M.A., Multiscale vessel tracking, IEEE Transactions on Medical Imaging, Vol. 23, No. 1, pp.130–133, 2004.

223. Anzalone, A., Bizzarri, F., Parodi, M. and Storace, M., A modular supervised algorithm for vessel segmentation in red-free retinal images, Computers in Biology and Medicine, Vol. 38, No. 8, pp.913–922, 2008.

224. Farnell, D.J.J., Hatfield, F.N., Knox, P., Reakes, M., Spencer, S., Parry, D. and Harding, S.P., Enhancement of blood vessels in digital fundus photographs via the application of multiscale line operators, Journal of the Franklin Institute, Vol. 345, No. 7, pp.748–765, 2008.

225. Moghimirad, E., Rezatofighi, S.H. and Soltanian-Zadeh, H., Multi-scale approach for retinal vessel segmentation using medialness function, 2010 7th IEEE International Symposium on Biomedical Imaging: From Nano to Macro, ISBI 2010 – Proceedings, pp.29–32, 2010.

226. Läthén, G., Jonasson, J. and Borga, M., Blood vessel segmentation using multi-scale quadrature filtering, Pattern Recognition Letters, Vol. 31, No. 8, pp.762–767, 2010.

227. Nguyen, U.T.V., Bhuiyan, A., Park, L.A.F. and Ramamohanarao, K., An effective retinal blood vessel segmentation method using multi-scale line detection, Pattern Recognition, Vol. 46, No. 3, pp.703–715, 2013.

228. Su, R., Sun, C., Zhang, C. and Pham, T.D., A new method for linear feature and junction enhancement in 2D images based on morphological operation, oriented anisotropic Gaussian function and Hessian information, Pattern Recognition, Vol. 47, No. 10, pp.3193–3208, 2014.

229. Saffarzadeh, V.M., Osareh, A. and Shadgar, B., Vessel segmentation in retinal images using multi-scale line operator and K-means clustering, Journal of Medical Signals and Sensors, Vol. 4, No. 2, pp.122–129, 2018.

230. Zhang, L., Fisher, M. and Wang, W., Retinal vessel segmentation using multi-scale textons derived from keypoints, Computerized Medical Imaging and Graphics, Vol. 45, pp.47–56, 2015.

231. Espona, L., Carreira, M.J., Penedo, M.G. and Ortega, M., Retinal vessel tree segmentation using a deformable contour model, 19th International Conference on Pattern Recognition, pp.1–4, 2008.

232. Al-Diri, B., Hunter, A. and Steel, D., An active contour model for segmenting and measuring retinal vessels, IEEE Transactions on Medical Imaging, Vol. 28, No. 9, pp.1488–1497, 2009.

233. Kee, Y.P., Lila, I.I., Ahmad, F.M.H., Hanung, A.N., Hermawan, N. and Vijanth, S.A. (2009) 'Segmentation of retinal vasculature in colour fundus images', 2009 Innovative Technologies in Intelligent Systems and Industrial Applications, CITISIA 2009, pp.398–401.

234. Zhao, Y., Rada, L., Chen, K., Harding, S.P., and Zheng, Y., Automated Vessel Segmentation Using Infinite Perimeter Active Contour Model with hybrid region information with application to retinal images, IEEE Transactions on Medical Imaging, https://doi.org/10.1109/TMI.2015.2409024, 2015.

235. Kovács, G. and Hajdu, A., A self-calibrating approach for the segmentation of retinal vessels by template matching and contour reconstruction, Medical Image Analysis, Vol. 29, pp.24–46, 2016.

236. Zhou, L., Yu, Q., Xu, X., Gu, Y. and Yang, J., Improving dense conditional random field for retinal vessel segmentation by discriminative feature learning and thin-vessel enhancement, Computer Methods and Programs in Biomedicine, Vol. 148, No. 7, pp.13–25, 2017.

237. Tolias, Y. a and Panas, S.M., A fuzzy vessel tracking algorithm for retinal images based on fuzzy clustering, IEEE Transactions on Medical Imaging, Vol. 17, No. 2, pp.263–273, 1998.

238. Kande, G.B., Subbaiah, P.V. and Savithri, T.S., Unsupervised fuzzy-based vessel segmentation in pathological digital fundus images, Journal of Medical Systems, Vol. 34, No. 5, pp. 849–858, 2010.

239. Ng, J., Clay, S.T., Barman, S.A., Fielder, A.R., Moseley, M.J., Parker, K.H. and Paterson, C., Maximum likelihood estimation of vessel parameters from scale space analysis, Image and Vision Computing, Vol. 28, No. 1, pp.55–63, 2010.

240. Villalobos-Castaldi, F.M., Felipe-Riverón, E.M. and Sánchez-Fernández, L.P., A fast, efficient and automated method to extract vessels from fundus images, Journal of Visualization, Vol. 13, No. 3, pp.263–270, 2010.

241. Allen, K., Joshi, N. and Noble, J.A., Tramline and NP windows estimation for enhanced unsupervised retinal vessel segmentation, Proceedings - International Symposium on Biomedical Imaging, pp.1387–1390, 2011.

242. Oliveira, W.S., Teixeira, J.V., Ren, T.I., Cavalcanti, G.D.C. and Sijbers, J., Unsupervised retinal vessel segmentation using combined filters, PLoS ONE, Vol. 11, No. 2, pp.1–21, 2016.

243. Câmara Neto, L., Ramalho, G.L.B., Rocha Neto, J.F.S., Veras, R.M.S., and Medeiros, F.N.S., An unsupervised coarse-to-fine algorithm for blood vessel segmentation in fundus images, Expert Systems with Applications, Vol. 78, pp.182–192, 2017.

244. Sinthanayothin, C., Boyce, J.F., Cook, H.L. and Williamson, T.H., Automated localisation of the optic disc, fovea, and retinal blood vessels from digital colour fundus images, The British Journal of Ophthalmology, Vol. 83, No. 8, pp.902–910, 1999.

245. Niemeijer, M., Staal, J., van Ginneken, B., Loog, M. and Abramoff, M.D., Comparative study of retinal vessel segmentation methods on a new publicly available database, Medical Imaging 2004: Image Processing, Vol. 5370, p.648,2004.

246. Staal, J., Abràmoff, M.D., Niemeijer, M., Viergever, M.A. and Van Ginneken, B., Ridge-based vessel segmentation in color images of the retina, IEEE Transactions on Medical Imaging, Vol. 23, No. 4, pp.501–509, 2004.

247. Hoover, A., Kouznetsova, V. and Goldbaum, M., Locating blood vessels in retinal images by piecewise threshold probing of a matched filter response, IEEE Transactions on Medical Imaging, Vol. 19, No. 3, pp.203–210, 2010.

248. Soares, J.V.B., Leandro, J.J.G., Cesar, R.M., Jelinek, H.F. and Cree, M.J., Retinal vessel segmentation using the 2-D Gabor wavelet and supervised classification, IEEE Transactions on Medical Imaging, Vol. 25, No. 9, pp.1214–1222, 2006.

249. Ricci, E. and Perfetti, R. Retinal blood vessel segmentation using line operators and support vector classification, IEEE Transactions on Medical Imaging, Vol. 26, No. 10, pp.1357–1365, 2007.

250. Osareh, A. and Shadgar, B., Automatic blood vessel segmentation in color images of retina, Iranian Journal of Science and Technology, Transaction B: Engineering, Vol. 33, No. 2, pp.191–206, 2009.

251. Lupascu, C.A., Tegolo, D. and Trucco, E., FABC: retinal vessel segmentation using AdaBoost, IEEE Transactions on Information Technology in Biomedicine, Vol. 14, No. 5, pp.1267–1274, 2010.

252. Marín, D., Aquino, A., Gegúndez-Arias, M.E. and Bravo, J.M., A new supervised method for blood vessel segmentation in retinal images by using gray-level and moment invariants-based features, IEEE Transactions on Medical Imaging, Vol. 30, No. 1, pp.146–158, 2011.

253. Rahebi, J. and Hardalaç, F., Retinal blood vessel segmentation with neural network by using gray-level co-occurrence matrix-based features patient facing systems, Journal of Medical Systems, Vol. 38, No. 8, p.85, 2014.

254. Aslani, S. and Sarnel, H., A new supervised retinal vessel segmentation method based on robust hybrid features', Biomedical Signal Processing and Control, Vol. 30, pp.1–12, 2016.

255. Zhu, C., Zou, B., Zhao, R., Cui, J., Duan, X., Chen, Z. and Liang, Y., Retinal vessel segmentation in colour fundus images using extreme learning machine, Computerized Medical Imaging and Graphics, Vol. 55, No. 12, pp.68–77, 2017.

256. Crosby-Nwaobi, R., Heng, L.Z., Sivaprasad, S., Retinal vascular calibre, geometry and progression of diabetic retinopathy in type 2 diabetes mellitus. Ophthalmologica. http://dx.doi.org/10.1159/000337252. Online First, 2012.

257. Li, L.J., Cheung, C.Y.L., Ikram, M.K., Gluckman, P., Meaney, M.J., Chong, Y.S., Kwek, K., Wong, T.Y., Saw, S.M., Blood pressure and retinal microvascular characteristics during pregnancy/novelty and significance. Hypertension 60, 223e230, 2012.

258. Cheung, C.Y., Tay, W.T., Mitchell, P., Wang, J.J., Hsu, W., Lee, M.L., Lau, Q.P., Zhu, A.L., Klein, R., Saw, S.M., Wong, T.Y., Quantitative and qualitative retinal microvascular characteristics and blood pressure. Journal of Hypertension 29, 1380e1391, 2011.

259. Lim, L.S., Cheung, C.Y.L., Lin, X., Mitchell, P., Wong, T.Y., Mei-Saw, S., Influence of refractive error and axial length on retinal vessel geometric characteristics. Investigative Ophthalmology & Visual Science 52, 669e678, 2011.

260. Cheung, C.Y., Zheng, Y., Hsu, W., Lee, M.L., Lau, Q.P., Mitchell, P., Wang, J.J., Klein, R., Wong, T.Y., Retinal vascular tortuosity, blood pressure, and cardiovascular risk factors. Ophthalmology 118, 812e818, 2011.

261. Koh, V., Cheung, C.Y.L., Zheng, Y., Wong, T.Y., Wong, W., Aung, T., Relationship of retinal vascular tortuosity with the neuroretinal rim: the Singapore Malay eye study. Investigative Ophthalmology & Visual Science 51, 3736e3741, 2010.

262. Sasongko, M.B., Wang, J.J., Donaghue, K.C., Cheung, N., Benitez-Aguirre, P., Jenkins, A., Hsu, W., Lee, M.L., Wong, T.Y., Alterations in retinal microvascular geometry in young type 1 diabetes. Diabetes Care 33, 1331e1336, 2010.

263. Sasongko, M.B., Wong, T.Y., Wang, J.J., Retinal microvascular structure: determinants and potential utility of novel imaging measurements. Expert Review of Ophthalmology 5, 353e363, 2010.

264. Sasongko, M., Wong, T., Nguyen, T., Cheung, C., Shaw, J., Wang, J., Retinal vascular tortuosity in persons with diabetes and diabetic retinopathy. Diabetologia 54, 2409e2416, 2011.

265. Sasongko, M.B., Wong, T.Y., Donaghue, K.C., Cheung, N., Jenkins, A.J., Benitez- Aguirre, P., Wang, J.J., Retinal arteriolar tortuosity is associated with retinopathy and early kidney dysfunction in type 1 diabetes. American Journal of Ophthalmology 153, 176e183, 2012.

266. Sasongko, M.B., Wong, T.Y., Nguyen, T.T., Kawasaki, R., Jenkins, A.J., Shaw, J., Robinson, C., Wang, J.J., Serum apolipoproteins are associated with systemic and retinal microvascular function in people with diabetes. Diabetes 61, 1785e1792, 2012.

267. Hughes, A., Wong, T., Witt, N., Evans, R., Thom, S., Klein, B., Chaturvedi, N., Klein, R., Determinants of retinal microvascular architecture in normal subjects. Microcirculation 16, 159e166, 2009.

268. Witt, N., Wong, T.Y., Hughes, A.D., Chaturvedi, N., Klein, B.E., Evans, R., McNamara, M., Thom, S.A.M., Klein, R., Abnormalities of retinal microvascular structure and risk of mortality from ischemic heart disease and stroke. Hypertension 47, 975e981, 2006.

269. Hart, W.E., Goldbaum, M., Côté, B., Kube, P., Nelson, M.R., Automated measurement of retinal vascular tortuosity. In: Proceedings of the AMIA Annual Fall Symposium. American Medical Informatics Association, p. 459, 1997.

270. Hart, W.E., Goldbaum, M., Côté, B., Kube, P., Nelson, M.R., Measurement and classification of retinal vascular tortuosity. International Journal of Medical Informatics 53, 239e252, 1999.

271. Benitez-Aguirre, P.Z., Sasongko, M.B., Craig, M.E., Jenkins, A.J., Cusumano, J., Cheung, N.,Wong, T.Y., Donaghue, K.C., Retinal vascular geometry predicts incident renal dysfunction in young people with type 1 diabetes. Diabetes Care 35, 599e604, 2012.

272. Benitez-Aguirre, P., Craig, M.E., Sasongko, M.B., Jenkins, A.J., Wong, T.Y., Wang, J.J., Cheung, N., Donaghue, K.C., Retinal vascular geometry predicts incident retinopathy in young people with type 1 diabetes. Diabetes Care 34, 1622e1627, 2011.

273. Zepeda-Romero, L.C., Martinez-Perez, M.E., Ruiz-Velasco, S., Ramirez-Ortiz, M.A., Gutierrez-Padilla, J.A., Temporary morphological changes in plus disease induced during contact digital imaging. Eye 25, 1337e1340, 2011.

274. Mahal, S., Strain, W.D., Martinez-Perez, M.E., Thom, S.A.M., Chaturvedi, N., Hughes, A.D., Comparison of the retinal microvasculature in European and African-Caribbean people with diabetes. Clinical Science 117, 229e236, 2009.

275. Hughes, A.D., Stanton, A.V., Jabbar, A.S., Chapman, N., Martinez-Perez, M.E., McG Thom, S.A., Effect of antihypertensive treatment on retinal microvascular changes in hypertension. Journal of Hypertension 26, 1703e1707, 2008.

276. Chiang, M.F., Gelman, R., Jiang, L., Martinez-Perez, M.E., Du, Y.E., Flynn, J.T., Plus disease in retinopathy of prematurity: an analysis of diagnostic performance. Transactions of the American Ophthalmological Society 105, 73e84, 2007.

277. Koreen, S., Gelman, R., Martinez-Perez, M.E., Jiang, L., Berrocal, A.M., Hess, D.J., Flynn, J.T., Chiang, M.F., Evaluation of a computer-based system for plus disease diagnosis in retinopathy of prematurity. Ophthalmology 114, e59ee67, 2007.

278. Ferrara, D.C., Koizumi, H., Spaide, R.F., Early Bevacizumab treatment of central retinal vein occlusion. American Journal of Ophthalmology 144, 864e871, 2007.

279. Hughes, A.D., Martinez-Perez, E., Jabbar, A.S., Hassan, A., Witt, N.W., Mistry, P.D., Chapman, N., Stanton, A.V., Beevers, G., Pedrinelli, R., Parker, K.H., Thom, S.A., Quantification of topological changes in retinal vascular architecture in essential and malignant hypertension. Journal of Hypertension 24, 889e894, 2006.

280. Gelman, R., Martinez-Perez, M.E., Vanderveen, D.K., Moskowitz, A., Fulton, A.B., Diagnosis of plus disease in retinopathy of prematurity using retinal image multiScale analysis. Investigative Ophthalmology & Visual Science 46, 4734e4738, 2005.

281. Eze, C.U., Gupta, R., Newman, D.L., A comparison of quantitative measures of arterial tortuosity using sine wave simulations and 3D wire models. Physics in Medicine and Biology 45, 2593e2599, 2000.

282. Smedby, Ö., Högman, N., Nilsson, S., Erikson, U., Olsson, A., Walldius, G., Twodimensional tortuosity of the superficial femoral artery in early atherosclerosis. Journal of Vascular Research 30, 181e191, 1993.

283. Thom, S., Stettler, C., Stanton, A., Witt, N., Tapp, R., Chaturvedi, N., Allemann, S., Mayet, J., Sever, P., Poulter, N., O'Brien, E., Hughes, A., Differential effects of antihypertensive treatment on the retinal microcirculation: an Anglo-Scandinavian cardiac outcome trial substudy. Hypertension 54, 405e408, 2009.

284. Tapp, R.J., Williams, C., Witt, N., Chaturvedi, N., Evans, R., Thom, S.A.M., Hughes, A.D., Ness, A., Impact of size at birth on the microvasculature: the Avon longitudinal study of parents and children. Pediatrics 120, e1225ee1228, 2007.

285. Dougherty, G., Varro, J., A quantitative index for the measurement of the tortuosity of blood vessels. Medical Engineering & Physics 22, 567e574, 2000.

286. Bhuiyan, A., Nath, B., Ramamohanarao, K., Kawasaki, R., Wong, T., Automated analysis of retinal vascular tortuosity on color retinal images. Journal of Medical Systems 36, 689e697, 2010.

287. Tam, J., Dhamdhere, K.P., Tiruveedhula, P., Manzanera, S., Barez, S., Bearse, M.A., Adams, A.J., Roorda, A., Disruption of the retinal parafoveal capillary network in type 2 diabetes before the onset of diabetic retinopathy. Investigative Ophthalmology & Visual Science 52, 9257e9266, 2011.

288. Capowski, J., Kylstra, J., Freedman, S., A numeric index based on spatial frequency for the tortuosity of retinal vessels and its application to plus disease in retinopathy of prematurity. Retina 15, 490e500, 1995.

289. Wallace, D.K., Kylstra, J.A., Chesnutt, D.A., Prognostic significance of vascular dilation and tortuosity insufficient for plus disease in retinopathy of prematurity. Journal of American Association for Pediatric Ophthalmology and Strabismus 4, 224e229, 2000.

290. Wallace, D.K., Jomier, J., Aylward, S.R., Landers, M.B., Computer-automated quantification of plus disease in retinopathy of prematurity. Journal of American Association for Pediatric Ophthalmology and Strabismus 7, 126e130, 2003.

291. Gelman, R., Martinez-Perez, M.E., Vanderveen, D.K., Moskowitz, A., Fulton, A.B., Diagnosis of plus disease in retinopathy of prematurity using retinal image multiscale analysis. Investigative Ophthalmology & Visual Science 46, 4734e4738, 2005.

292. Wallace, D.K., Zhao, Z., Freedman, S.F., A pilot study using ROP tool to quantify plus disease in retinopathy of prematurity. Journal of American Association for Pediatric Ophthalmology and Strabismus 11, 381e387, 2007.

293. Gelman, R., Jiang, L., Du, Y.E., Martinez-Perez, M.E., Flynn, J.T., Chiang, M.F., Plus disease in retinopathy of prematurity: pilot study of computer-based and expert diagnosis. Journal of American Association for Pediatric Ophthalmology and Strabismus 11, 532e540, 2007.

294. Boone, M., Farber, M., Jovanovic-Peterson, L., Peterson, C., Increased retinal vascular tortuosity in gestational diabetes mellitus. Ophthalmology 96, 251e254, 1989.

295. Sutter, F.K.P., Helbig, H., 2003. Familial retinal arteriolar tortuosity: a review. Survey of Ophthalmology 48, 245e255.

296. Nischler, C., Egger, S.F., Reitsamer, H.A., Retinal vessel analysis in familial retinal arteriolar tortuosity. Spektrum Der Augenheilkunde 25, 8e12, 2011.

297. Incorvaia, C., Parmeggiani, F., Costagliola, C., Perri, P., D'Angelo, S., Sebastiani, A., Quantitative evaluation of the retinal venous tortuosity in chronic anaemic patients affected by [beta]-thalassaemia major. Eye 17, 324e329, 2003.

298. Longmuir, S.Q., Mathews, K.D., Longmuir, R.A., Joshi, V., Olson, R.J., Abramoff, M.D., Retinal arterial but not venous tortuosity correlates with facioscapulohumeral muscular dystrophy severity. Journal of American Association for Pediatric Ophthalmology and Strabismus 14, 240e243, 2010.

299. Gonzalez RC, Wintz P. Digital Image Processing. Reading, MA: Addison-Wesley; 1987.

300. Gonzalez RC, Woods RE. Digital Image Processing. Reading, MA: Addison-Wesley; 1992.

301. Rosenfeld A, Kak A. Digital Picture Processing. New York: Academic Press; 1982.

302. Russ J. The Image Processing Handbook, 2nd ed. Boca Raton, FL: CRC Press; 1994.

303. Wahl F. Digital Image Signal Processing. Norwood, MA: Artech House; 1987.

304. Halder, N., Bandyopadhyay, S., et al. Fusion-Based Segmentation and Classification of Novel Coronavirus or Pneumonia from Chest X-ray Images Using Machine Learning Techniques, IEEE International Interdisciplinary Conference on Mathematics, Engineering and Science (MESIICON), 11-12 Nov. 2022.

305. K.-Q. Huang, Q. Wang, and Z.-Y. Wu, Natural color image enhancement and evaluation algorithm based on human visual system, Computer Vision and Image Understanding, vol. 103, no. 1, pp. 52–63, 2006.

306. Reza, A. M., Realization of the contrast limited adaptive histogram equalization (CLAHE) for real-time image enhancement, Journal of VLSI Signal Processing Systems for Signal, Image and Video Technology, vol. 38, no. 1, pp. 35–44, 2004.

307. Gastal, E. S. L., and Oliveira, M. M., Domain transform for edge-aware image and video processing, ACM Transactions on Graphics, vol. 30, no. 4, article 69, pp. 1244–1259, 2011.

308. Rajan, J., Kannan, K., and Kaimal, M. R., An improved hybrid model for molecular image denoising, Journal of Mathematical Imaging and Vision, vol. 31, no. 1, pp. 73–79, 2008.

309. Hamza, A. B., Luque-Escamilla, P. L., Mart´ınez-Aroza, J., and Rom´an-Rold´an, R., Removing noise and preserving details with relaxed median filters, Journal of Mathematical Imaging and Vision, vol. 11, no. 2, pp. 161–177, 1999.

310. Knutsson, H. and Westin, C. F., Normalized and differential convolution methods for interpolation and filtering of incomplete and uncertain data, in Proceedings of the IEEE Conference on Computer Vision and Pattern Recognition (CVPR ’93), pp. 515–523, New York, NY, USA, June 1993.

311. Tomasi, C. and Manduchi, R., Bilateral filtering for gray and color images, in Proceedings of the IEEE 6th International Conference on Computer Vision (ICCV ’98), pp. 839–846, IEEE, Bombay, India, January 1998.

312. Dougherty, E. R., Digital Image Processing Methods, Optical Engineering, CRC Press, Boca Raton, Fla, USA, 1994.

313. You, Y. L., and Kaveh, M., Fourth-order partial differential equations for noise removal, IEEE Transactions on Image Processing, vol. 9, no. 10, pp. 1723–1730, 2000.

314. Naka, K., Rushton, W., 1966. S-potentials from colour units in the retina of fish (cyprinidae). The Journal of Physiology 185, 536–555.

315. Carandini, M., Heeger, D.J., 2012. Normalization as a canonical neural computation. Nature Reviews Neuroscience 13, 51–62.

316. Aujol, J.F., et al., 2006. Structure-texture image decomposition modeling, algorithms, and parameter selection. International Journal of Computer Vision 67, 111-136.

317. Yang, K.F., Zhang, X.S., Li, Y.J., 2020. A biological vision-inspired framework for image enhancement in poor visibility conditions. IEEE Transactions on Image Processing 29, 1493–1506.

318. Sauvola, J. and Pietikainen, M., Adaptive document image binarization, Pattern Recognition, vol.33, 225-236, 2000.

319. Sahoo, P. K., Soltani, S., Wong, A. K., and Chan, Y. C., A survey of thresholding techniques, Computer Vision Graphics, and Image Processing, vol.41, 1998(233-260)

320. Otsu, N., A threshold selection method from gray-level histogram, IEEE Transactions on Systems Man Cybernet, SMC-8, 1978. (62-66)

321. Lee, H. and Park, R. H., Comments on an optimal threshold scheme for image segmentation, IEEE Transation System Man Cybern, SMC-20, 1990. (741-742)

322. Aguiree, F., Brown, A., Cho, N. H., Dahlquist, G., Dodd, S., Dunning, T., Hirst, S. M., C. Hwang, Magliano, D., Patterson, C., Scott, C., JShaw, J., Soltesz, G., Usher-Smith, J., and Whiting, D., IDF Diabetes Atlas: sixth edition. 2013.

323. Wild, S., Roglic, G., Green, A, Sicree, R., and King, H., Estimates for the year 2000 and projections for 2030, World Health, vol. 27, no. 5, pp. 1047–1053, 2004.

324. Bottomley, J., Economic costs of diabetes in the US in 2007 – Implications for Europe, Br. J. Diabetes Vasc. Dis., vol. 8, no. 2, pp. 96–100, 2008.

325. Abdullah, M. and M.M. Fraz. Application of grow cut algorithm for localization and extraction of optic disc in retinal images. in 2015 12th International Conference on High-capacity Optical Networks and Enabling/Emerging Technologies (HONET). 2015. IEEE.

326. Joshi, G.D., J. Sivaswamy, and S. Krishnadas, Depth discontinuity-based cup segmentation from multiview color retinal images. IEEE Transactions on Biomedical Engineering, 2012. 59(6): p. 1523-1531.

327. Lee, S. and M. Brady, Optic disk boundary detection, in BMVC91. 1991, Springer. p. 359-362.

328. Xu, J., et al., Optic disk feature extraction via modified deformable model technique for glaucoma analysis. Pattern recognition, 2007. 40(7): p. 2063-2076.

329. Yu, H., et al., Fast localization and segmentation of optic disk in retinal images using directional matched filtering and level sets. IEEE Transactions on Information Technology in Biomedicine, 2012. 16(4): p. 644-657.

330. Zhang, D. and Zhao, Y., Novel accurate and fast optic disc detection in retinal images with vessel distribution and directional characteristics, IEEE Journal of Biomedical and Health Informatics, p. 10.1109/JBHI.2014.2365514, 2014.

331. Halder, N., Roy, D., Bandyopadhyay, S., et al. Automatic Detection and Segmentation of Optic Disc (ADSO) of Retinal Fundus Images Based on Mathematical Morphology, National Conference on Emerging Trends on Sustainable Technology and Engineering Applications, IEEE,2020.

332. Susman, E. J., Tsiaras, W. J., Soper, K. A. “Diagnosis of diabetic eye disease”, JAMA 247(23), 3231-3234, 1982.

333. Almotiri, J., K. Elleithy, and A. Elleithy. “Retinal Vessels Segmentation Techniques and Algorithms: A Survey”, Applied Sciences, 8, 155, 2018.

334. Srinidhi, C.L., P. Aparna, and J. Rajan. “Recent advancements in retinal vessel segmentation”, Journal of medical systems, 41, 70, 2017.

335. Almazroa, A., R. Burman, K. Raahemifar, and V. Lakshminarayanan. “Optic disc and optic cup segmentation methodologies for glaucoma image detection: a survey”, Journal of ophthalmology, Article ID 180972, 28, 2015.

336. Fraz, P. Remagnino, A. Hoppe, B. Uyyanonvara, A. R. Rudnicka, C. G. Owen, et al., “Blood vessel segmentation methodologies in retinal images–a survey”, Computer methods and programs in biomedicine, 108, 407-433, 2012.

337. Aguiree, F., A. Brown, N.H. Cho, G. Dahlquist, S. Dodd, T. Dunning, S. M. Hirst, C. Hwang, D. Magliano, C. Patterson, C. Scott, J. Shaw, G. Soltesz, J. Usher-Smith, and D. Whiting, IDF Diabetes Atlas: sixth edition. 2013.

338. Wild, S., G. Roglic, A. Green, R. Sicree, and H. King, “Estimates for the year 2000 and projections for 2030”, World Health, 27(5), 1047–1053, 2004.

339. Bottomley, J. “Economic costs of diabetes in the US in 2007 – Implications for Europe,” Br. J. Diabetes Vasc. Dis., 8(2), 96–100, 2008.

340. Saeid F., SevinSamadi, ParisaNadirkhanlou, “A Novel Retinal Vessel Segmentation Based on Local Adaptive Histogram Equalization”, 8-th Iranian Conference on Machine Vision and Image Processing (MVIP) IEEE, 2013.

341. Bob Z., Lin Zhang, Lei Zhang, FakhriKarrayRetinal vessel extraction by matched filter with first-order derivative of Gaussian,” ELSEVIER, Computers in Biology and Medicine, 40, 438–445, 2010.

342. M.-A. Al-Betar and A.-T. Khader, “A harmony search algorithm for university course timetabling,” Ann. Oper. Res., vol. 194, no. 1, pp. 3–31, 2012.

343. Senthilkumari, S., Neethu, M., et al., Identification of glaucomatous optic nerve head changes in Indian donor eyes without clinical history, Indian Journal of Ophthalmology, vol. 63, no. 7, pp. 600-605 (2015).

344. Narasimhan, K., Neha, V. C., Vijayarekha, K., et al., Hypertensive retinopathy diagnosis from fundus images by estimation of AVR, ICMOC – 2012, Elsevier Ltd., pp. 980 – 993 (2012).

345. Kingman S., Glaucoma is second leading cause of blindness globally, Bull World Health Organ, vol. 8 pp. 82-887 (2004).

346. George, R., Ve, R. S., Vijaya, L., Glaucoma in India: Estimated burden of disease, J Glaucoma, vol. 7, pp. 19-391 (2010).

347. Wong, T. Y., Klein, R., Sharrett, A. R., et al., Retinal arteriolar diameter and risk for hypertension, Ann. Intern. Med., vol. 140, pp. 248-255 (2004).

348. Wong, T. Y., Klein, R., Nieto, F. J., et al., Retinal microvascular abnormalities and 10-year cardiovascular mortality: a population-based case-control study, Ophthalmology, vol. 110, pp. 933-940 (2003).

349. Wong, T. Y., Klein, R., et al., Hypertensive retinopathy and risk of stroke, published online in Hypertension (2013).

350. Kondermann, C., Kondermann, D., Yan, M., Blood Vessel Classification into Arteries and Veins in Retinal Images, Article in Proceedings of SPIE - The International Society for Optical Engineering, (2007).

351. Kirsch, R., Computer determination of the constituent structure of biomedical images, Comput. Biomed. Res. Vol. 4(3), pp. 315-328 (1971).

352. Chaudhuri, S., Chatterjee, S., Katz, N., Nelson, M., Goldbaum, M., Detection of blood vessels in retinal images using two-dimensional matched filters, IEEE Transactions Medical Imaging, Vol.8(3), pp. 263-269 (1989).

353. Zana, F., Klein, J. K., Segmentation of vessel like patterns using mathematical morphology and curvature evaluation, IEEE Trans. Image Processing, Vol. 10(7), pp. 1010-1019 (2001).

354. JStaal, J., Ginneken, B., Niemeijer, M, Viegever, A., Abramoff, M. D., Ridge-based vessel segmentation in color images of the retina, IEEE Trans. Med. Imaging, Vol. 23(4), pp. 501-509 (2004).

355. Heneghan, C., Cahill, M., et al.: Characterization of changes in blood vessel width and tortuosity in retinopathy of prematurity using image analysis. Medical Image Analysis, Elsevier, 6, 407–429 (2002).

356. Kumar, D., Pramanik, A., Kar, S. S., and Maity, S. P., Retinal blood vessel segmentation using matched filter and Laplacian of Gaussian, in Signal Processing and Communications (SPCOM), International Conference on. IEEE, 2016, pp. 1–5, 2016.

357. Halder, N., Bandyopadhyay, S. et al., “Automatic Segmentation of Blood Vessels (ASBV) of Retinal Fundus Images using CLAHE and Multilevel Thresholding based on Harmony Search”, Contemporary Issues in Computing, Jan, 2020.

Appendix – I

Datasets

There is a number of public retinal datasets available with blood vessel details. It is the key step for blood vessel segmentation to train and test the classifier on the retinal database. Some databases i.e. STARE and DRIVE etc. are publicly available for the researchers along with the ground truth images of the vessels. The performance of the classifier can be evaluated using these datasets.

STARE stands for Structured Analysis of the Retina. This dataset consists of 400 retinal images, captured using TOP-CON TRV-50 fundus camera with additional settings of 35^0 field of view (FOV) and $8 bits / color$ channel at 605×700 pixels. The average diameter of the FOV is 650×700 . STARE has 20 vessel ground truth images used for blood vessel segmentation of which 9 are healthier while the rest of them has shown a different type of retinal diseases. Two experts manually segmented these images in which the first expert segmented 10.4% of vessel pixels, while the second expert segmented 14.9% of the thinner vessel. Generally, the segmentation of the first observer is used to compute the performance as the ground truth.

Digital Retinal Images for Vessel Extraction (DRIVE) is one of the commonly used datasets for retinal blood vessel segmentation. DRIVE consists of 40 retinal images, of which 33 are healthier images while 7 have shown signs of mild diabetic retinopathy. Canon CR5 non-mydriatic camera with 45^0 FOV and 8 $bit\ per\ color$ channel at 768×584 pixels have been used to capture the images in JPEG format. Every image has a circular FOV of 54^0 pixels in diameter. The DRIVE dataset has been divided into training and test set with 20 images each. In the training set, 14 images were segmented by the first expert, and 6 images were segmented by the second expert. In the test set, segmentation has been performed twice in two cases. In case 1, the first and second experts segmented 13 and 7 images respectively while the case 2 has been performed by the third expert. In case 1 and case 2, the observers marked 12.7% and 12.3% pixels as vessels respectively.

Child Health and Heart Studies in England (CHASE) contains images of different diseases in which retinal images along with ground truth vessels can be found in the first database entitled CHASE_DB1. The images were captured with an NM-200D funduscamera with 35^0 FOV, 1280×960 pixels resolution, and in TIF format. The images were captured under full-field illumination and around the center of the optic disc. The CHASE DB1 database incorporated 28 pictures altogether, which were gathered from the left and right eyes of 14 kids. The vessel ground truth pictures were

physically sectioned by two experts. There was no record of the disease in the 28 retinal pictures, however, they are all of great quality and differentiation.

This is the database of high-resolution fundus images created by Jan Odstrcilik to perform a comparative analysis of automatic segmentation algorithms. HRF database contains 45 photographs including 15 of normal patients, 15 images of the patient with glaucomatous, and 15 of diabetic retinopathy patients. The images in this dataset have 3504×2336 resolutions, which is higher than other retinal databases. Binary gold standard images are available for each image and these ground truth images are manually segmented by the experts in the retinal image analysis field. Canon CR-1 camera was used to capture fundus images along with 45^0 FOV and different acquisition settings.

The retinal image processing dataset utilized in this study is a comprehensive collection of high-resolution retinal images, specifically curated to facilitate the development and evaluation of advanced image processing techniques for retinal health assessment. The dataset encompasses a diverse range of retinal conditions, including diabetic retinopathy, age-related macular degeneration, glaucoma, and normal retinal morphology. These images have been acquired through various imaging modalities such as fundus photography, optical coherence tomography (OCT), and fluorescein angiography. Additionally, the dataset includes annotated ground truth labels, identifying key features, lesions, and abnormalities within the retinal images. This richly annotated dataset serves as a vital resource for training and validating algorithms aimed at early disease detection, classification, and progression monitoring, ultimately contributing to the enhancement of clinical decision support systems and advancements in retinal image processing technology.

Appendix – II

Publications

Automatic Detection and Segmentation of Optic Disc (ADSO) of Retinal Fundus Images Based on Mathematical Morphology

Niladri Halder
Department of Electronics & Communication Engineering
University Institute of Technology
The University of Burdwan
Purba Burdwan, India

Dibyendu Roy
Department of Electronics & Communication Engineering
University Institute of Technology
The University of Burdwan
Purba Burdwan, India

Rajib Banerjee
Department of Electronics and Communication Engineering
B. C. Roy Engineering College
Durgapur, India

Pulakesh Roy
Department of Electronics & Communication Engineering
University Institute of Technology
The University of Burdwan
Purba Burdwan, India

Partha Pratim Sarkar
Department of Electronics & Communication Engineering
University Institute of Technology
The University of Burdwan
Purba Burdwan, India

Subhankar Bandyopadhyay
Department of Instrumentation and Electronics Engineering
Jadavpur University
Jadavpur, Kolkata, India

***Abstract*— The main objective of medical image processing field is to design computational tools which will assist quantification and visualization of remarkable pathology and anatomical structure. Diabetic retinopathy is a medical disorder where the retina is damaged due to fluids leak from the blood vessels into the retina of human eye. The identification of optic disk in retinal fundus images and quantitative study of the evolution of its shape and size plays an important role in diagnosing different pathologies, and the abnormalities related to the retina of human eye. Most of the abnormalities which are related to optic disc may leads to a structural changes in the inner and the outer area of the optic disc. Optic disc identification and segmentation on the level of the whole retinal image reduces the detection sensitivity for those parts. In this research, an advanced classification based on hierarchical process for the detection and segmentation of optic disc has been proposed. The exact boundary of optic disc is obtained by calculating the region of interest and applying an innovative morphological transformation based adaptive thresholding. The presented technique helps to reduce the process area needed for segmentation techniques leading to a distinguished performance enhancement and reducing the amount of the needed computational cost for each retinal fundus image. The proposed technique has been evaluated on publicly available data sets of retinal images which are DIARETDB1, DRIVE, HRF, DRIONS-DB, IDRiD and STARE, and a remarkable improvement has been found over the existing techniques in terms of accuracy and processing time.**

Keywords— Keywords: Retinal image analysis, Region-of-Interest, CLAHE, optic disc, morphological operation, segmentation, and classification.

I. INTRODUCTION

Diabetes associated with different serious complications to human organs such as heart failure, complete vision loss, types of strokes etc., is more likely to develop different problems related to eye such as glaucoma and cataract but the effect of diabetes on the retina is the main risk to vision [1]. Adverse effect of diabetes causing different complications in retina including complete vision loss is called diabetes retinopathy [1].

Retinal images captured by fundus camera with different camera settings are used by ophthalmologists to diagnose several eye related diseases. Analysis of retinal images includes identification and extraction of many retinal anatomical structures which are directly related to the disease. Retinal optic disc, optic cup, vessels, fovea, exudates, hemorrhages etc. in figure (1) are several examples of retinal anatomical structures that depict the target features for different segmentation techniques [2-5].

In this research, authors are precisely focussing on the outcome of diabetes on retinal optic disc of human eye. Optic disc is the brightest part of a retinal image where the blood vessels are merging and from where fovea can be found out at a fixed distance. Optic disc identification can be used to identify the blood vessels and fovea. Moreover, optic disc, share's similar characteristics with different features like exudates and cotton wool spots of diabetic retinopathy disease.

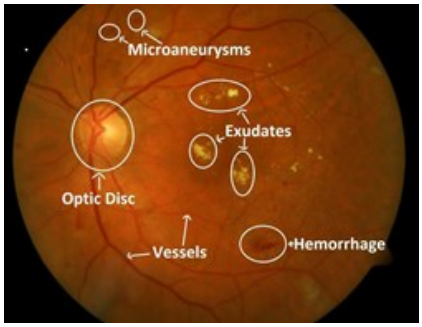

Figure 1: Different features of retinal images of human eye related to diabetics. Source [6].

According to [7-9] more than 382 million people globally suffering from the disease diabetes are aged in between 40 to 59 years. While India, China, and USA are in

the top considering to other countries and to screen such a large population, a large no of the ophthalmologist is essentially required. Thus, it is very advantageous to design an automatic diabetic retinopathy detection algorithm to support the ophthalmologist.

This research presents an advanced technique for the fast and accurate identification and segmentation of optic disc in different special filtering, contrast limited advanced histogram equalization and different morphology based techniques. First the red component of the input image has been considered as it provides the brighter part of the image more clearly. Special filters remove unwanted frequency components from the applied signal and enhance wanted ones. Histogram of red part of the input fundus image provides the different intensity characteristics. The most the image with the highest intensity has been considered as the optic disc. Experimental evaluation shows proposed technique is computationally fast in processing, robust to the variation in image contrast and illumination, and comparable with the state of the art methodologies in terms of quantitative performance metrics.

II. Related Work

Automatic analysis of optic disc may be divided in two different parts, optic disc detection and segmentation.
Sinthanayothin et al. [10] identified optic disc due to change in intensities occurring for blood vessels. Image feature vector projection to localize optic disc has been applied by Mahfouz et al. [11]. Watershed thresholding has also been applied to identify the optic disc. Watershed thresholding suggested by Walter et al. [12] has been used to find out optic disc contour. Thresholding based binary image performed on the intensity parameters, has been used to obtain the centroid of the brightest and the largest connected object. Hoover et al. [13] performed the fuzzy convergence logic by using voting type algorithm technique for optic disc detection considering the vessels origin and there after identified the centre of optic disc by considering the optic disc as a circular object or an elliptical shape [14] and performed the template matching algorithm[15,16]. Abdullah et al. [17, 18] proposed the optic disc detection without any template matching or vascular parameter information. The different morphology based operations has been used to identify the enhanced optic disc without any pathologies or retinal vasculature. Hough transformation has been used to approximate the optic disc centre.
For optic disc edge segmentation, Joshi et al. [6, 19] applied vessels kinks property to detect the optic disc edges properly. The irregular shape of the optic disc has been captured using gradient based active contour models. The algorithm initially performs the optic disc detection task by applying the gradient vector flow based on active contour method [20] and minimizes the high gradient values at the blood vessel locations i.e. minimizing the gradient energy. In [21] the deformable model based algorithm has been proposed where snake model [21] has been used to increase the vessels occlusion more prominently. The mentioned algorithm has been divided into two groups which are knowledge based clustering and smoothing. The cluster groups have been updated by the information collected locally as well as globally.
Abdullah et al. [16] identified the OD boundary using the grow-cut technique. Level set method and directional matching algorithm has been done by Yu.et al. [22] to segment the optic disc boundary.
It has been found that the presence of the blood vessels within and all over the optic disc, irregular shape of optic disc, the existence of the pathological features, existence of uneven illumination and noise in the image disturbs the proper segmentation of optic disc. A novel Optic Disc segmentation technique is proposed in this research that works even in the presence of these obstacles without the use of any prior information and template or Vessel map.

III. Materials and Methodology

In this research, a novel supervised method of optic disc identification and segmentation has been proposed which is robust to variations in illuminated images and retinal abnormalities. Optic disc may be the brightest region of the retinal image but the whole optic disc region part is not equally brightly illuminated. For exactly detection of optic disc boundary it is vital to detect the total bright optic disc regions. To achieve this a four step approach has been proposed, where in the first step retinal images are collected from different publicly available data set and converted into red plane so that the bright regions of the images are found in a brighter way. The second step is basically related to image enhancement where different image calibration, registration, optimization, transformation and filtering techniques are used. In the third step bright regions in close vicinity of major blood vessels are detected by thresholding a morphological reconstruction and region-based classification is performed to retain only the bright probable OD regions among all the bright regions previously detected. In the fourth step, Image analysis has been done. Here OD portion are cropped leaving rest of part and the OD is segmented out form the cropped ROI and the segmented OD are correlated with the ground truth data of the optic disc to validate the segmented result found by the proposed algorithm. A flowchart outlining these three steps for OD detection is shown in Figure (2).

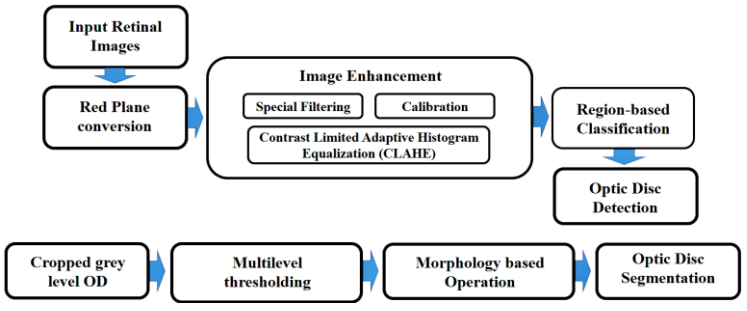

Figure 2: Detection of optic disc from retinal fundus image and segmentation of optic disc from retinal fundus images.

A. Dataset:

For the performance analysis of optic disc identification and segmentation, retinal images are manually marked for the optic disc boundary using GIMP software. The proposed optic disc identification and segmentation algorithm is examined on the fundus images found from the publicly available data set.

DRIVE [23] data set contains 40 images taken by CANON CR5 fundus camera with 45^0 field of view and size of $[564\times584]$ pixels in TIFF format. Among 40 images 33 are normal and 7 are diseased.

DIARETDB1 [23] data set contains 89 images taken by Nikon F5 fundus camera with 50^0 field of view and size of $[1500\times1152]$ pixels in PNG format. Among 89 images 5 are normal and 84 are diseased.

STARE [23] data set contains 81 images taken by TopCon TRV-50 fundus camera with 35^0 field of view and size of $[400\times600]$ pixels in TIFF format. Among 81 images 31 are normal and 50 are diseased.

DRIONS-DB [23] data set contains 110 images of size $[400\times600]$ pixels each in JPEG format.

IDRiD [23] data set contains 597 images of size $[2848\times4288]$ pixels each in JPEG format.

B. Pre-processing:

In RGB color space, each color is composed by three primary additive color spectral components, red, green and blue. A color image in this spectral is being represented in terms of intensity function as

$$I_{RGB}=\left(F_R,F_G,F_B\right) \tag{1}$$

Here $F_R(x,y), F_G(x,y)$ and $F_B(x,y)$ denotes the intensity of the pixel position (x,y) in the red, green and blue channels respectively. As the brightest optic disc is the target feature of this research, the RGB color image is being transformed into a gray level image. The transformation has been done by using the mentioned equation (2).

$$I_y=0.333F_R+0.5F_G+0.1666F_B \tag{2}$$

Here I_y represents the equivalent intensity of the gray component image transformed from RGB. The intensity related to red component is being considered for next step of the proposed algorithm. The reason is that it provides the brighter part of a gray image in more bright way.

A special filter is used to remove the noise by enhancing the intensities of pixels related to the target features on the image according to the intensities of the typically small rectangular sized neighbourhood pixels. Consider $F(x,y)$ denotes the input image and $G(x,y)$ is the output image, hence (x,y) represents the as integer coordinates of the pixels, with parameter ranges $0\le x\le M-1$ and $0\le y\le N-1$ where each image of F and G are of size $M\times N$. The neighbourhood pixel canter at the point (x,y) is defined as

$$S_{(x,y)}=\left[(x+s,y+t),\quad -a\le s\le a,\quad -b\le t\le b\right] \tag{3}$$

where $a,b>0$ are the integers. The size of $S_{(x,y)}$ is equal to $(2a+1)(2b+1)$, and denoted by $m=2a+1$ and $n=2b+1$, thus the size of $S_{(x,y)}$ becomes $M\times N$ and, $a=\frac{m-1}{2}, b=\frac{n-1}{2}$.

A window mask is defined as $w=w(s,t)$, for all $-a\le s\le a,\ -b\le t\le b$ of size $M\times N$. The output image $G(x,y)$ is defined as

$$G(x,y)=\sum_{s=-a}^{a}\sum_{t=-b}^{b}w(s,t)F(x+s,y+t) \tag{4}$$

The condition of the boundary image, F, must be taken care of in case of when $F(x+s,y+t)$ is not defined. Smoothing of the image F(x, y) of size $M\times N$ has been done by using the following expression.

$$G(x,y)=\frac{\sum_{s=-a}^{a}\sum_{t=-b}^{b}w(s,t)F(x+s,y+t)}{\sum_{s=-a}^{a}\sum_{t=-b}^{b}w(s,t)} \tag{5}$$

In equation (5) $G(x,y)$ is calculated for all (x,y) positions with x = 0, 1, 2, 3, 4… M-1 and y = 0, 1, 2, 3, 4… N-1. As the denominator of the mentioned equation is constant, it is needed to calculate only once. The blurry image F(x, y) of size $M\times N$ found after smoothing has been made sharper through the process mentioned in equation (6).

$$\Delta F(x,y)=\frac{\partial^2F}{\partial x^2}(x,y)+\frac{\partial^2F}{\partial y^2}(x,y) \tag{6}$$

In contrast limited adaptive histogram equalization (CLAHE), the input image is divided into two parts which are non-overlapping contextual area or tiles and local histogram of those tiles. Before the approximation of cumulative probability density and intensity of enhanced contrast, histogram of individual tile is clipped using some user defined clip limit which is the multiple of the histogram's average height of the contextual region.

$$Average\ Height\ of\ Histogram = \frac{number\ of\ pixels\ in\ the\ contextual\ region}{total\ number\ of\ pixels\ in\ gray\ level}$$

For the contextual region of size say $X\times Y$ and P be the number of histogram bars, the clip-limit is given by,

$$n_c=\begin{cases}1 & if\ \ \frac{\alpha XY}{P}<1\\ 1 & otherwise\end{cases}\qquad 0<\alpha\le1 \tag{7}$$

Where α = contrast factor defined by user. The actual height of the histogram of the contextual area 'n_k' is being clipped using the clip limit 'n_c' as mentioned in equation (8) where h_k the histogram of is given region.

$$h_k=\begin{cases}n_c & if\ \ n_k\ge n_c\\ n_k & otherwise\end{cases}\qquad k=1,2,3,.....,P-1 \tag{8}$$

Note that,
$$\sum_{k=0}^{P-1}n_k=XY \tag{9}$$

Total clipped pixels,
$$n_T=XY-\sum_{k=0}^{P-1}h_k \tag{10}$$

Renormalizing the histogram or bringing the area under the curve back to its original range, the clipped pixel values are spread back to the histogram plots. The rearrangement may be uniform otherwise the clipped pixel values may not be uniformly spread into the histogram plots with values of pixels below the clip limit. The pixels distributed to each histogram bins can be found from equation (11)

$$n_\mu = \frac{n_T}{P} = \frac{XY - \sum_{k=0}^{P-1} h_k}{P} \tag{11}$$

In equation (11) h_k defines the clipped histogram range. Now the clipped histogram is being renormalized as,

$$h_k = \begin{cases} n_c \; if \quad n_k + n_\mu \geq n_c \\ n_k + n_\mu \quad otherwise \end{cases} \tag{12}$$

The number of pixels not distributed can be calculated from equations (10) to (11) and the transformation shown in equation (12) is repeated until all the clipped pixel values get spread uniformly to the histogram plots and the histogram develops back to its original range. The accumulative histogram of the contextual region is being computed as,

$$C_k = \frac{1}{XY} \sum_{j=0}^{k} h_j \tag{13}$$

Using the above mentioned technique the largest region of maximum intensity is being considered as the area of interest.

C. *Post Processing*

In this section of the research, the optic disc from the cropped image has been segmented out by using multilevel thresholding followed by some morphological based operation.

In multilevel thresholding technique, a number of thresholds points $[T_1, T_2, T_3, ..., T_L]$ in the histogram image $f(x,y)$ is used to separate the image pixels. By using the separated threshold points, the original cropped image is being segmented to get image $T(f(x,y))$. Specifically:

$$T(f(x,y)) = \begin{cases} g_0 & if \quad f(x,y) \leq T_1 \\ g_1 \quad if & S_1 < f(x,y) \leq T_2 \\ ..... & ..... \\ g_L & if \quad f(x,y) > T_L \end{cases} \tag{14}$$

Such that g_i denotes the gray-level allocated to all pixel points at the region i that eventually signifies the object i. As in equation (14), the $L+1$ areas are calculated by the L number of thresholds $\{T_1, T_2, T_3, ..., T_L\}$. The maximum values of gray-level i.e. 255 can be used to dispense the gray-level regions correspondingly. Precisely, $g_i = i\left[\frac{255}{L}\right]$ so that the function returns an integer value of the argument. In contrast, the value of g_i can be selected as the mean value of gray-levels of the region's pixels.

IV. RESULT AND DISCUSSION

In this part of the research, the experimental results obtained by using the proposed method have been explored and discussed. The above mentioned system has been developed and tested under MATLAB 2018a software with the help of image processing toolbox.

The proposed method for detection and segmentation of optic disc have been extensively tested on above mentioned standard diabetic retinopathy databases. The choice of successful detection and failed detection of optic disc is based on the observation of human eye. To verify the optic disc localization results, optic discs of each image are manually categorized by the ophthalmologists [16]. The manually separated optic discs by human observer are considered as the ground truth data set. After successful detection of the optic disc, the proposed post processing algorithm has been applied to segment out the detected optic disc from different dataset. The step by step result of detection and segmentation of optic disc is shown in figure (3) and the optic disc detection result for different data set has been shown in figure (4).

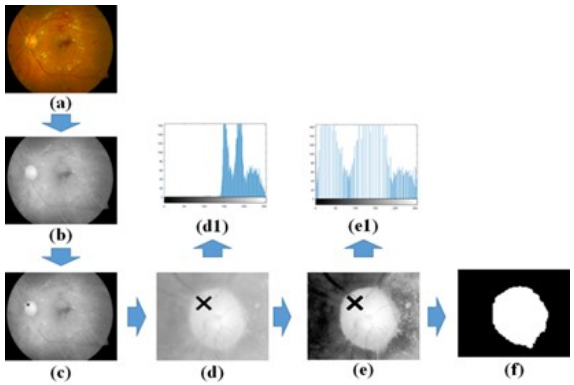

Figure 3: OD detection and segmentation steps; (a) Input fundus image, (b) red component of input, (c) OD detection, (d) OD cropping, (d1) histogram of figure (d), (e1) equalized histogram of figure (e), (e) OD enhancement, (f) OD segmentation

A comparison of the performance analysis of the proposed method with the result set different authors to detect the optic disc is shown in table (1) which simply shows that the performance of the proposed method is better than the mentioned existing methods.

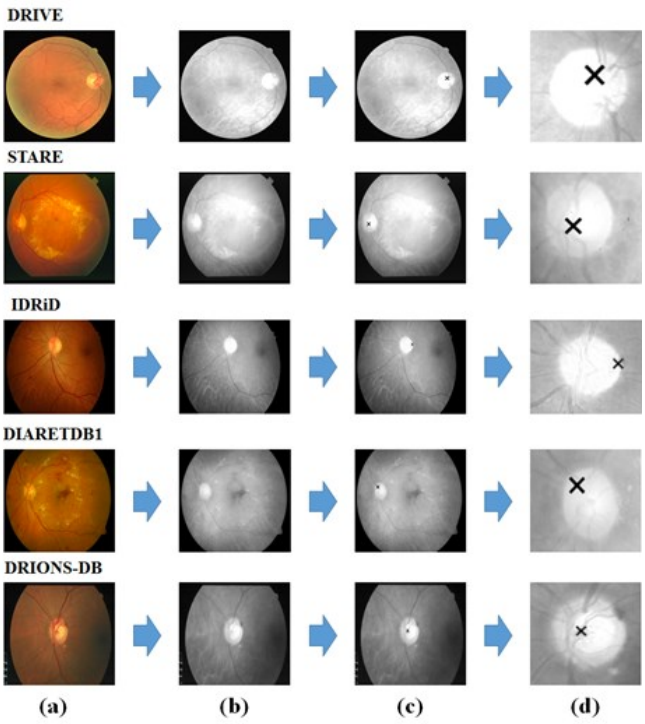

Figure 4: Optic Disc Identification and selection of AOI: (a) Input fundus images, (b) red components of inputs, (c) OD identification by marking, (d) OD cropping

TABLE I. Performance comparison of proposed method to detect OD with other existing methods

Algorithm	Dataset	Number of samples taken	Success rate (%)
Mohanta [18]	STARE	81	64.10
Park [19]	DRIVE	35	90.25
Niemeijer [20]	DRIVE	40	89.00
Manish Kumar Aggarwal [21]	DRIVE	40	95.00
	DIARETDB1	89	98.80
Foracchia et al. [22]	STARE	81	97.50
Mahfouz et al. [23]	DIARETDB1	89	97.80
	STARE	81	92.60
Youssif et al. [24]	STARE	81	98.77
ADSO Method	DRIONS-DB	110	99.09
	DRIVE	40	97.50
	STARE	81	98.76
	IDRiD	597	93.80
	DIARETDB1	89	98.87
	HRF	15	100.00

The optic disc segmented results for different databases using above mentioned proposed technique is shown in figure (5) where column (a) shows the input RGB fundus images of different dataset used, column (b) shows the identified and cropped optic disc and column (c) provides the optic disc segmented results of mentioned data set.

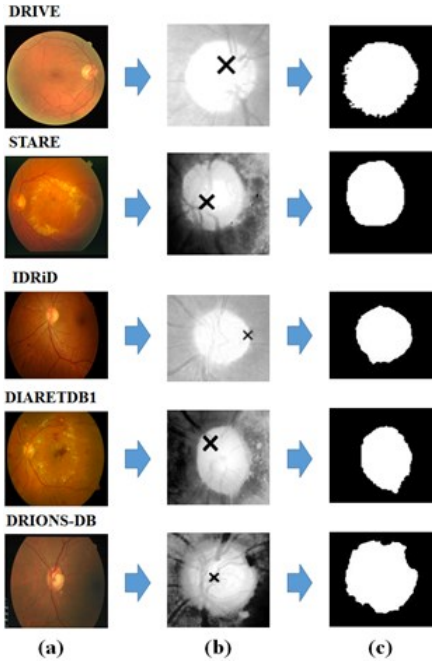

Figure 5: OD segmentation result for different dataset: (a) Input fundus image, (b) OD identification, (c) OD segmentation

In this research, as the optic disc has been identified first and cropped version of the optic disc has been used for segmentation purpose. The advantage is that the other parameters of the retina can be avoided and not need to be excluded separately. It will make the segmentation process faster and more accurate.

The sensitivity, specificity, accuracy and the overlapping ratio of the for the output result found using the proposed method has been calculated using the below mentioned simple mathematical expressions

$$Sensitivity = \frac{\sum correctly\ classified\ foreground\ pixels}{\sum foreground\ pixels\ in\ ground\ truth}$$

$$Specificity = \frac{\sum correctly\ classified\ background\ pixels}{\sum background\ pixels\ in\ groundtruth}$$

$$Accuracy = \frac{\sum correctly\ classified\ pixels}{total\ number\ of\ pixels\ in\ groundtruth}$$

$$Overlapping\ Ratio = \frac{ODB_G \cap ODB_R}{ODB_G \cup ODB_R}$$

Where,

$ODB_G = optic\ disc\ boundary\ from\ dgound\ truth$

$ODB_R = resultant\ optic\ disc\ boundary$

For segmentation purpose to get the best fitted result morphological dilation, erosion, opening and closing steps have been used depending on the requirements. To do so a structuring element has been considered. It is basically a user defined matrix that classifies the pixel in the processed image and explains the neighbourhood required to process each and every pixel. Due to change in the structuring element the quality of the output result changes as well as performance analysis also varies. Figure (6a), (6b), (6c) and (6d) shows the performance analysis of sensitivity,

specificity, accuracy and overlapping ratio with respect to the structuring element.

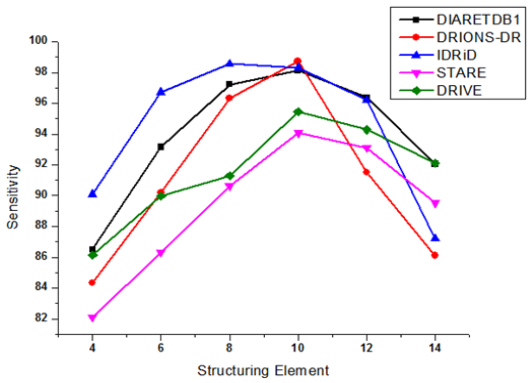

Figure (6a): Sensitivity graph of different database used with respect to different Structuring Elements

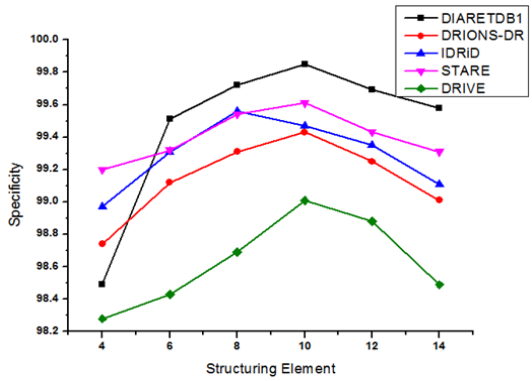

Figure (6b): Specificity graph of different database used with respect to different Structuring Elements

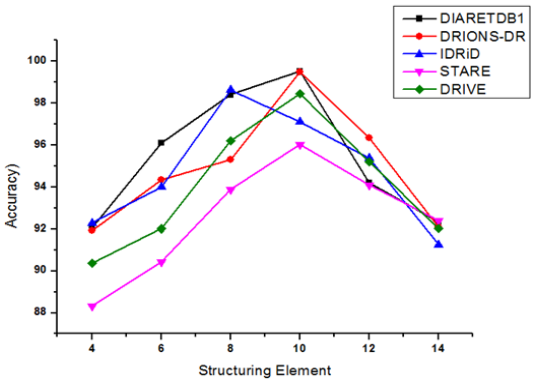

Figure (6c): Accuracy graph of different database used with respect to different Structuring Elements

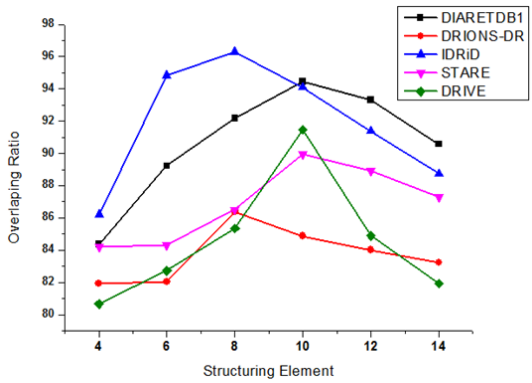

Figure (6d): Overlapping ratio graph of different database used with respect to different Structuring Elements

V. REFERENCES

[1] Susman, E. J., Tsiaras, W. J., Soper, K. A., “Diagnosis of diabetic eye disease” JAMA 247(23), 3231-3234 (1982).

[2] J. Almotiri, K. Elleithy, and A. Elleithy, "Retinal Vessels Segmentation Techniques and Algorithms: A Survey," Applied Sciences, vol. 8, p. 155, 2018.

[3] C. L. Srinidhi, P. Aparna, and J. Rajan, "Recent advancements in retinal vessel segmentation," Journal of medical systems, vol. 41, p. 70, 2017.

[4] A. Almazroa, R. Burman, K. Raahemifar, and V. Lakshminarayanan, "Optic disc and optic cup segmentation methodologies for glaucoma image detection: a survey," Journal of ophthalmology, Volume 2015, Article ID 180972, 28 pages, 2015.

[5] M. M. Fraz, P. Remagnino, A. Hoppe, B. Uyyanonvara, A. R. Rudnicka, C. G. Owen, et al., "Blood vessel segmentation methodologies in retinal images–a survey," Computer methods and programs in biomedicine, vol. 108, pp. 407-433, 2012.

[6] Joshi, G.D., J. Sivaswamy, and S. Krishnadas, Optic disk and cup segmentation from monocular color retinal images for glaucoma assessment. IEEE Transactions on Medical Imaging, 2011. 30(6): p. 1192-1205.

[7] F. Aguiree, A. Brown, N. H. Cho, G. Dahlquist, S. Dodd, T. Dunning, S. M. Hirst, C. Hwang, D. Magliano, C. Patterson, C. Scott, J. Shaw, G. Soltesz, J. Usher-Smith, and D. Whiting, IDF Diabetes Atlas: sixth edition. 2013.

[8] S. Wild, G. Roglic, A. Green, R. Sicree, and H. King, “Estimates for the year 2000 and projections for 2030,” World Health, vol. 27, no. 5, pp. 1047–1053, 2004.

[9] J. Bottomley, “Economic costs of diabetes in the US in 2007 – Implications for Europe,” Br. J. Diabetes Vasc. Dis., vol. 8, no. 2, pp. 96–100, 2008.

[10] Sinthanayothin, C., et al., Automated localisation of the optic disc, fovea, and retinal blood vessels from digital colour fundus images. British Journal of Ophthalmology, 1999. 83(8): p. 902-910.

[11] Mahfouz, A.E. and A.S. Fahmy, Fast localization of the optic disc using projection of image features. IEEE Transactions on Image Processing, 2010. 19(12): p. 3285-3289.

[12] Walter, T. and J.-C. Klein. Segmentation of color fundus images of the human retina: Detection of the optic disc and the vascular tree using morphological techniques. In International Symposium on Medical Data Analysis. 2001. Springer.

[13] Hoover, A. and M. Goldbaum, Locating the optic nerve in a retinal image using the fuzzy convergence of the blood vessels. IEEE transactions on medical imaging, 2003. 22(8): p. 951-958.

[14] Pallawala, P., et al. Automated optic disc localization and contour detection using ellipse fitting and wavelet transform. in European conference on computer vision. 2004. Springer.

[15] Lalonde, M., M. Beaulieu, and L. Gagnon, Fast and robust optic disc detection using pyramidal decomposition and Hausdorff-based template matching. IEEE transactions on medical imaging, 2001. 20(11): p. 1193-1200.

[16] Abdel-Ghafar, R. and T. Morris, Progress towards automated detection and characterization of the optic disc in glaucoma and diabetic retinopathy. Medical informatics and the Internet in medicine, 2007. 32(1): p. 19-25.

[17] Abdullah, M., M.M. Fraz, and S.A. Barman, Localization and segmentation of optic disc in retinal images using circular Hough transform and grow-cut algorithm. PeerJ, 2016. 4: p. e2003.

[18] Abdullah, M. and M.M. Fraz. Application of grow cut algorithm for localization and extraction of optic disc in retinal images. in 2015 12th International Conference on High-capacity Optical Networks and Enabling/Emerging Technologies (HONET). 2015. IEEE.

[19] Joshi, G.D., J. Sivaswamy, and S. Krishnadas, Depth discontinuity-based cup segmentation from multiview color retinal images. IEEE Transactions on Biomedical Engineering, 2012. 59(6): p. 1523-1531.

[20] Lee, S. and M. Brady, Optic disk boundary detection, in BMVC91. 1991, Springer. p. 359-362.

[21] Xu, J., et al., Optic disk feature extraction via modified deformable model technique for glaucoma analysis. Pattern recognition, 2007. 40(7): p. 2063-2076.

[22] Yu, H., et al., Fast localization and segmentation of optic disk in retinal images using directional matched filtering and level sets. IEEE Transactions on Information Technology in Biomedicine, 2012. 16(4): p. 644-657.

[23] D. Zhang and Y. Zhao, “Novel accurate and fast optic disc detection in retinal images with vessel distribution and directional characteristics,” IEEE Journal of Biomedical and Health Informatics, p. 10.1109/JBHI.2014.2365514, 2014.

Volkson Press

ISBN: 978-1-948012-16-4

Contemporary Issues in Computing (CIC)

DOI: http://doi.org/10.26480/cic.01.2020.103.108

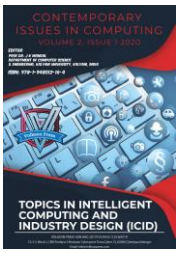

CrossMark

AUTOMATIC SEGMENTATION OF BLOOD VESSELS (ASBV) OF RETINAL FUNDUS IMAGES USING CLAHE AND MULTILEVEL THRESHOLDING BASED ON HARMONY SEARCH

Niladri Halder[a], Dibyendu Roy[a], Pulakesh Roy[a], Subhankar Bandyopadhyay[b]

[a]Department of ECE, University Institute of Technology, The University of Burdwan, Purba Burdwan, India
[b]Department of Instrumentation and Electronics Engineering, Jadavpur University, Jadavpur, Kolkata, India

ARTICLE DETAILS

Article History:

Received 26 October 2020
Accepted 27 November 2020
Available online 03 December 2020

ABSTRACT

The main objective of the medical image-processing field is to design computational tools that will assist the quantification and visualization of remarkable pathology and anatomical structure. Diabetic retinopathy is a medical disorder where the retina is damaged due to fluids leak from the blood vessels into the retina of the human eye. The identification of blood vessels in retinal fundus images and quantitative study of the evolution of its shape and size plays an important role in diagnosing different abnormal conditionscorrelated to the retinal structure of the human eye. Most of the abnormalities, which relate to blood vessels, may tends to a structural changes of the blood vessels. Segmentation of blood vessels corresponding to entire retinal image reduces the sensitivity for those areas. In this research, an advanced algorithm related to CLAHE and multilevel thresholding based on harmony search for the detection and segmentation of blood vessels has been proposed. The presented technique helps to reduce the process area needed for segmentation methodrelated to notable performance enhancement and reducing computational cost for each fundus image of human eye. The proposed technique has been evaluated on publicly available data sets of retinal images, which are CHASEDB1, DRIVE, HRF and STARE, and a remarkable improvement has been found over the existing techniques in terms of accuracy and processing time.

KEYWORDS

Retinal image analysis, Region-of-Interest, CLAHE, blood vessels, multilevel thresholding, harmony search, segmentationand classification.

1. INTRODUCTION

Diabetes associated with different serious complications to human organs such as heart failure, complete vision loss, types of strokes, etc., is more likely to develop different problems related to the eye such as glaucoma and cataract but the effect of diabetes on the retinal system causes the main risk in vision system that may cause different complications in retina including complete vision loss is called diabetes retinopathy (Niladri et al., 2020; Susman et al., 1982).

Ophthalmologists diagnose several eye-related diseases by using the retinal images, which captured by the fundus camera with different settings of the camera. Analysis of retinal images includes the identification and extraction of many retinal anatomical structures, which directly related to the disease. There are several examples of retinal structures are shown in the following figure 1 that depicts the target features for different segmentation techniques such as Retinal optic disc, optic cup, vessels, fovea, exudates, hemorrhages, etc. (Almotiri et al., 2018; Srinidhi et al., 2017; Almazroa et al., 2015; Fraz et al., 2012).

In this research, authors are precisely focusing on the outcome of diabetes on retinal vessel structures of the human eye. Blood vessel diameter changes due to the change in vessel fluid pressure, which relates to the sugar level of the human body. Generally, in retinal image optic disc is the brightest part where the blood vessels are merging. Optic disc identification can be used to identify the blood vessels.

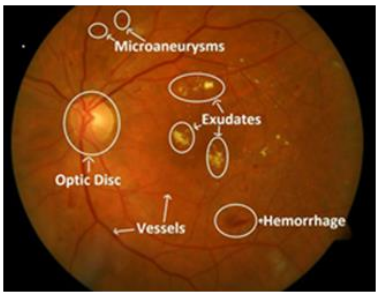

Figure 1: Different features of retinal images of human eye related to diabetics. Source (Joshi et al., 2011).

Quick Response Code	This paper was presented at	Access this article online	
	International Conference on Contemporary Issues in Computing (ICCIC-2020) - Virtual IETE Sector V, Salt Lake, Kolkata From 25th-26th July 2020	**Website:** www.intelcomp-design.com	**DOI:** 10.26480/cic.01.2020.103.108

According to more than 382 million people (age 40 to 59 years) are suffering from diabetes disease (Aguiree et al., 2013; Wild et al., 2004; Bottomley et al., 2008). While India, USA, and China are considered as the top with respect to other countries and for screening this kind of large population, a very large no of the ophthalmologist is primarily needed. For this, it is very much essential to design an algorithm to detect diabetic retinopathy automatically. This research presents an advanced technique for the fast and accurate segmentation of retinal vessels in different special filtering; contrast limited advanced histogram equalization and multilevel thresholding technique based on harmony search.

First, the optic disc has been identified after that segmented from the fundus image. The red component of the input image has considered as it provides the brighter part of the image more clearly. Special filters remove unwanted frequency components from the applied signal and enhance wanted ones. Histogram of the red part of the input fundus image provides different intensity characteristics. Most of the images with the highest intensity has considered as the optic disc. The different morphological technique has been used to segment out the optic disc. Secondly, the image has been enhanced so that the vessels can be found more clearly. CLAHE with different clip limits has been used to achieve the best-enhanced result. Finally, multilevel thresholding based on harmony search has been introduced to segment out the vessel structure. After the experimental evaluation, it is observed that the proposed technique shows better results in terms of image contrast, illumination, and quantitative performance and is computationally faster in terms of processing.

2. Literature Review

There are different kinds of work that have been done related to this field, some of the work have discussed below. In the author deeply researches on the advanced classification of optic disc for the segmentation and detection of vessels based on the hierarchical process (Niladri et al., 2020). Here an innovative morphological based thresholding technique is implemented for exacting the boundary of the optic disc. The proposed technique is very much helpful to reduce the process area for the vessel segmentation techniques. For this, the computational cost for each retinal fundus image is reduced. After the experiment, it is observed that the proposed technique shows a better result in terms of accuracy and processing time.

In the author compares the OTSU thresholding with Morphology based thresholding for the segmentation of vessels (Niladri et al., 2016). Generally, threshold segmentation is an important step for image segmentation and it has a lot of scopes available on the research field of image processing of this technique. The thresholding is the simplest method of image processing to separate any object from the background image. Here two different techniques are applied for the vessel segmentation and after the experiment; it is observed Morphology gives a better result than the OTSU thresholding for the segmentation of vessels.

In the author proposed a concept of blood vessel segmentation of the retinal image (Rattathanapad et al., 2012). In this paper, the author exhibits the technique of line detection in the multi-scale framework for vessel segmentation with systematically combines the Gaussian line detection output, which sequentially applied to the input. The Blood vessels of a retinal image are very much an important factor for the diagnosis of different types of diseases such as diabetes, arteriosclerosis, and hypertension. Normally, the images, which are taken from the retinal cameras, are usually poorly contrasted. To detect the diseases from that image, the ophthalmologist takes a lot of time. For making, the process in the easiest way multiple algorithms developed to segment blood vessels of the retinal images.

Various changes in morphology, branching, diameter, the pattern of blood vessels indicate various clinical disorders of body and eye. In the author discusses the vessel segmentation of retinal images by using the supervised method (Fraz et al., 2012). For the classification of the retinal image in this work, a Bayesian classifier has been used.

Blood vessel segmentation of the retinal fundus image is the initial step for the detection of different types of diseases, which related to retina such as diabetic retinopathy. The retinal fundus image of the patients shows some abnormalities, which predict the presence of diseases (NehaGour et al., 2017). In another paper, the author proposed an efficient method for the segmentation of vessels with the help of morphological top-hat transformation by using the hybrid median filter. In this paper, the method evaluated in terms of the accuracy of the segmentation, specificity, and sensitivity.

In another paper the author proposed the method for blood vessel segmentation of retinal images (SaeidFazli et al., 2013). The structure of blood vessels of retinal images is a very much important factor in terms of the diagnosis of different kinds of diseases. Here, the author proposed a scheme on the preprocessing of the retinal image by enhancing the histogram of the images. In this paper, the author discusses the effect of the non-linear and linear intensity transformation in segmented vessels of the retinal image. Here the author focuses mainly on two methods for the segmentation of a vessel that includes the Gaussian matched filter and the first derivative of Gaussian matched filter. These methods are helpful in many research works but still, there are some problems, which may occur during the detection of vessels (Chaudhuri et al., 1989; Hoover et al., 2000; Al-Rawi et al., 2007; Bob et al., 2010). To overcome this problem adaptive histogram equalization technique is used. In this experiment, the improved match filter shows better results of accuracy.

The most important factor to manage the different diseases is the automatic detection of the structures of the blood vessel. In another paper [20] the author proposes an algorithm for the segmentation in retinal images based on the features of the integral channel. Here, a preprocessing technique performed for obtaining the pixels of vessels of each candidate.

3. Proposed Scheme

In this research, a novel supervised method has proposed for the segmentation of the vessel to detect the retinal abnormalities. Generally, the optic disc is the brightest section of the retinal image but the total section of the optic disc is not equally bright. Therefore, for the detection of the optic disc boundary efficiently, it is very much essential to detect the total brightest part of the optic disc. To achieve an effective result a six steps approach has proposed in this paper. At the first stage of this technique all, the retinal images collected from different sources, which are publically available. The second stage related to the filtering technique and enhancement of vessels. To achieve this median filter plays a very vital role in removing the noise from the input image. After that, the Contrast Limited Adaptive Histogram Equalization (CLAHE) technique is applied to those images for the enhancement of vessels. In the third stage of the scheme, Morphological opening and Top-Hat operation performed. After that, in the fourth stage Multilevel Thresholding technique is applied to detect the major blood vessels. The fifth stage includes the morphology-based operation to detect the specific edges and shapes in the image and in the final step image analysis done for the detection of segmented vessels from the retinal images.

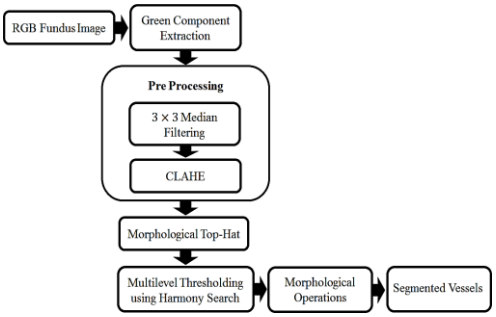

Figure 2: Proposed System Architecture

3.1 Data set of Retinal fundus image:

For the segmentation of the input fundus image, all the retinal images marked manually by using GIMP software. The proposed scheme examined on the fundus images collected from the publically available data set.

DRIVE contains a data set of 40 TIFF images taken by the CANON CR5 fundus camera with the 45 fields of view and the pixel size is pixel size 584564 (Zhang and Zhao, 2014). This dataset contains 40 images among them 7 images are diseased image and rest part is normal. In another data set, DIARETDB1 consists of 89 PNG images captured by the Nikon F5 fundus camera with the 50 fields of view and the pixel size is 11521500. This dataset contains 89 images among them 84 images are diseased image and rest part is normal. In STARE data set there are 81 TIFF images taken by TopCon TRV-50 fundus camera with the 35 fields of view and the pixel size is 400600. This dataset contains 81 images among them 50 images are diseased image and rest part is normal. In DRIVES-DB data set there are 110 JPEG images with the pixel size is 600400 and in Madrid, data set there are 597 images with the pixel size 28484288.

For smoothing the image here median filter is used as it is an effective solution for smoothing the image as it is very much efficient to reduce the noise and preserve the information about the edge of the resultant image (Niladri et al., 2013). It also does not create any unrealistic pixel intensity.

3.2 Median Filter

The Median filter is used to remove the noise from the input figure after the top-hat transform technique. Generally, the median filter used as a quality improvement process in the spatial domain. In the Median filter, pixel values are sort in the upward window for smoothing the image and remove the noise. After the sorting process, the median values obtain the original pixel value at the center of the window. During the process, if the pixel sequence is even, then, in that case, the average of two middle pixel values are taken for the future work. The mathematical equation for the median filter given below.

$$f(x,y) = median[g(a,b)|(a,b) \in W)] \quad (1)$$

Working function:

Take the 3×3 windows and check the fifth pixel and if the pixel is noisy then in that case the pixel value replaced with the median value. After that, the diagonal pixel value selected from window for checking if the diagonal window is noisy or not. Finally, after the checking, if it is found noisy, then in that case, the values replaced with the median value. In the same way, the horizontal and vertical pixel values are check and if it is found noisy then the horizontal and vertical pixel values are replaced by median values of the element.

3.3 Contrast Limited Adaptive Histogram Equalization (CLAHE):

For the vessel segmentation, image enhancement is an important step to increase the quality of the image and improved comprehension ability. Histogram equalization is one of the important techniques for contrast enhancement that will increase the intensity of the pixel for the proper utilization of the entire dynamic range. From the histogram, it is observed that the input fundus images have a low contrast value which is narrow and are only concentrates on a certain amount of gray level. Generally, it is very much difficult to observe every detail from the retinal image, which may cause delayed diagnosis or even the wrong diagnosis of diseases. To avoid this kind of situation histogram equalization plays a very important role. In this work, the CLAHE technique is implemented which is an efficient technique for the biomedical image. This technique is very much helpful to increase the background in-homogeneities. We proposed an image enhancement technique, which is based on the CLAHE method to divide the image into small contextual segments (Tiles).

CLAHE is one of the effective methods for the contrast enhancement to overcome the problem of low contrast value in the digital images (Example Medical images). Generally, it is the advanced version of the Adaptive Histogram Equalization and Histogram Equalization technique for the probability of a grayscale image. In CLAHE, a patch is used to process the input retinal fundus image to get a better contrast value (Sahu et al., 2018). In this process, the contrast of each small area of the image (tiles) increases the histogram of the image. After that, the neighbouring tiles merged to avoid the induced boundaries. The contrast enhancement technique mainly used to avoid the noise of the image. Let the Histogram equalization technique is applied on image y and j is the value of the gray level. Here the probability of the image at j level can calculate as$p_y(j) = p_{(y=j)} = \frac{n_j}{n}$ $(where\ 0 \le 0 < L)$ (2)

In the above image, the total number of gray level is L (generally, L = 256) and n is termed as total number of image pixels.

3.4 Morphological Processing

Generally, in image processing is the most suitable and acceptable technique to detect the shapes in images. For this Morphology is one of the efficient techniques which is introduced by Matheron to analyze the geometric structure of geologic and metallic samples (Serra et al., 1982). For the analysis of any image, mathematical morphology is a nonlinear tool, which plays a very important role in terms of quantifying the retinal pathology. There are four important steps of morphological operation such as Morphological Opening, Morphological Closing, dilation, and erosion (NehaGour et al., 2017). Generally, the morphological operation opening is the form of erosion, which followed by the dilation used for erasing any object and has a smaller size than the structuring element from the input image. So, for the enhancement of any object, which erased by using the operation opening, can be easily obtained by doing the operation between the original image and opened image (Fraz et al., 2011). The main assumption from the proposed scheme is that the vessels are the brightest part with the Gaussian shape cross-section when the background is dark, which piecewise connected with each other, and are generally linear in nature. Therefore, for the enhancement of the vessels from the input retinal figure the morphological filters used with the linear structuring element. Generally, the morphological opening operation oriented at a particular point, which remove the vessel or a particular part of the vessel when the vessel does not contain the structuring element due to the orthogonal directions of structuring element and vessel and the structuring element size is longer than the vessel width. On the other hand, the vessel will almost unchanged, when the orientation of structuring element is parallel with the vessel of retinal fundus image.

In the morphological process Dilation, the input image is superimposed by the Structuring Element. The main purpose of the Dilation operation is to increase the size of the pixels of the original image. It is also very much useful to fill the gaps in the image.

$$\epsilon_B\ (A) = max_{(f,k\epsilon B)}[A_{(m+f,n+k)} + B_{(f,k)}] \quad (3)$$

Like the Dilation, Erosion is another important morphological operation in which the main image is thinned by subtracting the main image by using the Structuring Element. It is the shrinking operation where the Structuring Element superimposed on the original image. In this technique, the resultant central pixel values are taken and the image details, which are smaller than the structuring element, removed from the main image.

$$\delta_B(A) = min_{(f,k\epsilon B)}[A_{(m-f,n-k)} - B_{(f,k)}] \quad (4)$$

The morphological opening consists of Erosion, which followed by the Dilation. This technique is used for the smoothing of the image, break the narrow joint, and remove the thin protrusions.

$$\gamma_B(A) = \epsilon_B[\gamma_B(A)] \quad (5)$$

The morphological closing operation consists of Dilation, which is followed by Erosion. This technique is very much helpful for smoothing

the image by fusing the narrow breaks and removes the small holes.

$$\emptyset_B(A) = \delta_B[\in_B (A)] \quad (6)$$

Another technique of morphology can be used for better extraction and remove the noise from the input fundus image known as morphological top-hat to get more details of the vessels from the input retinal image.

3.4.1 Morphological Top Hat

The morphological top-hat transformation used for extracting the brighter regions from the input image. Basically, top-hat transformation is the difference between the original image and its opening (Dalwinder et al., 2014). The top-hat transformation classified into two categories one is black top-hat transformation and another one is white top-hat transformation (NehaGour et al., 2017). In black top-hat, the objects are selected from the input image which has a smaller size with respect to the structuring element and also darker than the background. Generally, the blood vessels of the green channel are usually darker. For this, in this work, black top-hat is very much efficient. The equation of top-hat is written below.

$$T_H = A - \gamma_B(A) \quad (7)$$

3.5 Multilevel Thresholding

In the multilevel thresholding technique, several numbers of thresholds points such as $[Th_1, Th_2, Th_3, \dots\dots Th_L]$ have been used in the histogram image $f(x,y)$ to separate each image pixel. By using the separated threshold points, the original cropped image is being segmented to get the image $Th\big(f(x,y)\big)$. Specifically:

$$T\big(f(x,y)\big) = \begin{Bmatrix} G_0 \quad if \quad f(x,y) \leq Th_1 \\ G_1 \; if \; S_1 < f(x,y) \leq Th_2 \\ \quad - - - - - - - - \\ \quad - - - - - - - - \\ G_L \quad if \quad f(x,y) > \; Th_L \end{Bmatrix} \quad (8)$$

Such that G_i denotes the gray-level allocated to all pixel points at the region i that eventually signifies the object i . As in equation, the L+1areas are calculated by the L number of thresholds$[Th_1, Th_2, Th_3, \dots\dots\dots, Th_L]$. The maximum values of gray-level i.e. 255 can be used to dispense the gray-level regions correspondingly. Precisely $G_i = i\left[\frac{255}{L}\right]$, for this, an integer value of the argument is returned by the function. The value can be selected as the mean of gray levels of the pixels.

Performance Analysis:

Here true positive (TP) denotes the segmentation of vessel pixel as the vessel pixel on the other hand true negative (TN) denotes the segmentation of vessel pixel as the non-vessel pixel. In the same way, false positive (FP) indicates the non-vessel pixels segmentation of vessel pixels on the other hand false negative (FN) denotes the correct segmentation of vessel pixels as the non-vessel pixels.

The sensitivity, specificity, accuracy and the overlapping ratio for the output result found using the proposed method has been calculated using the below mentioned simple mathematical expressions:

$$Sensitivity = \frac{\sum correctly\ classified\ foreground\ pixels}{\sum foreground\ pixels\ in\ groundtruth} \quad (9)$$

$$Specificity = \frac{\sum correctly\ classified\ background\ pixels}{\sum background\ pixels\ in\ groundtruth} \quad (10)$$

$$Accuracy = \frac{\sum correctly\ classified\ pixels}{total\ number\ pixels\ in\ groundtruth} \quad (11)$$

$$Overlapping\ Ratio = \frac{ODB_G \cap ODB_R}{ODB_G \cup ODB_R} \quad (12)$$

$$where, ODB_G = Optic\ Disc\ Boundary\ from\ groundtruth$$
$$ODB_R = Resultant\ Optic\ Disc\ Boundary$$

The AUC is the area under the curve of the receiver operating characteristic (ROC) that shows the segmentation performance and determined by the combination of both the specificity and sensitivity. In this study, AUC calculated by using the following formula:

$$AUC = \frac{Sensitivity + Specificity}{2} \quad (13)$$

It should always remember that an AUC with a value of 0.50 or less than to it for this it can be stated that it is not very much useful as the segmentation is purely based on random guessing. On the other hand, an AUC with a value of 1.0 indicates that using the segmentation algorithm all the pixels can easily be segmented.

4. Result and Discussion

In this part of the research, the experimental results obtained by using the proposed method have been explored and discussed. The above-mentioned system has been developed and tested under MATLAB 2018a software with the help of image processing toolbox.

The proposed method for segmentation of vessel structure has been extensively tested on the above-mentioned publicly available databases. The choice of successful detection and failed detection of vessel structure is based on the observation of the human eye. To verify the results, vessels of each image are manually categorized by the ophthalmologists. The manually separated vessel structure by the human observer is considered as the ground truth data set. The proposed method has been used to detect the vessel structure automatically. Validation of the result set has been done by comparing it with the ground truth data.

To automatically identify the vessel structure, first pre-processing has been done to enhance the given fundus image of the human eye. As a first step of pre-processing, the green components of input RGB fundus image of the human eye has been considered as it gives the best-fitted result in the contrast of blood vessels (darker blood vessels on a brighter background). Next, a 3×3 median filter has been used to remove noise like salt and pepper noises. Finally, the CLAHE (contrast limited adaptive histogram equalization) technique is implemented for better enhancement of the image. The result set of CLAHE for different limits has been shown in figure (3) which an image data is taken from DRIVE.

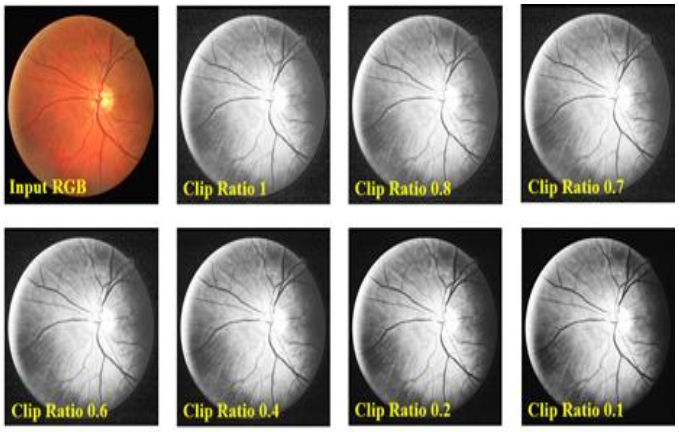

Figure 3: Result shows the contrast limited adaptive histogram equalization on DRIVE data (04_test.tif)

In the post-processing part, the enhanced results found from CLAHE have processed through the morphological top-hat transform technique with the help of the structuring elements to extract the small elements and details from the given input images. The result is shown in the following figure (4).

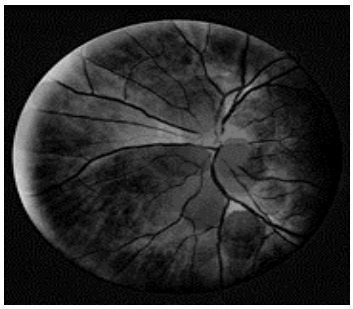

Figure 4: Result shows morphological Top-hat transformation of DRIVE (04_test.tif)

In multilevel thresholding with the help of harmony search, best fitted five different intensity levels of the top hat transformed image are being calculated and shown into the different threshold. The fitness graph comparing the gray levels with probability is shown in figure (5). After multilevel thresholding morphological dilation and erosion are being used simultaneously to remove the unwanted variables and finally morphological closing is used to get the final result.

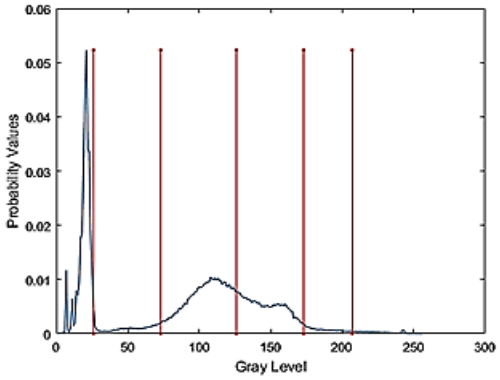

Figure 5: The result shows the fitness graph of multilevel thresholding comparing the gray levels with probability values

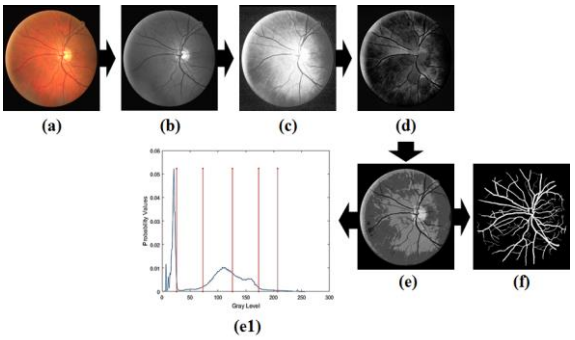

Figure 6: Result shows the outputs of DRIVE_04_test.tif: (a) input retinal fundus image (RGB), (b) Green components of the RGB image of retina, (c) result after using contrast limited adaptive histogram equalization technique with the limit 0.1, (d) morphological Top hat, (e) Multilevel thresholding using harmony search, (e1) Threshold limit of multilevel thresholding, (f) segmented vessels.

The segmented results compared to respective ground truth results using the mentioned different datasets are shown in figure (7). Table (1) shows the result of the performance analysis of the proposed technique compare to the previously established methods.

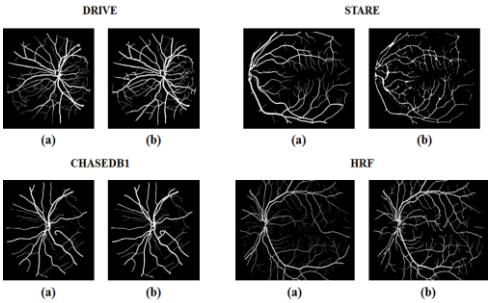

Figure 7: Result shows the images of segmented vessels (a) ground truth result, (b) automatic segmented result using proposed method.

Table 1: The performance analysis result of the proposed technique with compare to the previously established methods

Algorithm	Dataset	Number of samples taken	Sensitivity (SE) (%)	Specificity (SP) (%)	Accuracy (ACC) (%)	Overlapping Ratio (%)	AUC
SaeidFazli et al. [14]	DRIVE	40	-	-	93.53	-	-
Zhun Fan et al. [20]	DRIVE	20	71.9	98.5	96.1	-	-
	STARE	20	70	97.9	95.9	-	-
ASBV	DRIVE	40	99.63	96.69	97.00	98.73	98.16
	STARE	81	98.53	96.45	97.33	98.07	97.49
	HRF	15	99.71	97.62	98.22	98.79	98.66
	CHASEDB1	28	98.47	95.31	98.11	96.28	96.89
Ming Li et al. [19]	DRIVE	40	83.47	97.96	95.10	-	97.92
	STARE	20	82.31	97.82	95.60	-	97.43
Yitian Zhao et al [30]	DRIVE	40	77.4	97.9	95.8	-	97.5
	STARE	20	78.8	97.6	95.7	-	95.9
	HRF	45	74.9	94.2	94.1	-	97.1

REFERENCES

Aguiree, F., A. Brown, N.H. Cho, G. Dahlquist, S. Dodd, T. Dunning, S. M. Hirst, C. Hwang, D. Magliano, C. Patterson, C. Scott, J. Shaw, G. Soltesz, J. Usher-Smith, and D. Whiting, IDF Diabetes Atlas: sixth edition. 2013.

Almazroa, A., R. Burman, K. Raahemifar, and V. Lakshminarayanan. 2015. Optic disc and optic cup segmentation methodologies for glaucoma image detection: a survey, Journal of ophthalmology, Article ID 180972, 28.

Almotiri, J., K. Elleithy, and A. Elleithy. 2018. Retinal Vessels Segmentation Techniques and Algorithms: A Survey, Applied Sciences, 8, 155.

Al-Rawi, M.S., M.A. Qutaishat, M.R. Arrar. 2007. An improved Matched filter for blood vessel detection of digital retinal images, Comp. Biol. Med. 37(2), 262–267.

Bob Z., Lin Zhang, Lei Zhang, FakhriKarray. 2010. Retinal vessel extraction by matched filter with first-order derivative of Gaussian," ELSEVIER, Computers in Biology and Medicine, 40, 438–445.

Bottomley, J. 2008. Economic costs of diabetes in the US in 2007 – Implications for Europe," Br. J. Diabetes Vasc. Dis., 8(2), 96–100.

Chaudhuri, S., S. Chatterje, N. Katz, M. Nelson, M. Goldbaum, 1989Detection of blood vessels in retinal images using two dimensional matched filters", IEEE Trans. Med. Imaging, 8(3), 263–269.

Dalwinder, S., Dharmveer, Birmohan Singh. 2014. A New Morphology based Approach for Blood Vessel Segmentation in Retinal Images, Annual IEEE India Conference (INDICON).

Fraz, M.M., P. Remagnino, A. Hoppe, Sergio Velastin, B. Uyyanonvara, S. A. Barman. 2011. A Supervised Method for Retinal Blood Vessel Segmentation Using Line Strength, Multiscale Gabor and Morphological Features, IEEE International Conference on Signal and Image Processing Applications.

Fraz, P. Remagnino, A. Hoppe, B. Uyyanonvara, A. R. Rudnicka, C. G. Owen, et al., 2012. Blood vessel segmentation methodologies in retinal images– a survey, Computer methods and programs in biomedicine, 108, 407-433.

Hoover, A., V. Kouzntesova, M. Goldbaum. 2000. Locating blood vessels in retinal images by piecewise threshold probing of a matched filter responses, IEEE Trans. Med. Imaging, 19(3), 203–210.

Joshi, G.D., J. Sivaswamy, and S. Krishnadas. 2011. Optic disk and cup segmentation from monocular color retinal images for glaucoma assessment. IEEE Transactions on Medical Imaging, 30(6), 1192-1205.

Madalina S., Dan Popescu, Loretta Ichim. 2017. Blood Vessel Segmentation in Eye Fundus Images, 978-1-5386-2101-1/17, IEEE.

Ming, L., Qingbo Yin, Mingyu Lu. 2018. Retinal Blood Vessel Segmentation Based on Multi-Scale Deep Learning, Proceedings of the Federated Conference on Computer Science and Information Systems, 117–123.

NehaGour, Pritee Khanna. 2017. Blood Vessel Segmentation using Hybrid Median Filtering and Morphological Transformation, 13-th International Conference on Signal-Image Technology & Internet-Based Systems (SITIS).

NehaGour, Pritee Khanna. 2017. Blood Vessel Segmentation using Hybrid Median Filtering and Morphological Transformation, 13th International Conference on Signal-Image Technology and Internet-Based System.

Niladri H., Dibyendu Roy, Pulakesh Roy, Poushali Roy. 2016. Qualitative Comparison of OTSU Thresholding with Morphology Based Thresholding for Vessels Segmentation of Retinal Fundus Images of Human Eye, IOSR Journal of VLSI and Signal Processing (IOSR-JVSP), 6(3), 41-48.

Niladri H., Dibyendu Roy, Pulakesh Roy, Rajib Banerjee, Partha Pratim Sarkar, Subhankar Bandyopadhyay. 2020. Automatic Detection and Segmentation of Optic Disc (ADSO) of Retinal Fundus Images Based on Mathematical Morphology, National Conference on Emerging Trends on Sustainable Technology and Engineering Applications, IEEE.

Niladri S.D., HimadriSekhar Dutta, Mallika De, SaurajeetMondal. 2013. An Effective Approach: Image Quality Enhancement for Microaneurysms Detection of Non-Dilated Retinal Fundus Image, International Conference on Computational Intelligence: Modeling Techniques and Applications (CIMTA), ELSVIEWER.

Rattathanapad, S., P. Mittrapiyanuruk, P. Kaewtrakulpong, B. Uyyanonvara, and C. Sinthanayothin. 2012. Vessel Extraction in Retinal Images using Multilevel Line Detection, Proceedings of the IEEE-EMBS International Conference on Biomedical and Health Informatics (BHI 2012) Hong Kong and Shenzhen, China, 2-7 Jan IEEE.

Saeid F., SevinSamadi, ParisaNadirkhanlou. 2013. A Novel Retinal Vessel Segmentation Based on Local Adaptive Histogram Equalization, 8-th Iranian Conference on Machine Vision and Image Processing (MVIP) IEEE.

Sahu, S., A. Kumar, S. P. Ghrera, and M. Elhoseny. 2018. An approach for de-noising and contrast enhancement of retinal fundus image using CLAHE, Opt. Laser Technol.

Serra, J. 1982. Image Analysis and Mathematical Morphology, Academic Press, New York.

Serra, J. 1983. Image Analysis and Mathematical Morphology. Orlando, FL, USA: Academic Press, Inc.

Srinidhi, C.L., P. Aparna, and J. Rajan. 2017. Recent advancements in retinal vessel segmentation," Journal of medical systems, 41, 70.

Susman, E. J., Tsiaras, W. J., Soper, K. A. 1982. Diagnosis of diabetic eye disease, JAMA 247(23), 3231-3234.

Wild, S., G. Roglic, A. Green, R. Sicree, and H. King, 2004Estimates for the year 2000 and projections for 2030, World Health, 27(5), 1047–1053.

Yitian Zhao et al. 2018. Automatic 2-D/3-D Vessel Enhancement in Multiple Modality Images Using a Weighted Symmetry Filter, IEEE Transactions on Medical Imaging, 37(2).

Zhang, D. and Y. Zhao. 2014. Novel accurate and fast optic disc detection in retinal images with vessel distribution and directional characteristics, IEEE Journal of Biomedical and Health Informatics, 10.1109/JBHI.2014.2365514,.

Zhun, F., Yibiao, R., Jiewei, L., Jiajie, M., Fang, L., Xinye C. and Tiejun, Y. 2016. Automated Blood Vessel Segmentation in Fundus Image Based on Integral Channel Features and Random Forests, 12th World Congress on Intelligent Control and Automation (WCICA).

PSO-HRVSO: SEGMENTATION OF RETINAL VESSELS THROUGH HOMOMORPHIC FILTERING ENHANCED BY PSO OPTIMIZATION

Niladri Halder[1*], Dibyendu Roy[2], Partha Pratim Sarkar[2], Sankar Narayan Patra[1], Subhankar Bandyopadhyay[1]

[1*]Instrumentation and Electronics Engineering, Jadavpur University, Saltlake Campus, Kolkata, 700098, West Bengal, India
[2]Electronics and Communication Engineering, UIT, Burdwan University, Golapbag, Burdwan, 713104, West Bengal, India

ABSTRACT

The structure of retinal blood vessels is crucial for the early detection of diabetic retinopathy, a leading cause of blindness worldwide. Yet, accurately segmenting retinal vessels poses significant challenges due to the low contrast and noise present in capillaries.The automated segmentation of retinal blood vessels significantly enhances Computer-Aided Diagnosis for diverse ophthalmic and cardiovascular conditions. It is imperative to develop a method capable of segmenting both thin and thick retinal vessels to facilitate medical analysis and disease diagnosis effectively. This article introduces a novel methodology for robust vessel segmentation, addressing prevalent challenges identified in existing literature.

The methodology PSO-HRVSO comprises three key stages: pre-processing, main processing, and post-processing. In the initial stage, filters are employed for image smoothing and enhancement, leveraging PSO optimization. The main processing phase is bifurcated into two configurations. Initially, thick vessels are segmented utilizing an optimized top-hat approach, homo-morphic filtering, and median filter. Subsequently, the second configuration targets thin vessel segmentation, employing the optimized top-hat method, homomorphic filtering, and matched filter. Lastly, morphological image operations are conducted during the post-processing stage.

The PSO-HRVSO method underwent evaluation using two publicly accessible databases (DRIVE and STARE), measuring performance across three key metrics: specificity, sensitivity, and accuracy. Analysis of the outcomes revealed averages of 0.9891, 0.8577, and 0.0.9852 for the DRIVE dataset, and 0.9868, 0.8576, and 0.9831 for the STARE dataset, respectively.

The PSO-HRVSO technique yields numerical results that demonstrate competitive average values when compared to current methods. Moreover, it sur-passes all leading unsupervised methods in terms of specificity and accuracy. Additionally, it outperforms the majority of state-of-the-art supervised methods without incurring the computational costs associated with such algorithms. Detailed visual analysis reveals that the PSO-HRVSO approach enables a more precise segmentation of thin vessels compared to alternative procedures.

KEYWORDS

Optimization using PSO, Segmentation of retinal blood vessels, Optimized Top-hat transformation, Homomorphic Filtering.

1. INTRODUCTION

The examination of the eye fundus is extensively utilized by ophthalmologists and other medical practitioners as a standard clinical procedure for preventing, diagnosing, and monitoring the treatment of various ocular conditions including retinal thrombosis, glaucoma, and senile maculopathy, among others [1]. This examination involves a color imaging method of the retinal surface of the human eye, enabling the observation of key anatomical features such as the optic disc, macula, and vascular tree [66].

The segmentation of the retinal vascular tree holds significant importance in the realm of medical imaging because the retina offers a unique avenue to observe blood microcirculation non-invasively, allowing for the detection of various systemic diseases such as hypertension, diabetes, arteriosclerosis, and liver diseases, among others [3,4,6]. By delineating the retinal vessels, valuable morphological data including size, length, width, branching patterns, and angles of the retinal vasculature can be quantified [5]. However, manually performing this segmentation is a laborious process that demands expertise and experience from medical professionals [2]. Moreover, inconsistencies may arise due to subjective interpretations, as experts might employ different criteria for pixel classification [9–11].

Hence, it is imperative to advance and implement automated techniques for robust vessel extraction in Computer-Aided Diagnosis to facilitate early detection and assessment of disorders, aiming to mitigate medical expenses and enhance efficiency [8,7]. Nonetheless, segmentation encounters numerous hurdles. The foremost challenge emanates from the presence of various optical components in the eye fundus, including the optic disk, macula, and artifacts generated by pathologies, impeding the automated segmentation of vessels. The second challenge stems from the variability in vessel width and the subdued contrast of thin vessels against the background. Lastly, the third challenge arises from the diversity in shape, size, and intensity of vessel pixels, complicating accurate segmentation [3,16,14].

In recent decades, numerous techniques have emerged for automatically segmenting retinal vessels using fundus examination, garnering considerable attention from the scientific community due to their increasingly accurate outcomes [13]. These methods are typically categorized as supervised or unsupervised. Supervised methods involve training a classifier with a dataset (training set) to differentiate between vessel and non-vessel pixels, further classified into machine learning and deep learning algorithms. Machine learning approaches typically involve feature extraction, selection, and classification stages, with various feature extractors and classifiers PSO-HRVSO for medical image classification, including bag-of-visual-words, Gaussian filter, and Gabor filter, along with classifiers like K-Nearest Neighbors (K-NN), Random Forest, Support Vector Machine (SVM), and Artificial Neural Networks (ANN) [12–31].

Deep learning techniques offer an advantage over traditional methods by automatically extracting features from raw data, eliminating the need for handcrafted features [34,32]. While supervised methods yield satisfactory results for healthy retinal vessel extraction, a notable limitation is the necessity for ground-truth images, which can be challenging to obtain. Additionally, both machine learning and deep learning algorithms demand time-consuming and computationally expensive training processes to effectively handle new sets of images [9].

Conversely, unsupervised methods in medical image processing involve image segmentation without relying on a training dataset. These approaches utilize various image processing techniques. Initially, the image undergoes enhancement procedures, typically employing morphological operations [33], matched filter responses [39], the complex continuous wavelet transform [37], adaptive histogram equalization [35], Hessian-based filters [36, 38, 44], among others. Sub-

sequently, segmentation occurs through multilevel thresholding [40–43, 48] or region-oriented techniques such as region growing [45, 49] or active contours [46, 47]. These conventional unsupervised methods heavily rely on manual feature extraction for image element representation and segmentation. Generally, supervised methods exhibit higher efficiency and yield superior results [8]. However, unsupervised systems possess a significant advantage in performing vessel segmentation without prior knowledge of ground-truth labels, particularly beneficial for datasets lacking pixel-level labeling information [16]. Additionally, unsupervised methods offer computational efficiency and faster results. Recent research has utilized both supervised and unsupervised methodologies, demonstrating promising performance in retinal vessel segmentation. Nevertheless, the challenge of accurately segmenting thin vessels remains a significant hurdle for optimal performance in existing literature. Thin vasculature offers crucial information for detecting neovascular diseases [14], underscoring the importance of achieving improved vessel segmentation for enhanced detection and diagnosis of eye diseases [64].

This article presents a novel methodology aimed at accurately segmenting retinal vasculature to tackle prevalent challenges encountered in retinal vessel segmentation from eye fundus images. The PSO-HRVSO approach comprises three distinct phases: pre-processing, main processing, and post-processing. During the initial phase, a Gaussian filter is employed to yield a smoothed gray-scale fundus image, followed by PSO optimized image enhancement for obtaining an optimized enhanced fundus image. The main processing phase entails two configurations: the first configuration targets thick vessel segmentation through a combination of filters (Optimized top-hat, Homomorphic, and Median), whereas the second configuration focuses on thin vessel segmentation using a similar combination of filters (Optimized top-hat, Homomorphic, and Matched). Subsequently, morphological image processing is applied during the post-processing phase. Extensive experiments are conducted on two publicly available databases, DRIVE (51) and STARE (50), to evaluate the methodology's performance. The results of performance metrics underscore the method's advantages, demonstrating comparable or superior values in contrast to many contemporary techniques, which often entail higher computational complexity for retinal vessel segmentation.

The major contributions of this article can be outlined as follows:

- Introducing a novel methodology for segmenting thin and thick retinal blood vessels.
- Presenting a new variant of the classical top-hat operation termed as the optimized top-hat.
- Investigating the variation of parameters in the optimized top-hat filter and the homomorphic filter based on the vessel thickness.
- Developing an automated method for robust retinal vessel segmentation suitable for Computer Aided Diagnosing tools.
- Achieving a minimal false positive rate through this PSO-HRVSO method.
- Demonstrating superior specificity and accuracy compared to recent unsupervised methods and competitive performance with supervised methods, while maintaining low computational costs.

2. LITERATURE REVIEW

In the preceding section, numerous relevant papers in contemporary research focus on retinal vascular tree segmentation within fundus images, broadly categorized as supervised and unsupervised methods. Noteworthy advancements in retinal vessel segmentation are briefly outlined below, serving as benchmarks against which the PSO-HRVSO methodology is evaluated.

Recent unsupervised methodologies, such as those introduced by Wang et al. [85] in 2019, involved modifications to top-hat and bottom-hat transformations aimed at enhancing images by mitigating disturbances and noise. Their segmentation approach utilized a novel technique known as flattening of minimum circumscribed ellipse to identify vessels. Similarly, Diaz et al. [84] in the same year PSO-HRVSO employing the Lateral Inhibition technique (LI) to enhance contrast between fundus and retinal vessels. They employed the minimization of cross-entropy via the differential evolution (DE) algorithm for vessel segmentation, optimizing for efficient segmentation.

In 2020, Shukla et al. [89] introduced a fractional filter to eliminate artifacts and noise while preserving thin vessel edges. Their method involved extracting central line pixels using a proprietary algorithm and applying Principal Component Analysis (PCA) to assess eigenvalue maps, followed by region growing operations and localized thresholding for vessel segmentation. Likewise, Dos Santos et al. [88] in the same year utilized Contrast Limited Adaptive Histogram Equalization (CLAHE) and the Wiener filter to enhance image contrast and reduce noise. An Artificial Neural Network (ANN) was employed to optimize filter parameters for optimal results.

Furthermore, Zhou et al. [87] PSO-HRVSO an enhanced line detector followed by Hidden Markov Model (HMM) application for detecting thin vessel lines effectively. Finally, Pachade et al. [90] recommended a novel segmentation configuration involving contrast enhancement, 2D median linear filtering, morphological operations, background estimation, and iterative thresholding to achieve segmentation completeness.

On the contrary, recent developments in supervised methodologies are outlined. In 2019, Adapa et al. [74] introduced a supervised technique involving initial image preprocessing. This involved enhancing the image using a CLAHE filter to improve local contrast, followed by a top-hat transform. Subsequently, feature extraction utilized Zernike moments for binary classification through an Artificial Neural Network (ANN). Similarly, Yang et al. [71] employed the K-Singular Value Decomposition (K-SVD) to derive multiple complementary features using six distinct enhancement algorithms. However, their PSO-HRVSO method required manually annotated ground-truth data for training, essential for vessel classification into thin or thick vessels using the K-SVD algorithm for vessel segmentation dictionary training. Jin et al. [72] introduced the Deformable U-Net (DUNet) for segmentation, a hybrid of the traditional U-Net and Deformable Convolutional Network (Deformable-ConvNet). In 2020, Cheng et al. [73] PSO-HRVSO a novel U-Net architecture specifically tailored for retinal vessel segmentation, enhancing accuracy for vessels of various thicknesses by incorporating a dense block into the network configuration. Lastly, Wu et al. [75] introduced NFN+, a novel configuration comprising two cascading backbones connected by inter-network skip connections. The initial network processes image patches to generate probability maps of primary vessels, while the subsequent network refines these maps to produce segmented results. Supervised approaches entail learning from a model to predict pixel categorization, demonstrating superior performance compared to unsupervised methods. However, certain unsupervised models, including those highlighted here and those PSO-HRVSO in this study, achieve comparable or even superior results with reduced computational overhead and time constraints.

3. METHODOLOGY

This section provides a concise overview of the PSO-HRVSO algorithm, as illustrated in the flowchart depicted in Figure 1. Key concepts integral to the PSO-HRVSO methodology are outlined herein. Notably, the eye fundus image exhibits both thick and thin blood vessels, with the latter often overlooked by previous algorithms. The primary objective of this approach is to effec-

tively segment thick and thin vessels, resulting in two distinct images. These images are subsequently merged to produce a final segmentation outcome.

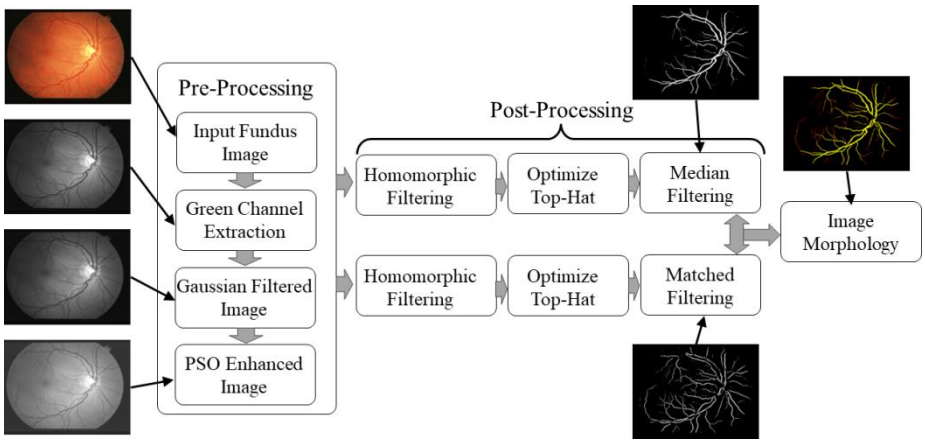

Figure 1:PSO-HRVSO method of vessels segmentation

3.1. Pre-processing

Prior to executing the thick and thin vessels processing phases, it is crucial to implement a pre-processing stage on a retinal eye fundus image, which significantly enhances the outcomes. This pre-processing task encompasses three stages: extracting the green channel of the image, employing a two-dimensional Gaussian filter, and enhancing it through PSO optimization.

3.1.1. Green Component Extraction

The input eye fundus image is presented in RGB format, indicating it's a 24-bit image, with each channel (red, green, and blue) comprising 8 bits. Consequently, the input can be viewed as a three-layered image, and its representation is as follows:

$$I_{Input} = [I_{Red} + I_{Green} + I_{Blue}] \quad (1)$$

The RGB input image, denoted as I_{Input}, consists of three channels: red (I_{Red}), green (I_{Green}), and blue (I_{Blue}). Each channel is represented by its respective layers. Upon analyzing individual channels, the green channel (I_{Green}) exhibits a significant contrast between vessels and the background. In contrast, the red (I_{Red}) and blue (I_{Blue}) channels display higher levels of noise and comparatively lower contrast [56]. Moreover, human visual perception is more responsive to the green channel compared to both red and blue channels [54]. Consequently, the green channel (I_{Green}) is extracted as a grayscale image for further processing.

3.1.2. Gaussian Filtering

While the green-channel of the eye fundus image exhibits commendable vessel-background contrast compared to the RGB input image, incorporating a noise removal step prior to subsequent stages yields positive and productive outcomes. The utilization of Gaussian smoothing filtering algorithm proves advantageous for enhancing image structures, including previously contrasted elements. This filtering technique operates by employing a Gaussian function, rooted in the normal distribution widely utilized in statistics, to compute the transformation applied to each pixel within the two-dimensional set. The Gaussian filtering representation $G(x, y)$ of an image is obtained through the convolution of the input image $I_{Green}(x, y)$ and the two-dimensional Gaussian kernel $g(x, y)$, the mathematical representation as follows:

$$g(x,y) = \frac{1}{2\pi\sigma^2} exp\left(-\frac{x^2+y^2}{2\sigma^2}\right) \quad (2)$$

The parameter σ represents the standard deviation within the Gaussian distribution, governing the extent or breadth of the filter's dispersion. Then the Gaussian distribution can be found from the equation 3.

$$G(x,y) = g(x,y) * I_{Green}(x,y) \quad (3)$$

In the event that the variance value approaches zero, the filter demonstrates an impulse function response, as articulated in Equation 4.

$$G(x,y) = I_{Green}(x,y) \quad (4)$$

With increasing σ^2, the filter's smoothing effect becomes more pronounced. Within this filter, image details significantly smaller than the standard deviation are entirely eliminated. Following various experiments, the variance is determined to be 0.472. The outcome of the pre-processing stage is depicted in Figure 2c.

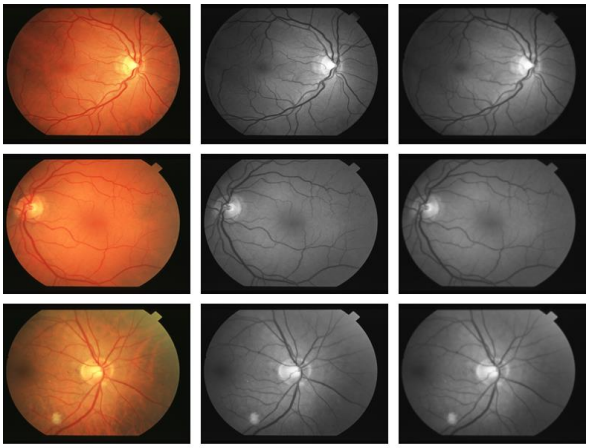

Figure 2: Shows the Gaussian Distributed results (a) Input RGB, (b) Green Component, (c) Gaussian Distribution

3.1.3. PSO Optimization

Particle swarm optimization (PSO) stands out as a widely recognized population-based optimization technique rooted in the principles of swarm intelligence. It leverages the collective behavior of a swarm to efficiently explore a designated search space in pursuit of the optimal solution. PSO operates by employing dynamic entities called "particles" that continually adjust their positions and velocities in a stochastic manner. These adjustments are directed both towards the most promising positions discovered by individual particles and across the entire search space. In a D-dimensional search space, with a swarm size denoted as X, each particle's position is represented as $P_i(p_{i_1}, p_{i_2}, p_{i_3}, \dots\dots\dots\dots, p_{i_D})$, offering a feasible solution to the optimization problem at hand. Correspondingly, the velocity of each particle is characterized by $U_i(u_{i_1}, u_{i_2}, u_{i_3}, \dots\dots\dots\dots, u_{i_D})$.The best previous position for each particle is denoted as $Q_i(q_{i_1}, q_{i_2}, q_{i_3}, \dots\dots\dots\dots, q_{i_D})$, while the overall best position identified by the entire swarm is represented as $Q_g(q_{g_1}, q_{g_2}, q_{g_3}, \dots\dots\dots\dots, q_{g_D})$. These equations, as cited in [53, 52, 55], govern the behaviour of the particles within the PSO framework.

$$u_{i_d}^{k+1} = \omega^k * u_{i_d}^k + a_1 * rand() * \left(q_{i_d} - p_{i_d}^k\right)\Delta t + a_2 * rand() * \left(q_{g_d} - p_{i_d}^k\right)/\Delta t \quad (5)$$

$$p_{i_d}^{k+1} = p_{i_d}^k + \Delta t * u_{i_d}^k \quad (6)$$

$$\omega^k = \omega_{max} - k * (\omega_{max} - \omega_{min})/k_{max}$$

The acceleration coefficients, identified as a_1 and a_2, and the inertia weight, represented by w where w_{max} and w_{min} denote the maximum and minimum values of w, are utilized within a random function $rand()$ adhering to a uniform distribution. The updated value and the maximum number of iterations are denoted by $u_{i_d}^{k+1}$ and $p_{i_d}^{k+1}$ respectively, where $d \in [1,\ D]$. The unit time is commonly denoted as Δt, and the conditions governing the restrictions on $u_{i_d}^{k+1}$ and $p_{i_d}^{k+1}$ are outlined as follows:

$$u_{i_d}^{k+1} = \begin{cases} u_{i_d}^{k+1} & -u_{max} \le u_{i_d}^{k+1} \le u_{max} \\ u_{max} & u_{i_d}^{k+1} > u_{max} \\ -u_{max} & u_{i_d}^{k+1} < -u_{max} \end{cases} \quad (7)$$

$$p_{i_d}^{k+1} = \begin{cases} p_{i_d}^{k+1} & -p_{max} \le p_{i_d}^{k+1} \le p_{max} \\ p_{init} & p_{i_d}^{k+1} > p_{max} \\ p_{init} & p_{i_d}^{k+1} < p_{min} \end{cases} \quad (8)$$

$$p_{init}^{k+1} = p_{min} + rand() * (p_{max} - p_{min}) \quad (9)$$

The term u_{max} denotes the peak value of u while p_{max} and p_{min} signify the upper and lower limits of p, respectively. Presented below is a concise overview of the fundamental stages engaged in the processing of PSO and figure 3 depict the outputs of PSO optimization with a swarm size of 28 and 100 iteration:

1. Commence by establishing the parameters of the Particle Swarm Optimization (PSO) framework, which encompass the maximum and minimum iteration weights, cognitive and social acceleration coefficients, population size, local window size, and the maximum iteration limit.
2. Select an RGB Fundus image as input and subsequently transform it into its green component.
3. Initialize the particles by defining their initial positions and velocities.
4. Evaluate the fitness values for the initialized particles.
5. Identify the optimal individual position for each particle within the swarm.
6. Employ equations 1, 2, and 3 to adjust the positions and velocities of the particles.
7. Update the best individual position for each particle and determine the best group position for the entire swarm.
8. Assess whether the maximum iteration limit has been reached. A. If the limit has been reached, output the particle with the highest HIS value. B. If not, return to step 6 and iterate the process.
9. Conclude the optimization process.

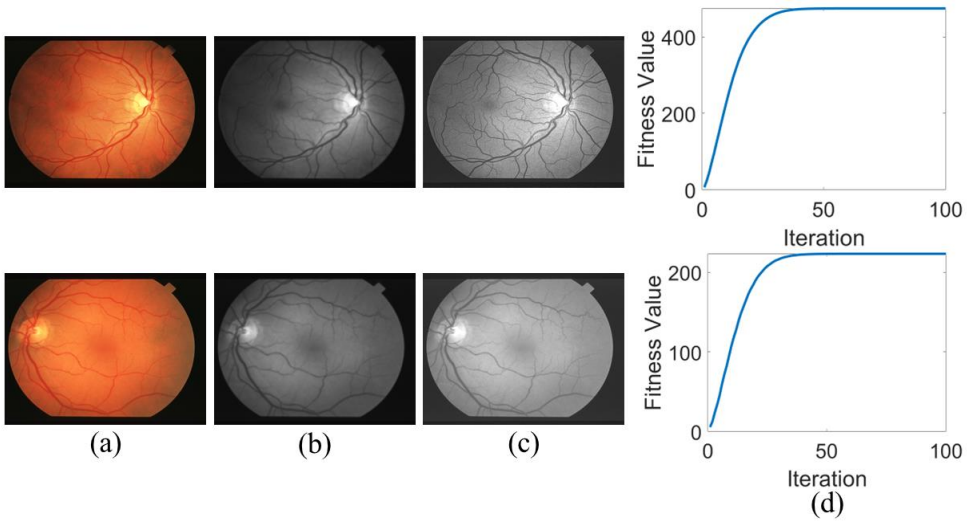

Figure 3: PSO Optimization: (a) RGB Image, (b) Gaussian Distribution, (c) PSO Enhanced, (d) Fitness Curve

3.2. Thick Vessels Segmentation

As illustrated in Figure 1, the thick vessel segmentation procedure comprises three distinct stages, which will be elaborated upon subsequently.

3.2.1. Optimized Top-Hat Algorithm

Morphological image operations serve as a robust tool for image manipulation. Mathematical morphology encompasses algebraic arithmetic operators that are employed on a grayscale 2-D eye fundus image. The top-hat morphological operation entails the disparity between the original image and its morphologically closed-form. This operation elucidates the interplay between the image and a structuring element characterized by specific size and shape [59]. It is utilized to amplify bright objects of interest set against a dark background, such as prominent blood vessels discerned from an image complement (a concept clarified later) of the green channel image where the background transitions to darkness. Denoting a grayscale 2-D image as I_{Input} and the structuring element as SE, the top-hat operation is defined by the following equation:

$$I_{Top\_Hat} = I_{Input} - \left(I_{Input} \circledcirc SE_O\right) \tag{10}$$

Various adaptations of the modified top-hat approach were introduced by Salembier et al. [57]. Mendonça et al. [58] and Bahadar Khan et al. [63] have previously applied these variations to blood vessel segmentation. This study proposes a novel optimized top-hat technique aimed at addressing certain issues identified in the conventional top-hat operation, as discussed in the aforementioned literature. One limitation is the failure to detect minor intensity fluctuations, which are crucial for identifying slender vessels. In this PSO-HRVSO method, the top-hat operator is first applied to a complementary image, and subsequently, morphological image operations are inverted. The PSO-HRVSO optimized top-hat can be described as follows:

$$I_{Optimized\_TH} = I^C_{Input} - \left(I^C_{Input} \circledcirc SE_O\right) \odot SE_C \tag{11}$$

SE_O and SE_E represent the structuring elements utilized for opening ⊙ and closing ⊙ operators correspondingly, while I^C_{Input} denotes the image complement of I_{Input}, delineated as follows:

$$I^C_{Input} = \frac{U}{I_{Input}} \tag{12}$$

The universe U represents all possible values that each pixel can assume. Subsequently, the operation defining the complement of an image is established as follows:

$$I^C_{Input}(x, y) = max(U) - I_{Input}(x, y) \tag{13}$$

The enhancement process for thick vessels utilizes a disk-shaped structuring element for both opening ⊙ and closing ⊙ operations, employing a radius of eight pixels for opening and sixteen pixels for closing.

Figure 4dand 4e illustrate the outcome of employing the PSO-HRVSO optimized top-hat filter and binarized top hat respectively on the input fundus image depicted in Figure 3a whereas figure 4b and 4c illustrate the outcome of employing global top-hat optimization and its binary part. Both Figure 4b and Figure 4d were generated using a structuring element of the same shape and size for both opening and closing operations (a disk with a radius of 10 pixels). A qualitative examination of the images reveals that the PSO-HRVSO optimized top-hat filter significantly improves the contrast of the vessels compared to the classical top-hat filter, enhancing both thick and thin vessels.

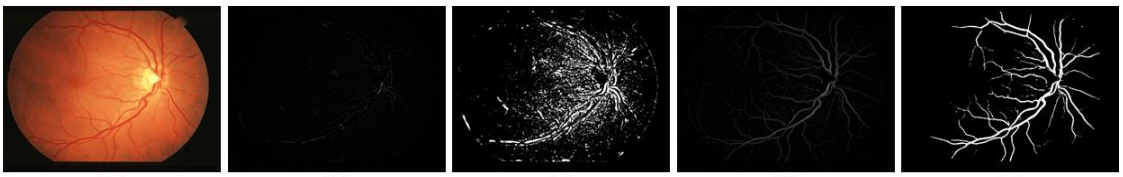

Figure 4: Optimized Top-Hat: (a) Input RGB, (b) Conventional Top-Hat, (c) Binary of (b), (d) Optimized Top-Hat, (e) Binary of (d).

3.2.2. Homomorphic Filtering

If we view it through the lens of the classical intensity model for digital images, an image can be seen as the outcome of light reflected from a scene, subsequently captured by a camera to create the image. Typically, this model is described in relation to the spatial distributions of intensity [60] within a two-dimensional function (such as an image represented by $I_{fundus}(x, y)$), and it is typically depicted as:

$$I_{fundus}(x, y) = l_{fundus}(x, y) r_{fundus}(x, y) \tag{14}$$

In this context, $l_{fundus}(x, y)$ denotes the brightness of the illumination, while $r_{fundus}(x, y)$ delineates the spatial spread of the reflectance, which is formed and influenced by the inherent characteristics of the object and the surrounding environment.

Homomorphic filtering operates in the frequency domain, enabling the adjustment of both illumination and reflectance intensities across the spectral range of an image. This capability facilitates diverse analyses through the application of multiple frequency-domain filters. Typically, the re-

flectance component, $r_{fundus}(x,y)$, spans the entire frequency spectrum, while the illumination component's intensity $l_{fundus}(x,y)$, exhibits gradual changes characterized by low spatial frequencies. Consequently, the illumination component is often centralized within the 2D-Fourier frequency domain. A common challenge in vessel segmentation involves enhancing the reflectance from the fundus image while minimizing the influence of the illumination component's intensity. To address this, a linear frequency-domain filter is employed to attenuate low-frequency components and enhance high-frequency intensities.

The natural logarithm serves as a mathematical tool that transforms multiplication into addition. By applying this principle to Equation 14, we derive the subsequent equation:

$$z_{fundus}(x,y) = ln\left(I_{fundus}(x,y)\right) = ln\left(l_{fundus}(x,y)r_{fundus}(x,y)\right) = ln\left(l_{fundus}(x,y)\right) + ln\left(r_{fundus}(x,y)\right) \quad (15)$$

The logarithm functions as a homomorphism, thus named the filtering process, which translates from a multiplicative number group to an additive number group. This transition enables the application of linear filtering processes. Equation 15 undergoes Fourier transformation, a step that isn't directly feasible due to the inseparability of function multiplication in the Fourier domain.

$$Fn\left[z_{fundus}(x,y)\right] = Fn_z(u,v) + Fn_r(u,v) \quad (16)$$

Filtering is achieved through the multiplication of the image $Fn_z(u,v)$ by a frequency-domain filter $H_{fn}(u,v)$. Among various transfer functions experimented with, the Gaussian high-pass response proves particularly effective for eye fundus images, as represented in Equation 17 in the frequency domain.

$$H_{fn}(u,v) = 1 - exp\left(\frac{-D^2(u,v)}{2\sigma^2}\right) \quad (17)$$

Where $D(u,v) = \sqrt{u^2+v^2}$ and σ represents the measure of the dispersion of the Gaussian curve. The greater the value of σ, the higher the cut-off frequency and the gentler the filtering effect. Upon implementing the filter, we derive the following equation:

$$G_{fn}(u,v) = Fn_z(u,v)H_{fn}(u,v) = Fn_l(u,v)H_{fn}(u,v) + Fn_r(u,v)H_{fn}(u,v) \quad (18)$$

The filtered spectrum of the processed signal is restored by applying a subsequent inverse Fourier transformation in the following manner:

$$Fn^{-1}\left[G_{fn}(u,v)\right] = Fn^{-1}\left[Fn_l(u,v)H_{fn}(u,v)\right] + Fn^{-1}\left[Fn_r(u,v)H_{fn}(u,v)\right] \quad (19)$$

$$g_{fundus}(x,y) = l'_{fundus}(x,y) + r'_{fundus}(x,y) \quad (20)$$

Ultimately, the filtered image, denoted as $l'_{fundus}(x,y)$, undergoes an exponential transformation to reverse the effects of the logarithmic transformation. Equation 21 encapsulates the formulation of this final step in the process.

$$I'_{fundus}(x,y) = exp\left[g_{fundus}(x,y)\right] = exp\left[l'_{fundus}(x,y)\right]exp\left[r'_{fundus}(x,y)\right] \quad (21)$$

Although the illumination and reflectance components aren't completely distinguished in the spectral domain, the homomorphic approach remains a valuable tool that produces significantly

enhanced images [61]. In this scenario, a sigma (σ) value of two is employed to amplify thick vessels, which have considerably higher reflectance values compared to thin vessels.

3.2.3. Median Filtering

Prior to the final operation, salt and pepper noise, induced by a low value of σ during the homomorphic filtering procedure, is eliminated using a median filter. It is noteworthy that the median filter is adept at retaining edges while eliminating noise. It possesses the capability to differentiate between isolated noise and intrinsic features of the input image, such as sharp edges and other details. This capability pertains to high spatial frequencies, thereby preserving previously enhanced thick vessels. The median filter operates by substituting each pixel in the image with the median intensity value within a designated neighborhood $R_n(m,n)$. Mathematically, the resultant image $I'_{median}(x,y)$ after the median filtering process of an image $I_{input}(x,y)$ can be expressed as:

$$I'_{median}(x,y) = M_e\big(I_{input}(m,n), (m,n) \in R\big) \tag{22}$$

The median value of pixels within the region $R_n(m,n)$ is denoted as M_e. Although the noise generated in earlier stages is minimal, it significantly impacts the outcome. The neighborhood size is represented by a matrix of dimensions [2, 2].

Recently, the optimized top-hat method has been reintroduced to enhance the profile of thick vessels, effectively filling small black pixel regions within them. In this instance, the dimensions of the disk-shaped structuring element are notably increased compared to the previous optimized top-hat approach. Operations involving both opening and closing are suggested, with radii of thirty-two and eighty-six, respectively. Figure 5 illustrates the outcome of these concepts.

3.3. Thin Vessels Segmentation

The process of segmenting thin vessels involves two stages similar to those used for thick vessels, as outlined in figure 5. However, the specific methods are not elaborated upon in this section. Nevertheless, the PSO-HRVSO parameters for these shared stages will be outlined here.

Building upon the methodology described in the preceding section, and considering the finer scale of thin blood vessels which occupy smaller pixel sizes, a disk-shaped structuring element with radii of 5 and 25 pixels is PSO-HRVSO for opening and closing operations, respectively. As thin vessels encompass only a small percentage of the image, their total reflectance component value is comparatively lower than that of thick vessels. To enhance the visibility of these small white regions, a σ value of twenty is utilized to expand the cut-off regions of the filter. This enhancement improves all white components of the image, including the small vessels, albeit at the expense of thinning the thick and major veins of the vascular tree. However, this thinning effect will later be rectified by merging the segmented image of thick veins with the resultant image of subsequent steps.

When analyzing a gray-scale image in segments, the parts within it often resemble certain distribution curves. Two-dimensional matched filters are specifically crafted to amplify image sections that correspond to a particular distribution. Thus, this filtering technique seeks a level of correlation between the specified distribution and the local image area. The strategy behind employing a matched filtering method aims to identify segmented linear segments of blood vessels in fundus images. These segments' grayscale profile can typically be approximated by a Gaussian-shaped curve [62]. This Gaussian distribution, referred to as the kernel, undergoes rotation by an angular

step θ. Subsequently, it is convolved with the input image areas to enhance the matched regions. The rotation of the kernel is achieved through a rotation matrix RM, represented as follows:

$$RM = \begin{bmatrix} cos\theta & -sin\theta \\ sin\theta & cos\theta \end{bmatrix} \tag{23}$$

Non-vessel regions (i.e. low value of response) are not enhanced. The matched filter kernel is defined as follows:

$$f_{matched}(x,y) = -k\ exp\left(\frac{-x^2}{2\sigma^2}\right), for\ |y| \leq L/2 \tag{24}$$

Considerations should be made regarding the length (L) of the vessel's piecewise element and the spread (σ) of the kernel intensity profile. It is notable in the literature that blood vessels typically exhibit low curvatures. Therefore, it is crucial to search for rotations of anti-parallel pairs within estimated piecewise elements. Additionally, small blood vessels often lack significant local contrast. Despite previous homomorphic enhancement techniques, small vessels exhibit a low reflectance component compared to other inner surfaces of the human eye. Their appearance is characterized by lower illumination than the relative background, and their width decreases as they traverse the vascular tree.

To address these factors, vessel orientation may vary, and it is assumed that the vessel direction aligns with the y-axis. For thin vessel segmentation, the kernel undergoes rotation at seven-degree intervals, spanning angles from θ = 0, 7, 14 to 182 degrees, resulting in 26 different rotations. Recommended parameters for this methodology include a σ value of 0.8 and a kernel size of 7 × 7 pixels. This choice is informed by the common widths of retinal blood vessels, which typically range from 2 to 10 pixels (equivalent to 36 to 180μm). By employing this method, the likelihood of false detection of vasculature is reduced, consequently lowering the false positive rate.

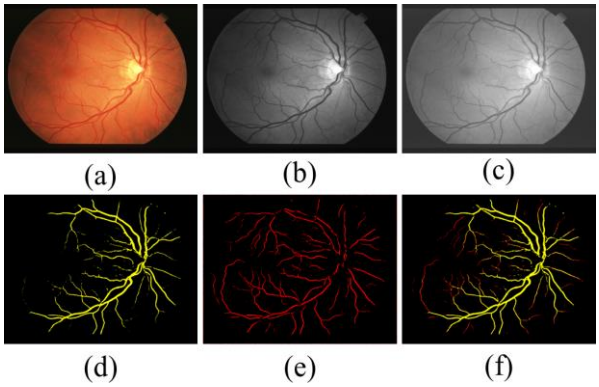

Figure 5: Vessels Segmentation: (a) Input RGB, (b) Green Component, (c) PSO Optimized, (d) Segmented Thick Vessels, (e) Segmented Thin Vessels, (f) Combined Vessels

3.4. Post Processing

The integration of thick and thin vessel segmentation in binary form involves applying a bitwise OR operation, followed by the generation of a final segmentation image illustrating the outcomes from both branches depicted in Figure 1. To eliminate small undesired components and noise generated in prior phases, a final post-processing step is executed. This step employs morphological image techniques including dilation, erosion, and a connectivity assessment to eliminate binary elements smaller than a predetermined pixel size, resulting in a definitive binary image for

subsequent evaluation. The ultimate outcome of the segmentation procedure is depicted in Figure 5(f).

4. RESULTS AND DISCUSSION

This section presents the performance outcomes of the PSO-HRVSO method applied to two eye fundus datasets for retinal vessel segmentation: DRIVE [51] and STARE [50], both publicly accessible. The DRIVE dataset comprises 40 images divided into two subsets of 20 elements each, designated as the training and test sets. All images were captured using a Canon CR5 nonmydriatic 3CCD camera with a 45^0 field of view and a spatial resolution of 565 × 584 pixels [91]. Additionally, the DRIVE image dataset includes manual segmentation conducted and validated by three trained human observers with medical expertise. The training subset involves the manual segmentation of one set by a single human observer, while the test subset underwent manual segmentation by two human observers, offering dual perspectives and establishing ground-truth images for performance analysis.

On the other hand, the STARE dataset comprises 397 digitized eye fundus images acquired using a TopCon TVR-50 fundus camera with a 35^0 field of view and a spatial resolution of 605×700 pixels [50]. Among these images, manual segmentation was performed for only 25 by two observers. The first observer segmented 11.2% of the entire image pixels as vascular tree pixels, while the second observer segmented a total of 14.6%. Both datasets encompass healthy and diseased fundus images, including various vascular abnormalities, diabetic retinopathy, choroidal neovascularization, arteriosclerotic retinopathy, among others.

To conduct a mathematical analysis and determine the accuracy of segmentation, three performance metrics are employed: Specificity (Spe), Sensitivity (Sen), and Accuracy (Acc). These metrics are defined mathematically as follows:

$$Sensitivity(Sen) = \frac{True\ Positive(T_P)}{True\ Positive(T_P) + False\ Negative(F_N)}$$

$$Specificity(Spe) = \frac{True\ Negative(T_N)}{True\ Negative(T_N) + False\ Positive(F_P)}$$

$$Accuracy(Acc) = \frac{T_P + T_N}{T_P + T_N + F_P + F_N}$$

Table 1: Results of the PSO-HRVSO methodology applied to DRIVE dataset

Images	Observer 1			Observer 2		
	Sen	Spe	Acc	Sen	Spe	Acc
01_test	0.8358	0.9742	0.9754	0.8437	0.9834	0.9715
02_test	0.8159	0.9867	0.9823	0.8164	0.9847	0.9794
03_test	0.8422	0.9831	0.9854	0.8519	0.9881	0.9837
04_test	0.7891	0.9928	0.9745	0.7974	0.9943	0.9829
05_test	0.7843	0.9936	0.9942	0.8036	0.9942	0.9918
06_test	0.8251	0.9849	0.9937	0.8284	0.9837	0.9916
07_test	0.8735	0.9874	0.9821	0.8734	0.9862	0.9864
08_test	0.8715	0.9942	0.9825	0.8839	0.9911	0.9838
09_test	0.8694	0.9837	0.9875	0.8734	0.9871	0.9827
10_test	0.8846	**0.9957**	0.9943	0.8858	0.9958	0.9918
11_test	0.8723	0.9943	0.9843	0.8868	0.9969	0.9837
12_test	0.8264	0.9785	0.9826	0.8234	0.9741	0.9784
13_test	0.8531	0.9938	0.9746	0.8519	0.9961	0.9721
14_test	0.8591	0.9892	0.9853	0.8587	0.9873	0.9864
15_test	0.8664	0.9875	0.9746	0.8738	0.9834	0.9766
16_test	0.8697	0.9828	0.9748	0.8769	0.9845	0.9784
17_test	0.8856	0.9914	0.9872	0.8821	0.9961	0.9867
18_test	**0.8946**	0.9849	0.9836	0.8937	0.9837	0.9817
19_test	0.8935	0.9932	0.9941	**0.8981**	0.9957	0.9969
20_test	0.8816	0.9941	0.9843	0.8776	**0.9971**	0.9792
21_test	0.8829	0.9852	0.9971	0.8872	0.9831	0.9944
22_test	0.8426	0.9847	0.9876	0.8265	0.9881	0.9848
23_test	0.8247	0.9911	**0.9982**	0.8319	0.9935	**0.9971**
24_test	0.8167	0.9927	0.9934	0.8264	0.9938	0.9964
25_test	0.8935	0.9857	0.9861	0.8897	0.9862	0.9908
Mean	0.8542	0.9882	0.9856	0.8577	0.9891	0.9852

True Positive (T_P) denotes the number of pixels identified as vessels in both the ground-truth and the segmented image. True Negative (T_N) indicates the count of pixels accurately classified as non-vessels in both the ground-truth and the segmented image. False Positive (F_P) represents the number of pixels identified as vessels in the segmented image but are non-vessel pixels in the ground-truth. Finally, False Negative (F_N) illustrates the number of pixels incorrectly classified as non-vessels in the segmented image when they correspond to vessels in the ground-truth.

Table 1 displays the performance results of applying segmentation metrics from the PSO-HRVSO methodology to the DRIVE dataset against observer 1 and observer 2. The method achieves a specificity of 0.9882, sensitivity of 0.8542, and average precision of 0.9856 compared to observer 1.

Similarly, against observer 2, the method achieves averages of 0.9891, 0.8577, and 0.9852 for these metrics, respectively. The maximum specificity values against observers 1 and 2 occur in image 10_test, reaching 0.9957 and in image 20_test, reaching 0.9971, respectively. Conversely, the minimum specificity values against observers 1 and 2 are 0.9742 and 0.9741, observed in images 01_test and 12_test, respectively.

Table 2 presents the metrics results of comparing the segmentation performed by the PSO-HRVSO method with both observers for the STARE data-set. The average sensitivity, specificity,

and accuracy achieved when comparing the segmented image with the ground-truth of observer 1 are 0.8577, 0.9868, and 0.9836, respectively. Similarly, when compared with the ground-truth of observer 2, these metrics are 0.8576, 0.9868, and 0.9831. The highest specificity values against observers 1 and 2 are 0.9974 in image im0038 and 0.9967 in image im0021, respectively. Conversely, the lowest specificity values against observers 1 and 2 are 0.9718 in image im0278 and 0.9739 in image im0056.

Table 2: Results of the PSO-HRVSO methodology applied to STARE dataset

Images	Observer 1			Observer 2		
	Sen	Spe	Acc	Sen	Spe	Acc
im0001	0.7925	0.9921	0.9951	0.7895	0.9878	0.9955
im0006	0.8244	0.9937	0.9927	0.8235	0.9938	0.9884
im0008	0.8257	0.9841	0.9842	0.8284	0.9926	0.9824
im0009	0.8317	0.9964	0.9934	0.8321	0.9897	**0.9968**
im0012	0.8341	0.9859	0.9763	0.8364	0.9918	0.9719
im0015	0.8347	0.9811	0.9748	0.8369	0.9792	0.9737
im0017	0.8522	0.9842	0.9822	0.8581	0.9846	0.9818
im0021	0.8761	0.9964	0.9851	0.8743	**0.9967**	0.9841
im0024	0.8795	0.9937	0.9837	0.8784	0.9896	0.9862
im0038	0.8628	**0.9974**	0.9942	0.8617	0.9933	0.9921
im0047	0.8748	0.9833	0.9901	0.8788	0.9818	0.9912
im0056	0.8691	0.9719	0.9871	0.8738	0.9739	0.9887
im0081	0.8824	0.9848	0.9833	0.8654	0.9864	0.9837
im0090	0.8857	0.9927	0.9858	0.8855	0.9899	0.9868
im0102	0.8749	0.9967	0.9869	0.8765	0.9927	0.9829
im0138	0.8869	0.9924	0.9925	0.8815	0.9964	0.9924
im0154	0.8871	0.9817	0.9847	0.8911	0.9791	0.9843
im0197	0.8215	0.9824	0.9723	0.8233	0.9867	0.9755
im0243	0.8166	0.9861	0.9611	0.8167	0.9865	0.9581
im0251	0.8546	0.9913	0.9637	0.8516	0.9922	0.9655
im0274	0.8612	0.9743	0.9728	0.8644	0.9854	0.9737
im0278	**0.8927**	0.9718	0.9738	**0.8917**	0.9739	0.9716
im0289	0.8715	0.9738	0.9829	0.8719	0.9718	0.9867
im0294	0.8657	0.9955	0.9954	0.8655	0.9897	0.9891
im0305	0.8852	0.9862	**0.9973**	0.8837	0.9857	0.9944
Mean	0.8577	0.9868	0.9836	0.8576	0.9868	0.9831

In Table 3, the results obtained are numerically contrasted against contemporary supervised and unsupervised methods, showcasing the efficiency and computational time across both datasets. Notably, the table highlights the highest average values among the three metrics for both supervised and unsupervised methods, which are denoted in bold. Specifically, in terms of specificity and accuracy, PSO-HRVSO attains the highest values of 0.9846 and 0.9856, respectively, whereas sensitivity peaks at 0.9230 with Liskowski et al. [64] for the DRIVE dataset. Similarly, for the STARE dataset, PSO-HRVSO achieves the highest specificity and accuracy scores of 0.9868 and 0.9833, while Liskowski et al. [64] secures the highest sensitivity at 0.9207. Despite not yielding the optimal outcomes, it's noteworthy that the approach is closely comparable in numerical terms

to methods necessitating training processes and ground-truth data, such as supervised methods, albeit with higher computational expenses.

Table 3: Comparative analysis of outcomes obtained from implementing the PSO-HRVSO methodology on both the DRIVE and STARE datasets, juxtaposed with state-of-the-art supervised and unsupervised methods.

Method	Year	DRIVE Dataset			STARE Dataset			Processing Time
		Sen	Spe	Acc	Sen	Spe	Acc	
Supervised methods								
Liskowski et al. [64]	2016	**0.9230**	0.9241	0.9160	**0.9207**	0.9304	0.9309	92.0s
Zhang et al. [65]	2017	0.7861	0.9712	0.9466	0.7882	0.9729	0.9547	23.40s
Orlando et al. [66]	2017	0.7897	0.9684	-	0.7680	0.9738	-	-
Dasgupta et al. [67]	2017	0.7691	0.9801	0.9533	-	-	-	-
Yan et al. [68]	2018	0.7653	0.9818	0.9542	0.7581	0.9846	0.9612	-
Thangaraj et al. [69]	2018	0.8014	0.9753	0.9606	0.8339	0.9536	0.9435	180.86s
Guo et al. [70]	2018	0.7046	0.9806	0.9613	0.5629	0.9816	0.9540	-
Yang et al. [71]	2019	0.756	0.9696	0.9421	0.7202	0.9733	0.9477	-
Jin et al. [72]	2019	0.7963	0.9800	0.9566	0.7595	0.9858	0.9641	17.65s
Cheng et al. [73]	2020	0.7672	0.9834	0.9559	-	-	-	-
Adapa et al. [74]	2020	0.6994	0.9811	0.9450	0.6298	0.9839	0.9486	81.0s
Wu et al. [75]	2020	0.7996	0.9813	0.9582	0.7963	0.9863	0.9672	88.0s
Unsupervised methods								
Zhang et al. [76]	2016	0.7743	0.9725	0.9476	0.7791	0.9758	0.9554	20.0s
Shahid et al. [77]	2017	0.7300	0.9790	0.9580	0.7900	0.9650	0.9510	-
Fan et al. [78]	2018	0.7360	0.9810	0.9610	0.7910	0.9710	0.9570	13.23s
Aguirre et al. [79]	2018	0.7854	-	0.9503	0.7116	0.9454	0.9231	-
Abdallah et al. [80]	2018	0.6887	0.9765	0.9389	0.6801	0.9711	0.9388	-
Pal et al. [81]	2018	0.6129	0.9744	0.9431	-	-	-	-
Yue et al. [82]	2018	0.7528	0.9731	0.9447	-	-	-	4.60s
Biswal et al. [83]	2018	0.7100	0.9700	0.9500	0.7000	0.9700	0.9500	3.30s
Diaz et al. [84]	2019	0.8464	0.9701	0.9619	0.8331	0.9619	0.9559	-
Wang et al. [85]	2019	0.7287	0.9775	0.9446	0.7526	0.9733	0.9503	4.50s
Roy et al. [86]	2019	0.4392	0.9622	0.9295	0.4317	0.9718	0.9488	0.10s
Zhou et al. [87]	2020	0.7262	0.9803	0.9475	0.7865	0.9730	0.9535	63.2s
Dos Santos et al. [88]	2020	0.7702	0.9695	0.9519	-	-	-	-
Shukla et al. [89]	2020	0.7015	0.9836	0.9476	0.7023	0.9863	0.9573	1.41s
Pachade et al. [90]	2020	0.7738	0.9721	0.9552	0.7769	0.9688	0.9543	4.78s
PSO-HRVSO	2024	0.8559	**0.9846**	**0.9854**	0.8577	**0.9868**	**0.9833**	24.0s

The mean processing times derived for each method as detailed in Table 3 were sourced from existing literature. Analysis of Table 3 reveals that the PSO-HRVSO method demonstrates shorter processing times compared to both supervised and unsupervised methods based on performance data. Furthermore, the PSO-HRVSO algorithm demonstrates competitive processing times compared to both supervised and unsupervised methods. Moreover, it exhibits superior efficiency values across all three-performance metrics.

5. PSEUDOCODE

Begin /* (Pseudocode) */

Begin /* (Gaussian Flitering over RGB Image) */
rgbImage = imread(Input RGB image.jpg'); */* Read the input RGB image */*
greenImage = rgbImage(:, :, 2); */*RGB to Green Component conversion */*
gaussianKarnel = Gaussian kernel size = 3;
σ = Standard Deviation
/ Compute the size of the Gaussian kernel based on the standard deviation */*
/ Calculate the Gaussian function for each pixel in the kernel */*

$$G(x,y) = (1 / (2 * \pi * sigma^2)) * exp(-((x^2 + y^2)/(2 * sigma^2)))$$

End /* (Gaussian Flitering over RGB Image) */

Begin /* *(Image Enhancement using PSO)* */
objectiveFunction = @(x) computeObjective(x, grayscaleImage); */* Define the objective function for image enhancement */*
numParticles = 100; */* Set PSO parameters */*
numIterations = 100;
maxVelocity = 2;
c1 = 2; */* Cognitive component weight */*
c2 = 2; */* Social component weight */*
/ Initialize particles and velocities */*
particlePositions = initializeParticles(numParticles);
particleVelocities = initializeVelocities(numParticles);
/ Initialize the best positions and global best position */*
particleBestPositions = particlePositions;
globalBestPosition = particlePositions(1, :);
/* Perform PSO iterations */
for iteration = 1:numIterations
particleFitness = evaluateFitness(objectiveFunction, particlePositions); */* Evaluate the fitness of each particle */*
for particle = 1:numParticles */* Update particle best positions */*
if particleFitness(particle) < evaluateFitness(objectiveFunction, particleBestPositions(particle, :))
particleBestPositions(particle, :) = particlePositions(particle, :);
end
end
[~, globalBestIndex]=min(particleFitness); */*Update global best position */*
globalBestPosition = particlePositions(globalBestIndex, :);
particleVelocities = updateVelocities(particleVelocities, particlePositions, particleBestPositions, globalBestPosition, c1, c2, maxVelocity); /* Update particle velocities and positions */
particlePositions = updatePositions(particlePositions, particleVelocities);
end
enhancedImage = performEnhancement(globalBestPosition, grayscaleImage); /* Perform image enhancement using the global best position */
End /* *(Image Enhancement using PSO)* */

Begin /* (Homomorphic Filtering) */

$$I(x,y) = luminance(x,y) * reflectance(x,y)$$

$$Z(x,y) = ln\big(I(x,y)\big) = ln\big(luminance(x,y) * reflectance(x,y)\big)$$
$$= ln\big(luminance(x,y)\big) + ln\big(reflectance(x,y)\big)$$

$$Fn[Z(x,y)] = Fn_z(u,v) + Fn_r(u,v)$$

$$H_{fn}(u,v) = 1 - exp\left(\frac{-D^2(u,v)}{2\sigma^2}\right)$$

$$G_{fn}(u,v) = Fn_z(u,v)H_{fn}(u,v) = Fn_l(u,v)H_{fn}(u,v) + Fn_r(u,v)H_{fn}(u,v)$$

$$Fn^{-1}\big[G_{fn}(u,v)\big] = Fn^{-1}\big[Fn_l(u,v)H_{fn}(u,v)\big] + Fn^{-1}\big[Fn_r(u,v)H_{fn}(u,v)\big]$$

$g(x,y) = luminance'(x,y) + reflectance'(x,y)$
$I'(x,y) = exp[g(x,y)] = exp[luminance'(x,y)]exp[reflectance'(x,y)]$
End /* (Homomorphic Filtering) */

Begin /* (Optimized Top-Hat Algorithm)
inputImage = enhancedImg; */* Read the input image */*
/ Apply morphological operations for noise removal or smoothing */*
SE = strel('disk', size); */* Define a disk-shaped structuring element with specified size */*
morphImage = imopen(grayImage, SE); */* Perform opening operation */*
tophatImage = imtophat(morphImage, SE); */* Perform TOP-HAT transform for image enhancement */*
End /* (Optimized Top-Hat Algorithm)
Thick_Threshold = median_filtering(tophatImage)
Thin_Threshold = matched_filtering(tophatImage)
Segmented_Vessels = Thick_Threshold + Thin_Threshold.

End /* (Pseudocode) */

6. CONCLUSION & FUTURE WORK

We introduce a novel approach aimed at enhancing the segmentation of the retinal vascular tree in human eye fundus images. The methodology hinges on a segmentation process divided into two branches: thin and thick vessel detection. Notably, our method achieves high specificity without necessitating manual segmentation or resource-intensive training techniques. Comparative analysis of our method, applied to both the DRIVE and STARE datasets, reveals its superiority over existing unsupervised methods in the literature. Particularly, it excels in extracting thin vessels with greater precision compared to current methodologies.

Central to our framework is the parameter variation of optimized top-hat and homomorphic filtering stages, tailored to the segmentation results of thin and thick vessels. This adaptive feature significantly enhances segmentation accuracy and specificity. However, a limitation of our proposal is its relatively lower sensitivity compared to state-of-the-art values. To address this, we plan to explore reinforced learning algorithms to optimize the methodology's parameters and improve sensitivity.

Looking ahead, we aim to integrate this method as a preprocessing step in a robust computer-aided diagnosis (CAD) system for classifying healthy and unhealthy fundus images based on retinal vessel segmentation. The crux lies in achieving high specificity segmentation, minimizing false positives, and ensuring accurate diagnostic interpretations—an aspect we prioritize in our proposal's development.

DECLARATION OF COMPETING INTEREST

The authors assert that they do not possess any identifiable competing financial interests or personal relationships that might have been perceived to impact the findings presented in this paper.

REFERENCES

[1] I.P. Chatziralli , E.D. Kanonidou , P. Keryttopoulos , P. Dimitriadis , L.E. Papazisis , The value of fundoscopy in general practice, The open ophthalmology journal 6 (2012) 4 .
[2] R. Vega , G. Sanchez-Ante , L.E. Falcon-Morales , H. Sossa , E. Guevara , Reti- nal vessel extraction using lattice neural networks with dendritic processing, Computers in biology and medicine 58 (2015) 20–30 .

[3] X. Xiao , S. Lian , Z. Luo , S. Li , Weighted res-unet for high-quality retina vessel segmentation, in: 2018 9th International Conference on Information Technol- ogy in Medicine and Education (ITME), IEEE, 2018, pp. 327–331 .

[4] J.J. Kanski , B. Bowling , Clinical ophthalmology: a systematic approach, Elsevier Health Sciences, 2011 .

[5] M. Ortega , M.G. Penedo , J. Rouco , N. Barreira , M.J. Carreira , Personal verifica- tion based on extraction and characterisation of retinal feature points, Journal of Visual Languages & Computing 20 (2) (2009) 80–90 .

[6] Y.Q. Zhao , X.H. Wang , X.F. Wang , F.Y. Shih , Retinal vessels segmentation based on level set and region growing, Pattern Recognition 47 (7) (2014) 2437–2446 .

[7] Y. Zhao , J. Xie , H. Zhang , Y. Zheng , Y. Zhao , H. Qi , Y. Zhao , P. Su , J. Liu , Y. Liu , Retinal vascular network topology reconstruction and artery/vein classifica- tion via dominant set clustering, IEEE transactions on medical imaging (2019) .

[8] Q. Li , B. Feng , L. Xie , P. Liang , H. Zhang , T. Wang , A cross-modality learn- ing approach for vessel segmentation in retinal images, IEEE transactions on medical imaging 35 (1) (2015) 109–118 .

[9] B. Yin , H. Li , B. Sheng , X. Hou , Y. Chen , W. Wu , P. Li , R. Shen , Y. Bao , W. Jia , Vessel extraction from non-fluorescein fundus images using orienta- tion-aware detector, Medical image analysis 26 (1) (2015) 232–242 .

[10] Y. Gavet , M. Fernandes , J. Debayle , J.-C. Pinoli , Dissimilarity criteria and their comparison for quantitative evaluation of image segmentation: applica- tion to human retina vessels, Machine vision and applications 25 (8) (2014) 1953–1966 .

[11] L.C. Neto , G.L. Ramalho , J.F.R. Neto , R.M. Veras , F.N. Medeiros , An unsupervised coarse-to-fine algorithm for blood vessel segmentation in fundus images, Ex- pert Systems with Applications 78 (2017) 182–192 .

[12] J.M. Patel , N.C. Gamit , A review on feature extraction techniques in con- tent based image retrieval, in: 2016 International Conference on Wireless Communications, Signal Processing and Networking (WiSPNET), IEEE, 2016, pp. 2259–2263 .

[13] M.M. Fraz , P. Remagnino , A. Hoppe , B. Uyyanonvara , A.R. Rudnicka , C.G. Owen , S.A. Barman , Blood vessel segmentation methodologies in retinal images–a survey, Computer methods and programs in biomedicine 108 (1) (2012) 407–433 .

[14] L. Mou , L. Chen , J. Cheng , Z. Gu , Y. Zhao , J. Liu , Dense dilated network with probability regularized walk for vessel detection, IEEE transactions on medi- cal imaging (2019) .

[15] R. Vaddi , M. Prabukumar , Comparative study of feature extraction techniques for hyper spectral remote sensing image classification: a survey, in: 2017 In- ternational Conference on Intelligent Computing and Control Systems (ICI- CCS), IEEE, 2017, pp. 543–548 .

[16] J. Mo , L. Zhang , Multi-level deep supervised networks for retinal vessel seg- mentation, International journal of computer assisted radiology and surgery 12 (12) (2017) 2181–2193.

[17] D. Liu , S. Wang , D. Huang , G. Deng , F. Zeng , H. Chen , Medical image classifica- tion using spatial adjacent histogram based on adaptive local binary patterns, Computers in biology and medicine 72 (2016) 185–200 .

[18] Y. Zhang , R. Liu , X. Wang , H. Chen , C. Li , Boosted binary harris hawks opti- mizer and feature selection, structure 25 (2020) 26 .

[19] R.A . Ibrahim , A .A . Ewees , D. Oliva , M. Abd Elaziz , S. Lu , Improved salp swarm algorithm based on particle swarm optimization for feature selection, Journal of Ambient Intelligence and Humanized Computing 10 (8) (2019) 3155–3169 .

[20] B.S. Vidya , E. Chandra , Entropy based local binary pattern (elbp) feature ex- traction technique of multimodal biometrics as defence mechanism for cloud storage, Alexandria Engineering Journal 58 (1) (2019) 103–114 .

[21] A .A . Ewees , M. Abd El Aziz , A.E. Hassanien , Chaotic multi-verse optimiz- er-based feature selection, Neural computing and applications 31 (4) (2019) 991–1006 .

[22] J. Sivic , A. Zisserman , Video google: A text retrieval approach to object match- ing in videos, in: null, IEEE, 2003, p. 1470 .

[23] M. Ahmad , S. Shabbir , D. Oliva , M. Mazzara , S. Distefano , Spatial-prior gener- alized fuzziness extreme learning machine autoencoder-based active learning for hyperspectral image classification, Optik 206 (2020) 163712 .

[24] H. Tang , Y. Xu , A. Lin , A.A. Heidari , M. Wang , H. Chen , Y. Luo , C. Li , Predicting green consumption behaviors of students using efficient firefly grey wolf-as- sisted k-nearest neighbor classifiers, IEEE Access 8 (2020) 35546–35562 .

[25] V. Nguyen , M. Blumenstein , An application of the 2d gaussian filter for enhancing feature extraction in off-line signature verification, in: 2011 In- ternational Conference on Document Analysis and Recognition, IEEE, 2011, pp. 339–343 .

[26] H. Chantar , M. Mafarja , H. Alsawalqah , A .A . Heidari , I. Aljarah , H. Faris , Fea- ture selection using binary grey wolf optimizer with elite-based crossover for arabic text classification, Neural Computing and Applications 32 (16) (2020) 12201–12220 .

[27] D.J. Reddy , T.A. Prasath , M.P. Rajasekaran , G. Vishnuvarthanan ,Brain and pan- creatic tumor classification based on glcm??k-nn approaches, in: Interna- tional Conference on Intelligent Computing and Applications, Springer, 2019, pp. 293–302 .

[28] B.A. Devi , M.P. Rajasekaran , Performance evaluation of mri pancreas image classification using artificial neural network (ann), in: Smart Intelligent Com- puting and Applications, Springer, 2019, pp. 671–681 .

[29] E. Rodríguez-Esparza , L.A. Zanella-Calzada , D. Oliva , M. Pérez-Cisneros , Au- tomatic detection and classification of abnormal tissues on digital mammo- grams based on a bag-of-visual-words approach, in: Medical Imaging 2020: Computer-Aided Diagnosis, 11314, International Society for Optics and Pho- tonics, 2020, p. 1131424 .

[30] Y. Hamamoto , S. Uchimura , M. Watanabe , T. Yasuda , Y. Mitani , S. Tomita , A ga- bor filter-based method for recognizing handwritten numerals, Pattern recog- nition 31 (4) (1998) 395–400 .

[31] A. Subudhi , M. Dash , S. Sabut , Automated segmentation and classification of brain stroke using expectation-maximization and random forest classifier, Biocybernetics and Biomedical Engineering 40 (1) (2020) 277–289 .

[32] Y. Zaychenko , G. Hamidov , Hybrid fuzzy cnn network in the problem of med- ical images classification and diagnostics, in: The International Conference on Natural Computation, Fuzzy Systems and Knowledge Discovery, Springer, 2019, pp. 883–891 .

[33] V. Aggarwal , A. Gupta , Integrating morphological edge detection and mu- tual information for nonrigid registration of medical images, Current Medical Imaging Reviews 15 (3) (2019) 292–300 .

[34] L. Nanni , S. Ghidoni , S. Brahnam , Handcrafted vs. non-handcrafted features for computer vision classification, Pattern Recognition 71 (2017) 158–172 .

[35] L. Satapathy , R. Tripathy , P. Das , A combination of variational mode decompo- sition and histogram equalization for image enhancement, National Academy Science Letters 42 (4) (2019) 333–336 .

[36] T. Jerman , F. Pernuš, B. Likar , Ž. Špiclin , Enhancement of vascular structures in 3d and 2d angiographic images, IEEE transactions on medical imaging 35 (9) (2016) 2107–2118 .

[37] J. Liu , J. Li , K. Zhang , U.A. Bhatti , Y. Ai , Zero-watermarking algorithm for medi- cal images based on dual-tree complex wavelet transform and discrete cosine transform, Journal of Medical Imaging and Health Informatics 9 (1) (2019) 188–194 .

[38] R.K. Meleppat , E.B. Miller , S.K. Manna , P. Zhang , E.N. Pugh Jr , R.J. Zawadzki , Multiscale hessian filtering for enhancement of oct angiography images, in: Ophthalmic Technologies XXIX, 10858, International Society for Optics and Photonics, 2019, p. 108581K .

[39] M. Raman , R. Korah , K. Tamilselvan , An automatic localization of optic disc in low resolution retinal images by modified directional matched filter., Int. Arab J. Inf. Technol. 16 (1) (2019) 1–7 .

[40] H. Andrea , I. Aranguren , D. Oliva , M. Abd Elaziz , E. Cuevas , Efficient im- age segmentation through 2d histograms and an improved owl search algorithm, International Journal of Machine Learning and Cybernetics (2020) 1–20 .

[41] G.R. Hernández , M.A. Navarro , N. Ortega-Sánchez , D. Oliva , M. Pérez-Cis- neros , Failure detection on electronic systems using thermal images and metaheuristic algorithms, IEEE Latin America Transactions 18 (08) (2020) 1371–1380 .

[42] S. Hinojosa , K.G. Dhal , M.A. Elaziz , D. Oliva , E. Cuevas , Entropy-based imagery segmentation for breast histology using the stochastic fractal search, Neuro- computing 321 (2018) 201–215 .

[43] M. Abd Elaziz , A .A . Ewees , D. Oliva , Hyper-heuristic method for multilevel thresholding image segmentation, Expert Systems with Applications 146 (2020) 113201 .

[44] F. Shaik , J. Chittemma , S.M. Islam , B.L. Reddy , S.D. Reddy , Enhancement of cerebral and retinal vascular structures using hessian based filters, in: ICCCE 2020, Springer, 2020, pp. 461–474 .

[45] T.M. Khan , M. Mehmood , S.S. Naqvi , M.F.U. Butt , A region growing and lo- cal adaptive thresholding-based optic disc detection, Plos one 15 (1) (2020) e0227566 .
[46] A. Rampun , B.W. Scotney , P.J. Morrow , H. Wang , J. Winder , Segmentation of breast mr images using a generalised 2d mathematical model with inflation and deflation forces of active contours, Artificial intelligence in medicine 97 (2019) 44–60 .
[47] E.R. Arce-Santana , A.R. Mejia-Rodriguez , E. Martinez-Peña , A. Alba , M. Mendez , E. Scalco , A. Mastropietro , G. Rizzo , A new probabilistic active contour region-based method for multiclass medical image segmentation, Medical & biological engineering & computing 57 (3) (2019) 565–576 .
[48] I. Aranguren , A. Valdivia , B. Morales-Castañeda , D. Oliva , M. Abd Elaziz , M. Perez-Cisneros , Improving the segmentation of magnetic resonance brain images using the lshade optimization algorithm, Biomedical Signal Processing and Control 64 (2021) 102259 .
[49] S. Chakraborty , S. Chatterjee , A. Das , K. Mali ,Penalized fuzzy c-means enabled hybrid region growing in segmenting medical images, in: Hybrid Machine In- telligence for Medical Image Analysis, Springer, 2020, pp. 41–65 .
[50] A. Hoover , V. Kouznetsova , M. Goldbaum , Locating blood vessels in retinal im- ages by piecewise threshold probing of a matched filter response, IEEE Trans- actions on Medical imaging 19 (3) (20 0 0) 203–210 .
[51] J. Staal , M.D. Abràmoff, M. Niemeijer , M.A. Viergever , B. Van Ginneken , Ridge-based vessel segmentation in color images of the retina, IEEE trans- actions on medical imaging 23 (4) (2004) 501–509 .
[52] Zhou C, Gao HB, Gao L: Particle swarm optimization (PSO) algorithm, Appl Res Comput, 20(12), 7-11, (2003).
[53] Li L, Li D: Applied PSO-RBF to aerial and satellite remote sensing image texture classification, Geomatics Inform. Sci.Wuhan Univ. 34(9): 1051-1054, (2009).
[54] M.S. Livingstone , D.H. Hubel , Psychophysical evidence for separate channels for the perception of form, color, movement, and depth, Journal of Neuro- science 7 (11) (1987) 3416–3468 .
[55] Marinakis Y, Iordanidou GR, Marinaki M: Particle swarm optimization for the vehicle routing problem with stochastic demands, Applied Soft Computing, 13(4): 1693-1704, (2013).
[56] J.V. Soares , J.J. Leandro , R.M. Cesar , H.F. Jelinek , M.J. Cree , Retinal vessel seg- mentation using the 2-d gabor wavelet and supervised classification, IEEE Transactions on medical Imaging 25 (9) (2006) 1214–1222 .
[57] P. Salembier , Comparison of some morphological segmentation algorithms based on contrast enhancement. application to automatic defect detection., in: 5. European Signal Processing Conference., 2, 1990, pp. 833–836 .
[58] A .M. Mendonca , A . Campilho , Segmentation of retinal blood vessels by com- bining the detection of centerlines and morphological reconstruction, IEEE transactions on medical imaging 25 (9) (2006) 1200–1213 .
[59] E.R. Dougherty , Mathematical morphology in image processing, Marcel Dekker, 1992 .
[60] A.V. Oppenheim , R.W. Schaffer , Digital Signal Processing, Prentice-Hall, 1975 .
[61] L.I. Voicu , H.R. Myler , A.R. Weeks , Practical considerations on color image enhancement using homomorphic filtering, Journal of Electronic Imaging 6 (1) (1997) 108–114 .
[62] S. Chaudhuri , S. Chatterjee , N. Katz , M. Nelson , M. Goldbaum , Detection of blood vessels in retinal images using two-dimensional matched filters, IEEE Transactions on medical imaging 8 (3) (1989) 263–269 .
[63] K. BahadarKhan , A .A . Khaliq , M. Shahid , A morphological hessian based ap- proach for retinal blood vessels segmentation and denoising using region based otsu thresholding, PloS one 11 (7) (2016) .
[64] P. Liskowski , K. Krawiec , Segmenting retinal blood vessels with deep neural networks, IEEE transactions on medical imaging 35 (11) (2016) 2369–2380 .
[65] J. Zhang , Y. Chen , E. Bekkers , M. Wang , B. Dashtbozorg , B.M. ter Haar Romeny , Retinal vessel delineation using a brain-inspired wavelet transform and ran- dom forest, Pattern Recognition 69 (2017) 107–123 .
[66] J.I. Orlando , E. Prokofyeva , M.B. Blaschko , A discriminatively trained fully con- nected conditional random field model for blood vessel segmentation in fun- dus images, IEEE transactions on Biomedical Engineering 64 (1) (2016) 16–27 .

[67] A. Dasgupta , S. Singh , A fully convolutional neural network based structured prediction approach towards the retinal vessel segmentation, in: 2017 IEEE 14th International Symposium on Biomedical Imaging (ISBI 2017), IEEE, 2017, pp. 248–251 .

[68] Z. Yan , X. Yang , K.-T. Cheng , Joint segment-level and pixel-wise losses for deep learning based retinal vessel segmentation, IEEE Transactions on Biomedical Engineering 65 (9) (2018) 1912–1923 .

[69] S. Thangaraj , V. Periyasamy , R. Balaji , Retinal vessel segmentation using neural network, IET Image Processing 12 (5) (2017) 669–678 .

[70] Y. Guo , Ü. Budak , A. ¸S engür , A novel retinal vessel detection approach based on multiple deep convolution neural networks, Computer methods and pro- grams in biomedicine 167 (2018) 43–48 .

[71] Y. Yang , F. Shao , Z. Fu , R. Fu , Discriminative dictionary learning for retinal ves- sel segmentation using fusion of multiple features, Signal, Image and Video Processing 13 (8) (2019) 1529–1537 .

[72] Q. Jin , Z. Meng , T.D. Pham , Q. Chen , L. Wei , R. Su , Dunet: A deformable net- work for retinal vessel segmentation, Knowledge-Based Systems 178 (2019) 149–162 .

[73] Y. Cheng , M. Ma , L. Zhang , C. Jin , L. Ma , Y. Zhou , Retinal blood vessel seg- mentation based on densely connected u-net, Mathematical Biosciences and Engineering 17 (4) (2020) 3088 .

[74] D. Adapa , A.N. Joseph Raj , S.N. Alisetti , Z. Zhuang , G. Naik , A supervised blood vessel segmentation technique for digital fundus images using zernike mo- ment based features, Plos one 15 (3) (2020) e0229831 .

[75] Y. Wu , Y. Xia , Y. Song , Y. Zhang , W. Cai , Nfn+: A novel network followed net- work for retinal vessel segmentation, Neural Networks (2020) .

[76] J. Zhang , B. Dashtbozorg , E. Bekkers , J.P. Pluim , R. Duits , B.M. ter Haar Romeny , Robust retinal vessel segmentation via locally adaptive derivative frames in orientation scores, IEEE transactions on medical imaging 35 (12) (2016) 2631–2644 .

[77] M. Shahid , I.A. Taj , Robust retinal vessel segmentation using vessel's loca- tion map and frangi enhancement filter, IET Image Processing 12 (4) (2018) 494–501 .

[78] Z. Fan , J. Lu , C. Wei , H. Huang , X. Cai , X. Chen , A hierarchical image matting model for blood vessel segmentation in fundus images, IEEE Transactions on Image Processing 28 (5) (2018) 2367–2377 .

[79] H. Aguirre-Ramos , J.G. Avina-Cervantes , I. Cruz-Aceves , J. Ruiz-Pinales , S. Ledesma , Blood vessel segmentation in retinal fundus images using gabor filters, fractional derivatives, and expectation maximization, Applied Mathe- matics and Computation 339 (2018) 568–587 .

[80] M.B. Abdallah , A.T. Azar , H. Guedri , J. Malek , H. Belmabrouk , Noise-estima- tion-based anisotropic diffusion approach for retinal blood vessel segmenta- tion, Neural Computing and Applications 29 (8) (2018) 159–180 .

[81] S. Pal , S. Chatterjee , D. Dey , S. Munshi , Morphological operations with itera- tive rotation of structuring elements for segmentation of retinal vessel struc- tures, Multidimensional Systems and Signal Processing 30 (1) (2019) 373–389 .

[82] K. Yue , B. Zou , Z. Chen , Q. Liu , Improved multi-scale line detection method for retinal blood vessel segmentation, IET Image Processing 12 (8) (2018) 1450–1457 .

[83] B. Biswal , T. Pooja , N.B. Subrahmanyam , Robust retinal blood vessel segmen- tation using line detectors with multiple masks, IET Image Processing 12 (3) (2017) 389–399 .

[84] D. Primitivo , R. Alma , C. Erik , V. Arturo , C. Edgar , P.-C. Marco , Z. Daniel , A hybrid method for blood vessel segmentation in images, Biocybernetics and Biomedical Engineering 39 (3) (2019) 814–824 .

[85] W. Wang , W. Wang , Z. Hu , Segmenting retinal vessels with revised top-bot- tom-hat transformation and flattening of minimum circumscribed ellipse, Medical & biological engineering & computing 57 (7) (2019) 1481–1496 .

[86] S. Roy , A. Mitra , S. Roy , S.K. Setua , Blood vessel segmentation of retinal image using clifford matched filter and clifford convolution, Multimedia Tools and Applications 78 (24) (2019) 34839–34865 .

[87] C. Zhou , X. Zhang , H. Chen , A new robust method for blood vessel segmen- tation in retinal fundus images based on weighted line detector and hidden markov model, Computer Methods and Programs in Biomedicine 187 (2020) 105231 .

[88] J.C.M. dos Santos , G.A. Carrijo , C.d.F. dos Santos Cardoso , J.C. Ferreira , P.M. Sousa , A.C. Patrocínio , Fundus image quality enhancement for blood ves- sel detection via a neural network using clahe and wiener filter, Research on Biomedical Engineering (2020) 1–13 .

[89] A.K. Shukla , R.K. Pandey , R.B. Pachori , A fractional filter based efficient algo- rithm for retinal blood vessel segmentation, Biomedical Signal Processing and Control 59 (2020) 101883 .

[90] S. Pachade , P. Porwal , M. Kokare , L. Giancardo , F. Meriaudeau , Retinal vascu- lature segmentation and measurement framework for color fundus and slo images, Biocybernetics and Biomedical Engineering (2020) .

[91] M. Niemeijer , J. Staal , B. van Ginneken , M. Loog , M.D. Abramoff, Compara- tive study of retinal vessel segmentation methods on a new publicly avail- able database, in: Medical imaging 2004: image processing, 5370, Interna- tional Society for Optics and Photonics, 2004, pp. 648–656 .

Morphological Filter-based Detection of Retinal AVR and CDR through Blind Deconvolution and CLAHE Fusion (BDCLF)

Niladri Halder[1], Dibyendu Roy[2], Partha Pratim Sarkar[2], Sankar Narayan Patra[1] and Subhankar Bandyopadhyay[1]

[1]Instrumentation & Electronics Engineering, Jadavpur University, West Bengal, India
[2]University Institute of Technology, The University of Burdwan, West Bengal, India

Abstract

Several retinal disorders, including Hypertensive Retinopathy (HR), Glaucoma, Diabetic Retinopathy (DR), and macular degeneration, can lead to optic nerve damage and result in permanent vision loss. These disorders are commonly identified through clinical observations, such as abnormal changes in the diameter of retinal blood vessels and the ratio of the diameter of optic cup to disc (CDR). High blood pressure can lead to thinning of retinal vessels and dilation of the optic cup, which can alter the normal arteriovenous ratio (AVR) and CDR which cause nerve fiber damage, leading to hemorrhages and cotton wool spots. This paper proposes an automated algorithm for segmenting the optic cup, optic disc, and blood vessels from pre-processed retinal images. The segmentation was done using a ring mask created by superimposing two circles with the optic disk center and radii of 3D/2 and 1.5D/2, where D denotes the diameter of the optic disk. The maximum AV crossing was avoided within the retinal mask to simplify the process. Validations were performed by comparing the results with a predefined manually segmented dataset, achieving accuracies of 98.6% and 97.8% for retinal optic disk and optic cup, respectively, and 98.55% for retinal vessels. This algorithm could aid ophthalmologists in identifying retinal disorders accurately and automatically.

Keywords – Contrast Limited Adaptive Histogram Equalization, Blind Deconvolution, Region-based classification, Morphological analysis, Top-Hat Transformation, Artery Vein Ratio, Cup Disk Ratio.

1. Introduction:

Glaucoma, the world's second leading cause of vision loss, results in an estimated 12% of total blindness cases and is anticipated to affect almost 11 million people with bilateral blindness. The most common type of glaucoma globally is Primary Open-Angle Glaucoma (POAG), which impacts 74% of individuals diagnosed with the condition. According to stratified estimates based on population studies, it is projected that approximately 11.2 million people in India, accounting for approximately 4.6% of the population over the age of 40, are affected by glaucoma [4]. Detecting and treating this disease, which can potentially lead to blindness, presents significant challenges since the majority of those affected remain undiagnosed.

The narrowing of blood vessels in the eye due to hypertension can decrease blood flow to the optic nerve, leading to potential vision loss. Likewise, elevated pressure within the eye in cases of glaucoma can cause optic nerve damage and impair vision. Research has suggested that individuals with hypertension may be at a higher risk of developing open-angle glaucoma, the most common form of glaucoma. The likelihood of this risk seems to increase among people with severe or poorly managed hypertension over a prolonged period.

Unfortunately, the majority of associated instances do not exhibit symptoms, although they can be detected using retinal fundus imaging. Proper diagnosis and management of glaucoma in a clinical setting require careful assessment of changes in the optic nerve head (ONH), measurement of intraocular pressure (IOP), and identification of defects in the visual field. Diagnosing typical ONH changes in the donor's eyes can be more challenging due to the optic

disk's paleness and edema. Additionally, early vascular changes associated with high blood pressure can cause retinal arteriolar narrowing, alterations in the arteriolar junction (arteriovenous nicking), and changes in the arteriolar light reflections [5]. Additionally, vessel bending has been identified as a potential risk factor for hypertension and coronary disorders [6]. It is crucial to measure heart rate, as research has shown that it is strongly associated with an elevated long-term risk of stroke [7]. As such, the aim of this work is to create a method to detect potential cases of glaucoma and hypertension in donor eyes by examining the cup-to-disc ratio (CDR) and arteriole-to-venule ratio (AVR).

Table 1 explains the AVR for normal to accelerated hypertensive retinopathy cases with different risk factors [2] and CDR ranges for normal and affected retina [1].

Table 1: AVR [2] and CDR [1] for various stages of Hypertensive Retinopathy.

Grading of HR	AVR	Indications	Systematic Association	CDR
Normal	0.66-0.75 (Approx.)	Normal	Normal	0.00-0.60 (Approx.)
Grade 1 (Mild)	0.5 (Approx.)	Arteriolar narrowing, nicking of arteries and veins, the opacity of arteriolar wall	Weakly associated with cardiovascular disorders	>0.60 (Approx.)
Grade 2 (Moderate)	0.33 (Approx.)	Haemorrhages, hard and soft exudates.	Heart attack, stroke, and even cardiovascular mortality	>0.60 (Approx.)
Grade 3 (Combined)	0.25 (Approx.)	Haemorrhages, hard and soft exudates.	Heart attack, stroke, and even cardiovascular mortality	>0.60 (Approx.)
Grade 4 (Accelerated HR)	Fine Cords <0.2 (Approx.)	Optic disk swelling and vision loss.	Renal failure and mortality	>0.60 (Approx.)

Motivation:

Due to the potential cases of diabetes, glaucoma, and hypertension, examination of the cup-to-disc ratio (CDR) and arteriole-to-venule ratio (AVR) is an important aspect. Retinal image processing is one of the possible solutions for the early detection of those diseases. Retinal image processing is fueled by the desire to improve diagnostic precision and gain valuable knowledge about different eye conditions and diseases. The objective of retinal image processing is to extract significant information from retinal images, including the identification of specific features like the optic disk, retinal vessels, and hemorrhages, as well as the detection of abnormalities and indicators of ocular diseases. The motivation lies in the enhancement of the early detection, monitoring, and treatment of eye disorders, thereby improving patient outcomes and overall eye health.

Contribution:

The contribution to the development of BDCLF for retinal AVR and CDR detection involves several key aspects.

- The contribution encompasses the utilization of multiple algorithms for activities like enhancing, segmenting, extracting the retinal features, and the classification to derive significant and valuable information from the retinal images.
- We need to gather a large and varied sets of data of the retinal fundus images for the development and evaluation of the BDCLF technique. Authors contribution in this

research includes selecting, organizing and labeling these sets of data to confirm they comprehensively represent various retinal features conditions and their variations.

- In conclusion, the major contributions are accomplished through the detailed testing, assessment, and authentication of the developed technique. This comprises comparing with current methods, evaluating performance metrics like accuracy, sensitivity, and specificity, and performing clinical studies to confirm the algorithms' efficiency and consistency in real-world scenarios.

In summary, the effort to develop algorithms for retinal features image processing includes system design, dataset organization, interdisciplinary partnership, and comprehensive assessment, all focused on enhancing the accurateness and medical usefulness of retinal image features analysis.

Dataset:

In order to establish a completely automated monitoring system, the proposed technique is tested on a few of the publicly available datasets like INSPIRE-AVR, HRF, and STARE.

INSPIRE-AVR is one of the publicly accessible datasets containing 40 retinal images pointing to the marked vascular pathology, optic disc region, and artery vein ratio and is specifically used for the classification and grading of distinct complications related to hypertension. The markings in this dataset were executed by two specialists through their semi-automated software, developed by the University of Wisconsin in Madison, WI, USA [32].

The HRF imaging dataset, developed by different collaborative research groups to aid in the creation of clinical decision-making systems for diagnosing several retinal abnormalities, entails of 45 retinal images. This includes 15 images each from healthy individuals, glaucomatous patients, and those with diabetic retinopathy (DR) [33]. The images are captured at a resolution of 3504×2336 pixels with a color depth of 24 bits per pixel, using a CANON CF-60 UVI camera with a 60-degree field of view.

The STARE dataset includes roughly 400 images, including 50 images of vascular shapes and 80 images with ground truth for optic nerve detection [34]. It was created by capturing images at a resolution of 605×700 pixels in a 24-bit color space, using a TOPCON TRV-50 fundus camera with a 35-degree field of view.

2. Literature Review:

The retinal vessels play a crucial role in transporting blood from the heart to the retina, and evaluating their caliber can offer valuable information in identifying diseases like hypertension, diabetes, and stroke at an early stage. The retinal artery to vein width ratio (AVR) and optic the cup to optic disc diameter ratio (CDR) are the two frequently used metrics for assessing retinal vessels. This literature review will explore the different techniques employed for calculating AVR and CDR.

The CDR serves as a metric for evaluating the severity of glaucoma by measuring the ratio of the vertical height of the optic cup to that of the optic disc. A greater CDR value is suggestive of a larger optic cup, which has been linked to a heightened risk of glaucoma. Ophthalmologists or optometrists usually calculate the CDR during a comprehensive eye examination by using a specialized instrument called a fundus camera to capture images of the optic disc. The images are subsequently analyzed to determine the vertical height of the optic cup and disc. Some recent studies related to CDR measurement have been mentioned below.

The authors of a study, Al Shalchi, et al. [44], introduced a Grasshopper optimization algorithm as an automated approach for identifying the optic disc in retinal images. The algorithm takes

inspiration from the social behavior of grasshoppers and is known as the intelligent Grasshopper algorithm. The study's findings demonstrate that the algorithm is highly capable and accurate in its ability to detect the optic disc.

In their study, Buket Toptas and colleagues (Toptas et al., [45]) suggested a technique for identifying the retinal optic disc. They accomplished this by applying an optimized color space to the images, which involved converting them from RGB to a novel color space utilizing an artificial bee colony algorithm. The results demonstrated that in this new color space, the localization of the optic disc was more distinct than in the original RGB color space.

The objective of Mahum R. and colleagues in their study [46] was to utilize deep learning-based feature extraction to detect glaucoma at early stages. To train and test their proposed model, they utilized retinal fundus images. The first step involved pre-processing the images, followed by segmenting and extracting the region of interest (ROI). Next, the hybrid feature descriptors were used to extract features of the optic disc (OD) from the images that contained optic cup (OC).

A new technique for detecting glaucoma called Densenet-77-based Mask-RCNN has been introduced by Nazir T. and colleagues in their study [47]. To address the challenges associated with glaucoma detection, they initially applied data augmentation and added blurriness to samples to increase data diversity. Ground-truth (GT) images were then used to generate annotations, and the Densenet-77 framework was utilized for feature extraction at the Mask-RCNN layer to calculate deep key points Finally, the customized Mask-RCNN model employed the derived features used to localize and segment the OD and OC.

An improved version of the Harris corner location algorithm was suggested by Deng L, et al. [48]. The proposed algorithm takes into account the dense blood vessels and significant gray-level variations in the retinal fundus image, with the optic disc area exhibiting the highest concentration of corners. The primary approach involves extracting the target area by applying a matching filter, performing vessel removal, image improvement, and other techniques. The Harris corner detection algorithm is then upgraded based on comparison to extract the bend of the region of interest.

The segmentation of blood vessels is a crucial aspect of medical image analysis that has been extensively explored in the literature. In this document, a concise review of some commonly employed methods for retinal blood vessel segmentation is presented.

In their study, Rehman A. et al. [49] suggest a supervised algorithm to segment retinal vessels. The algorithm comprises two refinement stages that involve filtering and relative histogram analysis following pre-processing and enhancement of the quality of the image. Statistical attributes such as vessel trailing, maximum bend, and curvelet constant are then extracted for every pixel. These structures are then separated using a SVM algorithm and the k-nearest neighbors' method.

In their study, Arsalan M and colleagues [50] introduce two novel narrow deep learning models, (DSF-Net) and (DSA-Net), that can effectively identify retinal vasculature. The authors utilize semantic segmentation to analyze raw color fundus images and screen for diabetic and hypertensive retinopathies with high precision.

In their work, Pal M and colleagues [51] suggest an automated technique for segmenting the retinal vasculature. This technique utilizes a Gabor filter bank that has been optimized using a grid search across the entire parameter space. Additionally, a novel strip-wise categorization method is employed. The authors also incorporate Top-Hat attributes and ridge info, based on eigenvalues of the Hessian matrix, to further enhance the precision of vessel capture, in addition to the optimized Gabor features.

In their study, Boudegga H et al. [52] introduce a novel DL approach for retinal vessel tree segmentation. The key innovation of their work lies in the proposal of a U-shaped DL architecture that employs lightweight convolution blocks to achieve a higher segmentation performance while minimizing computational complexity. Additionally, the authors present preprocessing and data augmentation techniques tailored to the characteristics of retinal images and blood vessels, which constitute their second major contribution.

In their study, Ooi A et al. [53] propose a technique for extracting blood vessels from retinal fundus images interactive techniques based on Canny edge detection. The pre-processing phase involves extracting the green color channel, applying Contrast Limited Adaptive Histogram Equalization (CLAHE), and removing the retinal outline. Subsequently, the Canny algorithm-based edge detection techniques are employed.

The literature review highlights the effectiveness and promise of the image-processing methods examined in these studies for measuring significant parameters like the arteriovenous ratio (AVR) and cup-to-disc ratio (CDR). However, it is crucial to recognize that there are still specific constraints and opportunities for improvement.

Some retinal image processing techniques are sensitive to image quality factors such as low resolution, noise, uneven illumination, and motion artifacts. In real-world clinical settings, where image quality may vary, these techniques may yield suboptimal results or require pre-processing steps.

Certain retinal image processing techniques may be computationally demanding, requiring substantial computational resources or long processing times. This can limit their practical application in real-time or resource-constrained environments.

Obtaining accurate and comprehensive ground truth annotations for retinal images can be challenging and time-consuming. This limitation can affect the development and evaluation of image-processing techniques, making it difficult to establish their true efficacy.

The processing algorithm currently lacks compactness techniques that can effectively handle multiple target features, such as optic disks, retinal vessels, hemorrhages, and others.

3. Materials & Methods:

CDR Measurement: Fig. 1 provides an organizational chart of the CDR measurement. In the RGB color model, each individual color is made up of three basic additive color spectral elements that are generally red, green, and blue that are depicted as the intensity function as follows:

$$Img_{RGB} = [F_R(x,y), F_G(x,y), F_B(x,y)] \quad (1)$$

Where$F_R(x,y)$, $F_G(x,y)$ and $F_B(x,y)$signify the intensities of the pixel (x,y)in red, green, and blue channels respectively. For standard RGB space they are as follows:

$$red = \begin{pmatrix}0.64\\0.33\end{pmatrix}, green = \begin{pmatrix}0.30\\0.60\end{pmatrix}, blue = \begin{pmatrix}0.15\\0.06\end{pmatrix} \quad (2)$$

If only brightness information is required, color images may be converted to grayscale images using the proposed transformation equation (3).

$$\mathrm{I_G} = 0.333\mathrm{F_R} + 0.600\mathrm{F_G} + 0.060\mathrm{F_B} \quad (3)$$

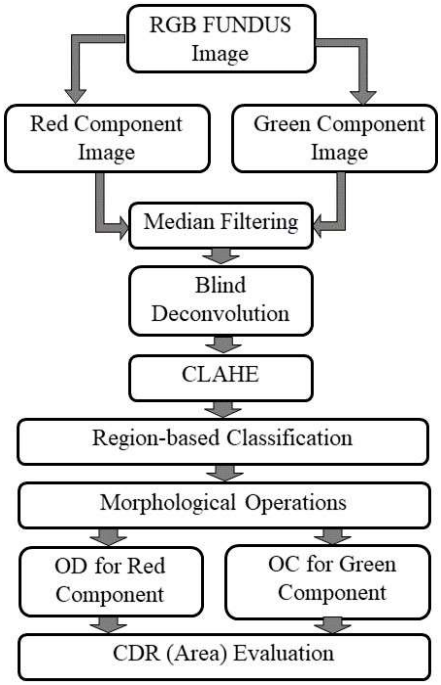

Fig.1: Block diagram explaining the CDR Evaluation

AVR Measurement: The vessel's segmentation and AVR calculation have been made in two steps shown in fig. 2(a) and fig. 2(b). In the first step, vessels of the overall RGB retinal image have been segmented by using an advanced CLAHE technique followed by Top Hat and different morphological image processing skills. In the second step, firstly the optic disk (OD) and its average diameter (D) and then the overlapping area between $\pi(3D/2)^2$ and $\pi(1.5D/2)^2$have been measured.

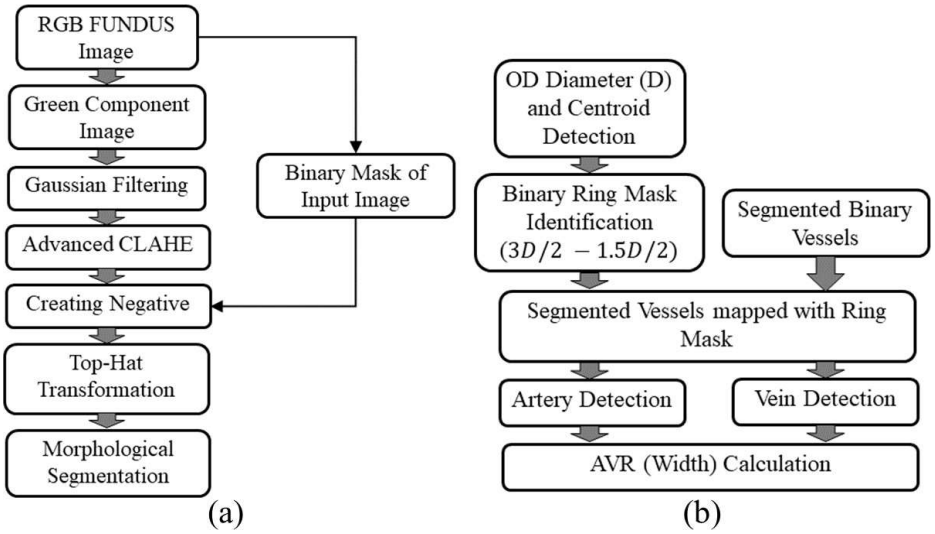

Fig. 2: Block diagram representing (a) Vessels Detection and (b) AVR Calculation.

The AVR and CDR of a retinal fundus image can be measured using the proposed BDCLF, which is a technique based on image processing. In the beginning, the BDCLF approach utilizes median filtering and Gaussian filtering. Subsequently, the subsections elaborate on the primary contributions, including Blind Deconvolution, CLAHE, and morphological operations.

Median Filtering:

The median filter is a nonlinear signal processing approach based on statistical analysis, where the noise data in a numeric image or sequence is swapped with the median data of its adjacent neighborhood. Equation (4) can be used to measure the result of the median filter.

$$g(x,y) = med\{f(x-i, y-j), i, j \in W\} \quad (4)$$

Here $f(x,y), g(x,y)$ are the input and output images respectively, $W$is the 2D mask: the mask size is $n \times n$ where n is usually odd such as $3 \times 3{,}5 \times 5$ etc.

Since the median filter is a non-linear filter, its mathematical analysis is relatively complicated for randomized noise images. For the image where the average noise is zero in a normal distribution, the median filter noise variance is approximate.

$$\sigma_{mid} = \frac{1}{4nf^2(\bar{n})} \approx \frac{\sigma_i^2}{n+\frac{\pi}{2}-1}.\frac{\pi}{2} \quad (5)$$

Where $\sigma_i^2$is the input power (the variance) noise, $n$is the mask size of the median filter, $f^2(\bar{n})$ is noise density function. The noise variance of average filtering can be measured from equation (6).

$$\sigma_0^2 = \frac{1}{n}\sigma_i^2 \quad (6)$$

Gaussian Filtering:

Gaussian filter, a linear class windowed filter, is typically used for image blurring or noise reduction. The unshaped masking that is the edge can be detected simply by subtracting two filtered results from each other. The Gaussian or normal distribution is a probability function that is referred to as a bell function due to its shape. The most common function formula is shown in equation (7).

$$G(x,y) = \frac{1}{2\pi\sigma^2} e^{\{-(x^2+y^2)/2\sigma^2\}} = G(x).G(y) \quad (7)$$

Equation (7) explains that the 2D Gaussian filter is separable. To obtain the Gaussian filtering of the 2D image, the following algorithm is employed.

- Measure the weights of 1D window $G_n^{/}$.
- Filter every image row as a 1D indicator.
- Filter every image column as a 1D indicator.

2D Gaussian filter with window $[2n+1] \times [2n+1]$ is compacted to a few 1D filters with window $[2n+1]$. This signifies a substantial acceleration, especially for large images due to the move from $O(N^2)$ to $O(N)$ number of operators.

Blind Deconvolution:

It is a method in image analysis used to improve the image quality by eradicating fuzziness triggered by a defocused or fuzzy imaging system. This method includes simultaneously approximating both the input image data and the blur data without any former information of either. To reach this, blind deconvolution systems generally minimize an objective function in an iterative manner, which measures the difference between the estimated deblurred image and the original blurred image.

To begin the blind deconvolution method, the first step is to estimate the point-spread function (PSF) that causes the image data degradation. A common approach for this is to use the Richardson-Lucy algorithm, that iteratively guesstimates the PSF by associating the degraded

image with an estimated reinstated image. The mathematical expression for the Richardson-Lucy algorithm is provided in equation (8).

$$P_{k+1}(x,y) = P_k(x,y)\frac{\sum_{i,j}\frac{I(x-i,y-j)}{(P_k * I)(x-i,y-j)}}{\sum_{i,j}\frac{P_k(x-i,y-j)}{(P_k * I)(x-i,y-j)}} \quad (8)$$

The expression includes the estimated point spread function (PSF) at iteration k symbolized as P_k the tainted image represented by I, and the convolution operator signified by $*$. The process begins by making an initial guesstimate of the PSF, denoted as P_0, and then continuously refines this guess until it converges. In this approach, the numerator represents the rebuilding of the tainted image using the existing PSF approximation, while the denominator signifies the distorting of the restored data by the PSF. The procedure refines the PSF guess by weighting neighboring pixels in the tainted data based on their resemblance to the present PSF estimate.

Hessian Blind Deconvolution is an data rebuilding method that concurrently controls the point-spread function (PSF) and recuperates the image. The following is a high-level algorithm describing the Hessian Blind Deconvolution process:

Inputs: degraded image I, regularization parameter λ, maximum number of iterations T.

Outputs: estimated PSF P and restored image R.

1. Set the initial values of P and R by randomly assigning values.
2. For t = 1 to T:
    a. Calculate the gradient and Hessian of the cost function regarding P and R.
    b. To obtain the updates ΔP and ΔR for P and R respectively, solve the linear system $H\Delta X = -\nabla f$.
    c. Update P and R using ΔP and ΔR respectively: $P \leftarrow P + \Delta P$ and $R \leftarrow R + \Delta R$.
3. Return P and R as the estimated PSF and restored image, respectively.

Typically, a combination of a data fidelity term and a regularization term is used as the cost function f in the above algorithm. The term data fidelity evaluates the degree of similarity between the estimated image and the observed degraded image, whereas the regularization term discourages solutions that lack smoothness or do not meet other desired criteria.

To estimate the point-spread function (PSF) and the restored image simultaneously using the Hessian Blind Deconvolution algorithm, the Hessian matrix is calculated as the second-order derivative of the cost function. An iterative method, such as conjugate gradient, is then used to solve the linear system HΔX = -∇f. The regularization parameter λ is used to balance the trade-off between data fidelity and regularization, while the maximum number of iterations T sets the times the algorithm will run before returning the estimated PSF and restored image.

Modified CLAHE:

Histogram equalization improves image contrast by allocating the pixel values more evenly over the histogram. In this study, a improved version of CLAHE was employed to improve retinal grayscale images. Initially, the contrast of the grayscale image was increased using the formula specified in equation (9).

$$Im(x,y) = \frac{fn(x,y) - fn(min)}{fn(max) - fn(min)} * 2^{bpp} \quad (9)$$

Here $Im(x,y)$ denotes the input image,$fn(x,y)$, $fn(min)$, and $fn(max)$ refer to the values of each pixel intensity, including the minimum and maximum intensities. The output is the contrast-stretched image, which serves as the input for CLAHE.

In CLAHE, the input image is separated into two non-overlapping contextual areas, called tiles, and a local histogram is formed for each of these tiles. Before estimating the cumulative probability, density and enhancing contrast intensity, the histogram of each individual tile is clipped using a clip limit determined by the user. This clip limit is a multiple of the average height of the histogram of the contextual region, as illustrated in equation (10).

$$[Hist\_Hight]_{Avg} = \frac{[Pixel(total)]_{contextual}}{[Pixel(total)]_{gray}} \tag{10}$$

For a contextual region of dimensions $M \times N$, with P representing the number of histogram bars, the clip limit is defined by equation (11).

$$Clip_{Limit} = \begin{cases} 1 & if \quad \frac{\alpha_{cf} MN}{[P_n]_{hist}} < 1 \quad for \quad 0 < \alpha \leq 1 \\ 0 & otherwise \end{cases} \tag{11}$$

In this scenario, α_{cf} is the contextual factor defined by the used. The accurate height of the histogram of the contextual area $n_k$is being trimmed using the $Clip_{Limit}$as indicated in equation (12) in which $[Hist]_k$is the histogram of the given area.

$$[Hist]_k = \begin{cases} Clip_{Limit} \; if \; n_k = Clip_{Limit} \; for \; k = 1,2,\dots,[P_n]_{hist} - 1 \\ n_k \qquad\qquad otherwise \end{cases} \tag{12}$$

Note that,

$$\sum_{k=0}^{[Pn]_{Hist}-1} n_k = MN \tag{13}$$

Total clipped pixels,

$$Clip_{total} = MN - \sum_{k=0}^{[Pn]_{Hist}-1} [Hist]_k \tag{14}$$

Re-normalizing the histogram or restoring the area under the curve to its original value restructures the clipped pixel values back into the histogram. This reordering may be uniform; if not, the clipped pixel values might be unevenly spread all over the histogram plots with pixel values below the clip limit. The allocation of distributed pixels to each histogram bin can be determined as outlined in equation (15).

$$[Pixel]_{\mu} = \frac{Clip_{total}}{[Pn]_{Hist}} = \frac{MN - \sum_{k=0}^{[Pn]_{Hist}-1} [Hist]_k}{[Pn]Hist} \tag{15}$$

The clipped histogram is being re-normalized by using equation (16).

$$[Hist]_k = \begin{cases} CLip_{Limit} \quad if \quad n_k + [Pixel]_{\mu} \geq Clip_{Limit} \\ n_k + [Pixel]_{\mu} \qquad\qquad otherwise \end{cases} \tag{16}$$

Morphological Operations:

All morphological filters are derived from various combinations of the two fundamental operations: dilation and erosion, along with a kernel known as a structuring element. This structuring element is represented as a binary mask with a specific shape and a designated reference point. The shape of this structuring element influences how the filter impacts the image. An image I (the input object), a structuring element SE and the two basic operations, erosion and dilation, can be defined as shown in equations (17) and (18).

$$I \ominus SE = \{x \;\; such\ that \quad SE_x \subseteq I\} \tag{17}$$

$$I \oplus SE = \{x \quad such\ that \quad SE_x^s \cap I \neq \Phi\} \tag{18}$$

where SE_x means the structural element SE with the position value x, whereas SE_x^ssignifies the reflective rotation of the structuring element in x.

Several composite morphological filters can be defined as combinations of the aforementioned elements. The most general composite operators are the opening and closing operators, which are defined as the sequences of erosion followed by dilation and dilation followed by erosion, respectively, as shown in equations (19) and (20).

$$I \circledcirc SE = I \ominus SE \oplus SE \quad (19)$$

$$I \odot SE = I \oplus SE \ominus SE \quad (20)$$

The Top-Hat morphological operation is highly effective for distinguishing point targets against various backgrounds. However, it is less effective for addressing image removal issues involving localized targets that are heavily corrupted by noise. Consequently, an improved morphological Top-Hat filtering process is needed.

The Structuring Element of the innovative Top-Hat operator is calculated as follows: develop an internal structural element and a peripheral structural element as $SE_0(m \times m)$, complying $SE_i \subset SE_0$. Define Edge Structuring Element as $SE_{Edge} = SE_0 - SE_i$. Thus, the upgraded Top-Hat action can be defined as in equation (21).

$$Top\_Hat_{I,SE}(x) = \left[\left\{I - \left(I\Theta SE_{Edge}\right) \oplus SE_i\right\}.x\right] \quad (21)$$

Pseudocode:

Below is a sample pseudocode that demonstrates how to perform a Top Hat Transformation on an image by utilizing the opening morphological operation.

Input: I is a binary image with dimensions $M \times N$, and SE is a structuring element with dimensions $m \times n$.

Output: After applying the Top Hat Transformation, the binary image J will have a size of $M \times N$.

1. Create a function named $Top\_Hat(I, SE)$ that utilizes the morphological opening function to execute the Top Hat Transformation.
    a. Consider a structuring element (SE) of 'disk' shape with a specific size: $SE = strel$('disk', size).
    b. Compute the morphological opening operation on the binary input image, I. $morph_{open} = imopen(I, SE)$.
    c. Subtract the $morph_{open}$ image from the input binary image, I to grt the top hat transformed image, J.
    $$J = I - morph_{open}$$
    d. Return the resulting top hat image, J.
2. End

3. Results:

To evaluate the performance of the BDCLF technique, arbitrarily selected 50 fundus retinal images from HRF, CHASEDB1, DRIVE, and STARE have been considered where 25 of the retinal images are from the normal patients, with zero disorders, and 25 others are from patients with clinical abnormality. For these 50 fundus retinal images optic cups, optic disks, and vessel's structure are segmented, and then optic cup diameter, optic disc diameter, and vessel width have been measured by a mentioned automatic process. Cup-Disc Ratio (CDR), and Artery-Vein Ratio (AVR) have been calculated and compared to the manual data respectively. Fig. 3 implies the image enhancement by applying the advanced CLAHE and BDCLF techniques.

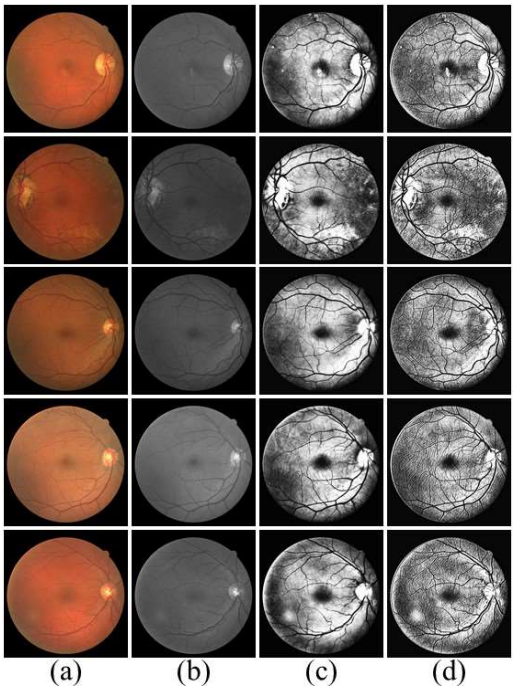

Fig. 3: Result shows the image enhancement techniques using CLAHE and BDCLF: (a) Input RGB Fundus Image, (b) Green Components, (c) Enhancement by CLAHE, and (d) Enhancement by BDCLF.

Table 2 presents a comparison of the quality measures between images that have been enhanced using CLAHE and BDCLF techniques. BDCLF achieves a higher PSNR, indicating superior image quality. Additionally, BDCLF exhibits a lower MSE than CLAHE, leading to enhanced image fidelity, improved visual quality, and increased accuracy. Furthermore, the higher SSIM measure of BDCLF compared to CLAHE ensures minimal distortion in the image structure. The results clearly demonstrate that BDCLF surpasses CLAHE in terms of image enhancement.

Table 2: Quality measures of BDCLF and CLAHE

Image	MSE $(Pixel^2)$		PSNR(dB)		SSIM	
	BDCLF	CLAHE	BDCLF	CLAHE	BDCLF	CLAHE
6(a1)	3151.30	4273.50	15.85	11.82	0.4428	0.3390
6(a2)	5316.20	6322.50	16.63	10.12	0.2760	0.1752
6(a3)	3992.91	5161.00	14.89	11.01	0.3379	0.2365
6(a4)	1953.30	2737.30	17.43	13.75	0.6469	0.5456
6(a5)	3162.4	4058.3	18.93	12.05	0.4582	0.3480

The system successfully segmented the optic disc and cup of the images. The mean CDR values across the dataset were consistent with previous studies that report CDR values in healthy and glaucomatous eyes. Significant differences were observed between normal and glaucomatous subjects, with the latter exhibiting larger CDR values. To categorize OD and OC the red and green elements of the RGB image are considered respectively, as shown in fig. 3. For the reduction of noise, median filtration, and improvement, the advanced technique of CLAHE has been employed. Secondly, the use of the regional classification made it possible to detect OD and OC. The operations based on morphology such as dilation, erosion, opening, and closing are considered for segmenting the OD and OC features.

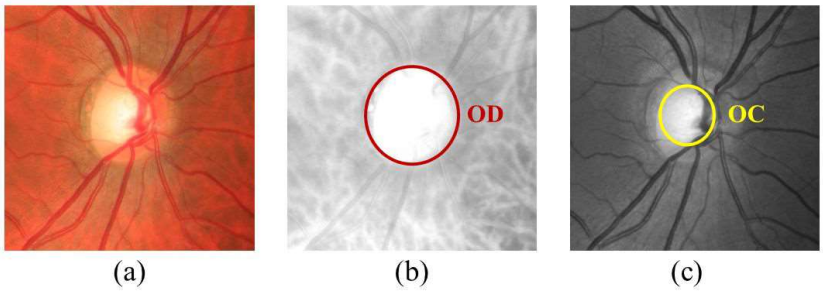

Fig. 3: Random image of HRF dataset represents (a) cropped OD and OC, (b) red channel marking OD, and (c) green channel marking OC.

Fig. 4 represents the input RGB fundus images of the macula with segmented results of the optic disk and optic cup using mentioned morphological techniques.

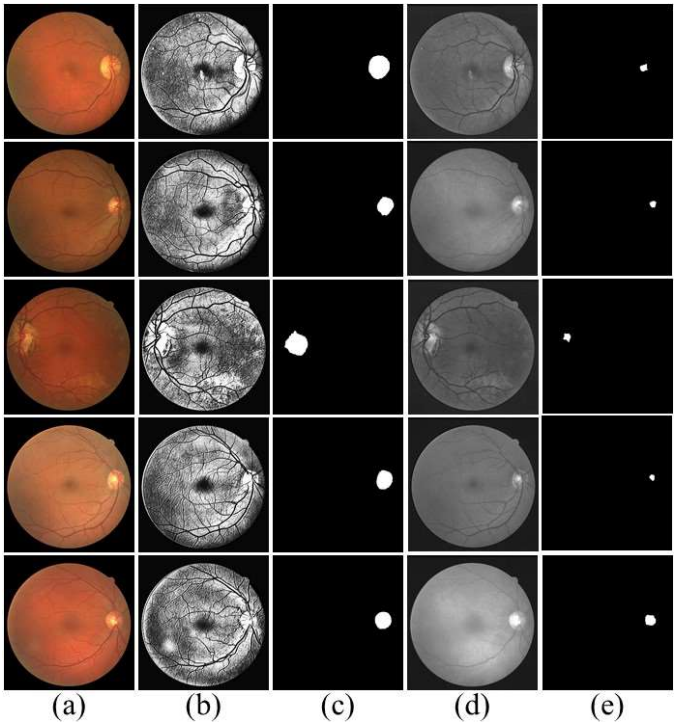

Fig. 4: In this figure, (a) represents the input RGB fundus image, (b), (c), (d) and (e) represents the BDCLF Enhancement, segmented Optic Disk, green components of input image and segmented Optic Cup respectively.

Table 3 provides a comparison between the automatic and manual Cup-to-Disc Ratio (CDR) measurements. The automatic diameter measurements of the Optic Disc (OD) and Optic Cup (OC) in terms of pixels are performed by BDCLF, while the manual diameters are obtained from the specified dataset. The CDR values are computed for both automatic and manual measurements by taking the ratio of their respective areas. The CDR errors are determined by calculating the difference between the manual and automatic CDR values.

Table 3: Result shows the comparison of automatic CDR and manual CDR

Sl. No.	$Dia_{OD}(Pixel)$		$Dia_{OC}(Pixel)$		CDR $(Pixel^2)$		$Error_{CDR}$
	Auto	Manual	Auto	Manual	Auto	Manual	
1	230	234	186	190	0.65	0.66	0.01
2	226	224	194	190	0.74	0.72	-0.02
3	218	223	184	186	0.71	0.70	-0.01
4	226	232	178	184	0.62	0.63	0.01
5	228	224	182	178	0.64	0.63	-0.01
6	203	194	179	175	0.78	0.81	0.04
7	216	230	175	178	0.66	0.60	-0.06
8	224	218	184	175	0.67	0.64	-0.03
9	226	225	128	130	0.32	0.33	-0.01
10	224	225	128	125	0.33	0.31	-0.02

The average diameter error for both OD and OC is ±4% approximately. Graphs depicting the correlation between the automatically detected diameter and manually measured diameter for the OD and OC can be observed in Fig. (5a) and (5b) respectively.

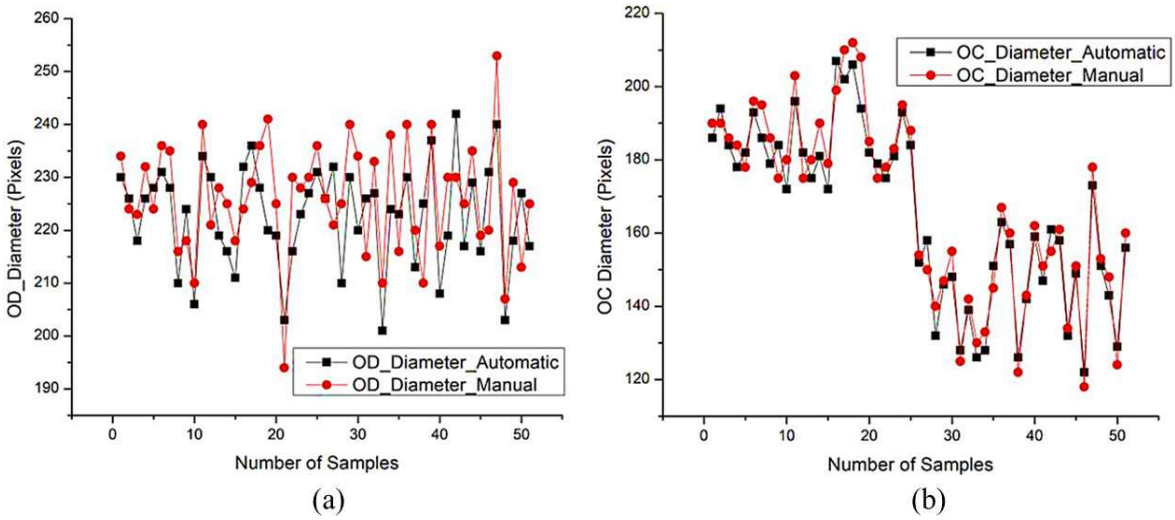

Fig. 5: This figure represents the comparison of (a) diameter of Optic Disk and (b) diameter of Optic Cup segmented by using manual and automated process.

The calculation of the CDR, an essential indicator in the detection of glaucoma and hypertension, involves measuring the optic cup and optic disc areas and determining their ratio. Normal patients typically have a CDR below 0.6, while patients with abnormalities tend to have a CDR above 0.6. Fig. 6 depicts the error comparison between the automated CDR and manual CDR, serving as an evaluation of the approach's performance. This figure illustrates the distribution of errors across 50 sample images. From the results shown in fig. 6, it is evident that our proposed BDCLF method achieves a maximum error for the CDR of approximately less than ±4%. Additionally, the average mean error is calculated to be approximately 6.11%, demonstrating the higher accuracy of the CDR measurement. These findings indicate that BDCLF outperforms other methods in this context.

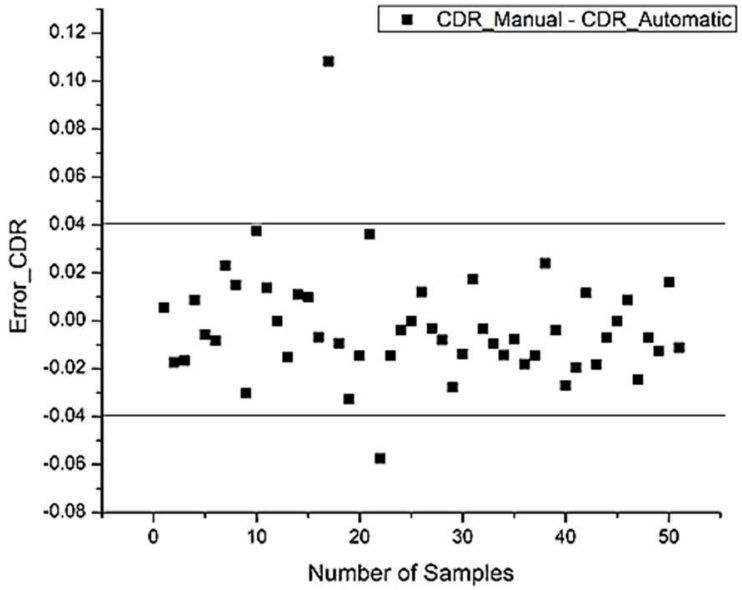

Fig. 6: Result shows the error in Cup-Disk Ratio calculated automatically and manually.

To assess the effectiveness of the proposed method, Figure 7 is presented. It illustrates the detection of glaucoma using both our proposed method and the manual method. A CDR value exceeding 0.60 is used to classify a patient as a potential abnormal case. The findings indicate that the proposed method has average sensitivity, specificity, and accuracy of 95.83%, 98.23%, and 96.49%, respectively.

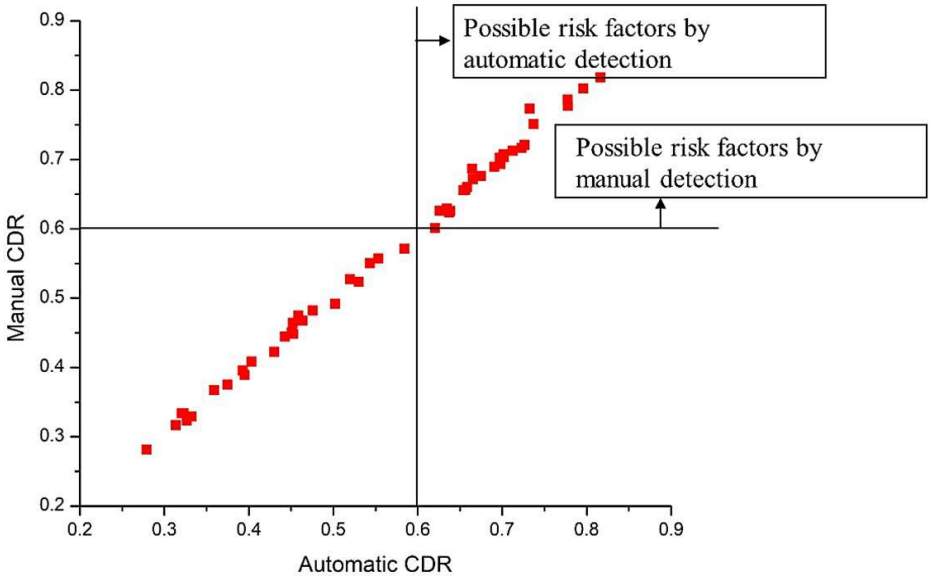

Fig. 7: This figure represents the dataset ranging from normal to possible risk factors [1].

The performance quality of various classifiers is determined by computing evaluation metrics as sensitivity, accuracy, specificity which are found using equations (23), (24), and (25).

$$Accuracy = \frac{TP+TN}{TP+TN+FP+F} \quad (23)$$

$$Specificity = \frac{TN}{TN+F} \quad (24)$$

$$Sensitivity = \frac{TP}{TP+F} \quad (25)$$

where $TN = True\ Positive$, $TN = True\ Negative$, $FP = False\ Positive$ and $FN = False\ Negative$.

Table 4 presents the computation results for various metrics in the context of optical disc (OD) and optic cup (OC) analysis. Specifically, it covers sensitivity, specificity, overlapping error (OD and OC), balanced accuracy (OD and OC), and absolute error in cup-to-disc ratio (CDR), denoted as A_{OD}, A_{OC}, E_{OD}, E_{OC}, δ_E, respectively. When focusing on OD segmentation, the BDCLF method achieves a sensitivity of 98.6%, specificity of 99.7%, and accuracy of 98.5%, accompanied by an absolute error of 2.8%. Similarly, for OC segmentation, the BDCLF method demonstrates a sensitivity of approximately 97.7%, specificity of 98.7%, accuracy of 96.8%, and a minimum error of 2.8%. These results further establish the superiority of the BDCLF technique over alternative methods.

Table 4: Statistical results of optic cup and optic disk

Dataset	Sensitivity		Specificity		Accuracy		E_{OD}	E_{OC}	δ_E
	OD	OC	OD	OC	OD	OC			
CHASEDB1	0.962	0.953	0.997	0.983	0.975	0.968	0.103	0.103	0.049
DRIVE	0.968	0.947	0.984	0.972	0.971	0.945	0.087	0.294	0.045
HRF	0.986	0.977	0.984	0.987	0.985	0.962	0.074	0.241	0.028
STARE	0.950	0.932	0.976	0.975	0.953	0.960	0.093	0.285	0.069

The algorithm identified arterioles and venules within the retinal vasculature and calculated the AVR for each image. Then the segmented vessels within that masked area have been mapped. The reason behind this mask is that within this range the maximum vessels which are mostly affected by hypertension are found and also complexity reduces. In the final stage of the second step, arteries and veins are separated to measure the area of artery and vein separately. Arteries and veins are identified using the following parameters [8].

- The color of the arteries is brighter than that of the veins.
- Arteries tend to be thinner than their neighboring veins.
- The central reflex (luminous reflex from inside the vessels) is larger in the arteries and smaller in the veins.
- Arteries and veins generally different in the vicinity of the optical disk before branching out.

Fig. 8(a) and fig. 8(b) show the marking arteries and veins and the proposed region of interest. Finally, AVR concerning the area has been calculated. The measured AVR helps the Ophthalmologist to detect the stages of hypertensive retinopathy.

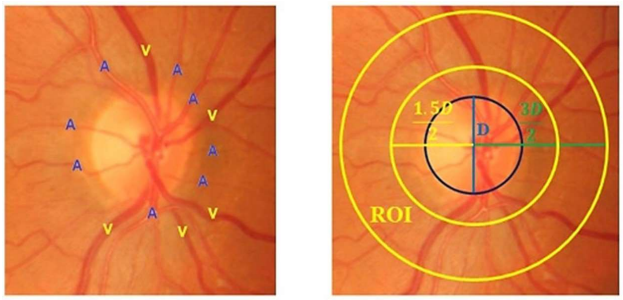

(a) (b)

Fig. 8: Random Image cropped from HRF datasets represents (a) marking arteries and veins, and (b) proposed region of interest (ROI).

The segmentation of vessels structure of overall image by using the proposed technique is shown in fig. 9. The Gaussian filtering helps to enhance and detect the edges and the edges of the vessel's structures. Top-Hat transformation is used to extract the vessels features that helps to segment the vessel's structure.

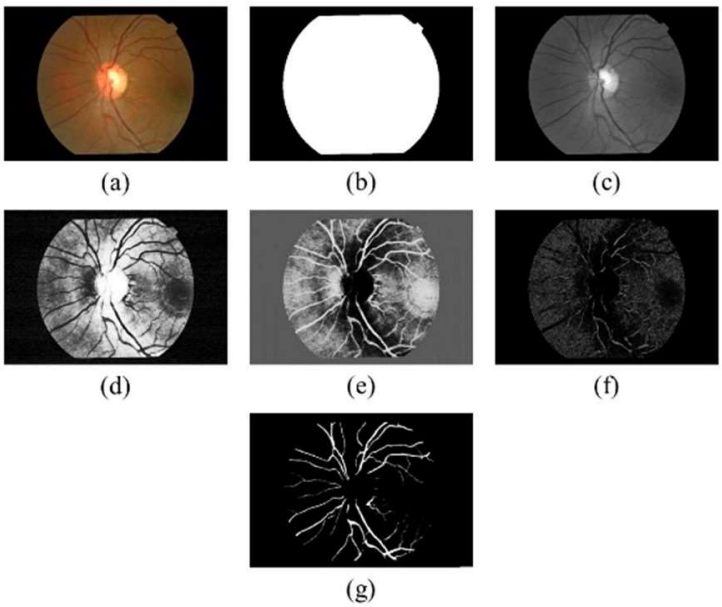

Fig. 9: Result shows the overall vessels segmentation steps: (a) Input RGB fundus image, (b) Binary mask, (c) Gaussian Filtering, (d) Advanced CLAHE, (e) Negative, (f) Top-Hat transform, and (g) Segmented vessels.

Fig. 10 compares the manual and automatic results of the vessel's structure with respective input images. Compared to other pre-existing techniques, this method offers superior accuracy and faster processing time. The proposed automated method for segmenting vessels achieves an average accuracy of 98.4% and a sensitivity of 97.6%.

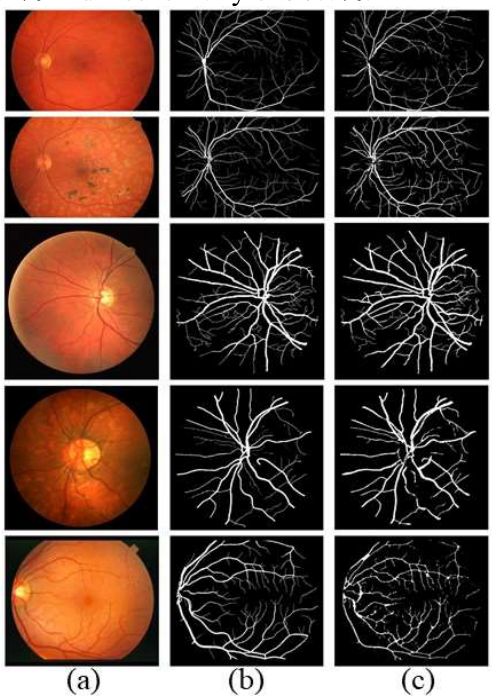

Fig. 10: This figure shows the results of segmented vessels: (a) Input RGB fundus images, (b) Manually Segmented vessels, and (c) Automatically segmented vessels.

Fig. 11 explains the vessels mapping and artery-vein separation within the mentioned specific ring mask. The ring mask has been chosen to complexity due to vessel's branching.

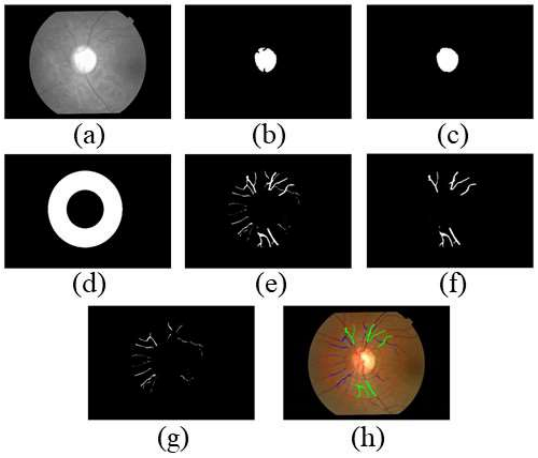

Fig. 11: Result shows the separation of arteries and veins within specified ring mask: (a) Red components of RGB fundus image, (b) Segmented optic disk, (c) Segmented optic disk filling, (d) (3D-1.5D) mask, (e) Segmented vessels within mask, (f) Separated veins, (g) Separated arteries, and (h) Segmented vessel's labelling.

The evaluation metrics, accuracy and sensitivity, are calculated for various classifiers to assess their qualitative performance. Table 5 presents the results of comparing the performance of the projected method with predefined methods. The table clearly indicates that our BDCLF method outperforms the other techniques in retinal vessel segmentation, with a sensitivity ranging from 96.16% to 98.53%. Additionally, our BDCLF method surpasses the conventional methods in terms of accuracy, achieving an accuracy of 98.55%.

Table 5: The results display the performance study of the BDCLF technique related to the formerly recognized approaches.

Algorithm	Dataset	Samples	Sen (%)	Spe (%)	Acc (%)
Li et al [54]	DRIVE	40	75.69	98.16	95.27
	STARE	20	77.26	98.44	96.28
	CHASEBD1	28	75.07	97.93	95.81
Srinidhi et al. [55]	DRIVE	40	**86.44**	96.67	95.89
	STARE	20	83.25	97.46	95.02
	CHASEBD1	28	82.97	96.63	94.74
Yan et al. [56]	DRIVE	40	76.31	98.20	95.38
	STARE	20	77.35	98.57	96.38
	CHASEBD1	28	76.40	98.06	96.07
Jin et al. [57]	DRIVE	40	79.63	98.00	95.66
	STARE	20	75.95	**98.78**	96.41
	CHASEBD1	28	81.55	97.52	96.37
Yuchen Yuan et al. [58]	DRIVE	40	80.46	98.05	95.81
	STARE	20	79.14	98.70	96.65
	CHASEBD1	28	84.02	98.01	**96.73**

BDCLF	HRF	45	**96.16**	97.65	**98.55**
	DRIVE	40	**97.63**	96.69	**97.49**
	CHASEDB1	28	**98.47**	95.31	**98.17**
	STARE	20	**98.53**	96.45	**98.39**

To measure vessel width, the center line and the edges of the first vessels are computed from the segmented binary vessels using thinning and canny edge detection methods. These images are then mapped to locate the vessel width for a pixel position on the specific vessel center line, fig. 12.

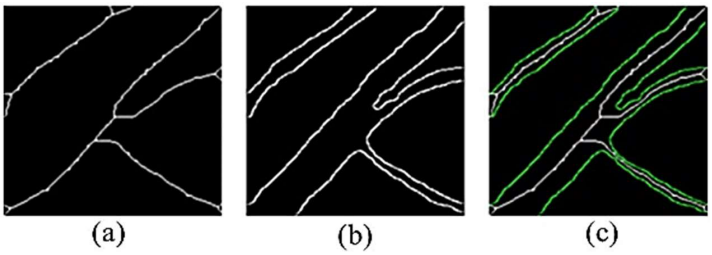

Fig.12: Results representing: (a) vessel's skeleton, (b) vessel's edge, (c) mapping of (a) and (b).

To measure the vessel's width, a pixel from the vessel's centerline image is selected, and a mask is applied with that center pixel at its core. This mask is designed to identify potential edge pixels on either side of the centerline pixel. To determine all pixel positions within the mask, the pixel is shifted one unit at a time up to the mask size, while simultaneously rotating each position from 0^0 to 180^0 around the center pixel. To increase the rotation resolution, the step size for the angle is set to be less than 180^0 divided by the mask length.

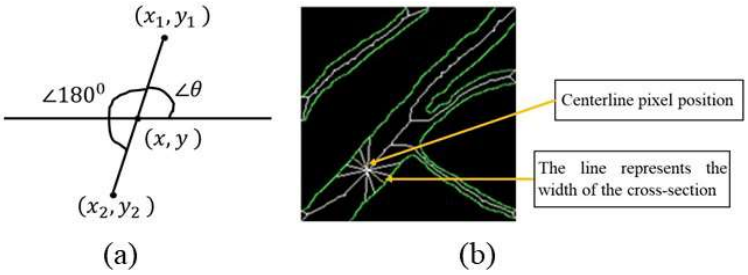

Fig. 13: This figure represents the process (a) to find the edge pixels and (b) the vessel's width or minimum distance of pair pixels.

For each identified position, the grayscale value of the edge image was examined to determine if it corresponds to an edge pixel. Once an edge pixel was detected, its counterpart was located by rotating the angle by 180 degrees and extending the distance from one to the maximum size of the mask [fig. 13]. This process generated a rotationally invariant mask, which captured all potential pixel pairs to measure the width or diameter of the cross-sectional area.

$$x_1 = x + r\,cos(\theta) \tag{26}$$

$$y_1 = y + r\,sin(\theta) \tag{27}$$

where (x, y) is the vessel centerline pixel position, $r = 1,2,3,\ldots\ldots,(mask \quad size/2)$and $\theta = 0^0,\ldots\ldots\ldots,180^0$. For any pixel position, if the binary value in the edge image is *1* then the pixel (x_2, y_2) in the opposite edge has been measured by considering $\theta = 180^0 + \theta$and by varying r.

After performing the operation, a pair of pixels was discovered on the opposite edge. The minimum Euclidean distance, $\sqrt[2]{(x_1 - x_2)^2 + (y_1 - y_2)^2}$, was calculated from this pair of pixels to determine the width of the vessel's cross-section. Table 5 displays the resulting widths at 20 distinct cross-sections of the vessel as shown in figure 13b.

Measuring the width of the vessel is crucial because it helps determine the AVR, which indicates the severity of the disease based on the condition of the retinal image. Table 6 provides a comparison of vessel widths obtained using the proposed automated technique and manual measurements. Two images from each dataset (HRF, INSPIRE-AVR, DRIVE, CHASEDB1, and STARE) were chosen for analysis.

Table 6: Result of Euclidean Width of 20 cross section of figure (14b).

Cross Sections	Centerline Pixel Position	Width-Line End Point		Vessel's Width (Euclidean Distance)
	(x, y)	(x_1, y_1)	(x_2, y_2)	
1	(17,27)	(13,69)	(20,75)	9.22
2	(45, 48)	(41,42)	(50,53)	14.21
3	(53,42)	(48,37)	(58,46)	13.45
4	(58,38)	(53,33)	(61,43)	12.80
5	(41,166)	(29,155)	(55,177)	34.06
6	(50,157)	(36,147)	(62,170)	34.71
7	(65,142)	(52,128)	(79,152)	36.12
8	(74,131)	(59,119)	(88,143)	37.64
9	(69,125)	(65,114)	(92,137)	35.47
10	(108,80)	(100,75)	(116,87)	20.00
11	(116,70)	(108,63)	(123,78)	21.21
12	(125,63)	(117,55)	(133,70)	21.93
13	(136,52)	(128,45)	(144,60)	21.93
14	(124,95)	(121,92)	(129,98)	10.00
15	(135,88)	(133,85)	(137,90)	6.40
16	(143,80)	(140,76)	(146,84)	10.00
17	(147,77)	(143,74)	(150,82)	10.63
18	(132,153)	(135,150)	(129,156)	8.48
19	(144,161)	(147,158)	(141,163)	7.81
20	(159,170)	(162,168)	(156,173)	7.81

Table 7 presents the automated measurements of retinal vessel width using BDCLF, along with manually collected data. It also illustrates the automatic and manual calculations of AVR, showcasing a marginal average error of less than ±4% as shown in fig. 15. A normal retinal image is characterized by an AVR range exceeding 6.6, whereas a range below this threshold indicates abnormalities related to glaucoma or hypertension [1]. Consequently, the BDCLF technique proposed in this study is capable of effectively assessing retinal data abnormalities, rendering it highly favorable.

Table 7: The outcome presents a comparison between the widths of the vessel acquired through the automated method proposed and those obtained through manual measurements.

Sl. No.	$Width_{Automatic}$		$Width_{Manual}$		AVR		ERROR
	Artery	Vein	Artery	Vein	Auto	Manual	
1	11.75	21.40	12.20	23.40	0.549	0.521	-0.027
2	18.02	27.31	17.46	26.57	0.659	0.657	-0.002
3	17.69	38.83	17.85	40.02	0.455	0.446	-0.009
4	14.87	28.28	15.65	31.14	0.525	0.502	-0.023
5	3.16	4.47	6.41	8.94	0.706	0.717	0.010
6	2.76	3.61	2.81	3.60	0.764	0.780	0.016
7	10.50	15.80	9.4	13.60	0.664	0.691	0.026
8	10.63	13.45	10.76	13.41	0.790	0.802	0.012
9	6.83	10.82	5.32	7.81	0.631	0.681	0.050
10	2.03	6.08	2.06	6.32	0.333	0.325	-0.007

Fig. 14 displays the evaluation of automatic and manually identified AVR and error of the projected technique whereas fig. 15 represents the percentage of error in detection of AVR.

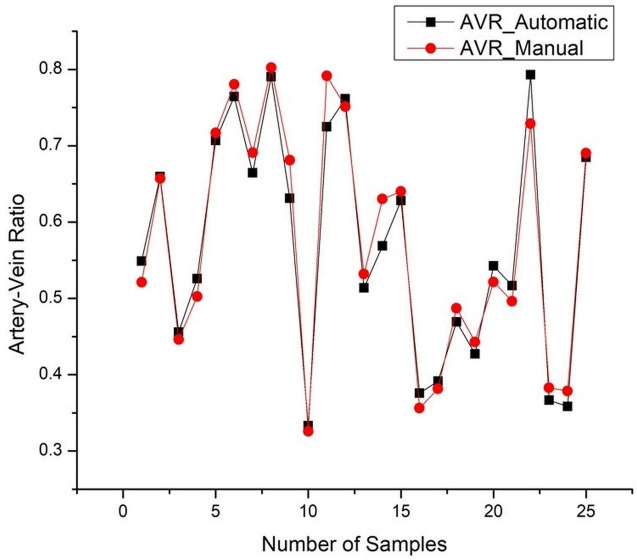

Fig.14: Results shows the comparison of automatic measured AVR with manual AVR.

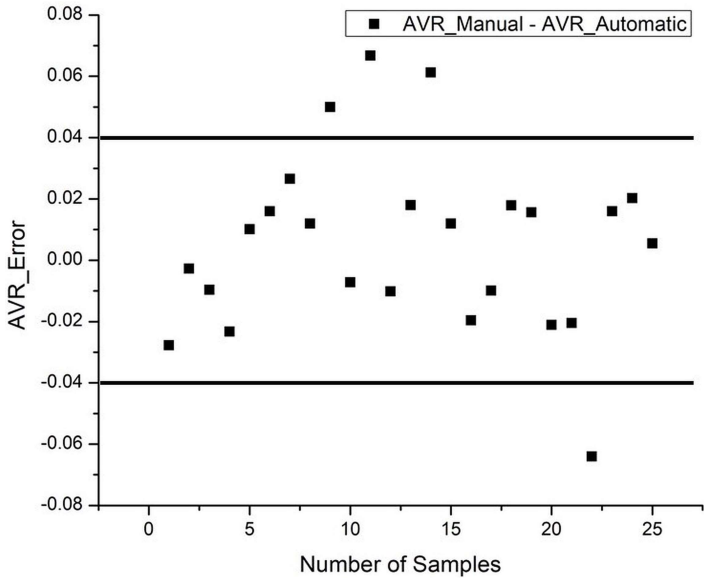

Fig 15: Result shows the percentage of error in detection of automatic AVR

The performance evaluation of a binary classifier system was conducted using the ROC curve displayed in figure 16. This curve demonstrates how the true positive rate (sensitivity) relates to the false positive rate (1 - specificity) as the classification threshold is modified. By visualizing the classifier's performance at various thresholds, the ROC curve enables the assessment of its ability to distinguish between positive and negative instances. Additionally, it facilitates the comparison of different classifiers or models. In this particular ROC curve, the dataset from the drive was used to evaluate the performance of five different techniques, including the proposed BDCLF technique. Results indicate that the BDCLF method outperforms existing techniques in terms of ROC, as evidenced by its faster and more stable curve. A stable ROC curve signifies that the classifier's performance remains consistent and reliable across diverse datasets or conditions, thereby instilling confidence in its generalization capability to new and unseen data. Furthermore, these findings establish the superiority of the proposed BDCLF method over existing approaches.

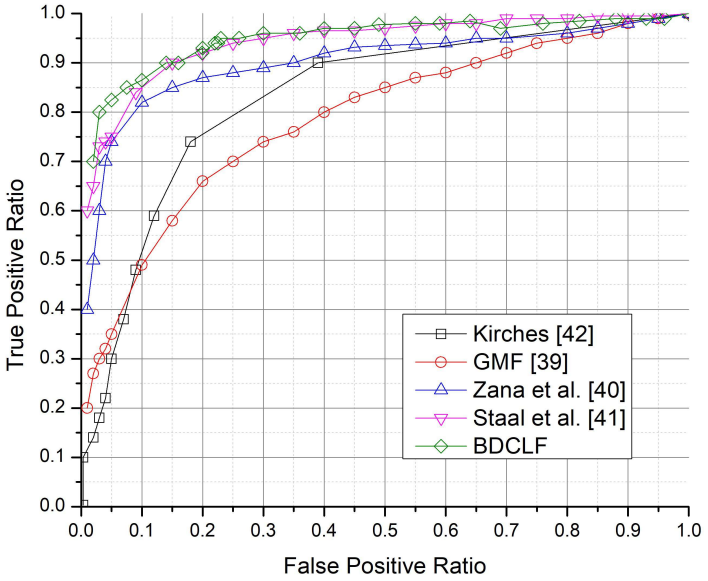

Fig. 16: Graph depicts the aggregate ROC curve for the 40 DRIVE datasets using five different techniques.

The AVR and CDR values obtained through the BDCLF method, as shown in Table 8, are utilized to assess the condition of the patent in terms of diabetes, glaucoma, and overall health. To accomplish this, a selection of retinal images from the HRF dataset, encompassing diabetic, glaucoma, and healthy cases, were randomly chosen. The results obtained were promising, revealing an average CDR of 0.68 for diabetic patients, 0.62 for glaucoma patients, and 0.41 for healthy individuals. Similarly, the average AVR values were found to be 0.52 for diabetics, 0.43 for glaucoma patients, and 0.75 for those without any eye-related conditions.

Table 8: Result shows the AVR and CDR for patient's different health conditions.

HRF Image	Patent's Condition	OD (Avg.)	OC (Avg.)	W_{Artery} (Avg.)	W_{Vein} (Avg)	CDR	AVR
01_dr	Diabetic	372	294	13.15	32.37	0.63	0.41
02_dr		375	306	12.32	22.62	0.67	0.54
03_dr		327	281	14.05	23.18	0.74	0.61
04_dr		336	268	13.19	26.39	0.64	0.50
01_h	Healthy	410	248	17.39	20.81	0.37	0.84
02_h		408	267	16.18	23.41	0.43	0.69
03_h		396	237	17.02	22.11	0.36	0.77
07_h		416	278	17.36	24.79	0.45	0.70
01_g	Glaucoma	338	261	12.27	26.58	0.60	0.46
08_g		367	292	11.43	28.91	0.63	0.39

4. Conclusion:

An automated approach has been proposed to evaluate two specific target features in the human eye, namely CDR and AVR, for the purpose of detecting abnormalities associated with conditions like diabetes, glaucoma, and hypertension. The results obtained so far are promising, demonstrating high levels of accuracy: 98.6% for OD, 97.8% for OC, and 98.55% for AVR, with only minor errors. This technique surpasses other established methods in terms of speed due to its fully automated nature, and it requires minimal expertise for implementation, making it accessible to individuals with any level of medical knowledge. The positive outcomes achieved through this method allow for the measurement of various parameters (such as nicking, narrowing, and branching coefficients), which can assist in diagnosing different diseases.

The upcoming study goals to quantitatively evaluate a collection of clinical data found from publicly available datasets to recognize retinopathy of prematurity (ROP).

References:

1. Srinivasan Senthilkumari, Mohan Neethu, Radhakrishnan Santhi, Subbiah Ramaswami Krishnadas, and Veerappan Muthukkaruppan, Identification of glaucomatous optic nerve head changes in Indian donor eyes without clinical history, Indian Journal of Ophthalmology, vol. 63, no. 7, pp. 600-605 (2015).
2. K. Narasimhan, V. C. Neha, K. Vijayarekha, et al., Hypertensive retinopathy diagnosis from fundus images by estimation of AVR, ICMOC – 2012, Elsevier Ltd., pp. 980 – 993 (2012).
3. Kingman S., Glaucoma is second leading cause of blindness globally, Bull World Health Organ, vol. 8 pp. 82-887 (2004).

4. George R, Ve RS, Vijaya L., Glaucoma in India: Estimated burden of disease, J Glaucoma, vol. 7, pp. 19-391 (2010).
5. T. Y. Wong, R. Klein, A. R. Sharrett, et al., Retinal arteriolar diameter and risk for hypertension, Ann. Intern. Med., vol. 140, pp. 248-255 (2004).
6. T. Y. Wong, R. Klein, F. J. Nieto, et al., Retinal microvascular abnormalities and 10-year cardiovascular mortality: a population-based case-control study, Ophthalmology, vol. 110, pp. 933-940 (2003).
7. T. Y. Wong, R. Klein, et al., Hypertensive retinopathy and risk of stroke, published online in Hypertension (2013).
8. Claudia Kondermann, Daniel Kondermann, Michelle Yan, Blood Vessel Classification into Arteries and Veins in Retinal Images, Article in Proceedings of SPIE - The International Society for Optical Engineering, (2007).
9. Pooja Chaudhari, Prof. Girish A. Kulkarni, Using Artificial Neural Network to Detect Glaucoma with the Help of Cup to Disk Ratio, International Journal of Advanced Research in Electronics and Communication Engineering, vol. 5, no. 7, pp. 1967-1972 (2016).
10. Kurnika Choudhary, ANN Glaucoma Detection using Cup-to-Disk Ratio and Neuroretinal Rim, International Journal of Computer Applications, vol. 111, no. 11, pp. 8-14 (2015).
11. Tehmina Khalil, Samina Khalid and Adeel M. Syed, Review of Machine Learning Techniques for Glaucoma Detection and Prediction, Science and Information Conference, London, UK, pp. 27-29 (2014).
12. T. Teng, M. Lefley, and D. Claremont, Progress towards automated diabetic ocular screening: A review of image analysis and intelligent systems for diabetic retinopathy, Med. Biol. Eng. Comput., vol. 40, pp. 2–13 (2002).
13. R. M. Cesar, Jr, and H. F. Jelinek, Segmentation of retinal fundus vasculature in nonmydriatic camera images using wavelets, in Angiography and Plaque Imaging, Advanced Segmentation Techniques, J. S. Suri and S. Laxminarayan, Eds. Boca Raton, FL: CRC, pp. 193–224 (2003).
14. J. Staal, M. D. Abramoff, M. Niemeijer, M. A. Viergever, and B. van Ginneken, Ridge-based vessel segmentation in color images of the retina, IEEE Trans. Med. Imag., vol. 23, no. 4, pp. 501–509 (2004).
15. C. Heneghan, J. Flynn, M. O'Keefe, and M. Cahill, Characterization of changes in blood vessel width and tortuosity in retinopathy of prematurity using image analysis, Med. Image Anal., vol. 6, pp. 407–429 (2002).
16. A. J. Campilho, A. M. Mendonça, and J. R. Nunes, Image analysis techniques for avascular region detection in retinal angiography, in Proc. ICIAP, pp. 624–628 (1992).
17. E. Grisan and A. Ruggeri, A divide and imperial strategy for the automatic classification of retinal vessels into arteries and veins, in Proc. 25th Int. Conf. IEEE Eng. Med. Biol. Soc., pp. 890–893 (2003).
18. Y. Hatanaka, H. Fujita, M. Aoyama, H. Uchida, and T. Yamamoto, Automated analysis of the distributions and geometries of blood vessels on retinal fundus images, Proc. SPIE Med. Imag. 2004: Image Process., vol. 5370, pp. 1621–1628 (2004).
19. M. Foracchia, E. Grisan, and A. Ruggeri, Extraction and quantitative description of vessel feature hypertensive retinopathy fundus images, in Book Abstracts 2nd Int. Workshop Comput. Asst. Fundus Image Anal., pp. 6 (2001).
20. X. Goa, A. Bharath, A. Stanton, A. Hughes, N. Chapman, and S. Thom, A method of vessel tracking for vessel diameter measurement on retinal images, in Proc. ICIP, pp. 881–884 (2001).

21. M. E. Martinez-Perez, A. D. Hughes, A. V. Stanton, S. A. Thom, N. Chapman, A. A. Bharath, and K. H. Parker, Retinal vascular tree morphology: A semiautomatic quantification, IEEE Trans. Biomed. Eng., vol. 49, no. 8, pp. 912–917 (2002).
22. J. Lowell, A. Hunter, D. Steel, A. Basu, R. Ryder, and R. L. Kennedy, Measurement of retinal vessel widths from fundus images based on 2-D modeling, IEEE Trans. Med. Imag., vol. 23, no. 10, pp. 1196–1204 (2004).
23. D. E. Becker, A. Can, J. N. Turner, H. L. Tanenbaum, and B. Roysam, Image processing algorithms for retinal montage, synthesis, mapping, and real-time location determination, IEEE Trans. Biomed. Eng., vol. 45, no. 1, pp. 115–118 (1998).
24. H. Shen, B. Roysam, C. V. Stewart, J. N. Turner, and H. L. Tanenbaum, Optimal scheduling of tracing computations for real-time vascular landmark extraction from retinal fundus images, IEEE Trans. Inf. Technol. Biomed., vol. 5, no. 1, pp. 77–91 (2001).
25. Subhasis Choudhury, Shankar Chatterjee, Norman Kata,z et al. Detection of blood vessels in retinal images using two dimensional matched filter, IEEE Transactions on Medical Images, vol. 8, No. 3, pp. 264 – 269 (1987).
26. James Lowell, Andrew Hunter et al. Measurement of retinal vessels width from fundus images based on 2-D modeling, IEEE Transactions on Medical Imaging, vol. 3, No. 10, pp. 1200 – 1203 (2004).
27. Di Wu, Ming Zhang et al. Adaptive detection of blood vessels in retinal images, IEEE Transactions on Biomedical Engineering, vol. 53, No. 2, pp. 341-343 (2006).
28. Zhang, Zhuo, Beng Hai Lee, Jiang Liu, Damon Wing Kee Wong, Ngan Meng Tan, Joo Hwee Lim, Fengshou Yin, Weimin Huang, Huiqi Li, and Tien Yin Wong., Optic disc region of interest localization in fundus image for glaucoma detection in ARGALI, In 2010 5th IEEE Conference on Industrial Electronics and Applications, IEEE, pp. 1686-1689 (2010).
29. Dehghani, Amin, Hamid Abrishami Moghaddam, and Mohammad- Shahram Moin., Optic disc localization in retinal images using histogram matching, EURASIP Journal on Image and Video Processing 2012, no. 1, pp. 19 (2012).
30. Akram, M. Usman, Aftab Khan, Khalid Iqbal, and Wasi Haider Butt., Retinal images: optic disk localization and detection, In International Conference Image Analysis and Recognition, Springer, Berlin, Heidelberg, pp. 40-49 (2010).
31. M. Kirubaa, R; Dr. Lavanya R.; Nazneen P Kotwal; Devi Vijayan, change detection in mammogram images using fuzzy C-means clustering, International Journal of Applied Engineering Research 10(11):29825-29834 (2015).
32. “Inspire Datasets”, University of Iowa, Carver College of Medicine, Department of Ophthalmology and Visual Science, available online at https://medicine.uiowa.edu/eye/inspire-datasets.
33. “High-resolution fundus (HRF) image database” available online at https://www5.cs.fau.de/research/data/fundus-images/.
34. “Structured analysis of the retina dataset” is available online at http://www.ces.clemson.edu/~ahoover/stare/.
35. Saeid F., Sevin Samadi, Parisa Nadirkhanlou, Novel Retinal Vessel Segmentation Based on Local Adaptive Histogram Equalization, 8-th Iranian Conference on Machine Vision and Image Processing (MVIP) IEEE, (2013).
36. Yitian Zhao et al., Automatic 2-D/3-D Vessel Enhancement in Multiple Modality Images Using a Weighted Symmetry Filter, IEEE Transactions on Medical Imaging, 37, (2018).

37. Ming, L., Qingbo Yin, Mingyu Lu, Retinal Blood Vessel Segmentation Based on Multi-Scale Deep Learning, Proceedings of the Federated Conference on Computer Science and Information Systems, p. 117–123 (2018).

38. Zhun, F., Yibiao, R., Jiewei, L., Jiajie, M., Fang, L., Xinye C. and Tiejun, Y, Automated Blood Vessel Segmentation in Fundus Image Based on Integral Channel Features and Random Forests, 12th World Congress on Intelligent Control and Automation (WCICA) (2016).

39. S. Chaudhuri, S. Chatterjee, N. Katz, M. Nelson, M. Goldbaum, Detection of blood vessels in retinal images using two dimensional matched filters, IEEE Trans. Med. Imaging, Vol.8(3), pp. 263-269 (1989).

40. F. Zana, J.C. Klein, Segmentation of vessel like patterns using mathematical morphology and curvature evaluation, IEEE Trans. Image Processing, Vol. 10(7), pp. 1010-1019 (2001).

41. J. Staal, B. Ginneken, M. Niemeijer, A. Viegever, M.D. Abramoff, Ridge based vessel segmentation in color images of the retina, IEEE Trans. Med. Imaging, Vol. 23(4), pp. 501-509 (2004).

42. R. Kirsch, Computer determination of the constitute structure of biomedical images, Comput. Biomed. Res. Vol. 4(3), pp. 315-328 (1971).

43. Mohammed Al-Rawi, Munib Qutaishat, Mohammed Arrar, An improved matched filter for blood vessel detection of digital retinal images, Computers in Biology and Medicine, Vol. 37, pp. 262-267 (2007).

44. Nassrallah Faris, Abdukader Al Shalchi, & Javad Rahebi, Human retinal optic disc detection with grasshopper optimization algorithm, Multimedia Tools and Applications, Springer, volume 81, pages24937–24955 (2022)

45. Buket Toptaş, Murat Toptaş & Davut Hanbay, Detection of Optic Disc Localization from Retinal Fundus Image Using Optimized Color Space, Journal of Digital Imaging, Springer, 35, pages302–319 (2022).

46. Mahum R Rehman, S Okon, OAlabrah, AMeraj, TRauf H, A novel hybrid approach based on deep cnn to detect glaucoma using fundus imaging, Electronics (Switzerland) (2022).

47. Nazir TIrtaza, AStarovoitov V, Optic Disc and Optic Cup Segmentation for Glaucoma Detection from Blur Retinal Images Using Improved Mask-RCNN, International Journal of Optics (2021).

48. Deng I, Wang Y Han J, Optical Disc Location Based on Similarity to Improved Harris Algorithm, Chinese Control Conference, CCC (2021) 2021-July 2185-2189

49. Rehman AHarouni, MKarimi, MSaba, TBahaj, & S Awan, Microscopic retinal blood vessels detection and segmentation using support vector machine and K-nearest neighbors, Microscopy Research and Technique (2022) 85(5) 1899-1914.

50. Arsalan M Haider, A Choi, J Park K, Diabetic and hypertensive retinopathy screening in fundus images using artificially intelligent shallow architectures, Journal of Personalized Medicine (2022) 12(1).

51. Pal M, Banerjee M, Retinal vessel segmentation using a strip wise classification approach with grid search-based parameter selection, International Journal of Computational Vision and Robotics (2022) 12(2) 194-218.

52. Boudegga, H Elloumi, Y Akil, M Hedi, Bedoui, M Kachouri, R Abdallah A, Fast and efficient retinal blood vessel segmentation method based on deep learning network, Computerized Medical Imaging and Graphics (2021) 90.

53. Ooi, A Embong, Z Abd, Hamid A Zainon, R Wang, S Ng, T Hamzah, R Teoh, S Ibrahim H, Interactive blood vessel segmentation from retinal fundus image based on canny edge detector, Sensors, MDPI, (2021) 21(19).

54. Q. Li, B. Feng, L. Xie, P. Liang, H. Zhang, and T. Wang, A crossmodality learning approach for vessel segmentation in retinal images, IEEE transactions on medical imaging, vol. 35, no. 1, pp. 109–118, 2015.

55. C. L. Srinidhi, P. Aparna, and J. Rajan, A visual attention guided unsupervised feature learning for robust vessel delineation in retinal images, Biomedical Signal Processing and Control, vol. 44, pp. 110–126, 2018.

56. Yan, Zengqiang and Yang, Xin and Cheng, Kwang-Ting, A three-stage deep learning model for accurate retinal vessel segmentation, IEEE journal of biomedical and health informatics, vol. 23, no. 4, pp. 1427–1436, 2018.

57. Q. Jin, Z. Meng, T. D. Pham, Q. Chen, L. Wei, and R. Su, Dunet: A deformable network for retinal vessel segmentation, Knowledge-Based Systems, vol. 178, pp. 149–162, 2019.

58. Yuchen Yuan, Lei Zhang, Lituan Wang, and Haiying Huang, Multi-level Attention Network for Retinal Vessel Segmentation, ieee journal of biomedical and health informatics, DOI 10.1109/JBHI.2021.3089201.

PSO-Optimized CLAHE for Image Enhancement and Active Contour-Based Segmentation of Retinal Vessels

Niladri Halder[1*], Dibyendu Roy[2], Partha Pratim Sarkar[2], Sankar Narayan Patra[1], and Subhankar Bandyopadhyay[1]

[1] *Instrumentation and Electronics Engineering, Jadavpur University, Saltlake Campus, Kolkata, 700098, West Bengal, India.
[2] Electronics and Communication Engineering, UIT, Burdwan University, Golapbag, Burdwan, 713104, West Bengal, India.

Abstract. Accurate segmentation of retinal vessels is crucial for diagnosing and monitoring various ocular and systemic diseases. However, challenges such as low contrast, noise, and uneven illumination in retinal images hinder precise segmentation. This study proposes a novel framework combining Particle Swarm Optimization (PSO) with contrast-limited Adaptive Histogram Equalization (CLAHE) for image enhancement, followed by an Active Contour Model (ACM) for the segmentation of retinal vessels.

The PSO algorithm is employed to optimize the parameters of CLAHE, ensuring enhanced image contrast and clarity while preserving critical vessel details. The enhanced images are subsequently segmented using an ACM, which effectively delineates vessel boundaries by minimizing a hybrid energy function. Integrating PSO-optimized CLAHE ensures superior preprocessing, enabling the active contour model to achieve more accurate and robust segmentation results.

Experimental evaluations were conducted on publicly available retinal image datasets, and the proposed method demonstrated improved performance in terms of accuracy, sensitivity, and specificity compared to traditional enhancement and segmentation approaches. The framework's adaptability to varying image qualities and its potential for integration into automated diagnostic systems highlight its significance in retinal image analysis.

Keywords: Retinal Vessel Segmentation, Particle Swarm Optimization, Contrast-limited Adaptive Histogram Equalization, Image Enhancement, Active Contour Model, Medical Imaging.

1 Introduction

The segmentation of retinal vessels plays a crucial role in diagnosing and monitoring various ocular and systemic diseases, including diabetic retinopathy, glaucoma, and hypertension. Retinal vessel extraction aids in the analysis of vascular structures, which are pivotal indicators of pathological changes. However, accurate segmentation remains a challenging task due to the complex and intricate patterns of retinal vasculature, as well as variations in image quality caused by illumination inconsistencies, noise, and patient-specific anatomical differences.

To address these challenges, image preprocessing techniques that enhance vessel visibility and segmentation algorithms that precisely delineate vascular structures are essential. Contrast Limited Adaptive Histogram Equalization (CLAHE) has emerged as a powerful image enhancement technique, especially in medical imaging, due to its ability to enhance local contrast while mitigating noise amplification. However, its performance is highly dependent on the appropriate selection of parameters such as clip limit and grid size, which can significantly influence the quality of the enhanced image.

Particle Swarm Optimization (PSO), a swarm intelligence-based optimization algorithm, offers an effective solution for parameter tuning in complex problems. By employing PSO to optimize the CLAHE parameters, the enhanced images can achieve superior contrast and vessel visibility, setting the stage for improved segmentation results.

In addition to enhancement, segmentation techniques play a pivotal role in accurately extracting retinal vessels. Active contour models (ACMs) have been widely utilized for this purpose due to their ability to refine contours based on energy minimization principles iteratively. ACMs effectively balance internal forces (ensuring contour smoothness) and external forces (driven by image features such as edges or gradients). When applied to enhanced retinal images, ACMs can achieve precise vessel delineation, even in challenging cases.

This research proposes a novel framework that combines PSO-optimized CLAHE for image enhancement with active contour-based segmentation for extracting retinal vessels. Integrating these techniques leverages each component's strengths, ensuring enhanced image quality and robust segmentation. The proposed methodology is evaluated on publicly available retinal image datasets, demonstrating its potential to achieve high segmentation accuracy and reliability, even in noise and complex vascular structures.

The remainder of this paper is structured as follows: Section 2 reviews related work in retinal image enhancement and segmentation. Section 3 presents the proposed methodology, detailing the PSO-optimized CLAHE process and the active contour-based segmentation approach. Section 4 discusses the experimental setup, datasets, and evaluation metrics. Section 5 analyzes the results and compares the proposed framework with existing methods. In conclusion, Section 6 wraps up the paper and highlights potential areas for future research.

2 Literature Review

Retinal vessel segmentation plays a vital role in diagnosing ocular and systemic diseases such as diabetic retinopathy and hypertension. Accurate segmentation requires effective preprocessing to enhance vessel structures, especially in noisy or low-contrast retinal images. The combination of Particle Swarm Optimization (PSO), Contrast Limited Adaptive Histogram Equalization (CLAHE), and Active Contour Models (ACMs) has emerged as a promising approach. This review highlights recent advancements and applications of these methods in retinal image analysis.

CLAHE has gained significant attention for enhancing retinal images by improving local contrast and preserving edge details. Recent studies have addressed its limitations, such as over-amplification of noise, by optimizing its parameters. In 2023, Priyadharsini C. presented enhancement techniques for retinal images based on the Lab color space [1]. Although the study doesn't focus solely on CLAHE, it emphasizes the significance of color dominance in retinal image enhancement. The authors explore how manipulating different color channels can enhance image quality, which is relevant when applying CLAHE to specific channels for focused enhancement. A 2022 study by Cheng Wan et al., published in Frontiers in Medicine, explores adaptive CLAHE methods for enhancing retinal fundus images [2]. The research emphasizes how CLAHE improves image contrast and reduces noise, aiding in the clearer visualization of retinal structures. The results indicate that CLAHE is a useful tool for enhancing retinal images, leading to more accurate analysis and diagnosis. In 2020, Alwazzan MJ introduced a hybrid algorithm that integrates CLAHE with other enhancement methods to improve the quality of color retinal fundus images [3]. The authors tackle issues like artificial boundaries and noise amplification that are commonly associated with CLAHE. Their approach involves preprocessing the green channel of the image with a Wiener filter before applying CLAHE, which leads to better image quality, reduced noise, and clearer vessel structures. Esra Kaya et al. (2020) investigated a technique for supervised segmentation of retinal vessel structures utilizing Artificial Neural Networks (ANN), focusing on the use of CLAHE preprocessing [4]. In their study, CLAHE was applied to the green channel of retinal images to improve the visibility of the vascular structures. This preprocessing step played a crucial role in enhancing the ANN's segmentation performance, resulting in more accurate delineation of vessels within the retinal images.

These studies underscore the versatility and effectiveness of CLAHE in enhancing retinal images, thereby facilitating better visualization and analysis of retinal structures. The integration of CLAHE with other advanced techniques, such as neural networks and hybrid algorithms, further enhances its applicability in medical imaging.

Particle Swarm Optimization (PSO) has emerged as a powerful technique for enhancing retinal images, addressing challenges such as uneven illumination, low contrast, and noise. By simulating the social behavior of particles, PSO effectively adjusts image parameters to improve visual quality and facilitate subsequent analysis. In 2022, Jyotirmaya Sahoo and colleagues introduced an autonomous augmentation technique utilizing real-encoded PSO to enhance medical images [5]. This approach resulted in notable improvements in image quality, supporting more precise medical decision-making. V. Sathananthavathi proposed a method in 2021 to enhance fundus images with uneven illumination and contrast by adjusting luminance and contrast through Particle Swarm Optimization (PSO) [6]. This approach effectively improved the image quality, making it more suitable for clinical analysis. In 2020, Swarup Kr. Ghosh and colleagues introduced a novel enhancement method that utilizes Particle Swarm Optimization (PSO) within a fuzzy framework to tackle challenges in retinal image enhancement [7]. This approach successfully improved image quality, enabling more effective analysis of retinal conditions. In 2019, Qiang Huo proposed a data-efficient semi-supervised learning framework that integrates deep learning networks with Generative Adversarial Networks (GAN) and self-training, optimized through Particle Swarm Optimization (PSO) [8]. This approach demonstrated performance on par with supervised learning while utilizing only a small portion of labeled data, showcasing the effectiveness of PSO in optimizing deep learning models for retinal vessel segmentation.

PSO has proven to be a valuable tool in retinal image enhancement, effectively addressing various challenges and improving image quality for clinical applications. Ongoing research continues to explore its potential, integrating PSO with advanced techniques like deep learning and fuzzy logic to further enhance retinal image analysis.

Active contour models, commonly known as snakes, have been extensively utilized for retinal vessel segmentation due to their ability to adapt to vessel boundaries and effectively delineate complex structures. Recent advancements in this area have introduced innovative methodologies to enhance segmentation accuracy and robustness.

In 2018, Prakash Kumar Karn introduced Hybrid Active Contour Models that integrate various techniques to enhance segmentation performance [9]. For example, one study presented a hybrid active contour model that included an innovative preprocessing method to segment retinal blood vessels in different fundus images. This approach showed improved robustness and accuracy over traditional methods. The Infinite Perimeter Active Contour Model was introduced by Zhao Y in 2015, incorporating hybrid region information to segment retinal vessels [10]. This model effectively tackles issues like low contrast and noise, delivering high specificity and accuracy in vessel segmentation. Another important contribution is the "Ribbon of Twins" active contour model, which uses two pairs of contours to accurately capture the edges of each vessel while ensuring consistent width. Developed by Bashir Al-Diri et al., this approach employs a generalized

morphological order filter for initialization and an implicit neural cost function to address junction configurations, enabling efficient segmentation and measurement of retinal vessels [11].

The literature review emphasizes the effectiveness and potential of the image-processing methods discussed in these studies for segmenting blood vessels. However, it is important to acknowledge the existing limitations and areas for improvement. Some retinal image processing methods are sensitive to factors like low resolution, noise, uneven illumination, and motion artifacts. In real-world clinical environments, where image quality can vary, these methods may produce suboptimal results or necessitate additional pre-processing steps. Additionally, certain techniques can be computationally intensive, requiring significant computational resources or extended processing times, which may hinder their use in real-time or resource-limited settings. Acquiring accurate and comprehensive ground truth annotations for retinal images is another challenge, as it can be time-consuming and difficult, impacting the development and evaluation of image-processing algorithms and complicating efforts to determine their true effectiveness. Moreover, the processing algorithms currently lack efficient techniques for handling multiple target features, such as optic disks, retinal vessels, hemorrhages, and others.

3 Motivation and Contribution

Motivation:

Enhancing and segmenting retinal blood vessels plays a critical role in advancing medical imaging, diagnosis, and treatment planning. Below are the key motivations:

- Early Disease Detection: Retinal vessel segmentation can help detect microaneurysms, hemorrhages, and neovascularization, which are early signs of diabetic retinopathy. Changes in blood vessel structure, such as narrowing or irregularity, can indicate hypertension-related damage. Analysis of the retinal blood vessels and optic disc region aids in identifying glaucoma. Retinal vessels provide insights into systemic vascular conditions, as the retina is the only place where microvasculature can be observed non-invasively.
- Improved Diagnosis Accuracy: Enhancing and segmenting retinal vessels improves image clarity, enabling clinicians and AI systems to differentiate between normal and pathological features more accurately.
- Treatment Monitoring: Changes in vessel structure or density can indicate how well a patient is responding to treatments like laser photocoagulation or anti-VEGF injections. Segmentation allows clinicians to monitor disease progression over time, ensuring timely interventions.
- Cost and Time Efficiency: Automated segmentation reduces the workload for healthcare professionals, enabling faster and more consistent analysis of retinal images, which is crucial in large-scale screening programs.

By enhancing and segmenting retinal blood vessels, we not only improve diagnostic and therapeutic outcomes but also contribute to a deeper understanding of the interconnection between ocular and systemic health.

Contribution:

The study introduces an innovative approach for segmenting retinal blood vessels by leveraging Particle Swarm Optimization (PSO) to enhance contrast-limited adaptive Histogram Equalization (CLAHE) for image enhancement and employing active contour methods for segmentation. The contributions of this method are as follows:

- By using PSO to optimize the parameters of CLAHE, the proposed method achieves superior contrast enhancement. This ensures that retinal blood vessels, particularly thin and low-contrast vessels, are more distinguishable from the background, facilitating accurate segmentation.
- Traditional CLAHE methods rely on manually chosen parameters that may not generalize well across diverse datasets. PSO automates the selection of optimal parameters, ensuring consistent performance across various image conditions, such as varying lighting, noise, and contrast levels.
- The active contour model, when applied to the enhanced images, benefits from the optimized contrast, leading to precise delineation of retinal blood vessels. This is particularly effective in addressing challenges posed by complex retinal structures and varying vessel thickness.
- Combining PSO-optimized CLAHE with active contour models introduces a hybrid approach that synergistically leverages the strengths of both methods. This integration minimizes noise interference and false positives, which are common in traditional segmentation techniques.
- The algorithm can be extended to other medical imaging modalities where contrast enhancement and precise segmentation are critical, such as magnetic resonance imaging (MRI) or computed tomography (CT) scans.

The proposed approach significantly advances retinal vessel segmentation by combining PSO-optimized CLAHE for image enhancement with active contour-based segmentation. It offers a robust, accurate, and clinically valuable tool for retinal image analysis.

4 Dataset

Dataset:

The Active-BDCLF algorithm was estimated by freely accessible datasets like DRIVE, HRF, STARE, CHASEDB1, INSPIRE-AVR, and others to develop a fully automated monitoring system.

The DRIVE dataset was created as part of a diabetic testing campaign in The Netherlands. The trial involved 400 diabetic individuals ranging in age from 25 to 90 years. Out of this collection, 40 images were selected at random: 33 exhibiting no signs of diabetic retinopathy and 7 showing early-stage, mild diabetic retinopathy. These visuals were obtained with a Canon CR5 non-mydriatic 3CCD camera featuring a 45-degree field of view (FOV). Each image was confirmed at a resolution of 768×584 pixels, using an 8-bit color model, with a circular field of view covering approximately 540 pixels. The photos were reaped around the FOV, and every photo was accompanied by a 'mask' delineating the FOV.

The collection of 40 images was divided into a training set and a test set, each containing 20 images. The training collection comprises a solitary manual segmentation of the vascular structure. In relation to the test set, two manual delineations are included: one acts as the standard, and the other facilitates a comparison between the computer-generated segmentation and an independent human observer. Each retinal image also comes with a mask defining the region of interest. The human observers responsible for manual segmentations were trained by an experienced ophthalmologist and instructed to label pixels as vessels only if they were at least 70% confident in their assessment.

The INSPIRE-AVR dataset is publicly available and consists of 40 annotated retinal images with significant vascular abnormalities, optic disc region, and artery-vein ratio. It is specifically used for classifying and grading various hypertension-related complications. The annotations were made by two specialists using a hybrid automated tool developed by the University of Wisconsin, Madison, WI, USA [18].

The HRF imaging dataset, created by a collaborative research group, is designed to aid in the formulation of clinical decision-support tools for diagnosing different retinal irregularities. It covers 45 retinal images from participants, with 15 from healthy individuals, 15 from glaucomatous cases, and 15 from diabetic retinopathy (DR) cases [19]. These pictures are recorded at 3504×2336 pixels resolution, 24 bits per pixel, utilizing a CANON CF-60 UVI camera with a 60-degree viewing angle.

The STARE dataset comprises approximately 400 images, with 50 images depicting vascular patterns and 80 featuring Reference standards for optic nerve localization [20]. These pictures were taken at a resolution of 605×700 pixels with a 24-bit color depth using a TOPCON TRV-50 fundus camera, offering a 35-degree field of view.

5 Methodology

The proposed methodology for the PSO-Optimized CLAHE for Image Enhancement and Active Contour-Based Segmentation of Retinal Vessels is structured in two primary phases: image enhancement and vessel segmentation. Below are the detailed steps:

5.1 Image Enhancement Using PSO-Optimized CLAHE

This method effectively enhances images by combining Particle Swarm Optimization (PSO) and Contrast Limited Adaptive Histogram Equalization (CLAHE). The goal is to optimize the CLAHE parameters using PSO, ensuring the enhanced image balances contrast improvement and naturalness. Fig. 1 illustrates the retinal vessel enhancement techniques utilizing the proposed PSO-CLAHE fusion method.

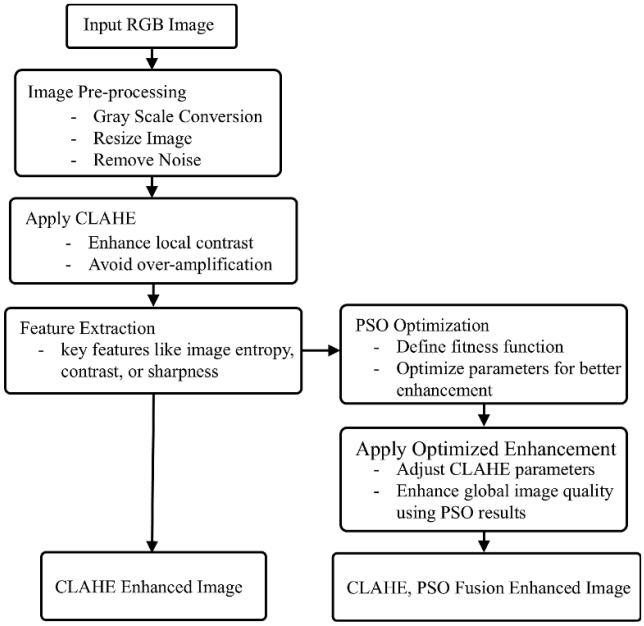

Fig. 1: PSO-optimized CLAHE to enhance retinal vessels

5.1.1 Introduction to CLAHE

CLAHE is an extension of Adaptive Histogram Equalization (AHE), which enhances local contrast by dividing an image into smaller regions (tiles) and performing histogram equalization locally on each region. However, AHE can lead to over-amplification of noise in homogeneous regions. CLAHE addresses this by limiting the contrast enhancement, thus preventing noise amplification. The CLAHE algorithm involves the following steps:

a. The input image is divided into non-overlapping tiles or regions, typically of uniform size $m \times n$.

b. For each tile, compute the histogram of pixel intensities:

$$H_k(i) = \sum_{(x,y)} \delta(I(x,y) - i), \qquad i = 0,1,2, \dots \dots \dots \dots, L-1 \tag{1}$$

Where $H_k(i)$ is the histogram for tile k at intensity level i. δ is the Kronecker delta function. $I(x,y)$ is the intensity at the pixel (x,y). L is the total number of intensity levels.

c. To limit noise amplification, the histogram is clipped at a predefined threshold T. Excess intensity values are redistributed across the histogram. The clipped histogram $H'_k(i)$ is given by

$$H'_k(i) = \begin{cases} H_k(i), & if\ H_k(i) \le T \\ T & if\ H_k(i) > T \end{cases} \tag{2}$$

The excess pixels $E = \sum_i max(0, H_k(i) - T)$ are redistributed uniformly:

$$H''_k(i) = H'_k(i) + \frac{E}{L} \tag{3}$$

d. The normalized CDF for the clipped histogram is computed:

$$CDF_k(i) = \frac{\sum_{j=0}^{i} H''_k(j)}{\sum_{j=0}^{L-1} H''_k(j)} \tag{4}$$

e. The new intensity values are mapped using the CDF.

$$I'_k(x,y) = CDF_k\big(I(x,y)\big).(L-1) \tag{5}$$

f. To avoid discontinuities at tile boundaries, bilinear interpolation is used to blend the intensities of adjacent tiles. The final pixel value is calculated as:

$$I'(x,y) = (1-w_x)\big(1-w_y\big)I'_A + w_x\big(1-w_y\big)I'_B + (1-w_x)w_y I'_C + w_x w_y I'_D \tag{6}$$

Where I'_A, I'_B, I'_C, I'_D are the intensity values of the four nearest tiles, and w_x, w_y are the interpolation of time.

Figure 2 illustrates the enhanced result of a fundus image from the DRIVE dataset, processed using Histogram Equalization (HE), Adaptive Histogram Equalization (AHE), and CLAHE. The individual histogram analysis highlights the characteristics of each enhanced image. The histogram-equalized image shows an overall improvement in contrast but may appear unnatural or overly harsh in regions with distinct brightness variations. The adaptive histogram-equalized image effectively enhances local regions, bringing out finer details, though it may amplify noise or artifacts, particularly in uniform areas. In contrast, the CLAHE-enhanced image achieves a balanced enhancement of local details, minimizing noise and artifacts. This results in a smoother and more visually appealing outcome compared to AHE.

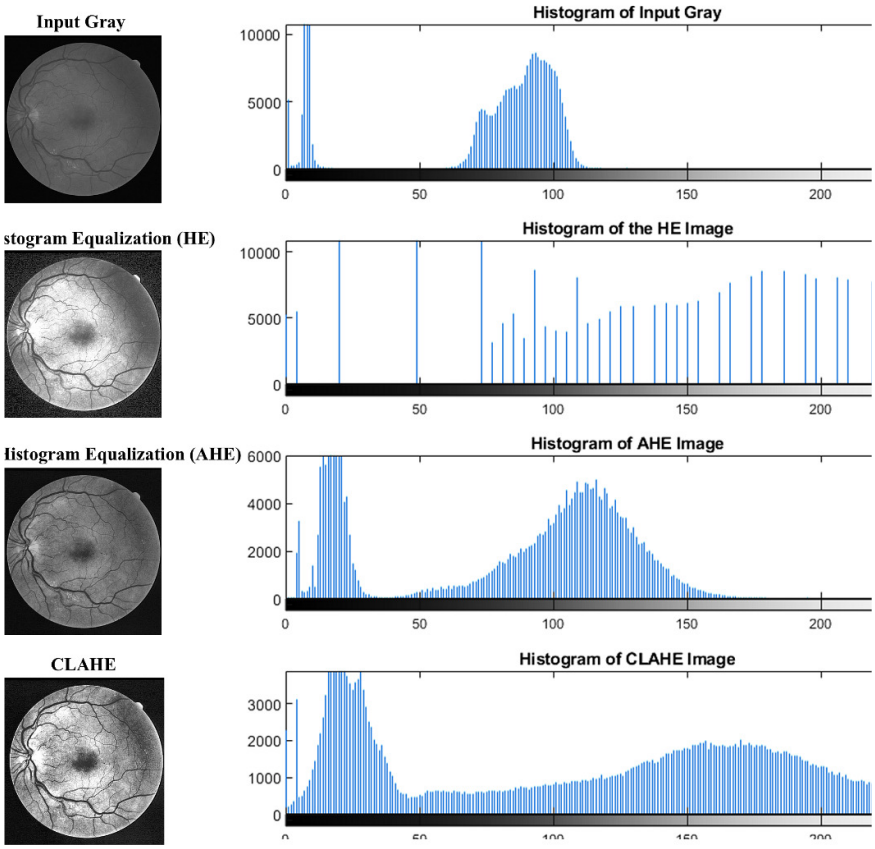

Fig. 2: Enhanced fundus image from the DRIVE dataset using Histogram Equalization (HE), Adaptive Histogram Equalization (AHE), and Contrast Limited Adaptive Histogram Equalization (CLAHE).

5.1.2 Introduction to Particle Swamp Optimization

Particle swarm optimization (PSO) [12, 13, 14] is a widely recognized population-based optimization technique inspired by the principles of swarm intelligence [15, 16, 17]. This approach excels in efficiently exploring the optimal solution within a given search domain. PSO achieves this by employing a specialized group of agents called 'particles,' which dynamically adjust their positions and velocities in a probabilistic manner, guided by the best-known position within the group and the global search area. Assuming X is the size of the swarm in a D-dimensional search space, each particle's position at any given moment is defined as $P_i\left(p_{i_1}, p_{i_2}, p_{i_3}, \dots\dots\dots\dots, p_{i_D}\right)$, which represents a feasible solution to an optimization problem. The velocity of each particle is denoted by $U_i\left(u_{i_1}, u_{i_2}, u_{i_3}, \dots\dots\dots\dots, u_{i_D}\right)$. The best previous position of the swarm is represented by $Q_i\left(q_{i_1}, q_{i_2}, q_{i_3}, \dots\dots\dots\dots, q_{i_D}\right)$ for each particle, while the best position determined by the entire swarm is denoted as $Q_g\left(q_{g_1}, q_{g_2}, q_{g_3}, \dots\dots\dots\dots, q_{g_D}\right)$. These equations [7, 8, 9] are used to control the behaviour of the particles.

$$u_{i_d}^{k+1} = \omega^k * u_{i_d}^k + a_1 * rand() * \left(q_{i_d} - p_{i_d}^k\right)\Delta t + a_2 * rand() * \left(q_{g_d} - p_{i_d}^k\right)/\Delta t \quad (7)$$

$$p_{i_d}^{k+1} = p_{i_d}^k + \Delta t * u_{i_d}^k \quad (8)$$

$$\omega^k = \omega_{max} - k * (\omega_{max} - \omega_{min})/k_{max} \quad (9)$$

The acceleration coefficients, represented by a_1 and a_2 and the inertia weight, denoted by w where w_{max} and w_{max} are the maximum and minimum values of w are used in a random function $rand()$ that follows a uniform distribution. The updated value and maximum number of iterations are indicated by $u_{i_d}^{k+1}$ and $p_{i_d}^{k+1}$ respectively, where $d \in [1,\ D]$. The unit time is usually denoted by Δt and the conditions under which $u_{i_d}^{k+1}$ and $p_{i_d}^{k+1}$ must be restricted are as follows:

$$u_{i_d}^{k+1} = \begin{cases} u_{i_d}^{k+1} & -u_{max} \le u_{i_d}^{k+1} \le u_{max} \\ u_{max} & u_{i_d}^{k+1} > u_{max} \\ -u_{max} & u_{i_d}^{k+1} < -u_{max} \end{cases} \quad (10)$$

$$p_{i_d}^{k+1} = \begin{cases} p_{i_d}^{k+1} & -p_{max} \le p_{i_d}^{k+1} \le p_{max} \\ p_{init} & p_{i_d}^{k+1} > p_{max} \\ p_{init} & p_{i_d}^{k+1} < p_{min} \end{cases} \quad (11)$$

$$p_{init}^{k+1} = p_{min} + rand() * (p_{max} - p_{min}) \quad (12)$$

where u_{max} represents the highest value of u while p_{max} and p_{min} indicate the maximum and minimum values of p, respectively. The following is a summary of the primary stages involved in the processing of PSO:

1. Define the PSO parameters: Establish the PSO (Particle Swarm Optimization) settings, such as the upper and lower iteration weights, cognitive and social acceleration constants, swarm size, neighborhood scope, and the iteration limit.
2. Select an RGB Fundus image: Pick a Fundus image in RGB format and extract its green channel.
3. Initialize particle positions and velocities: Set up the initial locations and speeds of the particles.
4. Evaluate particle fitness: Calculate the fitness scores for the initially placed particles.
5. Identify the best position for each particle: Pinpoint the optimal individual location for every particle in the swarm.

$$pos_{new} = pos_{old} + v$$
$$v = I \times v_{old} + C_1 \times rand(\quad) \times (pos_{individual} - pos_{old}) + C_2 \times rand(\quad) \times (pos_{swarm} - pos_{old})$$

Where v is the velocity, I is the inertia weight, C_1, C_2 are the cognitive and social coefficients respectively.

6. Apply equations 1, 2, and 3 to modify the particles' positions and velocities [33].
7. Refresh the optimal individual position for each particle and the optimal group position for the entire swarm.
8. Determine if the maximum allowed iterations have been completed or not.
    a. If completed, return the particle with the highest HIS value.
    b. If not, loop back to step 6 and continue the process.
9. Terminate the algorithm

PSO functions by iteratively updating the position and velocity of a group of particles within a search domain, where each particle signifies a potential solution. The quality of each particle is evaluated using a fitness function, and PSO leverages interactions among particles to explore the search domain and converge toward an optimal solution. The result of the PSO algorithm is the most favorable solution identified during the process, which might represent a local rather than a global optimum. The results of improving the PSO algorithm are illustrated in Fig. 3.

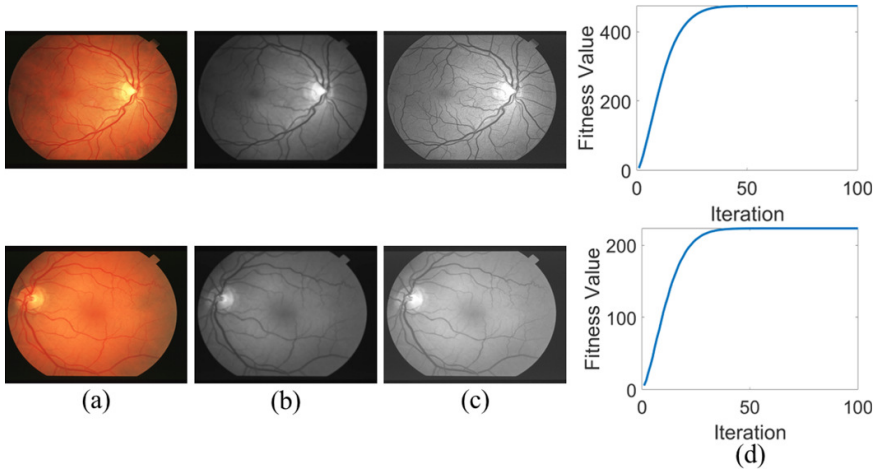

Fig. 3: Enhanced Image using PSO: (a) Input RGB fundus image, (b) Gray Image, (c) PSO enhanced Image, (d) Fitness values of PSO enhanced Images.

Particle Swarm Optimization (PSO)-enhanced Contrast Limited Adaptive Histogram Equalization (CLAHE) integrates the strengths of optimization algorithms with image processing techniques to effectively improve image quality. By fine-tuning CLAHE parameters, PSO maximizes contrast while minimizing noise and distortion. This automated optimization

process eliminates the need for manual parameter adjustments, making it ideal for large-scale image processing applications. Fig. 4 illustrates the enhanced vessels of a retinal fundus image achieved using PSO-optimized CLAHE.

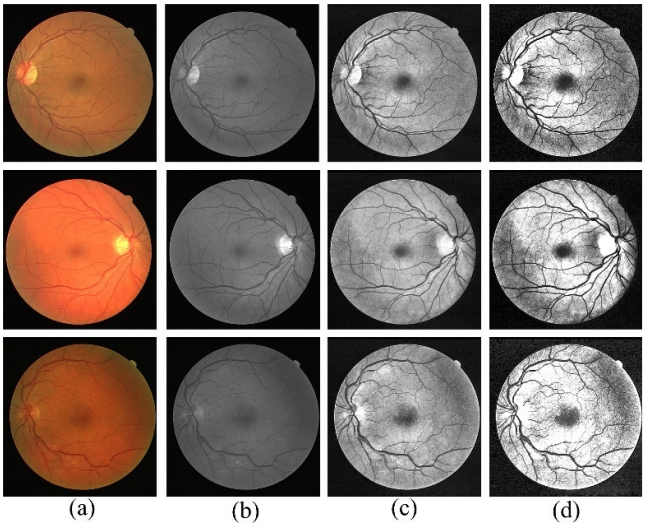

Fig. 4: Vessel's enhancement using PSO optimized CLAHE: (a) Input fundus image, (b) Gray image, (c) CLAHE enhanced image, (d) PSO optimized CLAHE enhancement

5.2 Vessel's segmentation using Active Contour

Active Contour-based Vessel Segmentation is a widely used technique in medical imaging for extracting and analyzing blood vessels in retinal fundus images. Active contour models, also known as "snakes," are energy-minimizing curves that evolve under specific constraints to delineate object boundaries. Fig. 5 illustrates the active contour method employed for segmenting retinal vessels.

This method leverages the joint capabilities of the gradient force snake model and the balloon model to detect blood vessels in fundus images effectively. An image-based contour model is a deformable spline curve guided by an internal force that resists deformation, allowing it to move toward objects in the image [21]. This behavior is comparable to the way a snake moves through a hollow space. A snake typically avoids the center of a hollow space, instead moving along the walls and corners, constantly searching for openings. Upon finding a hole, it enters, explores, and retreats if the path is blocked. Similarly, when applied to retinal blood vessels, the snake follows the vessel boundaries, where the vessel walls act as the boundaries and the openings or cracks represent potential entry points.

To ensure the snake adheres to the vessel boundaries without deforming them, its energy must remain lower than the internal energy of the vessels. The Gradient Vector Flow (GVF) technique limits the snake's energy [22]. The total energy function of the snake, calculated at a point v_q, where $q = 0, \ldots, n-1$ is the addition of its inner energy (E_{int}), image energy (E_{img}), and user-defined constraint force E_{Cns}. This relationship is expressed through the equation (13):

$$E_s^* = \int_0^1 E_s(v_q')dq = \int_0^1 [E_{int}(v_q') + E_{img}(v_q') + E_{cns}(v_q')]dq \qquad (13)$$

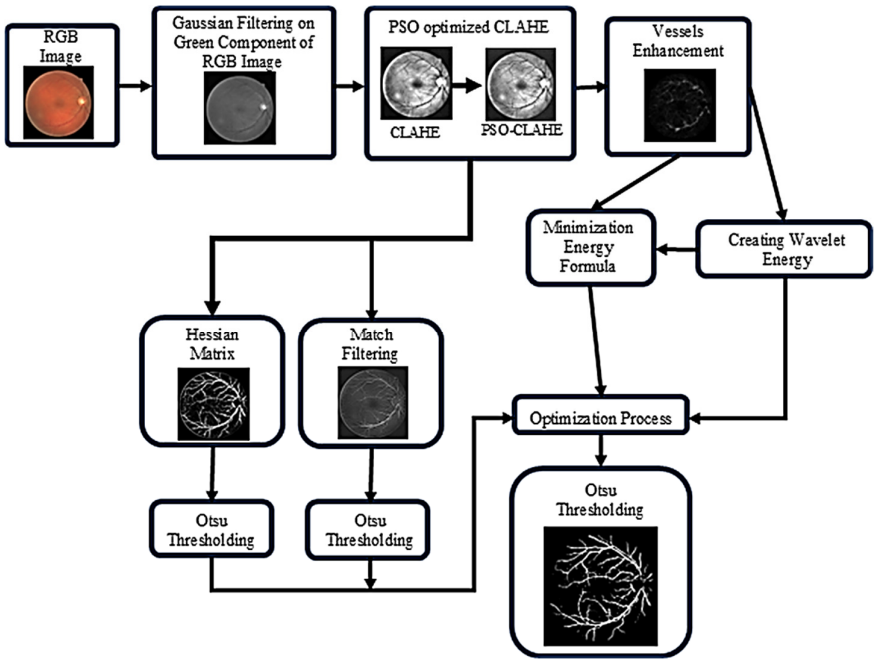

Fig. 5: Retinal vessel segmentation using Active Contour

5.2.1 Internal energy of snake:

The stored power of the snake is influenced by the fluidity of the curve E_{smth} and continuity of contour E_{con}.

$$E_{int}^{snake} = E_{con} + E_{smth} \quad (14)$$

Moreover the aforementioned equation can be articulated as in an expanded form as:

$$E_{int}^{snake} = \frac{1}{2}\left(\alpha'(q)\left|v_q'\right|^2\right) + \frac{1}{2}\left(\beta'(q)\left|v_q'\right|^2\right)$$

$$= \frac{1}{2}\left(\alpha'(q)\left\|\overline{\frac{\partial v'}{\partial q}}(q)\right\|^2 + \beta'(q)\left\|\overline{\frac{\partial^2 v'}{\partial q^2}}(q)\right\|^2\right) \quad (15)$$

To regulate the sensitivity of the snake's length, user-controlled weights $\alpha'(q)$ and $\beta'(q)$ are introduced.

5.2.2 Energy of Image:

Consider an image, $Img(m,n)$, with attributes like boundaries, closures, and lines. The vitality of the image can then be expressed as:

$$\ddot{E}_{img} = W_{line}E_{line} + W_{edge}E_{edge} + W_{cls}E_{cls} \quad (16)$$

The proportions of attributes such as line, edge, and closure are displayed by $W_{line}, W_{edge}, W_{cls}$ while their corresponding energies are denoted as $E_{line}, E_{edge}, E_{cls}$. The various energies associated with these features are illustrated below.

Line functional: This refers to the intensity of the image, which can be expressed using the following equation:

$$E_{line} = X(m,n) \quad (17)$$

The scale and sign of W_{line} dictate whether the snake gravitates towards dark or light vessels. In this study, a Gaussian filter is employed on the image to shield the snake from being disturbed by inaccessible noisy pixels. After applying the filter, the equation becomes:

$$E_{line} = Gaussian\_Filter\left(X(m,n)\right) \quad (18)$$

Edge function: This parameter is influenced by the gradient of the image

$$E_{edge} = -|\nabla X(m,n)|^2 \quad (19)$$

A snake preliminary beyond the target item may sometimes congregate to a localized noise artifact or minimum. To tackle this problem, a distorting filter is first used and the level of blurriness is gradually reduced to refine the snake-fitting process.

$$E_{edge} = -\left|\ddot{G}_\sigma \times \nabla X(m,n)\right|^2 \quad (20)$$

The term $\ddot{G}_\sigma$ refers to a Gaussian blur where σ represents the standard deviation (SD). The blurry filter can be useful either in the line or the edge function. Given the Marr–Hildreth philosophy of edge detection, the least values of the function occur at the zero-crossings of $\ddot{G}_\sigma \times \nabla X(m,n)$.

Closure function: To sense the corners and endpoints of the line, the data is blurred using $\ddot{G}_\sigma$. Let $J(m,n)$ represent the image after smoothing.

$$J(m,n) = \ddot{G}_\sigma \times x(m,n) \quad (21)$$

Having gradient angle

$$\hat{\theta} = arctan\left(\frac{J_n}{J_m}\right) \quad (22)$$

The normalized vector pointing along the gradient is

$$\hat{n} = \left(cos\hat{\theta}, sin\hat{\theta}\right) \quad (23)$$

A normalized vector $\hat{n}_\perp$ perpendicular to the gradient path

$$\hat{n}_\perp = \left(-sin\hat{\theta}, cos\hat{\theta}\right) \quad (24)$$

The strength of the exit function is specified by

$$E_{cls} = \frac{\partial\hat{\theta}}{\partial\hat{n}_\perp} = \frac{\partial^2 J/\partial^2\hat{n}_\perp}{\partial J/\partial\hat{n}} = \frac{J_{nn}J_m^2 - 2J_{mn}J_mJ_n + J_{mm}+J_n^2}{\left(J_m^2+J_n^2\right)^{3/2}} \quad (25)$$

5.2.3 Constrain Energy:

The accumulated energy managed by the snake's movement, either towards or away from specific object features typically specified by the user. Using the two energy formulas debated earlier, the snake's concluding energy equation can be derived from equation (36). To prevent the snake from penetrating the vessels and to ensure it follows the wall, the internal energy must be minimized accordingly. Several optimization techniques can be employed for this, such as the gradient descent method [23], discrete approximation methods, and others.

$$\ddot{E}_{img} = W_{line}.Gaussian\_Filter\left(X(m,n)\right) + W_{edge}\left(-\left|\ddot{G}_\sigma \times \nabla X(m,n)\right|^2\right) + W_{cls}\frac{J_{nn}J_m^2 - 2J_{mn}J_mJ_n + J_{mm}+J_n^2}{\left(J_m^2+J_n^2\right)^{3/2}} \quad (26)$$

$$\ddot{E}_{GVF} = \iint \mu\left(\widehat{u_m^2} + \widehat{u_n^2} + \widehat{v_m^2} + \widehat{v_n^2}\right) + \left|\nabla\hat{f}\right|^2\left|\hat{V} - \nabla\hat{f}\right|^2 \partial m\, \partial n \quad (27)$$

The gradient vector flow method is applied in this work to mitigate the external energy exerted on the vessels, which is related to the snake's internal energy.

This GVF model [22] tackles issues such as:

i. Difficulty in achieving convergence when starting from minimum.
ii. Inadequate fusing at concave limits.

The bidimensional energy of the GVF vector field is presented in equation (27), where μ represents the tunable smoothing factor. By applying Euler's method to equation (27), the resulting equations are explained:

$$\mu\nabla^2\hat{u} - \left(\hat{u} - \frac{\partial}{\partial m}\widehat{F_{ext}}\right)\left(\frac{\partial}{\partial m}\widehat{F_{ext}}(m,n)^2 + \frac{\partial}{\partial n}\widehat{F_{ext}}(m,n)^2\right) = 0 \quad (28)$$

$$\mu\nabla^2\hat{v} - \left(\hat{v} - \frac{\partial}{\partial n}\widehat{F_{ext}}\right)\left(\frac{\partial}{\partial m}\widehat{F_{ext}}(m,n)^2 + \frac{\partial}{\partial n}\widehat{F_{ext}}(m,n)^2\right) = 0 \quad (29)$$

Solving through iteration with a steady-state value we have

$$\widehat{u_{i+1}} = \hat{u}_i + \mu\nabla^2\hat{u}_i - \left(\hat{u}_i - \frac{\partial}{\partial m}\widehat{F_{ext}}\right)\left(\frac{\partial}{\partial m}\hat{F}_{ext}(m,n)^2 + \frac{\partial}{\partial n}\hat{F}_{ext}(m,n)^2\right) \quad (30)$$

$$\widehat{v_{i+1}} = \hat{v}_i + \mu\nabla^2\hat{v}_i - \left(\hat{v}_i - \frac{\partial}{\partial n}\widehat{F_{ext}}\right)\left(\frac{\partial}{\partial m}\hat{F}_{ext}(m,n)^2 + \frac{\partial}{\partial n}\hat{F}_{ext}(m,n)^2\right) \quad (31)$$

This result can be substituted with the default external force.

$$F_{ex}^* = \hat{F}_{GVF}$$

5.3 Pseudocode

Below is a sample pseudocode that demonstrates how to perform a Top Hat Transformation on an image by utilizing the opening morphological operation.

5.3.1 PSO optimized CLAHE

1. ***Input:*** Original image
2. ***Preprocessing:***
- Convert the image to grayscale (if not already).
- Normalize the pixel intensity values.

3. ***Apply Optimal CLAHE:***
- Use the global best parameters ($gBest$) to apply CLAHE on the original image.

4. ***Initialize PSO Parameters:***
- Number of particles (N)

- Maximum iterations (Max_Iter)
- Inertia weight (w), cognitive coefficient (c_1), social coefficient (c_2)
- Randomly initialize the position and velocity of each particle.
- Define the search space for CLAHE parameters:
  - Clip Limit (CL): $[CL\_min, CL\_max]$
  - Grid Size (GS): $[GS\_min, GS\_max]$

5. ***Define Fitness Function:***
- Apply CLAHE with the particle's parameters (CL, GS).
- Compute the fitness score based on image quality metrics, such as:
  - Entropy
  - Peak Signal-to-Noise Ratio (PSNR)
  - Structural Similarity Index (SSIM)

6. ***Optimization Loop:***
- For each iteration (t = 1 to Max_Iter):
  - For each particle:
    a. Evaluate the fitness of the particle using the fitness function.
    b. Update the particle's personal best position ($pBest$) if the fitness improves.
  - Update the global best position ($gBest$) based on all particles' $pBest$.
  - Update particle velocity and position using the PSO equations:
    - Velocity: $v[i] = w * v[i] + c1 * rand(\ \ ) * (pBest[i] - position[i]) + c2\ * rand() * (gBest - position[i])$
    - Position: $position[i] = position[i] + v[i]$
  - Ensure the particle's position stays within the parameter bounds.

7. ***Output:***
- Enhanced image.
- Optimal CLAHE parameters (CL and GS).

5.3.2 Active Contour Model for Vessel Segmentation

Input: Image I, Initial contour C_0, Smoothing parameter μ, Number of iterations N

Output: Final contour C

Begin

1. Initialize the starting contour of the snake C_0.
2. For each iteration i from 1 to N:
   a. Compute internal forces:
      - Curvature force (based on second derivatives of the contour)
      - Elastic force (based on first derivatives of the contour)
   b. Compute external forces (based on the image gradient or desired edges):
      - Image gradient or edge information (e.g., from a gradient map or energy function)
   c. Combine internal and external forces to compute the new contour:
      - Update contour points by minimizing the energy function:
        $C_{new} = C_{old} + (Force_{internal} + Force_{external})$
   d. Apply smoothing term μ to adjust the contour's smoothness (optional)
   e. If the change in contour position is below a threshold, exit the loop early
1. Return the final contour C

End

6 Result

The performance of the proposed method for vessel segmentation was evaluated on the DRIVE dataset. The results demonstrate the effectiveness of the PSO-optimized CLAHE for image enhancement and the active contour model for accurate vessel segmentation. To enhance vessel visibility and contrast, PSO-optimized CLAHE was applied. Particle Swarm Optimization was used to determine the optimal parameters for the CLAHE algorithm. The resulting enhanced images showed

a significant improvement in contrast and clarity of features, as demonstrated by several quantitative metrics: MSE decreased from 249.5186 in the original image to 208.4254 in the enhanced image, indicating better information content; the Peak Signal-to-Noise Ratio (PSNR) rose from 11.59 dB to 15.6130 dB, highlighting reduced noise and improved image quality; and the Structural Similarity Index (SSIM) improved from 0.6218 to 0.8516, reflecting a closer alignment to the ideal image. Table 2 compares the quality measures of images enhanced using CLAHE versus PSO-optimized CLAHE.

Table 1: Quality measures of PSO-CLAHE and CLAHE

Image	MSE $(Pixel^2)$		PSNR(dB)		SSIM	
	CLAHE	PSO-CLAHE	CLAHE	PSO-CLAHE	CLAHE	PSO-CLAHE
01_test	206.8080	176.7352	12.1448	14.6792	0.6846	0.8830
02_test	202.9524	159.3982	11.8737	15.3431	0.5246	0.8476
03_test	225.6509	210.3323	8.1633	11.6705	0.7063	0.9223
04_test	295.7462	237.3071	13.7519	17.4351	0.6456	0.8469
05_test	316.4354	258.3542	12.0519	18.9327	0.5480	0.7582

In the preceding section, wavelet terms were applied for energy minimization. However, thin vessels can sometimes be removed when their orientations differ from those of the wavelet terms. Additionally, non-vessel structures, such as pathological regions, can exhibit high intensity. In such scenarios, edges have struggled to accurately detect the active contour, often resulting in misclassifying pathological regions as vessels. For example, as shown in Fig. 6, this issue is demonstrated in a portion of an image containing signs of pathology. Here, edges are not detected effectively by the active contour, leading to the misinterpretation of pathological regions as vessels. The ability of the active contour to update the evolution function in subsequent iterations can be further hindered by high-intensity regions. Edge detection errors are often caused by factors such as the presence of pathology, intensity variations within the image, or inconsistencies in the level set function that arise during the evolution process, potentially destabilizing it.

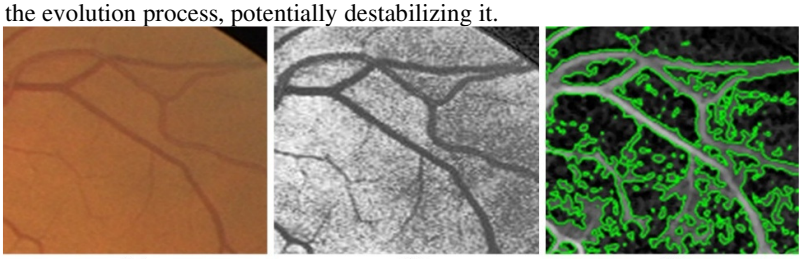

(a) (b) (c)

Fig. 6: Image part from DRIVE dataset (a) the input image, (b) image with applied enhancement, (c) active contour result after 100 iterations.

Therefore, a solution for modification called 'reinitialize' is used, but it is difficult to implement. 'Reinitialize' is not available in the active contour. A performance enhancement framework is used to prevent the evolutionary equilibrium from being destroyed, which strives to maintain the outline along the borders of the image. An equation for modifying the evolution function is developed by the proposed algorithm as shown below:

$$E_{optimal}(x,y) = \alpha_1 E_n(x,y) + \alpha_2 I_{Hessian}(x,y) E_n(x,y) + \alpha_3 I_{match}(x,y) E_n(x,y)$$

Where $\alpha_1 > 0, \alpha_2 > 0, and\ \alpha_3 > 0$ are the coefficients that regulate the importance of each term. $E_n(x,y)$ can be achieved from the following equation.

$$E_n(x,y) = E_{n-1}(x,y) + \Delta t.F(\phi,x,y)$$

Where $F(\phi,x,y)$is the potential operator, Δt is the time phase, and n is the iteration frequency. E_0 is the initial curve and its obtained as $E_0(x,y) = \phi_0(x,y)\phi(0,x,y)$. $I_{Hessian}$ and I_{match} in equation 6 are Binary representations derived from the Hessian matrix [24] and matched filter [25], respectively. A matched filter is considered a framework for vessels. It is typified by a second-dimensional Gaussian filter and is merged with the main picture. The convolution matrix is utilized in various iterations. The kernel completes twelve rotations in 15° stages and adapts to differently oriented vessels. The peak performance of the filter is determined per pixel, and a boundary criterion is next utilized to supply a binary vessel structure. In [24], a vessel enhancement filter utilizing the Hessian matrix components is discussed. The Hessian is a square array that holds the second-order partial derivatives. These frameworks can be molded by the intricacies of the image and three-second derivatives $Gaussian_x x$, $Gaussian_y y$, $Gaussian_x y$ as $H(f) = \begin{bmatrix} f_{xx} & f_{xy} \\ f_{xy} & f_{yy} \end{bmatrix}$. Eigenvalues γ_1 and γ_2 are measured as $\gamma_1 = 1/2\left(f_{xx} + f_{yy} + temp\right)$ and $\gamma_2 = 1/2\left(f_{xx} + f_{yy} - temp\right)$. The $temp$ function is achieved as $temp = \sqrt{\left(\left(f_{xx} - f_{yy}\right)^2 + 4f_{xy}^2\right)}$. The hessian filter is measured as:

$$Hessian = \begin{cases} 0 & if\ \gamma_2 > 0 \\ exp\left(-\frac{R_\beta^2}{2\beta^2}\right)\left(1 - exp\left(-\frac{s}{2c^2}\right)\right) & otherwise \end{cases}$$

Where $R_\beta = \frac{\gamma_1}{\gamma_2}$ and $s = \sqrt{\gamma_1^2 + \gamma_2^2}$. The Hessian matrix demonstrates qualities including noise removal, recognition of linear structures, and spot-like appearances.

The final step involves the extraction of the vessel tree. Different strategies for sorting are available. In this approach, basic thresholding with a global threshold criterion obtained from Otsu's method [26] was used. Two classes of pixels are present in the vessel segmentation: the pixel (i, j) is assigned to either the foreground or the background. The optimum threshold separating these classes is calculated by the Otsu algorithm, ensuring that their interclass variance is maximized [26]. The optic discs or bright lesions can increase false positives. Additionally, some thin vessels are fragmented. Therefore, post-processing is required to restore fragmented edges and the eliminate of noise. Morphological operators were used for this work. Noise pixels, which are not part of the vascular network, were eliminated by considering a threshold level based on the number of pixels, with regions having fewer pixels than the threshold being discarded. For linking edges, the bridge morphologies operator was used. The bridge operator ties pixels together that each have two nonzero neighboring pixels. The separation of the vessel of the overall image by using the proposed active contour technique is shown in Fig. 7.

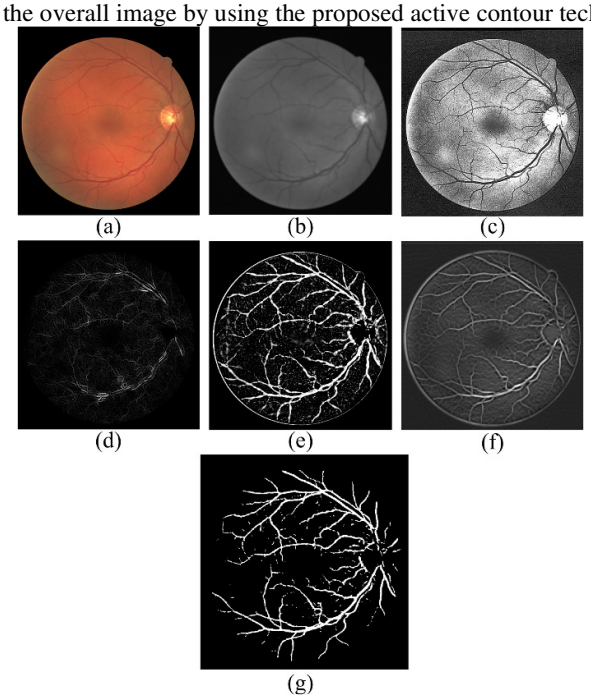

Fig. 7: Active Contour: (a) RGB input, (b) Grey image, (c) PSO-CLAHE enhancement, (d) Vessel's enhancement, (e) Hessian matrix image, (f) Match filtering, and (g) Segmented vessel structure.

Fig. 8 compares the manual and automatic results of the vessel's structure with respective input images. Compared to other pre-existing techniques, this method offers superior accuracy and faster processing time. The proposed automated method for segmenting vessels attains an average accuracy of 98.4% and a sensitivity of 97.6%.

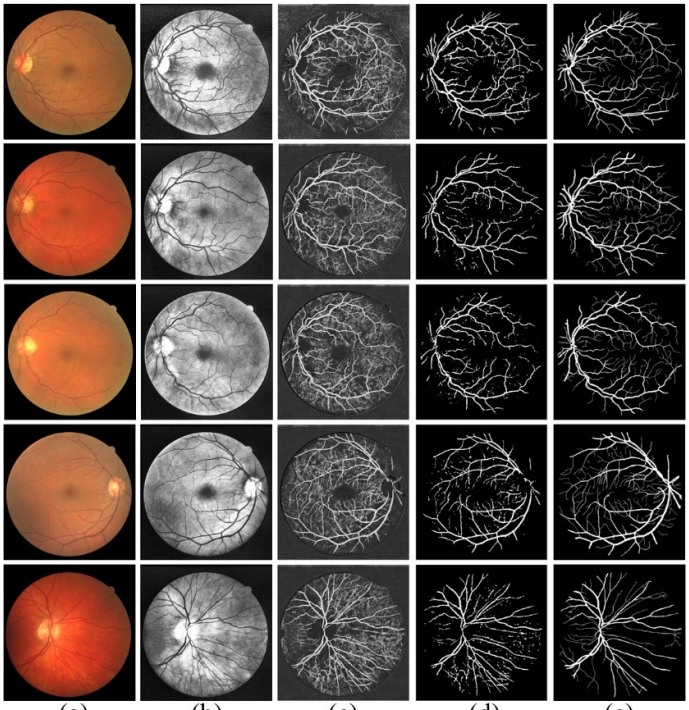

Fig. 8: Result shows the overall vessels segmentation using active contour by PSO-CLAHE: (a) Input RGB fundus image, (b) PSO-CLAHE based Enhancement, (c) Vessels after applying Active Contour function, (d) Active Contour based segmentation, (e) Manual Segmentation.

The performance quality of various classifiers is determined by computing assessment metrics such as accuracy, specificity, and sensitivity, which are obtained using equations (23), (24), and (25).

$$Accuracy = \frac{TP+TN}{TP+TN+FP+FN} \quad (23)$$

$$Specificity = \frac{TN}{TN+FP} \quad (24)$$

$$Sensitivity = \frac{TP}{TP+FN} \quad (25)$$

Where, $TN = True\ Positive,\ TN = True\ Negative, FP = False\ Positive$ and $FN = False\ Negative$.

The evaluation metrics, accuracy, and sensitivity are calculated for various classifiers to assess their qualitative performance. Table 2 presents the results of comparing the recital of the PSO-CLAHE-based Active Contour Model system with previously established methods. The table indicates that our proposed method outperforms the other techniques in retinal vessel segmentation, with a sensitivity ranging from 96.04% to 98.87%. Additionally, our proposed method surpasses the conventional methods in terms of accuracy, achieving an accuracy of 98.82%.

Table 2: The results show the performance analysis of the proposed technique compared to the previously established methods.

Algorithm	Dataset	Samples	Sensitivity (%)	Specificity (%)	Accuracy (%)
Li et al [23]	DRIVE	40	75.69	98.16	95.27
	STARE	20	77.26	98.44	96.28
	CHASEBD1	28	75.07	97.93	95.81
Srinidhi et al. [27]	DRIVE	40	86.44	96.67	95.89
	STARE	20	83.25	97.46	95.02
	CHASEBD1	28	82.97	96.63	94.74
Yan et al. [28]	DRIVE	40	76.31	98.20	95.38
	STARE	20	77.35	98.57	96.38
	CHASEBD1	28	76.40	98.06	96.07
Jin et al. [29]	DRIVE	40	79.63	98.00	95.66
	STARE	20	75.95	98.78	96.41
	CHASEBD1	28	81.55	97.52	96.37

Yuchen Yuan et al. [30]	DRIVE	40	80.46	98.05	95.81
	STARE	20	79.14	98.70	96.65
	CHASEBD1	28	84.02	98.01	96.73
PSO-CLAHE-based Active Contour Model	HRF	45	96.04	97.14	98.63
	DRIVE	40	97.72	98.39	97.35
	CHASEDB1	28	**98.87**	95.20	**98.82**
	STARE	20	98.13	**99.17**	98.09

7 Conclusion

This paper presents an effective approach for retinal vessel segmentation through a combination of PSO-optimized CLAHE-based image enhancement and active contour-based segmentation. The PSO-optimized CLAHE method improves the visibility and contrast of retinal images by automatically determining the optimal parameters, leading to enhanced vessel features and better overall image quality. The results show significant improvements in key image quality metrics, such as entropy, PSNR, and SSIM, when compared to traditional CLAHE techniques.

Following enhancement, the active contour model was employed to segment retinal vessels accurately. The model demonstrated excellent performance in delineating vessel boundaries, even in the presence of noise and thin vessels. Quantitative evaluation using metrics such as the Dice Similarity Coefficient (DSC) and Jaccard Index showed high accuracy in the segmentation process.

Overall, the proposed PSO-CLAHE-based enhancement and active contour-based segmentation framework proved to be a robust and efficient method for retinal vessel segmentation, providing high-quality results suitable for medical image analysis and disease diagnosis. The combined approach is particularly useful in clinical applications, where accurate vessel detection and analysis are crucial for early disease detection and monitoring.

Declaration

Ethical Approval

This paper provides an image processing technique to detect retinal disorders. The experiment was performed by taking some images from the open-source repository which were processed and analyzed. The experimental procedure or results have no direct contact or involvement of humans or animals. Hence, in that respect, there is no objection to giving the consent to publish.

As the results are encouraging, we are trying to integrate the software into some embedded systems in our future endeavors. We are also trying to collaborate with some government and private hospitals for a trial run when we will develop our futuristic model. In that case for future purpose, we will provide ethical clearance. However, the present paper requires no such clearance.

Competing Interest

It is declared that there is no competing interest financially or non-financially that might be perceived to influence the result of the findings

Authors Contribution

The concept was developed by Niladri Halder and Dr. Dibyendu Roy, with the experimental work conducted by Niladri Halder. Guidance and expertise regarding the experiment were provided by Dr. Partha Pratim Sarkar, Dr. Sankar Narayan Patra, and Prof. Subhankar Bandyopadhyay. The paper was authored by Niladri Halder, Dr. Dibyendu Roy, and Dr. Partha Pratim Sarkar, while editing was carried out by Dr. Sankar Narayan Patra and Prof. Subhankar Bandyopadhyay. The contributions from all the authors were integral to the completion of the work.

Funding

Not applicable. There is no Funding source applicable for this work.

Availability of data and materials

Data and materials for the current research if required will be made available.

References:

1. Priyadharsini C. & Jagadeesh Kannan R.: Retinal image enhancement based on color dominance of image. Sci Rep 13, 7172 (2023).

2. Cheng Wan, Xueting Zhou et al.: Retinal Image Enhancement Using Cycle-Constraint Adversarial Network, Front. Med., 12 January 2022.

3. Alwazzan MJ, Ismael MA, Ahmed AN: A Hybrid Algorithm to Enhance Colour Retinal Fundus Images Using a Wiener Filter and CLAHE. J Digit Imaging. 2021 Jun;34(3):750-759.
4. Esra Kaya, İsmail Sarıtaş, Ilker Ali Ozkan: Supervised Segmentation of Retinal Vessel Structures Using ANN, arXiv:2001.05549, 2020.
5. J. Sahoo and P. Sapra: PSO based Medical Image Enhancement for Quality Decisions, 2022 11th International Conference on System Modeling & Advancement in Research Trends (SMART), Moradabad, India, 2022, pp. 1424-1428.
6. Sathananthavathi, V., Indumathi, G.: Particle Swarm Optimization Based Retinal Image Enhancement. Wireless Pers Commun 121, 543–555 (2021).
7. Swarup Kr Ghosh, Biswajit Biswas, Anupam Ghosh: A novel Approach of Retinal Image Enhancement using PSO System and Measure of Fuzziness, Procedia Computer Science, volume 167, 2020, pp. 1300-1311.
8. Qiang Huo: Particle Swarm Optimization for Great Enhancement in Semi-Supervised Retinal Vessel Segmentation with Generative Adversarial Networks, arXiv:1906.07084, 2019.
9. Prakash Kumar Karn, Birendra Biswal, and Subhransu Ranjan Samantaray: Robust retinal blood vessel segmentation using hybrid active contour model, IET Image Processing, Volume 13, Issue 3, 2018.
10. Zhao Y, Rada L, Chen K, Harding SP, Zheng Y.: Automated Vessel Segmentation Using Infinite Perimeter Active Contour Model with Hybrid Region Information with Application to Retinal Images, IEEE Trans Med Imaging, 2015 Sep;34(9):1797-807.
11. Bashir Al-Diri, Andrew Hunter, David Steel: An active contour model for segmenting and measuring retinal vessels, IEEE Trans Med Imaging, 2009 Sep,28(9):1488-97.
12. Zhou C, Gao HB, Gao L: Particle swarm optimization (PSO) algorithm, Appl Res Comput, 20(12), 7-11, (2003).
13. Li L, Li D: Image texture classification based on immune particle swarm optimization, Acta Geodaetica et Cartographica Sinica. 37(2): 185-189, (2008).
14. Li L, Li D: Fuzzy entropy image segmentation based on particle swarm optimization, Progress in Natural Science. 18: 1167-1171, (2008).
15. Marinakis Y, Iordanidou GR, Marinaki M: Particle swarm optimization for the vehicle routing problem with stochastic demands, Applied Soft Computing, 13(4): 1693-1704, (2013).
16. Yitian Zhao, Yalin Zheng, Yonghuai Liu, Yifan Zhao, Lingling Luo, Si-yuan Yang, Tong Na, Yongtian Wang, Jiang Liu: Automatic 2-D/3-D Ves-sel Enhancement in Multiple Modality Images Using a Weighted Symmetry Filter, IEEE Transactions on Medical Imaging, 37, (2018).
17. Yan, Zengqiang and Yang, Xin and Cheng, Kwang-Ting: A three-stage deep learning model for accurate retinal vessel segmentation, IEEE journal of biomedical and health informatics, vol. 23, no. 4, 1427–1436, (2018).
18. “Inspire Datasets”, University of Iowa, Carver College of Medicine, Department of Ophthalmology and Visual Science, available online at https://medicine.uiowa.edu/eye/inspire-datasets.
19. “High-resolution fundus (HRF) image database” available online at https://www5.cs.fau.de/research/data/fundus-images/.
20. “Structured analysis of the retina dataset” is available online at http://www.ces.clemson.edu/~ahoover/stare/.
21. Kass, M., Witkin, A., Terzopoulos, D.: Snakes: active contour models, Int. J. Comput. Vis., 1988, 1, (4), pp. 321–331.
22. Xu, C., Prince, J.L.: Gradient vector flow: a new external force for snakes. Proc., 1997 IEEE Computer Society Conf. Computer Vision and Pattern Recognition, San Juan, Puerto Rico, 1997, pp. 66–71.
23. Q. Li, B. Feng, L. Xie, P. Liang, H. Zhang, and T. Wang: A crossmodality learning approach for vessel segmentation in retinal images, IEEE transactions on medical imaging, vol. 35, no. 1, pp. 109–118, 2015.
24. Modava, M., Akbarizadeh, G.: Coastline extraction from SAR images using spatial fuzzy clustering and the active contour method, Int. J. Remote Sens., 2017, 38, (2), pp. 355–370.
25. Fraz, M.M., Remagnino, P., Hoppe, A., et al.: Blood vessel segmentation methodologies in retinal images – A survey, Comput. Methods Programs Biomed., 2012, 108, (1), pp. 407–433.
26. Modava, M., Akbarizadeh, G.: Coastline extraction from SAR images using spatial fuzzy clustering and the active contour method, Int. J. Remote Sens., 2017, 38, (2), pp. 355–370.
27. C. L. Srinidhi, P. Aparna, and J. Rajan: A visual attention guided unsupervised feature learning for robust vessel delineation in retinal images, Biomedical Signal Processing and Control, vol. 44, pp. 110–126, 2018.
28. Yan, Zengqiang and Yang, Xin and Cheng, Kwang-Ting: A three-stage deep learning model for accurate retinal vessel segmentation, IEEE journal of biomedical and health informatics, vol. 23, no. 4, pp. 1427–1436, 2018.
29. Q. Jin, Z. Meng, T. D. Pham, Q. Chen, L. Wei, and R. Su, Dunet: A deformable network for retinal vessel segmentation, Knowledge-Based Systems, vol. 178, pp. 149–162, 2019.
30. Yuchen Yuan, Lei Zhang, Lituan Wang, and Haiying Huang: Multi-level Attention Network for Retinal Vessel Segmentation, ieee journal of biomedical and health informatics, DOI 10.1109/JBHI.2021.3089201.

Detection of Retinal AVR and CDR Using Active Contours with Blind Deconvolution and CLAHE Fusion (Active-BDCLF)

Niladri Halder[1], Dibyendu Roy[2], Rajib Banerjee[3], Pulakesh Roy[2], Sankar Narayan Patra[1] and Subhankar Bandyopadhyay[1]

[1]Instrumentation & Electronics Engineering, Jadavpur University, West Bengal, India
[2]University Institute of Technology, The University of Burdwan, West Bengal, India
[3]School of Computer Science (SoCS), University of Petroleum and Energy studies (UPES), Dehradun, India

Corresponding Author: **Rajib Banerjee**

Abstract: Various retinal disorders, commonly diabetic and hypertensive retinopathy, can damage the optic nerve, potentially leading to permanent vision loss. Clinical observations often detect these conditions, such as abnormalities in retinal blood vessel diameter and the optic cup-to-disc ratio. High blood pressure can cause retinal vessel thinning and optic cup dilation, disrupting the normal arterio-venous ratio (AVR) and cup-to-disc ratio (CDR). This disruption may result in nerve fiber damage, hemorrhages, and cotton wool spots. This study proposes an automated retinal optic disk and vessel segmentation from pre-processed retinal images. The segmentation was done using a ring mask created by superimposing two circles with the optic disk center and radii of 3D/2 and 1.5D/2, where D denotes the diameter of the optic disk. The maximum AV crossing was avoided within the retinal mask to simplify the process. Validations were performed by comparing the results with a predefined manually segmented dataset, achieving accuracies of 98.6% and 97.8% for retinal optic disk and optic cup, respectively, and 98.73% for retinal vessels. This algorithm could aid ophthalmologists in identifying retinal disorders accurately and automatically.

Keywords: Active Contour, Contrast Limited Adaptive Histogram Equalization, Blind Deconvolution, Region-based classification, Cup Disc Ratio, Artery Vein Ratio

1. Introduction

Glaucoma, considered one of the major reasons for blindness, results in an estimated 12% of total blindness cases and is anticipated to affect almost 11 million people with bilateral blindness. The most common type of glaucoma globally is Primary Open-Angle Glaucoma (POAG), which impacts 74% of individuals diagnosed with the condition. Based on stratified estimates derived from population studies, it is expected that almost

11.2 million people in India, accounting for nearly 4.6% of the people over the age of 40, are affected by glaucoma [4]. Detecting and treating this disease, which can potentially lead to blindness, presents significant challenges since the majority of those affected remain undiagnosed.

Hypertension can narrow the vessels inside the eye, reducing blood flow to the optical nerve and potentially resulting in blindness. Likewise, elevated pressure within the eye in cases of glaucoma can harm the optic nerves and affect vision. Research has suggested that individuals with hypertension may be at an increased likelihood of developing open-angle glaucoma, a group of eye conditions that damage the optic nerve. The possibility of this risk seems to surge among people with severe or poorly managed hypertension over a prolonged period.

Unfortunately, most associated instances do not exhibit symptoms, although they can be detected using retinal Fundus imaging. Appropriate diagnosis and managing the disease in a clinical setting require careful valuation of variations in the optical nerve head (ONH), measurement of intraocular pressure (IOP), and identification of defects in the visual field. Diagnosing typical ONH alterations in the donor's eyes may be more difficult to assess because of the optic disk's pallor and swelling. Additionally, early vascular changes associated with high blood pressure can cause a narrowing of the retinal arterioles, changes at the arteriolar junction, such as arteriovenous nicking, and arteriolar light reflexes.[5]. Additionally, vessel bending is acknowledged as a likely cause of hypertension and coronary disorders [6]. It is crucial to measure heart rate, as studies have demonstrated a strong link to an elevated long-term likelihood of stroke [7]. As such, this effort seeks to develop a way to detect probable cases of glaucoma and hypertension in donor eyes by examining the optic disc cupping ratio and micro vascular ratio.

2. CDR Measurement

Fig. 1 provides an organizational chart of the CDR measurement. In the RGB color model, each color composed of 3 primary additive color elements—red, green, and blue—which are represented by the following intensity function:

$$\mathrm{Img}_{\mathrm{RGB}} = [\mathrm{Fn}_{\mathrm{R}}(x,y), \mathrm{Fn}_{\mathrm{G}}(x,y), \mathrm{Fn}_{\mathrm{B}}(x,y)] \quad (1)$$

Where$\mathrm{Fn}_{\mathrm{R}}(x,y)$, $\mathrm{Fn}_{\mathrm{G}}(x,y)$ and $\mathrm{Fn}_{\mathrm{B}}(x,y)$ represent the intensities of the pixel (x,y) in the red, the green, and the blue channels correspondingly. In the standard RGB color space, these are as follows:

$$\text{red} = \begin{pmatrix}0.64\\0.33\end{pmatrix}, \text{green} = \begin{pmatrix}0.30\\0.60\end{pmatrix}, \text{blue} = \begin{pmatrix}0.15\\0.06\end{pmatrix} \quad (2)$$

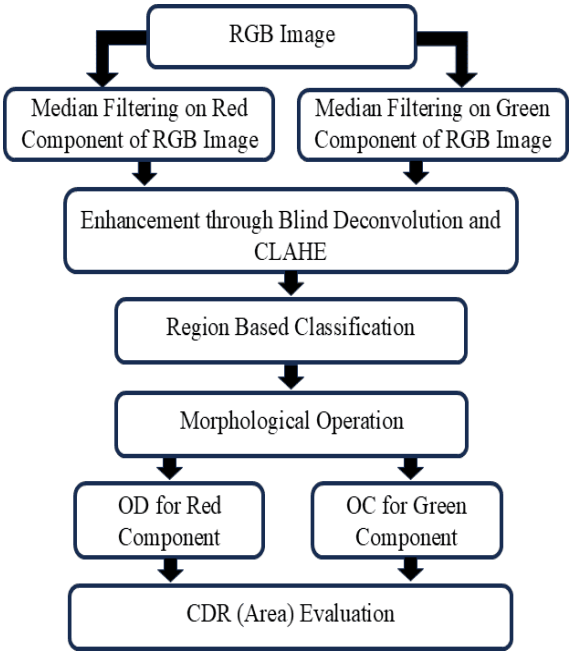

Fig.1: Block diagram explaining the CDR Evaluation

If only brightness information is required, color images may be converted to grayscale images using the proposed transformation equation (3).

$$I_G = 0.333F_R + 0.600F_G + 0.060F_B \quad (3)$$

Here I_G represents the gray equivalent intensity of the RGB image. The red and the green elements of the image Img_{RGB} can be quantified using equation (3). The red and green components of the color image are employed to categorize OD and OC, respectively, as mentioned in Fig. 2.

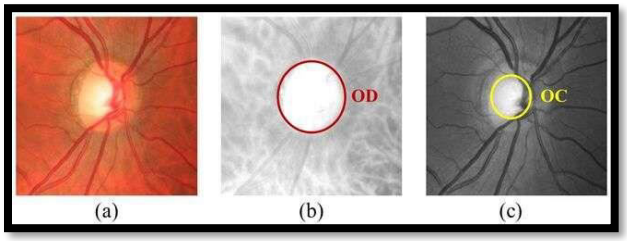

Fig. 2: Random image of HRF dataset represents (a) cropped OD and OC, (b) red channel marking OD, and (c) green channel marking OC.

The advanced technique of CLAHE has been employed to reduce noise through median filtration and enhance the image. Secondly, the use of the regional classification made it possible to detect OD and OC. The operations based on morphology such as dilation, erosion, opening, and closing are used to isolate the OD and OC features.

3. AVR Measurement

The vessel's segmentation and AVR calculation have been made in two steps mentioned in Fig. 3(a) and Fig. 3(b). In the first step, vessels of the overall RGB retinal image have been segmented by fusioning Blind Deconvolution and advanced CLAHE technique followed by Active Contour-based vessel segmentation skills. In the second step, firstly the optic disk (OD) and its average diameter (D) and then the overlapping area between$\pi(3D/2)^2$ and $\pi(1.5D/2)^2$ has been measured.

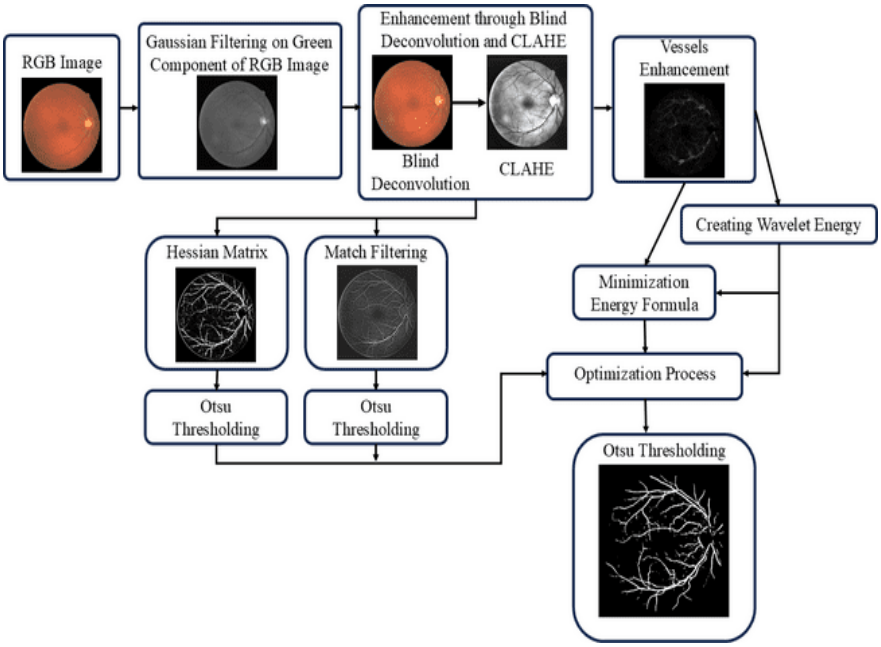

Fig. 3a: Block diagram representing vessels Detection

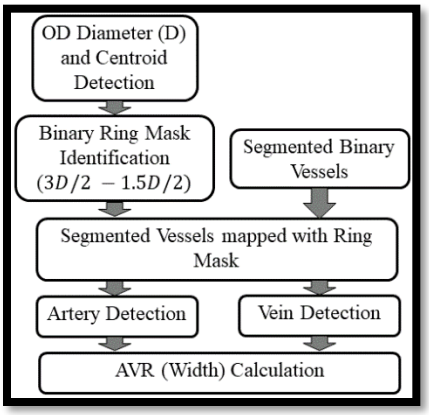

Fig. 3b: Block diagram representing AVR Calculation.

Then the segmented vessels within that masked area have been mapped. The reason behind this mask is that within this range the maximum vessels that are mostly affected by hypertension are found and also complexity is reduced. In the final stage of the second

step, arteries and veins are separated to measure the area of the artery and vein separately. Arteries and veins are identified using the following parameters [8].

- The color of the arteries is brighter than that of the veins.
- Arteries are generally narrower than the adjacent veins.
- The central reflex (luminous reflex from within the vessels) is more pronounced within the blood arteries and less pronounced in the blood veins.
- Blood vessels typically alternate near the optic disc before branching out.

Fig. 4(a) and fig. 4(b) shows the marking arteries and veins and the proposed region of interest. Finally, AVR concerning the area has been calculated. The measured AVR helps the Ophthalmologist to detect the stages of hypertensive retinopathy.

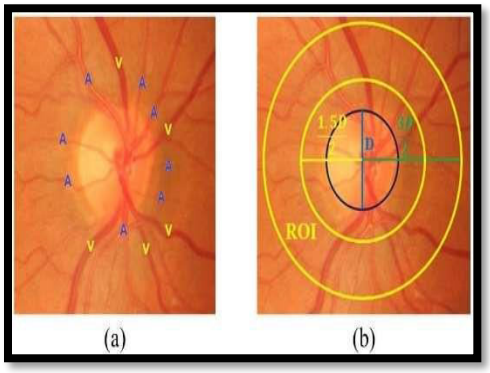

Fig. 4: Random Image cropped from HRF datasets represents (a) marking arteries and veins, and (b) proposed area of interest.

The final step is the validation step where the binary parts of automatic segmented and manual segmented images are considered to identify the true positive and false negative parameters. From here TP, FP, TN, and FN values have been calculated to validate the proposed result set. These steps are depicted in Fig. 5.

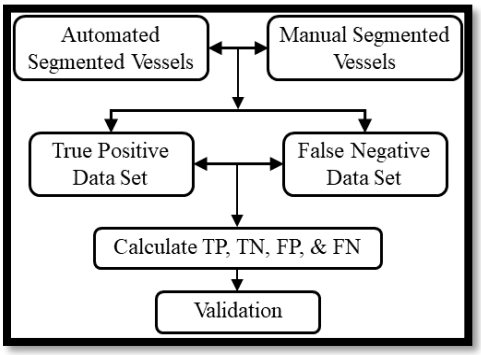

Fig. 5: Functional diagram representing the validation of vessel structure.

Table 1 explains the AVR for normal to accelerated hypertensive retinopathy cases with different risk factors [2] and CDR ranges for normal and affected retina [1].

Table 1: AVR [2]and CDR [1] for different stages of Hypertensive Retinopathy.

Grading of HR	**AVR**	**Indications**	**Systematic Association**	**CDR**
Normal	0.66-0.75 (Approx.)	Normal	Normal	0.00-0.60 (Approx.)
Grade 1 (Mild)	0.5 (Approx.)	Constricted arterioles, arterial and venous nicking, and thickening of the arteriolar wall.	Loosely linked to cardiovascular disorders	>0.60 (Approx.)
Grade 2 (Moderate)	0.33 (Approx.)	Hemorrhages, along with both hard and soft exudates.	Heart attacks, strokes, and even deaths from cardiovascular diseases.	>0.60 (Approx.)
Grade 3 (Combined)	0.25 (Approx.)	Hemorrhages, along with both hard and soft exudates.	Heart attacks, strokes, and even deaths from cardiovascular diseases.	>0.60 (Approx.)
Grade 4 (Accelerated HR)	Fine Cords <0.2 (Approx.)	Swelling of the optic disc and loss of vision.	Kidney failure and death	>0.60 (Approx.)

4. Literature Review:

The retinal vessels are essential for carrying blood from the heart to the retina, and evaluating their caliber can offer valuable information in identifying diseases like hypertension, diabetes, and stroke at an early stage. The AVR and CDR are two frequently used metrics for assessing retinal vessels. This literature review will explore the different techniques employed for calculating AVR and CDR.

The CDR serves as a metric for evaluating the severity of glaucoma by measuring the proportion of the perpendicular depth of the cup relative to that of the optic disc. A greater CDR value is suggestive of a larger optic cup, which has been linked to a heightened risk of glaucoma. Ophthalmologists or optometrists usually calculate the CDR

during a comprehensive eye examination using a specialized device known as a fundus camera to take images of the optic disc. The images are subsequently analyzed to measure the perpendicular dimensions of the ocular cup and the optic nerve head. Some recent studies related to CDR measurement have been mentioned below.

The authors of a study, Al Shalchi, et al. [44], introduced a Grasshopper optimization algorithm as an automated approach for identifying the optic nerve head in retinal images The algorithm is inspired by the social behavior of grasshoppers and is known as the intelligent Grasshopper algorithm. The results highlight the algorithm's exceptional capability and accuracy in detecting the optic disc.

In their study, Buket Toptas and colleagues (Toptas et al., [45]) recommended a method for recognizing the optical disc in retinal fundus images. They accomplished this by applying an optimized color space to the images, which involved converting them from RGB to an innovative color model by applying an artificial bee colony system. The results indicated that in this newly defined color space; the optic disc was more distinctly localized compared to the original RGB color space.

The objective of Mahum R. and colleagues in their study [46] was to utilize deep learning-based feature extraction to detect early-stage glaucoma. They used retinal scan images for training and validation of their proposed model. The first step involved pre-processing the images, followed by segmenting and selecting the focused region. Next, the hybrid feature descriptors were used to extract the features of the optic disc (OD) from images that include the optical cup region.

A new technique for detecting glaucoma called Densenet-77-based Mask-RCNN has been introduced by Nazir T. and colleagues in their study [47]. To address the challenges associated with glaucoma detection, they initially applied data augmentation and added blurriness to samples to increase data diversity. Ground-truth (GT) images were then used to generate annotations, and The Densenet-77 framework was leveraged for feature extraction at the Mask-RCNN stage to calculate deep key features. Finally, the customized Mask-RCNN model used the calculated structures to identify and segment the OD and OC.

An improved version of the Harris corner location algorithm was suggested by Deng L., et al. [48]. The proposed algorithm takes into account the thick vessels and prominent gray variations in the retinal photograph, with the optic disc area containing the highest number of corners. The main approach includes extracting the region of interest using a matching filter, followed by vascular detection, image optimization, and additional methods. The Harris corner detection algorithm is subsequently enhanced using similarity to identify the corner of the region of interest.

Vascular segmentation is a key component of medical image analysis that has been extensively researched in academic work. This document offers a concise review of some commonly employed methods to segment the retinal vessel's structure.

In their study, Rehman A. et al. [49] propose a trained method for extracting retinal blood vessels. The algorithm comprises two refinement stages that perform filtering and relative histogram analysis following image refinement and quality improvement. Data attributes, including vessel monitoring, peak curvature, and wavelet coefficients, are subsequently retrieved for each pixel. These attributes are then separated through a support vector machine and the k-nearest neighbors'.

In their study, Arsalan M and colleagues [50] present two innovative shallow deep learning models, referred to as DSF-Net and DSA-Net that can effectively identify retinal vasculature. The authors utilize semantic segmentation to analyze raw color fundus images and screen for diabetic and hypertensive retinopathies with high precision.

In their work, Pal M and colleagues [51] suggest an automated technique for segmenting the retinal vasculature. This technique utilizes a Gabor filter bank that has been optimized using a lattice search across the entire constraint space. Additionally, the author employed a novel strip-wise classification method and also incorporated Tophat attributes and ridge data, based on the Eigenvalue spectrum of the Hessian matrix, to improve the accuracy of vessel capture, in addition to the optimized Gabor features.

Boudegga H et al. [52] introduce an innovative DL method for retinal vessel structure segmentation in their study. The key innovation of their work lies in the suggestion of a U-shaped deep learning model that uses efficient convolution layers to improve segmentation accuracy while minimizing computational complexity. Additionally, the authors currently use Data preparation and enhancement methods tailored to the characteristics of retinal images and blood vessels, which constitutes their second major contribution.

In their study, Ooi A et al. [53] recommend a way for segmenting vessel structure from retinal images employing interactive methods grounded in Canny edge detection. The pre-processing phase involves removing the green components, CLAHE, and removing the retinal skeleton. Subsequently, the Canny algorithm-based edge recognition techniques is employed.

The literature review highlights the effectiveness and promise of the image-processing methods examined in these studies for measuring significant parameters like the AVR and CDR. However, it is crucial to recognize that there are still specific constraints and opportunities for improvement.

Some retinal image processing techniques are sensitive to image quality factors such as low resolution, noise, uneven illumination, and motion artifacts. In real-world clinical settings, where image quality may vary, these techniques may yield suboptimal results or require pre-processing steps.

Certain retinal image processing techniques may be computationally demanding, requiring substantial computational resources or long processing times. This can limit their practical application in real-time or resource-constrained environments.

Obtaining accurate and comprehensive ground truth annotations for retinal images can be challenging and time-consuming. This limitation can affect the expansion and evaluation of image-processing algorithms, making it difficult to establish their true efficacy.
The processing algorithm lacks compact techniques that can effectively handle multiple target features, such as optic disks, retinal vessels, hemorrhages, and others.

5. Motivation and Contribution

Motivation:

Due to the potential cases of diabetes, glaucoma, and hypertension, examination of the CDR and AVR is an imperative aspect. One possible approach for the early detection of these diseases is retinal image analysis. Retinal image processing is fueled by the desire to improve diagnostic precision and gain valuable knowledge about different eye conditions and diseases. Retinal image analysis focuses on analyzing and obtaining meaningful data derived from retinal scans, such as identifying key features like the optic disc, retinal vessels, and hemorrhages, along with detecting abnormalities and signs of eye diseases. The motivation lies in the enhancement of the early detection, monitoring, and treatment of eye disorders, thereby improving patient outcomes and overall eye health.

Contribution:

The contribution to developing the proposed retinal AVR and CDR detection involves several key aspects.

- The contribution encompasses the utilization of multiple algorithms for tasks such as enhancing, segmenting, extracting features, and classifying to derive significant and valuable information from the retinal images.
- We need to gather a comprehensive and heterogeneous dataset of retinal images to support the development and evaluation of the Active-BDCLF algorithm. Our role is to compile and tag these datasets to verify they comprehensively represent retinal conditions and their variations.
- Lastly, the developed algorithms are refined and enhanced through comprehensive testing, thorough evaluation, and meticulous validation. This includes comparing the algorithms to existing ones, evaluating performance metrics like accuracy, sensitivity, and specificity, and performing Clinical trials to validate their efficacy and dependability in practical settings. The development of algorithms for retinal image

processing involves designing algorithms, curating datasets, fostering interdisciplinary collaboration, and conducting rigorous evaluations, all to enhance the precision and medical relevance of retinal image evaluation.

6. Dataset:

The Active-BDCLF algorithm was estimated by freely accessible datasets like DRIVE, HRF, STARE, CHASEDB1, INSPIRE-AVR, and others to develop a fully automated monitoring system.

The DRIVE dataset was created as part of a diabetic testing campaign in The Netherlands. The trial involved 400 diabetic individuals ranging in age from 25 to 90 years. Out of this collection, 40 images were selected at random: 33 exhibiting no signs of diabetic retinopathy and 7 showing early-stage, mild diabetic retinopathy. These visuals were obtained with a Canon CR5 non-mydriatic 3CCD camera featuring a 45-degree field of view (FOV). Each image was confirmed at a resolution of 768 × 584 pixels, using an 8-bit color model, with a circular field of view covering approximately 540 pixels. The photos were reaped around the FOV, and every photo was accompanied by a 'mask' delineating the FOV.

The collection of 40 images was divided into a training set and a test set, each containing 20 images. The training collection comprises a solitary manual segmentation of the vascular structure. In relation to the test set, two manual delineations are included: one acts as the standard, and the other facilitates a comparison between the computer-generated segmentation and an independent human observer. Each retinal image also comes with a mask defining the region of interest. The human observers responsible for manual segmentations were trained by an experienced ophthalmologist and instructed to label pixels as vessels only if they were at least 70% confident in their assessment.

The INSPIRE-AVR dataset is publicly available and consists of 40 annotated retinal images with significant vascular abnormalities, optic disc region, and artery-vein ratio. It is specifically used for classifying and grading various hypertension-related complications. The annotations were made by two specialists using a hybrid automated tool developed by the University of Wisconsin, Madison, WI, USA [32].

The HRF imaging dataset, created by a collaborative research group, is designed to aid in the formulation of clinical decision-support tools for diagnosing different retinal irregularities. It covers 45 retinal images from participants, with 15 from healthy individuals, 15 from glaucomatous cases, and 15 from diabetic retinopathy (DR) cases [33]. These pictures are recorded at 3504 × 2336 pixels resolution, 24 bits per pixel, utilizing a CANON CF-60 UVI camera with a 60-degree viewing angle.

The STARE dataset comprises approximately 400 images, with 50 images depicting vascular patterns and 80 featuring Reference standards for optic nerve localization [34]. These pictures were taken at a resolution of 605 × 700 pixels with a 24-bit color depth using a TOPCON TRV-50 fundus camera, offering a 35-degree field of view.

7. Methodology:

The Active-BDCLF can measure the CDR and AVR of an ophthalmoscope image. In the beginning, the Active-BDCLF approach utilizes median filtering and Gaussian filtering. Subsequently, the subsections elaborate on the primary contributions, including Blind Deconvolution, CLAHE, and morphological operations.

7.1 Median Filtering:

The median filter is a statistical-based, non-linear approach to signal processing that replaces noisy values in a numerical image or sequence with the median of surrounding values. The outcome of applying the median filter can be determined using equation (4).

$$I_g(x,y) = \text{median}\{I_f(x-i, y-j), i, j \in W_{2d}\} \quad (4)$$

Here $I_f(x,y), I_g(x,y)$is the input and the resulting images accordingly, $W_{2d}$is the 2D mask: the size of the mask is N × N where N is commonly odd such as 3 × 3,5 × 5etc.

The mathematical analysis of a non-linear median filter is comparatively complicated for randomized noise images. For the image where the average noise is zero in a normal distribution, the median filter noise variance is approximate.

$$\sigma_{mid} = \frac{1}{4nf^2(\bar{n})} \approx \frac{\sigma_i^2}{n+\frac{\pi}{2}-1} \cdot \frac{\pi}{2} \quad (5)$$

Where $\sigma_i^2$the power of noise, the variance, is Nis the size of the mask of the filter, $f^2(\bar{n})$ is the function representing noise density. The variance of the filtering can be determined using equation (6).

$$\sigma_0^2 = \frac{1}{n}\sigma_i^2 \quad (6)$$

7.2 Gaussian Filtering:

Gaussian filter, a linear class windowed filter, is typically used for image blurring or noise reduction. The unshaped masking that is the edge can be detected simply by subtracting two filtered results from each other. The Gaussian or normal distribution is a probability

function that is referred to as a bell function due to its shape. The most common function formula is shown in equation (7).

$$G(x,y) = \frac{1}{2\pi\sigma^2} e^{\{-(x^2+y^2)/2\sigma^2\}} = G(x).G(y) \quad (7)$$

Equation (7) explains that the 2D Gaussian filter is separable. To obtain the Gaussian filtering of the 2D image, the following algorithm is employed.

- Measure the weights of the 1D window, denoted as $G_n^{/}$.
- Process each image line as a one-dimensional signal.
- Process each column of the filtered image as a 1D signal.

Two-dimensional filtering with window $[2n+1] \times [2n+1]$ is condensed to a few one-dimensional filters with a window $[2n+1]$. This signifies a substantial acceleration, particularly for large datasets resulting from the reduction in the number of operators, from $O(N^2)$ to $O(N)$.

7.3 Blind Deconvolution

Blind Deconvolution is an approach in image analysis used to improve image quality by fixing image smudges caused by stemming from problems like lens misalignment or imaging system blur. This system assesses both the original image and the blur kernel at the same time, without any previous information about either. Usually, unsupervised Deconvolution modalities operate by repetitively reducing an objective function that calculates the discrepancy between the evaluated deblurred image and the actual blurred image. Unsupervised Deconvolution helps restore images affected by convolution—such as those with motion blur or caused by an image response function—back to their original quality.

The first step in the blind deconvolution algorithm is to estimate the point-spread function (PSF) that causes the visual deterioration. A commonly employed technique for this is the Richardson-Lucy algorithm, which progressively refines the PSF by comparing the degraded image with an estimated version of the restored image. The Richardson-Lucy algorithm is mathematically expressed in equation (8).

$$P_{k+1}(x,y) = P_k(x,y) \frac{\sum_{i,j} \frac{I(x-i,y-j)}{(P_k * I)(x-i,y-j)}}{\sum_{i,j} \frac{P_k(x-i,y-j)}{(P_k * I)(x-i,y-j)}} \quad (8)$$

The appearance includes the projected PSF at repetition k signified asP_k, the tainted image signified as I, and the convolution kernel symbolized by $*$. Primarily, the approach approximations the PSF as P_0 and then constantly upgrades this approximation until merging. The dividend in appearance specifies recovering the degraded image with the

estimated PSF, while the divisor specifies the smearing of the revalidated image by the PSF. The procedure apprises the PSF estimation by conveying pixel proximity weights in the tainted image based on their resemblance to the present PSF estimation.

Hessian Blind Deconvolution is an image rebuilding method that concurrently estimates the point-spread function (PSF) and reinstates the image. Below is a high-level process exactness the Hessian Blind Deconvolution process:

Inputs: degraded image I, regularization parameter λ, maximum number of iterations T.

Outputs: estimated PSF P and restored image R.

1. Set the initial values of P and R by randomly assigning values.
2. For t = 1 to T:
    a. Calculate the gradient and Hessian of the cost function concerning P and R.
    b. To obtain the updates ΔP and ΔR for P and R respectively, solve the linear system $H\Delta X = -\nabla f$.
    c. Update P and R using ΔP and ΔRseparately: $P \leftarrow P + \Delta P$ and $R \leftarrow R + \Delta R$.
3. Return P and R as the estimated PSF and restored image, respectively.

Typically, a mixture of an information fidelity period and a regulation period is used as the cost function f in the above algorithm. The data fidelity term evaluates the degree of resemblance between the estimated image and the observed degraded image. In contrast, the regularization term discourages solutions that lack smoothness or do not meet other desired criteria.

To approximate the point-spread function (PSF) and the restored image simultaneously using the Hessian Blind Deconvolution algorithm, the Hessian matrix is calculated as the 2nd-order derivative of the cost function. Are iterative method, such as conjugate gradient, is then used to resolve the linear system $H\Delta X = -\nabla f$. The regularization parameter λ is used to balance the trade-off between data fidelity and regulation, while the iteration ceiling T sets the number of times the process will run before returning the estimated PSF and restored image. The improvement of the retinal dataset using proposed blind Deconvolution is illustrated in Fig. (6).

7.4 Modified CLAHE

Histogram equalization enhances the contrast ratio by redistributing the brightness levels across the frequency distribution. In this research, CLAHE, with specific adjustments, was applied to strengthen retinal grayscale images. Initially, the contrast of the grayscale image was enhanced using the formula outlined in the equation (9).

$$\mathrm{Im}(x,y) = \frac{\mathrm{fn}(x,y)-\mathrm{fn}(\min)}{\mathrm{fn}(\max)-\mathrm{fn}(\min)} * 2^{\mathrm{bpp}} \quad (9)$$

Here $\mathrm{Im}(x,y)$signifies the input data,$\mathrm{fn}(x,y)$, $\mathrm{fn}(\min)$, and $\mathrm{fn}(\max)$represent the pixel intensity values, and the least and greatest pixel intensities, respectively. The generated contrast-adjusted image is subsequently used as the input for CLAHE. In CLAHE, the source image is divided into non-overlapping contextual areas, or tiles, each with its local histogram. Before determining the total probability distribution, and amplifying contrast intensity, the histogram of each segment is truncated using a user-defined clipping threshold. The clipping threshold corresponds to a multiple of the average histogram peak within the surrounding region, as shown in equation (10).

$$[\mathrm{Hist\_Hight}]_{\mathrm{Avg}} = \frac{[\mathrm{Pixel(total)}]_{\mathrm{contextual}}}{[\mathrm{Pixel(total)}]_{\mathrm{gray}}} \quad (10)$$

For contextual scale say $M \times N$ and Pbe the number of histogram bins, the clip limit is assumed by the equation (11).

$$\mathrm{Clip}_{\mathrm{Limit}} = \begin{cases} 1 & \text{if } \frac{\alpha_{cf} MN}{[P_n]_{\mathrm{hist}}} < 1 \quad \text{for } 0 < \alpha \leq 1 \\ 0 & \text{otherwise} \end{cases} \quad (11)$$

In this situation, α_{cf}does the user define a contextual aspect. The precise elevation of the histogram in the contextual area $n_k$is being trimmed using the $\mathrm{Clip}_{\mathrm{Limit}}$as specified in equation (12) where $[\mathrm{Hist}]_k$is the histogram of the specified area.

$$[\mathrm{Hist}]_k = \begin{cases} \mathrm{Clip}_{\mathrm{Limit}} \text{ if } n_k = \mathrm{Clip}_{\mathrm{Limit}} \text{ for } k = 1,2,\dots,[P_n]_{\mathrm{hist}} - 1 \\ n_k \quad \text{otherwise} \end{cases} \quad (12)$$

Note that,

$$\sum_{k=0}^{[Pn]_{\mathrm{Hist}}-1} n_k = MN \quad (13)$$

Total clipped pixels,

$$\mathrm{Clip}_{\mathrm{total}} = MN - \sum_{k=0}^{[Pn]_{\mathrm{Hist}}-1} [\mathrm{Hist}]_k \quad (14)$$

By adjusting the histogram again, the area beneath the curve is reestablished to its original range, redistributing the clipped pixel values across the histogram. The reordering can be uniform; however, if not, the clipped pixel standards may be unevenly spread across histogram plots for pixel parameters below the clip limit. The pixels assigned to each histogram bin are determined as described in Equation (15).

$$[\mathrm{Pixel}]_{\mu} = \frac{\mathrm{Clip}_{\mathrm{total}}}{[\mathrm{Pn}]_{\mathrm{Hist}}} = \frac{MN - \sum_{k=0}^{[Pn]_{\mathrm{Hist}}-1} [\mathrm{Hist}]_k}{[\mathrm{Pn}]\mathrm{Hist}} \quad (15)$$

The histogram, once clipped, is being re-scaled by applying equation (16).

$$[Hist]_k = \begin{cases} CLip_{Limit} & \text{if} \quad n_k + [Pixel]_\mu \geq Clip_{Limit} \\ n_k + [Pixel]_\mu & \text{otherwise} \end{cases} \tag{17}$$

7.5 Morphological Operations:

Morphological filters are derived from various combinations of two primary operations—dilation and erosion—along with a kernel known as a structural component, a bit mask characterized by precise contour and focal point. The structural component's shape determines the filter's impact on the image. Correspondingly, the retinal input image I, the structural component, SE, and the two elementary operators, erosion and dilation, is considered to be in equations (18) and (19).

$$I \ominus SE = \{x \text{ such that } SE_x \subseteq I\} \tag{18}$$

$$I \oplus SE = \{x \text{ such that } SE_x^s \cap I \neq \Phi\} \tag{19}$$

Where SE_xsignifies the structural componentSE with the standard parameters located in x, while SE_x^ssignifies the symmetric rotation of the structural component located inx.

Multiple merged morphological filters can then be distinctly characterized as a mix of the superior components. The basic complex operators are the 'open' and 'close' operators, marked as the erosion-dilation and dilation-erosion operations, respectively, in Equation (20) and Equation (21).

$$I \circledcirc SE = I \ominus SE \oplus SE \tag{20}$$

$$I \odot SE = I \oplus SE \ominus SE \tag{21}$$

The morphological Top-Hatoperation is very effective for individual point marks with all kinds of backgrounds, but it is less useful for tackling the image removal problem with the localized target, that is severely corrupted by noise. It is therefore necessary to supply an improved morphological Top-Hat filter.

The structural component of the innovative Top-Hat filter is designed as follows: design an internal structural element and an external structural element as$SE_0(m \times m)$, complying $SE_i \subset SE_0$. Define Edge Structuring Element as$SE_{Edge} = SE_0 - SE_i$. Thus, the improved Top-Hat operation can be demarcated as in equation (22).

$$Top\_Hat_{I,SE}(x) = \left[\left\{I - \left(I \Theta SE_{Edge}\right) \oplus SE_i\right\}.x\right] \tag{22}$$

7.6 Modified active contour

This method leverages the joint capabilities of the gradient force snake model and the balloon model to detect blood vessels in fundus images effectively. An image-based contour model is a deformable spline curve guided by an internal force that resists deformation, allowing it to move toward objects in the image [59].This behavior is comparable to the way a snake moves through a hollow space. A snake typically avoids the center of a hollow space, instead moving along the walls and corners, constantly searching for openings. Upon finding a hole, it enters, explores, and retreats if the path is blocked. Similarly, when applied to retinal blood vessels, the snake follows the vessel boundaries, where the vessel walls act as the boundaries and the openings or cracks represent potential entry points.

To ensure the snake adheres to the vessel boundaries without deforming them, its energy must remain lower than the internal energy of the vessels. The Gradient Vector Flow (GVF) technique limits the snake's energy [60]. The total energy function of the snake, calculated at a pointv_q, where $q = 0, \ldots, n-1$ is the addition of its inner energy (E_{int}), image energy (E_{img}), and user-defined constraint force E_{Cns}. This relationship is expressed through the equation (23):

$$E_s^* = \int_0^1 E_s(v_q')dq = \int_0^1 [E_{int}(v_q') + E_{img}(v_q') + E_{cns}(v_q')]dq \qquad (23)$$

7.6.1 Internal energy of snake:

The stored power of the snake is influenced by the fluidity of the curve E_{smth} and continuity of contourE_{con}.

$$E_{int}^{snake} = E_{con} + E_{smth} \qquad (24)$$

Moreover the aforementioned equation can be articulated as in an expanded form as:

$$E_{int}^{snake} = \frac{1}{2}\left(\alpha'(q)|v_q'|^2\right) + \frac{1}{2}\left(\beta'(q)|v_q'|^2\right)$$

$$= \frac{1}{2}\left(\alpha'(q)\left\|\overline{\frac{\partial v'}{\partial q}}(q)\right\|^2 + \beta'(q)\left\|\overline{\frac{\partial^2 v'}{\partial q^2}}(q)\right\|^2\right) \qquad (25)$$

To regulate the sensitivity of the snake's length, user-controlled weights $\alpha'(q)$ and $\beta'(q)$are introduced.

7.6.2 Energy of Image:

Consider an image, Img(m, n), with attributes like boundaries, closures, and lines. The vitality of the image can then be expressed as:

$$\ddot{E}_{img} = W_{line}E_{line} + W_{edge}E_{edge} + W_{cls}E_{cls} \qquad (26)$$

The proportions of attributes such as line, edge, and closure are displayed by $W_{line}, W_{edge}, W_{cls}$ while their corresponding energies are denoted as $E_{line}, E_{edge}, E_{cls}$. The various energies associated with these features are illustrated below.

Line functional: This refers to the intensity of the image, which can be expressed using the following equation:

$$E_{line} = X(m, n) \tag{27}$$

The scale and sign of W_{line} dictate whether the snake gravitates towards dark or light vessels. In this study, a Gaussian filter is employed on the image to shield the snake from being disturbed by inaccessible noisy pixels. After applying the filter, the equation becomes:

$$E_{line} = \text{Gaussian\_Filter}\big(X(m, n)\big) \tag{28}$$

Edge function: This parameter is influenced by the gradient of the image

$$E_{edge} = -|\nabla X(m, n)|^2 \tag{29}$$

A snake preliminary beyond the target item may sometimes congregate to a localized noise artifact or minimum. To tackle this problem, a distorting filter is first used and the level of blurriness is gradually reduced to refine the snake-fitting process.

$$E_{edge} = -\left|\ddot{G}_\sigma \times \nabla X(m, n)\right|^2 \tag{30}$$

The term $\ddot{G}_\sigma$refers to a Gaussian blur whereσ represents the standard deviation (SD). The blurry filter can be useful either in the line or the edge function. Given the Marr–Hildreth philosophy of edge detection, the least values of the function occur at the zero-crossings of $\ddot{G}_\sigma \times \nabla X(m, n)$.

Closure function: To sense the corners and endpoints of the line, the data is blurred using $\ddot{G}_\sigma$. Let $J(m, n)$ represent the image after smoothing.

$$J(m, n) = \ddot{G}_\sigma \times x(m, n) \tag{31}$$

Having gradient angle

$$\hat{\theta} = \arctan\left(\frac{J_n}{J_m}\right) \tag{32}$$

The normalized vector pointing along the gradient is

$$\hat{n} = \left(\cos\hat{\theta}, \sin\hat{\theta}\right) \tag{33}$$

A normalized vector $\hat{n}_\perp$perpendicular to the gradient path

$$\hat{n}_\perp = \left(-\sin\hat{\theta}, \cos\hat{\theta}\right) \tag{34}$$

The strength of the exit function is specified by

$$E_{cls} = \frac{\partial \hat{\theta}}{\partial \hat{n}_{\perp}} = \frac{\partial^2 J / \partial^2 \hat{n}_{\perp}}{\partial J / \partial \hat{n}} = \frac{J_{nn} J_m^2 - 2 J_{mn} J_m J_n + J_{mm} + J_n^2}{(J_m^2 + J_n^2)^{3/2}} \quad (35)$$

7.6.3 Constrain Energy:

The accumulated energy managed by the snake's movement, either towards or away from specific objects features typically specified by the user. Using the two energy formulas debated earlier, the snake's concluding energy equation can be derived from equation (36). To prevent the snake from penetrating the vessels and to ensure it follows the wall, the internal energy must be minimized accordingly. Several optimization techniques can be employed for this, such as the gradient descent method [54], discrete approximation methods, and others.

$$\ddot{E}_{img} = W_{line}.\,\text{Gaussian\_Filter}\big(X(m,n)\big) + W_{edge}\left(-\left|\ddot{G}_{\sigma} \times \nabla X(m,n)\right|^2\right) + W_{cls}\frac{J_{nn} J_m^2 - 2 J_{mn} J_m J_n + J_{mm} + J_n^2}{(J_m^2 + J_n^2)^{3/2}} \quad (36)$$

$$\ddot{E}_{GVF} = \iint \mu\left(\widehat{u_m^2} + \widehat{u_n^2} + \widehat{v_m^2} + \widehat{v_n^2}\right) + \left|\nabla \hat{f}\right|^2 \left|\hat{V} - \nabla \hat{f}\right|^2 \partial m\ \partial n \quad (37)$$

The gradient vector flow method is applied in this work to mitigate the external energy exerted on the vessels, which is related to the snake's internal energy.

This GVF model [60] tackles issues such as:

i. Difficulty in achieving convergence when starting from minimum.
ii. Inadequate fusing at concave limits.

The bi-dimensional energy of the GVF vector field is presented in equation (37), where μ represents the tenable smoothing factor. By applying Euler's method to equation (37), the resulting equations are explained:

$$\mu \nabla^2 \hat{u} - \left(\hat{u} - \frac{\partial}{\partial m}\widehat{F_{ext}}\right)\left(\frac{\partial}{\partial m}\widehat{F_{ext}}(m,n)^2 + \frac{\partial}{\partial n}\widehat{F_{ext}}(m,n)^2\right) = 0 \quad (38)$$

$$\mu \nabla^2 \hat{v} - \left(\hat{v} - \frac{\partial}{\partial n}\widehat{F_{ext}}\right)\left(\frac{\partial}{\partial m}\widehat{F_{ext}}(m,n)^2 + \frac{\partial}{\partial n}\widehat{F_{ext}}(m,n)^2\right) = 0 \quad (39)$$

Solving through iteration with a steady-state value we have

$$\widehat{u_{l+1}} = \hat{u}_l + \mu \nabla^2 \hat{u}_l - \left(\hat{u}_l - \frac{\partial}{\partial m}\widehat{F_{ext}}\right)\left(\frac{\partial}{\partial m}\hat{F}_{ext}(m,n)^2 + \frac{\partial}{\partial n}\hat{F}_{ext}(m,n)^2\right) \quad (40)$$

$$\widehat{v_{l+1}} = \hat{v}_l + \mu \nabla^2 \hat{v}_l - \left(\hat{v}_l - \frac{\partial}{\partial n}\widehat{F_{ext}}\right)\left(\frac{\partial}{\partial m}\hat{F}_{ext}(m,n)^2 + \frac{\partial}{\partial n}\hat{F}_{ext}(m,n)^2\right) \quad (41)$$

This result can be substituted with the default external force.

$$F_{ex}^{*} = \hat{F}_{GVF} \quad (42)$$

7.7 Pseudo code

Below is a sample pseudo code that demonstrates how to perform a Top Hat Transformation on an image by utilizing the opening morphological operation.

1. Algorithm for Blind Deconvoluted CLAHE:

Input: Color retinal image
Output: Colorenhanced image`
Begin

```
blurredImage = imread('blurred_image.jpg');   /* Read the blurred image*/
numIterations = 100; /*Number of iterations for the algorithm*/   /*Set parameters for blind deconvolution*/
lambda = 0.01; /* Regularization parameter*/
psfSize = [15, 15];  /* Size of the point spread function (PSF) */
psfInitial = fspecial('gaussian', psfSize, 2); /* Initial estimate of PSF */
estimatedImage = deconvblind(blurredImage, psfInitial, numIterations, lambda); /* Perform blind deconvolution */
    if size(estimatedImage, 3) == 3  /* Convert estimatedImage to grayscale if needed */
        img = rgb2gray(estimatedImage);
    end
[row, column] = size(img);  /* Calculate the image size */
numBlocksRows = floor(rows / blockSize); /* Divide the image into non-overlapping blocks */
numBlocksCols = floor(cols / blockSize);
enhancedImg = zeros(rows, cols);  /* Initialize the output enhanced image */
/* Loop through each block */
    for i = 1 :numBlocksRows
        for j = 1 :numBlocksCols
            /* Extract the current block */
            block = img((i-1)*blockSize+1:i*blockSize, (j-1)*blockSize+1:j*blockSize);
            equalizedBlock = histeq(block);   /* Perform histogram equalization on the block */
```

```
                /* Clip the block's histogram to the specified limit */
                clippedBlock = min(max(equalizedBlock, 0), limit);
                /* Assign the enhanced block to the corresponding region in the
                output image */
                enhancedImg((i-1)*blockSize+1:i*blockSize,                    (j-
                1)*blockSize+1:j*blockSize) clippedBlock;
            end
        end
        /* Convert the output enhanced image to the original color space if needed */
        If size(estimatedImage, 3) == 3
            enhancedImg = repmat(enhancedImg, [1, 1, 3]);
        end
End
```

2. Algorithm for Morphological operation and TOP-HAT transform

Input: Enhanced gray image
Output: Segmented binary image
Begin

```
Image(input) =Image(enhanced);   /* Scan the input image */
/* Employ morphological transformations to clean noise or smooth out the data.*/
Structuring Element = strel('disk', size);  /* Develop a circular structuring element
with a specified size*/
Image(morph) = imopen(Image_gray, SE);  Execute opening function*/
Image(tophat) = imtophat(Image(morph), SE);  Implement TOP-HAT technique
for image sharpening*/
threshold = graythresh(Image(tophat));  /* Implement thresholding to segment the
target regions in the image*/
Image_binary = imbinarize(Image(tophat), threshold);
/*If applicable, apply additional steps to the binary image to achieve more
precision*/
/* (e.g., block holes, eliminate small objects) */
```

End

3. Algorithm for Active Contour Model for Vessels Segmentation

Input: Image I, Initial contour C_0, Smoothing parameter μ, Number of iterations N
Output: Final contour C
Begin

1. Initialize the starting contour of the snakeC_0.

2. For each iteration i from 1 to N:
    a. Compute internal forces:
        - Curvature force (based on second derivatives of the contour)
        - Elastic force (based on first derivatives of the contour)
    b. Compute external forces (based on the image gradient or desired edges):
        - Image gradient or edge information (e.g., from a gradient map or energy function)
    c. Combine internal and external forces to compute the new contour:
        - Update contour points by minimizing the energy function:
        $C_{new} = C_{old} + (Force_{internal} + Force_{external})$
    d. Apply smoothing term μ to adjust the contour's smoothness (optional)
    e. If the change in contour position is below a threshold, exit the loop early
3. Return the final contour C

End

7. Result

To assess the performance of the Active-BDCLF, a set of 40 fundus retinal images from the DRIVE database was selected. Of these, 33 images are from healthy patients with no clinical disorders, while 7 images are from patients with clinical abnormalities. For all 40 images, the optic cups, optic discs, and vessel structures were segmented, and measurements for the optic cup diameter, optic disc diameter, and vessel width were obtained using the described automatic process. The Cup-Disc Ratio (CDR) and Artery-Vein Ratio (AVR) were then calculated and compared with the manual data. Fig. 6 illustrates the image enhancement achieved using the advanced CLAHE and Blind Deconvolution fusion techniques.

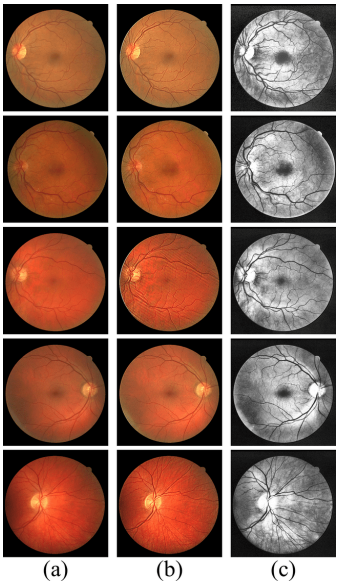

Fig. 6: Result shows the image enhancement techniques using CLAHE and Blind Deconvolution fusion: (a) Input RGB Fundus Image, (b) Enhancement by Blind Deconvolution, and (d) Enhancement by CLAHE after Blind Deconvolution.

Table 2 presents a comparison of the quality measures between images that have been enhanced using CLAHE and the Active-BDCLF techniques. The Active-BDCLF achieves a higher PSNR, indicating superior image quality. Additionally, the proposed technique exhibits a lower MSE than CLAHE, leading to enhanced image fidelity, improved visual quality, and increased accuracy. Furthermore, the higher SSIM measure of the proposed technique compared to CLAHE ensures minimal distortion in the image structure. The results demonstrate that the mentioned technique surpasses CLAHE in terms of image enhancement.

Table 2: Quality measures of PROPOSED and CLAHE

Image	MSE (Pixel^2)		PSNR(dB)		SSIM	
	Active-BDCLF	CLAHE	Active-BDCLF	CLAHE	Active-BDCLF	CLAHE
6(a1)	3151.30	4273.50	15.85	11.82	0.4428	0.3390
6(a2)	5316.20	6322.50	16.63	10.12	0.2760	0.1752
6(a3)	3992.91	5161.00	14.89	11.01	0.3379	0.2365
6(a4)	1953.30	2737.30	17.43	13.75	0.6469	0.5456
6(a5)	3162.4	4058.3	18.93	12.05	0.4582	0.3480

Fig. 7 represents the input RGB fundus images of the macula with segmented results of the optic disk and optic cup using the mentioned morphological techniques.

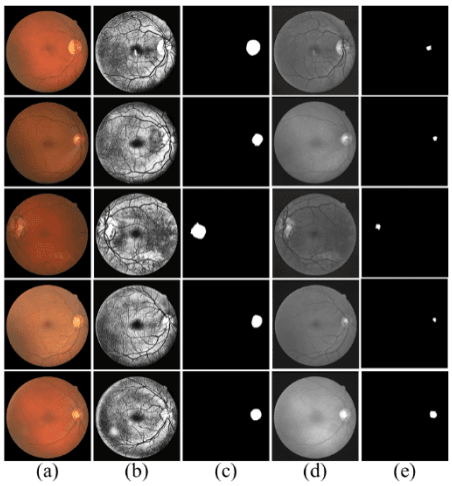

Fig. 7: In this figure, (a) represents the input RGB fundus image, (b), (c), (d) and (e) represent the PROPOSED Enhancement, segmented Optic Disk, green components of the input image, and segmented Optic Cup respectively.

Table 3 provides a comparison between the automatic and manual Cup-to-Disc Ratio (CDR) measurements. The automatic diameter measurements of the Optic Disc (OD) and Optic Cup (OC) in terms of pixels are performed by Active-BDCLF, while the manual diameters are obtained from the specified dataset. The CDR values are computed for both automatic and manual measurements by taking the ratio of their respective areas. The CDR errors are calculated by finding the difference between the manually and automatically determined CDR values.

Table 3: Result shows the comparison of automatic CDR and manual CDR

Sl. No.	Dia_{OD}(Pixel)		Dia_{OC}(Pixel)		CDR (Pixel^2)		$Error_{CDR}$
	Auto	Manual	Auto	Manual	Auto	Manual	
1	230	234	186	190	0.65	0.66	0.01
2	226	224	194	190	0.74	0.72	-0.02
3	218	223	184	186	0.71	0.70	-0.01
4	226	232	178	184	0.62	0.63	0.01
5	228	224	182	178	0.64	0.63	-0.01
6	203	194	179	175	0.78	0.81	0.04
7	216	230	175	178	0.66	0.60	-0.06
8	224	218	184	175	0.67	0.64	-0.03
9	226	225	128	130	0.32	0.33	-0.01
10	224	225	128	125	0.33	0.31	-0.02

The average diameter error for both the optic disc and cup is approximately ±4%. Graphs depicting the correlation between the automatically detected diameter and manually measured diameter for the optic disc and cup can be observed in Fig. 8a and Fig. 8b respectively.

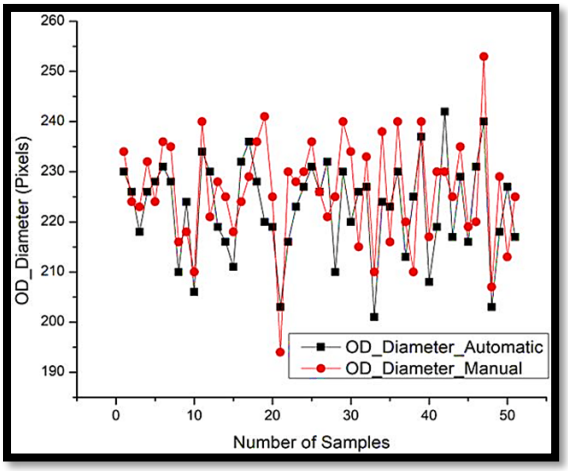

Fig. 8a: This figure represents the comparison of the diameter of the Optic Disk segmented by using manual and automated processes.

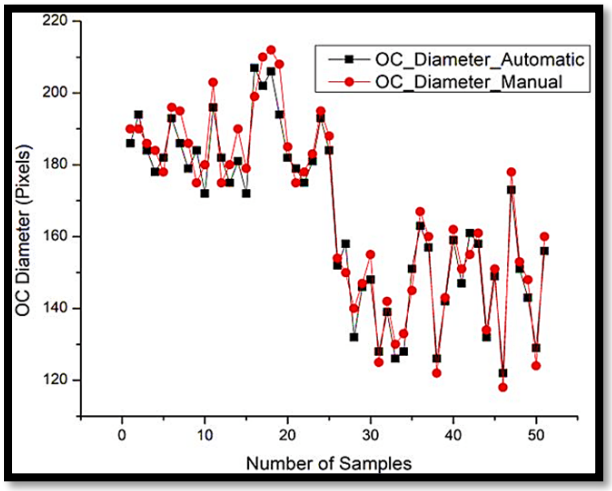

Fig. 8b: This figure represents the comparison of the diameter of the Optic Cup segmented by using manual and automated processes.

The calculation of the CDR, an essential pointer in the detection of glaucoma and hypertension, involves measuring the optic cup and optic disc areas and determining their ratio. Normal patients typically have a CDR below 0.6, while patients with abnormalities tend to have a CDR above 0.6. Fig. 9 depicts the error comparison between the automated CDR and manual CDR, serving as an evaluation of the approach's performance. This figure illustrates the distribution of errors across 50 sample images.

From the results displayed in Fig. 9, it is evident that our Active-BDCLF method achieves a maximum error for the CDR of approximately less than ±4%. Additionally, the average mean error is intended to be almost6.11%, demonstrating the higher accuracy of the CDR measurement. These findings indicate that Active-BDCLF outperforms other methods in this context.

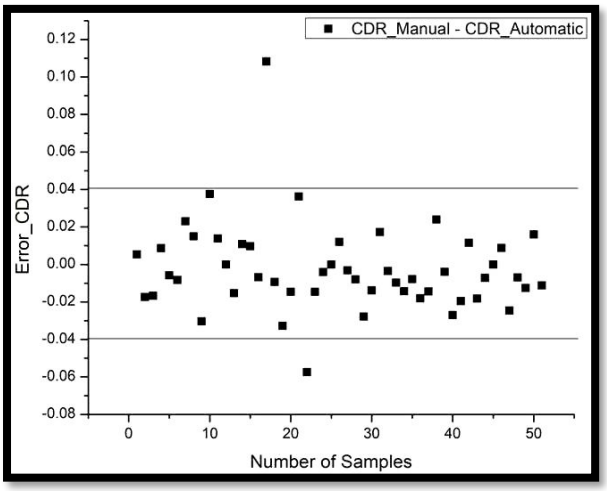

Fig. 9: The result shows the error in the Cup-Disk Ratio calculated automatically and manually.

Figure 10 is offered to gauge the effectiveness of the proposed method. It compares glaucoma detection results from our proposed method with those from the manual method. A CDR value greater than 0.60 is used to identify a patient as a potentially abnormal case. It is found that the Active-BDCLF process has average sensitivity, specificity, and precision are 95.83%, 98.23%, and 96.49%

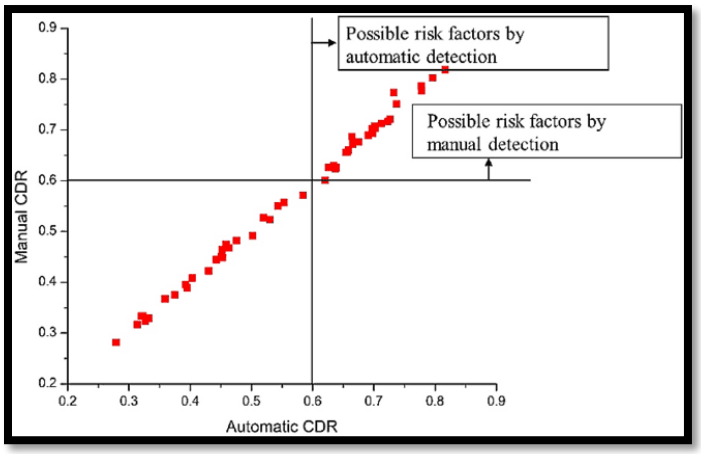

Fig. 10: This figure represents the dataset ranging from normal to possible risk factors [1].

The performance quality of various classifiers is determined by computing assessment metrics such as accuracy, specificity, and sensitivity, which are obtained using equations (23), (24), and (25).

$$\text{Accuracy} = \frac{TP+TN}{TP+TN+FP+FN} \quad (23)$$

$$\text{Specificity} = \frac{TN}{TN+FP} \quad (24)$$

$$\text{Sensitivity} = \frac{TP}{TP+FN} \quad (25)$$

Where, TN = True Positive, TN = True Negative, FP = False Positive and FN = False Negative.

Table 4 presents the computation results for various metrics in the context of optical disc (OD) and optic cup (OC) analysis. Specifically, it covers sensitivity, specificity, overlapping error (OD and OC), balanced accuracy (OD and OC), and absolute error in cup-to-disc ratio (CDR), denoted asA_{OD}, A_{OC}, E_{OD}, E_{OC}, δ_E, respectively. When focusing on OD segmentation, the Active BDCLF method accomplishes a sensitivity of 98.6%, specificity of 99.7%, and accuracy of 98.5%, accompanied by an absolute error of 2.8%. Similarly, for OC segmentation, the Active BDCLF method demonstrates a sensitivity of approximately 97.7%, specificity of 98.7%, accuracy of 96.8%, and a minimum error of 2.8%. These results further establish the superiority of the PROPOSED technique over alternative methods.

Table 4: Statistical results of optic cup and optic disk

Dataset	Sensitivity		Specificity		Accuracy		E_{OD}	E_{OC}	δ_E
	OD	OC	OD	OC	OD	OC			
CHASEDB1	0.962	0.953	0.997	0.983	0.975	0.968	0.103	0.103	0.049
DRIVE	0.968	0.947	0.984	0.972	0.971	0.945	0.087	0.294	0.045
HRF	0.986	0.977	0.984	0.987	0.985	0.962	0.074	0.241	0.028
STARE	0.950	0.932	0.976	0.975	0.953	0.960	0.093	0.285	0.069

In the preceding section, wavelet terms were applied for energy minimization. However, thin vessels can sometimes be removed when their orientations differ from those of the wavelet terms. Additionally, high intensity can be exhibited by non-vessel structures, such as pathological regions. In such scenarios, edges have struggled to be accurately detected by the active contour, often resulting in the misclassification of pathological regions as vessels. For example, as shown in Fig. 11, this issue is demonstrated in a portion of an image containing signs of pathology. Here, edges are not detected effectively by the active contour, leading to the misinterpretation of pathological regions as vessels. The ability of the active contour to update the evolution function in subsequent iterations can be further hindered by high-intensity regions. Edge detection errors are often caused by

factors such as the presence of pathology, intensity variations within the image, or inconsistencies in the level set function that arise during the evolution process, potentially destabilizing it.

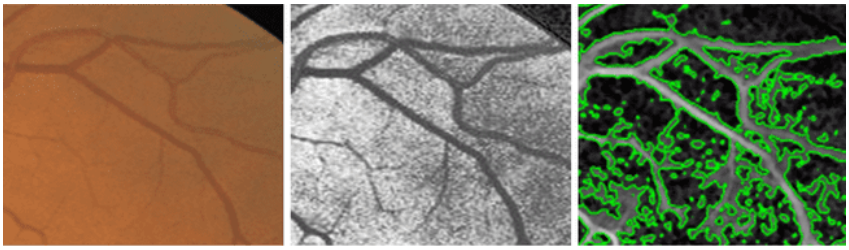

(a) (b) (c)

Fig. 11: Image part from DRIVE dataset (a) the input image, (b) image with applied enhancement, (c) active contour result after 100 iterations.

Therefore, a solution for modification called 'reinitialize' is used, but it is difficult to implement. 'Reinitialize' is not available in the active contour. A performance enhancement framework is used to prevent the evolutionary equilibrium from being destroyed, which strives to maintain the outline along the borders of the image. An equation for modifying the evolution function is developed by the proposed algorithm as shown below:

$$E_{optimal}(x,y) = \alpha_1 E_n(x,y) + \alpha_2 I_{Hessian}(x,y) E_n(x,y) + \alpha_3 I_{match}(x,y) E_n(x,y)$$

Where $\alpha_1 > 0, \alpha_2 > 0,$ and $\alpha_3 > 0$ are the coefficients that regulate the importance of each term. $E_n(x,y)$ can be achieved from the following equation.

$$E_n(x,y) = E_{n-1}(x,y) + \Delta t.\, F(\phi, x, y)$$

Where $F(\phi, x, y)$is the potential operator, Δt is the time phase, and n is the iteration frequency. E_0 is the initial curve and its obtained as $E_0(x,y) = \phi_0(x,y)\phi(0,x,y)$. $I_{Hessian}$ and I_{match} in equation 6 are Binary representations derived from the Hessian matrix [61] and matched filter [62], respectively. A matched filter is considered a framework for vessels. It is typified by a second-dimensional Gaussian filter and is merged with the main picture. The convolution matrix is utilized in various iterations. The kernel completes twelve rotations in 15° stages and adapts to differently oriented vessels. The peak performance of the filter is determined per pixel, and a boundary criterion is next utilized to supply a binary vessel structure. In [61], a vessel enhancement filter utilizing the Hessian matrix components is discussed. The Hessian is a square array that holds the second-order partial derivatives. These frameworks can be molded by the intricacies of the image and three-second derivatives $Gaussian_x x$, $Gaussian_y y$, $Gaussian_x y$ as $H(f) = \begin{bmatrix} f_{xx} & f_{xy} \\ f_{xy} & f_{yy} \end{bmatrix}$. Eigenvalues γ_1 and γ_2 are measured as $\gamma_1 = 1/2\left(f_{xx} + f_{yy} + temp\right)$ and $\gamma_2 = 1/2\left(f_{xx} + f_{yy} - temp\right)$. The temp function is achieved as $temp = \sqrt{\left(\left(f_{xx} - f_{yy}\right)^2 + 4f_{xy}^2\right)}$. The hessian filter is measured as:

$$\text{Hessian} = \begin{cases} 0 & \text{if } \gamma_2 > 0 \\ \exp\left(-\frac{R_\beta^2}{2\beta^2}\right)\left(1 - \exp\left(-\frac{s}{2c^2}\right)\right) & \text{otherwise} \end{cases}$$

Where $R_\beta = \frac{\gamma_1}{\gamma_2}$ and $s = \sqrt{\gamma_1^2 + \gamma_2^2}$. The Hessian matrix demonstrates qualities including noise removal, recognition of linear structures, and spot-like appearances.

The final step involves the extraction of the vessel tree. Different strategies for sorting are available. In this approach, basic thresholding with a global threshold criterion obtained from Otsu's method [63] was used. Two classes of pixels are present in the vessel segmentation: the pixel (i, j) is assigned to either the foreground or the background. The optimum threshold separating these classes is calculated by the Otsu algorithm, ensuring that their interclass variance is maximized [63]. The optic discs or bright lesions can increase false positives. Additionally, some thin vessels are fragmented. Therefore, post processing is required to restore fragmented edges and the eliminate of noise. Morphological operators were used for this work. Noise pixels, which are not part of the vascular network, were eliminated by considering a threshold level based on the number of pixels, with regions having fewer pixels than the threshold being discarded. For linking edges, the bridge morphologies operator was used. The bridge operator ties pixels together that each has two nonzero neighboring pixels. The separation of the vessel of the overall image by using the proposed active contour technique is shown in Fig. 12. Fig. 12 compares the manual and automatic results of the vessel's structure with respective input images. Compared to other pre-existing techniques, this method offers superior accuracy and faster processing time. The proposed automated method for segmenting vessels attains an average accuracy of 98.4% and a sensitivity of 97.6%.

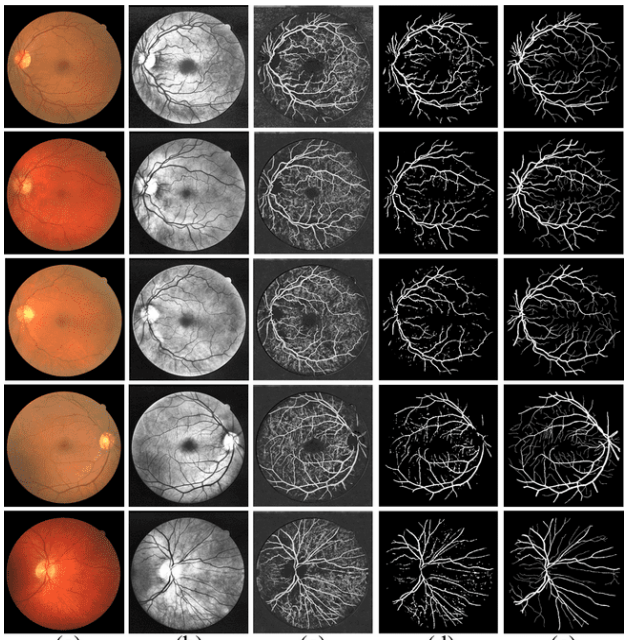

Fig. 12: Result shows the overall vessels segmentation using active contour by fusioning CLAHE and Blind Deconvolution: (a) Input RGB fundus image, (b) CLAHE and Blind Deconvolution fusion-based Enhancement, (c) Vessels after applying Active Contour function, (d) Active Contour based segmentation, (e) Manual Segmentation.

Fig. 13 explains the vessel mapping and artery-vein separation within the mentioned specific ring mask. The ring mask has been chosen for complexity due to the vessel's branching.

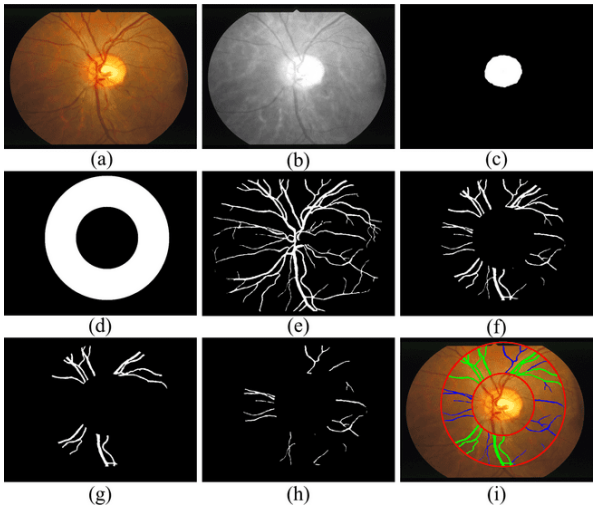

Fig. 13: Result shows the separation of arteries and veins within specified ring mask: (a) The Input RGB Image, (b) Red components of RGB image, (c) Segmented optic disk, (d) (3D-1.5D) mask, (e) Segmented Vessels (f) Segmented vessels within mask, (g) Separated veins, (h) Separated arteries, and (I) Segmented vessel's labeling.

The evaluation metrics, accuracy, and sensitivity are calculated for various classifiers to assess their qualitative performance. Table 5 presents the results of compilation the recital of the Active-BDCLF system with previously established methods. The table indicates that our proposed method outperforms the other techniques in retinal vessel segmentation, with a sensitivity ranging from 96.58% to 98.73%. Additionally, our Active-BDCLF method surpasses the conventional methods in terms of accuracy, achieving an accuracy of 98.56%.

Table 5: The results show the performance analysis of the proposed technique compared to the previously established methods.

Algorithm	Dataset	Samples	Sensitivity (%)	Specificity (%)	Accuracy (%)
Li	DRIVE	40	75.69	98.16	95.27

et al [54]	STARE	20	77.26	98.44	96.28
	CHASEBD1	28	75.07	97.93	95.81
Srinidhi et al. [55]	DRIVE	40	86.44	96.67	95.89
	STARE	20	83.25	97.46	95.02
	CHASEBD1	28	82.97	96.63	94.74
Yan et al. [56]	DRIVE	40	76.31	98.20	95.38
	STARE	20	77.35	98.57	96.38
	CHASEBD1	28	76.40	98.06	96.07
Jin et al. [57]	DRIVE	40	79.63	98.00	95.66
	STARE	20	75.95	**98.78**	96.41
	CHASEBD1	28	81.55	97.52	96.37
Yuchen Yuan et al. [58]	DRIVE	40	80.46	98.05	95.81
	STARE	20	79.14	98.70	96.65
	CHASEBD1	28	84.02	98.01	96.73
Active-BDCLF	HRF	45	**96.58**	97.65	**98.56**
	DRIVE	40	**97.23**	96.69	**97.39**
	CHASEDB1	28	**98.41**	95.31	**98.14**
	STARE	20	**98.73**	96.45	**98.37**

To measure vessel width, the center line and the edges of the first vessels are computed from the segmented binary vessels using thinning and canny edge detection methods. These images are then mapped to locate the vessel width for a pixel position on the specific vessel center line, fig. 14.

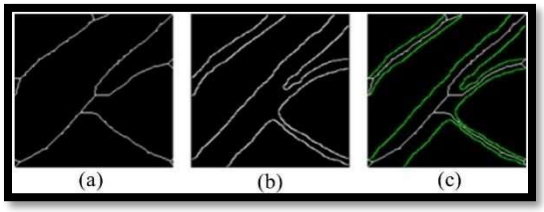

Fig.14: Results representing: (a) vessel's skeleton, (b) vessel's edge, (c) mapping of (a) and (b).

To measure the vessel's width, a pixel from its centerline image is taken into account, subsequently, a mask is applied with the center pixel at its core. This mask aims to identify the edge pixels near the centerline pixel. Every pixel location within the mask is established by advancing the pixel position incrementally until the mask's size is reached and rotating each position from 0° to 180° relative to the center pixel simultaneously. To extend the angle of rotation, the step size is considered to be less than 180° divided by the mask length.

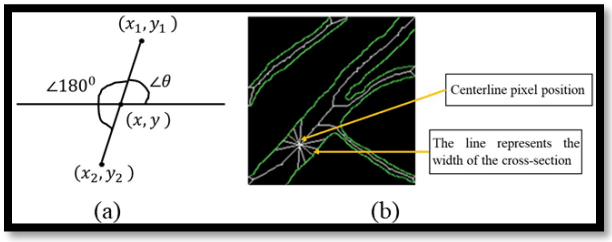

Fig. 15: This figure represents the process (a) finding the edge pixels and (b) the vessel's width or minimum distance of pair pixels.

Edge pixel intensity has been searched for each obtained position to determine whether it is border pixel or not. Once the pixel's boundary is measured, its minor is identified by shifting the angle by 180 degrees and expanding the distance from one to the mask's maximum dimension [fig. 15]. Thus, a rotationally invariant mask is created, and all possible pixel pairings are picked to find the width or diameter of that cross-sectional area.

$x_1 = x + r\cos(\theta)$ (26)

$y_1 = y + r\sin(\theta)$ (27)

Where,(x, y) is the vessel centerline pixel position, $r = 1,2,3,\ldots\ldots,$(mask size/ 2)and $\theta = 0^0,\ldots\ldots\ldots,180^0$. For any pixel position, if the binary parameter in the edge image is 1 then the pixel (x_2, y_2) in the opposite edge has been measured by considering $\theta = 180^0 + \theta$and by varyingr.

After operating, a pair of pixels was discovered on the opposite edge. The minimum Euclidean distance, $\sqrt[2]{(x_1 - x_2)^2 + (y_1 - y_2)^2}$, was calculated from this pair of pixels to determine the width of the vessel's cross-section. Table 5 displays the resulting widths at 20 distinct cross-sections of the vessel as shown in figure 15b.

Measuring the width of the vessel is crucial because it helps determine the AVR, which indicates the severity of the disease based on the condition of the retinal image. Table 6 provides a comparison of vessel widths obtained using the proposed automated technique and manual measurements. Two images from each dataset (HRF and DRIVE) were chosen for analysis.

Table 6: Result of Euclidean Width of 20 cross section of figure (14b).

Cross Sections	Centerline Pixel Position	Width-Line End Point		Vessel's Width (Euclidean Distance)
	(x, y)	(x_1, y_1)	(x_2, y_2)	
1	(17,27)	(13,69)	(20,75)	9.22
2	(45, 48)	(41,42)	(50,53)	14.21
3	(53,42)	(48,37)	(58,46)	13.45
4	(58,38)	(53,33)	(61,43)	12.80
5	(41,166)	(29,155)	(55,177)	34.06
6	(50,157)	(36,147)	(62,170)	34.71
7	(65,142)	(52,128)	(79,152)	36.12
8	(74,131)	(59,119)	(88,143)	37.64
9	(69,125)	(65,114)	(92,137)	35.47
10	(108,80)	(100,75)	(116,87)	20.00
11	(116,70)	(108,63)	(123,78)	21.21
12	(125,63)	(117,55)	(133,70)	21.93
13	(136,52)	(128,45)	(144,60)	21.93
14	(124,95)	(121,92)	(129,98)	10.00
15	(135,88)	(133,85)	(137,90)	6.40

16	(143,80)	(140,76)	(146,84)	10.00
17	(147,77)	(143,74)	(150,82)	10.63
18	(132,153)	(135,150)	(129,156)	8.48
19	(144,161)	(147,158)	(141,163)	7.81
20	(159,170)	(162,168)	(156,173)	7.81

Table 7 presents the automated measurements of retinal vessel width using Active-BDCLF, along with manually collected data. It also illustrates the automatic and manual calculations of AVR, showcasing a marginal average error of less than ±4% as shown in Figure 17. A normal retinal image is characterized by an AVR range exceeding 6.6, whereas a range below this threshold indicates abnormalities related to glaucoma or hypertension [1]. Consequently, the Active-BDCLF technique proposed in this study is capable of effectively assessing retinal data abnormalities, rendering it highly favorable.

Table 7: The outcome presents a comparison between the widths of the vessel acquired through the automated method proposed and those obtained through manual measurements.

Sl. No.	**$Width_{Auton}$**		**$Width_{Manu}$**		**AVR**		**ERROR**
	Artery	**Vein**	**Artery**	**Vein**	**Auto**	**Manual**	
1	11.75	21.40	12.20	23.40	0.549	0.521	-0.027
2	18.02	27.31	17.46	26.57	0.659	0.657	-0.002
3	17.69	38.83	17.85	40.02	0.455	0.446	-0.009
4	14.87	28.28	15.65	31.14	0.525	0.502	-0.023
5	3.16	4.47	6.41	8.94	0.706	0.717	0.010

6	2.76	3.61	2.81	3.60	0.764	0.780	0.016
7	10.50	15.80	9.4	13.60	0.664	0.691	0.026
8	10.63	13.45	10.76	13.41	0.790	0.802	0.012
9	6.83	10.82	5.32	7.81	0.631	0.681	0.050
10	2.03	6.08	2.06	6.32	0.333	0.325	-0.007

Fig. 16 displays the assessment result of automatic and physically calculated AVR and error of the projected technique whereas fig. 17 represents the percentage of error in detection of AVR.

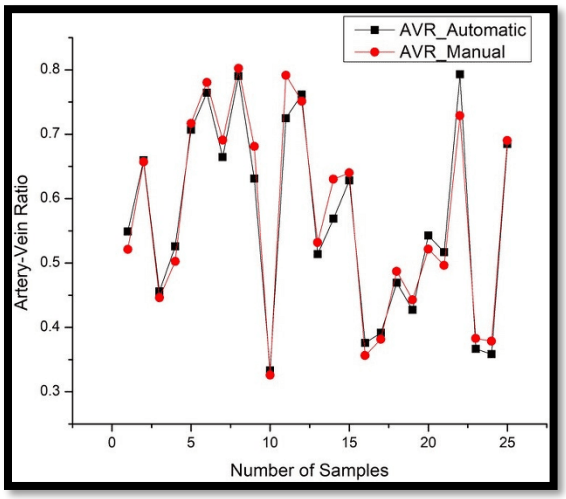

Fig.16: Results shows the comparison of automatic measured AVR with manual AVR.

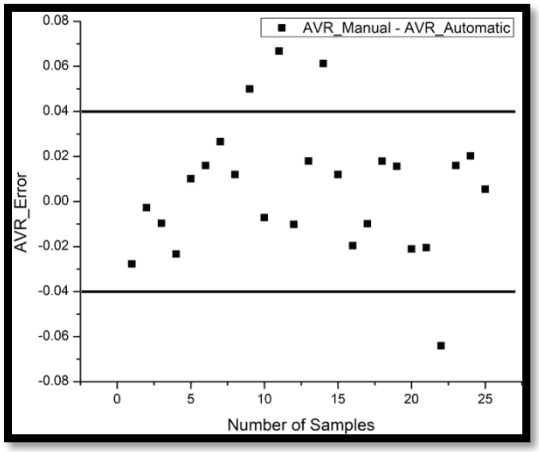

Fig 17: Result shows the percentage of error in the detection of automatic AVR

The presentation evaluation of a binary classifier system was conducted using the receiver operating characteristic (ROC) curve displayed in Fig. 18. This curve portrays the association between the true positive rate (sensitivity) and the false positive rate (1 - specificity) with varying classification thresholds. By visualizing the classifier's performance at various thresholds, the ROC curve enables the assessment of its ability to distinguish between positive and negative instances. Additionally, it facilitates the comparison of different classifiers or models. In this particular ROC curve, the dataset from the drive was utilized to analyze the performance of five distinct techniques, including the proposed Active-BDCLF method. Results indicate that the PROPOSED method outperforms existing techniques in terms of ROC, as evidenced by its faster and more stable curve. A stable ROC curve signifies that the classifier's performance remains consistent and reliable across diverse datasets or conditions, thereby instilling confidence in its generalization capability to new and unseen data. Furthermore, these findings establish the superiority of the proposed Active-BDCLF method over existing approaches.

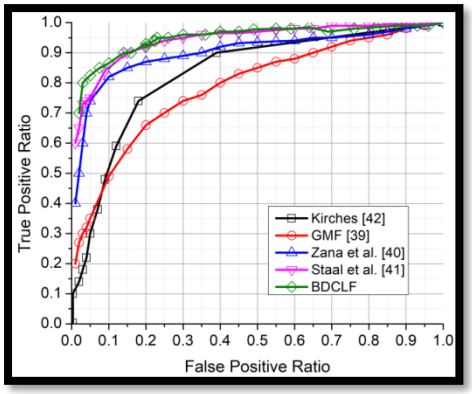

Fig.18: The average ROC plot for 40 DRIVE data is shown using five different methods.

The AVR and CDR values obtained through the Active-BDCLF method, as shown in Table 8, are applied to measure the condition of the patient in terms of diabetes, glaucoma, and overall health. To accomplish this, a selection of retinal images from the HRF dataset, encompassing diabetic, glaucoma, and healthy cases, were randomly chosen. The results obtained were promising, revealing an average CDR of 0.68 for diabetic patients, 0.62 for glaucoma patients, and 0.41 for healthy individuals. Similarly, the average AVR values were found to be 0.52 for diabetics, 0.43 for glaucoma patients, and 0.75 for those without any eye-related conditions.

Table 8: Result shows the AVR and CDR for patient's different health conditions.

HRF Image	Patent's Condition	OD (Avg.)	OC (Avg.)	W_{Artery} (Avg.)	W_{Vein} (Avg)	CDR	AVR
01_dr	Diabetic	372	294	13.15	32.37	0.63	0.41
02_dr		375	306	12.32	22.62	0.67	0.54
03_dr		327	281	14.05	23.18	0.74	0.61
04_dr		336	268	13.19	26.39	0.64	0.50
01_h	Healthy	410	248	17.39	20.81	0.37	0.84
02_h		408	267	16.18	23.41	0.43	0.69
03_h		396	237	17.02	22.11	0.36	0.77
07_h		416	278	17.36	24.79	0.45	0.70
01_g	Glaucoma	338	261	12.27	26.58	0.60	0.46
08_g		367	292	11.43	28.91	0.63	0.39

8. Conclusion:

An automated approach has been proposed to evaluate two specific target features in the human eye, namely CDR and AVR, to detect abnormalities associated with conditions like diabetes, glaucoma, and hypertension. The results obtained so far are promising, demonstrating high levels of accuracy: 98.6% for OD, 97.8% for OC, and 98.55% for AVR, with only minor errors. This technique surpasses other established methods in terms of speed due to its fully automated nature, and it requires minimal expertise for implementation, making it accessible to individuals with any level of medical knowledge. The positive outcomes achieved through this method allow for the measurement of various parameters (such as nicking, narrowing, and branching coefficients), which can assist in diagnosing different diseases.

A series of clinical images acquired from publicly available datasets will be quantitatively evaluated in the next study to find the retinopathy of prematurity (ROP).

References:

- Srinivasan Senthil Kumari, Mohan Neethu, Radhakrishnan Santhi, Subbiah Ramaswami Krishnadas, and Veerappan Muthukkaruppan, Identification of glaucomatous optic nerve head changes in Indian donor eyes without clinical history, Indian Journal of Ophthalmology, vol. 63, no. 7, pp. 600-605 (2015).

- K. Narasimhan, V. C. Neha, K. Vijayarekha, et al., Hypertensive retinopathy diagnosis from fundus images by estimation of AVR, ICMOC – 2012, Elsevier Ltd., pp. 980 – 993 (2012).
- Kingman S., Glaucoma is second leading cause of blindness globally, Bull World Health Organ, vol. 8 pp. 82-887 (2004).
- George R, Ve RS, Vijaya L., Glaucoma in India: Estimated burden of disease, J Glaucoma, vol. 7, pp. 19-391 (2010).
- T. Y. Wong, R. Klein, A. R. Sharrett, et al., Retinal arteriolar diameter and risk for hypertension, Ann. Intern. Med., vol. 140, pp. 248-255 (2004).
- T. Y. Wong, R. Klein, F. J. Nieto, et al., Retinal microvascular abnormalities and 10-year cardiovascular mortality: a population-based case-control study, Ophthalmology, vol. 110, pp. 933-940 (2003).
- T. Y. Wong, R. Klein, et al., Hypertensive retinopathy and risk of stroke, published online in Hypertension (2013).
- Claudia Kondermann, Daniel Kondermann, Michelle Yan, Blood Vessel Classification into Arteries and Veins in Retinal Images, Article in Proceedings of SPIE - The International Society for Optical Engineering, (2007).
- Pooja Chaudhari, Prof. Girish A. Kulkarni, Using Artificial Neural Network to Detect Glaucoma with the Help of Cup to Disk Ratio, International Journal of Advanced Research in Electronics and Communication Engineering, vol. 5, no. 7, pp. 1967-1972 (2016).
- Kurnika Choudhary, ANN Glaucoma Detection using Cup-to-Disk Ratio and Neuroretinal Rim, International Journal of Computer Applications, vol. 111, no. 11, pp. 8-14 (2015).
- Tehmina Khalil, Samina Khalid and Adeel M. Syed, Review of Machine Learning Techniques for Glaucoma Detection and Prediction, Science and Information Conference, London, UK, pp. 27-29 (2014).
- T. Teng, M. Lefley, and D. Claremont, Progress towards automated diabetic ocular screening: A review of image analysis and intelligent systems for diabetic retinopathy, Med. Biol. Eng. Comput., vol. 40, pp. 2–13 (2002).
- R. M. Cesar, Jr, and H. F. Jelinek, Segmentation of retinal fundus vasculature in nonmydriatic camera images using wavelets, in Angiography and Plaque Imaging, Advanced Segmentation Techniques, J. S. Suri and S. Laxminarayan, Eds. Boca Raton, FL: CRC, pp. 193–224 (2003).
- J. Staal, M. D. Abramoff, M. Niemeijer, M. A. Viergever, and B. van Ginneken, Ridge-based vessel segmentation in color images of the retina, IEEE Trans. Med. Imag., vol. 23, no. 4, pp. 501–509 (2004).

- C. Heneghan, J. Flynn, M. O'Keefe, and M. Cahill, Characterization of changes in blood vessel width and tortuosity in retinopathy of prematurity using image analysis, Med. Image Anal., vol. 6, pp. 407–429 (2002).
- A. J. Campilho, A. M. Mendonça, and J. R. Nunes, Image analysis techniques for avascular region detection in retinal angiography, in Proc. ICIAP, pp. 624–628 (1992).
- E. Grisan and A. Ruggeri, A divide and imperial strategy for the automatic classification of retinal vessels into arteries and veins, in Proc. 25th Int. Conf. IEEE Eng. Med. Biol. Soc., pp. 890–893 (2003).
- Y. Hatanaka, H. Fujita, M. Aoyama, H. Uchida, and T. Yamamoto, Automated analysis of the distributions and geometries of blood vessels on retinal fundus images, Proc. SPIE Med. Imag. 2004: Image Process., vol. 5370, pp. 1621–1628 (2004).
- M. Foracchia, E. Grisan, and A. Ruggeri, Extraction and quantitative description of vessel feature hypertensive retinopathy fundus images, in Book Abstracts 2nd Int. Workshop Comput. Asst. Fundus Image Anal., pp. 6 (2001).
- X. Goa, A. Bharath, A. Stanton, A. Hughes, N. Chapman, and S. Thom, A method of vessel tracking for vessel diameter measurement on retinal images, in Proc. ICIP, pp. 881–884 (2001).
- M. E. Martinez-Perez, A. D. Hughes, A. V. Stanton, S. A. Thom, N. Chapman, A. A. Bharath, and K. H. Parker, Retinal vascular tree morphology: A semiautomatic quantification, IEEE Trans. Biomed. Eng., vol. 49, no. 8, pp. 912–917 (2002).
- J. Lowell, A. Hunter, D. Steel, A. Basu, R. Ryder, and R. L. Kennedy, Measurement of retinal vessel widths from fundus images based on 2-D modeling, IEEE Trans. Med. Imag., vol. 23, no. 10, pp. 1196–1204 (2004).
- D. E. Becker, A. Can, J. N. Turner, H. L. Tanenbaum, and B. Roysam, Image processing algorithms for retinal montage, synthesis, mapping, and real-time location determination, IEEE Trans. Biomed. Eng., vol. 45, no. 1, pp. 115–118 (1998).
- H. Shen, B. Roysam, C. V. Stewart, J. N. Turner, and H. L. Tanenbaum, Optimal scheduling of tracing computations for real-time vascular landmark extraction from retinal fundus images, IEEE Trans. Inf. Technol. Biomed., vol. 5, no. 1, pp. 77–91 (2001).
- Subhasis Choudhury, Shankar Chatterjee, Norman Kata,z et al. Detection of blood vessels in retinal images using two dimensional matched filter, IEEE Transactions on Medical Images, vol. 8, No. 3, pp. 264 – 269 (1987).

- James Lowell, Andrew Hunter et al. Measurement of retinal vessels width from fundus images based on 2-D modeling, IEEE Transactions on Medical Imaging, vol. 3, No. 10, pp. 1200 – 1203 (2004).
- Di Wu, Ming Zhang et al. Adaptive detection of blood vessels in retinal images, IEEE Transactions on Biomedical Engineering, vol. 53, No. 2, pp. 341-343 (2006).
- Zhang, Zhuo, Beng Hai Lee, Jiang Liu, Damon Wing Kee Wong, Ngan Meng Tan, Joo Hwee Lim, Fengshou Yin, Weimin Huang, Huiqi Li, and Tien Yin Wong., Optic disc region of interest localization in fundus image for glaucoma detection in ARGALI, In 2010 5th IEEE Conference on Industrial Electronics and Applications, IEEE, pp. 1686-1689 (2010).
- Dehghani, Amin, Hamid Abrishami Moghaddam, and Mohammad- Shahram Moin., Optic disc localization in retinal images using histogram matching, EURASIP Journal on Image and Video Processing 2012, no. 1, pp. 19 (2012).
- Akram, M. Usman, Aftab Khan, Khalid Iqbal, and Wasi Haider Butt., Retinal images: optic disk localization and detection, In International Conference Image Analysis and Recognition, Springer, Berlin, Heidelberg, pp. 40-49 (2010).
- M. Kirubaa, R; Dr. Lavanya R.; Nazneen P Kotwal; Devi Vijayan, change detection in mammogram images using fuzzy C-means clustering, International Journal of Applied Engineering Research 10(11):29825-29834 (2015).
- “Inspire Datasets”, University of Iowa, Carver College of Medicine, Department of Ophthalmology and Visual Science, available online at: medicine.uiowa.edu.
- “High-resolution fundus (HRF) image database” available online at: www5.cs.fau.de
- “Structured analysis of the retina dataset” is available online at www.ces.clemson.edu.
- Saeid F., Sevin Samadi, Parisa Nadirkhanlou, Novel Retinal Vessel Segmentation Based on Local Adaptive Histogram Equalization, 8-th Iranian Conference on Machine Vision and Image Processing (MVIP) IEEE, (2013).
- Yitian Zhao et al., Automatic 2-D/3-D Vessel Enhancement in Multiple Modality Images Using a Weighted Symmetry Filter, IEEE Transactions on Medical Imaging, 37, (2018).
- Ming, L., Qingbo Yin, Mingyu Lu, Retinal Blood Vessel Segmentation Based on Multi-Scale Deep Learning, Proceedings of the Federated Conference on Computer Science and Information Systems, p. 117–123 (2018).

- Zhun, F., Yibiao, R., Jiewei, L., Jiajie, M., Fang, L., Xinye C. and Tiejun, Y, Automated Blood Vessel Segmentation in Fundus Image Based on Integral Channel Features and Random Forests, 12th World Congress on Intelligent Control and Automation (WCICA) (2016).
- S. Chaudhuri, S. Chatterjee, N. Katz, M. Nelson, M. Goldbaum, Detection of blood vessels in retinal images using two dimensional matched filters, IEEE Trans. Med. Imaging, Vol.8(3), pp. 263-269 (1989).
- F. Zana, J.C. Klein, Segmentation of vessel like patterns using mathematical morphology and curvature evaluation, IEEE Trans. Image Processing, Vol. 10(7), pp. 1010-1019 (2001).
- J. Staal, B. Ginneken, M. Niemeijer, A. Viegever, M.D. Abramoff, Ridge based vessel segmentation in color images of the retina, IEEE Trans. Med. Imaging, Vol. 23(4), pp. 501-509 (2004).
- R. Kirsch, Computer determination of the constitute structure of biomedical images, Comput. Biomed. Res. Vol. 4(3), pp. 315-328 (1971).
- Mohammed Al-Rawi, Munib Qutaishat, Mohammed Arrar, An improved matched filter for blood vessel detection of digital retinal images, Computers in Biology and Medicine, Vol. 37, pp. 262-267 (2007).
- Nassrallah Faris, Abdukader Al Shalchi, & Javad Rahebi, Human retinal optic disc detection with grasshopper optimization algorithm, Multimedia Tools and Applications, Springer, volume 81, pages24937–24955 (2022)
- Buket Toptaş, Murat Toptaş & Davut Hanbay, Detection of Optic Disc Localization from Retinal Fundus Image Using Optimized Color Space, Journal of Digital Imaging, Springer, 35, pages302–319 (2022).
- Mahum R Rehman, S Okon, OAlabrah, AMeraj, TRauf H, A novel hybrid approach based on deep cnn to detect glaucoma using fundus imaging, Electronics (Switzerland) (2022).
- Nazir TIrtaza, AStarovoitov V, Optic Disc and Optic Cup Segmentation for Glaucoma Detection from Blur Retinal Images Using Improved Mask-RCNN, International Journal of Optics (2021).
- Deng I, Wang Y Han J, Optical Disc Location Based on Similarity to Improved Harris Algorithm, Chinese Control Conference, CCC (2021) 2021-July 2185-2189
- Rehman AHarouni, MKarimi, MSaba, TBahaj, & S Awan, Microscopic retinal blood vessels detection and segmentation using support vector machine and K-nearest neighbors, Microscopy Research and Technique (2022) 85(5) 1899-1914.

- Arsalan M Haider, A Choi, J Park K, Diabetic and hypertensive retinopathy screening in fundus images using artificially intelligent shallow architectures, Journal of Personalized Medicine (2022) 12(1).
- Pal M, Banerjee M, Retinal vessel segmentation using a strip wise classification approach with grid search-based parameter selection, International Journal of Computational Vision and Robotics (2022) 12(2) 194-218.
- Boudegga, HElloumi, Y Akil, M Hedi, Bedoui, M Kachouri, R Abdallah A, Fast and efficient retinal blood vessel segmentation method based on deep learning network, Computerized Medical Imaging and Graphics (2021) 90.
- Ooi, A Embong, Z Abd, Hamid A Zainon, R Wang, S Ng, T Hamzah, R Teoh, S Ibrahim H, Interactive blood vessel segmentation from retinal fundus image based on canny edge detector, Sensors, MDPI, (2021) 21(19).
- Q. Li, B. Feng, L. Xie, P. Liang, H. Zhang, and T. Wang, A crossmodality learning approach for vessel segmentation in retinal images, IEEE transactions on medical imaging, vol. 35, no. 1, pp. 109–118, 2015.
- C. L. Srinidhi, P. Aparna, and J. Rajan, A visual attention guided unsupervised feature learning for robust vessel delineation in retinal images, Biomedical Signal Processing and Control, vol. 44, pp. 110–126, 2018.
- Yan, Zengqiang and Yang, Xin and Cheng, Kwang-Ting, A three-stage deep learning model for accurate retinal vessel segmentation, IEEE journal of biomedical and health informatics, vol. 23, no. 4, pp. 1427–1436, 2018.
- Q. Jin, Z. Meng, T. D. Pham, Q. Chen, L. Wei, and R. Su, Dunet: A deformable network for retinal vessel segmentation, Knowledge-Based Systems, vol. 178, pp. 149–162, 2019.
- Yuchen Yuan, Lei Zhang, Lituan Wang, and Haiying Huang, Multi-level Attention Network for Retinal Vessel Segmentation, ieee journal of biomedical and health informatics,
- Kass, M., Witkin, A., Terzopoulos, D.: 'Snakes: active contour models', Int. J. Comput. Vis., 1988, 1, (4), pp. 321–331.
- Xu, C., Prince, J.L.: 'Gradient vector flow: a new external force for snakes'. Proc., 1997 IEEE Computer Society Conf. Computer Vision and Pattern Recognition, San Juan, Puerto Rico, 1997, pp. 66–71.
- Modava, M., Akbarizadeh, G.: 'Coastline extraction from SAR images using spatial fuzzy clustering and the active contour method', Int. J. Remote Sens., 2017, 38, (2), pp. 355–370.
- Fraz, M.M., Remagnino, P., Hoppe, A., et al.: 'Blood vessel segmentation methodologies in retinal images – A survey', Comput. Methods Programs Biomed., 2012, 108, (1), pp. 407–433.

- Modava, M., Akbarizadeh, G.: 'Coastline extraction from SAR images using spatial fuzzy clustering and the active contour method', Int. J. Remote Sens., 2017, 38, (2), pp. 355–370.

Nilabdri Halder

Sulchankar Banerjee
07/11/2025

Professor
Dept. of Instrumentation & Electronics Engg
Jadavpur University
Salt Lake, 2nd Campus
Kolkata-700098

Dibyendu Roy
07/11/2025

Assistant Professor
Department of ECE,
University Institute of Technology
The University of Burdwan